EFFECT OF CUPROUS OXIDE PARTICLES ON THE DRAG CHARACTERISTICS OF MARINE COATINGS

Chang Li

Marine, Offshore and Subsea Technology Group, School of Engineering, Newcastle University, United Kingdom

A thesis submitted in partial fulfilment of the requirements for the degree of

Doctor of Philosophy

May, 2019

Abstract

Cu_2O is an active antifouling substance which is commercially produced with different particle sizes before being formulated into antifouling products, and this consequently leads to different surface finish roughness conditions. The further effects of particle size on the drag performance of antifouling coatings and hence on ship hull resistance, as well as biofilm attachment, has not been explored and studied systematically. Accordingly, about the question of how to make an optimised selection of Cu_2O size remains for the ship owners or paint developers.

In this research, a number of different sized Cu_2O ($2\mu m \leq D_{50} \leq 250\mu m$) were applied to Newcastle University's (UNEW) flat test panels. The boundary layer characteristics of the coated surfaces and the uncoated reference surface were measured using two-dimensional Laser Doppler Velocimetry (LDV) in the Emerson Cavitation Tunnel. Pressure drop measurements were carried out using a turbulent flow channel under dynamic flow conditions. The effect of biofilm on the drag characteristics of the Cu_2O surfaces under "in-service" conditions was investigated by mounting the test panels the research vessel, *The Princess Royal*, and examining them every six weeks during a six-month dynamic/static immersion period. The subsequent streamwise pressure drop measurements were conducted on all of the test panels along with uncoated reference panels. In addition, roughness characteristics were analysed by using an optical surface profilometer and the microstructure was studied using Scanning Electron Microscopy (SEM). Based on the roughness function results obtained from the tests, the additional resistance diagrams for full-scale ships were developed according to the Granville similarity scaling law by employing an in-house programme.

The research study has systematically explored the effect of different sized Cu_2O on the drag and roughness characteristics of marine coatings for the first time in the open literature and hence demonstrated the significant potential impact of this effect on ship performance in-service. It was found that the lowest roughness surface was not desmonstrated by the smallest sized particles because of aggregations which caused an unexpectedly rougher surface and higher fricitonal drag. Apart from the aggregated particles, the overall fricitonal drag was found to increase with particle size and this can be expressed by an empirical linear equation. Details of the time-dependent influence of biofilms on the Cu_2O surfaces have been presented. Based on this, the frictional drag changes on different size full-scale ships under similar surface conditions may become more predictable. It was also observed that significant fluctuation occurs on the roughness and frictional drag values for surfaces coated with larger sizes of Cu_2O

particles, e.g. D_{50}=60µm and therefore, similar behaviours are expected for ship surfaces which have similar or rougher characteristics than this particle size. It has to be noted that the test coatings were purely experimental, having exceptionally high Cu_2O contents in the dry film that do not correspond to any commercial antifoulings.

Acknowledgements

Firstly, I would like to express the highest gratitude to my supervisor Prof. Mehmet Atlar for all his guidance and edification. I especially appreciate his willingness to encourage me whenever I was overcautious or indecisive as to my course of action. It has been a great honour to be his student. Not only is he a learned man, but also enthusiastic and dedicated to his field of research. This spirit, which I feel is greatly contagious, has deeply affected me and I hope this is reflected in my work.

I also wish to extend my sincerest thanks to Dr. Colin Anderson, of American Chemet Corporation, for his endless help and continuous encouragement with this work. In addition, I would also like to express my thanks to American Chemet Corporation, USA, for their supporting this study and providing the samples necessary to complete the research.

My appreciation also goes to my supervisory team, Dr. Maryam Haroutunian, Dr. Rose Norman and Prof. Grant Burgess, for their insightful comments and advice throughout this work.

Throughout my studies I have had the good fortune to meet many interesting people, without whom, and the generous support they gave, it would have been impossible to complete this work successfully.

- My colleagues at the Emerson Cavitation Tunnel, particularly Dr Serkan Turkmen for advising me on how to use the turbulent flow channel for the pressure drop tests and helping me to deliver the test panels between Blyth and Newcastle University during the experiments.
- The staff at the Special Collection Library, Marine, Offshore and Subsea Technology Group, School of Engineering, particularly Dr Brian Newman and Mr. Richard Carter. Thank you, not only for providing me with invaluable reference material, but also for looking after me all the time. Further thanks must go to Dr. Brian who helped me to manufacture the immersion box and panel framework which played a significant role in my research. I have to say, that without Dr. Brian's contribution, the biofouling growth deployment would never have gone as smoothly as it did.
- The team at the Royal Northumberland Yacht Club, South Harbour, Blyth, particularly Mr. Peter Gay who generously agreed to let me to carry out biofouling growth deployment work from [one of their] the floating pontoons.

- Dr. Schultz at the US Naval Academy, for his comments and detailed explanations on boundary-layer experiments and pressure drop analysis.
- The team of technicians at Marine, Offshore and Subsea Technology Group, School of Engineering. Especially thank you to Mr. Robert Hindhaugh, Mr. Ian Howard-Row, Mr. Ian Paterson and Mr. Phil Letouze, all of whom responded rapidly whenever I encountered a problem during my experiments and were always able to fix any issue with their expert knowledge and skills.
- My beloved best friends, Dr. Ralitsa Mihaylova, Mr Oliver White and Mrs Arriya Leelachai. Thank you for your friendship, feeling like we are part of a family since the very beginning helped me to get into my new environment smoothly. Your good-tempered nature and your patience whenever I made a mistake have helped me to grow.
- Also, thank you to all my colleagues from office PGR2.66, Armstrong Building, for bringing the atmosphere of joy, friendship and determination.

I must thank my parents, and all other family members for their great support and encouragement. Providing the most solid foundation, my family have helped me to keep generating the energy and courage necessary to eliminate doubt so that I can take each step forward firmly and confidently.

Last but not least, I will say a very special thank you to all the difficulties I have met in the past, as well as to all those I will meet in the future. Thank you to the hard times that have provided me with the opportunity to strengthen myself before each new challenge. Thank you for the sleepless nights which taught me to squeeze my brain for better inspiration. And thank you to the hopeless situation that showed me that if you find one door closed to you, one can always turn-back to look for an alternative path. As they say: No pain, no gain".

Chang Li

1st May 2019

Table of Contents

Lists of Figures

Lists of Tables

Nomenclature

A	Defined as the slope of the logarithmic velocity law equation (or is equal to $1/\kappa$)
B	Smooth wall log-law intercept
B_1	The intercept of logarithmic velocity law. It has to be noted that B is the value of B_1 only for the smooth surface
B_R	The intercept of the rough wall
B_4	Smooth wall log-law intercept based on Thompson's theoretical reasoning, similar to Coles' law of the wake (Coles, 1956), whereby the constants B_4 was empirically determined 2.6
B_2	The velocity-defect factor which does not vary with roughness but does vary with streamwise pressure gradient (Granville, 1987)
C_F	Ship friction coefficient
C_f	Skin friction coefficient
D	Hydraulic Diameter
D_{10}	Particle diameter at 10% in the cumulative distribution.
D_{50}	Particle diameter at 50% in the cumulative distribution.
D_{90}	Particle diameter at 90% in the cumulative distribution
D_Z	The number of zero crossings with the mean line
D_e	Peak Count or defined as the number of peaks per unit length of a profile
H	The shape factor
I_1, I_2, I_3	The evaluation of outer-law integrals. They are constants if the outer law is considered a function of only y/δ right up to the wall ($y = 0$)
L_h	The hydrodynamic entry length
L_c	The cut-off length
P	Pressure
R_a	Arithmetic Average height
Re_D	Reynolds number based on duct hydraulic diameter
Re_δ	The Reynolds number based on the boundary layer thickness
$Re_{\delta 1}$	The Reynolds number based on the displacement thickness
Re_θ	The Reynolds number based on the momentum thickness
R_{ku}	Kurtosis
R_p	The height of roughness profile peaks
R_q	Root Mean Square Roughness height
R_{sk}	Skewness
R_t	Peak to trough roughness height
R_v	The depth of roughness profile valleys
R_z	Ten-point roughness of the roughness profile
S_i	The mean spacing between the i^{th} and $(i+1)^{th}$ profile peak
S_m	Defined as the mean spacing between profile peaks at the mean line, measured over the assessment length.

TI_x	The turbulence intensity in the streamwise direction
TI_y	the turbulence intensity in the wall-normal direction
U	Mean velocity in *x* direction
$\overline{U}$	Bulk mean velocity
U^+	The non-dimensional streamwise velocity, $U^+ = U/u_\tau$
U_e	The freestream fluid velocity outer boundary layer
c_f	Local friction coefficient
f	Fanning Friction Factor
g	Gravity
h, b	Inner dimension size of the channel height and beam
k	Roughness length scale
k^+	The non-dimensional roughness height or roughness Reynolds number
k_1, k_2, k_3	Defined as the geometrical description of the irregular rough wall
k_s	The sand grain size in the Nikuradse (1933) experiment
u_τ	Friction velocity
u'	Streamwise velocity discrete points
$\overline{u'^2}$	Streamwise Reynolds normal stresses
$-\overline{u'v'}$	Reynolds shear stress
$u_{x_{RMS}}$	The root-mean-square of the velocity fluctuations in the streamwise direction
$u_{y_{RMS}}$	The root-mean-square of the velocity fluctuations in the wall-normal direction
v'	Wall-normal velocity discrete points
$\overline{v'^2}$	Wall-normal Reynolds stresses
y^+	The normalized wall distance, $y^+ = yu_\tau/\nu$.
y_i	The roughness height at the i^{th} ordinates
y_j	The roughness height at the j^{th} ordinates
Δ_a	The mean slope of the profile along the roughness assessment length
ΔP	Pressure Drop values
ΔU^+	Roughness Function
Δx	Streamwise Pressure Dropping Distance
Π	The wake parameter
T	Defined as the texture of roughness, $T = \frac{k}{k_1}, \frac{k_1}{k_2}, \frac{k_2}{k_3}$
δ	The thickness of the boundary layer
δ_1, δ^*	The displacement thickness
δ_{x_i}	The sample interval along the roughness assessment length
ε	Wall origin error
η	Defined as non-dimensional boundary layer thickness which can be expressed as $\eta = u_\tau \delta/\nu$
θ	The momentum thickness
κ	Von Karman constant
λ_a	The average wavelength along the roughness assessment length

μ	Dynamic Viscosity
ν	Kinematic Viscosity
ρ	Density
σ	Defined as a convenient local coefficient of skin friction given from the definitions $\sigma = (\tau_w/\rho\overline{U}^2)^{-0.5}$
τ	Shear stress
τ_w	Wall shear stress

Superscript

$+$	Inner variable (normalized with U_τ or U_τ/ν

Subscript

max	Maximum value
min	Minimum value
R	Rough surface
S	Smooth surface

Acronyms and Abbreviations

CDP	Controlled Depletion Polymer
ECT	Emerson Cavitation Tunnel
FR	Foul-Release coating
FTFC	Fully Turbulent Flow Channel
HM	Hama's Method
LDV	Laser Doppler Velocimetry
MC	Modified Clauser method
PDF	Probability Density Functions
SEM	Scanning Electron Microscope
SPC	Self-Polishing Copolymer
TI	Turbulence Intensities
TS	Total Stress method

Chapter 1 Introduction

9.1 Chapter Overview

The research study conducted in this thesis is mainly experimental and is based on the systematically obtained and analysed data of rough surfaces, consisting of Cu_2O particles and including the effects of biofilms. In this chapter, the general perspectives of this experimental study are presented (**Section 1.2**) including the motivations behind the present research. The primary aim and specific objectives of the research study are described (**Section 1.3**) as well as the layout of the thesis (**Section 1.4**), and thus it presents an overall introduction of the thesis.

9.2 Research Motivations

Copper and copper compounds are typically used as biocides in marine antifouling (AF) to prevent the artificial surfaces from becoming fouled by organisms when exposed to seawater. As one of the most commonly used copper-based compounds, Cu_2O can provide an efficient mechanism for keeping surfaces fouling free, and consequently reducing fuel consumption and Greenhouse Gases (GHG) emissions from marine vessels.

Commercially, Cu_2O is manufactured with different particle sizes before being formulated into AF products. Compared with other solid component particles mixed into the antifouling system, Cu_2O has the largest particle size and therefore has a greater influence on the surface roughness. As a consequence, assuming similar antifouling performance, choosing different sized Cu_2O products could result in the roughness of the finished surface being quite different and subsequently lead to larger ship frictional drag differences. It remains unclear for the shipowner or the paint developer what the optimum selection of Cu_2O particle size should be before processing it into an antifouling product. Many papers in the open literature have reported biofouling impacts on ship performance or drag penalties after a certain period when coated with antifouling systems however, it would be helpful to know the time-dependent influence of fouling on these antifouling systems, especially with different surface roughness conditions (McEntee (1916); Visscher, 1928; Denny (1951); Lewthwaite *et al.* (1985); Haslbeck and Bohlander (1992); Holm *et al.* (2004)). In order to standardise surface treatment, practical insight is needed into the surface roughness and drag changes due to the fouling interaction with the physicochemical properties of the antifouling coating.

A comprehensive review of the state-of-the-art, as reported in the open literature, revealed that

there had been no systematic investigation of the impact of different sized Cu_2O particles on the roughness and frictional drag characteristics of Cu_2O based AF surfaces. Moreover, for such Cu_2O surfaces formed with different sized irregular particles, surface roughness and boundary-layer characteristics are still largely unknown. Also, the nature of marine fouling and its diversity can be affected by temperature, water current, light etc. therefore fouling impacts on such Cu_2O surfaces is still unpredictable. Although numerical methods may rely much less on the experimental data, as far as the present research field is concerned, these methods are not well established enough to resolve the research difficulties.

Within the above framework, the motivations for this research study were based on the following points:

- According to the state-of-the-art references (McEntee, 1916; Lewthwaite *et al.*, 1985; Haslbeck and Bohlander, 1992; Holm *et al.*, 2004; Schultz, 2004; Swain *et al.*, 2007; Schultz *et al.*, 2011), the information about the history of copper-based antifouling technologies and their evolutions are scattered. Therefore, it would be helpful to review this information and identify the gaps, to support the aim and objectives of this thesis;

- For copper-based marine antifouling surfaces, the Cu_2O particle contributions to the roughness and drag penalties are largely unknown. Therefore an investigation is needed to determine whether or not there exists a statistical relationship between the surface roughness and frictional drag characteristics and different sized Cu_2O particles of the surface coatings;

- There is a lack of information on rough-wall turbulent boundary layers of antifouling surfaces with irregular roughness, especially for surfaces coated with different sized Cu_2O particles;

- There is insufficient information regarding the impact of time-dependent biofilm development on the roughness and frictional drag of surfaces coated with Cu_2O antifouling. This can be obtained by periodical monitoring and measurements of such surfaces in real-life biofilm conditions.

- It is necessary to study the biofilm impacts on an AF system, especially under the in-service condition. There is a bespoke facility to simulate the real-life condition of biofilms on test surfaces that can be deployed on the Newcastle University (UNEW) research vessel, and

this allows biofilms to develop on the test surfaces while the vessel is in service conditions. At the same time, the roughness of biofilm fouled surfaces can be measured by using the UNEW optical profilometer device while keeping the tested panel immersed in the water;

- Rather than conducting tests with ship models or other alternative methods, the wall-similarity law procedure can be implemented to make more efficient and practical frictional drag estimations for a full-scale ship. Therefore, using this procedure in combination with the laboratory-based test data, the frictional drag changes on different size full-scale ships with newly painted surfaces or fouled by different periods of biofouling could be predicted. This will be very attractive for performance estimation of ships.

9.3 Aim and Objectives

The main aim of this research study is to contribute to the understanding of the effect of different size Cu_2O particles on the roughness and frictional drag characteristics of ship antifouling surfaces, including in the presence of biofilms.

Within the framework of the previously stated research motivations above, the specific objectives of the thesis are as follows:

1. To conduct a state-of-the-art literature survey on copper-based antifouling technology and biofouling effects on ship surface conditions and frictional resistance, and thus to define the research challenges and gaps within the literature;

2. To review and describe the basic concepts of the surface roughness and rough-wall zero pressure boundary layer theory. Also, to define the experimental procedures to determine the frictional drag coefficient and roughness function based on the boundary layer measurements and pressure drop tests;

3. To inspect the microstructure of the coated surfaces and surface fouling organisms by using Scanning Electronic Microscope (SEM) technology, and determine the roughness parameters of tested surfaces in clean and fouled conditions using the optical surface roughness analyser;

4. To obtain the boundary layer parameters of clean Cu_2O applied test surfaces based on velocity profiling measurements using a two-dimensional Laser Doppler Velocimetry (LDV) system. To determine and compare the skin friction coefficients and roughness

function data, using different approaches;

5. To further investigate the effect of the Cu_2O particle size on the frictional drag characteristics of the test surfaces by using a fully turbulent flow channel (FTFC) facility. Accordingly, to obtain and compare the skin frictional coefficients of Cu_2O surfaces by using the pressure drop test data using this facility and subsequently to determine the roughness functions including the biofilm effects which is one of the main benefits of the FTFC;

6. To measure the frictional drag coefficients of the fouled Cu_2O surfaces periodically (eg every 1.5 months) by conducting pressure drop measurements in the FTFC, and hence to explore the time-dependent impact of the biofilm effect;

7. Based on the roughness function data obtained from the tests in the water tunnel and FTFC facilities, develop the additional resistance diagrams to predict the frictional drag increases of ship surfaces coated with different sizes of Cu_2O particles, and also when fouled, by using an in-house programme to be developed based on the similarity scaling law.

9.4 Thesis Layouts

In achieving the above-stated aim and objectives, this research study is presented in nine chapters, summarised as follows:

Chapter 1 presents the general perspectives of the research study, the research motivations together with the aim and objectives of the study.

Chapter 2 provides a literature review to support this research study. The literature is to fulfil **Objective 1,** and hence the chapter starts with a review of biofouling and its impacts on the marine industry. Specifically, since the current study involves biofilm testing, detailed information on biofilm fouling is presented. This is followed by a discussion of all of the possible factors that may directly affect biofilm growth during deployment. A review of copper sheathing and copper-based antifouling technologies is then presented, and this is followed by further reviews of full-scale trials and experimental test results of copper-based antifouling. In complementing the main aim of this research study, a state-of-the-art review is also presented on the hydrodynamic results of surfaces coated with copper-based antifouling, with and without biofilms. Within the context of alternative fouling control systems, the chapter also discusses

non-toxic and other antifouling technologies which may potentially be future alternatives to the current copper-based antifoulings. Apart from fouling, the quality of the finished surfaces could also play a highly important role, and these are also reviewed in this chapter.

Chapter 3 presents a review of the basic methodologies used in this research study. These involve the measurement and analysis of surface roughness characteristics, as well as those of the hydrodynamic characteristics of rough surfaces, by using different experimental facilities and procedures. In order to meet **Objective 2**, the chapter first provides an understanding of surface roughness, along with the characterisation, measurement and analysis of irregularly rough surfaces. This is followed by outlining the fundamental turbulent boundary layer concept for both a flat plate boundary layer and turbulent pipe/channel flow. To complement the boundary layer concept, the boundary layer structure, scaling properties and surface roughness effects on these characteristics are also included. The procedure for the experimental roughness function determination, for both velocity profiling and pipe/channel flow measurements, is then presented. The measurement and calculation techniques of skin friction drag are also reviewed in the same chapter. In addition, due to the use of a range of cuprous oxide particle sizes and testing under different biofilm biofouling conditions in this work, the Granville (1958) similarity-law-based prediction procedure for ship's frictional resistance coefficients is reviewed.

Chapter 4 provides an understanding of the surface roughness along with the characterisation, measurement and analysis of irregularly rough surfaces, including the effect of biofilm on these surfaces. For this purpose, eight different size cuprous oxide particles were selected and applied on the Newcastle University standard size test panels. As for the investigation of the biofilm impact, four specimens were selected and submerged into the sea for biofilm growth in dynamic/static conditions. In order to meet **Objective 3**, this chapter first introduces the optical surface roughness measurement device and its set-up. This is followed by a detailed description of the test surfaces and experiments, including the selection of the cuprous oxide particles, test surface preparation and the instrument for the biofilm cultivation and fouled surfaces. The measurement and analyses of the essential roughness parameters of these surfaces, and the use of Scanning Electronic Microscopy (SEM) as well as the topographies for the clean and fouled surfaces, are described.

Chapter 5 provides an understanding of the relationship of the roughness characteristics with the turbulent boundary layers developing on copper-based antifouling surfaces. In this chapter,

Objective 4 was aimed to be achieved by conducting boundary layer experiments on flat surfaces coated with eight different sized cuprous oxide particles, along with one reference surface. The experimental campaign covered carefully conducted turbulent boundary layer tests on these surfaces fitted to a zero pressure gradient flat test bed in UNEW's Emerson Cavitation Tunnel, and by using a two-dimensional Laser Doppler Velocimetry (LDV) system. This chapter presents descriptions of the experimental facility, test set-up and boundary layer measurement tests as well as the analysis of these measurements. The results of the analysis, including the uncertainties where appropriate, are presented and discussed with regard to the mean velocity profiles, boundary layer parameters, local skin friction drag, roughness functions and Reynolds stresses of the measured surfaces.

Chapter 6 presents the hydrodynamic assessments of the Cu_2O surfaces by using an alternative testing facility, UNEW's fully turbulent flow channel (FTFC), as opposed to the measuring the boundary layer under external fluid conditions. This facility enables a study to be conducted of the drag impacts from copper-based antifouling surfaces under internal fluid conditions, which can be more practical and efficient. Accordingly, the chapter aimed to fulfil **Objective 5** with frictional drag measurements of the freshly applied different Cu_2O surfaces, based on particle size. The detailed specification of the UNEW FTFC facility, experimental set-up, repeatability and tests results are outlined, including the uncertainty of the tests. The frictional drag and roughness function results of all of the tested surfaces are presented and discussed in this chapter.

Chapter 7 repeats the work conducted in Chapter 6, but this time including the presence of biofilm to satisfy **Objective 6**, and thus explores the impact of biofilm on the hydrodynamic characteristics of the selected Cu_2O surfaces. Also, to associate with real-life conditions, these surfaces were deployed on the UNEW research vessel, *The Princess Royal*, to allow the biofilm to develop while the vessel was in service so that the biofilm time-dependent impact on surfaces coated with Cu_2O antifouling could be evaluated periodically. The chapter presents and discusses the results based on the periodic (1.5 monthly) measurements conducted in the UNEW FTFC, including the repeatability and uncertainty of the tests. The impact of the biofilm on the drag and roughness functions of the tested surfaces are discussed, and main conclusions from the work are outlined.

Chapter 8 is aimed to achieve **Objective 7** hence to demonstrate the ultimate effect of different sizes of Cu_2O particles on full-scale ship performance, including with the biofilm effect. For

this purpose, the Granville boundary layer scaling similarity law was used to predict the additional drag for different sizes and ranges of ships by using the experimental data (i.e. frictional drag coefficients and roughness functions) produced in this research study. The results of the findings are presented as practical added resistance, showing the impact of the different sized particles on the powering characteristics of the ships, and including the effect of biofilms.

Chapter 9 starts with an overall review of the research study regarding the contributions made to the state-of-the-art. It then continues with a statement of the main results and conclusions that support the aim and objectives of the research study, and how these objectives were addressed. The chapter finally concludes with the recommendations for future work, which could not be achieved in this study due to scope and time limitations.

9.5 Chapter Summary

This chapter presented the general perspectives of the research study presented in this thesis, the research motivations, the aim and objectives of the research as well as the layout of the thesis chapters.

Chapter 2 Literature review

2.1 Introduction

All artificial marine structures, such as ships, platforms, offshore structure, oil and gas pipelines, wave energy converters, tidal turbines, etc. are vulnerable to fouling organisms. Before looking at the effectiveness of antifouling measures, it is necessary to understand the fouling organisms and their adhesion mechanisms. Antifouling treatment is an effective process of preventing wet surfaces from fouling attachments. Traditionally, the organisms are killed or repelled with coatings using biocides. As one of the typical antifouling biocides, copper and its compounds have been widely applied in prevention marine structures from biofouling for centuries. Moreover, other industrial processes such as thermal treatments, pulses of energy and slippery surfaces can also prevent organisms from attaching.

In this chapter, a literature review supporting the current project work is presented and organised as follows: **Section 2.2** reviews biofouling and its impacts on the marine industry. Specifically, since the current project involves biofilm testing, detailed information on biofilm fouling is presented. In **Section 2.3**, all possible factors that may directly affect biofilm growth during deployments in the present project are discussed. Then, a review of copper sheathing and copper-based antifouling technologies is presented in **Section 2.4**. **Section 2.5** reviews full-scale trials and experimental tests results of copper-based antifouling. In this section, the hydrodynamic results of surfaces coated with copper-based antifouling with and without biofilms are discussed. **Section 2.6** discusses non-toxic and other antifouling technologies that may potentially be future alternatives to the current copper-based antifoulings. Apart from fouling, the finished surface qualities could also play a highly important role, and these are reviewed in **Section 2.7**. Finally, the chapter summary is presented in **Section 2.8**.

2.2 Fouling, its Components and Impacts

As early as the 4th century BC, fouling was described by Aristotle as small fish that were able to slow ships down. In this section, the introduction to fouling evolution on a substrate includes precondition accumulation, then the microbial fouling and finally the macroscopic fouling stages. This is followed by reviews of the major fouling issues of the shipping industry.

2.2.1 Conditioning Layer

When a clean substrate, such as a ship, offshore structure or pontoon is immersed in an aquatic environment, particularly in a marine environment, the result is the spontaneous adsorption of what is frequently referred to as a "conditioning layer", which was initially proposed by (Baier, 1973) and (Loeb and Neihof, 1975). This conditioning layer usually consists of dissolved organic matter, such as glycoproteins (Baier, 1980), humus (Loeb and Neihof, 1975) and proteins, lipids, nucleic acid, polysaccharides (Taylor *et al*., 1997); molecule attachments (Zaidi *et al*., 1984), exopolysaccharide (Berman and Passow, 2007) and possibly inorganic materials such as metallic oxides or very fine clay mineral particles (Chamberlain, 1992). All these nutrients drive bacterial movement (or chemotaxis) from their environment to the immersed surfaces. Thus bacteria and unicellular organisms gradually settle on the conditioning film and form a microbial slime film (Fletcher and Chamberlain, 1975).

2.2.2 Microfouling

2.2.2.1 Bacteria Biofilm

Hilen (1923) and Angst (1923) gave the earliest reports that the slime occurring on the surfaces was composed of different kinds of bacteria, as well as yeasts and moulds. Further early studies (Zobell and Allen, 1935; Zobell, 1938; Zobell, 1939) carried out in ship biofouling, with testing after a short period of one to seven days immersion, investigated the microscopic size of sea organisms that were found to attach to surfaces; most of the organisms were identified as bacteria. Moreover, Zobell and Allen (1935) indicated that the bacteria appeared singly or in pairs, instead of groups of bacterial colonies, showing up within a few hours of the surface being exposed to seawater.

For stainless steel immersed in seawater, Marszalek *et al.* (1979) reported that rod-shaped bacteria were the first colonisers. It should be noted that the firm attachment of bacteria after coming into contact with the surface is not immediate. They will show a logarithmic phase of growth and firmly attach on the surface only once the bacteria are of the correct attachment type (Zobell and Allen, 1935). A ship may be surrounded with different aquatic phases, and it will be impossible to prevent bacteria biofilm developing once the optimal adaptive bacteria species have settled on the surface.

2.2.2.2 Algal Biofilm

Slime consists of both bacteria and algae. Bacteria are found on the conditioning layer within a short period, usually attached by mucilaginous fibrils (Geesey *et al.*, 1978) but this is not an essential circumstance for subsequent colonisation by diatoms (Paul Jr *et al.*, 1977). In natural environments, algal biofilms usually develop on a moist illuminated surface (Leadbeater and Callow, 1992) and are dominated by diatoms such as cyanobacteria (blue-green algae), filamentous green algae, or mixed communities incorporating by these types (Characklis and Cooksey, 1983). The successful colonisation of the algae propagules (e.g. individual cells, vegetative fragments or spores) on a substrate surface, particularly in turbulent flow conditions, is achieved by having a strong adhering ability though secretion of adhesive polymers referred to as extracellular polymeric substances (EPS) (Hoagland *et al*., 1993).

Both diatoms and bacteria can produce EPS adhesive exudates in microbial colonies, which help to trap more particles and organisms (Hoagland *et al.*, 1982; Hoagland *et al.*, 1993). This key transition process from a microbial biofilm to a more complex community involves the settlement and the growth of larger marine fouling (macrofouling) organisms.

2.2.3 Macrofouling

Macrofouling can bring more significant impacts on offshore structures, ships and oceanographic instruments than microfouling. Macrofouling organisms are of many types, according to the investigations of Visscher (1928) who collected samples from over 250 vessels. It was reported that 48 species of animals were found on the ship bottoms, where most of them were barnacles, hydroids, worms and sea squirts. Also, 16 kinds of plants were identified, all algae. In general, macrofouling can be classified as “hard” and “soft” fouling types. A fouling species with a solid skeleton (such as a calcareous tube or shell) to protect the body within (e.g. calcareous algae, barnacles, mussels, tubeworms) is regarded as “hard” macrofouling whereas fouling organisms without such solid skeletons are referred to as “soft” macrofouling, such as sponges, seaweed and bryozoan.

2.2.4 Fouling Impacts

Capt. Henry Williams (1923) stated that coal was being wasted due to running fouled ships at full speed, with many tons of additional fuel being burned. The fuel consumption of a fouled ship was significantly higher than the consumption of a newly painted vessel. For new and clean

hull conditions, frictional resistance accounts for 80-85% of the total resistance in slow speed vessels and as much as 50% in high-speed vessels. Therefore minimising the ship resistance is significant in reducing the fuel consumption, as well as to reduce exhaust gas emissions. Before the successful application of antifouling paints, ship operators would accept from 0.25% to 0.5% increments in drag per day because of the expected accumulation of fouling (Woods Hole Oceanographic Institution, 1952). By effectively limiting fouling attachment using antifouling coatings, it is estimated that the global shipping industry has a fuel saving of $60 billion and reduced emissions of 384 million tons of carbon dioxide per annum (Bressy and Lejars, 2014).

Fouling can also promote and accelerate corrosion of metals. Microbial metal corrosion is the result of biofilm development on submerged metal surfaces. For example, bacterial corrosion occurs wherever non-sterile water is in contact with a metallic surface. Also, macroscopic organisms can aggravate the corrosion process. One example would be a barnacle that has penetrated through a soft bituminous coating in its growth process. As the barnacle shears open the coating film, the water can easily contact with the metal enabling the corrosion action to start. Moreover, when the barnacle settles down near the metal surface, uneven areas between the metal and the base of the barnacle may provide oxygen concentration cells which result in local galvanic corrosion. Another effect of marine fouling is the deterioration of coatings. For example, large and heavy shelled marine growths may attach firmly to a painted surface. Mechanical actions to remove these marine growths could result in the protection paints being stripped off and lead to an exacerbation of surface damage. If the settling of initial microorganisms can be prevented, certain fouling may be greatly decreased or eliminated (Saroyan, 1968). A consequence of fouling settlements is an increased demand for dry-docking operations, either because of additional hull cleaning or even for coating replacement or costly hull repairing.

Biofilms can block or reduce thermal efficiency in pipeline systems as the internal diameter may be reduced with biofilm development, thereby restricting the fluid flow through the pipe (Mittelman and Geesey, 1987; Bott, 1990). Algal biofilm has been found to release dissolved organic carbon (DOC) into the potable water supply system, and the result is to impart tastes and odours to the water (Hutson *et al*., 1987). Microbial accumulations also increase surface frictional forces and cause turbine power losses in hydroelectric systems (Tyler and Marshall, 1967). Moreover, fouled vessels are the most common marine species carrier which delivers

non-native fouling organisms into foreign areas, potentially leading to the introduction of invasive species (Bressy and Lejars, 2014).

2.3 Environmental Factors Affecting Fouling Growth

The factors that determine the fouling attachments on a surface are numerous and variable (Visscher, 1928; Saroyan, 1968). They can be classified into: ship aspects (vessel shape, route, harbour, speed etc.); environmental aspects (e.g. surface condition, season, temperature, pH, salinity, light etc.); and biochemical aspects (material, corrosion, nutrient substances, species composition etc.). In this section, only the factors related to the current project will be discussed: season and temperature (**Section 2.3.1**); freshwater (**Section 2.3.2**); light and colour (**Section 2.3.3**); surface conditions (**Section 2.3.4**); water movement and flow pattern (**Section 2.3.5**).

2.3.1 Season and Temperature:

The effects of seasonal changes in temperature and salt content on all living marine organisms are very evident. For seasonal effects on different fouling organisms on ship bottoms, Visscher (1928) conducted an investigation with 250 ships at harbours in Boston, New York, Norfolk, and Beaufort, N. C.. The results indicated that hydroids and algae are formed in late winter and early spring; many of the barnacles, oysters, and the bryozoan Bugula are formed in late spring and summer, whereas some barnacles and zebra mussels (Mackie, 1991) are formed in late summer or early autumn. Fouling would occur more significantly at certain periods of the year, and periods of active fouling vary with the kinds of fouling. It was also noted by Visscher (1928) that the breeding period for barnacles and some other fouling organisms might be extended when in warm water areas.

2.3.2 Freshwater:

According to Capt. Henry Williams (1923), it was generally believed that fouling growths would be removed if the fouled vessel was placed in freshwater, therefore experienced sea captains would put vessels into a freshwater harbour for this purpose whenever possible (Visscher, 1928). According to tests conducted on how freshwater can affect sea fouling organisms, Visscher (1928) stated that most of these fouling organisms (particularly larval and young forms) could easily be killed within 24 hours in a freshwater environment. Even though the larvae and younger forms of some species (i.e. Balanus eburneus, Ostrea, and Enteromorpha), can be killed within a short period, their mature forms were often not killed in

less than four days. Additionally, it was found that the shells of barnacles and structures of some other mature forms of fouling remained on the surface (Woods Hole Oceanographic Institution, 1952). As earlier stated by Visscher (1928), freshwater can kill fouling organisms. However, it does not mean the ship bottom would then be clean.

In freshwater environments, further observations have shown that the conditioning layer can be formed within one day even though nutrition deposits on a surface immersed in freshwater is slower than that in seawater (Meyer *et al.*, 1988). Even in high-quality waters with low nutrient levels, microbial growths are still likely to occur. Overall, a fouled ship can still gain a resistance benefit having spent time in freshwater as most of the macrofouling organisms will be killed, leaving their "houses" on the ship bottom without occupants, but this will effectively prevent the fouling structure from increasing in size.

2.3.3 Light and Colour:

During investigations of creatures on ships bottoms, Mast (1911) showed that the larvae of one of the hydroids (Eudendrium) reacted negatively to light, whereas spores of certain plant forms (algae) are positive in their reaction to light. Grave (1920) and Grave and McCosh (1923) both found similar reactions from the larvae of several tunicates. Moreover, the examination of a ship in dry dock revealed that the fouling was most dense beneath the bilge keels of the ship. The different distributions of fouling may be considered as "shaded" in different ship areas (Foster, 1975). Therefore Visscher (1928) deemed that light was the main effect.

Concerning the reaction of animals and plants to light, in one of the earliest demonstrations, Lubbock (1882) stated the fact that different sorts of animals may react to light of different colours. Gardner (1922) conducted tests with 12 steel panels coated with six different colour non-toxic paints. The subsequent inspections showed the panel coated with white paint was practically free from fouling, whereas the panels coated with yellow and green were slightly fouled. However, it was found the fouling was heavy on those panels coated with the red, blue and black paint. It has to be noted that colours would lose their influence once the panels had been exposed for a sufficient period and had become heavily fouled (Visscher, 1928).

2.3.4 Surface Condition:

The type of surface and surface texture play very significant roles in fouling attachment. Brooks (1880) noted that surface roughness could not stop but can affect the level of fouling attachment.

As demonstrated by several researchers (Coe and Allen, 1937; Pomerat and Weiss, 1946; Ogata, 1953; Den Hartog, 1959; Foster, 1975; Watanuki and Yamamoto, 1990) both animal and plant macrofouling organisms generally lean towards colonising a roughened surface rather than a smooth and nonporous surface. Other studies found Sargassum (Watanuki and Yamamoto, 1990), Porphyra (Rees, 1940) and Btidingia (Tittley, 1985) to be more abundant on smooth surfaces. Compared to smooth surfaces, roughened surfaces can provide higher water retention and protect the fouling organisms from desiccation (Saito and Atobe, 1970; Gonzalez and Goff, 1989). Russell and Morris (1971) carried out ship model towing tests with Enteromorpha spores attached on roughened and smooth glass slides, and results indicated the greater survival of spores attached to the roughened surfaces. Similarly, results from mechanical brush cleaning procedures of antifouling paints were reported (Moss and Marsland, 1976). Further studies found surface roughness can affect fouling processes (Neushul *et al*., 1976) (Foster, 1975) and the type of fouling organisms (Luther, 1976).

The surface topography and roughness can also affect the microbial attachment to surfaces (Christensen and Characklis, 1990; Bryers, 1994; Ammar *et al.*, 2015). It was found that the biofilm adhesion to scratched or rough surfaces is stronger than adhesion to flat surfaces (Tebbs *et al.*, 1994; Flint *et al.*, 2000; Medilanski *et al.*, 2002; Whitehead and Verran, 2006). Furthermore, rough surfaces were found to provide zones of low shear stress to minimise the biofilm removal (Alnnasouri *et al*., 2011); and more contact areas for microorganisms to attach (Geesey *et al*., 1996). Therefore, biofilms usually develop thinner layers on a flat surface rather than a rough surface (El Din *et al.*, 2003; Li and Logan, 2004; Chin *et al.*, 2007).

2.3.5 Water Movement and Flow Pattern:

Fouling abundance is also thought to be related to changes in water movement and flow pattern relative to a surface. The initial attachment of biofilm is weak and reversible. However once the attachment type microorganisms have selected and successfully adhered to a surface, faster flow can result in greater growth (Zobell and Allen, 1935; Heukelekian and Crosby, 1956a), with secretion of extracellular polymeric substances (EPS) from bacteria and diatoms to boost formation of a film (Horbund and Freiberger, 1970) giving more firm adherence to the surface. Moreover, increasing shear force at the walls can alter the biofilm thickness (Kornegay and Andrews, 1968; Rijnaarts *et al.*, 1993; Zheng *et al.*, 1994). The species distribution of microfouling organisms in the film also varies with the level of turbulence (Characklis, 1971).

For macrofouling organisms subjected to water flow current, Fischer-Piette (1932) came up with the possibility that water movement affects barnacle attachment. Moore (1933) and Phelps (1942) found that excessive water current inhibited barnacle attachment, but without given information of detailed water current speed. Further laboratory tests were conducted with disks rotating in the sea, using disks already covered with variously aged barnacles (Smith, 1946). The observations indicated that there were no barnacles left on the disk edge, some with stunted growth were in the intermediate area and continued growth in the centre. The conclusion noted that the average speed that affected barnacle attachment was 1.1 knots. The young forms were found to be easily removed under lower speed water flow, whereas a higher water speed was needed for dislodging the more mature forms. Compared to animal fouling larva, small algae spores are less likely to be removed from a surface in a slow-moving water current (Conover and Sieburth, 1964). Houghton *et al.* (1973) stated that Enteromorpha spores could even settle onto a surface subjected to water speeds of up to 10.7 knots.

Other studies (Moore, 1935; Moore and Kitching, 1939; North, 1970) stated that high flow speeds result in increased nutrient renewal and waste removal rates, thus boosting the growth of fouling abundance. The influence of water movement on fouling can be summarised into two aspects: a sufficient flow speed can either provide pressure and shear force to detach or prevent fouling attachments; or it can supply excess amounts of nutrition, oxygen and other organic and inorganic matters that promote faster growth.

For a ship moving in the water, apart from the water flow over the wetted surface, the surface profile could also alter the water-flow patterns, with the creation of eddies and reduced water speed over the ship hull (Neushul, 1972; Foster, 1975; DeNicola and McIntire, 1990). The water-flow pattern impact on fouling abundance over the substrata is also called "edge effect". A further explanation was given by Hoerner (1965) who compared the water flow region over the central flat area with the turbulent eddies over edges, which have lower water speed and which may encourage spore and larval settlement. Moreover, the water speed also drops when it meets vertical or sloping obstructions, and this can also lead to an additional settlement near edges.

2.4 Historical Development of Cu-based Antifouling Technology

Around 412 BC, a papyrus record detailed the very early ship painting process using a mixture of arsenic, sulphur and asphalt oil applied on the vessel sides (Grant and Culver, 1935). About

300 BC, the ancient Greeks were using tar and wax to coat ship bottoms. Around 200 BC, Atheneus recorded that the entire bottom of Archimedes ships was covered with lead sheathing fastened by copper bolts (Visscher, 1928) to effectively prevent fouling attachment on the wooden ship. From the thirteenth to the eighteenth century, pitch, oil, resin, tallow and lead were used to protect ships. During the following centuries, the main form of protection for wooden ships was either copper sheathing or the use of a mixture containing sulphur and arsenic. It was not until the development of iron hulls that copper sheathing was replaced with modern antifouling compounds. As a traditional and typical antifouling technology, copper and its compounds are commonly used against biofouling. In the following sections, detailed information of metallic copper and copper compound antifouling paints, and their coating types are introduced in **Section 2.4.1**, **Section 2.4.2** and **Section 2.4.3**, respectively.

2.4.1 Copper Sheathing

The first successful antifouling surface to receive general recognition was copper sheathing. However, no relevant case records were established prior to the 18th Century (Woods Hole Oceanographic Institution, 1952). The idea of applying copper sheathing on the Royal Navy ships was proposed by Charles Perry and others in 1708 (Harris, 1966) to the Lord High Admiral and the Navy Board for those ships on voyages to the East and West Indies. This proposal was later rejected due to the high costs involved and difficulty of repairing battle damage. In 1740, copper-zinc alloys were suggested by Nehemiah Champion and the Brass Company of Bristol (Staniforth, 1985) as sheathing on naval vessels, with an experiment conducted to prove it, but this produced no definite results. The Royal Navy experimented "coppering" in February 1758, with HMS *Invincible* partly copper-sheathed on a false keel (Bingeman *et al*., 2000). The first ship fully sheathed in copper was the 32-gun frigate HMS *Alarm* in 1761. During the sea trial of 1761 to 1765, the hull of *Alarm* was found to have a perfectly clean bottom after her four years of trials (Young, 1867). During the same period, another two ships, HMS *Dolphin* and HMS *Tamar*, were fully copper sheathed and repeated the *Alarm* trials (Bingeman *et al*., 2000).

The procedure of copper sheathing keeps the surface clean due largely to mechanical rather than chemical processes. When a coppered ship sails in the sea, the copper sheathing oxidises in very thin but parallel layers, the fouling organisms can be detached along with the continual thin oxidised exfoliation layers. Capt. Henry Williams (1923) and Woods Hole Oceanographic Institution (1952) also indicated the so-called exfoliation theory for copper sheathing.

Documents show thriving of the process of applying copper sheathing around the time of the American War of Independence (1775 to 1783), and its technical innovation was fully developed by the British Royal Navy (Monteiro, 2000). During the period 1775 to 1777, another thirteen Royal Navy ships' bottoms were coppered before they were sent off on their voyages (Fincham, 1851; Hay, 1863). Subsequently, all 32-gun (fifth rate) frigates were ordered to be finished with copper sheathing by 1779, and by January 1782, the whole battle fleet of the Royal Navy was coppered (Cock, 2001). During the same period, the USS *Alliance* was the first coppered American naval frigate in 1781 (Maurer, 1945), the USS *Constitution* was the second coppered frigate, completed in 1795 (Forbes, 1999).

There are also many flaws in using copper sheathing, as one of the drawbacks found in the ironwork from the *Alarm* illustrated; this was corrosion due to the galvanic action between the iron and the copper. At the same time, the iron prevented the copper from dissolving through galvanic action, and resulted in barnacles and tubeworms being able to adhere to it freely. Also, the copper was wasted or wore away at an excessive rate which shortened the service-life and increased the price (Saroyan, 1968). The same problems were found during the inspections on the *Dolphin* and the *Tamar*. Thus copper sheathing was removed from all three ships (Young, 1867). However, for wooden ships that were partially or fully plated with copper sheathing, Visscher (1928) noted algae and hydroids were absent, whereas barnacles were present on the copper (Young, 1867). The Age of Steam and Iron gradually replaced the Age of Sail as the Industrial Revolution unfolded in the 19th century, and the copper sheathing technology was unsuitable for the iron ships due to the serious corrosion issue (Ninnis, 1871; Atherton, 1899).

2.4.2 Copper Compound Antifouling

Driven by the corrosion and fouling issues, materials of the first antifouling generation were commonly based on toxic heavy metal compounds of arsenic, copper and mercury. The first patent of what was probably a copper-containing antifouling compound, by William Beale, was issued in 1625 (Sabin, 1900; Field, 1981). A notable copper compound antifouling was patented by James McInnes as ''hot plastic paint'' in 1854 using copper-sulphate as a biocide to be mixed in a metallic soap (Adamson, 1937). Moravian developed similar ''hot plastic paint'' compositions to McIness in 1862 in Trieste, Italy, by mixing rosin with copper, arsenic and mercury compounds. This composition also is known as ''Italian Moravian'' and demonstrated outstanding antifouling performance during the nineteenth century (Woods Hole Oceanographic Institution, 1952). The solvent antifouling formula with tar and copper oxide

was patented by James Tarr, and Augustus Wonson and shellac type paints were invented by Rahtjen in 1863 (Woods Hole Oceanographic Institution, 1952; Anderson, 2012).

According to Young (1867), in England alone, there were already more than 300 antifouling patents issued by 1865. Some of them were efficient in antifouling but expensive due to their short lives, whereas many of them were useless, with various ingredients which ranged from guano to plain kitchen salt (Barnaby, 1860; Mallet, 1872; Newman, 1896). By 1908, there were still no technical specifications for the U.S. Navy to unify their antifouling inspection, and the purchase of antifoulings was completely dependent on competitive bidding. It was no surprise that performance varied according to the differently priced products. Since the antifouling paint was highly military important, the US Navy finally decided to standardise the formula by developing its own antifouling, and this started with both shellac and hot plastic ship bottom paints (Williams, 1923). The tests of the first experimental ship-bottom paints were conducted with 21 different antifouling formulations at Norfolk Navy yard in June 1906. Two years later, the tests found that one of the shellac type antifouling paints containing red mercuric oxide had outstanding performance with an average of nine months service-life (Barnaby, 1860). However, due to being expensive and especially unobtainable during wartime, the mercury compounds were later replaced by copper compounds which were fairly cheap and were efficacious in preventing fouling attachment (Williams, 1923). The copper is released from the matrix into the water continuously in the form of copper ions Cu^{2+} or Cu^{+}. Under natural conditions, Cu^{+} ions will be oxidised immediately into Cu^{2+} ions, their main biocidal form, which is more stable (Zhao and Wang, 2015).

With the elaborate apparatus limitation for application, the hot plastic paints were replaced by alternative cold plastics, using an air-assisted spray to form dry film through evaporation of the solvent. The “cold plastic system” was typically a paint matrix with cuprous oxide as the toxic component, and it would typically require three coats of antifouling to provide the desired protection. This improved paint technology could keep the ship out of dry dock for as long as 12-18 months with negligible reduction in speed or increase in fuel consumption (Ingram, 1944; Honda, 1997). During World War II (1939-1945), the cuprous oxide was widely used as a biocide and mixed at a high weight ratio into US navy ship-bottom antifouling composites. For example, two famous products were Formula 15HP/1942 (30% wt) and Formula 143E/1943 (40% wt). After the war, this value was further increased in the following navy products: Formula 134/1960 (50% wt) and Formula 121/1963 (70% wt) (Saroyan, 1968). According to

Saroyan (1968), **Table 2.1** gives results of early US Navy tests of a cuprous oxide containing antifouling coatings, in terms of their effectiveness in preventing the attachment of marine growth for various periods. It was found that the service life of these antifouling paints could be enhanced by an increase in the film thicknesses.

When tributyltin self-polishing polymer (TBT-SPC) systems were successfully introduced into the antifouling marketing during the mid-1970s, cuprous thiocyanate (CuSCN) was added as an additional biocide, and eventually, this was replaced by cuprous oxide (Anderson, 2012). When TBT-SPC systems were banned in 2008 (International Maritime Organization, 2001), the main biocide used in TBT-free SPC and other alternative biocide antifouling systems became predominantly cuprous oxide, which is added as a pigment during paint manufacture.

Table 2.1: Effective period of U.S. Navy antifouling against fouling (Saroyan, 1968)

Products	Cuprous Oxide Percentage	Panel Tests	Ship Tests
Formula 134	50%	7-8 years	3-4 years
Formula 15HP/54	30%	6-7 years	3-4 years
Formula 121	70%	3-5 years	2-3 years

As a biocide, copper-compounds are limited in their effectiveness, especially to diatom and algae fouling. Therefore additional biocides are required to enhance the copper performance, and these are referred to as “boosting biocides”. It is, currently, estimated that copper-based antifouling paints protect more than 90% of the global vessels from fouling impacts. The high rate use of copper-based antifouling products, and their toxicity to the marine environment, if used excessively, can lead to environmental problems, especially for the local harbour water environment that has minimal water exchange with the open ocean. Regulations associated with copper-based paints, coupled with the high cost of biocide registration (e.g. more than $10 million to register a new compound in the U.S.) has increased the search to find a non-toxic alternative for AF protection.

In addition to seawater applications, several antifouling paints for freshwater use copper or copper salts (e.g. cuprous oxide or cuprous thiocyanate), sometimes adding algaecide as a booster (Callow, 1990; Callow and Edyvean, 1990; Kjaer, 1992). Copper-based antifoulings have a much lower release rate in fresh water than in seawater, and so can still meet fouling control requirements in many freshwater environments. Additionally, Callow (1993) stated that some of the copper-based antifouling formulas have a hard, smooth surface that results in poor bio-adhesion for zebra mussels. Combining this with the toxic effect of copper on the younger

fouling forms, both the chemical and physical properties of copper-based antifoulings have been effective in controlling zebra mussels on boats in the Great Lakes.

There are still some limitations in using copper and copper salt-containing antifoulings in freshwater, particularly in hard-water areas. The dissolved calcium salts can often be deposited within the biofilms, and these calcified biofilms can form a crust layer, up to several millimetres thick, on any submerged surface (Heath *et al.*, 1993). As a consequence, the calcium salt weakens the performance of the antifouling paints (Callow, 1990). It also becomes extremely difficult to remove calcified biofilms, and damage to the underlying coating substrate is unavoidable.

2.4.3 Types of Cu-base Antifouling

For biocidal antifouling paints, the leaching rate is the standard method for measuring the biocide release from the paint matrix. As the leach rate is usually directly affected by the binder system, there are four main categories of copper-based antifouling paint, based on the binder type:

2.4.3.1 Rosin-based Antifouling Paints

Rosin, commonly referred to as gum rosin or wood rosin, is slightly soluble in seawater. When it is used in antifouling coatings, the rosin matrix releases the biocides by a diffusion process. As illustrated in **Figure 2.1**, the biocide leaching rate of rosin-based paints usually begins with an excessive rate in the early days of immersion, and this value gradually drops in the following months as the biocide diffuses from deeper levels of the paint matrix. This continues until this value eventually falls below the effective critical level (i.e. 10 μg/cm^2/day) (Woods Hole Oceanographic Institution, 1952) and its antifouling performance fails (Anderson, 2012).

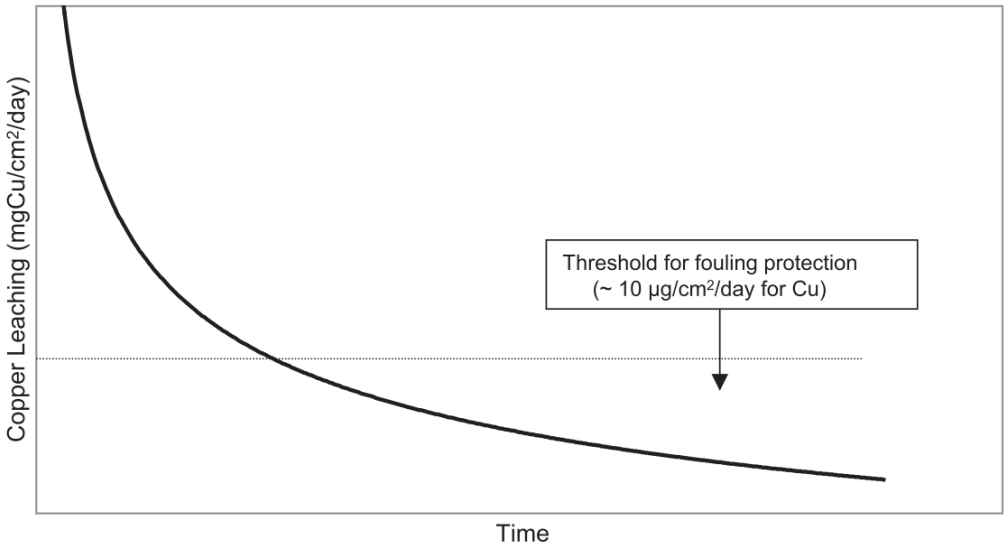

Figure 2.1: Biocide release of rosin-based antifoulings (Anderson, 2012)

To enhance the mechanical strength of a rosin-based paint matrix, some insoluble components are added at a specific ratio. High rosin content types of antifouling are known as "soluble matrix". The formula of the soluble matrix has been developed and improved so that these paints can fully dissolve and release biocides, and have reached a 36-month life-span. Such antifouling paints are given various names, such as Controlled Depletion Polymer antifouling (CDP) and Ablative antifouling. The biocide release mechanisms of such rosin-based paints are physical dissolution (i.e. bar soap like reaction in water) rather than by a chemical reaction. Low rosin content types of antifouling are known as "contact leaching matrix" because the high biocide content means that the biocide pigments are all in close contact with each other. As the biocide is released from the insoluble matrix, the leach layer (as shown in **Figure 2.2**) becomes thicker, and this eventually reduces the antifouling effectiveness. These paints could thus be ''reactivated'' by removing the leach layer mechanically through in-water cleaning. Without the reactivation process, in-service life of "contact leaching matrix" is limited to 24 months (Anderson, 2012).

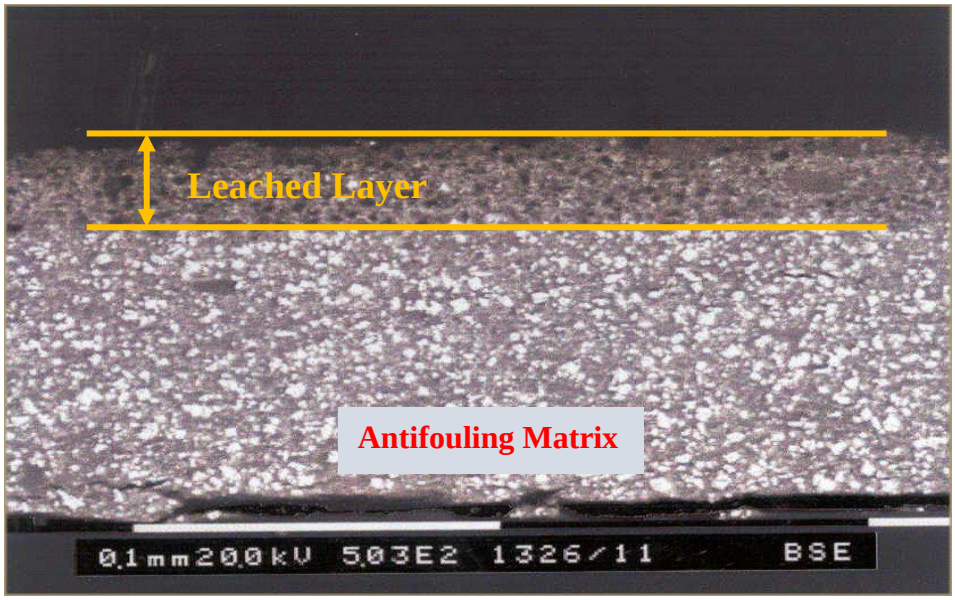

Figure 2.2: Antifouling and its leach layer (Anderson, 2008)

2.4.3.2 Self-polishing Acrylic Copolymer (SPC)

The SPC technology was introduced with TBT-SPC in 1974, using a chemical mechanism to release the biocide, through hydrolysis or ion exchange of an acrylic polymer at the surface. Compared to rosin-based paints, the SPC can keep an efficient control of biocide leaching until all of the paint is dissolved away, as shown in

Figure 2.3. Due to the polishing process, the roughness of the SPC surface decreases as the ship is underway at sea, and therefore the drag is reduced compared to rosin-based antifouling paints. The in-service period of SPC antifoulings can be extended up to 60 months, and once the vessel is in dry-dock, the maintenance and repair are relatively straightforward.

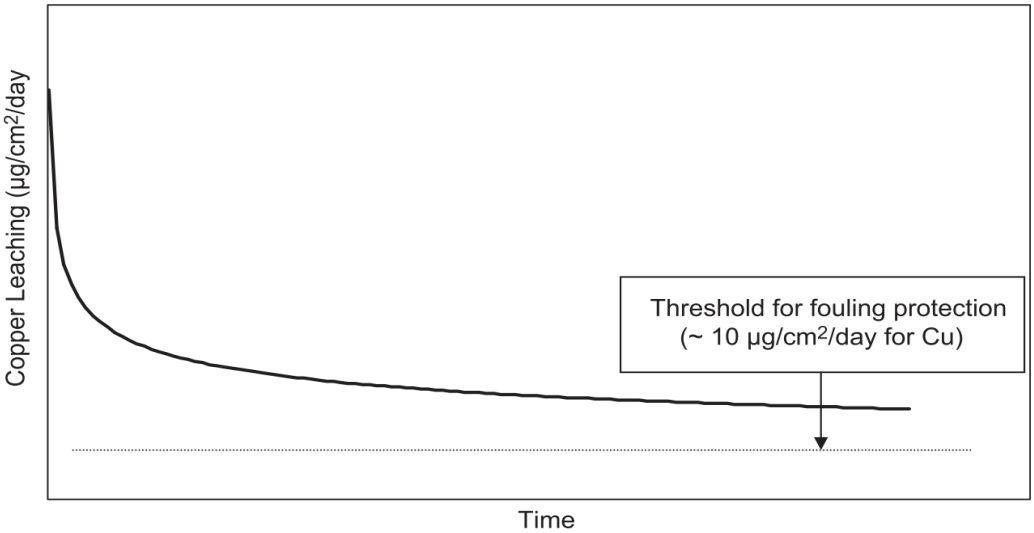

Figure 2.3: Biocide release of self-polishing copolymer antifouling (Anderson, 2012)

2.4.3.3 Water-based Latexes

Water-based latexes can form tough and durable films, with excellent long-term antifouling performance. Generally, there are two main types of water-based antifouling: hard and ablative. Similar to the rosin-based "contact leaching matrix", hard water-based latexes have a high biocide content and release the biocide in the same way as the solvent-based contact leaching matrix.

In contrast, the ablative water-based latexes have lower binder content, thus achieve a higher polishing rate. However, due to slow film formation by slow water evaporation from the coatings in a cold and damp environment, it takes a considerable time before the application of the coating can be finished. Most of the coating layer can even be washed off if a vessel is immersed before the paint is fully dry.

2.4.3.4 Hard and Scrubbable Antifouling Paints

This type of antifouling paint contains either metallic copper or cuprous oxide pigments in an epoxy or vinyl ester binder to form a hard coating layer. For a vessel operating in regions where it might suffer underwater scrubbing, such as vessels operating in ice, this type of antifouling could be regularly "reactivated" by scrubbing the hard leach layer away. An environmental benefit of these coatings is that they have very low (or no) solvent content, and being impervious to water, they can also provide anticorrosive protection (Anderson, 2012).

2.5 Experimental Studies of Cu-based Antifoulings and Biofilm Fouling Impacts

Capt. Henry Williams (1923) "[… considering that frictional resistance is the most important element in the resistance to propulsion of practically all ships, it is surprising there has been so little investigation of the possibility of reducing skin friction to a minimum. Ship owners seem to be satisfied that everything possible is accomplished by docking ships periodically for cleaning bottoms and painting with anti-fouling paints. …]"

McEntee (1916) investigated the potential of reducing the frictional resistance of a ship by testing friction planes coated with graphite, black lead, soaps, and oils. It was found that none of these materials offered an advantage over a smooth varnished surface. As no surface coated with antifouling can achieve lower frictional resistance than a simple smooth surface, coating technology can always be optimised according to the frictional drag and antifouling

performances. In **Section 2.5.1** full-scale trials and experimental hydrodynamic performance of copper-based coatings are discussed in. Full-scale records and experimental results of fouling conditions are discussed in **Section 2.5.2**.

2.5.1 Experimental Studies of Cu-based Antifouling Performance

Haslbeck and Bohlander (1992) and Holm *et al.* (2004) performed drag measurements on copper-component ablative AF coatings by using rotating disk apparatus, but without surface roughness evaluations at each experimental stage, nor fouling condition. Especially for an ablative coating matrix, it would be expected that the surface roughness would change while it is reacting with seawater, and therefore the roughness needs to be observed during the tests. Candries *et al.* (2003b) used rotating disk drag tests to study Foul-Release (FR) and Self Polishing Co-polymer (copper SPC) AF coatings. Two cylinders were coated with an FR scheme and a copper SPC scheme by spray application; one other cylinder was coated with an FR scheme by roller application. It was noted that the finished surfaces were expected to be rougher when the coating was applied with a roller in comparison to spray application. It was concluded that roughness comparisons under the same coating application methods are required for more accurate roughness estimations.

Towing tank measurements were carried out on flat plates allowing for the comparison of the frictional drag of Tin-free AF with that from FR coatings (Candries, 2001; Candries *et al.*, 2003a; Schultz, 2004). It was found that SPC copper had the highest roughness amplitudes and frictional force, followed by the ablative copper scheme, while the FR scheme exhibited the lowest roughness amplitude and frictional force. The results are in agreement with the work of Candries *et al.* (2003b), who found the roughness amplitudes and frictional resistance of SPC copper to be higher than that of the FR scheme under the same application procedure. Also, the SPC copper scheme was found to have a higher frictional resistance than the FR scheme according to water tunnel tests carried out by Candries and Atlar (2005).

2.5.2 Microfouling Experimental Results

McEntee (1916) performed towing tests with panels fouled with “unnoticeably” small barnacles, and it was found that the maximum increase in resistance was four times as great as the clean condition. One of the earliest trials of the fuel consumption related to “unnoticeable” fouling attachments was recorded by the U.S. Navy Department (Visscher, 1928). This investigation was made in early spring of 1923 near the Boston Harbour with a Navy submarine

USS S-34 (SS-139), eight weeks after it had been dry docked. During the trials, the speed was found to have decreased from 9.85 to 9.25 knots at low propeller energy input, and at a high power, the input speed was reduced from 15.0 to 14.5 knots. The fuel consumption increased considerably even though there was only a very small fouling present, which was almost unnoticeable. Similarly, Denny (1951) stated that resistance measurements on the Lucy Ashton increased by about 5% over 40 days, although the subsequent examination of the ship's bottom indicated no apparent fouling.

With the assist of a scanning electron microscope (SEM), Dempsey (1981) described the biofilm layer that was formed by extensive bacterial communities on a cuprous oxide antifouling substrate. Casse and Swain (2006) and Chen *et al*. (2013) both reported that slime films dominated the fouling on a copper-based antifouling coating. With regard to biofilm impacts on the performance of a copper-coated ship, an earlier full-scale trial was reported by Lewthwaite *et al*. (1985) for a 23m ship, RMAS LAMLASH, coated with copper-based AF. There was a 25% drag increase caused by a thin slime film after 240 days of operation. After 771 days, a 1mm thick layer of dense slime and extensive weed above the bilge keel resulted in a dramatic drag increase of 80%. A set of trails on the USS Brewton (FF-1086) coated with organotin and cuprous oxide antifouling were reported by Haslbeck and Bohlander (1992). The vessel was tested in terms of power and fuel consumption under a fully developed biofilm and after the biofilm had been removed. There was an 18% decrease in power required to achieve a given speed of 25 knots in the latter case. However there were slight roughness changes. An economic estimation was analysed by Schultz *et al*. (2011) based on an Arleigh Burke-class destroyer (DDG-51) which was coated with ablative copper antifoulings. Schultz *et al*. (2011) found that a heavy slime condition could result in 10.3% more fuel consumption for the DDG-51 with respect to the hydraulically smooth condition, and this was equivalent to $1.2M extra costs per ship per year.

Since the very first experimental investigation into the effect of hull roughness on frictional resistance was carried out (Froude, 1872; Froude, 1874), the laboratory scale information on the drag characteristics of biofilmed surfaces (McEntee, 1916) and roughness can pave the way to estimate the drag penalties at full-scale with boundary layer-similarity laws (Granville, 1958; Granville, 1987). However, this would require an efficient way of growing biofilms, measuring the roughness and drag characteristics using practical testing apparatus. Haslbeck and Bohlander (1992) and Holm *et al*. (2004) did exposure tests and drag measurements of rotating

disks that were coated with copper-component ablative AF coatings. They found that the frictional resistance coefficient increased due to the development of micro-biofouling. Frictional drag tests on several types of coated surfaces were carried out by (Schultz, 2004) using towing tank experiments. They tested those surfaces under non-fouled, fouled and cleaned conditions. After static immersion, they found there was a greater drag increase from both silicon FR compare to traditional copper-based (SPC and Ablative) and TBT-SPC coatings. As a side-by-side comparison (Swain *et al*., 2007) immersed flat plates coated with FR and copper-based AF exposed to river conditions for 75 days: 60 days static in the river and 15 days of lab dynamic conditions. The drag tests showed that the copper-based AF had a lower drag coefficient than FR after 60 days of static immersion. They also found, at the relatively low test speed, the ablative copper coating out-performed the self-polishing systems. However, the quantisation analyses of the above frictional drag tests relative to their surface roughness measurements of surfaces fouled with soft fouling (e.g. biofilm) could not be systematically addressed.

With pipe flow experiments, Picologlou *et al.* (1980) found a strong positive correlation between the frictional resistance and the biofilm thickness. Moreover, compared to a rigid surface roughness of similar height, it was found that the biofilm could cause higher energy consumption due to its viscoelastic character and natural filamentous shape. Stoodley *et al.* (1999) noted that biofilms grown under laminar flow were patchy and consisted of cell clusters separated by interstitial voids, whereas biofilms grown under turbulent flow were filamentous. Further pressure drop tests of dynamic growth diatomaceous biofilm were conducted using a turbulent water channel (Schultz *et al*., 2015). The results indicated that diatomaceous biofilm could significantly increase the skin-friction by up to 70% with the surface evaluated by biofilm thickness and percentage coverage. Similar observations from turbulent boundary layers tests in which the biofilm thickness varied from 160μm to 350μm, the skin friction coefficient increased from 33% to 190% (Schultz, 1998; Schultz and Swain, 1999).

2.5.3 Challenges of Biofilm Fouling Studies

Even though a great deal of research has been conducted to understand the effects of biofilm fouling on overall ship power and drag penalties, it is still challenging to understand soft fouling organisms, and there are several possible reasons for these effects. Firstly, the condition of biofouling starts within seconds of a surface being immersed. A film forms on this surface by both organic and inorganic matter adsorbed from the aquatic phase. This effectively generates

a new substratum interface with altered physicochemical properties (Lewis, 1998). However, Lewis (1998) and Donlan (2002) indicated subsequent microbial colonisation of this film is influenced by the composition of the conditioning film (Loeb and Neihof, 1975; Mittelman, 1996; Ofek and Doyle, 2012), the nature of the substratum (Zobell, 1943; Heukelekian and Crosby, 1956b; Characklis *et al.*, 1990), the nature of the aquatic phase (Piatek, 1967; Fera *et al.*, 1989; Donlan *et al.*, 1994) and the species composition of the microbial community in the aquatic phase (Maier, 1968; Curtis and Curds, 1971). These factors make biofilms complex assemblages of diverse organisms ranging from bacteria to diatoms and algae. It is therefore challenging to quantify the characteristics of biofilms (e.g. density, height, etc.) and in turn to accurately estimate the impacts on ship surface roughness and drag penalties.

Secondly, the initial attachment of a biofilm is weak and reversible but once established, faster flows result in greater growth (Heukelekian and Crosby, 1956a) with bacteria able to secrete extracellular polymeric substances (EPS) to boost formation of the film (Horbund and Freiberger, 1970) and adhere to the surface more firmly. Moreover, increasing shear force at the walls can alter the biofilm thickness (Kornegay and Andrews, 1968; Rijnaarts *et al.*, 1993; Zheng *et al.*, 1994). It also should be noted that species distribution of organisms in the film varies with the level of turbulence (Characklis, 1971) making for the process of water fluid modelling and drag prediction on a biofilmed surface more difficult. Furthermore, biofilms can be changed and dislodged by the flow which makes the drag characteristics time variable even at a constant flow speed. Because of these complex issues, the contribution of a biofilm to overall ship power and drag penalties is still largely unknown and challenging to understand.

2.6 Other Alternative Antifouling Technologies

Given current environmental concerns, people are seeking more environmentally friendly antifouling control methods as replacements for biocidal antifouling technologies. Alternative candidates include: biomimetic surfaces based on shark and dolphin skin that can reduce the surface drag and minimise fouling impacts; forming coating systems utilising surface properties (such as hydrophobic or low energy surfaces) to control fouling attachments; keeping the hull clean by electrolytic, ultrasonic, UV or other physicochemical treatments. In **Section 2.6.1** foul-release antifouling, as one of the state-of-the-art non-toxic fouling control measures, is reviewed. Other alternative copper-based antifouling technologies, electrolytic systems and copper alloys are also reviewed in **Section 2.6.3** and **Section 2.6.4**, respectively.

2.6.1 Foul-release Antifouling Paints

Meyer *et al.* (1988) stated that the interaction between the substrate properties and conditioning film is the key to assist in fouling removal. An earlier, similar comment was that a surface should behave as a fouling release substrate layer when it has particular surface properties: such as surface energy (Baier and DePalma, 1971; Baier, 1973; Kinloch, 1987) and surface tension (Kendall, 1971; Baier *et al.*, 1997), that can be characterised by contact angles and wettability (Kinloch, 1987; Good and van Oss, 1992; Schmidt *et al.*, 2004); and elastic modulus (Brady Jr, 1999). In 1972, silicone was reported as having been used in a fouling-release coating system (Swain, 1999), but due to the very successful use of TBT-SPC during the 1970s and 1980s, little attention was given to foul-release coatings. Meyer *et al.* (1988) found less fouling occurred on low energy surfaces compare to high energy surfaces. Further tests using non-toxic silicone-based coatings indicated that they had excellent performance in resisting zebra mussel adhesion (Leitch, 1992). These results have been further proved by the following researchers (Callow *et al.*, 1986; Swain and Schultz, 1996; Brady Jr and Singer, 2000), and silicone coatings based on polydimethylsiloxane (PDMS) systems have been shown to effectively prevent macrofouling attachment.

Unlike the two or three layers of a biocidal antifouling system, only a single top layer of an FR system is required to apply directly on the ship hull as the primer and/or tie-coat. This will require less dry-docking time, have lower paint consumption and lower application costs, and also has a longer lifetime in service (Bressy and Lejars, 2014). Also, full-scale trial case studies (Millett and Anderson, 1997; Anderson *et al.*, 2003) and laboratory tests (Candries *et al.*, 2000; Candries, 2001; Atlar *et al.*, 2002; Schultz, 2004; Townsin and Anderson, 2009; Ünal, 2012; Ünal *et al.*, 2012; Ünal, 2015) proved newly finished FR coatings have lower roughness profiles which can lead to lower drag resistance than biocidal. Moreover, due to the fact that it contains no biocide, this technology would hardly be affected by future environmental legislation.

However, apart from these advantages, it has to be noted that there are still some limitations in using such non-biocidal technologies. Research from various authors (Gerhart *et al.*, 1992; Kovach and Swain, 1998; Callow and Callow, 2002; Bressy and Lejars, 2014) has pointed out that some fouling organisms appear to prefer low energy surfaces. Typical case studies are given based on the behaviours of barnacles and bryozoans, which are both important macrofouling species. Attachment populations of barnacle larvae on a surface show a positive correlation with surface wettability, whereas bryozoan larvae have an inverse correlation with

surface wettability. A high percentage of bryozoan attachments, even up to 30 cm in diameter, were found on surfaces coated with silicone elastomers (Callow, 1993). Callow and Callow (2002) also found that diatom slimes, oysters and tubeworms can tenaciously stick on FR systems and become difficult to remove, even at high speed.

As there are no toxic components contained in such coatings, they are likely to become fouled on vessels that spend a long time in port, and extra in-water hull cleaning might be required for such vessels (Swain, 1999). Even though hydrodynamic forces will tend to keep the hull in a fouling free condition for those vessels that are continually operating at high speeds, the information about the required water velocities to remove other fouling types and communities (Swain and Schultz, 1996) from state-of-the-art FR is still not clear. This may be because of the different fouling adhesion strengths, coating conditions and variable hydrodynamic characteristics along a ship hull. FR systems are costly (Wells and Sytsma, 2013), about three times more expensive than tin-free SPC coatings, due to costs of the paint itself, the careful surface preparation required and any additional hull cleaning due to fouling growth (Callow and Callow, 2002). Also, the non-stick nature and softness mean that FR systems cannot be firmly coated on the substrate without using a tie-coat, and they have frequently suffered mechanical damage when there has not been particular hull care and mooring protection (Swain, 1999; Bressy and Lejars, 2014).

2.6.2 Surface Treated Coatings (STCs)

Surface Treated Coatings (STCs) are biocide-free antifouling coating and mainly formulated with vinyl ester resin with containing a high volume of glass flakes (Candries, 2009). It not only can supply impermeable barrier that protects submerged surfaces of ships or offshore installations against corrosion, but also can be used for antifouling purpose. The STCs has rendered harder, smoother and more impermeable by the surface alignment of embedded glass flakes making it more difficult for fouling organisms to attach. Also, as their so named, antifouling efficiency of STCs needs to be maintained by regular in-water treatment and remove any marine fouling at an early stage of development. The overall effect of this treatment consists of a conditioning aspect that involves special technology to improve the surface characteristics and a cleaning aspect that removes fouling in an early stage of development (Candries, 2010).

As the consequence, a large number of full-scale applications of STCs show excellent corrosion protection and resistance to fouling, a long service life due to high durability, and significant

drag reduction when compared to conventional antifouling methods (Van Rompay, 2013). Moreover, considering from the lifecycle and maintenance costs, cleaning and conditioning are an integral part of the STCs coating system and can be carried out rapidly at limited cost resulting in improved antifouling performance.

2.6.3 Electrolytic System

The initial studies in antifouling by electrolytic system were carried out by Parker (1924), who tested various metals for their response to fouling by submerging panels of zinc, iron, aluminium, tin, lead, and copper. Parker (1924) found the metal that was coupled with a more active one turned into the anode, with fouling organisms grow freely. At the same time, the cathode (the active metal) was totally fouling free. Therefore, Parker (1924) concluded that any metal's electrolytic action causing ionisation could prevent fouling attaching.

It should also be noted that to achieve a toxic antifouling level, a sufficient metallic ion concentration should be kept within a certain distance, at least 1 millimetre (Visscher, 1928), of the surface of the ship. Many researchers (Shibata *et al*., 1972; Nakasono *et al*., 1993; Matsunaga and Lim, 2000) proposed further electricity fouling prevention procedures utilising different materials. Even though the results have shown that this procedure can stop fouling occurring or even kill fouling attachments by creating anodic or cathodic poles at the paint surface, it has not been made to work for extended periods due to the voltage drop across the surface, cathodic chalk formation, and possible corrosion of the underlying steel.

2.6.4 Copper Alloy

It was found that copper-nickel 90/10, in which the copper is alloyed with 10% nickel and 1-2% iron, has a much-improved resistance to corrosion and fouling compared to the copper sheathing. The copper-nickel alloys were initially developed for condensers and piping systems in a seawater environment (Powell and Michels, 2000). A slime layer could not build up sufficiently on the alloy substrate, and therefore macrofouling could not be established. The copper-nickel 90/10 was also found to have a self-cleaning property, and surface accumulations can be effectively removed when surrounding velocities reach 3-8 knots (Manzolillo *et al.*, 1976), or they can be wiped off or removed with mild scraping (Powell, 1994). Two early solid copper-nickel hulled vessels, the *Asperida* and the *Copper Mariner*, were in service for 30 and 16 years respectively without hull cleaning because of the negligible fouling (Manzolillo *et al.*, 1976). After 8 years of in-service conditions, examination of *Asperida* indicated a maximum

reduction in copper-nickel sheathing thickness of 0.05 mm which corresponds to a corrosion rate of less than 0.01 mm/year (Glover, 1982). Therefore copper-nickel alloys can be expected to have an outstanding service life compared to any other antifouling materials.

However, as with copper sheathing, directly attaching the copper-nickel to a steel hull can cause galvanic corrosion. Also, due to cathodic protection, the antifouling performance can be significantly reduced. Therefore, copper-nickel has to be freely exposed to seawater without contact with any other active materials. Moreover, compared to antifouling coatings, its higher costs and unpredictable performance in polluted water have prevented its widespread adoption.

2.7 Other Resources Affect a Coated Surface Condition

Apart from the biological impacts of fouling attachments, other physical aspects such as coating material, corrosion, coating finished qualities and substrate surface conditions can directly affect vessel hydrodynamic performance. In the current project, the test surfaces were prepared using cast acrylic, commercially known as "Perspex", as a substrate surface with a manual air-assist spray application of the coatings. Therefore, the related factors of coating materials and coating finished qualities are reviewed in **Section 2.7.1** and **Section 2.7.2** in the next.

2.7.1 The Contributions of Particle Size

For any processed surface, understanding the impact of natural irregular particles on coating microstructure and surface roughness is essential. One of the main issues stems from the fact that it is harder to evaluate a three-dimensional irregular shaped particle, for example, a sand grain or a pigment, with a unique number (Rawle, 2002). As a result, a body of research focuses on the interaction of surface roughness and particle size, due to coating properties, addressing questions such as how particle size can affect viscosity, dispersion stability and surface roughness. Heslin *et al.* (1974) studied the surface roughness effect of different sized glass-sphere particles. Particle sizes of 10 to 40 and 40 to 80 microns were tested, and it was established that roughness increases with particle size. However, the limitation of the study is that only artificial regular shaped particles were tested instead of irregularly shaped particles. Kong *et al.* (2007) carried out studies of the average powder effect on surface roughness and powder deposition efficiency. Five groups of different sized Inconel 625 Nickel alloy, ranging from 37μm to 158μm, were tested. The study found that the highest powder deposition efficiency did not result from the largest or the smallest particle size powder. Both large and very small particles were associated with high roughness with evident waviness. However, for

minuscule particles, only coagulation within the nozzle was discussed by Kong *et al.* (2007). A discussion from Rawle (2002) indicated that the phenomena of agglomeration and aggregation could occur for very small particles which may cause suspension during the particle powder application. Further research focusing on particles from different materials of the same size ranges is lacking.

Moreover, the interaction between surface roughness and particle size may also be affected by other factors. Irzaman *et al.* (2011) investigated surface roughness and grain size under annealing temperature effects. They found that with increasing temperature, the Root-Mean-Square (RMS) roughness and grain size decreased, which showed a strong correlation with annealing temperature. Xin *et al.* (2010) studied thickness dependence of particle size and surface roughness. Furthermore, there is evidence that thickness increases with grain size, which causes higher surface roughness (Melo *et al.* (2004); Xin *et al.* (2010)). An investigation of surface roughness with Nano-crystalline Aluminium was conducted by Perron *et al.* (2008) using mean grain sizes of 5, 10, 15 and 20 nm. They evaluated the surface roughness changes from elastic and plastic deformation. Roughness insignificantly increased during the elastic deformation, but they found that it changed rapidly in the plastic domain. This research studied temperature, layer thickness and deformation aspects of nanometer-scale particles, but the results for larger scale grain sizes are not very clear.

2.7.2 Coating Application Failures and Damages

Based on the experience obtained from the present study, the quality of a finished condition caused by several factors, such as coating quality condition, human error, the powder application device and the environment (wind and mainly humidity), can significantly alter the surface characteristics and potentially increases the drag penalties. Therefore, in this literature review section, typical coating failures and damage that can directly affect a vessel hydrodynamic performance are listed and discussed.

2.7.2.1 Adhesion Failure

Adhesion failure, also known as “delamination” or “flaking”, is one of the typical coating application failures due to the coating failing to adhere to the substrate or underlying coats of paint. This is usually caused by a contaminated substrate condition. It may also be due to incompatibility between coating systems or exceeding the over-coating time (Morgan and Roger, 2015). Therefore, it is essential to ensure the substrate is clean and dry, and that any

defective areas are removed. At the same time, the coating specification and over-coating intervals must be closely followed.

2.7.2.2 Blistering and Bubbles

Blistering can be described as the dome-shaped projections in the dry coating film due to the local loss of adhesion. According to Morgan and Roger (2015), this application failure can be dominated by many factors, such as retained solvent, hydrogen vapour and soluble pigments. Another similar application failure, "Bubbles" or "Bubbling", is caused by air or solvent trapped in the coating before it dries.

2.7.2.3 Cratering

During the process of the coating drying, trapped air or solvent bubbles may burst and leave small craters on the top coat. The solution to this would usually be either to improve the spray technique or adjust the thinner to give sufficient time to let the coating flow into a uniform film (Morgan and Roger, 2015).

2.7.2.4 Brush Marks and Runs

This failure is also known as "ladders" or "ropiness". Brush marks are undesirable ridges and furrows remaining on the dry film after brush application. This is usually caused by applying a coating with too high a viscosity, which is not suitable for brushing, or by using insufficient thinner. However, excessive use of thinners can lead a coating to "runs" over the surface (Morgan and Roger, 2015).

(**a**). Adhesion failure

(**b**). Blistering

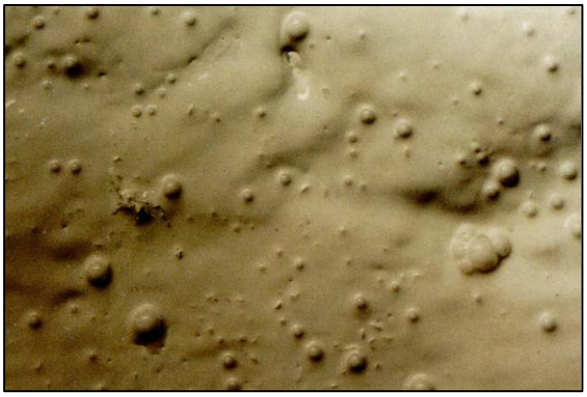

(**c**). Bubbles

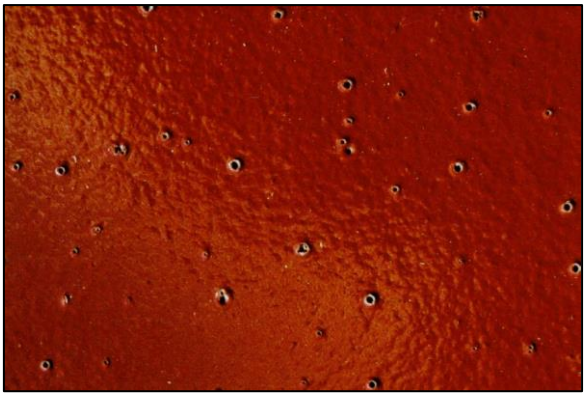

(**d**). Cratering

(**e**). Brush

(**f**). Runs

Figure 2.4 (**a**)−(**f**)**:** Coating Failures and in-service damages (Morgan and Roger, 2015)

2.8 Chapter Summary

This chapter presented an overview of marine fouling and antifouling technologies. In particular, it highlighted hull fouling control by copper-based antifouling systems and their further impacts on vessel hydrodynamic performance. The literature review identified research gaps that the effects of particle size on the drag performance of antifouling coatings and hence on ship hull resistance, as well as biofilm attachment, has not been explored and studied

systematically. For the ship owners or paint developers, this gap would result in a problematic issue of how to make an optimised selection of Cu_2O size.

Apart from the basic background review given in this chapter, for providing the data analysis theoretical support in this research work, the basic concepts of the surface roughness and rough-wall zero pressure boundary layer theory have been reviewed and presented in the next chapter (**Chapter 3**). This following chapter also includes several experimental procedures that were used for determining the frictional drag coefficient and roughness function based on different hydrodynamic assessment methods used in this research.

Chapter 3 Methodology Review

3.1 Introduction

This chapter aims to provide reviews of the basic methodologies for the following tasks which are mostly experimental and conducted in this research: roughness measurements (**Chapter 4**); boundary layer measurements (**Chapter 5**); pressure drop measurements (**Chapter 6** and **Chapter 7**) and full-scale frictional drag prediction based on the model scale data (**Chapter 8**). It has to be noted that, it is very difficult to analyse the fluid dynamics of viscous flow over an actual ship hull, plus considering different surface treatments, coating conditions and microbiological attachments. Instead, within the context of the rough boundary layer flow theory on flat plates which presents a good basis for the frictional drag estimation as used by many, it is justifiable to limit the boundary layer flow on flat plates and in pipes as reviewed in this chapter. Therefore, the experimental investigations in this research study were conducted under the flat plate boundary layer condition by attaching the testing panels in two different type water tunnels as described in **Chapter 5** and **6.**

In order to meet the above aim, the work carried out in this chapter is presented as follows: **Section 3.2** develops the reader's understanding of the surface roughness along with the characterisation, measurement and analysis of irregularly rough surfaces. The fundamental turbulent boundary layer concept for both a flat plate and turbulent pipe/channel flow is given in **Section 3.3**. This section also includes the boundary layer structure, scaling properties and surface roughness effects on these characteristics. **Section 3.4** introduces the experimental roughness function determination procedure for both velocity profiling and pipe/channel flow measurements. The measurement and calculation techniques of skin friction drag are summarised in **Section 3.5**. Also, due to the use of a range of cuprous oxide particle sizes and testing under different biofilm biofouling conditions in this work, a Granville (1958) similarity-law-based prediction procedure for ship's frictional resistance coefficients is discussed in **Section 3.6**, together with an overall summary of the chapter in **Section 3.7**.

3.2 Roughness and its Measurement

Surface roughness (or simply roughness) is a component of surface texture and plays a significant role in determining how a ship hull will interact with the marine environment and hence experience the frictional forces and fouling attachments. Because most of the conventional antifouling surfaces are irregularly rough, it is essential to have precise methods

of description and evaluation for the surface roughness. The definition of surface roughness and its categorisation are given in **Section 3.2.1**. The roughness and other surface texture compounds of a marine cuprous oxide surface are discussed in **Section 3.2.2**. **Section 3.2.3** discusses the data filtering procedures which can separate out the roughness profile from the measured raw profile to analyse the roughness and **Section 3.2.4** presents the roughness parameter calculation procedure that is used in the present work.

3.2.1 Surface Roughness

Surfaces represent the boundaries of materials and contain many intrinsic properties. Surface roughness, as one of these intrinsic properties, is not easily defined as it always depends on the technique or scale of measurements. For example, in the marine industry, one can understand the concept of a "rough sea", "rough hull" or "rough coating surface", compared to a "calm sea", "polished hull" or "smooth coated surface". If an ideal flat surface can be assumed to consist of straight lines with no defects, the general definition of the surface roughness would be the deviation of the actual surface from its ideal condition (Bhushan, 2000).

Most natural surfaces have irregular roughness characteristics (Thomas, 1999). For the marine industry, where it is important to control surface roughness, this is achieved by technology and material improvements. The most efficient way of evaluating surface roughness is by measuring the surface profile with various instruments, such as a stylus or optical device. Considering variation in 2 dimensions, the measured surface profile consists of a wavelength that is recognised by the measuring device. Typically, the range of measured wavelength is fixed by the measuring device itself. Similar to the visible light spectrum, the measuring device cannot "see" any wavelengths longer than its traverse length, or shorter than its sensor limit.

In manufacturing engineering, the measured profile can be classified according to the different surface wavelengths, as shown in **Figure 3.1**: (1) "error of form", which is associated with the longest wavelength and could be caused by thermal or stress distortions; (2) "waviness", which is associated with shorter wavelengths and might result from improper processing; (3) "roughness", which is associated with the shortest wavelength and could be generated by tool marks or impression from polishing (Thomas, 1999; Whitehouse, 2010). Moreover, it is prescribed that the ratio of wavelength to the amplitude of the error of form is at least 1000: 1, whereas this value for the waviness should be between 100:1 and 1000:1 (Deutsches Institut für Normung, 1982).

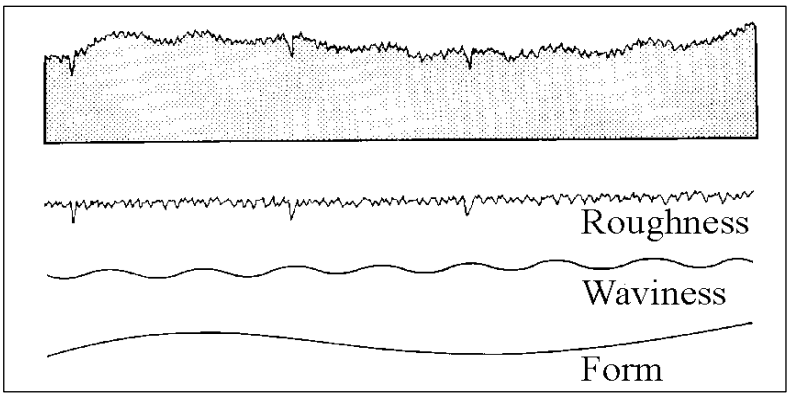

Figure 3.1: The measured profile consisting of roughness, waviness and form (Ettl *et al*., 1998)

3.2.2 The roughness of Marine Antifouling Coating

The frictional resistance is generally the largest part of the total resistance. For a new ship, the frictional resistance accounts for 50% of the total resistance in high-speed vessels, and as much as 80 – 90% in slow-speed vessels (Kempf, 1937; Todd and Taylor, 1967). The frictional resistance is governed by wetted surface (main dimensions and trim) and surface roughness of the hull (average hull roughness of coating). Private conversation with Dr Raouf Kattan, the Managing Director of Safinah coatings and engineering consultant, also confirmed that most of the ship's hulls from past to present time have been coated with antifouling paints containing cuprous oxide. These are usually applied either by spray, or roller, or brush. Each of these methods has different finished surface roughness (K Raouf, personal communication, September 2018). Meanwhile, particle size distribution (PSD) of cuprous oxide and its biocide boosters also affects the surface roughness. Figure 3.2 illustrates how solvent evaporates from a freshly applied binder film, eventually increasing initial surface roughness caused by the spherical cuprous oxide particles.

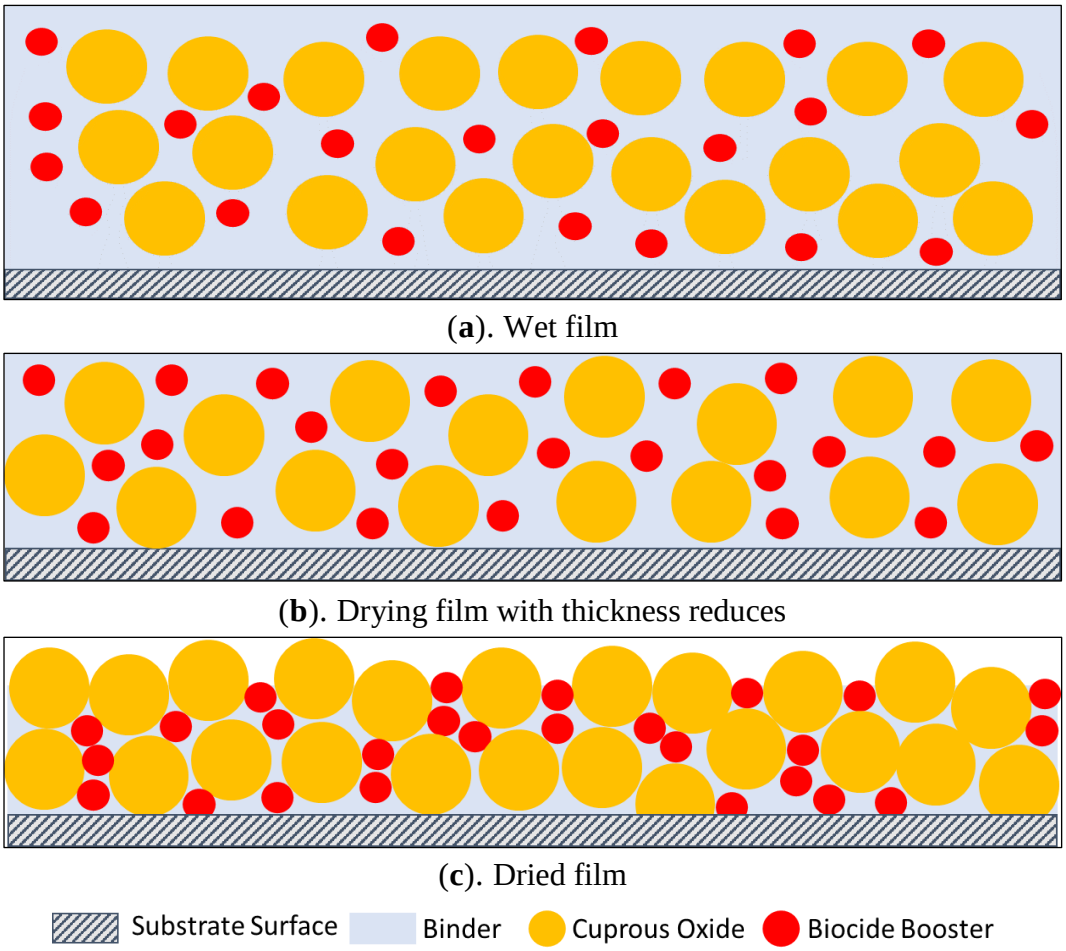

Figure 3.2 (a)−(c): Illustration of a cuprous oxide based antifouling coating drying after application (adapted from Howell and Behrends (2006))

For a coating surface, if expanding from a 2 dimensional profile into 3 dimensional topography, four essential surface elements are included in the surface topography, as described in **Figure 3.3**. These surface textures are flaws, lay, waviness and roughness.

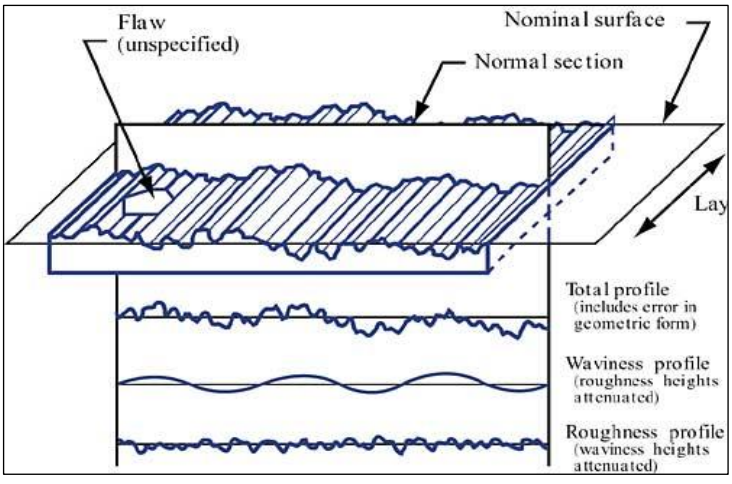

Figure 3.3: Representation of 3D surface texture (ASME, 2003)

These four elements are important in hydrodynamic efficiency of a marine surface. They exist with different levels of magnification and with one imposed upon the other. Flaws are usually caused by scratches in the paint or weld marks on the hull. Lay indicates the direction or pattern of the surface texture. The waviness is the carrier upon which roughness is superimposed. Referring to surface texture classification, Howell and Behrends (2006) summarised the three levels of roughness on a ship: structural roughness (flaw); the coating application process roughness (lay); and micro-roughness (waviness and roughness).

3.2.3 Roughness Data Filtering

When investigating marine antifouling coatings, rather than waviness, surface roughness has been the most common component used in the comparative assessment. For example, combining roughness measurements with a boundary layer method can give a simple and practical solution to frictional drag prediction (Granville, 1958; Granville, 1987; Mosaad, 1990). As roughness is imposed upon the waviness, care must be taken when analysing the surface roughness as the waviness profile is likely to dominate the roughness profile. To extract and analyse the waviness or roughness profile, a "cut-off" method is applied to numerically separate these two components from the measured raw surface profile data (Howell and Behrends, 2006). In roughness characterisation, three main wavelength cut-offs can be considered as shown in **Figure 3.4**. Firstly, the "traverse length", which is the maximum evaluation profile length and is associated with the measurement probe's travel distance across the surface. However, not all devices can collect data over the entire traverse length if it is too long. Secondly, the "assessment length", which is the length of measured data that is used in the analysis. The last category is "sampling length" or "cut-off length", which is the smallest distance over which the surface roughness parameters are assessed.

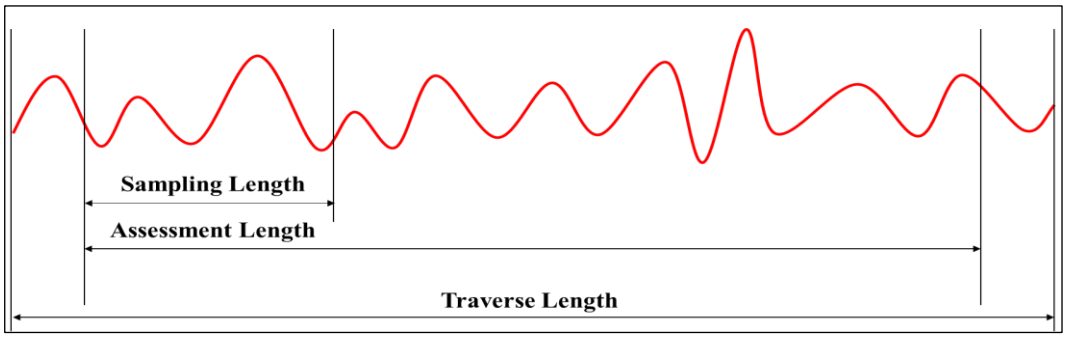

Figure 3.4: The lengths used in roughness evaluation (adapted from Whitehouse (2010))

The parameter used for evaluation of the roughness of a ship's hull is Rt_{50} which is the average

peak-to-trough height over a distance of 50mm cut-off lengths. The Rt_{50} parameter has become universally accepted for hull measurement, and can be obtained using the BMT Hull Roughness Analyser (HRA), which was used to measure roughness in the shipping industry for nearly 30 years according to Medhurst (1990) at that time and still is being used, although there are other alternatives.

Weinell *et al*. (2003) modelled the drag relationship of a painted surface with a ‘‘macro-roughness’’ (50mm cut-off length) and ‘‘micro-roughness’’ (10 mm cut-off length), respectively. The friction coefficient was found to be more attributable to “micro-roughness” impacts rather than “macro-roughness”. This is not to say that the use of roughness filtered with larger scale cut-off length is incorrect, but that choosing a more suitable cut-off length is important in different cases.

A “short wavelength cut-off” (or high-pass filter) would let the long wavelength components through and form the waviness profile. By contrast, a “long wavelength cut-off” (or low-pass filter) would let the short wavelength components through and form the roughness profile (Howell and Behrends, 2006). For surface roughness analysis, a cut-off length shorter than the waviness wavelength is normally used. The reason for this is that increasing the long wavelength cut-off generally increases the mean and the variation of height parameters (Mosaad, 1990). The International Organization for Standardization (ISO) has introduced cut-off filter lengths of 0.08, 0.25, 0.8 mm and 2.5 mm (ISO3274, 1996). However, for processing the surface analysis of different engineering surfaces, there is still no appropriate standard to use.

In the present work, the data filtering used a low-pass moving average filter to extract the roughness profile from the measured raw surface profile. This method, also referred to as the “boxcar method”, as expressed in Equation **3.1**, was fully described and discussed in Dey (1989), Byrne (1980), Medhurst (1990), Candries (2001) and Ünal (2012).

$$\overline{y_i} = y_i - \frac{1}{2M+1}\sum_{j=i-M}^{i+M} y_j \qquad \textbf{3.1}$$

where y_i and y_j are the roughness height at the i^{th} and j^{th} ordinates respectively, $2M$ is the window width (or the number of ordinates) based on the cut-off length; hence “$2M+1$” is the total number of points of the moving average used in this low-pass filter procedure.

Medhurst (1990) recommended the width of the filter window should be set to $2M = 0.8L_c$, where L_c is the cut-off length. Accordingly, as a cut-off length of 2.5µm was used for the current work, the width of the window is 2mm (or 80-points wide) with a sampling interval of 25µm. Therefore, this low-pass filter uses an 81-point moving average. **Figure 3.5** shows that the waviness and roughness data was separated by the 2.5mm cut-off length low-pass moving average filter method.

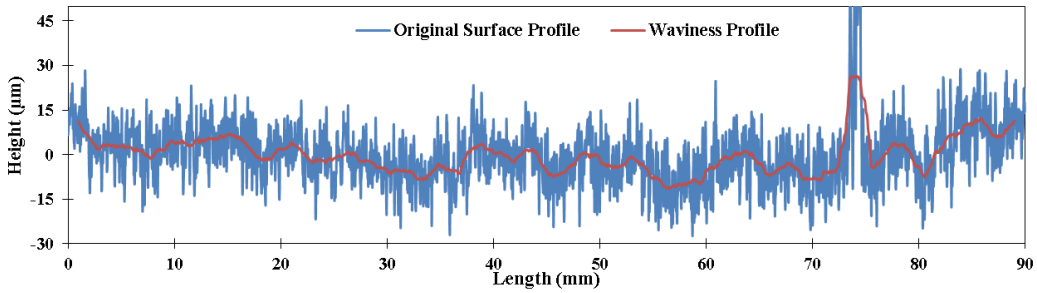

(**a**). Measured profile data included waviness profile before add filter

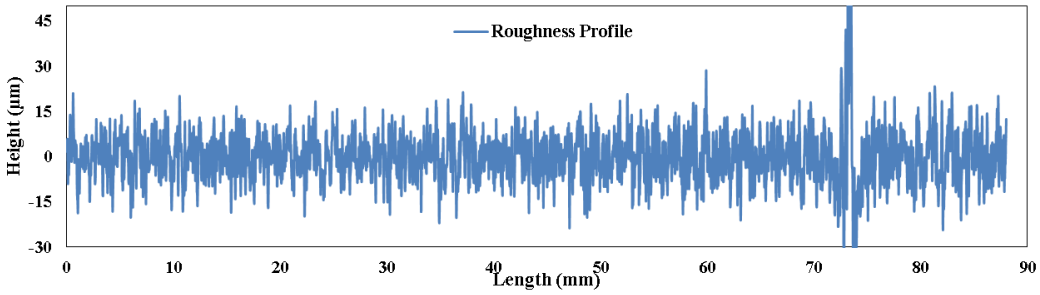

(**b**). Roughness profile after added filter

Figure 3.5 (a)−(b): Low-pass filter separates out roughness profile with 81-point moving

3.2.4 Roughness Parameters Calculations

When discussing surface roughness, usually the vertical deviations of the roughness are the first things to spring to mind. Actually, the surface roughness is a concept with three-dimensions. In this thesis, the form of the surface roughness is analysed in two principal planes: one is the vertical plane which is at right angles to the surface and represented by the roughness amplitude parameters; the other is the plane of surface and is characterised by the wavelength (or spacing) parameters.

According to ISO-4287, the parameters of the roughness profile can be classified into four broad families. Apart from amplitude parameters and spacing parameters, two other material ratio parameters and peak parameters are included. In this study, the roughness statistical analyses are described using six basic roughness amplitude parameters: arithmetic mean height

(R_a); root-mean-square deviation (R_q); total height (R_t); ten-point roughness of the roughness profile (R_z); skewness (R_{sk}); and kurtosis (R_{ku}). According to ISO4287 (1997), their calculation procedures are as below:

$$R_a = \frac{1}{\mathrm{n}}\sum_{\mathrm{i}=1}^{\mathrm{n}}|\mathrm{y_i}| \tag{3.2}$$

$$R_q = \sqrt{\frac{1}{\mathrm{n}}\sum_{\mathrm{i}=1}^{\mathrm{n}}|\mathrm{y_i}^2|} \tag{3.3}$$

$$R_t = \left|R_{pmax}\right| + |R_{vmax}| = {}^{max}_{i}y_i - {}^{min}_{i}y_i \tag{3.4}$$

$$R_z = \frac{|R_{v1} + R_{v2} + R_{v3} + R_{v4} + R_{v5}| + \left|R_{p1} + R_{p2} + R_{p3} + R_{p4} + R_{p5}\right|}{5} \tag{3.5}$$

$$R_{sk} = \frac{1}{nR_q^3}\sum_{i=1}^{n} y_i^3 \tag{3.6}$$

$$R_{ku} = \frac{1}{nR_q^4}\sum_{i=1}^{n} y_i^4 \tag{3.7}$$

where n is the total number of surface height samples, the y_i is the i^{th} sample height, R_v is the depth of valleys, R_p is the height of peaks.

Considering from the friction surface aspect, the five most influential spacing parameters associated with the roughness profile: High Spot Count (HSC); Peak Count (PC); mean spacing between profile peaks at the mean line (S_m); mean slope of the profile, (Δ_a); and average wavelength, (λ_a) are calculated (Gadelmawla *et al.*, 2002). Moreover, according to Gadelmawla *et al.* (2002), the HSC can also be defined as the number of high regions of the profile above the mean line (D_z). PC can be defined as the number of peaks per unit length of a profile (D_e) along the assessment length. The other roughness spacing parameters can be calculated as below:

$$S_m = \frac{1}{\mathrm{n}-1}\sum_{\mathrm{i}=1}^{\mathrm{n}} S_i \tag{3.8}$$

$$\Delta_a = \frac{1}{\mathrm{n}-1}\sum_{\mathrm{i}=1}^{n-1}\left(\frac{\delta_{y_i}}{\delta_{x_i}}\right) \quad \textbf{3.9}$$

$$\lambda_a = \frac{2\pi R_a}{\Delta_a} \quad \textbf{3.10}$$

where n is the total number of surface height samples, S_i is the mean spacing between the i^{th} and $(i+1)^{th}$ profile peak, the y_i is the i^{th} sample height and δ_{x_i} is the sample interval.

3.3 Turbulent Boundary Layer

In this section, a review of the general boundary layer concept over a flat smooth surface (**Section 3.3.1**) and its formulas (**Section 3.3.2**) are presented. **Section 3.3.3** discusses the boundary layer structure and scaling properties. The surface roughness effects on these characteristics, i.e. rough boundary layer flows, are presented in **Section 3.3.4**.

3.3.1 Turbulent Boundary Layer on a Flat Plate at Zero-Pressure Gradient

Ludwig Prandtl firstly described the boundary-layer concept during his presentation at Heidelberg in 1904. The paper was only eight pages long, entitled "Über Flüssigkeitsbewegung bei sehr kleiner Reibung" ("On the Motion of Fluids with Very Little Friction") and has proven to be one of the most important fluid-dynamics papers ever written (Krazer, 1905). At large Reynolds numbers, Prandtl assumed that fluid adheres to the wall and this leads to frictional forces retarding the motion of the fluid in a thin layer. Therefore, Prandtl theorised that the fluid adhesion was due to the "no-slip" condition at the solid wall which subsequently caused the immediately adjacent fluid to stick to the wall (Schlichting, 1974). This very thin layer concept is named the boundary layer, and it is shown schematically in **Figure 3.6**.

Even though the boundary layer is a hypothetical layer, it unequally divides the flows into outer and inner regions. In the bulk of the flow region (outer region), the viscosity can be neglected, and the flow is called the inviscid outer flow. The inner region is within the boundary layer where the viscosity must be taken into account. In **Figure 3.6**, at the leading edge of the plate, the constant incoming velocity distribution is perpendicular to the plate. As the distance from the leading edge increases, the thickness of the boundary layer increases as more particles are retarded by the skin friction.

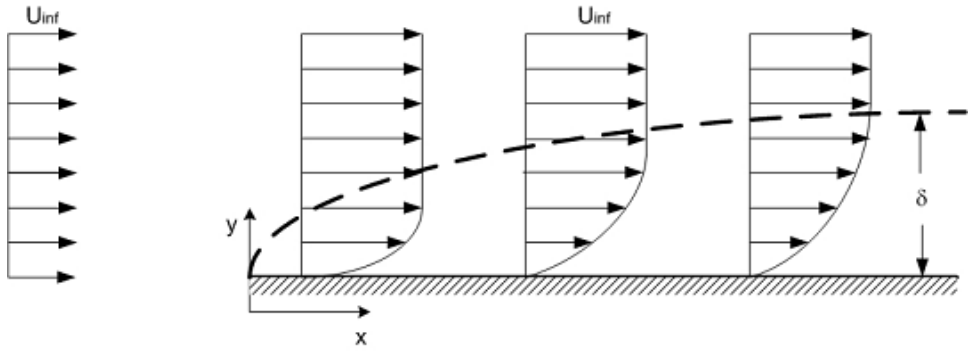

Figure 3.6: Schematic boundary layer on a flat plate at zero pressure gradient (Schlichting, 1974)

The velocity of the inner region fluid increases from zero at the wall (no slip) to its full free-stream value (inviscid outer flow). Thus the velocity changes enormously over a very short distance normal to the surface of a body immersed in a flow. In other words, the boundary layer is a region of very large velocity gradients. According to Newton's shear-stress law, the frictional shearing stresses, $\tau = \mu\, \partial U/\partial y$, are proportional to the velocity gradient. Even in fluids with very low viscosities, the local shear stress still can be considerable within the boundary layer. As a result, most of the drag force is due to skin friction.

Figure 3.6 clearly indicates that the thickness of the boundary layer, δ, increases along the plate from front to back. Therefore, the thickness of the boundary layer $\delta(x)$ increases monotonically as a function of the distance, x. The concept of the boundary layer thickness, was introduced by Prandtl in 1904 (White and Corfield, 2006) during the friction effects studies in the fluid boundary layer. As flow transition from the boundary layer region to the outer flow region is continuous, in reality, it is impossible to give a precise boundary thickness. The boundary thickness is therefore arbitrarily given as being at the point where the velocity reaches 99% of the outer velocity (i.e. $U = 0.99\, U_e$).

For fluid in a pipe/channel (internal flow), as shown in **Figure 3.7**, the boundary layer thickness increases in the flow direction until the boundary layer reaches the pipe centre and thus fills the entire pipe. The region from the pipe inlet to the point at which the boundary layer merges at the centre-line is called the hydrodynamic entrance region, and the length of the region is called the hydrodynamic entry length, L_h. Flow in the entrance region is called the hydrodynamically developing flow. Beyond the entrance region lies the fully developed region where the velocity profile is fully developed and remains unchanged. In the fully developed flow region, the velocity profile does not change downstream, and thus the wall shear stress remains constant as well.

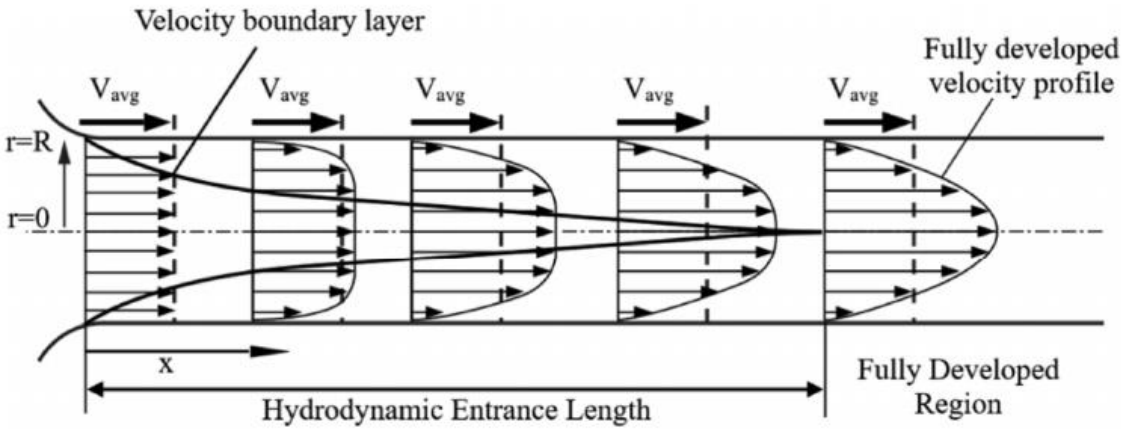

Figure 3.7: Development of the velocity boundary layer in a pipe (Gudala *et al*., 2018)

Apart from boundary layer thickness, δ, two other relevant length scales are also used to define the boundary layer thickness, namely the displacement thickness (δ_1) and the momentum thickness (θ). The displacement thickness, δ_1 defines how far the inviscid outer flow is displaced by the drop in velocity. The momentum thickness, θ is the distance by which the boundary should be displaced to compensate for the reduction in momentum of the flowing fluid on account of boundary layer formation. The calculations of these parameters are given in Equation **3.11** and **3.12**, respectively.

$$\delta_1 = \int_0^\infty \left[1 - \frac{U}{U_e}\right] dy \qquad \textbf{3.11}$$

$$\theta = \int_0^\infty \frac{U}{U_e}\left[1 - \frac{U}{U_e}\right] dy \qquad \textbf{3.12}$$

In either internal or external flow conditions, laminar or turbulent flow forms can both occur within a boundary layer developing over a long flat plate. One is called a laminar boundary layer, and the other is a turbulent boundary layer (Schlichting, 1974). As shown in Figure 3.8, over a flat plate, the flow remains laminar close to the leading edge. The laminar boundary layer becomes turbulent after a certain distance.

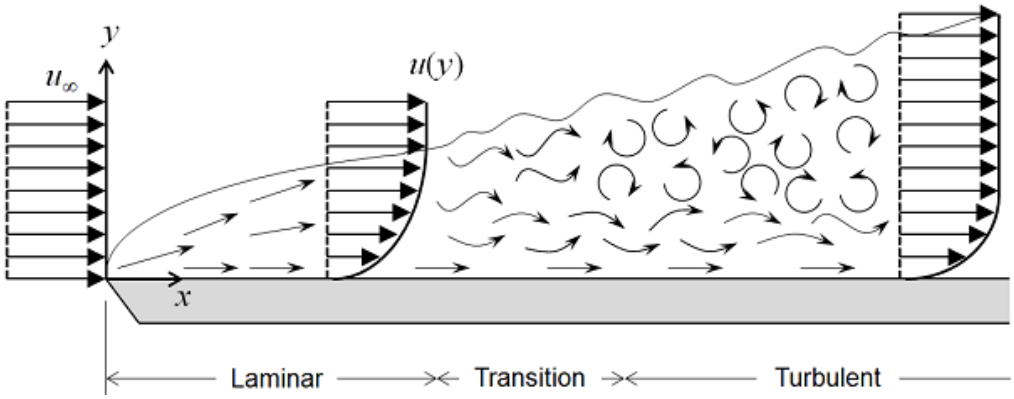

Figure 3.8: Schematic laminar and turbulent boundary layer on a flat plate at zero pressure gradient (Frei, 2013)

The transition region is marked by waves in the streamwise direction called Tollmien-Schlichting (T-S) waves. The transition process primarily depends on the Reynolds number, R_{e_x} which is the non-dimensional quantity and can be defined as:

$$\mathrm{R}_{e\_x} = \frac{U_e x}{\nu} \qquad \textbf{3.13}$$

where U_e is the fluid velocity, ν is the fluid kinematic viscosity, x is the length scale. Therefore, the position of the transition point, x_{crit}, can be determined by the critical Reynolds number $R_{e\_x_{crit}}$. Schlichting (1974) says that for the boundary layer on a flat plate, the critical Reynolds number for transition begins at about $R_{e\_x_{crit}} = 3 \times 10^5$ in strongly perturbed flow, whereas it can be up to $R_{e\_x_{crit}} = 3 \times 10^6$ for particularly smooth flow. Accordingly, Schlichting (1974) defines the following formula for the boundary layer thickness as a function of Reynolds number for a smooth flat plate:

$$\delta = \frac{0.37x}{\mathrm{R}_{e_x}^{1/5}} \quad (for\ \mathrm{R}_e \leq 10^7) \qquad \textbf{3.14}$$

Given the displacement thickness (δ_1) and the momentum thickness (θ), the shape factor H can be used to determine the nature of the boundary layer flow:

$$H = \frac{\delta_1}{\theta} \qquad \textbf{3.15}$$

The higher the value of H, the stronger the adverse pressure gradient. A high adverse pressure gradient can greatly reduce the Reynolds number at which transition into turbulence may occur.

According to Figure 3.9, for a flat-plate laminar boundary layer, the shape factor is $H \approx 2.6$. For a flat plate turbulent boundary layer, the shape factor decreases to $H \approx 1.4$

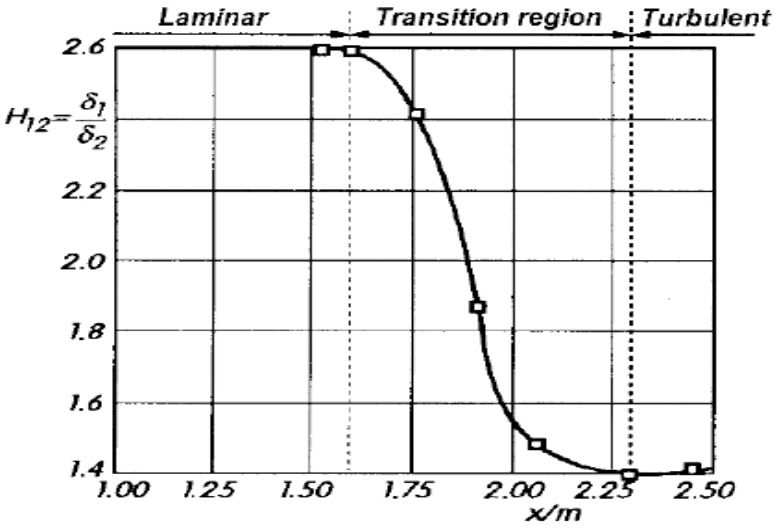

Figure 3.9: Changes of shape factor for the flat plate boundary layer (Schlichting, 1974)

Moreover, the onset of transition is also dependent on other factors such as surface roughness, pressure fluctuations and free-stream velocity fluctuations. For the boundary layer on a rough surface, Hinze (1975) suggested that the surface roughness could make T-S waves become unstable and result in the formation of U-shaped vortices. As illustrated in **Figure 3.8**, these vortices lift from the inner region of the boundary layer, burst, and eject lower velocity fluid into the faster moving outer region. As a result, a fully turbulent boundary layer flow develops where a large number of bursts occur. It should to be noted that the boundary layers are irregular in shape over time. Only when the time average of the flow is considered would a more defined boundary layer edge emerge. **Figure 3.10** shows the boundary layer on a flat surface at an instant in time.

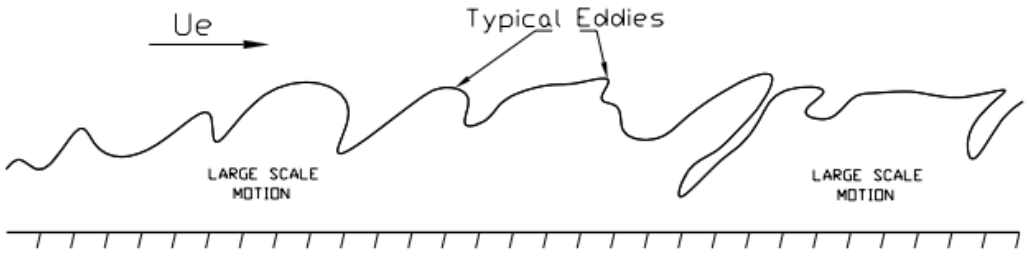

Figure 3.10: Boundary layer at an instant in time (Schultz, 1998)

3.3.2 Turbulent Boundary Layer Equations

In developing a mathematical theory of boundary layers, after approving the existence of the

boundary layer, the next step is to derivate its fundamental governing equations. The equations for the steady-state ($\partial U/\partial t = 0$) incompressible fluid boundary-layer can therefore be derived from the conservation of mass equation and the two-dimensional Navier-Stokes equations (N-S) which apply Newton's second law to a Newtonian viscous fluid. They can be given as below according to Ligrani (1989):

$$\frac{\partial U}{\partial x} + \frac{\partial V}{\partial y} = 0 \qquad \textbf{3.16}$$

$$U\frac{\partial U}{\partial x} + V\frac{\partial V}{\partial y} = -\frac{1}{\rho}\frac{\partial P}{\partial x} + \nu\frac{\partial^2 V}{\partial y^2} - \frac{\partial \overline{u'v'}}{\partial y} - \frac{\partial \overline{u'^2}}{\partial x} \qquad \textbf{3.17}$$

$$\frac{1}{\rho}\frac{\partial P}{\partial y} = -\frac{\partial \overline{v'^2}}{\partial y} \qquad \textbf{3.18}$$

Assuming that $W = 0, \partial(\,)/\partial z = 0, V \ll U, \partial()/\partial x \ll \partial()/\partial y, \delta \ll x$.

If Equation **3.18** is integrated over y, and the derivative of the result is taken over x and substituted into Equation **3.17** the following two-dimensional momentum equation is derived:

$$U\frac{\partial U}{\partial x} + V\frac{\partial V}{\partial y} = -\frac{1}{\rho}\frac{\partial P}{\partial x} + \frac{1}{\rho}\frac{\partial}{\partial y}\left[\mu\frac{\partial U}{\partial y} - \rho\overline{u'v'}\right] + \frac{\partial}{\partial x}\left[\overline{v'^2} - \overline{u'^2}\right] \qquad \textbf{3.19}$$

In order, from left to right: the terms on the left hand of the equals sign represent convection of momentum transport by the mean flow. The first term on the right hand of the equals sign represents the effects of the free-stream pressure gradient on the momentum contribution. The terms in square brackets indicate the viscous and turbulent diffusion of momentum, respectively. The last term in the square brackets represents the normal Reynolds stresses (Ligrani, 1989). In the boundary layer, the total shear stress, τ is made up of both viscous and turbulent stresses. Based on the viscous and turbulent diffusion terms, the total shear stress can be written as follows:

$$\tau = \mu\frac{\partial U}{\partial y} - \rho\overline{u'v'} \qquad \textbf{3.20}$$

In near-wall turbulence, the wall shear stress, τ_w can be directly used to calculate the local frictional coefficient:

$$cf = \frac{\tau_w}{\frac{1}{2}\rho U_e^2} \quad \textbf{3.21}$$

Therefore, the friction velocity, u_τ related to the wall shear stress can be calculated as:

$$u_\tau = \sqrt{\frac{\tau_w}{\rho}} = \sqrt{\frac{cf}{2}} U_e \quad \textbf{3.22}$$

3.3.3 Mean Velocity Profiles over the Smooth Wall

Based on the experimental data and physical interpretation, the turbulent boundary layer over a smooth surface consists of several sublayers. According to Ligrani (1989), there are three main sublayers: the viscous sublayer, the log-law region and the outer region. **Figure 3.11** shows these three main sublayers of the turbulent boundary layer scaled with the non-dimensional streamwise velocity, $U^+ = U/u_\tau$, and normalized by the wall distance, $y^+ = yu_\tau/\nu$. It shows that the viscous sublayer consists of two parts: the linear sublayer and the buffer layer. In a very thin zone in the proximity of the wall, the boundary lies in the linear sublayer in which the viscous sublayer extends to about $y^+ \approx 7$. In this region, the velocity profile is linear and is given by Equation **3.23**.

In **Figure 3.11**, the second zone of the viscous sublayer is called the buffer layer where the layer exists from about $7 < y^+ < 50$. In the buffer layer, the velocity profile departs from linearity. The formula (as shown by **Equation 3.24**) approximating the velocity profile across the entire inner layer including the buffer layer, was proposed by Spalding (1961) and others.

$$U^+ = y^+ \quad \textbf{3.23}$$

$$y^+ = U^+ + e^{-\kappa C}\left[e^{-\kappa U+} - 1 - \kappa U^+ - \frac{(\kappa U^+)^2}{2} - \frac{(\kappa U^+)^3}{6}\right] \quad \textbf{3.24}$$

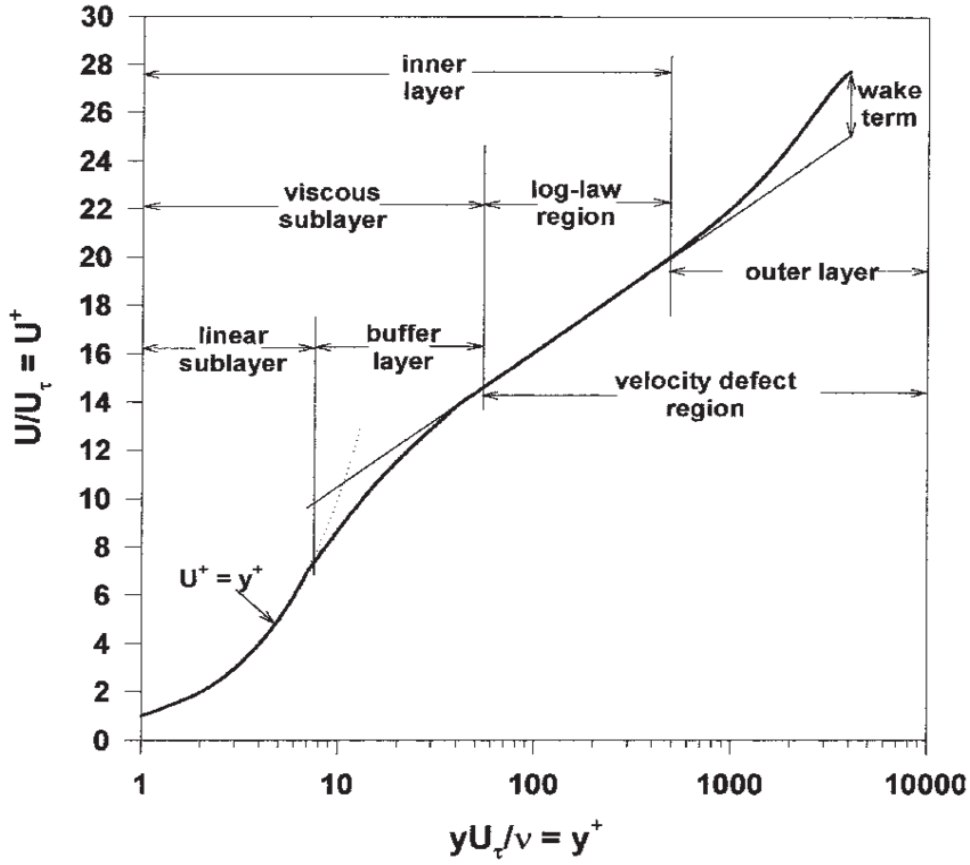

Figure 3.11: The sublayers in the normalized mean velocity profile in a turbulent boundary layer (Schultz *et al*., 2003)

As y^+ increases outside the viscous sublayer, an overlap region exists for $50< y^+ <300$. In this region, the mean fluid velocity has a logarithmic distribution (Townsend, 1980). Accordingly, this region is also known as the logarithmic layer. The logarithmic velocity profile (log-law) in this region of the boundary layer can be defined as below:

$$U^+ = \frac{1}{\kappa} ln\, y^+ + B \qquad \textbf{3.25}$$

where κ is the von-Karman constant and B is a smooth wall log-law intercept constant. There are no exactly defined values of κ and B. Clauser (1954b) used κ = 0.41 and B = 4.9 for the results of smooth plate data, whereas Coles (1956) reports values for κ = 0.40 and B = 5.0. And another group values of κ = 0.41 and B = 5 were used by Cebeci and Chang (1978). According to the Stanford Conference, the values of for κ = 0.41 and B = 5.0 were adopted (Kline *et al*., 1969).

The viscous sublayer and the log-law region make up the inner layer region. The thickness of this region is 10 to 20% (i.e. y/δ = 0.1 to 0.2) of the turbulent boundary layer thickness.

Moreover, in this inner layer region, the local mean velocity, U, is a function of the wall shear stress, u_τ, the fluid kinematic viscosity, ν and distance from the wall, y. Therefore, the fluid velocity in this layer can be described by Equation **3.26** which is called the law of the wall:

$$\frac{U}{u_\tau} = f\left(\frac{yu_\tau}{\nu}\right) \qquad \textbf{3.26}$$

Figure 3.12 shows the shear stress distribution within the inner layer region. In the linear sublayer, the fluid mean and turbulent motions are impeded by the fluid viscosity and wall condition. Over a smooth wall, the linear sublayer is dominated by the viscous stresses. As the thickness of the viscous sublayer increases, the viscous shear stress decreases along with a zero-pressure gradient smooth plate, and the no-slip boundary condition has less effect on the momentum fluctuation. Therefore, the turbulent shear stress (Reynolds shear stress) increases at the same time. The total shear stress is made up of the viscous stress and Reynolds stress in the buffer layer. In a zero-pressure gradient boundary layer, the total shear stress in the viscous sublayer almost equals to the wall shear stress, τ_w. In the log-law region, the turbulent stress dominates the shear stress and is almost entirely due to the fluctuating velocity components in the flow.

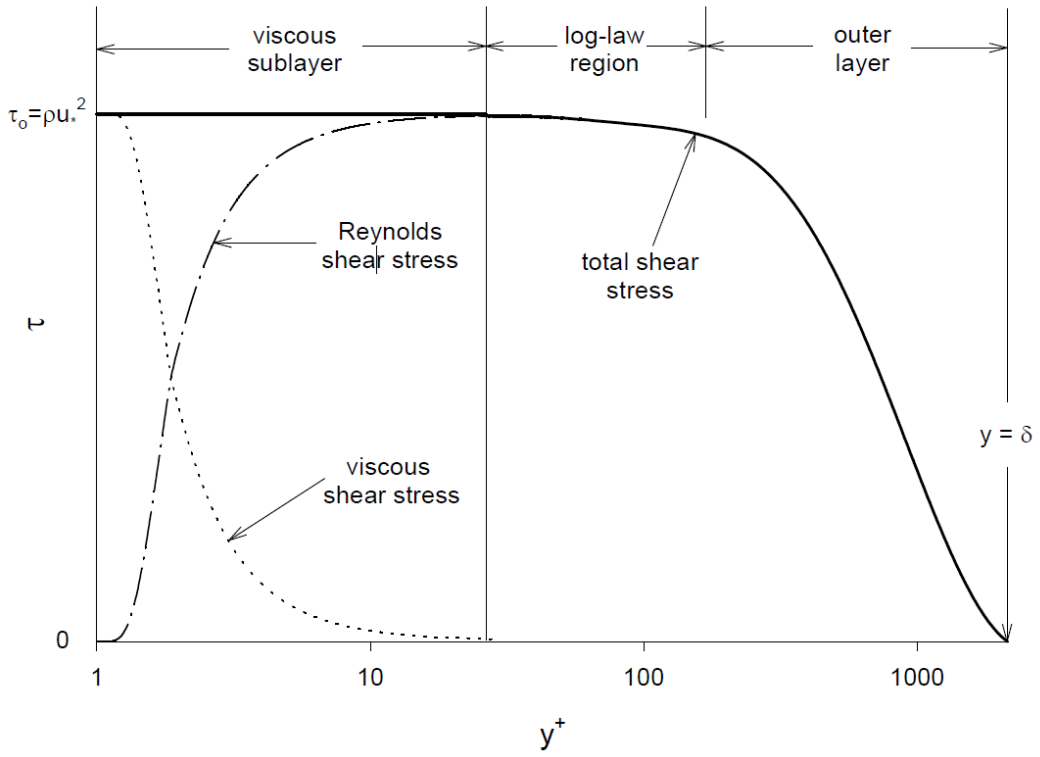

Figure 3.12: Turbulent boundary shear stress profile (Schultz *et al*., 2003) (adapted from Ligrani, 1989)

Similarly, for the pipe flow, the mean velocity profile is parabolic in fully developed laminar flow (**Figure 3.13**(**a**)) whereas it is much fuller in fully developed turbulent flow, with a sharp drop near the wall (**Figure 3.13** (**b**)).

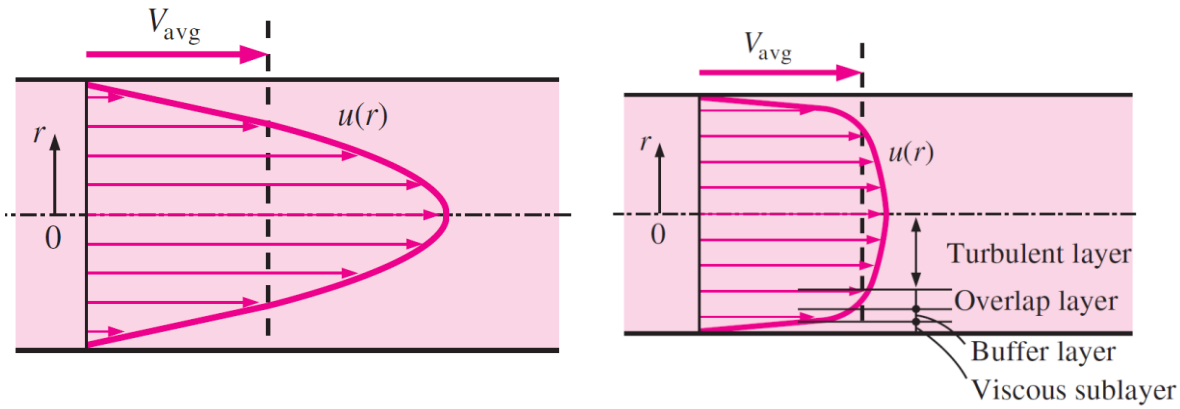

(**a**). Laminar pipe flow (**b**). Turbulent pipe flow

Figure 3.13 (**a**)-(**b**)**:** The velocity profile in fully developed pipe flow

For the flat plate boundary layer, the region of y/δ >0.1−0.2 is called the outer layer. In this region, instead of turbulence normalisation scaling laws by wall distance, y^+, the mean velocity profile can be expressed as a relationship between the velocity defect, $(U_e - U)/u_\tau$, and a non-dimensional distance y/δ (Schlichting, 1974). As shown in Equation **3.27**, this relationship is called the velocity defect law.

$$\frac{U_e - U}{u_\tau} = f\left(\frac{y}{\delta}\right) \qquad \textbf{3.27}$$

In the outer layer, the fluid motions far from the wall are independent of the fluid viscosity (Yaglom, 1979), and lead to surface roughness losing its influence further away from the wall. Therefore, the velocity defect law for both smooth and rough boundaries is expected to be geometrically similar at the same Reynolds numbers. The overlap region between the inner and outer region is formed by the log-law region in which the velocity defect also can be written as:

$$\frac{U_e - U}{u_\tau} = -\frac{1}{\kappa}\ln\left(\frac{y}{\delta}\right) + B_2 \qquad \textbf{3.28}$$

where the B_2 is a velocity-defect factor which does not vary with roughness but does vary with streamwise pressure gradient (Granville, 1987). B_2 is between 2.35 and 2.5 for a smooth plate with dP/dx =0, and 0.65 for pipe and channel flow. To extend the range of the log-law region,

Coles (1956) introduced the wake function which is corrected for the effect of the turbulent wake defect. The "law of the wake" for the smooth-wall boundary layer can be expressed as follows:

$$U^+ = \frac{1}{\kappa}\ln y^+ + B + \frac{2\Pi}{\kappa}\sin^2\left(\frac{\pi y}{2\delta}\right) \qquad \textbf{3.29}$$

where Π is the wake parameter. Hama (1954) and Coles (1956) gave the wake parameter as 0.55 for zero-pressure-gradient over a smooth surface in low free-stream turbulence conditions, whereas Schetz and Bowersox (1933) used 0.51. For the non-zero pressure gradient conditions, an adverse pressure gradient ($dP/dx > 0$) leads to an increase in the wake parameter or has the opposite effect when $dP/dx < 0$.

3.3.4 Effect of the Rough-Wall on Boundary Layers

The effects of roughness on turbulent flows were studied by many outstanding researchers in the past centuries (Darcy, 1857; Stanton, 1911; Mises, 1914; Hopf, 1923; Schiller, 1923). To investigate the effect of various degrees of relative roughness on turbulent flow, Nikuradse (1933) conducted experiments in rough pipes coated with artificial uniform sand grains. Nikuradse observed that the effect of the roughness on the flow conditions could be divided into three flow regimes, following the law of resistance in each range.

If the projections of roughness lie entirely within the viscous sublayer, the flow is called the "*hydraulically smooth"* regime. In this regime, the roughness has a negligible effect on the overall flow. Therefore the skin frictional drag is a function of the Reynolds number. The second flow condition is termed the "*transitionally rough"* regime where some of the projections of roughness penetrate the viscous sublayer due to the wall shear stress increases, or the higher surface roughness level. In this regime, form drag and eddy shedding are introduced by these extended roughness projections. Therefore roughness effects are a function of both Reynolds number and roughness characteristics. For the "*fully rough regime*", most of the roughness projections extend through the viscous sublayer and bring effects into the overlap layer. The drag is completely caused by form drag and eddy shedding of the roughness projections, whereas viscous effects entirely lose their impacts in this regime. The roughness effects are independent of Reynolds number but are still a function of roughness characteristics.

In those flow regimes, the roughness can be characterised by the non-dimensional roughness height, k^+, which is also called the roughness Reynolds number. The k^+ can be expressed as the ratio of the roughness length scale (k) to the viscous length scale (ν/u_τ):

$$k^+ = \frac{ku_\tau}{\nu} \qquad \textbf{3.30}$$

According to the closed-packed uniform sand grain roughness measurements of Nikuradse (1933), the hydraulically smooth regime ends by $k^+ \approx 5$. Whereas Schultz and Flack (2007) and Langelandsvik *et al*. (2008) reported the boundary value of the hydraulically smooth regime at $k^+ \approx 2.5$ and $k^+ \approx 1.4$, respectively. For the transitionally rough regime, Nikuradse (1933) gave a range of $15 < k^+ < 55$. However, Ligrani and Moffat (1986) indicated that roughness geometry can bring significant impacts on varying the range of the transitionally rough regime. Accordingly, their results showed a wider transitionally rough regime of $5 < k^+ < 70$. Schultz and Flack (2007) defined the range of the transitionally rough regime at $2.5 < k^+ < 25$ which agreed with the results of (Shockling *et al*., 2006) which were $3.5 < k^+ < 30$.

The velocity profile in the turbulent boundary layer of Nikuradse (1933) can be represented as in Equation **3.31** and Equation **3.32** based on the different flow regime (Schlichting, 1979).

$$U_s^+ = \frac{1}{\kappa}\ln y^+ + B \qquad \textbf{3.31}$$

$$U_r^+ = \frac{1}{\kappa}\ln\left(\frac{y}{k_s}\right) + B_R \qquad \textbf{3.32}$$

where k_s is the sand grain size in the Nikuradse (1933) experiment. The von Karman constant, κ and the intercept of the rough wall, B_R are 0.4 and 8.5 respectively, in the Nikuradse (1933) study. The intercept value, B, for a smooth wall is adopted as B = 5.0 according to the Stanford Conference (Kline *et al*., 1969). For velocity profile nearby the rough wall, the distance can be scalled based on the roughness length scale k_s. Therefore, y/k_s is applied into Equation **3.32** for determining the mean velocity profile. Subtracting Equation **3.31** and Equation **3.32,** the roughness function is obtained which indicates a function for the downward shift in velocity due to the roughness.

$$\Delta U^+ = U_s^+ - U_r^+ = \frac{1}{\kappa}\ln k_s^+ + B - B_R \qquad \textbf{3.33}$$

When k_s^+ is less than $e^{\kappa(B-B_R)}$, the roughness function, ΔU^+ is less than zero which means skin friction of the rough wall is lower than that of the smooth wall. For marine applications, there is no surface coated with antifouling that can achieve lower frictional resistance than a smooth surface (McEntee (1916). Therefore, to keep $\Delta U^+ <0$ is not practical. Hama (1954) and Clauser (1954a) found a downward shift on the mean velocity log-law profile when comparing a rough-wall to a smooth-wall under the primary effect of roughness. Therefore, for rough-wall boundary layers, the Equation **3.33** can be rewritten as

$$U^+ = \frac{1}{\kappa}\ln y^+ + B - \Delta U^+ \qquad \textbf{3.34}$$

According to the 'law of the wake', Coles (1956) extended Equation **3.34** to cover both the overlap and outer regions for the rough-wall boundary layer:

$$U^+ = \frac{1}{\kappa}\ln y^+ + B - \Delta U^+ + \frac{2\Pi}{\kappa}\sin^2(\frac{\pi y}{2\delta}) \qquad \textbf{3.35}$$

As shown in **Figure 3.14**, when plotting U^+ versus y^+, the roughness function, ΔU^+, can be observed as a downwards shift in the log-law region.

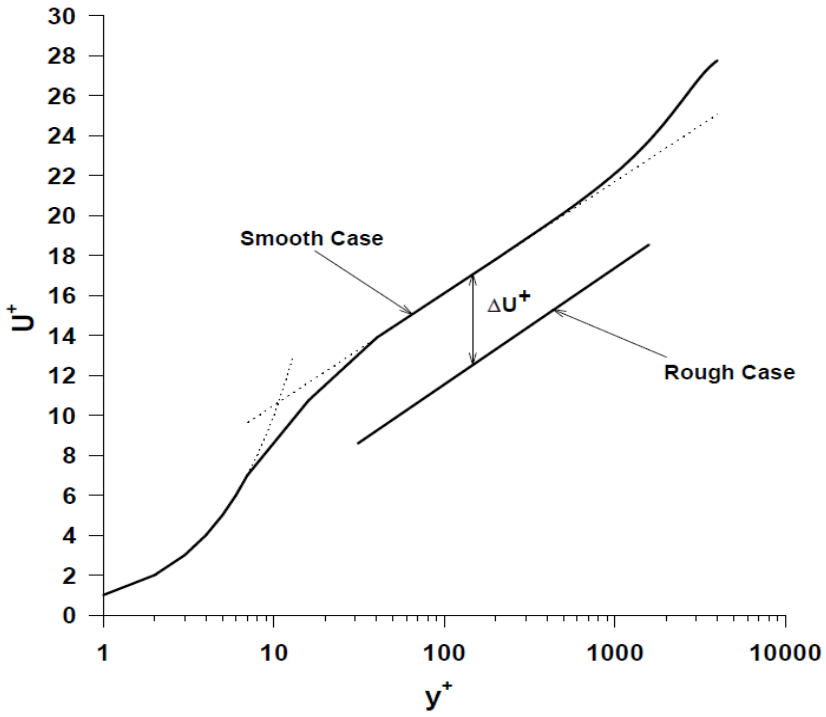

Figure 3.14: The roughness function (Schultz *et al*., 2003)

With regard to the flow characteristics, the roughness can be generally categorized into two types, k-type and d-type roughness. According to Perry *et al*. (1969), if the roughness function, ΔU^+, scales on the measured roughness height, k, the surface roughness is called "k-type" roughness. The classic example of k-type roughness is surface roughness formed by sand grains. For some fluid conditions, such as arrangements of span-wise grooves, the roughness function sometimes does not scale on, k. Perry *et al*. (1969) indicated that if the ratio of the roughness spacing to its height is less than one, stable vortices will be formed between the surface grooves and surface roughness will be "d-type". However, (Leonardi *et al*., 2004) stated that it is not completely correct as the ejection of vortices keeps happening for "d-type" roughness surfaces although they are less intense. The roughness function results of "d-type" roughness are found to scale on other, outer length scales, such as the pipe diameter, d, in pipe flow or the boundary thickness, δ, in a zero-pressure gradient boundary layer (Raupach *et al*., 1991).

3.4 Experimental Determination of Roughness Functions

Grigson (1990) states that the accurate roughness function determination is important for skin friction predictions of specific surfaces measured over a range of Reynolds numbers. In the present work, based on Granville (1978) and Granville (1987), reviews of two roughness function experimental determination methods are given below. **Section 3.4.1** reviews the

roughness function determination method from velocity profiling measurements over the flat plate, to support the experimental work presented in **Chapter 5**, whereas **Section 3.4.2** discuss the roughness function determination that is used in pipe/channel flow studies, to support the experimental work reported in **Chapter 6** and **Chapter 7**.

According to Granville (1987), the inner law relation, Equation **3.31**, can be rewritten in the form of roughness Reynolds-number mode, as below:

$$U_s^+ = \frac{1}{\kappa}\ln y^+ + B[k^+, T] \qquad \textbf{3.36}$$

where k^+ is roughness Reynolds number, T is texture of roughness, $T = \frac{k}{k_1}, \frac{k_1}{k_2}, \frac{k_2}{k_3}, \ldots k_1, k_2, k_3 \ldots$ are the geometrical description of the irregular rough wall. Therefore, the addition of the overlapping inner logarithmic relation, Equation **3.36**, to the outer logarithmic relation, Equation **3.28**, results in the logarithmic law of friction, which in the Reynolds-number mode can be expressed as:

$$\sigma = \frac{U}{u_\tau} = A\ln\eta + B_1[k^+, T] + B_2 \qquad \textbf{3.37}$$

where σ is a convenient local coefficient of skin friction given from the definitions $\sigma = (\tau_w/\rho\overline{U}^2)^{-0.5}$; η is non-dimensional boundary layer thickness which can be expressed as $\eta = u_\tau\delta/\nu$; A is the slope of the logarithmic velocity law equation (or is equal to $1/\kappa$); B_1 is the intercept of logarithmic velocity law. It has to be noted that B is the value of B_1 only for the smooth surface. B_2 is a velocity-defect factor.

Subsequent roughness function analyses based on the internal flow (turbulent flow channel measurements) or external flow (velocity profile measurements) results require the evaluation of outer-law integrals: I_1, I_2 and I_3 where their functions are given by Granville (1987):

$$I_1 = \int_0^1 \left(\frac{U_e - U}{u_\tau}\right) d\left(\frac{y}{\delta}\right) \qquad \textbf{3.38}$$

$$I_2 = \int_0^1 \left(\frac{U_e - U}{u_\tau}\right)^2 d\left(\frac{y}{\delta}\right) \qquad \textbf{3.39}$$

$$I_3 = \int_0^1 \left(\frac{U_e - U}{u_\tau}\right)\left(\frac{y}{\delta}\right) d\left(\frac{y}{\delta}\right) \qquad \textbf{3.40}$$

where I_1, I_2 and I_3 are constants if the outer law is considered a function of only y/δ right up to the wall (y =0).

3.4.1 Roughness Function Determination by Velocity Profile Method with Displacement Thickness

Based on the work of Hama (1954), Granville (1987) modified the indirect method with displacement thickness to determine the drag characterisation from the velocity profile close to the wall in the logarithmic region. According to Granville (1987), the logarithmic law of friction, Equation **3.37**, can be rewritten as:

$$\sigma = A \ln\left[\left(\frac{U_e \delta^*}{\nu}\right)\left(\frac{\delta}{\delta^*}\right)\frac{1}{\sigma}\right] + B_1 + B_2 \qquad \textbf{3.41}$$

where σ is a convenient local coefficient of skin friction given from the definitions $\sigma = (\tau_w/\rho\overline{U}^2)^{-0.5}$; A is the slope of the logarithmic velocity law which equals $1/\kappa$; δ^* is displacement thickness; B_1 is the intercept of the logarithmic velocity law and B_2 is a velocity-defect factor. By definition:

$$\frac{\delta^*}{\delta} = \frac{1}{\sigma}\int_0^1 \left(1 - \frac{U}{U_e}\right) d\left(\frac{y}{\delta}\right) \qquad \textbf{3.42}$$

Based on Equation **3.38**, therefore, Equation **3.42** can be rewritten as:

$$\frac{\delta^*}{\delta} = \frac{I_1}{\sigma} \qquad \textbf{3.43}$$

According to Granville (1987), the convenient local coefficient of the rough surface can consequently be expressed as:

$$\sigma = \left(\sqrt{\frac{2}{c_f}}\right)_{rough} = A \ln R_{\delta^*} + B + \Delta U^+ + B_2 - A \ln I_1 \qquad \textbf{3.44}$$

where the coefficient of local skin friction $c_f = 2\tau_w/\rho\overline{U}^2$, and the displacement-thickness Reynolds number $R_{\delta^*} = \delta^*\overline{U}/\nu$. For a smooth surface where $\Delta U^+ = 0$

$$\sigma = \left(\sqrt{\frac{2}{c_f}}\right)_{smooth} = A \ln R_{\delta^*} + B + B_2 - A \ln I_1 \qquad \textbf{3.45}$$

For sufficiently high Reynolds numbers and zero pressure gradient, the values of B_2 of smooth-wall and rough-wall are the same. At the same value of R_{δ^*}, for smooth and rough surfaces, the roughness function, ΔU^+ , can be given by the difference between Equations **3.44** and **3.45**, so that:

$$\Delta U^+ = \left(\frac{2}{c_f}\right)^{1/2}_{smooth} - \left(\frac{2}{c_f}\right)^{1/2}_{rough} \qquad \textbf{3.46}$$

According to (Granville, 1987) The associated roughness Reynolds number, k^+, is given by:

$$k^+ = R_{\delta^*}\left(\sqrt{\frac{c_f}{2}}\right)_{rough}\left(\frac{k}{\delta^*}\right) \qquad \textbf{3.47}$$

An alternative displacement thickness method is offered by Johansson (1985). Similar to the Granville (1987) method. However, a correction term is added to equation **3.47** to adjust for differences in Reynolds number, R_{δ^*}, between the smooth and rough surfaces.

$$\Delta U^+ = \left(\frac{2}{c_f}\right)^{1/2}_{smooth} - \left(\frac{2}{c_f}\right)^{\frac{1}{2}}_{rough} - A\left[\ln\left(R_{\delta^* smooth}\right) - \ln\left(R_{\delta^* rough}\right)\right] \qquad \textbf{3.48}$$

3.4.2 Roughness Function Determination for Pipe Flow

The indirect roughness function calculation method was derived by Granville (1987) and Granville (1978) for circular straight pipes which are coated inside with a uniform roughness level. Under fully developed turbulent flow, the pressure drop or the friction loss represented by the wall shear stress, τ_w, could be related to mean flow speed, $\overline{U}$, pipe diameter, D, and the geometrical description of the irregular rough wall, k_1, k_2, k_3… Therefore, the relationship can be expressed as:

$$\tau_w = f[\overline{U}, D, \rho, \nu, k_1, k_2, k_3 \dots] \quad \textbf{3.49}$$

The average velocity, $\overline{U}$, across a circular pipe can be calculated according the relationship below:

$$\pi R^2 \overline{U} = 2\pi \int_0^R U(R-y)dy \quad \textbf{3.50}$$

where R is the inside radius of the pipe. For fully developed pipe flow,

$$\frac{\overline{U}}{u_\tau} = 2\pi \int_0^R \frac{U}{u_\tau}\left(1-\frac{y}{\delta}\right) d\left(\frac{y}{\delta}\right) \quad \textbf{3.51}$$

where $\delta = R = D/2$ in the fully developed turbulent pipe/channel flow. Using the outer law, Equation **3.27**, the Equation **3.51** can be rewritten as:

$$\frac{\overline{U}}{u_\tau} = \sigma - 2\int_0^1 \left(\frac{U_e - U}{u_\tau}\right) d\left(\frac{y}{\delta}\right) + 2\int_0^1 \left(\frac{U_e - U}{u_\tau}\right)\left(\frac{y}{\delta}\right) d\left(\frac{y}{\delta}\right) \quad \textbf{3.52}$$

Or substituting Equation **3.38** and Equation **3.40** into Equation **3.52** which gives:

$$\frac{\overline{U}}{u_\tau} = \sigma - 2I_1 + 2I_3 \quad \textbf{3.53}$$

Substituting for σ from Equation **3.37** into Equation **3.53** yields:

$$\frac{\overline{U}}{u_\tau} = A\ln\eta + B_1 + B_2 - 2I_1 + 2I_3 \quad \textbf{3.54}$$

Moreover, in the pipe/channel flow, the Fanning friction factor, f, is defined as:

$$f = 2\left(\frac{u_\tau}{\overline{U}}\right)^2 = \left(\frac{\tau_w}{0.5\rho\overline{U}^2}\right) \quad \textbf{3.55}$$

and pipe Reynolds number Re_D is defined as:

$$Re_D = \frac{D\overline{U}}{\nu} \quad \textbf{3.56}$$

The Darcy-Weisbach friction factor (or Darcy friction factor) λ may also be used:

$$\lambda = 4f \qquad \textbf{3.57}$$

Then

$$\frac{\overline{U}}{u_\tau} = \sqrt{\frac{2}{f}} \qquad \textbf{3.58}$$

And

$$\eta = \frac{Re_D\sqrt{f}}{\sqrt{8}} \qquad \textbf{3.59}$$

Therefore for a rough surface:

$$\left(\sqrt{\frac{2}{f}}\right)_{rough} = A\ln\left(Re_D\sqrt{f}\right) + \left[B_1 + B_2 - A\ln\sqrt{8} - 2(I_1 - I_3)\right] \qquad \textbf{3.60}$$

and for a smooth surface:

$$\left(\sqrt{\frac{2}{f}}\right)_{smooth} = A\ln\left(Re_D\sqrt{f}\right) + \left[B + B_2 - A\ln\sqrt{8} - 2(I_1 - I_3)\right] \qquad \textbf{3.61}$$

Since B_2 is a velocity-defect factor which varies with a streamwise pressure gradient, it is the same for smooth or rough surfaces under fully developed pipe flow. The roughness function is the difference in skin friction data from the rough and the smooth surfaces when compared at the same $Re_D\sqrt{f}$.

$$\Delta U^+ = B - B_1 = \left(\frac{2}{f}\right)^{1/2}_{smooth} - \left(\frac{2}{f}\right)^{1/2}_{rough} \qquad \textbf{3.62}$$

According to Granville (1987) the associated roughness Reynolds number, k^+, is given by:

$$k^+ = \frac{\sqrt{2}}{2}\left(Re_D\sqrt{f}\right)\left(\frac{k}{2R}\right) \qquad \textbf{3.63}$$

3.5 Experimental Determination of Skin Friction Drag

Section 3.5.1 reviews the roughness function determination method from velocity profiling measurements over a flat plate, with the experimental work presented in **Chapter 5**, whereas **Section 3.5.2** discuss the roughness function determination in pipe/channel flow studies, as reported in **Chapter 6** and **Chapter 7**.

3.5.1 Skin Frictional Drag Determination over the Flat Plate

For practical skin frictional drag determination used in boundary profiling measurements, several methods can be used and reviewed in the following sections..

3.5.1.1 Sublayer Slope Method

The sublayer slope method (or viscous sublayer slope method) is a classical method used for determining the skin frictional drag coefficient, especially for a smooth-wall. Based on Equation **3.20**, the skin frictional coefficient can be directly calculated by using the wall shear stress, τ_w, which can be determined by measuring the velocity gradient in near-wall turbulence.

This method is based on the assumption that the turbulent shear stresses are negligible, and the shear stress is dominated by the viscous stress. Therefore the wall shear stress can be expressed as:

$$\tau_w = \mu \frac{\partial U}{\partial y}\Big|_{y=0} \qquad \textbf{3.64}$$

Even though the sublayer slope is a very straightforward method to calculate the skin frictional drag coefficient, it has limitations in that the viscous sublayer is too thin to measure the near-wall shear stress accurately. It is even harder to measure near a rough-wall as the viscous sublayer may not exist for all-over rough boundaries. Moreover, the effect of gaps, leakage, forces due to pressure gradients and especially misalignment could also lead to the results cannot be accurately measured.

3.5.1.2 Reynolds Stress Methods

According to **Figure 3.12**, the Reynolds stress method depends on the observation made in the constant stress region in the inner part of the boundary layer where the total shear stress is assumed to be only composed of the Reynolds stress (turbulent stress). Accordingly, the friction velocity, u_τ, can be determined as:

$$u_\tau = \sqrt{-\overline{u'v'}} \qquad \textbf{3.65}$$

Schultz and Flack (2007) used the "total stress" concept by summing the viscous and turbulent stress contributions. Therefore, the calculation is carried out at the plateau of the Reynolds shear stress profile, in the overlap region of the boundary layer. The total stress of this constant stress region is equal to the wall shear stress, and the relationship is shown in Equation **3.20**. The friction velocity, u_τ, can then be obtained using the combination of Equations **3.20** and **3.22**.

$$u_\tau = \sqrt{\nu \frac{\partial U}{\partial y} - \overline{u'v'}} \qquad \textbf{3.66}$$

Both the Reynolds stress method and total stress method are practical to work out the skin frictional drag coefficient as they can be carried out at each streamwise measurement position.

3.5.1.3 Inner layer Wall Similarity Techniques of the Clauser method

Clauser (1954a) proposed a similarity profile matching method in the inner region of the turbulent boundary layer for determining the friction velocity. In this method, the overlap region of the zero-pressure-gradient boundary layers over a smooth-wall obeys the "law-of-the-wall". Therefore, restating Equation **3.25** of the log-law as follows:

$$\frac{U}{U_e}\frac{U_e}{u_\tau} = \frac{1}{k}\log\left[\frac{yU_e}{\nu}\right] + \frac{1}{k}\log\left[\frac{u_\tau}{U_e}\right] + B \qquad \textbf{3.67}$$

as shown in Figure 3.15, by plotting U/U_e versus yU_e/ν, a series of curves similar to the Clauser chart can be drawn with different c_f values. The method uses an iterative least-squares optimization procedure to determine c_f, so that the logarithmic region of the measured mean velocity profile fits on the curve of the law-of-the-wall. This method is preferable for finding c_f values from a smooth-wall.

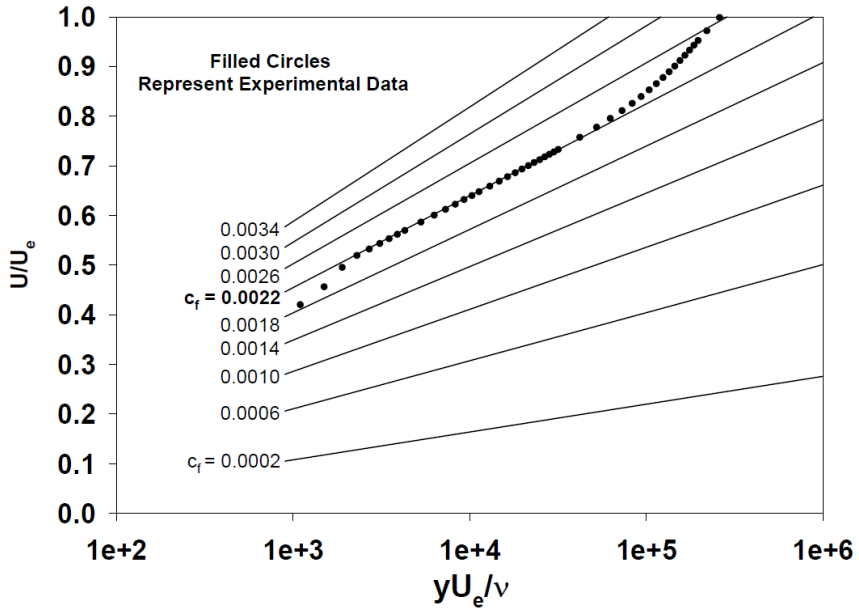

Figure 3.15: Clauser chart for experimental determination of skin frictional drag coefficient (Schultz, 1998)

3.5.1.4 Modified Clauser Method and Log-law Slope Method

Krogstad *et al*. (1992) observed the changing of the wake strength parameter from rough surfaces and reported the varying values of Coles' wake factor Π. Perry and Li (1990) proposed a method that is insensitive to Π value changes. Perry and Li (1990) took Π to be equal to 0.55. Therefore Equation **3.29** for the smooth-wall boundary layer "law of the wake" can be given as:

$$\frac{U}{U_e} = 1 + \frac{1}{k}\frac{u_\tau}{U_e} ln \frac{y}{\delta^*} + \frac{1}{k}\frac{u_\tau}{U_e} ln \frac{u_\tau}{U_e} + 0.493 \frac{u_\tau}{U_e} \qquad \textbf{3.68}$$

As shown in **Figure 3.16**, by plotting U/U_e versus y/δ^*, a series of curves similar to the Clauser chart can be drawn with different u_τ/U_e values. In the graph, U_1 is the freestream fluid velocity which equals U_e; z is the normal distance to the wall and is equal to y; e is the error in origin and it is represented by ε in the functions below.

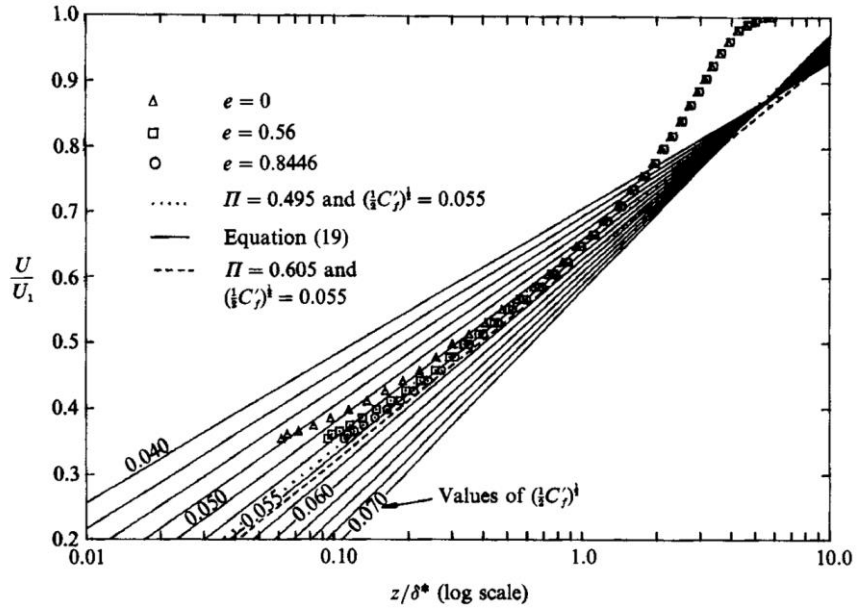

Figure 3.16: Modified Clauser method for determining skin friction over rough walls (Perry and Li, 1990)

Similar to the manner of the Clauser method, this method needs to determine two variables, the friction velocity (u_τ) and the error in the origin (ε) by using an iterative least-squares optimization procedure. The data points $0.1 \leq y/\delta^* \leq 1$ are used and compared with the constant u_τ/U_e lines. This method will be referred to as the modified Clauser method.

Moreover, due to a linear regression of the data points in the log-law region, the slope of this linear regression line can be calculated and used to observe c_f:

$$c_f = 2(\kappa)^2(slope)^2 \qquad \textbf{3.69}$$

Because the roughness function does not affect the slope of the log-law region; this method is valid for rough-walls as along as ε is taken into account.

3.5.1.5 Outer Layer Wall Similarity Techniques

Krogstad *et al*. (1992) and Krogstad and Antonia (1994) proposed another alternative profile matching method using the velocity defect law that allows the optimization of the wake strength, Π, rather than fixing the value. Ignoring the viscous sublayer, or the roughness sublayer in the rough case, according to Krogstad *et al*. (1992), the velocity distribution across the inner and outer regions is given by

$$U^+ = \frac{1}{k}\ln y^+ + B + \Delta U^+ + \frac{2\Pi}{k}\omega(\eta) \qquad \textbf{3.70}$$

where $\omega(\eta)$ is the wake function which defines the effect of the outer flow on the outer part of the boundary layer; $\eta = (y + \varepsilon)/\delta$ is the non-dimensionalized wall coordinate in the outer scale. The Equation **3.70** can be written in the velocity-defect form, as below:

$$U_e{}^+ - U^+ = \frac{2\Pi}{k}[\omega(1) - \omega(\eta')] - \frac{1}{k}ln(\eta') \qquad \textbf{3.71}$$

Moreover, according to the determination of the wake function by Granville (1987), the Π can be optimized using the following expression:

$$\omega(\eta) = (\frac{1}{2\Pi})[(1 + 6\Pi) - (1 + 4\Pi)\eta'](\eta')^2 \qquad \textbf{3.72}$$

Therefore, the strength of the wake, Π, friction velocity, u_τ, and the error in the origin, ε, are observed by using an iterative least-squares optimization procedure.

In **Chapter 5**, the friction velocities and local skin friction drag coefficients were calculated by using three different methods defined as in the following. The total stress method (TS) is from Schultz and Flack (2007). The inner layer wall similarity technique of the modified Clauser method (MC) is based on the study of Perry and Li (1990). The Hama Method (HM), also known as the outer layer wall similarity technique, is based on the work of Krogstad *et al*. (1992) and Krogstad and Antonia (1994).

3.5.2 Skin Frictional Drag Determination from the Pressure Drop Measurements of Turbulent Flow Channel

The pipe measurements of (Darcy, 1857) indicated that the resistance factor, λ, is a function of Reynolds number, R_e. The friction factor curve was also observed to decrease with increasing Reynolds number and the rate of decrease becomes slower for greater relative roughness, k/R (k is the average roughness, and R is the radius of the pipe). As for determining the friction factor, knowledge of the surface roughness and pressure loss through the pipe is required. Therefore, this section discusses how to obtain the friction factor by either reading from a Moody diagram, or using the appropriate functions.

3.5.2.1 Moody Diagram Method

According to Nikuradse (1933)'s resistance law ranges, as reviewed earlier in **Section 3.3.4**, there are three flow regimes: hydraulically smooth, transitionally rough and fully rough regimes. Within the first regime, as the roughness does not affect the resistance, the friction factor curve is a function of the Reynolds number:

$$\lambda = f\left(\frac{64}{R_e}\right) \qquad \textbf{3.73}$$

Within the fully rough regime, the resistance factor is independent of the Reynolds number, and friction factor curves become parallel to the horizontal axis. Nikuradse (1933) derived the relationships between friction factor and relative roughness in this regime (where k_s is the equivalent sand-grain roughness height):

$$\lambda = \frac{1}{\left(1.74 + 2\log\frac{R}{k_s}\right)^2} \qquad \textbf{3.74}$$

Colebrook and White (1937), Colebrook *et al*. (1939) and Moody (1944) extended Nikuradse's (1933) experimental observations and indicated that there was a gradual transition between the smooth and rough resistance laws. The friction factor curves within the transitionally rough regime follow the Colebrook function (Colebrook *et al*., 1939):

$$\frac{1}{\lambda} = -2\log_{10}\left(\frac{k_s/D}{3.7} + \frac{2.51}{R_e\sqrt{f}}\right) \qquad \textbf{3.75}$$

for $R_e < \sim 2300$ and $R_e > \sim 4000$

Accordingly, Moody diagram curves are drawn based on Equations **3.73**, **3.74** and **3.75**. As shown in **Figure 3.17**, the Moody diagram, which is one of the most common fluid engineering tools, relates pressure drop with relative pipe roughness (ratio of the roughness height to the hydraulic pipe diameter).

For general surface roughness cases, however, there are some limitations regarding the application of the Moody diagram. First of all, the roughness length scale, k_s (or ε as shown on the diagram) used in the Moody diagram is called the equivalent sand-grain roughness height which is not a physical measurement of the surface roughness. The k_s of a general surface is

determined according to Nikuradse's (1933) experiments as an equivalent uniform sand roughness height produces the same friction factor of this tested surface in the fully rough regime. Therefore, the k_s value of a tested surface is only valid in the fully rough regime. Moreover, any variations, such as manufacture traces, surface preparation and fouling, can significantly alter the equivalent sand roughness height for a surface (Flack and Schultz, 2014). Accordingly, the hydrodynamic test should be carried out in the fully rough regime with great care before determining the k_s of any surface.

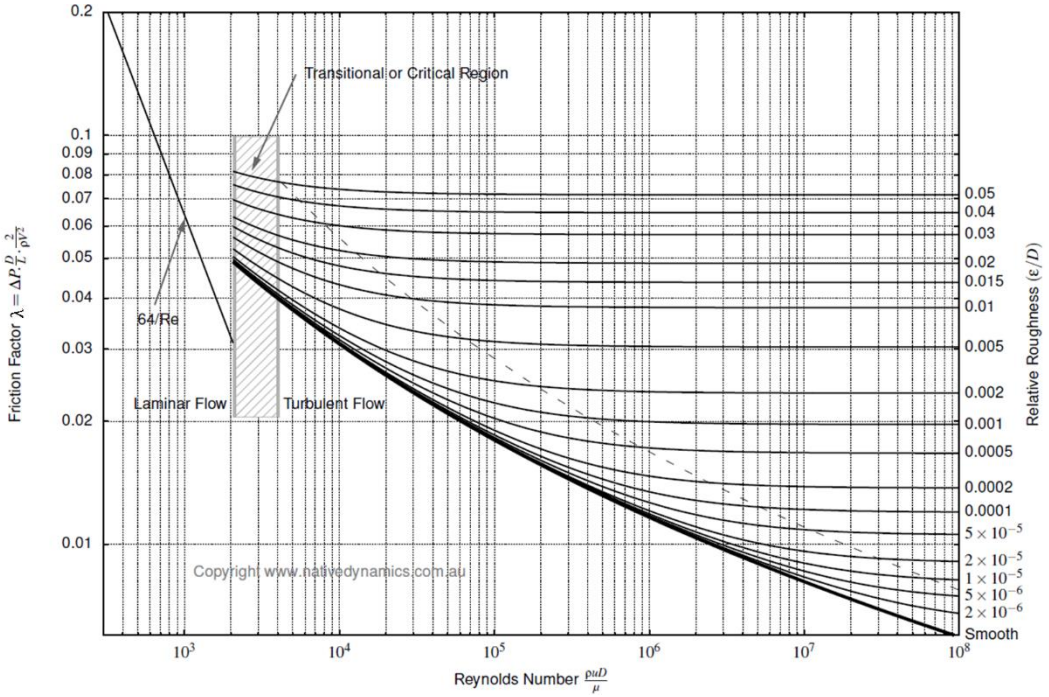

Figure 3.17: Moody Diagram (Moody, 1944)

Also, the Moody diagram implies that all roughness types share similar skin-friction behaviour in the transitionally rough regime. However, as shown in

Figure 3.18, some experiments found that in the transitionally rough regime of the Moody diagram, surfaces did not follow the Colebrook function (Nikuradse, 1933; Schultz and Flack, 2007). Allen *et al.* (2005) and Afzal *et al.* (2013) developed a universal transitional resistance diagram for honed finish pipes, and they found inflectional behaviour in the transitionally rough regime. Therefore, the Moody diagram would not be considered for the frictional drag calculation in the present work as it could not accurately describe the frictional curve at the transitionally rough regime.

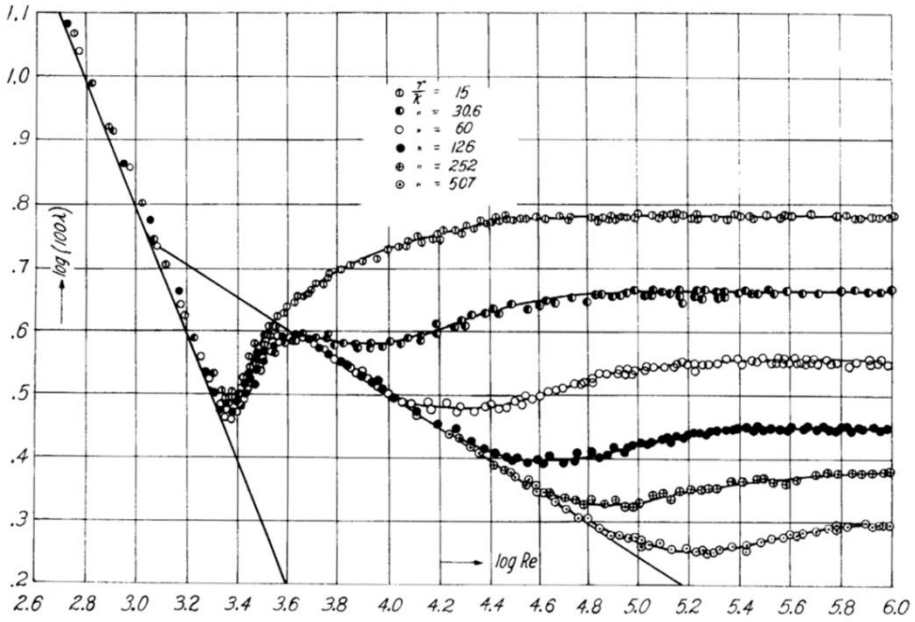

Figure 3.18: Friction factor curves versus Reynolds number (Nikuradse, 1933)

3.5.2.2 Pressure Drop Method

For incompressible fully developed pipe/channel flow, the wall shear stress, τ_w, can be experimentally determined by streamwise pressure drop values, dp at each pressure drop distance, dx. It is calculated as follows:

$$\tau_w = -\frac{D}{2}\frac{dp}{dx} \qquad \textbf{3.76}$$

where D is the hydraulic diameter, p is the static pressure value, x is the streamwise pressure drop distance. For a non-circular flow channel, the hydraulic diameter, D is commonly calculated as follows:

$$D = \frac{4hb}{2(h+b)} = \frac{2hb}{h+b} \qquad \textbf{3.77}$$

where h and b are the dimensions of the inner height and beam of the channel, respectively. The Reynolds number based on the hydraulic diameter, and bulk mean velocity, $\overline{U}$ (or mean velocity) can be expressed as:

$$Re_D = \frac{D\overline{U}}{\nu} \qquad \textbf{3.78}$$

where ν is the kinematic viscosity of the fluid. Accordingly. the skin-friction coefficient, C_f, of

the pipe/channel flow is typically expressed as:

$$C_f = \left(\frac{\tau_w}{0.5\rho\bar{U}^2}\right) = 2\left(\frac{u_\tau}{\bar{U}}\right)^2 \qquad \textbf{3.79}$$

where u_τ is the frictional velocity and ρ is the fluid density, taken as 998 kg/m^3 for fresh water (at the temperature 20 °C).

3.6 Granville's Similarity Law Scaling Procedure

As introduced by Granville (1958) and Granville (1978), the relationship between the roughness function and frictional drag may be determined by extrapolating the skin friction of various rough surfaces to full-scale, based on the experimentally derived roughness functions and boundary layer wall-similarity method. For this research study, the full-scale frictional drag predictions are based on roughness function results from velocity profiling and pressure drop measurements and following the boundary layer similarity law procedure. Schultz (1998) and Demirel (2015) gave detailed explanations of this procedure.

As shown in Figure 3.19, the first step of the procedure is to plot the smooth frictional resistance coefficient, $C_{F\,smooth}$, versus Reynolds number, $\log(R_e)$. For the flat plate prediction, the resistance coefficient for a smooth surface follows the relationship given by Granville (1978):

$$C_{F\,Smooth} = \frac{0.0776}{(\log(R_e) - 1.88)^2} + \frac{60}{R_e} \qquad \textbf{3.80}$$

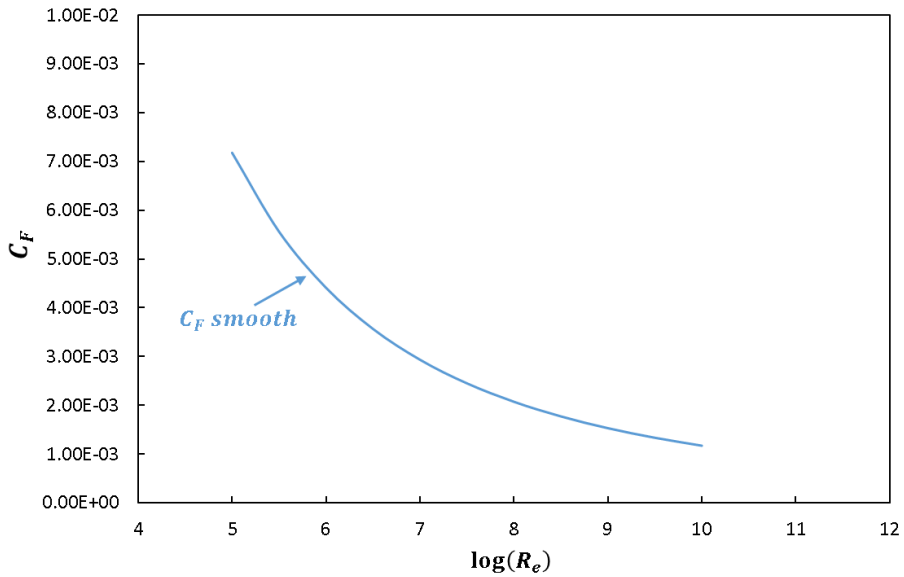

Figure 3.19: Schematic presentation of the first step of Granville's similarity method

The next step is to shift the smooth surface frictional resistance coefficient, $C_{F\,smooth}$ curve by a distance of "$\Delta U^{+}[\ln 10]^{-1}$" in the $\log(R_e)$ direction. The newly formed curve is known as the frictional resistance coefficient curve for the rough surface, $C_{F\,rough}$. The process is shown in **Figure 3.20**.

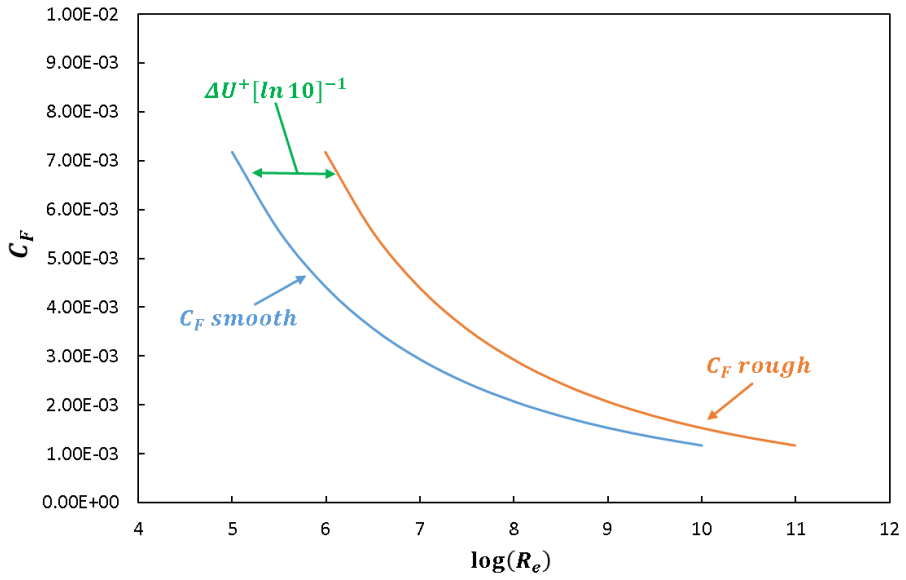

Figure 3.20: Schematic presentation of the second step of Granville's similarity method

The third step is to plot the frictional resistance coefficient line of the experimental flat plate scale, L^{+}_{plate}. Based on the given viscous length scale, ν/u_τ, therefore, the value of L^{+}_{plate} can be determined experimentally using the formula:

$$L^{+}_{plate} = \frac{L_{plate}\,u_\tau}{\nu} \qquad \textbf{3.81}$$

Accordingly, the line of constant L^{+}_{plate} value, shown in **Figure 3.21** can be plotted by solving Equation **3.82** iteratively. The intersection of the two loci represents (L^{+}_{plate} vs. $C_{F\,rough}$) the plate scale resistance.

$$Re = \frac{L^{+}_{plate}}{\left(\sqrt{\frac{C_F}{2}}\left(1-\frac{1}{\kappa}\sqrt{\frac{C_F}{2}}\right)\right)} \qquad \textbf{3.82}$$

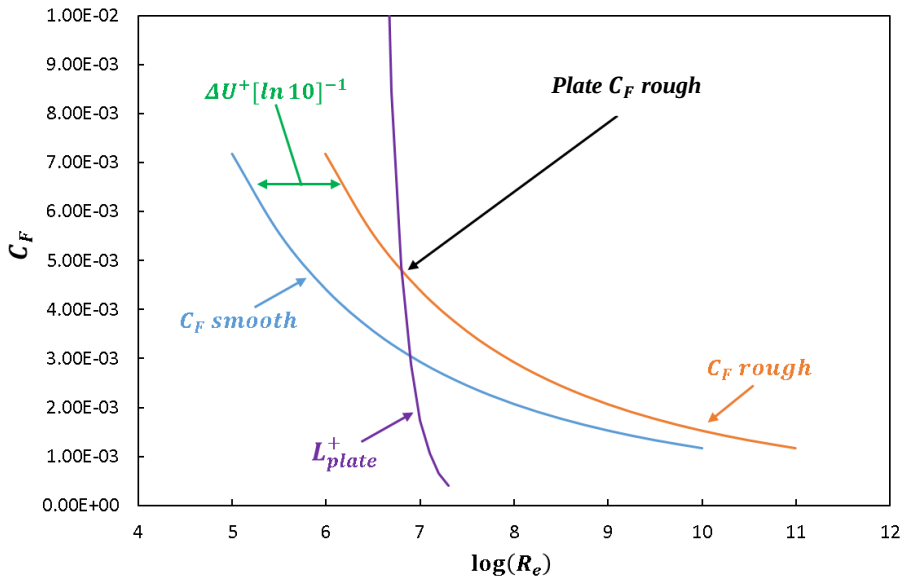

Figure 3.21: Schematic presentation of the third step of Granville's similarity method

The fourth step is to extrapolate to the desired ship scale length, L^+_{ship}, by shifting the line of constant L^+_{plate} at a distance of $\log(L_{ship}/L_{plate})$ along the $\log(R_e)$ axis. The intersection of the two loci represents (L^+_{ship} vs. $C_{F\,rough}$) the full scale resistance. **Figure 3.22** illustrates the whole procedure of Granville's method.

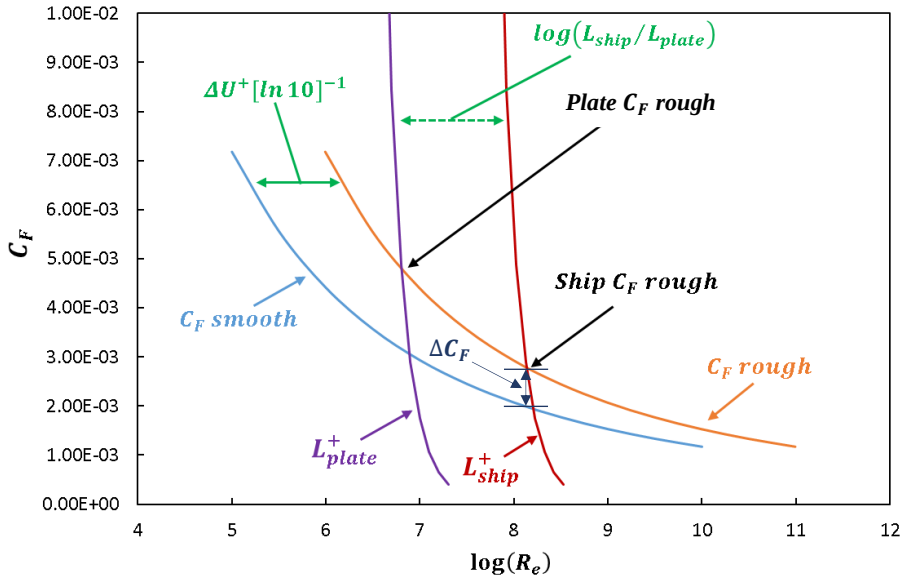

Figure 3.22: Schematic presentation of the fourth step of Granville's similarity method

Moreover, for the same Reynolds number, the difference between the evaluated $C_{F\,smooth}$ and the $C_{F\,rough}$ of the full scale length (using Equation **3.83**) gives the additional resistance coefficient, ΔC_F (%), due to surface roughness changes caused by roughness geometry may

also include fouling.

$$\Delta C_F\,(\%) = \frac{C_{F\,rough} - C_{F\,smooth}}{C_{F\,smooth}} \times 100 \qquad \textbf{3.83}$$

3.7 Chapter Summary

A methodology overview of the surface roughness and the turbulent boundary layer was given in this chapter to provide the basis for this research study, specifically for the tasks presented in Chapter 4 through 8.

The components of the surface roughness have been defined including 2D and 3D aspects. Before carrying out the roughness calculations, one important point is to choose the long or short wavelength cut-offs that are used to filter out the roughness data points from the raw measurement results. The definitions of the practical roughness parameters are presented (**Section 3.2.4**) and used in this research work to evaluate the surface roughness characteristics in **Chapter 4.**

The overall structure of the smooth wall turbulent boundary layers is well-defined according to the literature. However, there still remains a debate about the limits of the onset of the transitionally rough regime, as well as the limit of the fully rough regime. For evaluation of the rough-wall impacts on the turbulent boundary layer, two roughness function experimental determination methods were presented for velocity profiling and pipe/channel flow measurements.

Moreover, the skin friction drag experimental calculation from the rough wall boundary layer velocity profile data can be very straightforward using indirect methods or requires the calculation of a few additional parameters by using the wall similarity methods. The velocity profile fitting methods have generally proved their reliability on smooth surface and regular rough surfaces; however, great care should be taken when using these methods to calculate the skin friction drag of irregular rough surfaces.

For the experimental results described in **Chapter 5**, the friction velocities and local skin friction drag coefficients have been determined using the total stress method (**Section 3.5.1.2**), the modified Clauser method (**Section 3.5.1.4**) and Hama's Method (**Section 3.5.1.5**). Also, for the pipe/channel experiments in **Chapter 6** and **Chapter 7**, the pressure drop method (**Section 3.5.2.2**) can give a direct technique to evaluate the friction drag in pipe/channel flow.

Furthermore, for full-scale frictional drag predictions (**Section 3.6**) based on measurement results, MATLAB was used for developing an in-house code based on Granville's similarity law scaling procedure by employing experimental roughness function. The frictional drag prediction results and their diagrams are discussed in **Chapter 8**.

In the next chapter, the first experimental investigation work: "surface roughness measurement" has been conducted and described. Based on the earlier-described roughness analysis procedure, the roughness characteristics results of all the surface conditions have been presented and discussed.

Chapter 4 Surface Roughness Measurements

4.1 Introduction

This chapter aims to provide an understanding of the surface roughness along with its characterisation, measurement and analysis for the cuprous oxide particle (Cu_2O) applied surfaces, as well as the biofilm impacts on those surface.

As required by **Objective 3** of the research study (**Section 1.3**) the main tasks of this chapter include:

- To apply and describe the Cu_2O surface condition after coated with different size Cu_2O particles;
- To introduce and describe the "in-service" deployment set-up;
- To examine and compare the impacts of the Cu_2O particle size on the surface roughness characteristics, as well as repeat the experiment when the test surfaces were fouled with different period of biofilm present condition.

During the investigation, there were eight different sizes of Cu_2O particles selected and applied on the Newcastle University (UNEW) standard size test panels. Firstly, the impacts of the various Cu_2O particle sizes on surface roughness characteristics have been systematically investigated by using these test surfaces without any biofilm fouled condition.

For the investigation of the biofilm impacts on Cu_2O surface roughness changes, the standard sized UNEW test panels coated with four specimens (two commercial and two laboratorial specimens) were submerged into the open sea condition. The biofilm was cultivated for a total of six months which included 4.5 months of dynamic/static deployments (within 1.5 increments) at the beginning, and 1.5 months of static deployment later on. During the biofilm development process, the surface roughness characteristic evaluations were conducted by the end of every stage of the biofilm deployment activity.

In this chapter, the presentation of the surface roughness investigation work is organised and presented as follows: **Section 4.2** introduces the optical surface roughness measurement device and the experiment set-up. In **Section 4.3**, all the detailed information about the experiment preparations are presented such as the selection of the Cu_2O sizes, test surface preparation and the instrument for the biofilm cultivation. The essential roughness parameters and the use of Scanning Electronic Microscopy (SEM) as well as the topographies for no fouling and fouled

surfaces are discussed in **Section 4.4**. Finally, this chapter is summarised in **Section 4.5**.

It has to be noted that, the test coatings were purely experimental and the measured roughness values are not equivalent to the roughness values found on ships, which have had multiple coats of paint applied. However, this is the first step in systematically studying the effect of roughness from a single layer of thin paint, and can be used as a reference for newly built ships, which are smoother.

4.2 Roughness Measurement and SEM Scanning Device

For a ship, the frictional resistance is generally the largest part of the total resistance. For a given speed, the frictional resistance is governed by the ship's wetted surface and hull surface roughness (Bertram, 2011). Therefore, it is important to know the roughness of a surface in as much detail as possible before carrying out any hydrodynamic tests. In the current investigation, the surface roughness of the test surfaces was measured using Uniscan's Optical Surface Profiling (OSP) 100A system, which is a non-contact high accuracy topography mapping instrument. The schematic diagram of this device is illustrated in **Figure 4.1**.

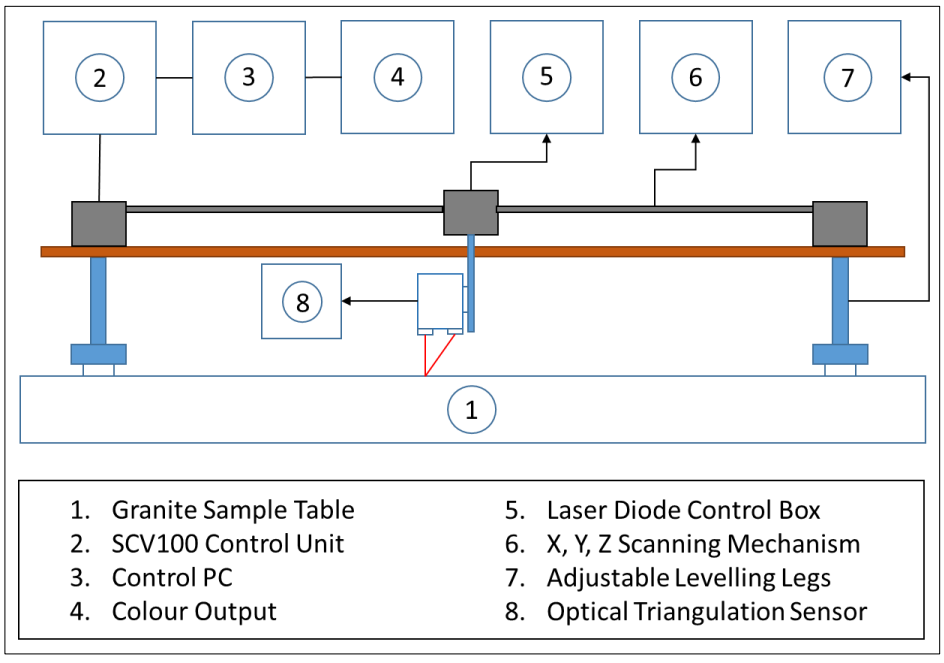

Figure 4.1: OSP100A laser profilometer schematic diagram

The whole OSP100A system consists of a precision x-y-z scanner, an operation bench with three adjustable legs, a granite bed, an optical probe, control electronics and computer control software. The laser probe was adjusted on the two-axis traverse with maximum positioning range of $100\text{mm} \times 90\text{mm}$ $(x \times y)$ with the adjustable scanning speed which ranges from

1 mms^{-1} to 25 mms^{-1} . For the present investigation, the scanning area was 90mm × 60mm (x × y), including 120 linear profiles that were measured at a scanning speed of 25 mms^{-1}.

The overview of the OSP100A is shown in **Figure 4.2**. The statistical analysis of surface roughness was calculated with a 2.5mm cut-off length, which is a commonly used value (Standard ISO 4287, 1997).

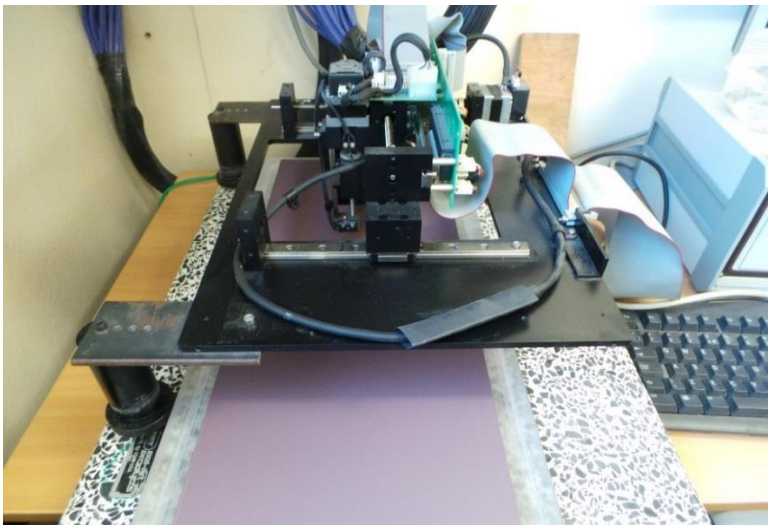

Figure 4.2: Photograph of OSP100A laser profilometer

Through the principle of optical interference profiling, which uses the wave properties of light to compare the optical path difference between a test surface and a reference surface, the OSP 100A uses the wavelength of light as the ruler and obtains accurate surface measurements.

As shown in **Figure 4.3**, inside an optical interference profiler, the laser beam is split by the beam splitter. One-half of the beam is reflected from the test surface and passed through the focal plane of a microscope objective lens, at the same time, the other half of the split beam is reflected from the reference mirror. When the path distance from the beam splitter to the reference mirror is the same as the distance between the beam splitter and the test surface, those two-half split beams are recombined. This creates the (constructive) light and (destructive) dark bands known as interference fringes which occurs in the combined beam wherever the path lengths of the light beams vary. Each transition from light to dark of the interference image represents one-half of a wavelength of difference between the reference path and the test path. Since the flatness of the reference mirror (which is close to the perfect flatness condition) and laser wavelength are known, it is possible to calculate the height differences across a test surface.

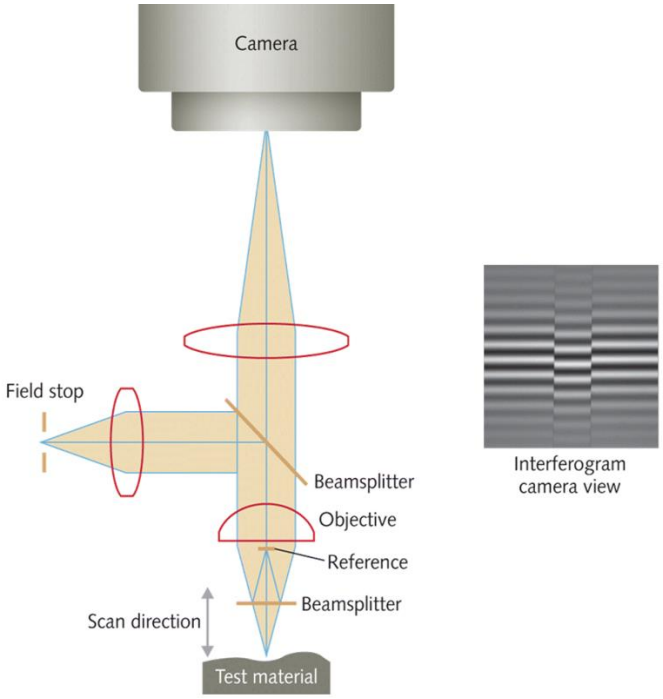

Figure 4.3: The working principle of the laser profilometer (Baysan *et al*., 2018)

Moreover, as shown in **Figure 4.4**, the XL30 ESEM was used for providing high resolution electron images in order to observe coating microstructures from finished surfaces, as well as their changes when surfaces were subsequently fouled with biofilm. The main benefit of the ESEM is that a high vacuum is not required in the microscope chamber. This means that a greater range of materials can be examined on this ESEM without the need for pre-treatment. During the present study, all samples were gold-coated before SEM examination.

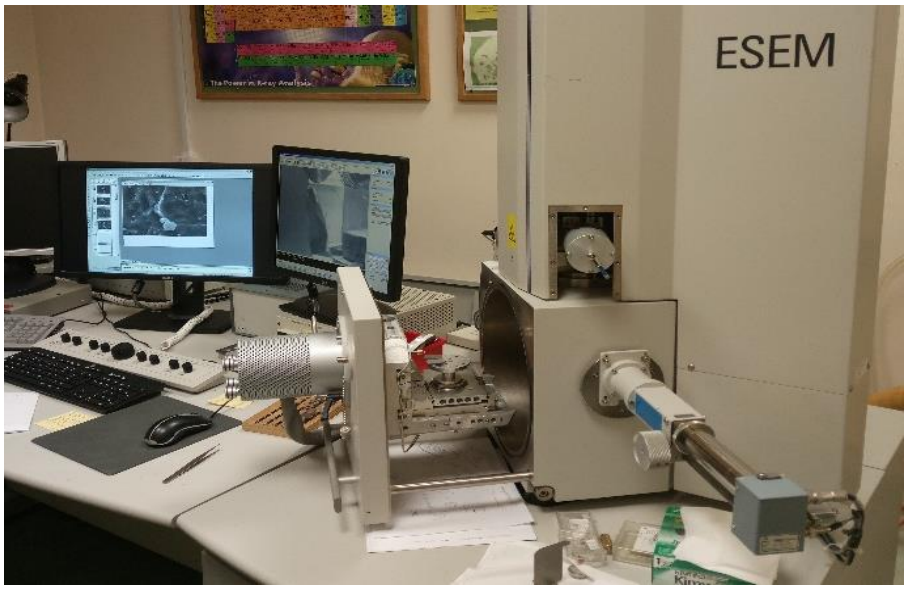

Figure 4.4: Photograph of the XL30 ESEM

4.3 Surface Preparations

The detailed descriptions of the test specimen powders are addressed in **Section 4.3.1**. The preparations of clean (no fouling) and fouled surfaces are introduced separately in **Section 4.3.2** and **Section 4.3.3**. Specifically, further information on the dynamic and static biofilm cultivation methods are provided in the following sub-section (**4.3.1**).

4.3.1 Powder Selection

To investigate the effects of surface roughness characteristics from various sized particles, eight different sized particles of Cu_2O were made by American Chemet Corporation. **Table 4.1** describes the Cu_2O particle diameters at 10% (D_{10}), 50% (D_{50}) and 90% (D_{90}) in the cumulative distribution, along with Cu_2O particle weight content (%) of each type of powder. In this research, these cuprous oxide particles are named hereafter as C2, C7, C12, C17, C25, C60, C100 and C250, where n in Cn stands for the rounded up value of the corresponding D_{50} in the cumulative distribution. It has to be noted that these eight specimens included three commercial products (C7, C12 and C17) and five experimental products (C2, C25, C60, C100 and C250).

Table 4.1: Statistical description of Cu_2O powder

Powder	D_{10} (μm)	D_{50} (μm)	D_{90} (μm)	Cu_2O (%)
C2	0.7	1.4	2.5	>95
C7	4	7	12	>95
C12	5	12	23	>95
C17	10	17	25	>95
C25	11	25	57	>95
C60	32	61	89	>95
C100	40	97	170	>95
C250	190	246	366	>95

From **Figure 4.5** it can be observed that the powder containing smaller size particles, i.e. D_{50}=2, appears as a bright orange colour. As the average particle size increased, the powder colour turned darker, from purple (i.e. D_{50}=17) to completely black (i.e. $D_{50}\geq25\mu m$). Due to the relationship between particle size and light wavelength, the larger size particles can absorb longer wavelengths which results in the powder containing larger size particles looking darker. For the powder status, in **Figure 4.5**(**a**) and (**b**), the specimen C2 and C7 have more powder caking than the larger size specimens, i.e. C12 (**Figure 4.5**(**c**)) and C17 (**Figure 4.5**(**d**)). For specimen particle sizes larger than $D_{50}\geq25\mu m$, the particles do not aggregate with one another.

(**a**). Specimen C2

(**b**). Specimen C7

(**c**). Specimen C12

(**d**). Specimen C17

(**e**). Specimen C25

(**f**). Specimen C60

(**g**). Specimen C100

(**h**). Specimen C250

Figure 4.5 (a)−(h): Tested cuprous oxide particle specimens

The microstructure of the test surfaces was evaluated using SEM. **Figure 4.6** gives SEM views

for tested specimens (i.e. C2−C250) along with their magnification ratio (i.e. 5000×, 1500×, 1000×, 800×, 200× and 100×).

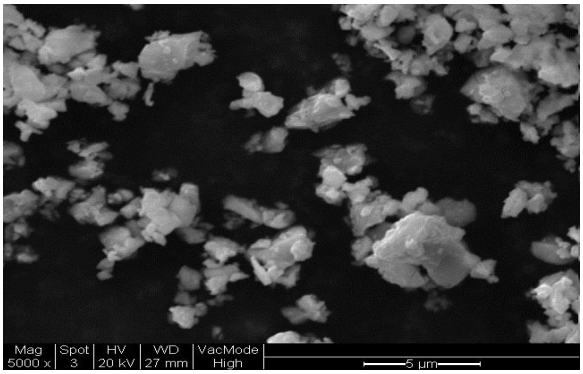

(**a**). Specimen C2 (5000× magnification)

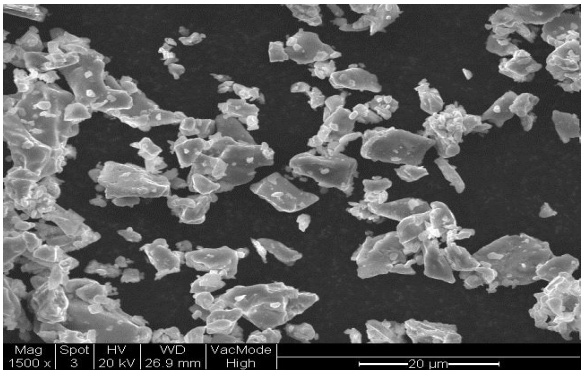

(**b**). Specimen C7 (1500× magnification)

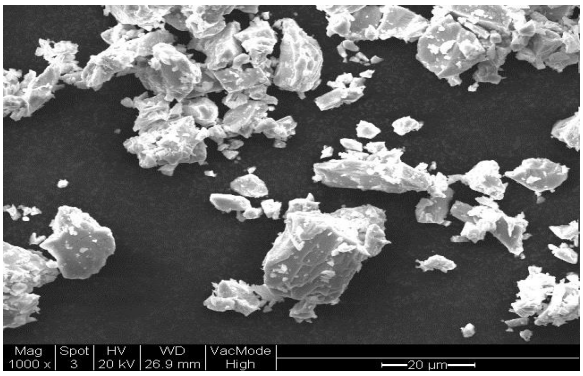

(**c**). Specimen C12 (1000× magnification)

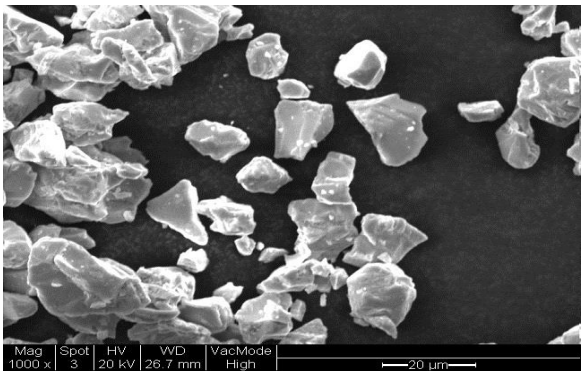

(**d**). Specimen C17 (1000× magnification)

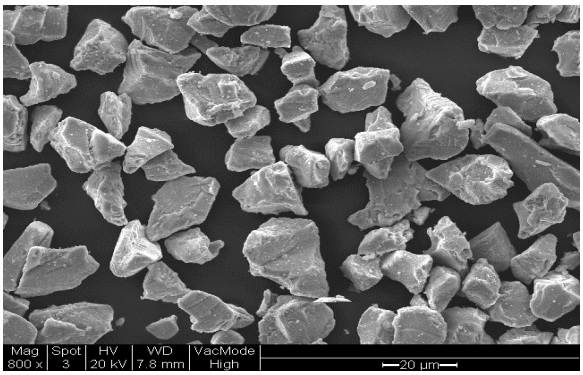

(**e**). Specimen C25 (800× magnification)

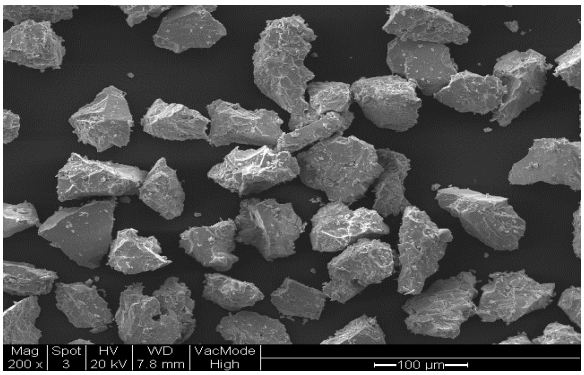

(**f**). Specimen C60 (200× magnification)

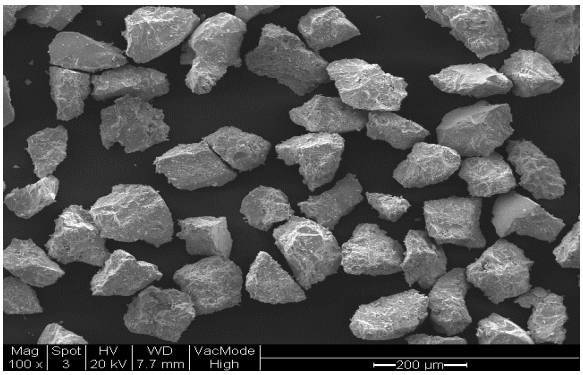

(**g**). Specimen C100 (100× magnification)

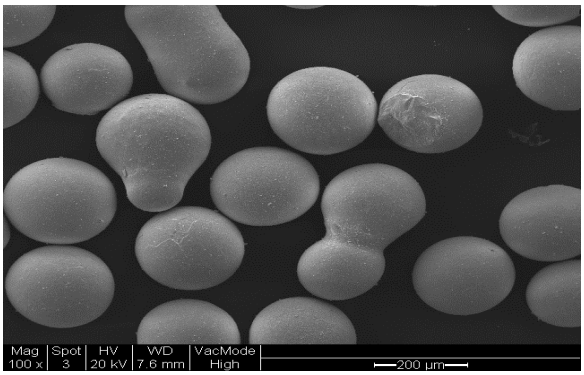

(**h**). Specimen C250 (100× magnification)

Figure 4.6 (a)−(h): SEM top-view of the test surfaces coated with Cu_2O

For the smallest size particles, the majority of specimen C2 particles were agglomerated together and this can be clearly identified in **Figure 4.6**(**a**). **Figure 4.6**(**b**) shows that most of the C7 particles appeared flake shaped and mixed with a few smaller agglomerated particles which were scattered among them. From **Figure 4.6**(**a**) to **Figure 4.6**(**h**), it can be seen that with the particle size increases, each irregular particle can be expressly observed.

4.3.2 Clean (Unfouled) Panel Preparations

The AF coatings were applied on Newcastle University's standard acrylic flat testing panels (as shown in **Figure 4.7** with air-assisted spray application.

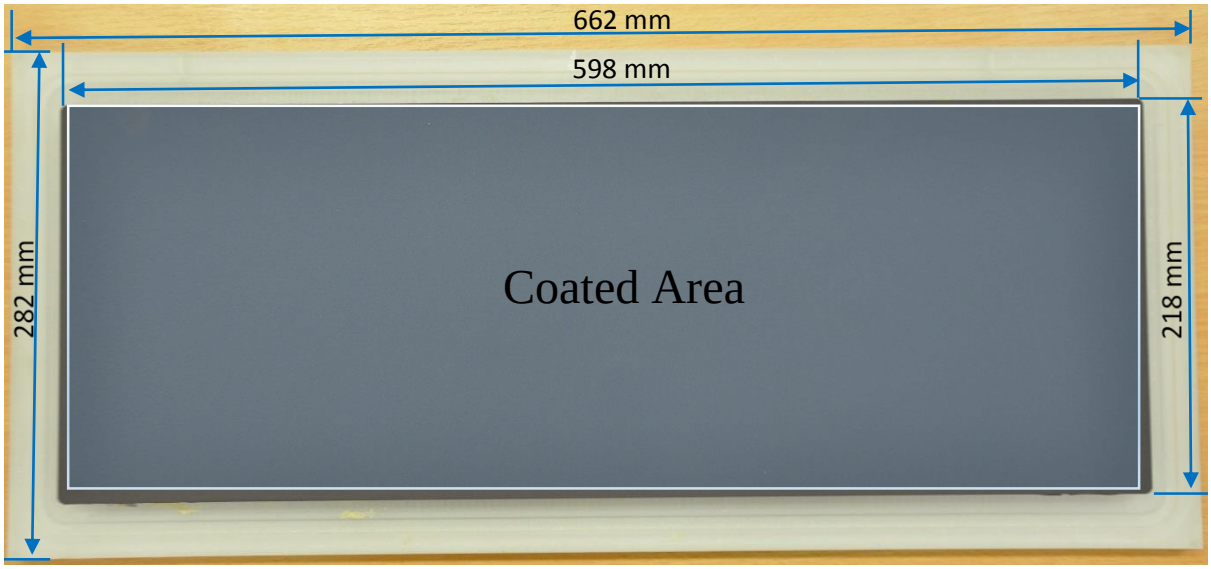

Figure 4.7: The locations of data collection lines on the actual coated standard panels

Before the application, all panels were hung on a metal framework with copper wire to let the panels stand vertically. To allow use of SEM to analyse the coatings' microstructure in more detail, microscope slides were prepared for each testing specimen as well. These microscope slides were placed beside the test panels so that the application of the surfaces could be processed together keeping the surface condition as similar as possible (**Figure 4.8**(**a**) and (**b**)).

(**a**). Coated test panels

(**b**). Coated microscope slides

(**c**). Process of spraying heavier particles on a test panel

Figure 4.8 (**a**)−(**c**)**:** Unfouled test surface preparation

The AF matrix was formulated with 75% cuprous oxide particles and 25% VC17M Extra-Part B. The VC17M Extra-Part B is formulated with a fluoro microadditive, which uses a volatile solvent as a carrier. Once it is mixed with antifuoling pigments and applied on a substrate surface, an extra strong thin film can be curing quickly. The reason why VC17M Extra-Part B was chosen as a binder material for this investigation was that only an extremely thin layer would remain after drying out. The dry binder film could block the original surface roughness characteristics. However VC17M Extra-Part B can eliminate this issue.

The applications were carried out during the winter time (December to January), with local average temperature and humidity changed from 3 °C − 7 °C and 84% − 86%, respectively. The paint applications were carried out in a closed paint workshop which had installed a good ventilation system. The technician held the spray gun and kept about 0.3 metres distance between the panel coating area and the gun nozzle. There were five rounds required, and each round included three repeats. Each repeat means continuously spraying from left-to-right and then from top-to-bottom. A 15-minute gap was requested between each application round in case over-application of paint in a short time resulted in the coating running. It has to be noted that specimen C60, C100 and C250 were larger and heavier particles which caused the spray gun pressure not to disperse or even deliver them fully. Instead of hanging vertically, for those specimens, the panels were placed on the ground with the coated area face up (**Figure 4.8**(**c**)). There were two duplications of each particle size. Finally, all of the finished panels were stored in a cool ventilated location for a minimum of 24 hours.

Therefore the finished dry film (20~150μm in thickness) consisted mainly of cuprous oxide particles, >90% by weight. The strength and insolubility of the matrix enabled the AF coating to sustain the slime growth during deployment and while tested under high water flow Reynolds number. Furthermore, as the dry AF coating contains over 90% cuprous oxide, it can correspond to a hypothetical surface of pure cuprous oxide (Carlton, 1998). It should be noted that these coatings were purely experimental, and not at all similar to commercially available antifoulings. Commercial antifoulings generally have a cuprous oxide content of < 50% (dry film weight) and are applied by airless spray at film thicknesses well in excess of 100 microns. **Figure 4.9** shows all of the specimen surfaces with a photograph area of 90mm×60mm (which corresponds to the roughness evaluation area).

After the application, the particle coagulation was observed with C2 and C7 and resulted in unexpected rougher finished surface condition. With the suspicion that external interference factors, such as human impacts (e.g. spraying speed and distance to the panels when doing the hand spray application), powder application device and the environmental influence (mainly humidity), have caused particle coagulation to be happened, therefore, the coatings from the 1st experiments were removed from the tested surfaces and recoated with the same size specimens while minimising these external interference factors. Therefore, the impacts from different particle sizes could be systematically studied by comparing the results from the two sets of experiments.

A large number of aggregated particles can be visually observed on the specimen C2 surfaces (**Figure 4.9** (**a**) and (**b**)) from both the 1st and the 2nd application. Compared to C2, the specimen C7 can be seen to have a better dispersion into the binder, without agglomeration. As a result, an improved surface for C7 in the 2nd application (**Figure 4.9** (**d**)) was achieved.

Compared with the surface conditions coated with smallest size particles, specimen C12 and C17 formed smoother surfaces without agglomerations. There was only imperceptible roughness, and waviness observed on surfaces coated with C25 and C60. In comparison, for surfaces consisting of larger size particles, i.e. C250, the cured surfaces became more obviously rougher.

(**a**). C2 surface 1st application

(**b**). C2 surface 2nd application

(**c**). C7 surface 1st application

(**d**). C7 surface 2nd application

(**e**). C12 surface

(**f**). C17 surface

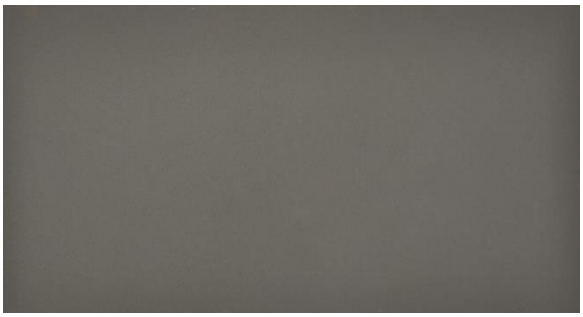

(**g**). C25 surface

(**h**). C60 surface

(**i**). C100 surface

(**j**). C250surface

Figure 4.9 (**a**)−(**j**)**:** Panels in no fouling condition (90mm × 60mm each square)

4.3.3 Fouled Panel Preparations

For the fouling tests, four different specimens were selected: two commercial products (C12 and C17) and two laboratory experimental products (C25 and C60). The setup of the dynamic growth condition is introduced in **Section 3.3.3.1**. The static condition for cultivating the biofilm is introduced in **Section 3.3.3.2**. Also, the deployment setup for the microscope slides which was used for the SEM observation is discussed in **Section 3.3.3.3**.

3.3.3.1 Dynamic Deployment of Test Panels (on Research Vessel: The Princess Royal)

To have biofilm develop naturally on the UNEW test panels under "in-service" conditions, a detachable fin structural system was designed and manufactured (Atlar *et al*., 2015b; Atlar *et al*., 2015c) in-house. This fin structural system is a field-based natural biofilm collection device which is a twin strut arrangement carrying the UNEW standard test panels and fitted to the UNEW catamaran research vessel, *The Princess Royal*. The twin strut system allows a maximum of eight standard test panels to be attached at the same time, namely two panels on each side of the strut, as illustrated in **Figure 4.10**. Further photographic records about the fouling deployment work have been provided in the **Appendix A**. Considering the operational direction of the vessel, to ensure the same fouling pattern development, the slots for holding the test panels are horizontally oriented on the struts making the test panels' longitudinal axes parallel to the vessel's longitudinal axis. Approximately a 0.30m depth of submergence from the top of the upper panels is kept (Atlar *et al*., 2015a) to ensure that there is sufficient depth of water and the test panels are fully submerged (wet) under all static and dynamic conditions (when the vessel is stationary and underway, respectively). During the current investigation, the static and dynamic conditions represented about 85% and 15% of the total vessel activities respectively. Test panels coated with specimens C12, C17, C25 and C60, were selected and installed on the twin strut. The reasons for making this selection was partly to have as many commercial products tested as possible with the "well-painted" surfaces, but also due to the limitations of the twin strut capability and the experimental schedule.

Figure 4.10: Panel arrangement along the starboard side of the twin strut

Figure 4.11 shows the arrangement of the twin strut system on The Princess Royal. The research vessel, has a top speed of 22 knots and is berthed and operated around the port of Blyth, on the northeast coast of England (55.1182° N, 1.4960° W) where the sea temperature changed between 6.7 and 15.3 °C on average during the current experiments seasons (autumn to winter).

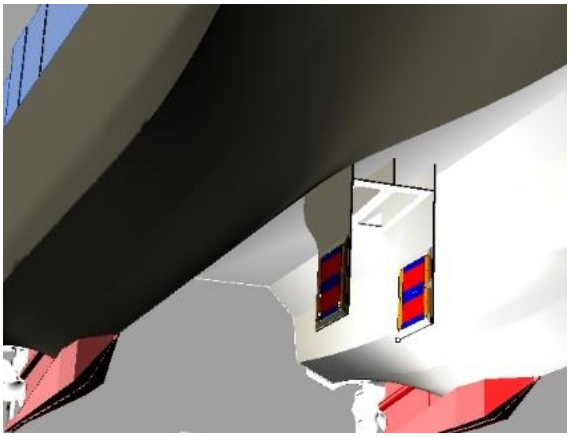

Figure 4.11: The arrangement of twin structural system under the moon pool deck

3.3.3.2 Static Deployment of Test Panels (at the Ship Harbour)

In addition to the vessel dynamic/static deployments, the eight panels were also submerged at the Northumberland Royal Yacht Club for a six-week static deployment. Each pair of panels

was placed back-to-back and fixed in a specially designed PVC framework (**Figure 4.12**(**a**)).

(**a**).Panel framework (**b**).Hanging and safety rope (**c**).Floating Pontoon

Figure 4.12 (**a**)−(**c**)**:** Static deployment arrangements

This specially designed PVC framework would allow panels to have rapid installation/uninstallation. There were four frames fastened along one side of the floating pontoon with polypropylene rope (blue), and thick stainless steel wire with plastic cover (yellow) was used as a safety rope (**Figure 4.12**(**b**)). In case the pontoon edge damaged the rope, the polypropylene rope was covered with a hard tube at each touching point. As shown in **Figure 4.12**(**c**) the floating pontoon was about seven meters away from the jetty, and this prevented the panels from being scratched when driven by the undercurrent. Also, since the framework would unavoidably have a small crosswise swing, 5 metres distance was kept between each fastening point. There was a variation from about 5 metres (low tide) to 9 metres (high tide) depth between the floating pontoon bottom and the seabed. All frameworks were submerged at 2 metres depth which would allow the panels to be close enough to the sea surface to get sufficient sunshine, but also minimised impacts from seabed mud attachment. **Figure 4.13** shows the tested panels after six months of dynamic and static biofilm cultivation deployment. Nevertheless, **Figure 4.13** also illustrates that the drag effect produced came from only a very light (green) slime, and not from big barnacles.

Figure 4.13: Panels in the six month fouled condition

3.3.3.3 Static Deployment for Microscope Slides (Ship Harbour)

To be able to conduct a biofilm study from the specimens, especially during the dynamic deployment, it would be necessary to have microscope slides attached on the vessel along with the test panels. However, there was no extra space on the twin strut to allow the coated microscope slides to be attached. Therefore, the microscope slides were deployed near to the vessel, within the harbour. A cage was made from PVC plates to support the microscope slides.

As shown in **Figure 4.14**(**a**), five concave slots were machined on the top and bottom plates of the cage. A 50mm gap was designed between the slots to make sure sufficient water current could pass through and control the local copper ion concentration. These slots allowed eight plates, with a maximum size of 210mm×297mm×5mm, to be installed at the same time. Along with the test panel arrangement, the microscope slides coated with specimens C12, C17, C25 and C60 were placed inside the cage. The deployment for the cage was the same as for the test panels installed on the fin strut.

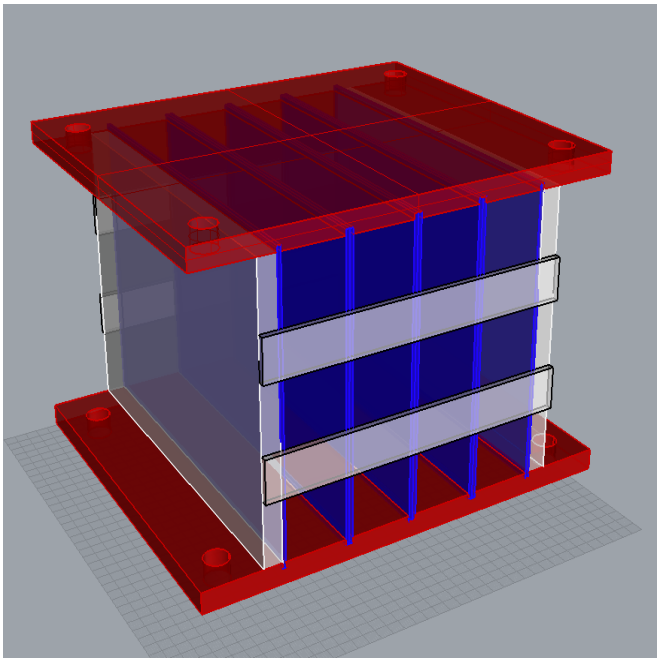

(**a**).The cage design drawing for installation small panels

(**b**).Process of deploying the cage

Figure 4.14 (**a**)−(**b**)**:** Static deployment setup for the microscope slides

Figure 4.14(**b**) shows the process of the deployment under the jetty. Even though the cage was not dynamically moving in the manner of a vessel, it has to be noted that the cage was still subject to the natural dynamic environment which included the changes of weather, waves, temperature, etc. This "static" deployment can be regarded as equivalent to the *Princess Royal* berthed at the port which accounted for nearly 85% of her total activities during the whole test period.

4.4 Roughness Characteristics Results of all Tested Panels

The roughness measurements and photographic results for the clean (no fouling) and fouled conditions are presented and discussed separately. For the clean panels after the 1st and 2nd applications, the statistical analysis for the roughness characteristics are included in **Section 4.4.1**. Meanwhile, the SEM images are shown in **Section 4.4.2**. For fouled panels, the roughness and SEM scanning images are discussed in **Section 4.4.3** and **Section 4.4.4** respectively. It must also be noted that the biofilm test was carried out on the 2nd applications only. Overall, to provide a clear view of the entire experimental arrangements, **Figure 4.15** shows the order of the panels used along with the experiment schemes.

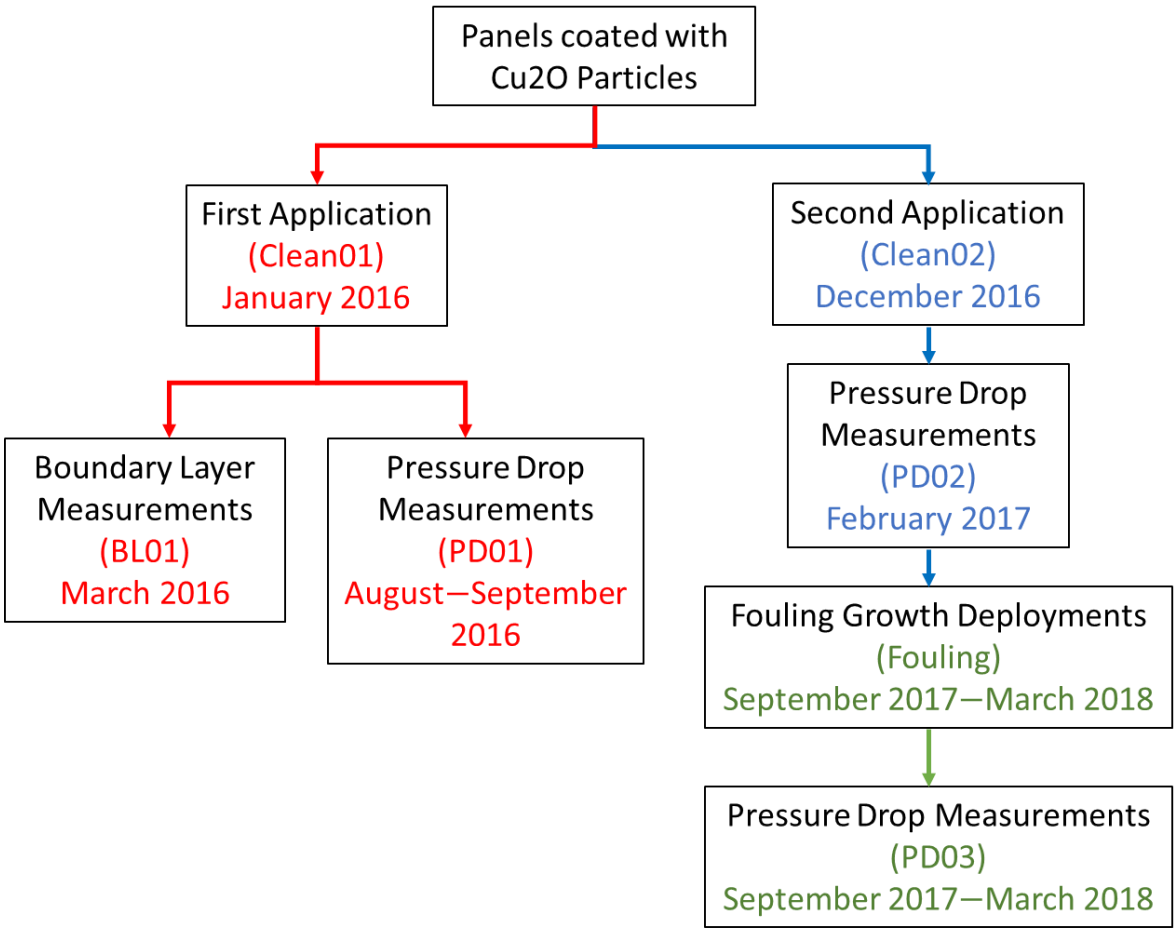

Figure 4.15: The arrangements of tested panels with experimental schemes and timeline

4.4.1 Roughness Parameters for the Clean Condition

In performing the uncertainty analysis for roughness measurements of clean specimens, the 95% precision confidence limits of the results were obtained by multiplying the standard error by the two-tailed t value (t=1.96) for the number of degrees of freedom divided by 120 (Coleman and Steele Jr, 1990).

Table 4.2 shows the analysis results of roughness statistics for all the test surfaces under the above-described conditions. To form a closed channel, two identical coated panels were installed on the top and bottom of the test section slots. In order to distinguish between the roughness statistics from each panel, the top and bottom panels were marked as "A" and "B", respectively. The topography maps of the clean (unfouled) test surfaces have been provided in **Appendix B**, which show further details about the surface conditions.

Table 4.2: Roughness Statistics (uncertainty represents the 95% confidence precision bounds for the measurements)

Specimen	Tests	Surface	R_a (μm)	R_q (μm)	R_t (μm)	R_{sk}	R_{ku}	Δ_a	λ_a (μm)
C2	Test_1	A	9.3±0.2	12.8±0.4	68.1±2.0	0.047±0.005	4.9±0.1	0.089±0.001	630.0±7.7
		B	5.3±0.1	7.3±0.2	39.4±1.3	0.046±0.009	5.1±0.2	0.055±0.000	587.1±8.6
	Test_2	A	8.4±0.2	12.4±0.4	68.2±2.2	0.071±0.006	6.1±0.2	0.085±0.001	592.3±8.9
		B	11.4±0.4	16.1±0.6	80.5±2.9	0.041±0.005	4.9±0.1	0.087±0.001	759.6±12.7
C7	Test_1	A	11.0±0.2	13.6±0.2	61.3±1.0	-0.017±0.002	3.0±0.1	0.078±0.000	875.7±8.1
		B	10.7±0.1	14.8±0.2	76.9±0.9	0.118±0.002	6.0±0.1	0.174±0.001	447.3±7.9
	Test_2	A	2.6±0.0	3.3±0.0	18.5±0.3	-0.049±0.009	3.5±0.1	0.055±0.000	297.0±2.8
		B	2.1±0.0	2.7±0.1	15.9±0.4	-0.022±0.010	3.7±0.1	0.051±0.000	260.1±2.6
C12	Test_1	A	2.4±0.0	3.0±0.0	17.7±0.2	0.022±0.007	3.7±0.1	0.052±0.000	275.8±2.1
		B	2.2±0.0	2.9±0.0	16.7±0.3	0.032±0.007	3.5±0.1	0.056±0.000	252.8±2.4
	Test_2	A	2.4±0.0	3.1±0.1	17.4±0.3	0.028±0.008	3.5±0.1	0.055±0.000	273.6±2.3
		B	2.6±0.0	3.3±0.1	18.5±0.3	0.003±0.009	3.5±0.1	0.057±0.000	284.8±3.3
C17	Test_1	A	2.8±0.0	3.5±0.0	20.0±0.2	0.031±0.006	3.5±0.1	0.064±0.000	264.1±3.6
		B	4.9±0.1	6.4±0.2	34.1±0.9	0.072±0.005	3.9±0.1	0.079±0.000	378.7±5.3
	Test_2	A	3.0±0.0	3.8±0.0	20.6±0.3	0.020±0.006	3.2±0.1	0.063±0.000	294.7±2.2
		B	2.8±0.0	3.5±0.0	19.4±0.3	0.031±0.006	3.3±0.1	0.063±0.000	273.1±1.8
C25	Test_1	A	4.8±0.0	6.1±0.0	32.8±0.3	0.003±0.003	3.3±0.1	0.085±0.000	330.1±2.0
		B	4.6±0.0	5.8±0.0	31.6±0.2	0.009±0.004	3.3±0.0	0.092±0.000	315.3±3.4
	Test_2	A	4.1±0.0	5.2±0.1	28.4±0.4	-0.033±0.006	3.5±0.1	0.078±0.000	326.2±2.6
		B	4.1±0.0	5.2±0.1	28.2±0.4	-0.013±0.006	3.4±0.1	0.078±0.000	327.0±2.5
C60	Test_1	A	6.6±0.1	8.3±0.1	43.7±0.4	0.018±0.003	3.3±0.1	0.097±0.000	427.3±4.5
		B	6.8±0.1	8.7±0.1	47.6±0.5	-0.037±0.003	3.6±0.1	0.121±0.000	364.0±3.8
	Test_2	A	14.6±0.2	18.1±0.2	88.2±0.9	-0.001±0.001	2.8±0.0	0.211±0.001	438.5±4.0
		B	16.1±0.2	19.9±0.2	95.6±1.0	0.001±0.001	2.7±0.0	0.216±0.001	471.3±4.4
C100	Test_1	A	20.7±0.2	26.8±0.3	131.4±1.8	0.052±0.001	4.9±0.1	0.264±0.001	492.5±3.4
		B	18.4±0.1	22.8±0.2	112.7±1.0	0.006±0.001	2.9±0.0	0.247±0.001	468.8±3.3
	Test_2	A	19.0±0.2	23.6±0.2	117.4±1.1	0.001±0.001	2.8±0.0	0.303±0.001	397.8±2.5
		B	19.5±0.2	24.2±0.2	121.6±1.3	-0.007±0.001	2.9±0.0	0.307±0.001	400.3±2.8
C250	Test_1	A	66.5±0.5	83.0±0.6	394.1±3.2	-0.001±0.000	2.9±0.0	0.631±0.002	673.6±8.2
		B	45.8±0.4	58.0±0.4	281.7±2.2	-0.003±0.000	3.1±0.0	0.436±0.002	679.5±8.6
	Test_2	A	65.1±0.7	77.3±0.7	307.5±2.6	0.003±0.000	2.4±0.0	0.461±0.002	902.6±9.2
		B	69.9±0.8	83.9±0.9	341.3±3.6	0.003±0.000	2.5±0.0	0.495±0.003	903.1±9.9

The analysis of roughness parameters for all tested particles indicated that, except for C2 and C7, amplitude parameters (R_a, R_q and R_t) are directly related to the particle size. For C12, C17, C25 and C60 specimens, roughness amplitude increases gradually with an increase in particle size. For particle sizes $D_{50} > 60$ μm (i.e. C100 and C250), the roughness parameters dramatically increased.

Comparing the roughness values between both applications, it can be seen that it was only in the case of the 2nd application of C60 where there was a significant difference, with the

roughness increasing to roughly twice that from the 1st application. However, no visual differences can be observed directly from the C60 surface between the 1st and 2nd applications. It seems likely that the roughness differences from specimen C60 between the 1st and 2nd applications were due to external interfering factors (human impacts, powder application device) and environmental influence. However this still needs to be further investigated with a number of duplications.

It is worth noting here that particle coagulation was observed with C2 and C7, which tended to block the spray nozzle and jam the chamber of the spray gun during the application process. According to the air-assisted spray principle, particles can be delivered only under sufficient air pressure. The minuscule particles, mixed with larger coagulated particles, were pushed out inconsistently and this resulted in pulsed spraying, giving rougher surface textures. As a consequence, even though C2 and C7 were regarded as very small sized particles in the present investigation, additional surface roughness was built up and roughness amplitudes specimens were found to be greater than those for four of the other tested specimens (i.e. C12, C17, C25 and C60). However, it was observed that specimen C7 can be better dispersed into the binder, without agglomeration in the 2nd application. An improved surface for C7 was achieved to have the lowest roughness characteristic.

Figure 4.16 and **Figure 4.17** show the normal distributions of the probability density functions (PDF) of all of the test surfaces after the 1st and 2nd applications, respectively. For an irregular surface profile, the mean average roughness height, R_a, is not a typical parameter to represent the general surface condition. Instead, the total roughness height (such as R_t50) has been widely adopted in the marine industry (Townsin and Dey, 1990; Townsin, 2003). Therefore the total roughness height, R_t, was selected as the roughness scale for the PDF.

When comparing PDF results from the 1st and 2nd applications, according to **Figure 4.16** and **Figure 4.17**, specimen C12 and C25 were found to have more spiky PDF shapes with narrower roughness distribution spans around their average values. In contrast, surfaces formed with larger specimens (i.e. C60, C100 and C250) had lower PDF shapes with larger roughness spans; In particular, C250 had an extremely wide roughness span range. Apart from C2, C7 and C60, most of the PDF results were almost the same between the 1st and 2nd applications, which means that the surface roughness characteristics were constantly distributed by those particles.

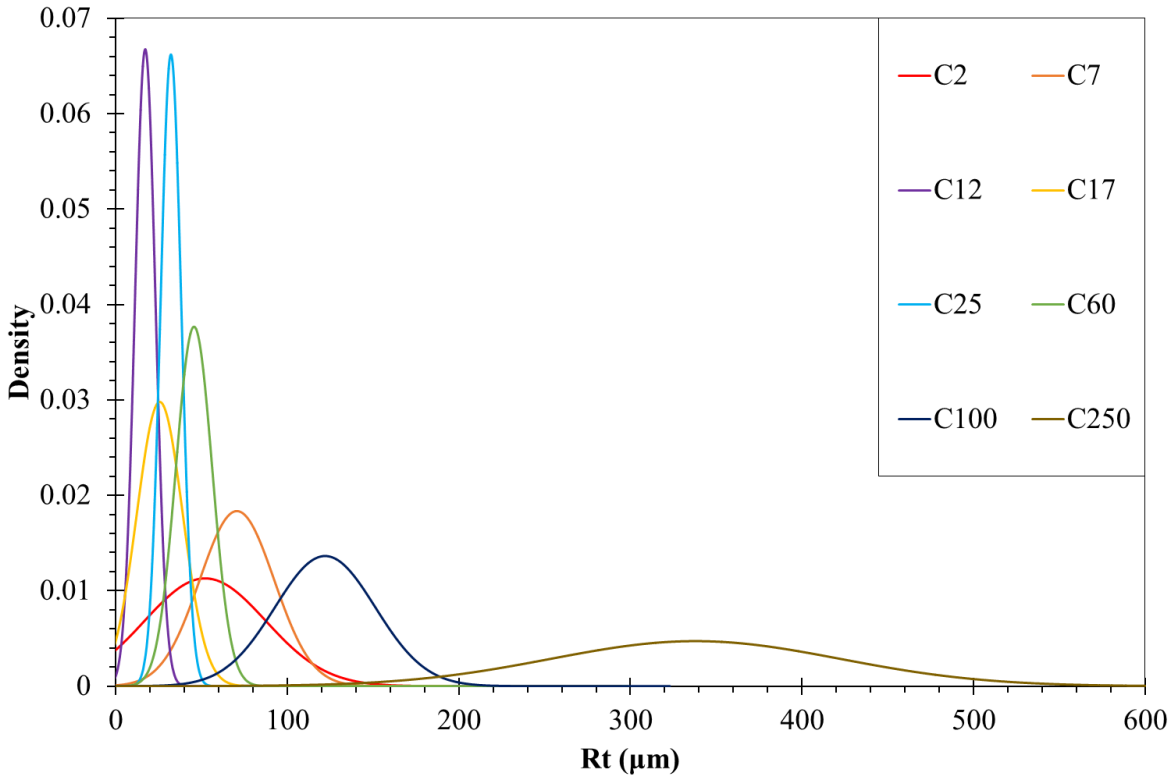

Figure 4.16: Probability density functions (PDF) of the roughness data of all of the 1st applications

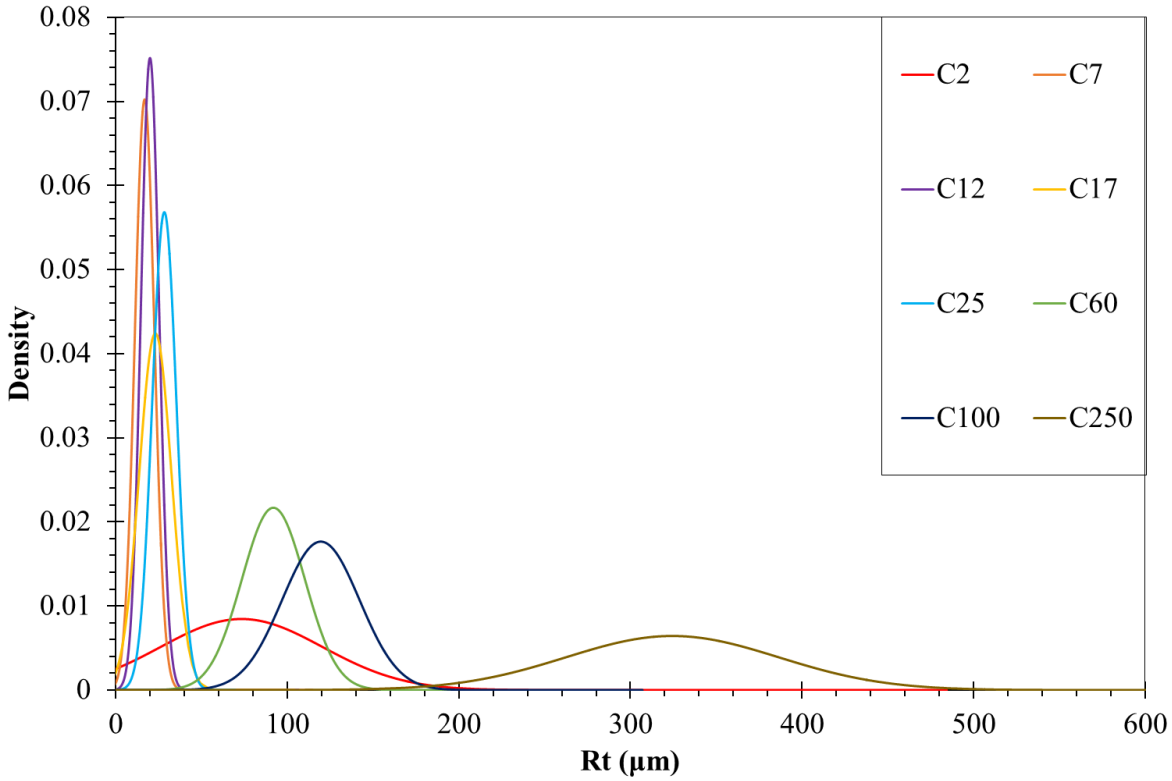

Figure 4.17: Probability density functions (PDF) of the roughness data of all of the 2nd applications

As for C2 and C7, the PDF results of those specimens agreed well with the previous discussion with regard to their particle agglomeration and low finish quality which can indirectly result in a rougher surface and enlarged the roughness span range of the PDF. Another apparent change which happened for specimen C60 should be noted as well. Unlike the case of C2 and C7, there was no C60 particle agglomeration found from either 1st or 2nd applications. However, as was discussed in **Section 4.3.2**, due to particles being heavier and not fully dispersed by the spraying air pressure during the surface preparation process for C60, they caused a locally uneven application. As a consequence, the 2nd application of C60 was rougher than the 1st application.

4.4.2 SEMs and Topography (Clean)

The microstructure of the test surfaces was evaluated using SEM. **Figure 4.18** gives SEM views for surfaces coated with tested specimens (i.e. C2−C250) along with their magnification ratio (i.e. 650×, 200× and 100×).

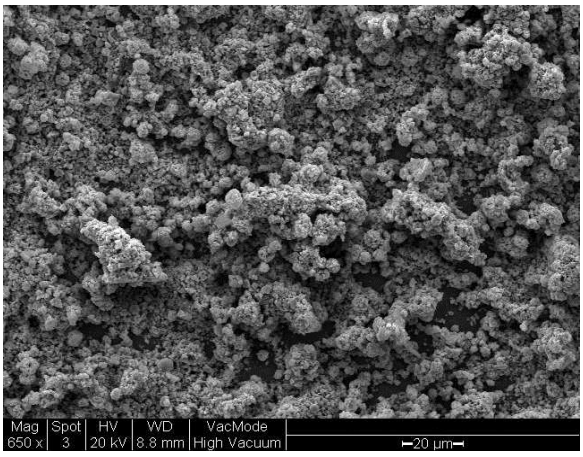

(**a**). C2 surface 1st application (650× magnification)

(**b**). C2 surface 2nd application (650× magnification)

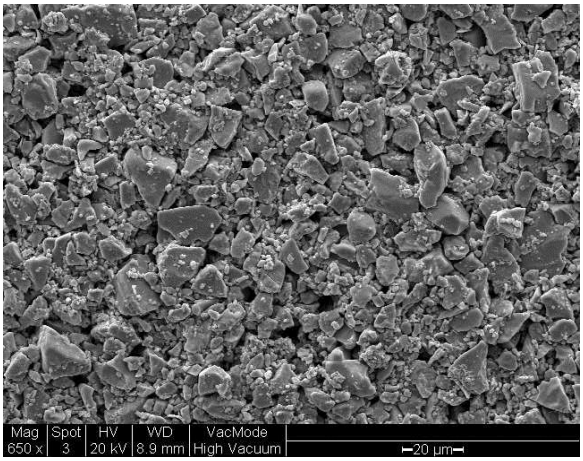

(**c**). C7 surface 1st application (650× magnification)

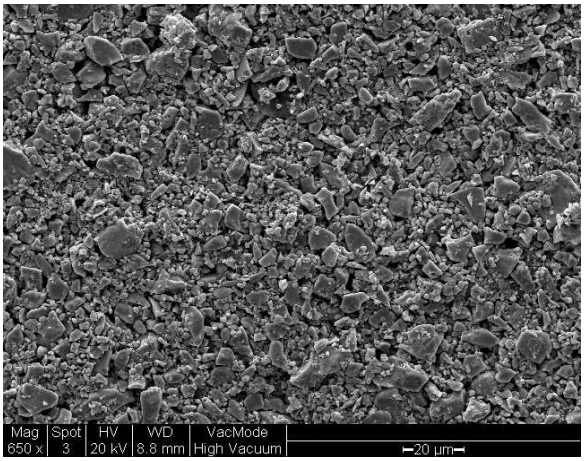

(**d**). C7 surface 2nd application (650× magnification)

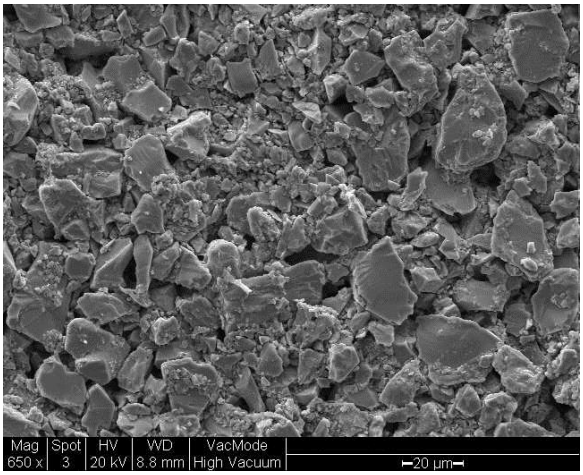

(**e**). C12 surface (650× magnification)

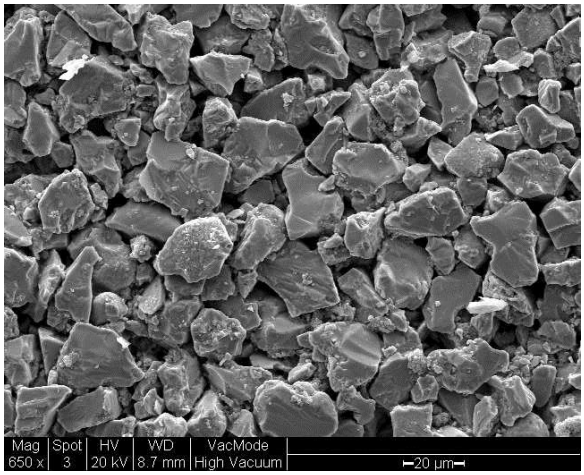

(**f**). C17 surface (650× magnification)

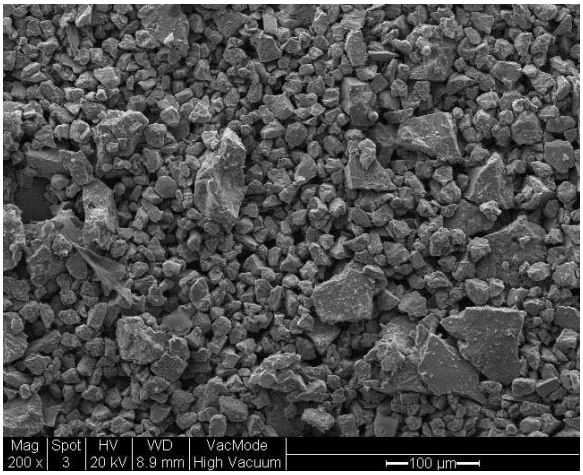

(**g**). C25 surface (200× magnification)

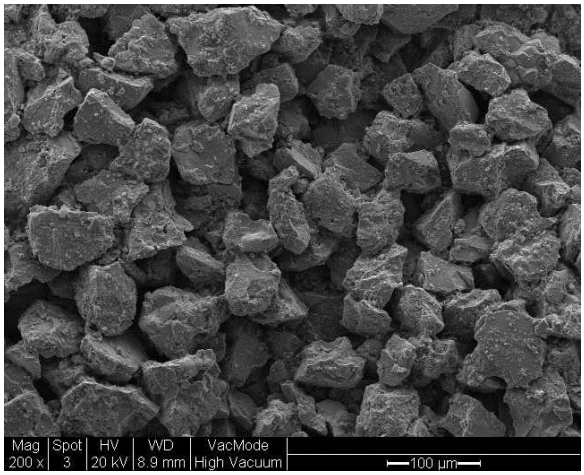

(**h**). C60 surface (200× magnification)

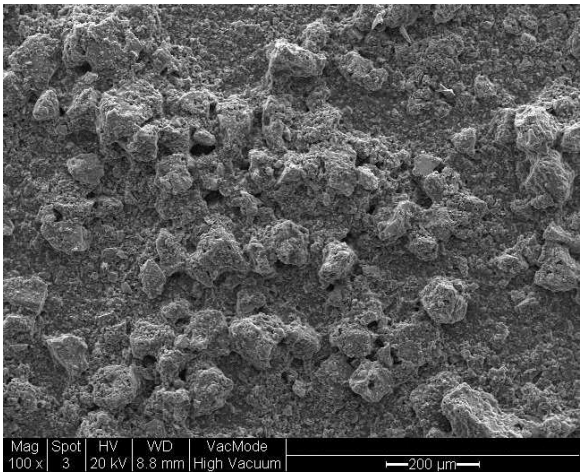

(**i**). C100 surface (100× magnification)

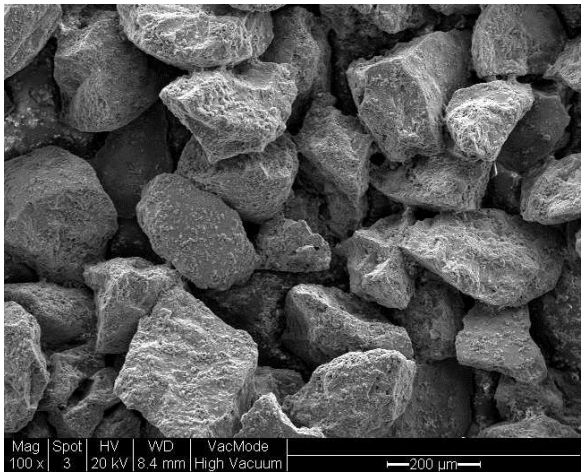

(**j**). C250 surface (100× magnification)

Figure 4.18 (a)−(j): SEM top-view of the test surfaces coated with Cu_2O

In the case of C2, **Figure 4.18** (**a**) shows a critically rough surface with significant "clumping" and wider interspaces between particles in the 1st application compared to the 2nd application (**Figure 4.18** (**b**)).

For the case of C7, the 2nd application condition (**Figure 4.18** (**d**)) compared to the 1st application (**Figure 4.18** (**c**)) shows a slightly higher particle density and smaller spaces between particles. As particle size increases (**Figure 4.18** (**e**), (**f**), (**g**), (**h**), (**i**) and (**j**)) the full contact between particles turns into a partial contact. As a result, wider and deeper gaps are formed, increasing the potential to have rougher waviness height from the surface coated with larger size particles.

The cross-section of the specimens and their magnification ratios (i.e. 1500×, 800×, 650×, 350× and 150×) are presented in **Figure 4.19**.

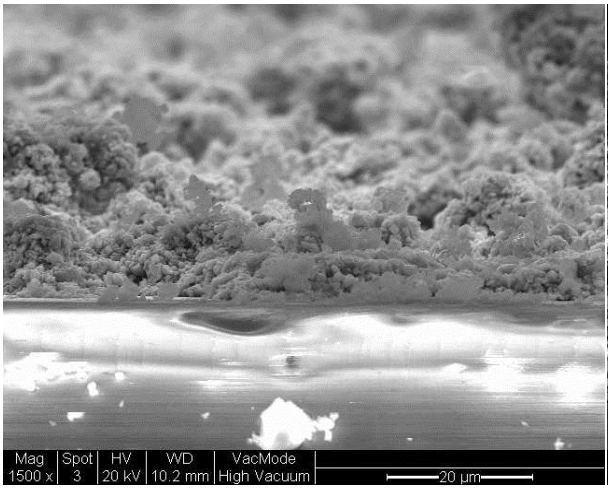

(**a**). C2 surface 1st application (1500× magnification)

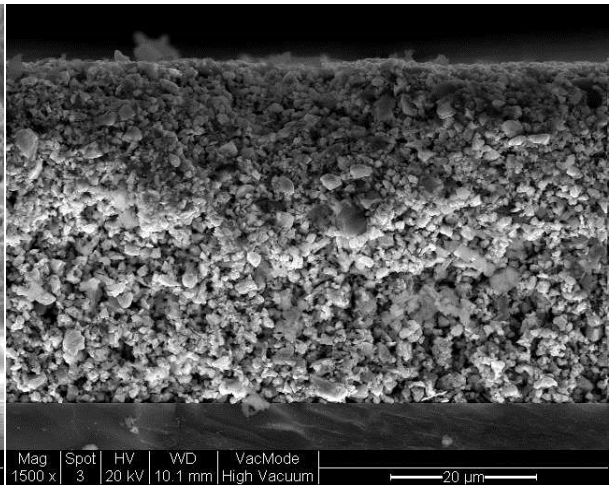

(**b**). C2 surface 2nd application (1500× magnification)

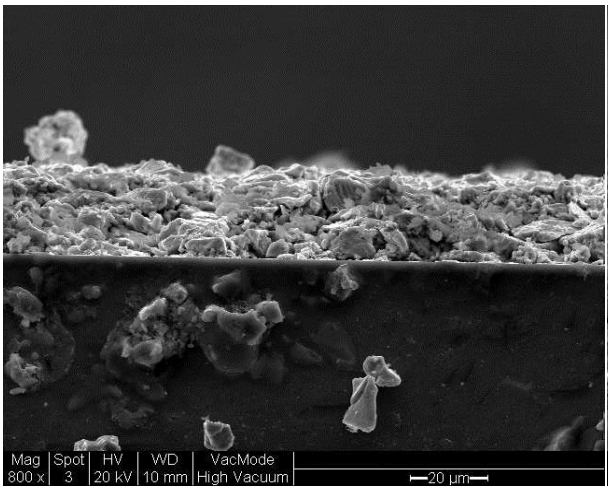

(**c**). C7 surface 1st application (800× magnification)

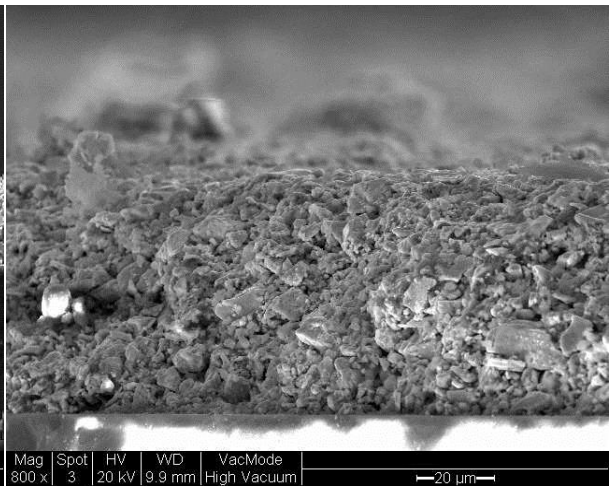

(**d**). C7 surface 2nd application (800× magnification)

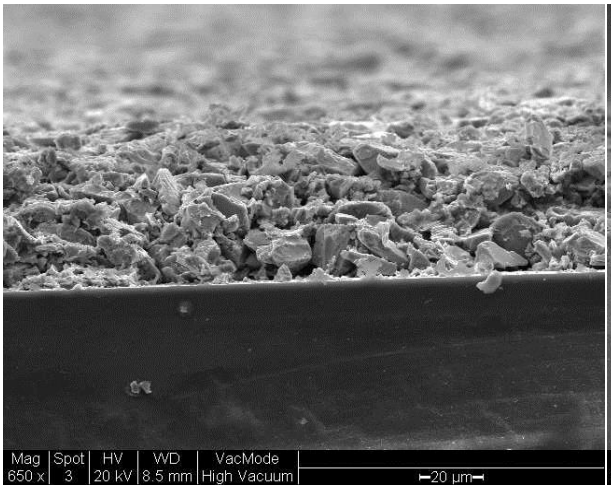

(**e**). C12 surface (650× magnification)

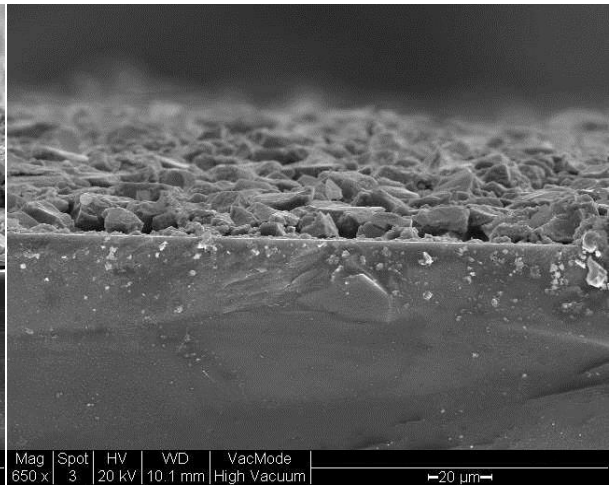

(**f**). C17 surface (650× magnification)

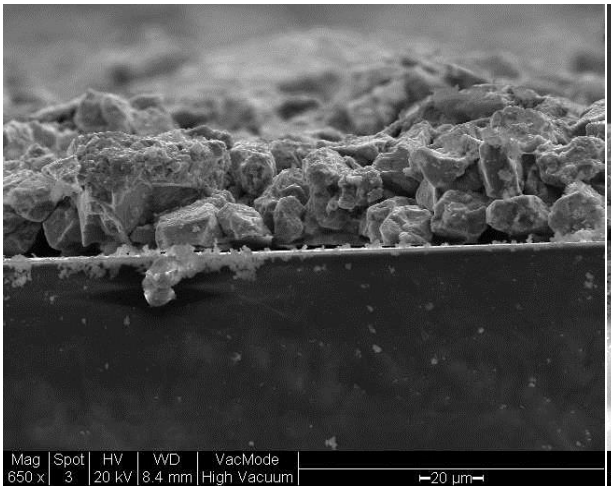

(**g**). C25 surface (650× magnification)

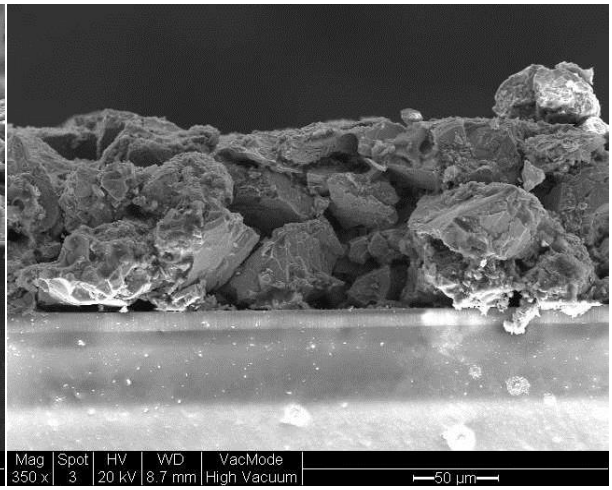

(**h**). C60 surface (350× magnification)

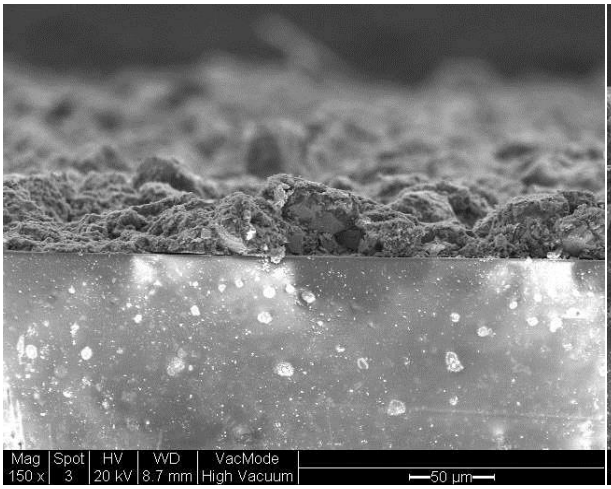

(**i**). C100 surface (150× magnification)

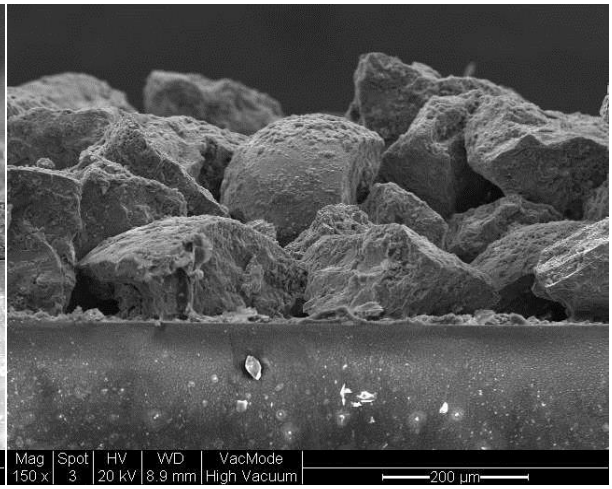

(**j**). C250 surface (150× magnification)

Figure 4.19 (a)−(j): SEM cross-sections of test surfaces covered with Cu_2O

Figure 4.19 (**a**) shows that the 1st application of C2 had a "coral" shape structure which dramatically increased the surface waviness profile. **Figure 4.19** (**b**) shows C2 from the 2nd application with increased layer thickness and a smoother top surface profile. However self-

aggregated materials with loose internal structures can be clearly observed. Surfaces with C7 have a low surface waviness profile. Compared with **Figure 4.19** (**c**), **Figure 4.19** (**d**) shows that C7 had a thicker layer of coating and carried a higher density of particles in the 2nd application. This leads to particles packing more closely and hence fewer interspaces were present. As particle size increases, (**Figure 4.19** (**e**), (**f**), (**g**), (**h**), (**i**) and (**j**)) surfaces become rougher due to the microstructures consisting of larger size specimens, with wider spacing gaps between particles.

4.4.3 Roughness Parameter for the Fouled Condition

In performing the uncertainty analysis for roughness measurements of fouled specimens, the 95% precision confidence for a given data quantity was obtained by multiplying its standard error by the two-tailed t value (t=1.96) for the number of degrees of freedom divided by 120 (Coleman and Steele Jr, 1990). **Table 4.3** shows the analysis results of roughness statistics for all of the test surfaces after the 1.5 months, 3 months, 4.5 months and 6 months biofilm deployments. The topography maps of the biofilm fouled test surfaces have been provided in **Appendix C**, which show further details about the surface conditions.

It has to be noted that, at the beginning of the roughness investigation for these biofilm fouled surface, the measurements were conducted on air dried surfaces. The results indicated that the roughness characteristics had substantially decreased and smoothed compared to their original unfouled condition. However, the higher frictional drag results that were obtained from the subsequent hydrodynamic measurements and proved that the roughness characteristics of dried biofilm surfaces were incorrect. According to the Fratesi *et al.* (2004) whom observed that biofilms appeared to have collapsed and the microstructure flattened after air drying. The roughness characteristics collected from the air dried surfaces cannot be used to describe the roughness characteristics of the wet surfaces. Therefore, the roughness measurements were collected by keeping the test panels immersed in seawater. Moreover, the environmental factors, such as water level and quality, and vibration movement of the water surface, were found to have impacts on the final surface roughness readings as well. Therefore, calibrations of the in-water measurements were carried out with great care by using two reference surfaces whose original surface roughness data had already be recorded. This allowed the fouled surfaces to be measured whenever the in-water calibrations of reference surfaces were similar to their original measurements.

Table 4.3: Roughness Statistics (uncertainty represents the 95% confidence precision bounds for the measurements)

Specimen	Tests	Surface	R_a (μm)	R_q (μm)	R_t (μm)	R_{sk}	R_{ku}	Δ_a	λ_a (μm)
C12	Test_2	A	2.4±0.0	3.1±0.1	17.4±0.3	0.028±0.008	3.5±0.1	0.055±0.000	273.6±2.3
		B	2.6±0.0	3.3±0.1	18.5±0.3	0.003±0.009	3.5±0.1	0.057±0.000	284.8±3.3
	1.5M	A	6.7±0.5	9.2±0.7	52.0±3.3	0.024±0.002	4.1±0.1	0.144±0.001	270.7±2.7
		B	6.5±0.1	8.6±0.2	48.9±1.6	0.023±0.004	3.9±0.2	0.150±0.002	263.5±2.5
	3M	A	8.6±0.1	10.8±0.1	60.0±0.7	-0.010±0.002	3.1±0.0	0.205±0.002	264.7±1.9
		B	8.2±0.1	10.4±0.1	57.1±0.7	-0.009±0.002	3.1±0.0	0.193±0.002	268.5±1.9
	4.5M	A	9.2±0.1	11.5±0.2	60.3±0.9	-0.011±0.002	2.9±0.0	0.186±0.002	312.5±3.9
		B	9.4±0.1	11.8±0.1	62.9±0.9	-0.009±0.002	3.0±0.0	0.200±0.002	298.1±3.4
	6M	A	9.2±0.1	11.5±0.2	63.2±1.1	-0.011±0.002	3.1±0.0	0.209±0.002	277.4±2.8
		B	9.5±0.1	11.9±0.1	64.0±0.9	-0.013±0.002	3.0±0.0	0.208±0.002	286.9±2.6
C17	Test_2	A	3.0±0.0	3.8±0.0	20.6±0.3	0.020±0.006	3.2±0.1	0.063±0.000	294.7±2.2
		B	2.8±0.0	3.5±0.0	19.4±0.3	0.031±0.006	3.3±0.1	0.063±0.000	273.1±1.8
	1.5M	A	5.7±0.4	7.7±0.8	44.6±3.6	0.037±0.004	4.4±0.2	0.131±0.002	264.7±2.9
		B	5.2±0.1	6.7±0.1	38.0±0.7	0.020±0.004	3.5±0.1	0.130±0.001	253.0±1.8
	3M	A	7.6±0.1	9.5±0.1	51.6±0.6	-0.007±0.002	3.0±0.0	0.173±0.001	274.8±2.3
		B	7.6±0.1	9.5±0.1	52.0±0.6	-0.005±0.002	3.0±0.0	0.177±0.001	270.0±2.0
	4.5M	A	8.4±0.1	10.5±0.2	55.6±1.0	-0.009±0.002	3.0±0.1	0.174±0.002	302.4±3.8
		B	8.5±0.1	10.7±0.2	57.4±1.0	-0.009±0.002	3.0±0.0	0.188±0.002	287.1±3.6
	6M	A	8.4±0.1	10.5±0.1	56.5±0.8	-0.010±0.002	3.0±0.0	0.182±0.002	289.6±2.8
		B	8.7±0.1	10.9±0.1	58.0±0.9	-0.007±0.002	3.0±0.1	0.178±0.002	309.0±3.3
C25	Test_2	A	4.1±0.0	5.2±0.1	28.4±0.4	-0.033±0.006	3.5±0.1	0.078±0.000	326.2±2.6
		B	4.1±0.0	5.2±0.1	28.2±0.4	-0.013±0.006	3.4±0.1	0.078±0.000	327.0±2.5
	1.5M	A	6.0±0.2	7.5±0.2	41.8±1.2	0.004±0.001	3.1±0.0	0.143±0.002	261.4±5.9
		B	5.8±0.3	7.5±0.4	41.5±1.7	0.003±0.001	3.1±0.0	0.133±0.002	267.0±6.8
	3M	A	7.7±0.2	9.7±0.2	53.9±1.1	-0.003±0.002	3.2±0.0	0.177±0.001	274.4±5.4
		B	8.1±0.2	10.2±0.3	56.7±1.2	-0.002±0.001	3.2±0.0	0.183±0.002	277.8±4.9
	4.5M	A	9.1±0.2	11.4±0.3	61.6±2.3	-0.009±0.002	3.0±0.1	0.202±0.003	284.9±4.5
		B	8.7±0.3	11.0±0.3	58.5±2.5	-0.010±0.002	3.0±0.1	0.185±0.003	297.9±5.3
	6M	A	9.7±0.6	12.6±1.3	70.3±7.0	-0.010±0.002	3.6±0.4	0.200±0.004	307.3±5.3
		B	9.4±0.3	11.9±0.6	64.0±6.6	-0.012±0.002	3.1±0.7	0.198±0.004	301.2±5.8
C60	Test_2	A	14.6±0.2	18.1±0.2	88.2±0.9	-0.001±0.001	2.8±0.0	0.211±0.001	438.5±4.0
		B	16.1±0.2	19.9±0.2	95.6±1.0	0.001±0.001	2.7±0.0	0.216±0.001	471.3±4.4
	1.5M	A	15.2±0.1	18.8±0.1	90.9±0.7	0.000±0.003	2.7±0.1	0.210±0.001	460.2±2.0
		B	18.5±0.4	22.8±1.1	107.7±5.8	0.002±0.003	2.7±0.1	0.226±0.002	513.8±3.1
	3M	A	15.0±0.1	18.5±0.1	90.7±0.8	-0.002±0.003	2.8±0.1	0.212±0.002	445.5±2.0
		B	17.0±0.1	21.0±0.1	100.8±0.8	-0.001±0.003	2.7±0.1	0.235±0.002	456.6±2.2
	4.5M	A	15.8±0.1	20.0±0.1	109.2±0.9	-0.010±0.002	3.5±0.0	0.253±0.002	393.1±2.8
		B	16.9±0.1	21.5±0.2	115.0±1.1	-0.005±0.002	3.4±0.0	0.252±0.002	425.9±3.6
	6M	A	15.8±0.1	20.5±0.4	111.0±4.5	-0.005±0.002	3.8±0.4	0.267±0.003	369.1±2.8
		B	16.8±0.1	21.8±0.1	114.0±1.0	-0.004±0.002	4.2±0.1	0.284±0.002	376.5±3.0

According to **Table 4.3**, compared with other tested surfaces, specimen C17 had the lowest surface roughness characteristics after 1.5 months of dynamic deployment. Compared to the C17 unfouled condition, there were about 170% and 180% increments in R_a and R_t respectively which indicated that the biofilm had dramatically increased the surface roughness of C17. Although surfaces coated with specimen C12 had the lowest roughness characteristics before submersion, after 1.5 months of submersion, these result values indicated that even rougher surfaces were developed on specimen C12 than on C17 and C25. The roughness

amplitude parameters R_a and R_t had increased by 90% and 107% respectively.

After the same dynamic exposure time, the roughness characteristics of C25 were between those of C12 and C17. On average, there was a 44% of roughness increment for C25 and this value was similar to the increment in total roughness height which was 47% higher than before. Even though specimen C60 had the roughest surfaces characteristics all of the time, it did have the lowest roughness increments which only increased by 10% and 8% for R_a and R_t .

In contrast to the above results, by the end of 3 months of deployment, the roughness increase rates for C12 and C17 had obviously slowed down. There were 27% and 39% increases in R_a, and 16% and 26% increases in R_t for specimens C12 and C17 respectively. Meanwhile, the C25 specimen had about 34% roughness increments in R_a and R_t which was slightly below the results for 1.5 month deployment. Unlike the other specimens, the roughness characteristics of C60 showed an unexpected decline. Although C60 still had the highest surface roughness condition, the R_a and R_t values were 5% and 4% lower respectively than those of the 1.5 months results. In contrast to C60, the C17 specimen still had the lowest roughness characteristics, and this was followed by C25.

The trendlines for the dynamic changes in roughness amplitude parameters (R_a and R_t) during the biofilm cultivation period are shown in **Figure 4.20** and **Figure 4.21**. When comparing the clean (unfouled) conditions with the 6 month deployment conditions, the roughness characteristics had increased significantly from the relatively smooth tested surfaces (i.e. C12, C17 and C25) , especially for the specimen C12. The biofilm had more obvious impacts on the C60 surface roughness during the 1.5 months to 4.5 months deployment period. These results indicated that the biofilm can produce more obvious surface roughness increments on a relatively smooth surface from the beginning of the immersion stage.

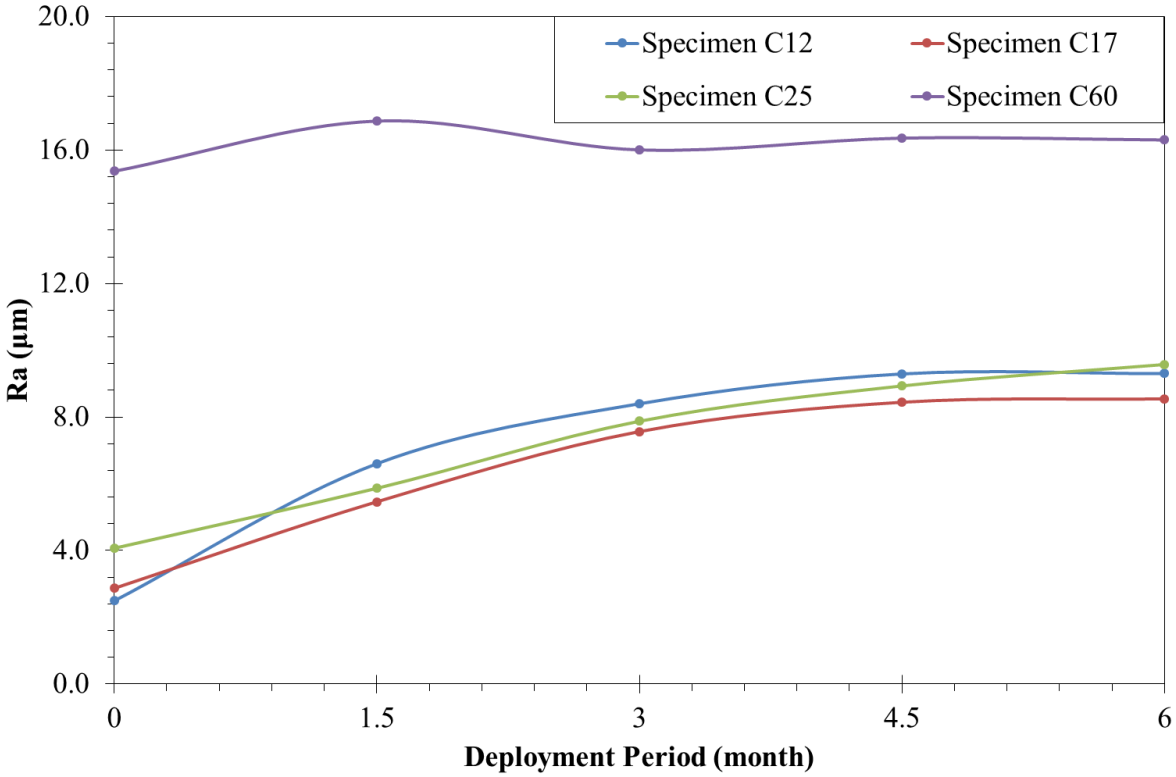

Figure 4.20: The trendline for the average roughness height (R_a) changes of all tested specimens along with each deployment stage

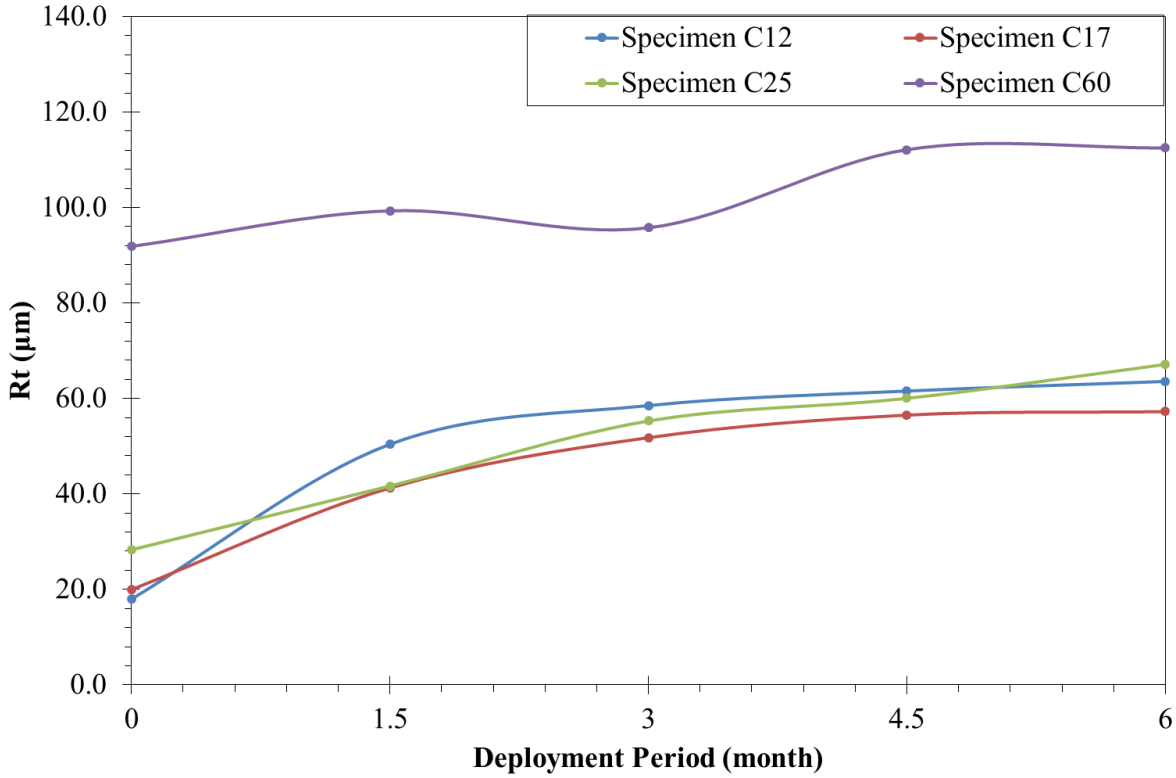

Figure 4.21: The trendline for the total roughness height (R_t) changes of all tested specimens along with each deployment stage

It can be seen from **Figure 4.20** and **Figure 4.21** that there was a less pronounced increase in surface roughness observed from a rougher surface. The rougher surface with polyporous microstructure, instead of simply being affected by biofilm, has an interaction between biofilm microorganisms and coating microstructure which should be taken into consideration. Overall, by the end of the biofilm growth test, the roughness characteristic of each tested specimen surface was approaching a dynamic stability value because the biofilm had fully developed over the entire surface. With regard to this, further SEM evidence and microstructure results of these tested surfaces will be presented and discussed in **Section 4.4.4**.

The PDF results of each tested specimen (i.e. C12, C17, C25 and C60) through all their biofilm fouled stages are plotted in **Figure 4.22** to **Figure 4.25** respectively. As it can be seen from each figure, the clean (unfouled) surface had a lower average roughness height and distributed its roughness with a narrower PDF shape than that of its fouled status.

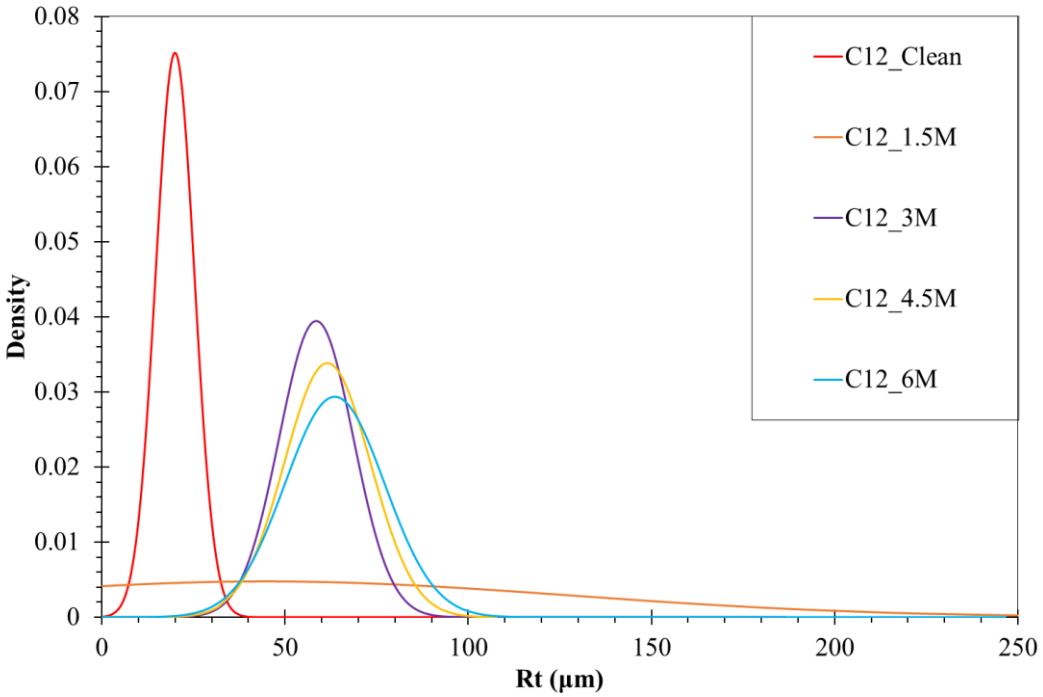

Figure 4.22: Probability density functions (PDF) of the roughness data of specimen C12 of all the biofilm present condition

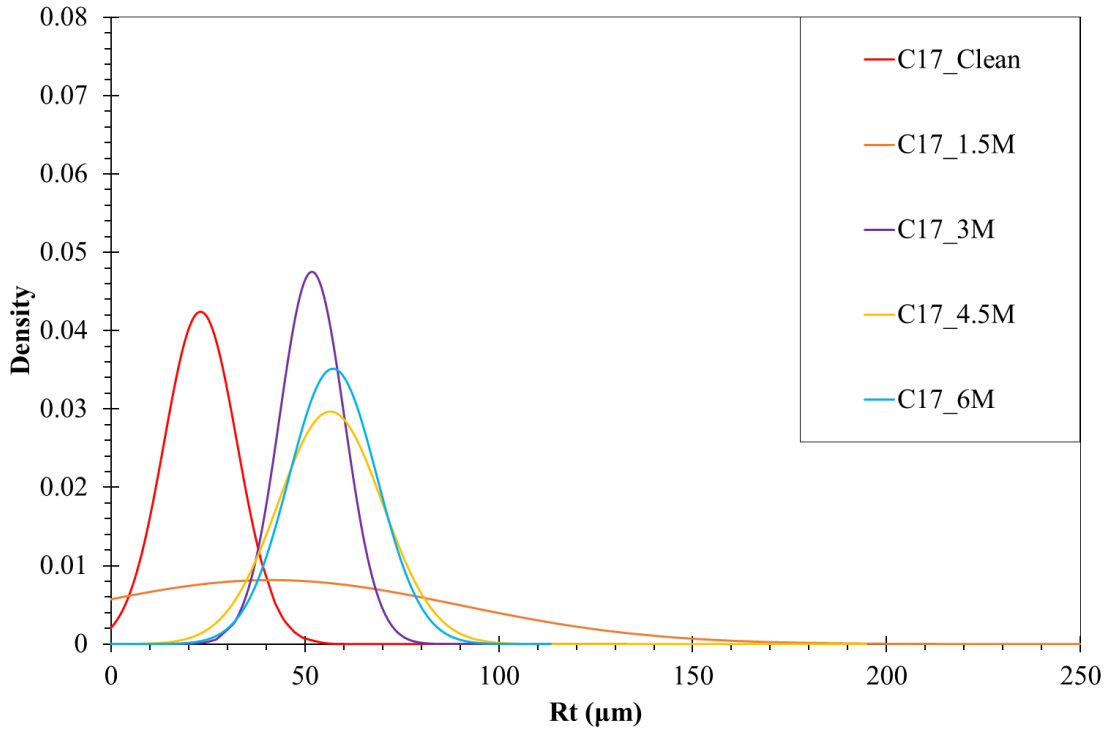

Figure 4.23: Probability density functions (PDF) of the roughness data of specimen C17 of all the biofilm present condition

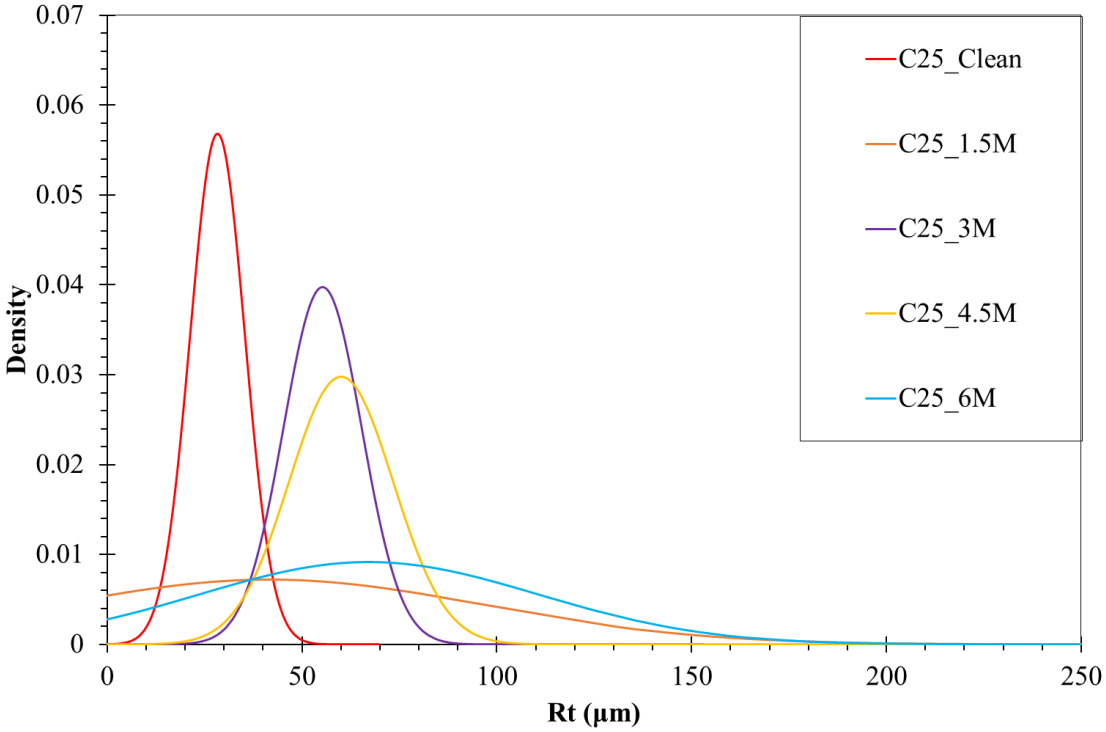

Figure 4.24: Probability density functions (PDF) of the roughness data of specimen C25 of all the biofilm present condition

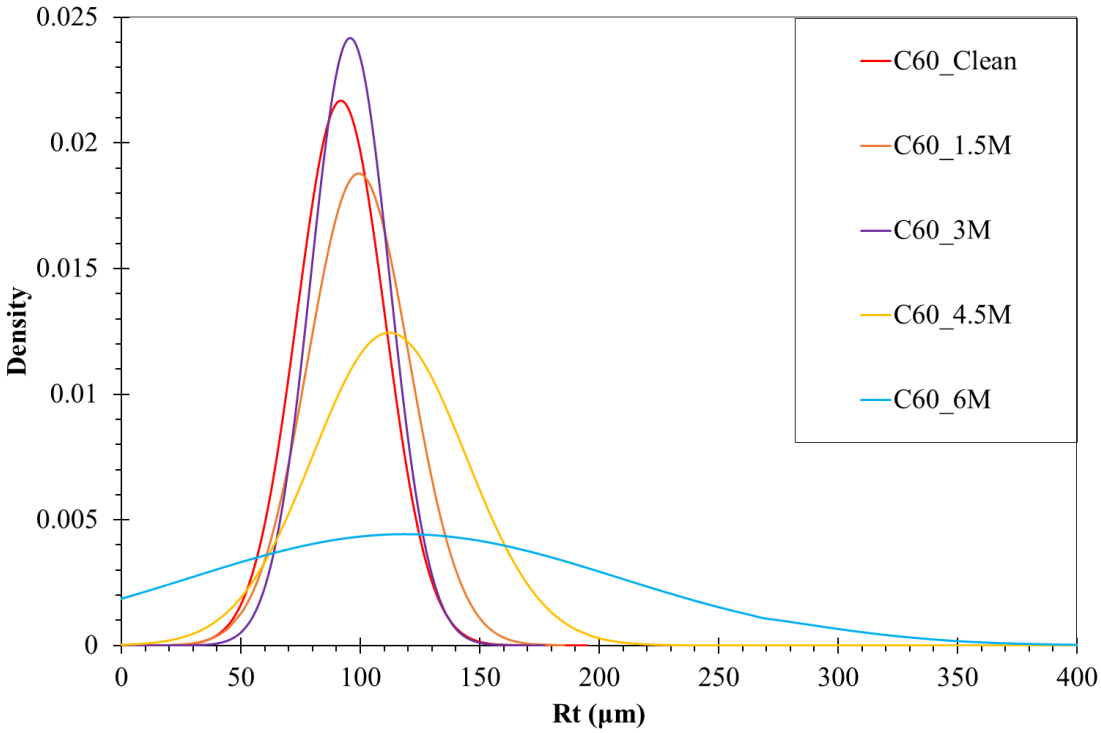

Figure 4.25: Probability density functions (PDF) of the roughness data of specimen C60 of all the biofilm present condition

Corresponding to the surface roughness results, after 1.5 months of deployment, the PDF of C12 had been expanded by six-fold which changed from 0-40µm to 0-250µm. After the same period, for roughness PDF results of C17 and C25, the span range enlarged by nearly 400% (i.e. 0-200µm) than before (i.e. 0-50µm). These PDF results further proved that biofilm can have great impacts on a surface with lower roughness profiles. By the end of 3 months of deployment, with average roughness values increasing, it was observed that the roughness span range had been obviously shortened by 75%, 70% and 65% from C12, C17 and C25, respectively, compared to those of 1.5 months. During the period from 4.5-6 months, less significant changes due to the biofilm can be observed from surfaces coated with specimen C12 and C17. Whereas, by the end of 6 months, the shapes of the PDF of specimens C25 became flatter with the roughness span gradually enlarged.

In comparison, after 1.5 months of deployment, the PDF for the C60 specimen had a weeny increment, about 100% (i.e. 0-200µm) than before (i.e. 50-150µm). The changes of PDF indicated that biofilm did not show a very immediate effect on the rougher surface at the beginning. For the PDF results after 4.5 months, the shapes of the PDF of C60 had slightly turned to be flatter with the roughness span gradually enlarged. By the end of 6 months, the PDF span of C60 surface roughness was amplified from 0-200µm to 0-400µm.

4.4.4 SEMs and Topography of Fouled Surfaces

The microstructure and surface characteristics of the test surfaces were evaluated using SEM. **Figure 4.26** gives surface top views of tested specimen C12 and C17 after 1.5 and 4.5 months deployment respectively along with a magnification ratio of 650×.

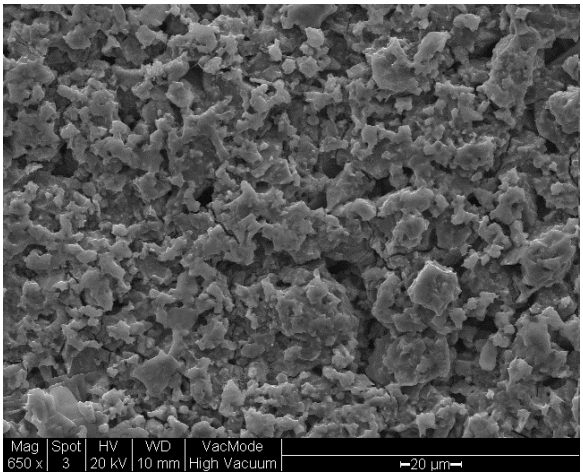

(**a**). C12 after 1.5-months dynamic deployment (650× magnification)

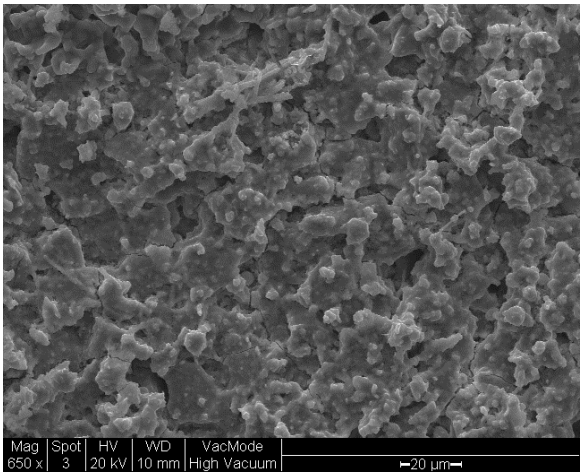

(**b**). C17 after 1.5-month dynamic deployment (650× magnification)

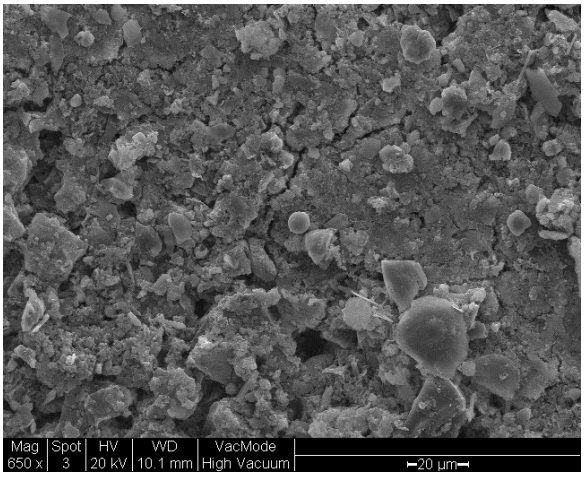

(**c**). C12 after 4.5-months dynamic deployment (650× magnification)

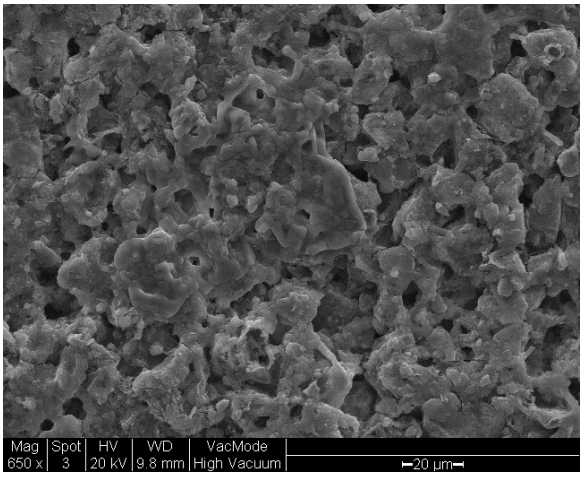

(**d**). C17 after 4.5-months dynamic deployment (650× magnification)

Figure 4.26 (**a**)-(**d**)**:** SEM top-view of the tested specimen C12 and C17 covered with 1.5/4.5 month biofilm

As can clearly be seen from the SEM images, after 1.5 months deployment, the surfaces coated with C12 (**Figure 4.26** (**a**)) and C17 (**Figure 4.26** (**b**)) were fully covered by the biofilm which completely altered the C12 and C17 original surface characteristics. By the end of 4.5 months, the biofilm covering those cuprous oxide particles became obviously thicker (**Figure 4.26** (**c**) and (**d**)). Specifically, C12 was unevenly distributed by the biofilm with wider and deeper interspaces remaining after 1.5-month deployment (**Figure 4.26** (**a**)). By the end of the 4.5

months, the surface characteristics of C12 became lower due to the majority of those interspaces being counteracted by the biofilm during the development. While there is still larger biofilm matter scattered around, the appearance of a diatom in particular (the rounded shell in the centre of **Figure 4.26** (**c**)) indicates that larger microorganisms had already started to attach. In contrast, as shown in **Figure 4.26** (**b**), a thick biofilm layer developed on top of C17 and this biofilm layer was evenly distributed after 1.5 months. Even though there are many larger interspaces distributed on top of C17, these interspaces with shallow valley regions resulted in smoother surface waviness. By the end of 4.5 months, **Figure 4.26** (**d**) shows that a more porous biofilm microstructure with deeper interspaces had formed over the C17.

Figure 4.27 gives surface top views of tested specimen C25 and C60 after 1.5 months deployment along with a magnification ratio of 200× and 650×.

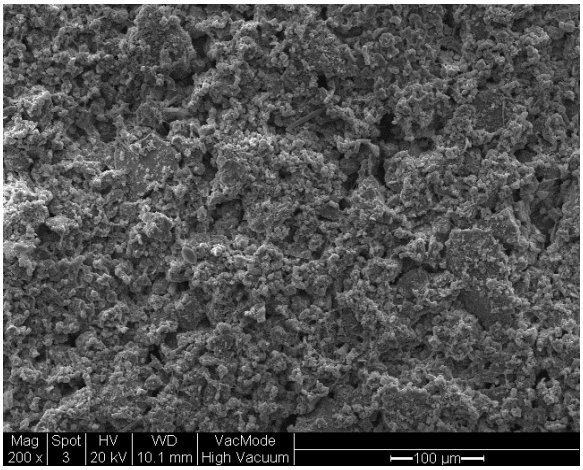

(**a**). C25 after 1.5-months dynamic deployment (200× magnification)

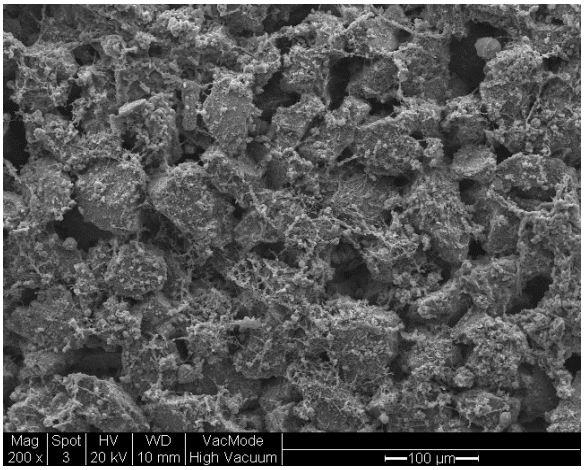

(**b**). C60 after 1.5-months dynamic deployment (200× magnification)

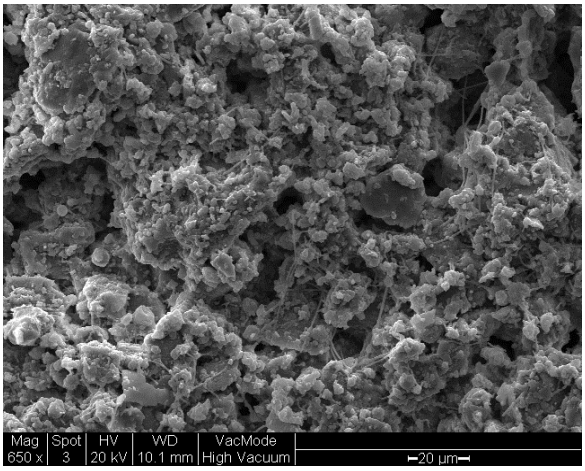

(**c**). C25 after 1.5-months dynamic deployment (650× magnification)

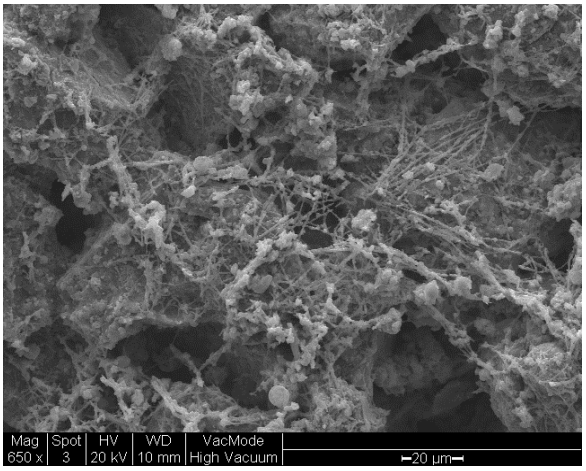

(**d**). C60 after 1.5-months dynamic deployment (650× magnification)

Figure 4.27 (**a**)−(**d**)**:** SEM top-view of the tested specimen C25 and C60 covered with 1.5 months biofilm

For these larger size specimens, the 650× magnification can give more local surface details, while the 200× magnification can provide an overview of the surface characteristics. According to **Figure 4.27** (***a***), even though the biofilm was not fully developed, the layer had already spread over the entire surface and started to change the surface characteristics. Meanwhile in **Figure 4.27** (**b**), due to the presence of only a few bacterial clusters (with network structure) on the C60, the surface waviness did not significantly change.

For further local details, **Figure 4.27** (**c**) indicates that the C25 particles had almost been fully covered by bacterial colonies with rougher surface characteristics resulting. Unlike the progress on C12 and C17, there were plenty of filiform fibres spread over these surfaces attempting to seal the interspaces. Especially for C60 surfaces (**Figure 4.27** (**d**)), the bacterial "bridges" were widely trussed over the "canyons" by those filiform fibres and connected with the bacterial colonies from the top of each C60 particle. Further SEM results about the bacterial colonies and filiform fibre and algae which were found from the test surfaces are presented in **Appendix D**.

Figure 4.28 gives surface top views of tested specimen C25 and C60 after 4.5 months of deployment with magnification ratios of 200× and 650×. **Figure 4.28** (**a**) shows that more original surface roughness characteristics C25 were eliminated by the biofilm after the 4.5 months of growth. Since all C25 particles were fully covered, the surface interspaces started to be filled by the biofilm. For the C60 (**Figure 4.28** (**b**)), the "bridges" have disappeared, and the filiform fibre networks are replaced by thin biofilm coverage on the top.

Figure 4.28 (**c**) indicates that the biofilm over C25 has a more layered structure, and a large amount of biofilm and bacterial colonies are piled together. **Figure 4.28** (**d**) shows that for C60, thin biofilm consists of many tiny bacterial colonies and those colonies have not been fully connected yet. Also, as shown in the centre of this image, a larger microorganism was observed which indicated the evolution of the fouling process from the biofilm to the microorganism.

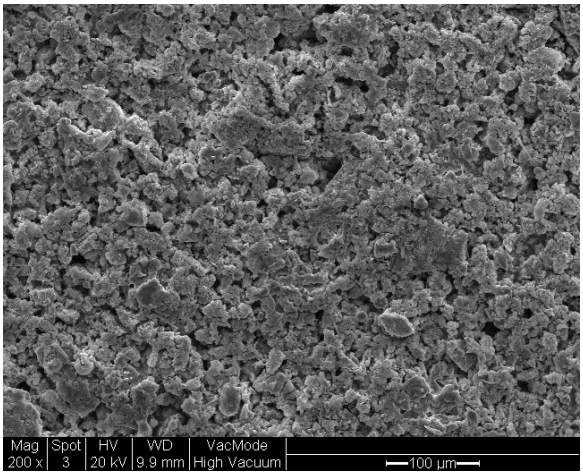

(**a**). C25 after 4.5-months dynamic deployment (200× magnification)

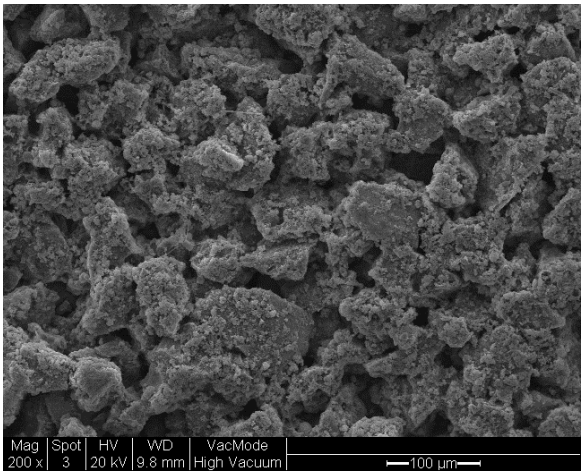

(**b**). C60 after 4.5-months dynamic deployment (200× magnification)

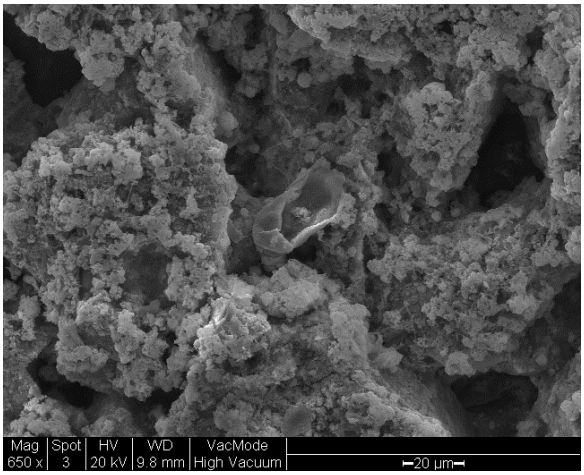

(**c**). C25 after-4.5 months dynamic deployment (650× magnification)

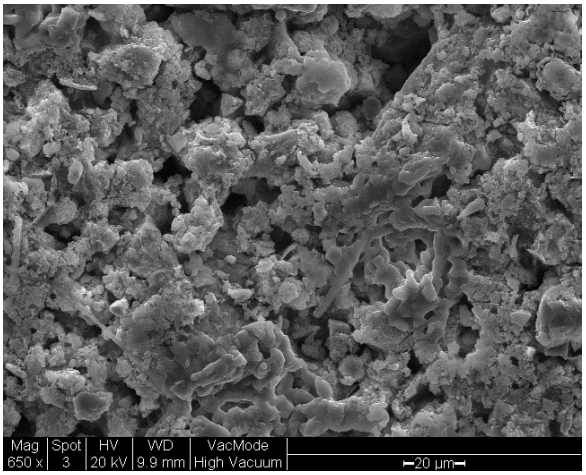

(**d**). C60 after 4.5-months dynamic deployment (650× magnification)

Figure 4.28 (**a**)−(**d**)**:** SEM top-view of the tested specimen C25 and C60 covered with 4.5 months biofilm

The cross-section of these specimens and their magnification ratio (i.e. 650×) are presented in **Figure 4.29**. Four weeks after the initial deployment, it can be seen that the biofilms are already fully distributed on top of the coating structure. With time passing by, the biofilm became thicker, and the original Cu_2O top surface characteristics were covered. However it can also be noticed that instead of completely filling every interspace inside the coating structure, the biofilm tended to expand over the top (**Figure 4.29**(**a**), (**b**), (**c**)).

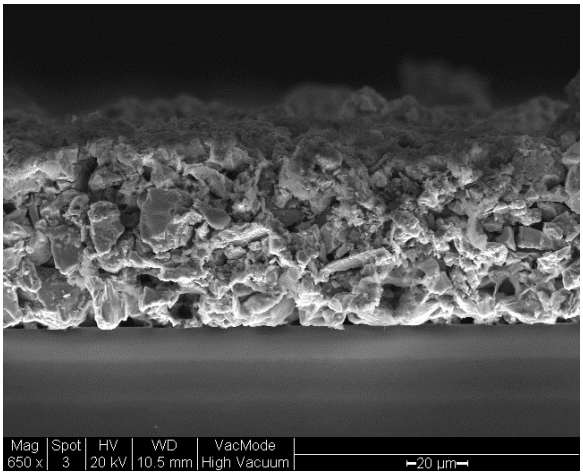

(**a**). C12 after 1.5-months dynamic deployment (650× magnification)

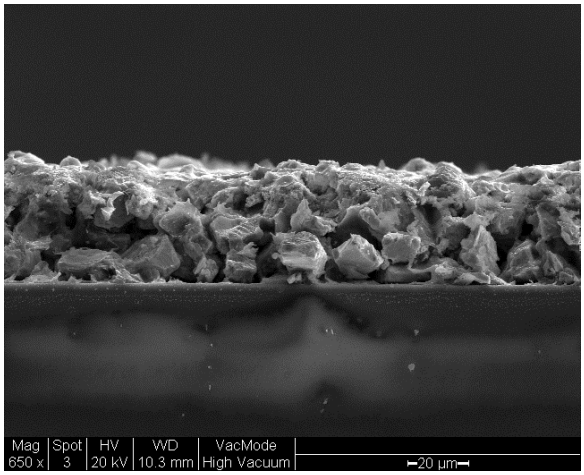

(**b**). C17 after 1.5-months dynamic deployment (650× magnification)

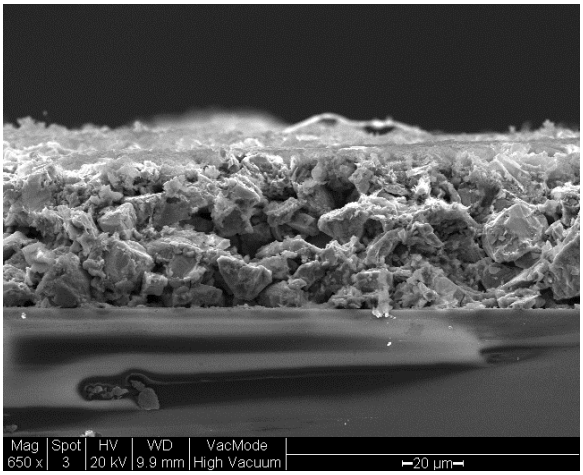

(**c**). C12 after 4.5-months dynamic deployment (650× magnification)

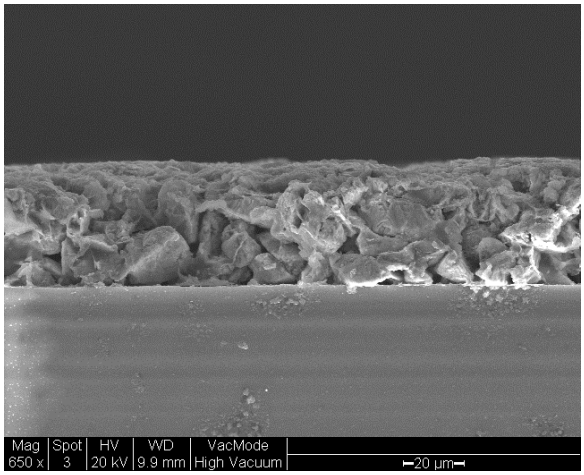

(**d**). C17 after 4.5-months dynamic deployment (650× magnification)

Figure 4.29 (**a**)−(**d**)**:** SEM cross-sections of the test specimen C12 and C17 covered with 1.5/4.5 months biofilm

Unlike forming a constant biofilm on the smaller sized specimens (i.e. C12 and C17), Figure 4.30 (**a**) and **Figure 4.30** (**b**) show that the bacterial colonies were unevenly attached on the C25 and C60 particles at the beginning. The surface waviness of the C25 and C60 top surfaces were rougher. At the end of 4.5 months, **Figure 4.30** (**c**) shows that a thick and continuous biofilm had formed on top of C25 only without invasion into the structure inside. Moreover, the waviness became smoother than that of 1.5 months. Meanwhile, due to C60 having more open and larger interspaces and these allowing bacteria and other microorganisms to have more chance to attach, a large number of bacterial clusters can be observed to be scattered throughout the C60 layer (**Figure 4.30** (**d**)).

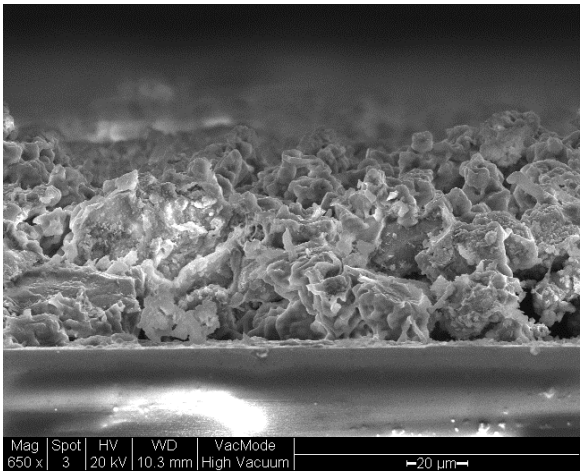

(**a**). C25 after 1.5-months dynamic deployment (650× magnification)

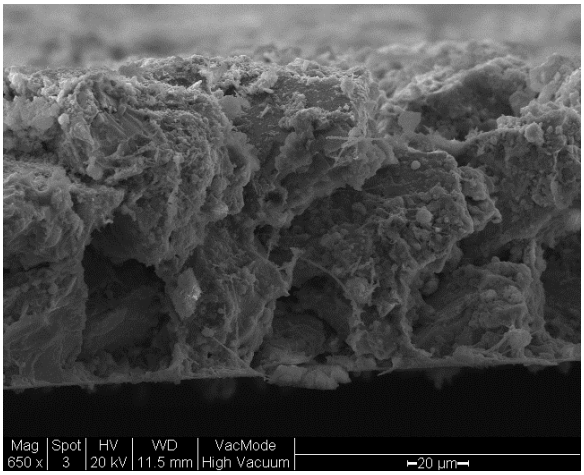

(**b**). C60 after 1.5-months dynamic deployment (650× magnification)

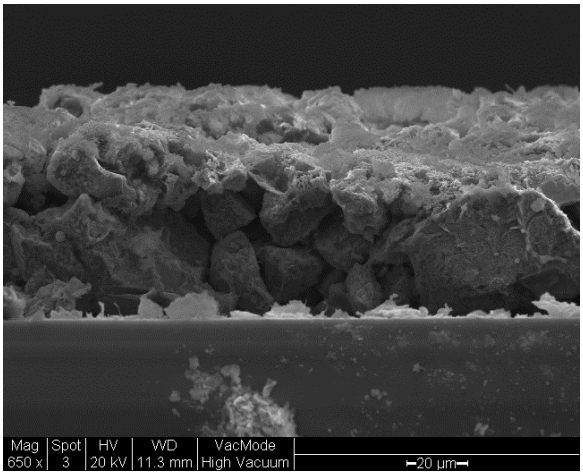

(**c**). C25 after 4.5-months dynamic deployment (650× magnification)

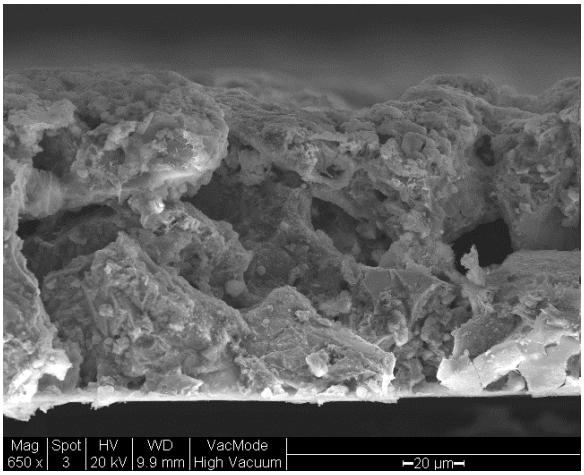

(**d**). C60 after 4.5-months dynamic deployment (650× magnification)

Figure 4.30 (**a**)−(**b**)**:** SEM cross-sections of the test specimens C25 and C60 covered with 1.5/4.5 months biofilm

4.5 Chapter Summary

For the measurements of roughness and analyses of the test surfaces coated with the Cu_2O particles under different biofilm conditions, the analysis results and SEM images are presented and discussed separately in this chapter. The main objectives of these measurements were to investigate the surface characteristics of AF coatings which were purely formed with different sized irregular Cu_2O particles and the changes of roughness characteristics affected by an interaction between surface profile waviness with biofilms. It is worth noting that, for the biofilm fouled surfaces, the roughness measurements were carried out using an optical roughness measurement device whilst keeping the plate in seawater

For those clean surfaces without biofilm, roughness results and observations of microscale

structures have clearly indicated that initial roughness of the surfaces was dependent on the particle size as well as the quality of coating application. A low coating application quality, such as particle agglomeration, can directly affect the surface roughness. In practical terms, the smallest size specimen (i.e. C2) did not give the expected lowest roughness characteristics.

For the fouled conditions with biofilm present, the microorganisms started to reproduce and expand their colonies during the beginning of the biofilm evolution stage (1.5 months), and these resulted in surface roughness increases. However, the roughness results and microstructure images indicated biofilm and microorganisms can block the top surface characteristics and reformed the surface waviness. Also, it was found that biofilm can bring more significant impacts on smoother surfaces which were evenly coated with smaller particle (i.e. C12 and C17). Moreover, the surface characteristics of the larger specimen (i.e. C25 and C60) changed slightly because the microorganisms could not immediately cover the larger interspaces. As the top surface and interspaces were gradually covered by microorganisms, the surface waviness profile got reformed. Therefore, with regard to the impacts on surface roughness, after an essential period (>3months), the biofilm and its microorganisms took on a more significant role than the particles.

After a sufficient period, with a thicker layer of the biofilm developed, the waviness of the top surface was kept at a dynamically constant level with roughness characteristics increasing slowly. At the same time, larger microorganisms and the subsequent macrofouling started to attach on those biofilm surfaces, and all these would lead to the surface characteristics becoming rougher.

It should be noted once again that the test coatings were purely experimental with exceptionally high Cu_2O contents in the dry film after applied on the top of flat acrylic surfaces. These surfaces would not represent any commercial antifouling surfaces which finished with multiple coats of paints. It is, therefore, the commercial products would result in different test results.

In the next chapter, the first hydrodynamic assessment (boundary layer measurement) on these Cu_2O surfaces were conducted by using a water tunnel (i.e. the Emerson Cavitation Tunnel) and a two-dimensional Laser Doppler Velocimetry (LDV) system. The detailed descriptions of the boundary layer test set-up and its subsequent result discussion have been presented.

Chapter 5 Zero-pressure Gradient Flat Plate Turbulent Boundary Layer Measurements

5.1 Introduction

This chapter describes the experimental study of the boundary layer flow over the Cu_2O antifouling surfaces which were finished by eight different sized Cu_2O particles.

To meet **Objective 4** of this research study (**Section 1.3**), the following tasks have been conducted in this chapter:

- To examine the different antifouling surface condition, which was formed by various size of Cu_2O particle, impacts on the mean velocities and boundary layer parameters subjected to different free-stream velocities;
- To examine and verify the similarity of the boundary layer flows on the overlap and the outer region of the smooth and rough walls which provided a theoretical basis for the roughness function calculation;
- To calculate and compare the local frictional coefficient, roughness functions and Reynolds stress of the different Cu_2O surfaces to understand the relationship between the roughness characteristics (generated by the different size Cu_2O particle) and the turbulent boundary layers characteristics.

The experimental turbulent boundary layer tests were conducted by fitting the testing surfaces to a dedicated zero pressure gradient flat test bed in the measuring section of the UNEW Emerson Cavitation Tunnel and using a two-dimensional Laser Doppler Velocimetry (LDV) system. The effects of the different size Cu_2O on the mean velocity profiles, boundary layer parameters, local skin friction drag, roughness functions and Reynolds stresses are presented and discussed. This chapter also includes descriptions of the experimental facility, test set-up and uncertainty analysis procedure for the flat plate boundary layer experiment results.

The above-summarised tasks are presented in this chapter as follows: **Section 5.2** introduces the Emerson Cavitation Tunnel, and **Section 5.3** gives detailed information about the experimental set-up. **Section 5.4** discusses the uncertainty analysis of the tests. After this, **Section 5.5** presents all of the boundary layer experimental results: the boundary layer parameters, the velocity profiling, the skin friction coefficient and roughness function, as well as the Reynolds stress results. Finally, conclusions of this chapter are addressed in **Section 5.6**.

5.2 Emerson Cavitation Tunnel

The boundary layer experiments on the test surfaces were conducted in the Emerson Cavitation Tunnel (ECT) of Newcastle University. As shown in **Figure 5.1**, the ECT is a closed circuit depressurised tunnel. The dimensions of the test section are 3.10 m in length (L), 1.22 m in width (W), and 0.81 m in height (H) and there is a contraction ratio of 4.271:1. The tunnel contains 60 tonnes of freshwater that is circulated by using a 400 HP DC motor driving a 1.4m diameter, 4-bladed impeller. The maximum attainable water speed in the measuring section is 8 m/s. The large observation windows on the side walls and floor of the measuring section of this facility provide laser and camera access and make it an ideal facility for measuring flow around various test bodies. Further detailed specification information of the ECT can be found in Atlar (2011).

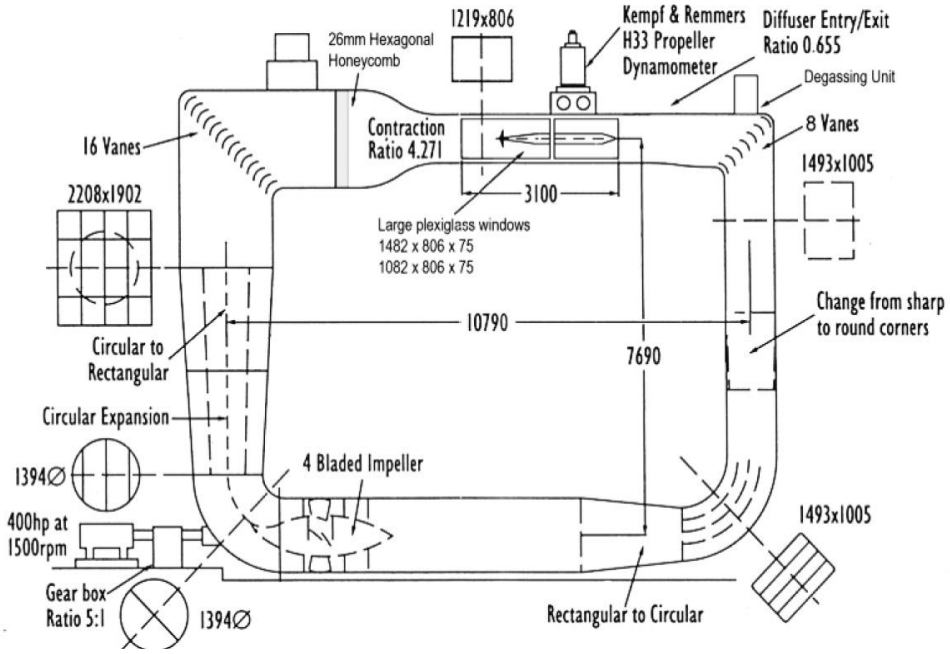

Figure 5.1: Schematic of the Emerson Cavitation Tunnel (Atlar, 2011)

5.3 Experimental Set-up

In order to conduct tests at higher Reynolds number with a sufficient length to achieve the fully developed turbulent boundary layer flows, the measuring section of the Emerson Cavitation Tunnel was upgraded in 2011 including a removable "high-speed insert" facility (Atlar, 2011). As shown in **Figure 5.2**, the removable insert section has an overall length of 3.924m and consists of three parts: an air-foil shaped leading edge (0.98m), the main bed body (2.044m) and an inclined tail section (0.90m). The deployment of such an air-foil shaped leading edge not only guides the incoming flow from the contraction part of the

tunnel slowly but can also effectively reduce the vibration of the insert bed by eliminating the flow which is passing behind it. The flat part of the main body was manufactured with a slot which allows the UNEW test panel (600mm × 220mm, $L \times W$) to be fitted flush with the insert surface to conduct dedicated boundary layer experiments with zero-pressure gradient test surfaces.

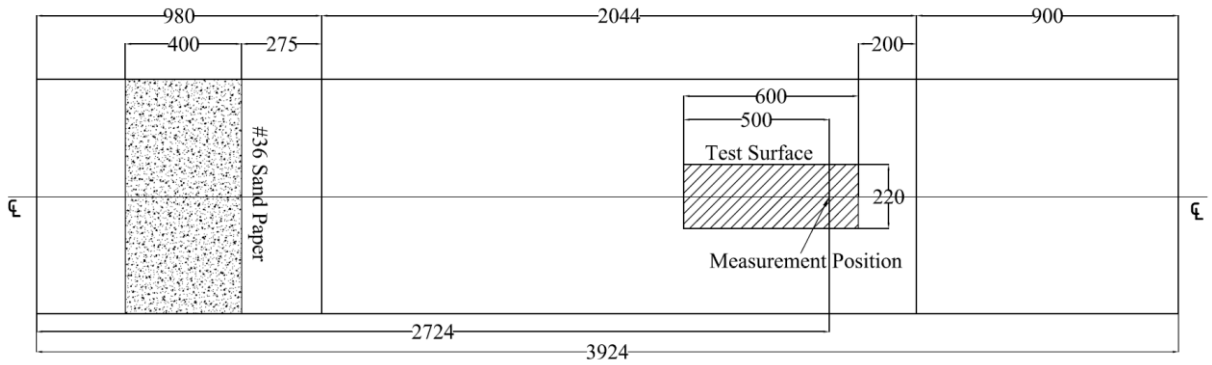

Figure 5.2: Schematic of the "high-speed insert" (dimensions unite in mm)

Furthermore, because the insert decreases the width of the original measuring section of the tunnel from 1.22m to 0.81m, the experiments can be carried out at lower impeller speeds for a higher inflow velocity. In order to thicken the boundary layer and hasten the transition to fully turbulent flow near the wall, a 400mm width #36 grit sandpaper was attached at 305mm from the leading edge of the high-speed insert and used as a turbulence stimulator. As shown in **Figure 5.3**, the test plate was arranged in the test section of the tunnel in the streamwise direction.

The leading edge of the test plate was 2224mm from the beginning of the leading edge of the test insert body. Six screws and handles were used to hold the test panel in place, and also allow the panel to be adjustable to obtain a zero-pressure gradient flow across the surface. The 0.9m tail section extended into the diffuser end of the tunnel test section to reduce the vibration at the high inflow speeds.

The boundary layer tests were carried out with hydraulically smooth reference plate and 16 Cu_2O coated panels which were all made from acrylic. The reference panel was used as a smooth reference surface. As introduced in **Chapter 4**, the 16 flat panels were coated with eight different sized Cu_2O particles which had a mean particle size ranging from 2μm (C2) to 250μm (C250). Moreover, as illustrated in **Figure 4.14**, the boundary layer tests of this chapter were carried out with those Cu_2O surfaces finished from the first application.

Figure 5.3: Photographs of the "high-speed insert" (left); the reverse side of the "insert" (right)

All of the boundary layer measurements were carried out at the midline of the test panels and 500mm from their leading edges. Therefore, a total distance of 2724mm from the insert leading edge was present for the boundary layer development. The measurements were performed against freestream velocities of 2 m/s, 4 m/s and 6 m/s, to cover a relatively large range of Reynolds numbers for fully turbulent boundary layer flow over the test panels.

Figure 5.4: Laser generator and processor

The data points of the boundary layer measurement were collected by using a two-dimensional DANTEC Laser Doppler Velocimetry (LDV) system. **Figure 5.4** presents

an overview of the LDV system which consists of two laser light sources (Spectra Physics), a beam separator, fibre-optic couplers, a multi-colour receiver, a signal processor, a fibre-optic probe, a chiller and a traverse controller. The primary function of the beam separator was to separate the beams coming from the Laser source into individual colour components and provide frequency shifting of the laser beam. Therefore, the laser beam was separated into two beams, green (λ=514.5nm) and blue (λ=488nm), by the DANTEC beam separator with a 40MHz frequency difference.

The 60mm laser probe was connected with a beam expander which had a beam expansion ratio of 2.97 and focal length of 500mm. As shown in **Figure 5.5**, the probe system was mounted on a three-axis traverse system which can reach maximum distances of 2510mm, 610mm and 410mm in X, Y and Z direction, respectively. During the experiment, the velocity-time data were collected for 180-second measurements or until 20,000 samples had been acquired, whichever was satisfied first. The data validation rate had a non-monotonous character that depended on the measurement location through the boundary layer. The seeding material used in the experiment was provided by Potters Industries Inc. and consisted of silver-coated glass spheres with a mean particle size of 10 μm. There were about 20−30 grams of seeding added to the tunnel water before the tests.

Figure 5.5: The LDV probe mounted on a computer-driven 3D traverse system

5.4 Uncertainty Analysis

The uncertainty analysis of the LDA turbulent velocity data was conducted with two procedures. One procedure was for the overall statistical uncertainty analysis, and it was applied to the sampling of a random process from individual LDA measurement without repetition, as explained in Benedict and Gould (1996). Accordingly, **Table 5.1** gives the basic turbulent flow study statistics and their associated estimator variances, where N represents the number of the samples, u' is the streamwise velocity discrete points, v' is the wall-normal velocity discrete points,

U is the streamwise velocity, V is the wall-normal velocity, $\overline{u'^2}$ is the streamwise Reynolds normal stresses, $\overline{v'^2}$ is the wall-normal Reynolds stresses and $\overline{u'v'}$ is the Reynolds shear stress.The 95% confidence bounds for each of the statistics can be calculated as $\pm\ 1.96 \times \sqrt{\sigma}$, where σ is the estimator variance. As an example, the 95% confidence bounds for streamwise velocity, U would be:

$$U \pm 1.96 \times \left(\overline{u'^2}/N\right)^{1/2} \qquad \textbf{5.1}$$

Table 5.1: Estimator variances

No.	Statistics		No.	Statistics	
1.	U	$\overline{u'^2}/N$	***2.***	V	$\overline{v'^2}/N$
3.	$\overline{u'^2}$	$\left[\overline{u'^4} - \left(\overline{u'^2}\right)^2\right]/N$	***4.***	$\overline{v'^2}$	$\left[\overline{v'^4} - \left(\overline{v'^2}\right)^2\right]/N$
5.	$\overline{u'v'}$	$\left[\overline{u'^2v'^2} - \left(\overline{u'^2v'^2}\right)^2\right]/N$			

Figure 5.6 and **Figure 5.7** respectively present the uncertainty percentage calculations of the mean streamwise velocity, U, and wall-normal velocity, V, for all of the tested surfaces by following the aforementioned procedure. For the very near wall region, $y/\delta < 0.01$, the uncertainty has relatively high values due to the lower data rates and smaller sample populations. Accordingly, the maximum uncertainty levels in the streamwise and transverse velocities are approximately 2% and 50% respectively for $y/\delta < 0.01$. For $y/\delta \approx 0.1$, both of the streamwise and wall-normal velocity uncertainty percentages quickly decrease and continue decreasing until the edge of the boundary layer measurement. The overall mean uncertainty range in the streamwise direction for $y/\delta > 0.2$ can be given as ranging from 0.12% for the smooth reference surface to 0.16% for the surface coated with the Cu2O size of 250μm; for the wall-normal velocity, the overall mean uncertainty ranges from 2.15% for the smooth reference surface to 2.89% for the surface coated with the Cu_2O size of 250μm.

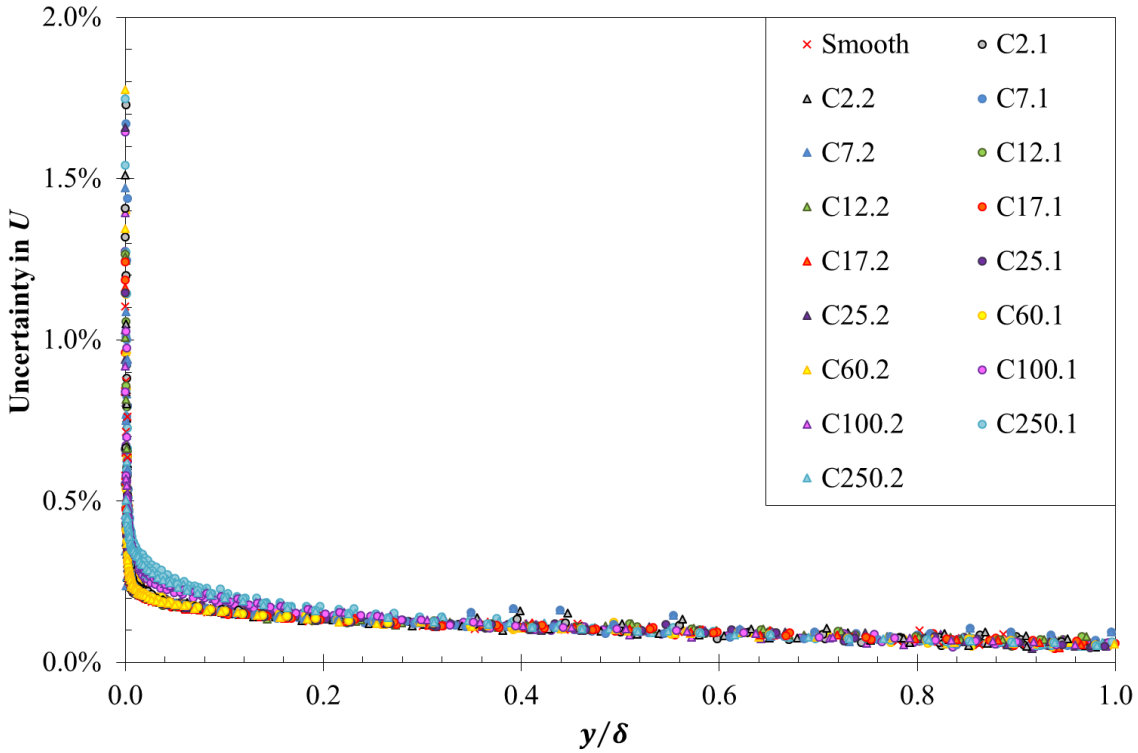

Figure 5.6: Uncertainty in streamwise velocity

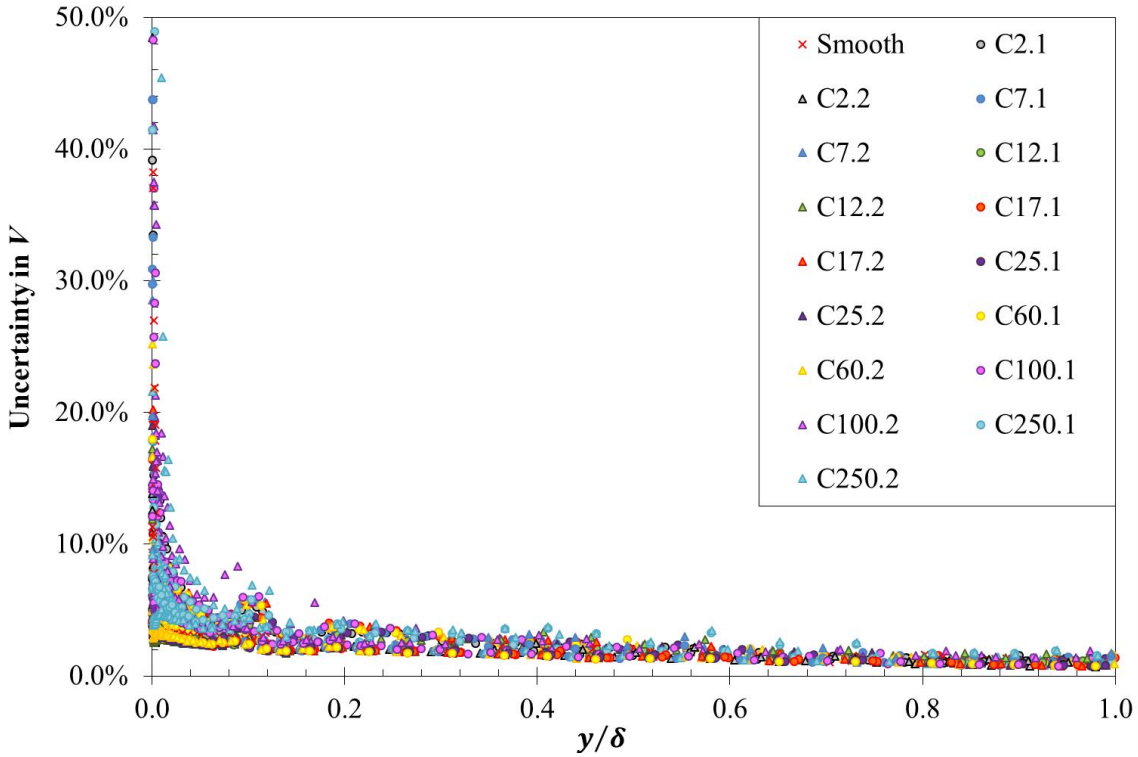

Figure 5.7: Uncertainty in wall-normal velocity

Figure 5.8 and **Figure 5.9** give the uncertainty percentages in the Reynolds stresses of streamwise and wall-normal compounds, respectively.

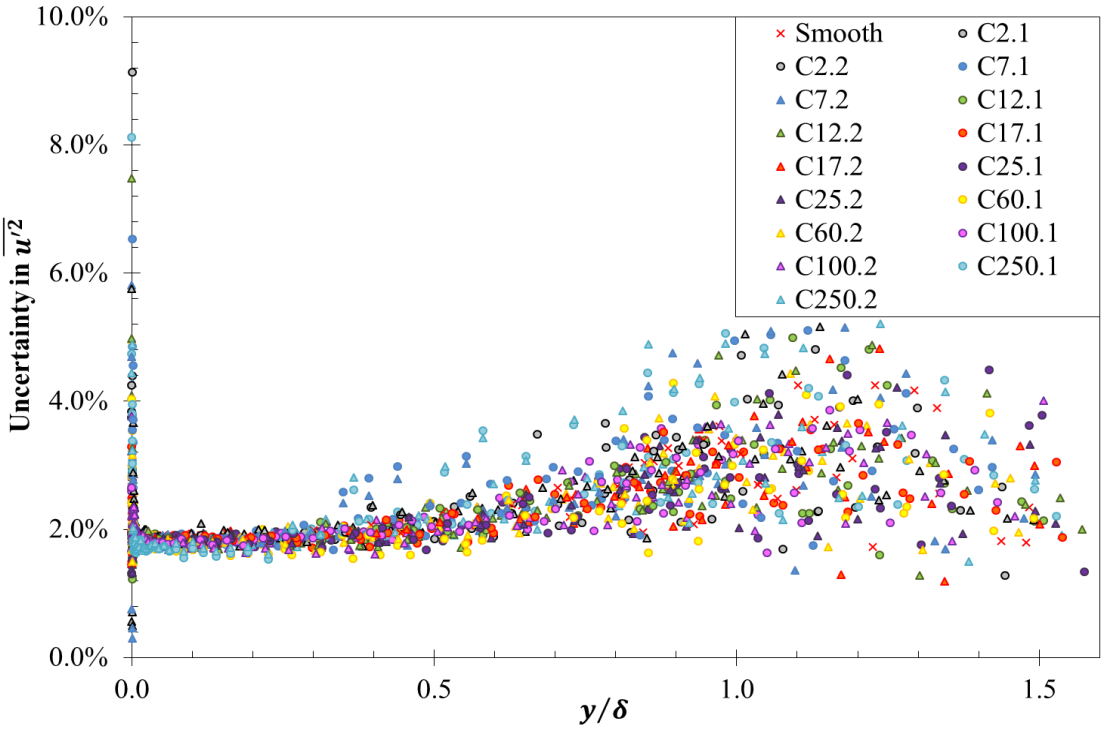

Figure 5.8: Uncertainty in Streamwise Reynolds normal stresses

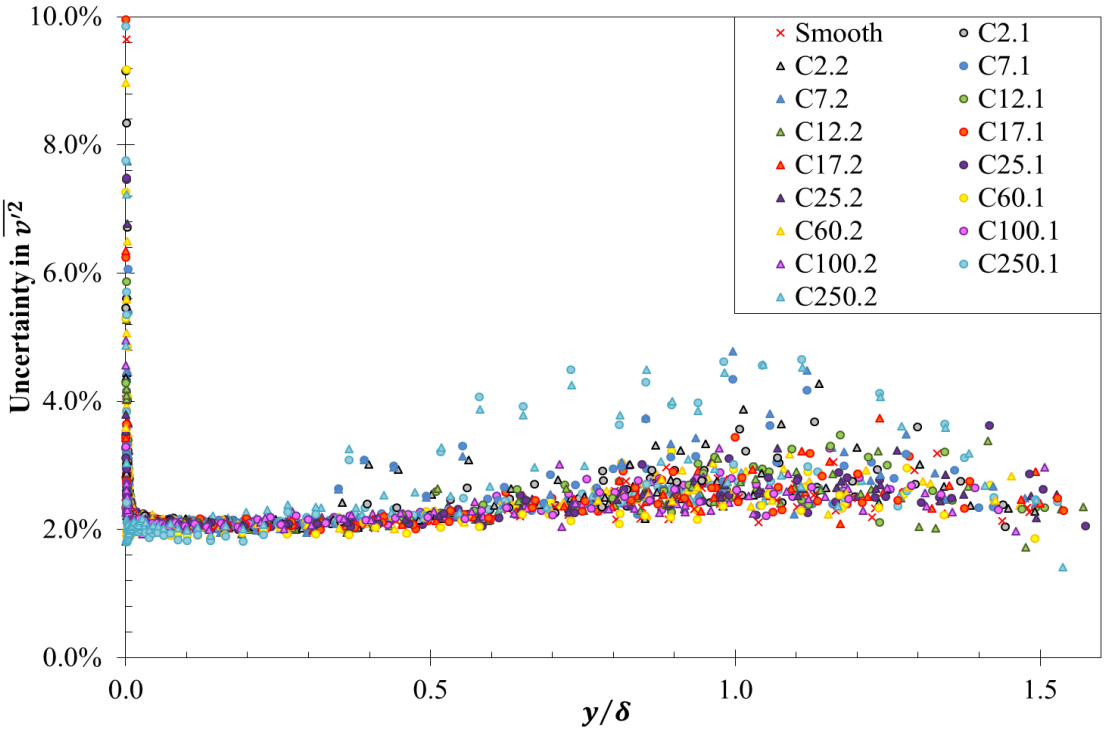

Figure 5.9: Uncertainty in Wall-normal Reynolds stresses

The maximum uncertainty levels in the streamwise and wall-normal Reynolds stress are about 10% of those encountered in a very near wall region, $y/\delta < 0.01$. For the distance away from the wall in the range, $0.01 < y/\delta < 0.3$, the uncertainty percentage was distributed as a platform region. The overall mean uncertainty percentages in this platform region for

streamwise and wall-normal Reynolds stress are 1.85% and 2.28% respectively. For $0.3 < y/\delta$, the uncertainty percentages gradually increase and reach the maximum values at $1.0 \leq y/\delta \leq 1.2$ for all of the tested surfaces. Similar phenomena were noted by Ünal (2012) who reported that, according to the result of the inflow measurements, this behaviour is due to the high turbulence intensities and unsettled fluctuations at the outer edge of the boundary layer.

Figure 5.10 presents the uncertainty percentages in the Reynolds shear stresses of all of the tested surfaces. The skin friction coefficients were calculated based on the total shear stress method (**Section 3.5.1.2)**. Therefore, the uncertainty analyses were taken at Reynolds shear stress data points located at $10 < y^+ < 100$ (the platform part of the turbulent boundary shear stress profile). This data range is equivalent to $0.01 \leq y/\delta \leq 0.1$ and the overall mean uncertainty percentage at this platform region for Reynolds shear stress is 3.77%.

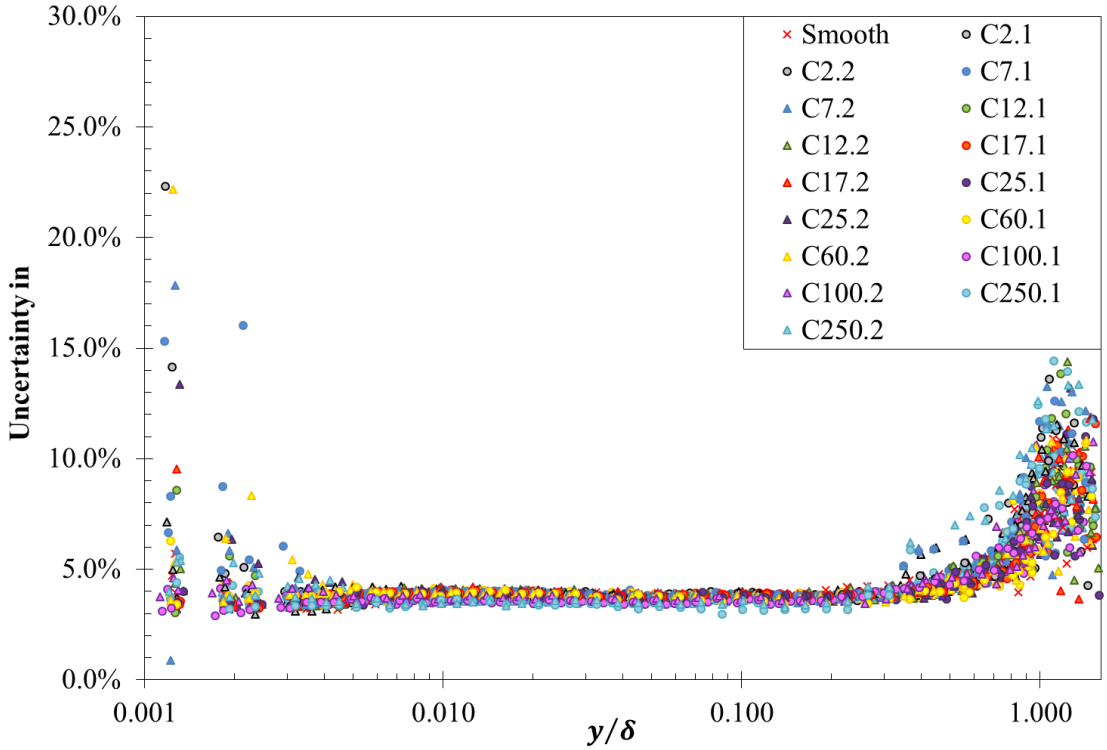

Figure 5.10: Uncertainty in Reynolds shear stresses

The other uncertainty calculations procedure used for the wall shear stress, τ_w, skin-friction coefficient, c_f, and roughness function, ΔU^+, for the single experiment was conducted by following the general uncertainty analysis procedure fully explained by Coleman and Steele Jr (1990). For the general case, if an experimental result, r, is a function of J variables X_i, then the reduction equation used for determining r from X_i can be written as:

$$r = r(X_1, X_2, X_3 \ldots X_J) \quad \textbf{5.2}$$

Therefore, the uncertainty result, U_r, can be given as:

$$U_r = \left[\left(\frac{\partial r}{\partial X_1} U_{X_1}\right)^2 + \left(\frac{\partial r}{\partial X_2} U_{X_2}\right)^2 + \cdots + \left(\frac{\partial r}{\partial X_J} U_{X_J}\right)^2\right]^{1/2} \quad \textbf{5.3}$$

It has to be noted that, in using Equation **5.3**, it is assumed that the uncertainty relationship is continuous and has continuous derivatives in the domain of interest. Also the measured variables,X_i, are independent of one another, and the uncertainties in the measured variables are independent of one another. Therefore, for skin-friction coefficients using the total stress method, the overall uncertainty with 95% confidence limits of all of the tested surfaces ranges from 3.9% to 3.93%. The overall uncertainty in roughness function ranges from 2.56% to 2.75%, and the overall uncertainty in wall shear stress ranges from 6.77% to 7.87%. The overall uncertainty level show a good agreement when comparing to the research works (Candries, 2001; Ünal, 2012) were done under the similar experimental setup by using the same water tunnel.

5.5 Results and Discussion

Section 5.5.1 details the basic findings with regard to the boundary layer properties such as the boundary layer thickness and shape factor and Reynolds number based on the integral thickness parameters. The results of the mean velocity profiles in outer variables are shown in **Section 5.5.2**. The local skin friction drag coefficients and roughness functions of all the tested surfaces are discussed in **Section 5.5.3**, and the results of Reynolds normal and shear stresses are presented in **Section 5.5.4**.

Two panels were coated with each sizes of Cu_2O particles according to the coating scheme of the 1st application. Therefore to distinguish the surface marks from other chapters, it has to be noted here that the tested surfaces of this chapter are referred to as: for example "C2.1" and "C2.2" which means the panel no.1 and no.2 coated with 2μm Cu_2O particles (C2).

5.5.1 The Turbulent Boundary Layer Parameters

At each test velocity, the basic boundary layer parameters are tabulated in **Table 5.2**, and they include: boundary layer thickness (δ), displacement thicknesses ($\delta 1$), momentum thicknesses (θ), shape factor (H), and Reynolds number based on the displacement and momentum

thickness ($Re_{\delta 1}$, Re_{θ}) for all of the test panels. It can be seen from the table that the boundary layer thickness of all cases varied between 44.4 mm and 53.4 mm, whereas the displacement thickness values ranged from 4.9 mm to 6.5 mm.

Table 5.2: Boundary layer parameters

Surface	U_e	δ	$\delta 1$	θ	H	$Re_{\delta 1}$	Re_{θ}
Smooth (Acrylic)	1.99	47.3	5.4	4.2	1.30	9473	7265
	4.05	47.2	5.1	3.9	1.31	17916	13709
	5.96	48.7	4.9	3.9	1.27	25705	20299
C2.1	2.01	48.5	5.5	4.1	1.34	9728	7244
	4.02	46.9	5.5	4.1	1.33	19186	14454
	5.99	48.6	5.6	4.2	1.34	29201	21777
C2.2	2.02	51.1	5.6	4.2	1.34	9924	7413
	4.01	50.5	5.4	4.1	1.32	18902	14306
	6.00	48.3	5.4	4.1	1.31	28109	21386
C7.1	2.01	51.5	5.7	4.3	1.33	10080	7597
	4.02	50.0	5.2	4.0	1.32	18400	13959
	5.99	49.2	5.4	4.0	1.34	28134	21040
C7.2	1.99	47.4	5.5	4.1	1.32	9520	7194
	4.01	46.8	5.2	3.9	1.33	18307	13805
	6.02	49.2	5.5	4.1	1.33	28877	21697
C12.1	2.01	46.9	5.8	4.3	1.33	10190	7648
	4.05	46.4	5.4	4.1	1.31	18940	14431
	6.03	47.6	5.3	4.0	1.32	28082	21312
C12.2	1.99	44.5	5.1	3.9	1.32	8912	6740
	4.00	45.6	5.2	4.0	1.32	18338	13905
	5.98	47.4	5.2	3.9	1.33	27388	20611
C17.1	2.00	49.0	5.6	4.2	1.33	9727	7332
	4.00	45.5	5.1	3.9	1.32	17708	13461
	5.96	45.8	5.1	3.9	1.31	26557	20246
C17.2	2.00	46.9	5.4	4.1	1.33	9492	7145
	4.01	46.6	5.3	4.0	1.31	18422	14028
	5.99	47.6	5.3	4.0	1.31	27794	21197
C25.1	2.00	44.4	5.4	4.0	1.34	9396	7023
	4.01	47.2	5.3	4.1	1.32	18730	14214
	5.96	46.5	5.2	4.0	1.31	27105	20696
C25.2	2.01	45.8	5.6	4.2	1.33	9760	7336
	3.99	46.8	5.1	3.9	1.32	17683	13436
	5.99	47.1	5.4	4.1	1.31	28110	21425
C60.1	2.01	49.1	5.4	4.0	1.34	9489	7089
	4.03	49.3	5.5	4.1	1.32	19351	14607
	5.99	46.9	5.3	4.0	1.32	27556	20806
C60.2	2.00	48.2	5.6	4.3	1.32	9846	7437
	4.02	47.7	5.4	4.1	1.33	18970	14294
	5.99	49.0	5.4	4.1	1.32	28101	21325
C100.1	2.01	50.2	6.1	4.4	1.39	10675	7696
	4.02	52.3	6.4	4.6	1.39	22514	16161
	6.02	48.9	6.3	4.4	1.43	33343	23378
C100.2	2.00	53.4	6.2	4.4	1.41	10950	7785
	4.03	46.4	6.0	4.3	1.41	21193	15001
	6.01	47.9	6.2	4.3	1.44	32440	22559
C250.1	2.01	45.8	6.1	4.2	1.45	10757	7419
	4.07	49.1	6.5	4.4	1.46	22958	15770
	6.01	46.9	6.5	4.4	1.48	34125	23117
C250.2	2.01	45.5	5.9	4.2	1.43	10467	7334
	4.01	49.6	6.4	4.5	1.42	22290	15694
	6.02	46.8	6.4	4.4	1.46	33478	22937

The minimum and maximum values of the momentum thickness changed between 3.9 mm and 4.6 mm and the shape factor of all tested surfaces varied between 1.27 and 1.48. The Reynolds number based on the displacement thickness changed between 8912 and 34125, and that based on the momentum thickness varied between 6740 and 23378.

Overall, the boundary layer thickness, displacement, momentum thickness and shape factor values generally increased along with coated Cu_2O particle size increase, or the surface roughness. It can be said that, apart from the smooth reference surface, the surfaces coated with particle sizes of 12µm (C12) and 17µm (C17) indicated the lowest boundary layer thickness and shape factor values. Thus a lower skin friction drag from these surfaces (i.e. C12 and C17) would be expected compared with other tested surfaces. Moreover, higher boundary layer parameters were observed from surfaces coated with Cu_2O particle size of 100µm (C100) and 250µm (C250). Therefore significantly higher frictional drag would be expected from those surfaces.

5.5.2 Mean Velocity Profiles in Outer Variables

The mean streamwise velocity profiles are plotted in **Figure 5.11**, using outer scaling for the entire test cases. Since the effect of higher roughness is to increase the drag, therefore, resulted in a less full velocity profile. In particular, it can be seen that the C100 and C250 surfaces exhibit significant drag as indicated by their velocity profiles had more obvious downward shift which is due to the extreme surface roughness resulting from the Cu_2O sizes.

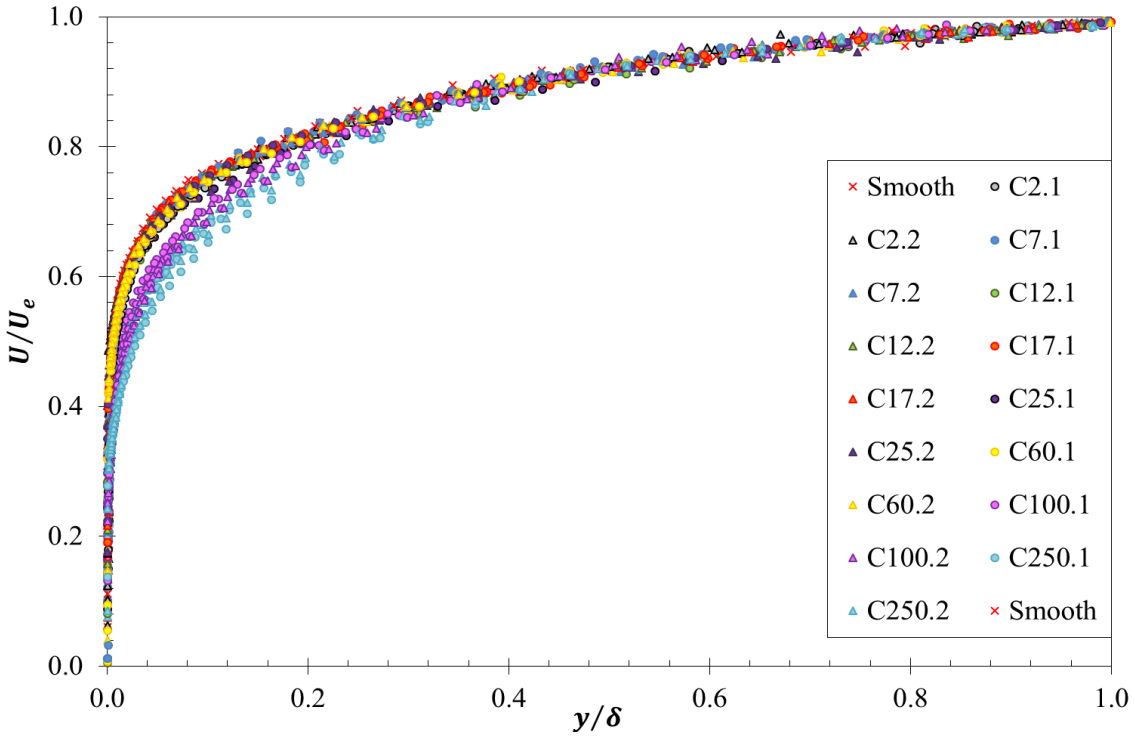

Figure 5.11: Mean velocity profiles in outer scaling for the entire test cases

For the mean flow similarity comparison, the velocity-defect law profiles from all test cases are plotted in **Figure 5.12**, using boundary layer thickness as the outer scaling parameter. A very good collapse of smooth and rough wall data was observed throughout the logarithmic and outer part of the boundary layer ($0.01 < y/\delta$). It has to be noted that, if the shapes of the mean profile in the overlap and outer region of the boundary layer are similar for smooth and rough walls, the roughness function can be expressed as the skin friction difference between the smooth wall (C_{fs}) and the rough wall (C_{fR}), at the same displacement thickness Reynolds number ($Re_{\delta 1}$). The detailed roughness function derivative process for the velocity profile measurement was introduced in Section 3.4.1. For the logarithmic and outer part of the boundary layer ($0.01 < y/\delta$), the excellent collapse of the smooth and rough profiles has been experimentally verified by a number of researchers (Bandyopadhyay, 1987; Raupach *et al.*, 1991; Antonia and Krogstad, 2001; Schultz and Flack, 2003; Castro, 2007; Flack *et al.*, 2007; Schultz and Flack, 2007).

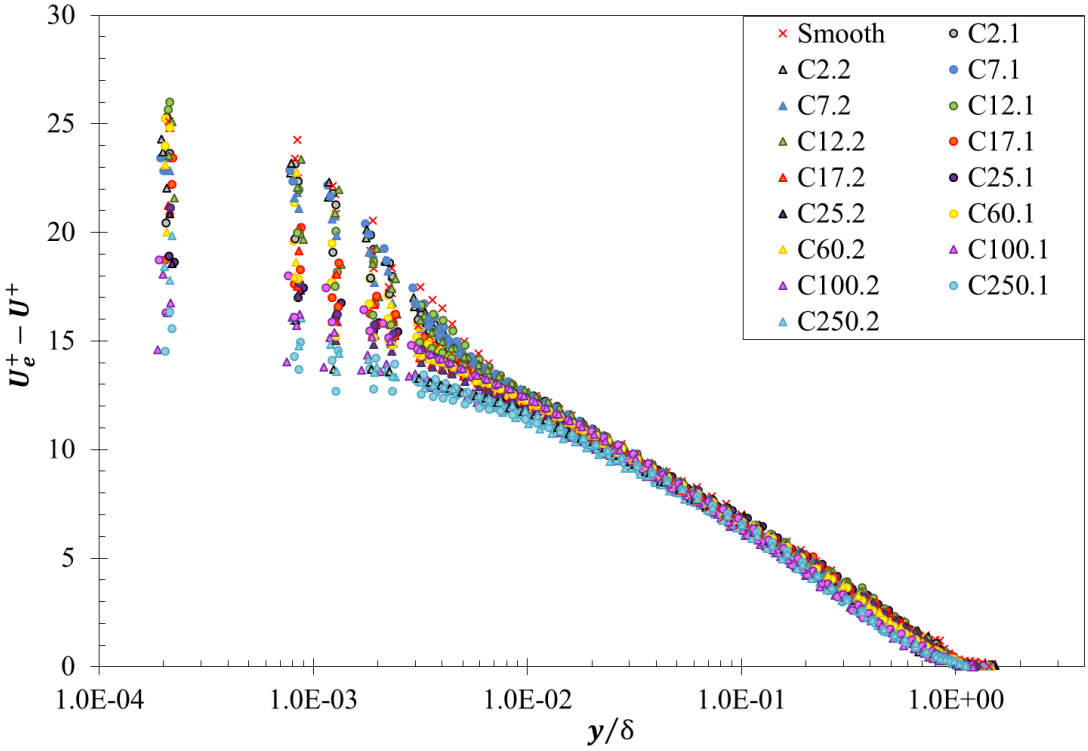

Figure 5.12: Velocity defect law in outer scaling for the entire test cases

Based on the acceptance of the universality of the velocity defect law, Hama (1954) derived the following equation to relate the shape parameter with the local skin friction coefficient by introducing a universal form parameter G for the cease of zero pressure gradient. The relation is expressed as:

$$H = \left(1 - G\left(\sqrt{\frac{c_f}{2}}\right)\right)^{-1} \qquad \textbf{5.4}$$

According to Hama (1954), G equals 6.1 for zero-pressure-gradient flat-plate turbulent boundary layer flows. The shape factors against the skin friction results of all tested surfaces are plotted in **Figure 5.13**. The results of most of the tested surfaces (smooth, C2−C60) are concentrated at the $25.6 < \sqrt{2/c_f} < 28.0$ with shape factor ranging between H = 1.27 (Smooth) to H =1.34 (C60). For the surfaces coated with larger size Cu_2O particles (i.e. C100 and C250), higher H values are expected due to the rougher surface profiles. The values of the shape factors for the surfaces C100 and C250 were between 1.39 and 1.48. Therefore, it is possible to state that the agreement of the overall experimental results with the given relationship is good and provides support to the universality of the velocity defect law.

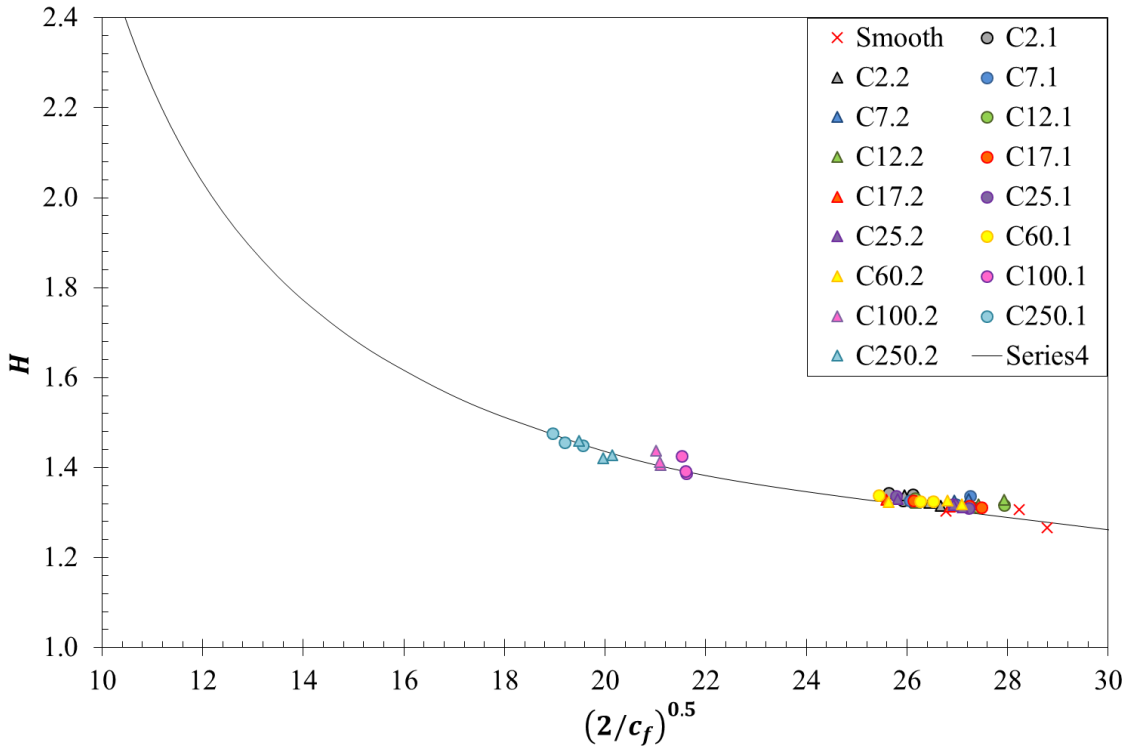

Figure 5.13: Shape parameter and local skin friction drag correlation

Figure 5.14 to **Figure 5.16** present the mean velocity profiles of the tested surfaces at tested freestream velocities of 2 m/s, 4 m/s and 6 m/s respectively, by using inner scaling. The friction velocities, used for the non-dimensionalisation, were calculated with the outer layer wall similarity technique (or Hama Method) which was introduced in **Section 3.5.1.5**. Shown for comparison, the viscous velocity profile ($U^+ = y^+$) and the logarithmic law for a smooth surface (Equation **3.25** are also included in the figures.

It is observed that the results of reference acrylic smooth surface follows the smooth logarithmic law (log-law) line as expected. At 2m/s (shown in **Figure 5.14**), the velocity profiles of the surfaces coated with specimens C12 and C17 almost overlapped with that of the smooth reference surface. The downwards shifts in the velocity profiles due to the surface roughness are not significant among these surfaces. Although there are slight downwards shifts for the surfaces coated with C2, C7, C25 and C60, however, they are all actually by a small amount. Therefore, the roughness function results from all of the above surfaces are expected to lie in the transitionally rough regime. According to **Figure 5.15** and **Figure 5.16**, as the inflow velocity increases, more obvious dissociation phenomena can be observed in these profiles, which displays larger deviations from the smooth log-law, and these indicate the increasing values of the roughness functions for these surfaces as the Reynold number increases. On the other hand, the velocity profile of the surfaces coated with C100 and C250 display very large

deviations from the smooth log-law with an obvious large downwards shift as expected in a fully rough flow regime.

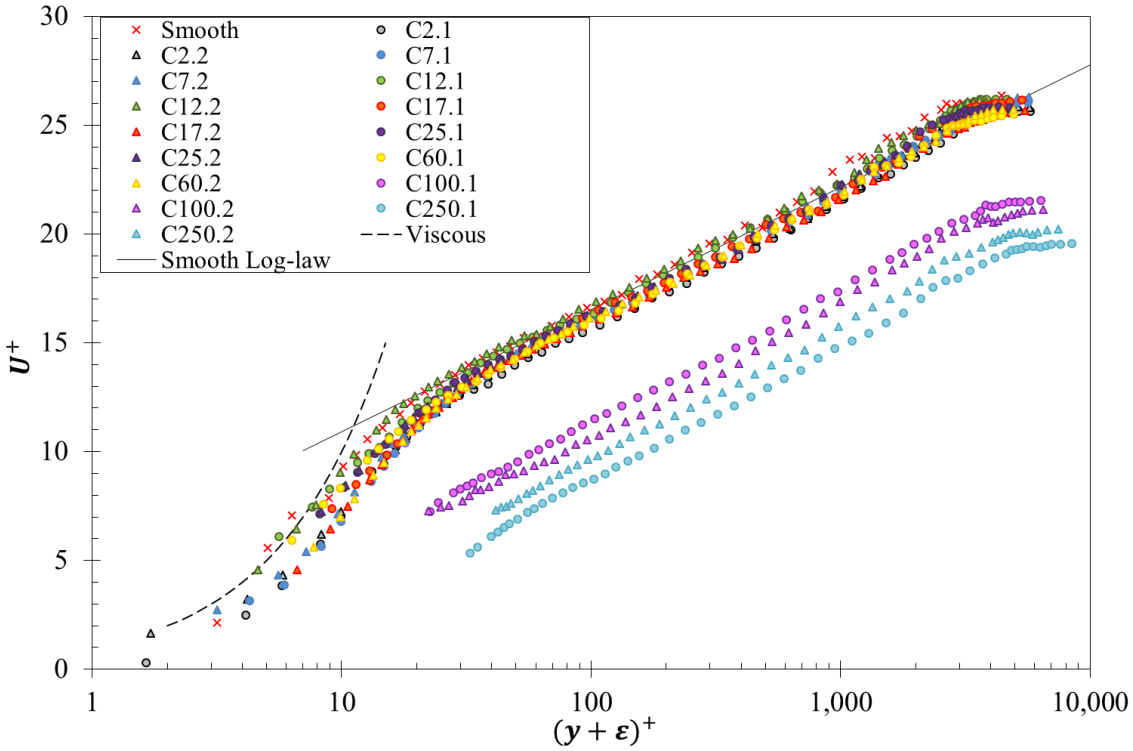

Figure 5.14: Streamwise velocity profiles in inner scaling at inflow velocity of 2m/s

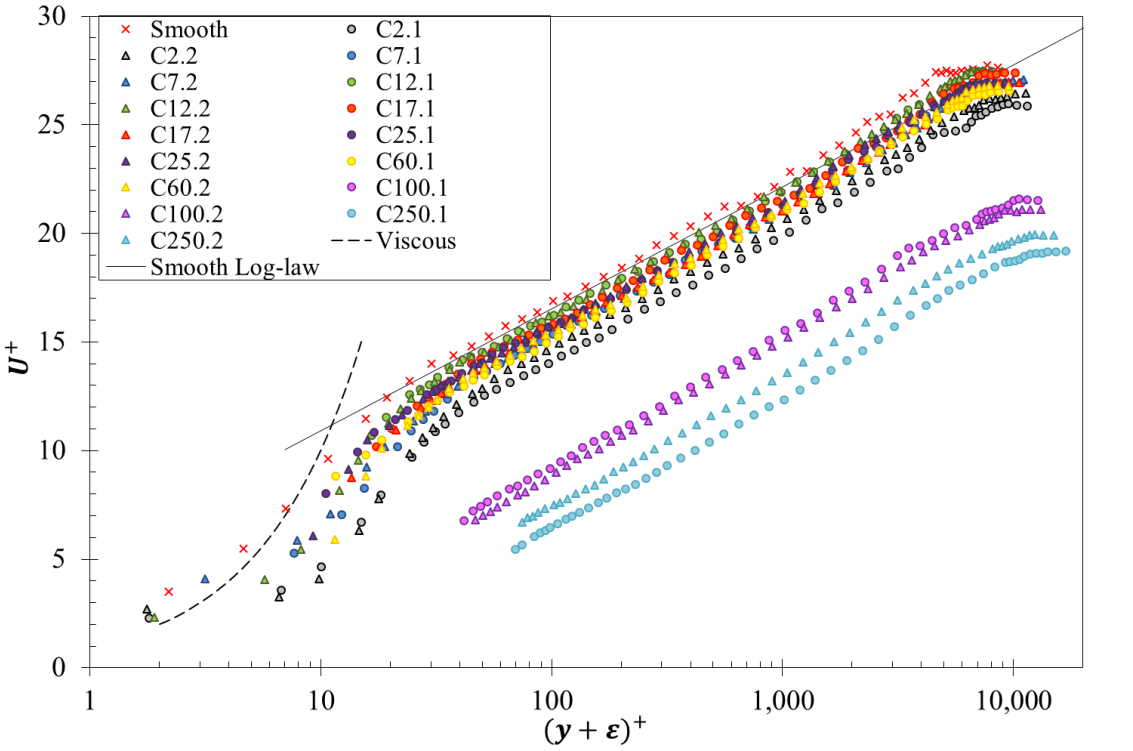

Figure 5.15: Streamwise velocity profiles in inner scaling at inflow velocity of 4m/s

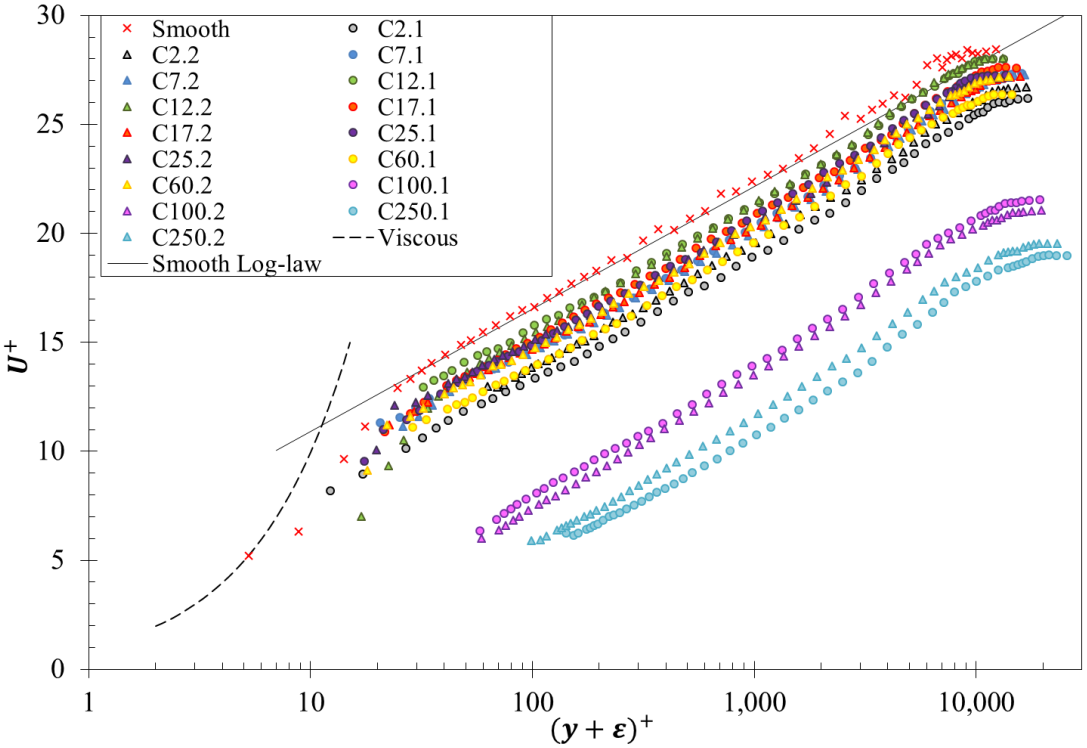

Figure 5.16: Streamwise velocity profiles in inner scaling at inflow velocity of 6m/s

5.5.3 Skin Friction Coefficient and Roughness Function

The results of friction velocities (u_τ) in m/s, local skin friction drag coefficients (c_f), and error in origin (ε) in mm are presented in **Table 5.3** for all of the test cases. The friction velocities and local skin friction drag coefficients were calculated by using three different methods:

1. Hama's Method (HM), also known as the outer layer wall similarity technique, based on Krogstad *et al*. (1992) and Krogstad and Antonia (1994);
2. The modified Clauser method (MC), based on Perry and Li (1990); and
3. The total stress method (TS) from Schultz and Flack (2007).

All three methods have already been explained in detail in **Section 3.5.1**. In using the three methods for the smooth surface friction velocity calculation, HM and MC provided very close results within a maximum difference of 0.97% (and 0.75% on average) while the average difference in the friction velocity for all coated surfaces (i.e. C2−C250) between the two methods was 1.4%, and 3% on average for the C100 and C250, respectively. The $\boldsymbol{u_\tau}$ values of the smooth surface with the TS method were found to be 8.52% higher than those from the HM and MC methods. For the full set of coated surfaces, the average difference in the friction velocity calculated by using the TS method was 6.6% higher than other two methods, and 2.5% on average for only C100 and C250.

Table 5.3: Skin friction coefficients for all tested surfaces

Surface	$Re_{\delta 1}$	ε	u_τ (HM)	c_f (HM)	u_τ (MC)	c_f (MC)	u_τ (TS)	c_f (TS)
Smooth (Acrylic)	9473	0.03	0.07	2.79E-03	0.08	2.83E-03	0.08	3.20E-03
	17916	-0.03	0.14	2.51E-03	0.14	2.53E-03	0.16	3.02E-03
	25705	0.01	0.21	2.41E-03	0.21	2.37E-03	0.23	2.78E-03
C2.1	9728	0.01	0.08	3.04E-03	0.08	3.05E-03	0.09	3.62E-03
	19186	0.02	0.16	2.98E-03	0.16	3.02E-03	0.17	3.54E-03
	29201	-0.08	0.23	2.93E-03	0.23	2.98E-03	0.25	3.46E-03
C2.2	9924	0.01	0.08	2.97E-03	0.08	2.99E-03	0.09	3.55E-03
	18902	0.02	0.15	2.86E-03	0.15	2.93E-03	0.17	3.38E-03
	28109	0.22	0.23	2.81E-03	0.23	2.90E-03	0.24	3.20E-03
C7.1	10080	0.03	0.08	2.95E-03	0.08	2.93E-03	0.08	3.41E-03
	18400	0.01	0.15	2.75E-03	0.15	2.82E-03	0.16	3.29E-03
	28134	-0.06	0.22	2.69E-03	0.22	2.77E-03	0.24	3.15E-03
C7.2	9520	0.03	0.08	2.92E-03	0.08	2.91E-03	0.08	3.47E-03
	18307	0.01	0.15	2.76E-03	0.15	2.77E-03	0.16	3.37E-03
	28877	-0.06	0.22	2.70E-03	0.22	2.74E-03	0.24	3.13E-03
C12.1	10190	0.03	0.08	2.92E-03	0.08	2.89E-03	0.08	3.32E-03
	18940	0.04	0.15	2.66E-03	0.15	2.64E-03	0.16	3.20E-03
	28082	0.03	0.22	2.56E-03	0.22	2.59E-03	0.24	3.04E-03
C12.2	8912	0.06	0.08	2.92E-03	0.08	2.93E-03	0.08	3.35E-03
	18338	0.02	0.15	2.66E-03	0.15	2.70E-03	0.16	3.15E-03
	27388	0.03	0.21	2.56E-03	0.22	2.64E-03	0.23	2.99E-03
C17.1	9727	0.11	0.08	2.93E-03	0.08	2.90E-03	0.08	3.32E-03
	17708	0.03	0.15	2.69E-03	0.15	2.74E-03	0.16	3.29E-03
	26557	0.03	0.22	2.65E-03	0.22	2.68E-03	0.23	3.03E-03
C17.2	9492	0.07	0.08	3.06E-03	0.08	2.91E-03	0.08	3.38E-03
	18422	0.03	0.15	2.77E-03	0.15	2.76E-03	0.16	3.23E-03
	27794	0.03	0.22	2.72E-03	0.22	2.74E-03	0.24	3.07E-03
C25.1	9396	0.10	0.08	3.01E-03	0.08	2.98E-03	0.08	3.50E-03
	18730	0.07	0.15	2.76E-03	0.15	2.83E-03	0.17	3.39E-03
	27105	0.03	0.22	2.70E-03	0.22	2.80E-03	0.24	3.13E-03
C25.2	9760	0.11	0.08	3.00E-03	0.08	3.02E-03	0.08	3.48E-03
	17683	0.07	0.15	2.76E-03	0.15	2.83E-03	0.16	3.39E-03
	28110	0.04	0.22	2.72E-03	0.22	2.79E-03	0.24	3.10E-03
C60.1	9489	0.03	0.08	3.09E-03	0.08	3.08E-03	0.09	3.60E-03
	19351	0.01	0.15	2.84E-03	0.15	2.91E-03	0.17	3.35E-03
	27556	0.05	0.23	2.90E-03	0.23	2.93E-03	0.24	3.16E-03
C60.2	9846	0.13	0.08	3.04E-03	0.08	3.03E-03	0.08	3.57E-03
	18970	0.01	0.15	2.78E-03	0.15	2.87E-03	0.17	3.38E-03
	28101	0.13	0.22	2.72E-03	0.22	2.81E-03	0.24	3.19E-03
C100.1	10675	0.13	0.09	4.28E-03	0.09	4.33E-03	0.10	4.48E-03
	22514	0.06	0.19	4.29E-03	0.19	4.57E-03	0.20	4.83E-03
	33343	0.10	0.28	4.32E-03	0.29	4.63E-03	0.30	4.80E-03
C100.2	10950	0.20	0.10	4.49E-03	0.10	4.68E-03	0.10	4.89E-03
	21193	0.10	0.19	4.50E-03	0.20	4.98E-03	0.20	4.80E-03
	32440	0.10	0.29	4.53E-03	0.30	5.05E-03	0.29	4.66E-03
C250.1	10757	0.20	0.10	5.23E-03	0.10	5.43E-03	0.10	5.22E-03
	22958	0.20	0.21	5.43E-03	0.22	5.71E-03	0.21	5.50E-03
	34125	0.30	0.32	5.57E-03	0.32	5.78E-03	0.31	5.46E-03
C250.2	10467	0.24	0.10	4.93E-03	0.10	5.18E-03	0.10	4.69E-03
	22290	0.20	0.20	5.02E-03	0.21	5.48E-03	0.20	5.21E-03
	33478	0.22	0.31	5.27E-03	0.32	5.58E-03	0.31	5.28E-03

Accordingly, since the good agreement was found between HM and MC in the calculation of the frictional velocities for smooth and coated surfaces, the friction drag coefficients and roughness function results calculated with HM were selected to plot. Moreover, the position errors in the origin values were observed to be in the range of 20μm for the smooth surface, and about 50μm on average for surfaces coated with C2−C60. The C100 and C250 surfaces were found to have the largest position error with an average of 120μm and 230μm, respectively.

The frictional resistance coefficients of all the tested surfaces are shown in **Figure 5.17** plotted against the displacement thickness Reynolds number, $Re_{\delta 1}$. For smooth surface comparison, an empirical power relation proposed by Monin *et al.* (1971) is given in below Equation **5.5**:

$$\frac{1}{\sqrt{c_f}} = \frac{1}{\kappa\sqrt{2}}\ln(Re_{\delta 1}) + B_4 \qquad \textbf{5.5}$$

This equation is based on Thompson's theoretical reasoning, similar to Coles' law of the wake (Coles, 1956), whereby the constants κ and B_4 were empirically determined as 0.4 and 2.6, respectively.

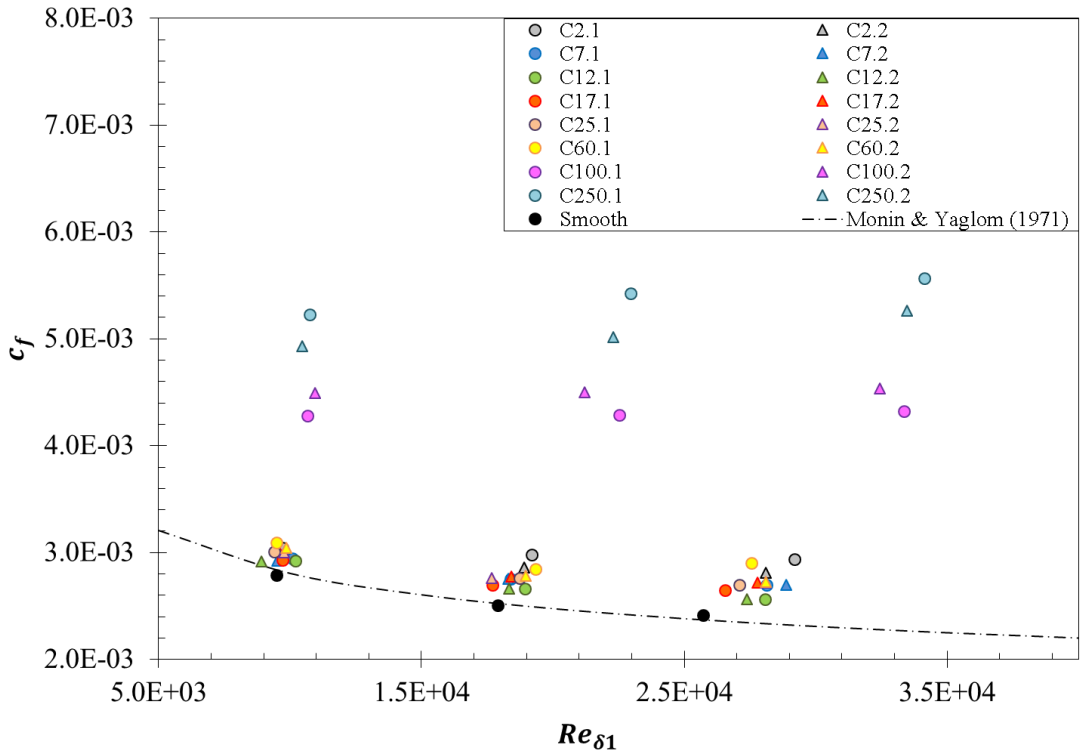

Figure 5.17: Frictional coefficient of all test surfaces (Hama's Method)

The experimental smooth surface results show a good agreement with the mean line of Monin *et al.* (1971) over the entire Reynolds number range. Within the same Reynolds number range,

the surfaces coated with C2−C60 display similar drag performance. Whereas, for the Reynolds number $Re_{\delta 1} > 2.3 \times 10^4$, the drag performance of surfaces coated with C100 and C250 presented Reynolds number independence which indicates the boundary layer reaching the fully rough regime.

To provide further insight into the friction drag versus different surface roughness conditions with their cuprous oxide specimens, **Table 5.4** shows the increase (%) in friction coefficient for the test surfaces compared to the smooth surface.

Table 5.4: Increase in overall c_f for the test specimens compared to the smooth surface

Specimen	R_t (μm) average	Average Increase in c_f (%)	Range of Increase in c_f
C2	53.7	14.4	6.5−21.5
C7	69.1	8.9	4.7−11.8
C12	17.2	5.7	4.7−6.2
C17	27.1	9.1	5.1−12.6
C25	32.2	10.0	7.6−12.7
C60	45.6	12.9	9.1−20.2
C100	122.0	71.9	53.5−87.7
C250	337.9	104.9	76.8−130.8

The lowest drag was demonstrated by specimen C12 (5.7%), and this was closely followed by C7 (8.9%) and C17 (9.1%). According to the discussion in **Section 4.4**, due to the coagulation of the very small particles, a large number of high macrostructure peaks formed on the C2 and C7 surfaces. However, based on the image observation (**Figure 4.16**) some smooth areas can be found to be scattered among these largely uneven top-surfaces. Therefore, the author speculates that during the measurements of C7, the laser intersection may have been located over the smooth area and measured the local velocity profile. Therefore, the C7 surface indicated slightly lower frictional coefficient values than C17, even though the C7 (R_t=69.1μm) has much higher R_t value than C17 (R_t=27.1μm). Nevertheless, the boundary layer gives the skin frictional coefficient of the local area, and the results can be easily varied by the surface condition of the chosen measurement location, especially for uneven surfaces. Further repeat tests at different measurement location are required for this case. The study of the overall surface condition impact on the frictional drag is presented in **Chapter 7**.

The smallest sized particle, C2 shows an average frictional coefficient of 14.4% of that of the smooth surface and is higher than C25 (10%) and C60 (12.9%) due to the application issues already discussed. The highest average friction was approximately 104.9%, and this was

obtained from C250. Then this is followed by C100 (71.9%). Except for the coagulation particles, i.e. C2 and C7, the experimental results from all tested surfaces indicated that the overall frictional coefficient increased from that of the smooth surface with the increase in particle size.

The results of the roughness function, ΔU^+, for all of the tested surfaces are plotted in **Figure 5.18** against the roughness Reynolds number, k^+. For comparison, the figure also includes the correlation of Townsin and Dey (1990), the well-known Colebrook-White type roughness function (Colebrook *et al*., 1939) and Nikuradse type roughness function (Nikuradse, 1933). The roughness function correlation of Townsin and Dey (1990) relies on a sizeable collection of data for rough ship surfaces. As reported, the resulting best fit found by Townsin and Dey (1990) is given in Equation **5.6**.

$$\Delta U^+ = \frac{1}{\kappa}\ln(1 + 0.18k^+) \qquad \textbf{5.6}$$

The Colebrook-White function was developed for engineering surfaces. The Colebrook type roughness function (Colebrook *et al*., 1939) is given by Aupoix (2015) as shown in Equation **5.7**:

$$\Delta U^+ = \frac{1}{\kappa}\ln(1 + \frac{k^+}{exp[\kappa(8.5 - C)]}) \qquad \textbf{5.7}$$

The Nikuradse (1933) roughness function based on uniform sand grain results was proposed by Ligrani and Moffat (1986) as below:

$$\begin{gathered} \Delta U^+ = (\frac{1}{\kappa}\ln + \mathrm{C} - 8.5)\sin(\frac{\pi g}{2}) \\ g = \frac{lnk_s^+ - lnk_S^+}{lnk_R^+ - lnk_S^+} \;\; k_S^+ < k_s^+ < k_R^+ \\ g = 1 \;\; k_R^+ < k_s^+ \\ g = 0 \;\; k_s^+ < k_S^+ \end{gathered} \qquad \textbf{5.8}$$

where the von Karman constant, κ, for the Townsin and Dey (1990) roughness function correlation and Colebrook type roughness function equals 0.41. The intercept constant, C is 5.25 for the Colebrook type roughness function and 5.1 for the Nikuradse type roughness function. The lower critical roughness Reynolds number is $k_S^+ = 2.25$ and the upper critical roughness Reynolds number is $k_R^+ = 90$.

The choice of a suitable roughness length scale only affects the abscissa of roughness function profiles along with the roughness Reynolds number, without affecting roughness function values. Therefore, several options have been considered for selecting a suitable roughness length scale. For example, a multiple of the centreline average roughness height, R_a (with model $k = AR_a$, where A is an arbitrary constant) (Schultz, 2002), or a multiple of the peak to trough roughness height, R_t (with model $k = AR_t$) (Schultz, 2004; Flack *et al*., 2012). In addition, some authors have proposed the application of combined roughness parameters to calculate the roughness length scale. For example, Candries (2001) used the mean slope of the profile, Δ_a, multiplied by the centreline average roughness height, R_a ($k = \Delta_a R_a/2$). Alternatively, a combination of root-mean-square, R_q, and skewness, R_{sk} (with model $k = AR_q(1 + R_{sk})^B$) was proposed by Flack and Schultz (2010) and later modified by Ünal (2015) who introduced the mean spacing between the zero-crossings, Sd_4, and therefore proposed as below Equation **5.9** or Equation **5.10**:

$$k = AR_q(1 + R_{sk})^B/Sd_4 \qquad \textbf{5.9}$$

$$k = AR_q^2(1 + R_{sk})^B/Sd_4 \qquad \textbf{5.10}$$

For the roughness function based on the frictional coefficient of Hama's Method (HM), the roughness length scale was given by $k = 230R_q^2(1 + R_{sk})^{10}/Sd_4$. Therefore, the subsequent regression analysis results indicated that the 98.6% (i.e. $R^2 = 0.986$) variance shows a good agreement with the Colebrook type roughness function behaviour in the transitionally rough regime, whereas the 96.2% (i.e. $R^2 = 0.962$) variance shows a reasonable agreement with the Townsin and Dey (1990) roughness function correlation.

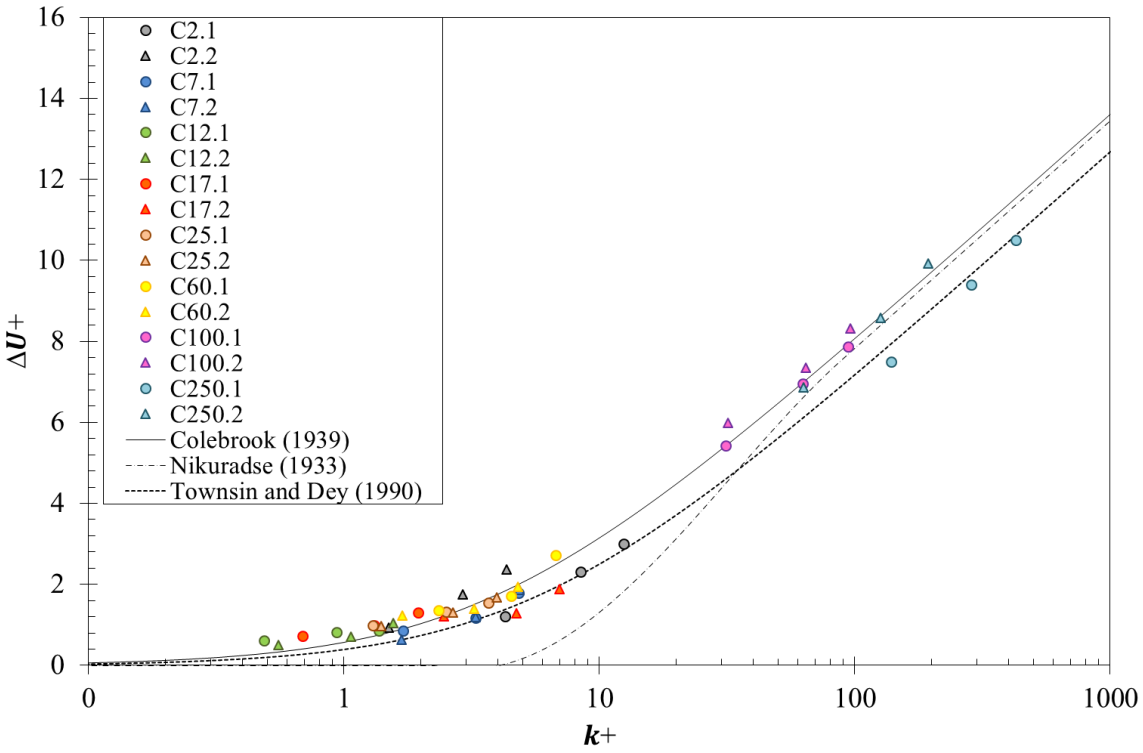

Figure 5.18: Roughness function of all test surfaces (Hama's Method)

Overall, observations of the roughness function values in the transitionally rough regime were generally concentrated between the Colebrook and Townsin and Dey curves. The roughness function behaviour of C100 and C250 fell between the fully rough asymptotic lines.

Further, detailed results of roughness function along with the associated k^+ from HM, MC and TS are presented in **Table 5.5**. There was no observation of k^+ value for the onset of the transitionally rough regime. Compared to results of the other surfaces, the surfaces coated with 12µm Cu_2O (C12) produced very close to zero ΔU^+ and the lowest roughness Reynolds number. This was followed by C17 and C7 whichever method is used. For the upper critical roughness Reynolds number, the fully rough regime of the HM results started at the roughness Reynolds number, $k^+ \approx 30$ for the surface of C100, and $k^+ \approx 40$ observed from the MC results. The TS results show the fully rough regime starts at $k^+ \approx 24$ for C100. These results show good agreement with Schultz and Flack (2007) and Shockling *et al.* (2006) who defined the upper critical range of the transitionally rough regime at $k^+ < 25$ and $k^+ < 30$ respectively.

Table 5.5: Roughness function for all tested surfaces

Surface	$Re_{\delta 1}$	k^+(HM)	ΔU^+(HM)	k^+(MC)	ΔU^+(MC)	k^+(TS)	ΔU^+(TS)
Smooth (Acrylic)	9473	-	-	-	-	-	-
	17916	-	-	-	-	-	-
	25705	-	-	-	-	-	-
C2.1	9728	4.27	1.22	5.20	1.05	4.46	1.52
	19186	8.43	2.31	10.33	2.58	8.82	2.76
	29201	12.47	3.00	15.30	3.51	12.99	3.46
C2.2	9924	1.49	0.94	1.82	0.85	1.87	1.31
	18902	2.91	1.75	3.59	2.16	3.63	2.17
	28109	4.31	2.36	5.34	3.08	5.28	2.41
C7.1	10080	1.70	0.87	2.06	0.62	1.80	0.72
	18400	3.28	1.17	4.04	1.62	3.56	1.78
	28134	4.84	1.78	5.97	2.45	5.20	2.23
C7.2	9520	1.68	0.64	2.03	0.37	2.47	0.95
	18307	3.27	1.19	4.00	1.35	4.90	2.05
	28877	4.86	1.86	5.96	2.39	7.08	2.20
C12.1	10190	0.49	0.62	0.59	0.27	0.80	0.56
	18940	0.93	0.82	1.13	0.57	1.58	1.49
	28082	1.36	0.86	1.67	1.29	2.30	1.77
C12.2	8912	0.55	0.51	0.68	0.31	0.93	0.40
	18338	1.07	0.71	1.31	0.98	1.81	1.24
	27388	1.56	1.05	1.93	1.72	2.63	1.48
C17.1	9727	0.69	0.73	0.83	0.40	1.07	0.48
	17708	1.32	0.99	1.62	1.07	2.13	1.67
	26557	1.95	1.30	2.39	1.75	3.05	1.57
C17.2	9492	2.47	1.22	2.93	0.37	3.07	0.92
	18422	4.72	1.29	5.74	1.33	5.96	1.53
	27794	6.99	1.88	8.55	2.30	8.70	1.88
C25.1	9396	1.30	0.99	1.57	0.65	1.78	1.19
	18730	2.50	1.32	3.09	1.54	3.50	2.16
	27105	3.68	1.56	4.56	2.33	5.00	2.06
C25.2	9760	1.40	0.97	1.71	0.92	1.90	0.84
	17683	2.66	1.31	3.28	1.56	3.76	2.04
	28110	3.97	1.67	4.90	2.57	5.36	1.81
C60.1	9489	2.34	1.37	2.84	1.10	2.80	1.05
	19351	4.50	1.72	5.54	2.13	5.50	2.11
	27556	6.75	2.73	8.25	3.13	7.93	2.21
C60.2	9846	1.69	1.24	2.05	0.98	2.10	0.96
	18970	3.24	1.40	4.00	1.89	4.18	2.17
	28101	4.78	1.93	5.91	2.64	6.05	2.36
C100.1	10675	31.27	5.42	38.27	5.38	24.06	4.08
	22514	62.53	6.97	78.59	7.83	49.91	6.54
	33343	94.14	7.88	118.70	9.01	74.70	7.41
C100.2	10950	31.94	5.98	39.70	6.27	25.08	5.05
	21193	64.22	7.34	82.27	8.55	49.94	6.35
	32440	96.16	8.33	123.61	9.81	73.39	7.04
C250.1	10757	138.64	7.50	169.60	7.44	76.02	5.67
	22958	285.36	9.40	356.40	10.09	157.66	7.87
	34125	426.69	10.50	529.28	11.25	231.92	8.74
C250.2	10467	62.77	6.86	78.33	7.18	37.73	4.52
	22290	126.17	8.57	160.47	9.61	79.30	7.28
	33478	193.96	9.92	243.00	10.86	119.69	8.36

It has to be noted that, the roughness length scale models used for the MC and TS calculations were also based on Equation **5.10**. The regression analysis results of 97.3% (i.e. $R^2 = 0.973$) and 96.6% (i.e. $R^2 = 0.966$) from MC and TS both indicated that these results are in good agreement with the Colebrook type roughness function. For the correlation with the Townsin and Dey's roughness function, 94.7% (i.e. $R^2 = 0.947$) and 95.4% (i.e. $R^2 = 0.954$) variances were given by MC and TS respectively. These values also show the good agreement of MC and TS results with Townsin and Dey's roughness function.

5.5.4 Reynolds Stress

Figure 5.19 presents the streamwise Reynolds normal stress component, $\overline{u'^2}$, normalised with u_τ^2, for smooth and all coated surfaces by using inner scaling. As shown in **Figure 5.19**, for surfaces coated with C2−C60, a near-wall high peak is observed at $(y+\varepsilon)^+ \approx 20$, which is similar to that observed on the smooth wall. The near-wall high peak values are associated primarily with the viscous effects and streamwise vortices (Grass, 1971; Jimenez, 2004). For $20 < (y+\varepsilon)^+$, the high peak near the wall disappears as the roughness Reynolds number, k^+, increases. According to Ligrani and Moffat (1986) and Brzek *et al.* (2007), the destruction of the near-wall high peak profile happens due to the breakdown of the viscous region by the roughness. Moreover, the absence of the near-wall peak in , $\overline{u'^2}^+$, was shown by Ligrani and Moffat (1986) to be a sensitive indicator of a boundary layer reaching the fully rough regime. Therefore, compared to the smooth wall, the near-wall high peak values of the C2−C60 surfaces decrease as the roughness Reynolds number increases. For the C100 and C250 surfaces, the near-wall high peak values totally disappear due to roughness elements extending further from the wall and breaking up the viscous region and some parts of the inner region and reaching the fully rough regime. When the boundary layer reaches the fully rough regime, the frictional drag is dominated by the form of the roughness elements as the viscous effects on the frictional drag of the wall become negligible.

It can also be seen that, for $(y+\varepsilon)^+ < 100$, the streamwise Reynolds normal stress profiles do not appreciably change with the flow Reynolds number increase. In contrast, the magnitudes of the profiles significantly increase for all wall distances greater than $100 < (y+\varepsilon)^+$. It was noted by Brzek *et al.* (2009) that this is due to the additional inactive motions over most of the boundary layer. Moreover, Reynolds number dependence is noticed for the tested surfaces in the outer region.

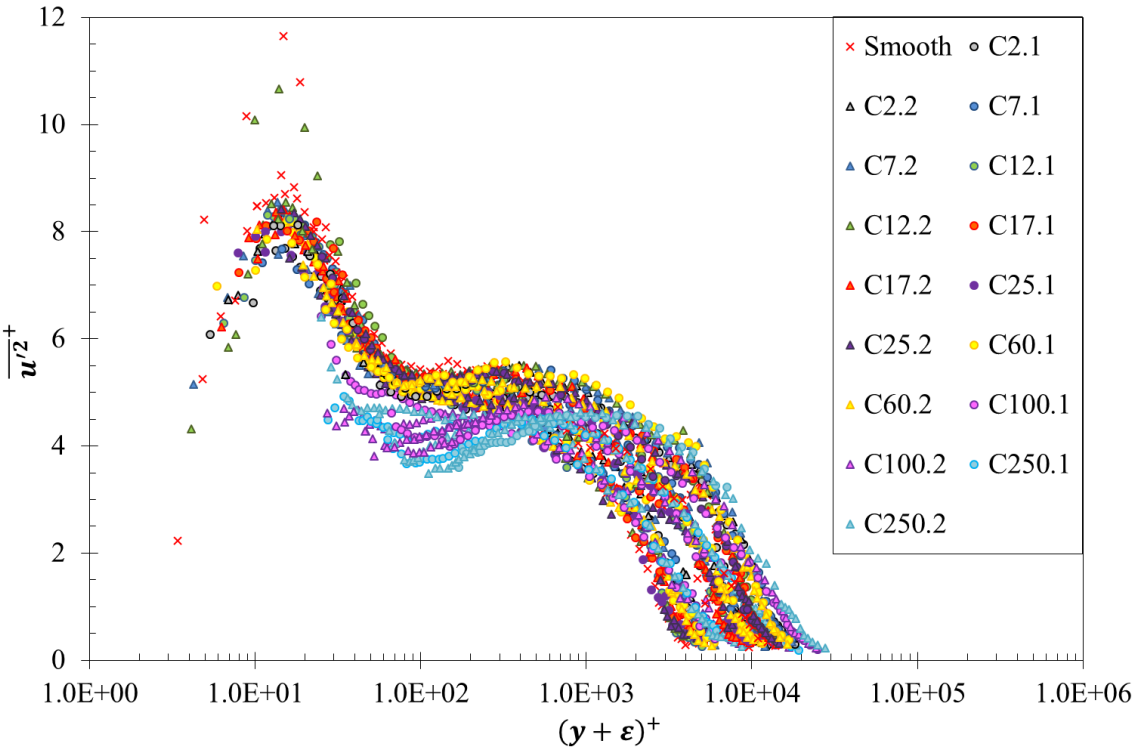

Figure 5.19: Streamwise Reynolds normal stresses in inner scaling

From the near-wall peak to $(y+\varepsilon)^+ \approx 100$, the decreasing tendency in $\overline{u'^2}^+$ profiles is observed from all the tests cases. However, for the fully rough $\overline{u'^2}^+$ profiles (i.e. C100 and C250), the rise in $\overline{u'^2}^+$ starts at $100 < (y+\varepsilon)^+$ and continues until reaching the large plateau region in the outer layer region for $400 < (y+\varepsilon)^+ < 2000$ of the boundary layer. For the surfaces C2−C60, the tendency of $\overline{u'^2}^+$ profiles continues to decrease for $100 < (y+\varepsilon)^+$. It can also be seen that at the edge of the boundary layer, the $\overline{u'^2}^+$ profiles do not go to zero for all the tested cases with high free-stream turbulence but converge to the free-stream values (Brzek *et al.*, 2009).

As for the streamwise Reynolds normal stresses for each surface against normalised wall distance, **Figure 5.20** indicates that the profiles of the smooth and surfaces coated with C2−C60 surfaces collapse within the uncertainty in the outer boundary layer. However, the surfaces of C100 and C250 display lower values over the range of $0.15 < (y+\varepsilon)/\delta$. This presents a discrepancy with regards to other investigations, e.g. Schultz (2000), Schultz and Flack (2003), Flack *et al.* (2007) and Brzek *et al.* (2007) who showed good agreement of the smooth- and rough-wall results in the overlap and outer region of the boundary layer when similar Reynolds number cases are compared.

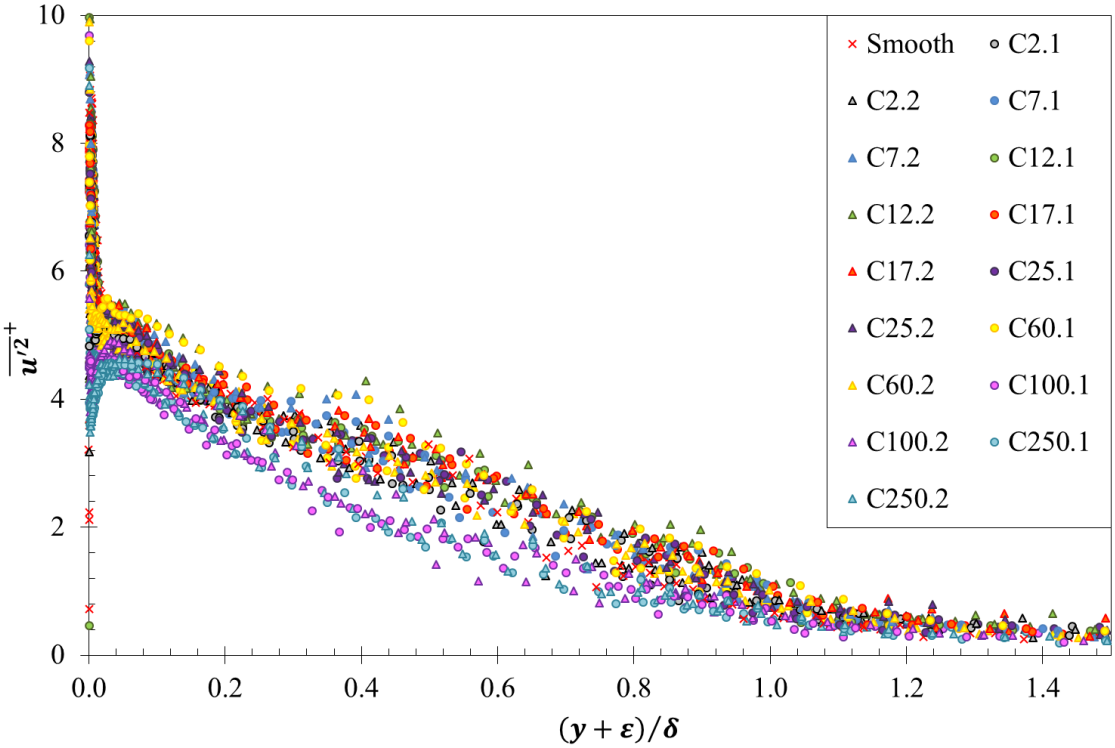

Figure 5.20: Streamwise Reynolds normal stresses in outer scaling

Similar issues were noted from other studies, for example, Schultz and Swain (1999) reported lower wall-normal fluctuations for some of their fouled specimens, whereas Ünal *et al.* (2012) found lower wall-normal Reynolds stresses for the fully rough sandpaper surface. According to Ünal *et al.* (2012) the step change in surface roughness, which exists in the present experimental configuration, may have affected the results. Antonia and Luxton (1971) proposed that a distance of almost 20δ from smooth to the rough junction is required in order to obtain the self-preserving nature of turbulence properties for a rough boundary layer. Whereas, Bandyopadhyay (1987) showed a distance of nearly 35δ for the sand roughness to reach the self-preserving state following the step change from smooth to rough. In the present investigation, the step change distance for C100 and C250 was 10δ and 10.6δ, respectively, which are shorter than the values suggested by Antonia and Luxton (1971) or Bandyopadhyay (1987). Therefore, the low values of the streamwise Reynolds normal stresses obtained from C100 and C250 could be associated with the sudden transition from smooth to the rough surface.

Based on the work of George and Castillo (1997), the outer scaling normalisation is based on the freestream velocity, U_e^2, instead of u_τ^2 which has a direct effect on the results. Accordingly, **Figure 5.21** presents the same variable. As it can clearly be seen, the profiles of all of the test cases collapsed well within the uncertainty for $0.5 < (y+\varepsilon)/\delta$. Furthermore, the effect of the

surface roughness of each test surface is clearly visible in the overlap region. The near wall peaks discussed in the previous paragraph may also be observed at $(y+\varepsilon)/\delta$ to be approximately $0.01-0.08$ with varying values for the different cases in this figure.

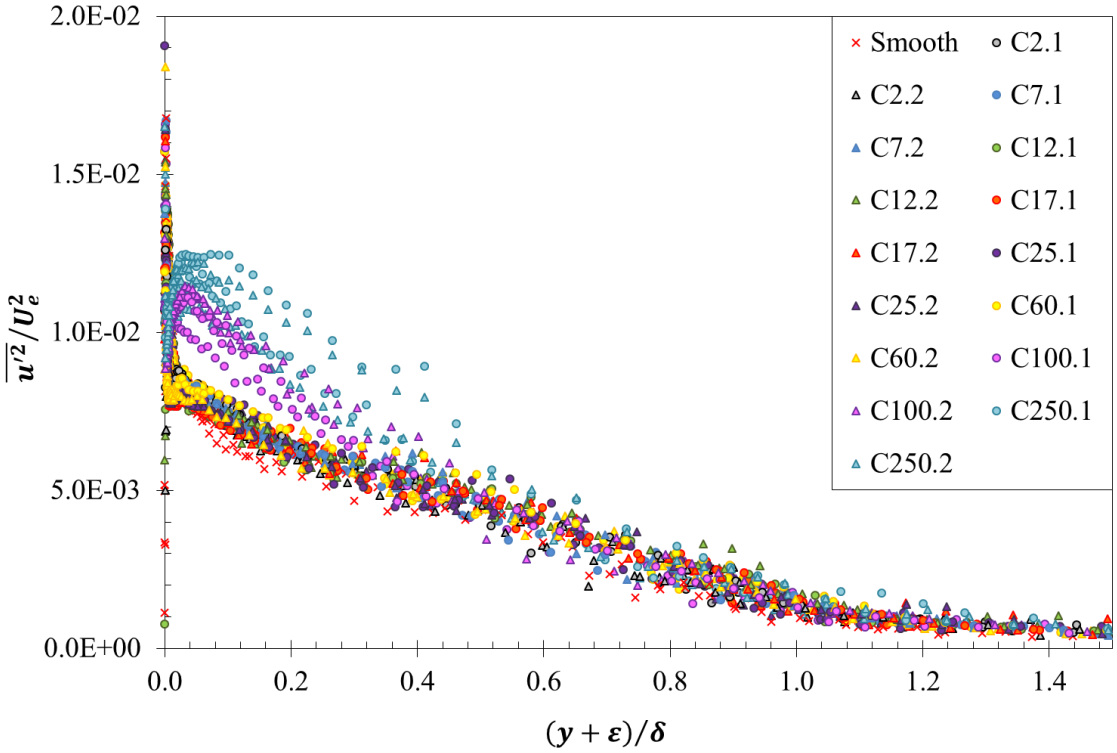

Figure 5.21: Streamwise Reynolds normal stresses in outer scaling (U_e^2)

The profiles of wall-normal Reynolds stress components, $\overline{v'^2}$, normalised with u_τ^2, for smooth and all coated surfaces by using inner scaling are presented in **Figure 5.22**. It can be seen that there is less effect from roughness on the $\overline{v'^2}^+$ profiles compare to the $\overline{u'^2}^+$ profiles, and only modest deviations are shown between smooth and rough surfaces in inner variables when the Reynolds number is similar. Furthermore, the shape of the smooth and transitionally rough profiles are nearly identical. Compared to the smooth surface profiles, the rough surfaces are found to have slight roughness dependence in the profiles. It can be said that the $\overline{v'^2}^+$ profiles vary mostly due to Reynolds number. Moreover, for different Reynolds number, the profiles of both smooth and rough surfaces show an approximate collapse up to $(y+\varepsilon)^+ \approx 80$ which is in good agreement with Brzek *et al.* (2007) and Ünal (2012). For $80 < (y+\varepsilon)^+$, profiles show a large plateau region at $1.2 < \overline{v'^2}^+ < 1.4$ and the range of the plateau region extends with increasing of the Reynolds number. Similar phenomena can also be found and proved by other investigation results such as Brzek *et al.* (2007), Flack *et al.* (2007), Brzek *et al.* (2008) and Brzek *et al.* (2009).

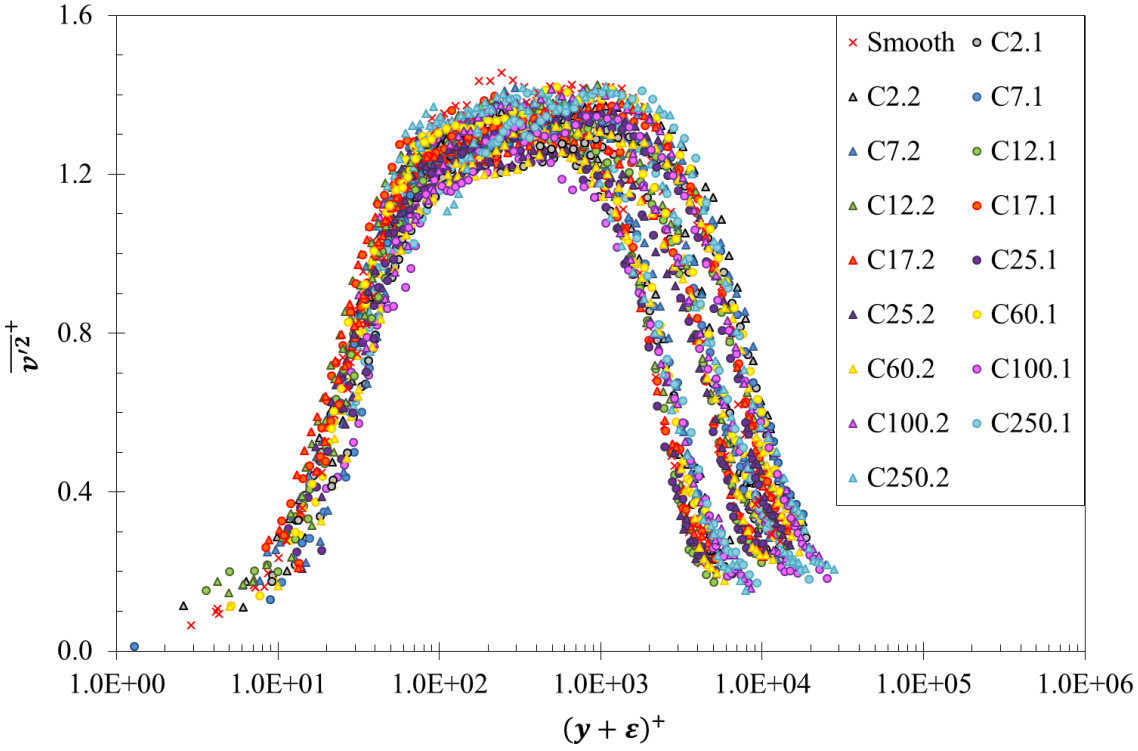

Figure 5.22: Wall-normal Reynolds stresses in inner scaling

Figure 5.23 presents the wall-normal Reynolds stress component, $\overline{v'^2}$, normalised with U_e^2 for each surface against normalised wall distance. As it clearly can be seen, the profiles of smooth and rough surfaces collapsed within the uncertainty for the range $0.44 < (y+\varepsilon)/\delta$. For outside the roughness (or viscous) sublayer of rough and smooth walls, Raupach *et al.* (1991) noted that there was similarity in $\overline{v'^2}^+$ profiles, which agreed with other well demonstrated studies, for instance, Schultz and Flack (2003) and Flack *et al.* (2007). However, there are also several studies that indicated that the wall-normal fluctuations outside the viscous sublayer were affected by the surface roughness. For example, Krogstad *et al.* (1992) and Krogstadt and Antonia (1999) found significant increases in transverse turbulence intensities with the effect of the different surface roughness types. Krogstad *et al.* (2005) inferred that internal flows such as channel and pipe flows may respond differently to roughness than do boundary layer flows. Nevertheless, the good agreement between smooth and rough surfaces provides support to the wall similarity concept in the boundary layers in which the relative roughness and the Reynolds number are both large. Furthermore, the effect of the surface roughness of each test surface is clearly visible in the overlap region. The near wall peaks seen in **Figure 5.23** may also be observed at $(y+\varepsilon)/\delta$ to be approximately $0.01-0.08$ with varying values for the different cases in this figure.

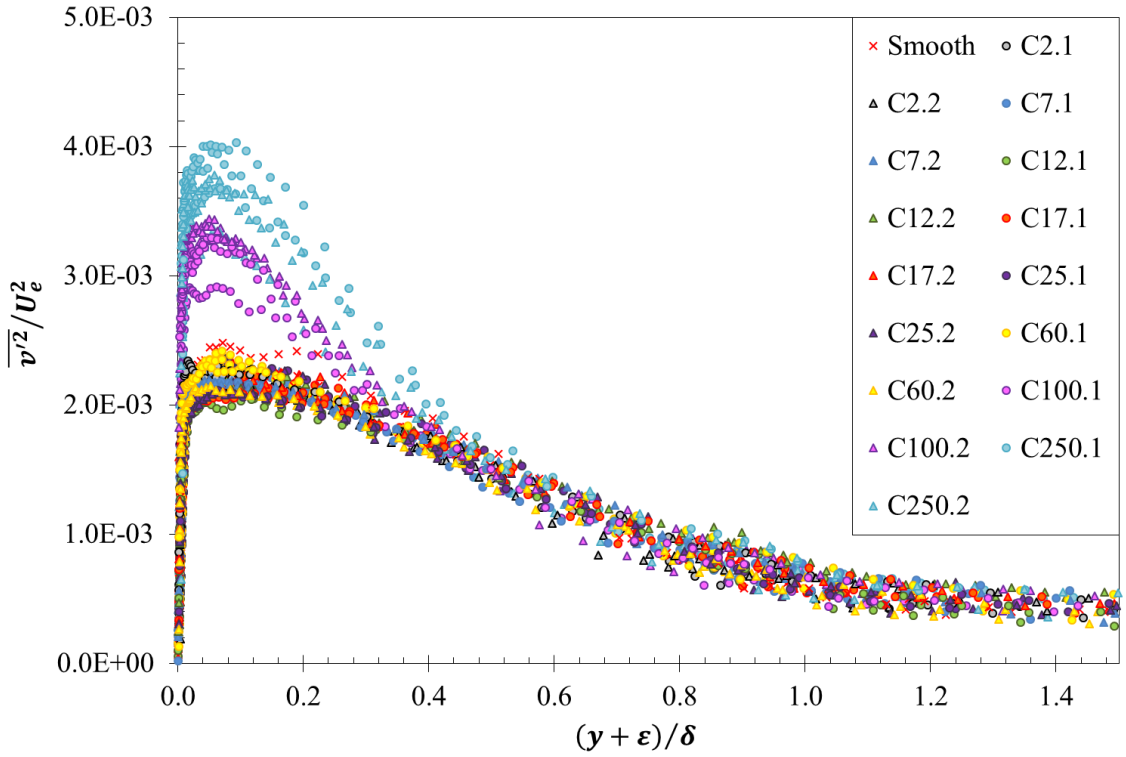

Figure 5.23: Wall-normal Reynolds stresses in outer scaling (U_e^2)

The Reynolds shear stress $-\overline{u'v'}$ profiles normalised with u_τ^2 for the set of test cases are given in inner scaling in **Figure 5.24**. Similar to the wall normal component, in the inner region, the roughness and Reynolds number only show a moderate influence on shear stress profiles $-\overline{u'v'}^+$. The Reynolds shear stress profiles of the C100 and C250 surface seemed to display slightly lower values compared to the other tested surfaces. In the outer region, a Reynolds number dependence and influence of roughness can be seen and resulted in the profiles being spread over a comparatively wide band. Moreover, the plateau region of the $-\overline{u'v'}^+$ profiles formed at approximately $30 < (y+\varepsilon)^+ < 500$ with peak values ranging between 0.85 and 1.0.

For similar Reynolds numbers, the $-\overline{u'v'}^+$ profiles associated with the smooth and rough surfaces form groups by collapsing on each other and no significant difference was observed between the tested surfaces in the outer layer. These findings are in good agreement with Ligrani and Moffat (1986), Schultz and Flack (2007), Brzek *et al.* (2007), Brzek *et al.* (2008) and Ünal *et al.* (2012) who did not find an influence of roughness on the Reynolds shear stresses.

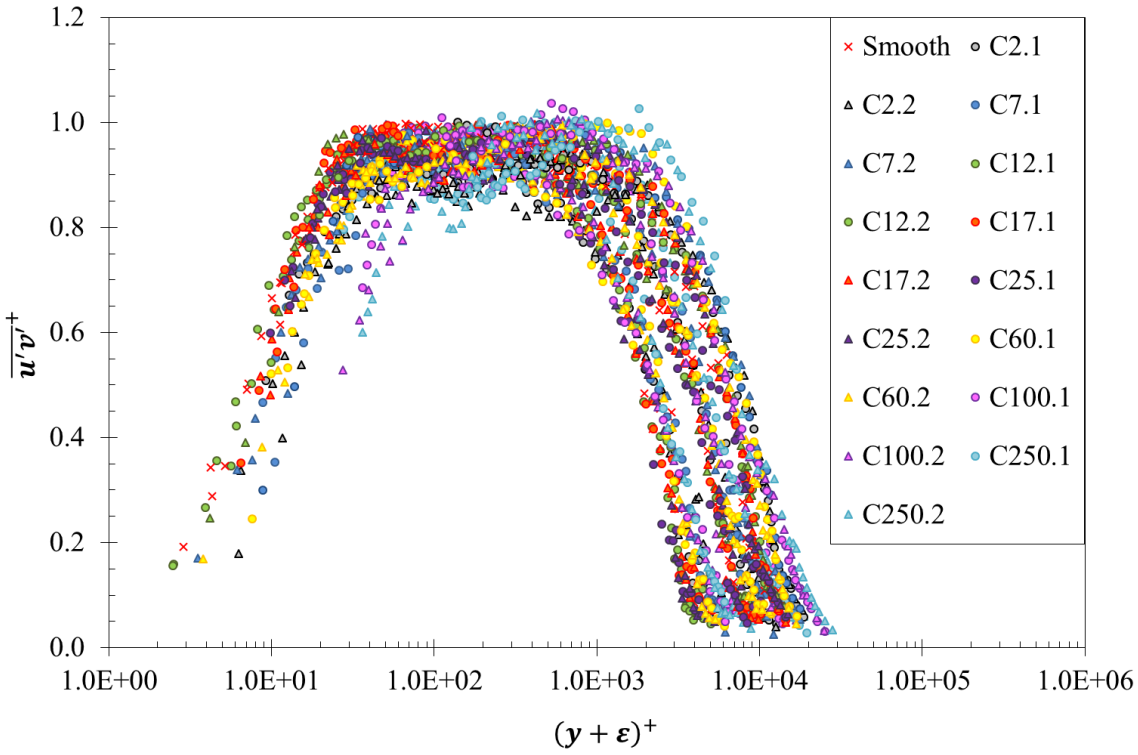

Figure 5.24: Reynolds shear stresses in inner scaling

Figure 5.24 presents the Reynolds shear stress component, $-\overline{u'v'}$, normalised with U_e^2 for each surface against normalised wall distance. Again, similar to the wall-normal fluctuations, no significant difference in the smooth and rough surface profiles can be observed in the outer layer of the boundary layer. However, Krogstad *et al.* (1992), Krogstadt and Antonia (1999) and Flack *et al.* (2005) all reported an increment in Reynolds shear stresses of various types of rough surfaces compared to a smooth wall in the outer layer. Overall, the profiles of smooth and rough surfaces collapsed well within the uncertainty for $0.44 < (y+\varepsilon)/\delta$. The near wall peaks seen in **Figure 5.24** may also be observed at $(y+\varepsilon)/\delta$ to be approximately $0.01-0.08$ with varying values for the different cases in this figure.

Furthermore, in the present investigation, the behaviours of the profiles of C100 and C250 surfaces are observed to be of very similar to those of other shear stress profiles in the outer scaling. Therefore, the effects of the step change in the surface roughness in the present experimental set-up were kept the same throughout all the shear stress collapse between C100, C250 surfaces and the other tested surfaces.

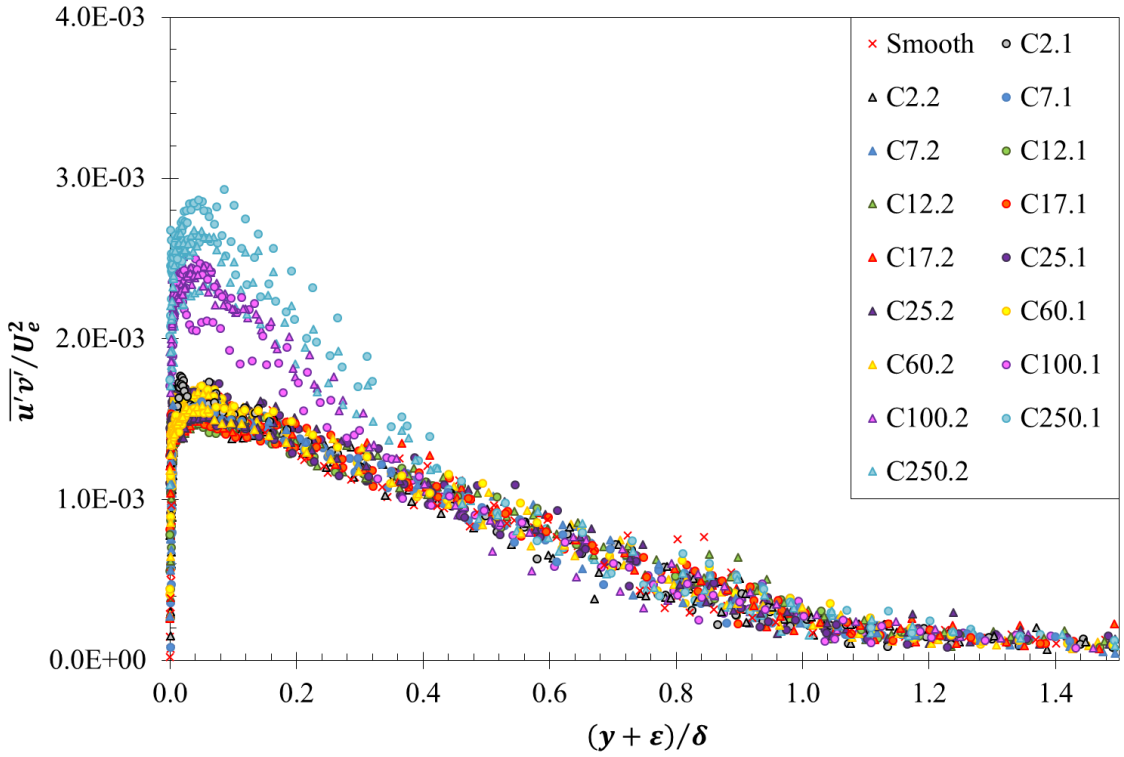

Figure 5.25: Reynolds shear stresses in outer scaling (U_e^2)

5.5.5 Turbulence Intensities

According to Schlichting (1974), the turbulence intensity in the streamwise direction and wall-normal direction can be calculated by dividing the root-mean-square of the velocity fluctuations at each direction with the mean velocity at the calculation point. Therefore, the turbulence intensity in the streamwise direction and wall-normal direction can respectively be expressed as:

$$TI_x = u_{x_{RMS}}/U_e \quad \textbf{5.11}$$

$$TI_y = u_{y_{RMS}}/U_e \quad \textbf{5.12}$$

Figure 5.26 and **Figure 5.27** presents turbulence intensities (TI_x and TI_y) at inflow velocity of 2m/s for smooth and all coated surfaces by using inner and outer scaling, respectively. Meanwhile, the **Appendix E** has provides further turbulence intensity results at other inflow velocities (4m/s, 6m/s). From **Figure 5.26**, a significant increase in the streamwise and wall-normal intensities over surfaces coated with C100 and C250 can be noticed. Many similar findings from the (Kutlar and Lewkowicz, 1990; Musker, 1990; Schultz and Swain, 1999;

Candries, 2001) also pointed out this increases in both components when compared against the smooth surface. Moreover, expect the turbulence intensities profiles of C100 and C250, the effect of increasing surface roughness can slightly be distinguished in the log law region (approximately $300 < (y + \varepsilon)^+ < 1000$) for the streamwise intensities, whereas not for the wall-normal intensities. Because of the higher free-stream turbulence levels, the turbulence intensities over rougher Cu_2O surface decay more slowly and remain higher in the outer layer. Therefore, it can be observed that C12 resulted in the lowest drag among all the test surfaces, whereas C250 brought the significant highest frictional resistant.

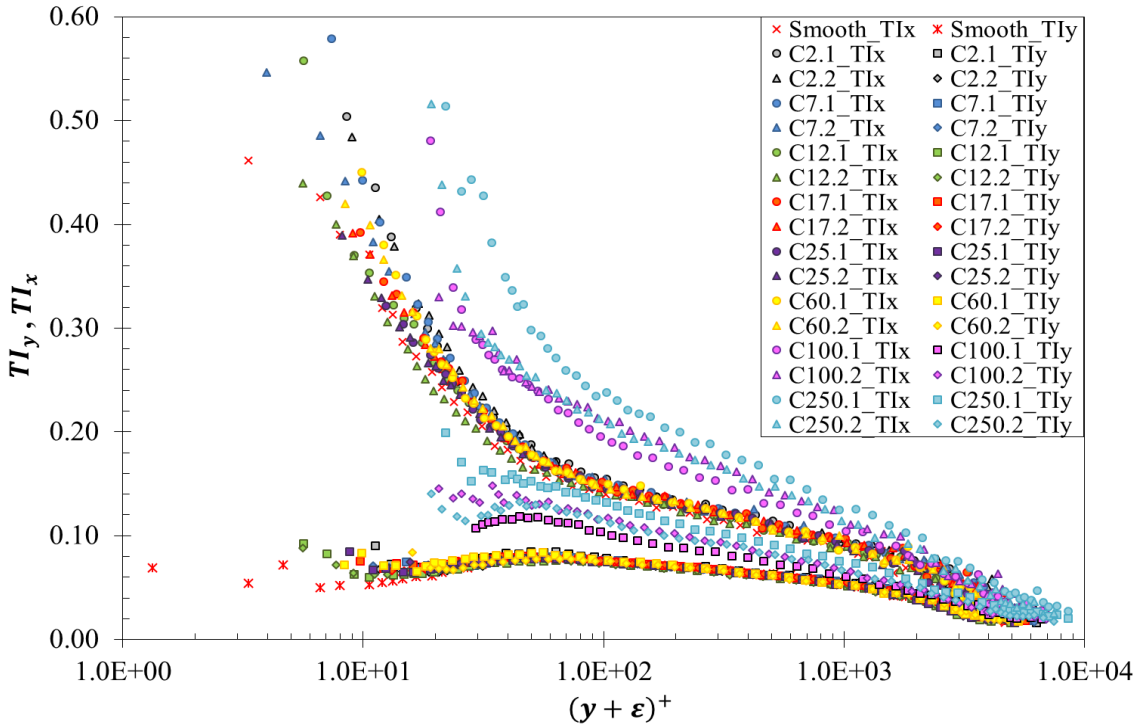

Figure 5.26: Turbulence intensity profiles in inner scaling at inflow velocity of 2m/s

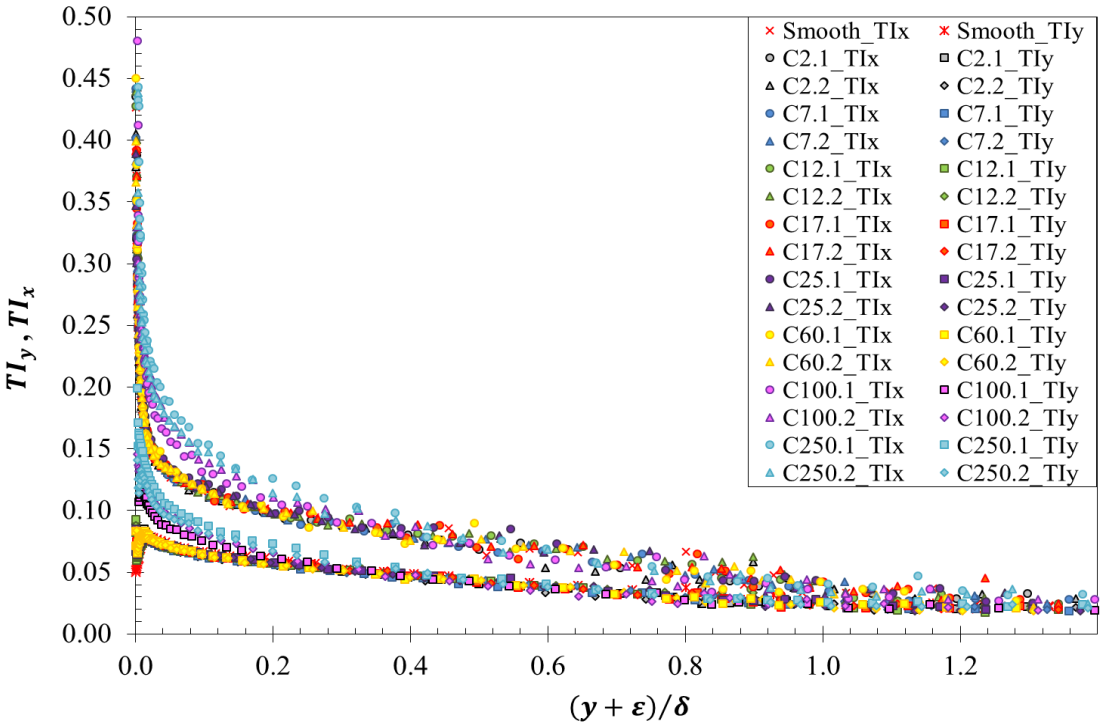

Figure 5.27: Turbulence intensity profiles in outer scaling at inflow velocity of 2m/s

Figure 5.27 presents turbulence intensities (TI_x and TI_y) for smooth and all coated surfaces by using outer scaling. The effect of increasing roughness still can clearly be observed, especially the outstanding increase in the turbulence intensities over surfaces coated with C100 and C250 at $(y+\varepsilon)/\delta$ to be approximately $0.01-0.4$. Overall, the profiles of smooth and rough surfaces collapsed well for $0.44 < (y+\varepsilon)/\delta$ which shows a good agreement with George and Castillo (1997) and Candries (2001) whose results collapse from $0.7 < (y+\varepsilon)/\delta$. The good agreement between the smooth and rough surface profiles support the wall similarity hypothesis and justifies the use of similarity techniques to calculate the friction velocity.

5.6 Chapter Summary

The results of two-dimensional LDV boundary layer measurements were presented in this chapter, carried out with eight different sized Cu_2O particle covered surfaces along with a smooth surface. The transitionally and fully rough surfaces were produced by the different Cu_2O particles size. The basic parameters of the boundary layer properties such as the boundary layer thickness, the integral parameters and the Reynolds number based on these thickness parameters were detailed in the chapter. Also, the results of local skin friction drag coefficients, roughness functions, turbulent normal and shear stresses were discussed.

According to the results of the boundary layer parameters, compared to the smooth reference

surface, the surfaces coated with particle sizes of 12μm (C12) and 17μm (C17) indicated lower displacement and momentum thicknesses and shape factor. In contrast, the tested surfaces coated with Cu_2O particle size of 100μm (C100) and 250μm (C250) were shown to have significantly higher values of these parameters compared to the smooth reference surface, as expected.

Based on the velocity defect profiles, a very good collapse of smooth and rough wall data is observed throughout the logarithmic and outer part of the boundary layer ($0.01 < y/\delta$). Moreover, the good correlation of the shape factors of all the tested surfaces with the curve proposed by Hama (1954) also provides support to the universality of the velocity defect law. The further velocity log-law profiles indicated, with the low freestream speed increasing, more downwards shift can be observed in the velocity profiles due to the surface coated Cu_2O particle size increasing. Unlike the other transitionally rough surfaces (i.e. C2−C60), C100 and C250 showed very large deviations from the smooth log-law which confirmed that these surfaces were in a fully rough flow regime.

For the skin frictional coefficient calculation, three methods were used in this chapter: Hama's Method (HM), the modified Clauser method (MC) and the total stress method (TS). It was observed that the surfaces coated with C2−C60 displayed similar drag performance within the uncertainty, whereas C100 and C250 presented obvious Reynolds number independence at the higher Reynolds number range of $Re_{\delta 1} > 2.3 \times 10^4$ with noticeably higher skin friction drag than the other tested surfaces.

On average, the lowest difference between the c_f values of the coated surfaces and the smooth reference was 5.7% which was from the C12, whilst a slightly higher skin friction drag resulted from C7 (8.9%) and C17 (9.1%). Even though the surface roughness and SEM analyses indicated that the C7 surfaces had dramatically higher roughness levels than C17, the subsequent analysis found that the LDV laser intersection was located at a smooth area of the C7 surface and therefore this resulted in C7 presenting a lower frictional drag than expected. On the other hand, the highest average skin friction drag was 104.9% from the C250, followed by the C100 with 71.9% higher than the smooth surface. As for the surface coated the smallest Cu_2O particles, C2, the average c_f difference was 14.4% which was higher than the 10.0% of C25 and 12.9% of C60.

The trends in the variation of skin friction drag were reflected in the calculated roughness functions which showed that all of the tested surfaces displayed increasing roughness function values as the Reynolds number increased. Moreover, by using a multiplied parameter roughness length scale function (Equation **5.10**), the presented roughness function results of all the coated surfaces show a good agreement with Townsin and Dey (1990) and Colebrook *et al*. (1939) type roughness functions. The roughness function results indicated that the surfaces coated with C100 and C250 were lying in the fully rough regime, and the rest of the coated surfaces were all in the transitionally rough regime. No hydraulically rough regime was found from any coated surfaces within the test Reynolds number range. The surfaces coated with C12 were found to have the smallest roughness function.

For the results of the Reynolds stresses, it was observed that the streamwise Reynolds stress shows considerable surface roughness effects near the wall with the increasing surface roughness with the different size Cu_2O particles. Due to the breakdown of the viscous region by the roughness, the streamwise Reynolds stress high peak near the wall partially disappeared below $(y+\varepsilon)^+ \approx 50$ and totally disappeared for the fully rough surfaces (i.e. C100 and C250). However, the surface roughness did not show much effect on the wall-normal component of the Reynolds stresses and the Reynolds shear stress. Overall, in the outer region, Reynolds number dependence was noticed for the tested surfaces. The Reynolds stress results of similar Reynolds number profiles had good collapse beginning from $(y+\varepsilon)^+ \approx 400-700$ for the coated (C2−C60) and smooth surfaces and $(y+\varepsilon)^+ \approx 1000$ for the fully rough surfaces (C100 and C250), respectively.

Moreover, the C2 − C60 and smooth surfaces showed good collapse when observing all Reynolds stress results in the outer scaling. However, those of the C100 and C250 surfaces had a discrepancy at lower values over the range $0.15 < (y+\varepsilon)/\delta$ due to the effect of the step change in the surface roughness in the present experimental set-up. With the outer scaling normalisation based on the freestream velocity, U_e^2, instead of u_τ^2, the profiles of all test cases were found to be well collapsed within the uncertainty for the range $0.5 < (y+\varepsilon)/\delta$.

According to the results of the turbulence intensity, both a significant increase in intensities can be observed from the streamwise and wall-normal components from surfaces coated with very large Cu2O particles (i.e. C100 and C250). This indicated that the turbulence intensity decay more slowly from these surfaces and remain higher in the outer layer and resulted in higher

frictional drag. In the outer region, a good collapse between the smooth and rough surface profiles at the range $0.44 < (y + \varepsilon)/\delta$, which support the wall similarity hypothesis.

Have to say that, due to the test set-up and device calibration should be taken with great care, plus longer period for the data collection, it may not always be convenient to conduct the hydrodynamic tests by using the water tunnel and two-dimensional Laser Doppler Velocimetry (LDV) system. Alternatively, the experimental work can also be achieved by using the turbulent flow channel through the pressure drop measurements. In the next chapter (**Chapter 6**), the hydrodynamic assessments of the test panels by using an alternative testing facility, UNEW's fully turbulent flow channel, have been described and discussed.

Chapter 6 Pressure Drop Measurements of Clean Cu_2O Surfaces

6.1 Introduction

In addition to the boundary layer measurements under external fluid conditions, the study of the drag impacts from copper-based antifouling surfaces may also be investigated under internal fluid conditions. This chapter describes the experimental pressure drop measurements using the fully turbulent flow channel (FTFC) by presenting the associated results and discussions.

According to **Objective 5** of this research study **(Section 1.3**), the details of the tasks conducted in this chapter as follows:

- To examine the effect of the Cu_2O particle size on the frictional drag characteristics of the test surfaces by using a FTFC facility under the internal fluid conditions with subjecting to the different free-stream velocities;
- To calculate and compare the frictional coefficient and roughness functions of each testing surface;
- To find if there is any empirical function can be deduced to describe the relationship between the frictional drag of the Cu_2O applied test surfaces with the Cu_2O particle size.

Therefore, frictional drag measurements of the different Cu_2O surfaces, based on particle size, were conducted with the pressure drop measured by using a FTFC. The specifications of the FTFC are presented in **Section 6.2**. The details of the experimental set-up are given in **Section 6.3,** and the repeatability and uncertainty of the tests are addressed in **Section 6.4**. The frictional drag and roughness function results of all of the tested surfaces are discussed in **Section 6.5**. Finally, the chapter is summarised in **Section 3.7**.

It should be noted that, as already discussed in **Chapter 4**, there were some practical application difficulties for the very small Cu_2O particles (i.e. C2 and C7) and these resulted in a random surface roughness condition. Apart from the measurements of the original coated surfaces, the pressure drop tests were also conducted on these surfaces after the coating had been reapplied.

6.2 The UNEW Fully Turbulent Flow Channel (FTFC)

The pressure drop measurements were performed in the UNEW Fully Turbulent Flow Channel located in the Hydrodynamics Laboratory at Newcastle University, as shown in **Figure 4.7**. The test section of the FTFC is 10 mm in height (H), 180 mm in width (W), and 2.7 m in length (L) which gives an aspect ratio (W/H) of 18:1 for the present experiments. Dean (1978)

postulated that a minimum aspect ratio of 7:1 is required to ensure two-dimensional flow in a turbulent channel, whereas Schultz and Flack (2013) conducted their tests with a channel aspect ratio of 8:1. Monty (2005) reported that an aspect ratio of 12:1 should be more than sufficient to provide two-dimensional flow in the centre of the channel. Accordingly, the aspect ratio of the presented channel is deemed to be more than sufficient to provide two-dimensional flow along the centreline of the channel.

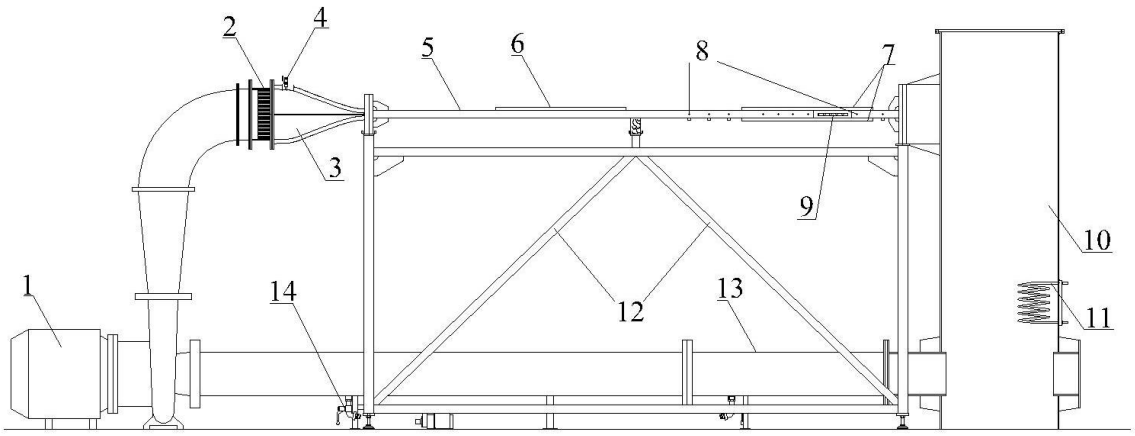

1. Centrifugal Pump	6. Inspection Test Plate	11. Cooling Coil
2. Honeycomb	7. Test Plates	12. Support Construction
3. Contraction	8. Pressure Taps	13. Duct
4. Ball Valve	9. LED Window	14. Draining Valve
5. Measuring Test Section	10. Reservoir	

Figure 6.1: Outline of the turbulent flow channel integral structure

Figure 6.2 shows the cross-section of the test section from the inlet direction. It can be seen that from each side of the channel wall there is a protruding bar which extends from the inlet to the outlet (as marked by the yellow ring in **Figure 6.2**. The protruding bar has a thickness of 10mm which effectively maintains the closed channel inner height at this value (H=10mm) constantly.

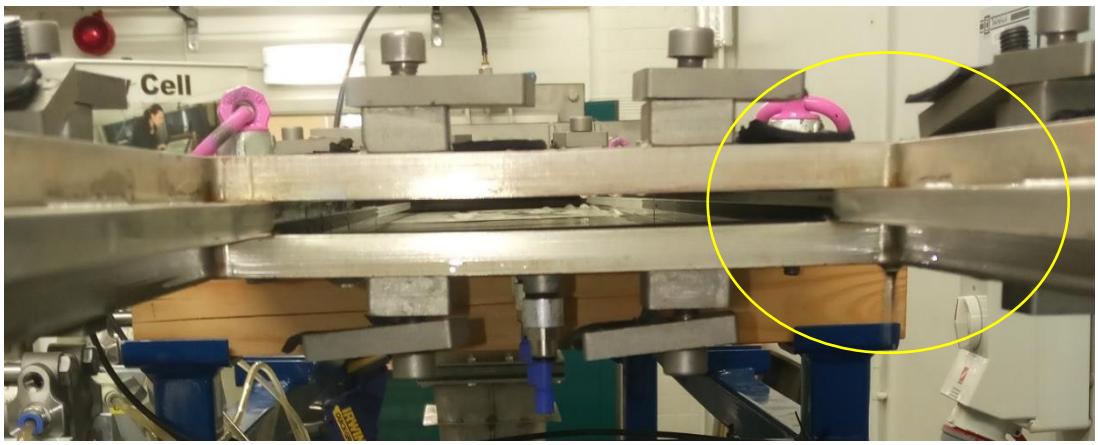

Figure 6.2: The cross-section of the test section

The discharge tank of the facility can hold 3000 L of freshwater, and the temperature of the water was controlled at 20 ± 0.25 ℃ via a cooling coil fitted in the discharge tank. The flow is produced by a 15kW centrifugal pump which can provide flow rates of up to 300 Ls^{-1}, and it is computer controlled by a variable frequency drive unit. The pump generates a bulk mean velocity of $1.62-8.30\ \mathrm{ms}^{-1}$ in the test section. The resulting Reynolds number, based on the channel height and bulk mean velocity, Re_m ranges between 3×10^4 and 1.6×10^5.

A stainless steel honeycomb flow straightener with 5 mm diameter cells, and 100 mm in length is fitted in the settling chamber upstream of the test section. The flow was tripped at the entrance to the test section by using 36# sandpaper covering the top and bottom walls of the contraction section, which has the contraction ratio of 34.7:1. Based on the work of Durst *et al.* (1998) and Schultz *et al.* (2000), a slot for fitting UNEW's standard test panel ($\mathrm{L} \times \mathrm{W} = 598\mathrm{mm} \times 218\mathrm{mm}$) is located at a~192H (about 1920mm, where H is the channel height) downstream of the channel inlet to obtain a fully-developed turbulent channel at Reynolds number > 3000. This allows two identical test panels to be placed at the top and bottom of the pressure drop test section to form the top and bottom boundaries of the test section.

Along one of the side walls of the test section, there are nine pressure taps located at 164H–262H downstream of the trip at the inlet to the channel. As illustrated in **Figure 6.3**, these are 0.75 mm holes located along the centreline of the side wall of the test section.

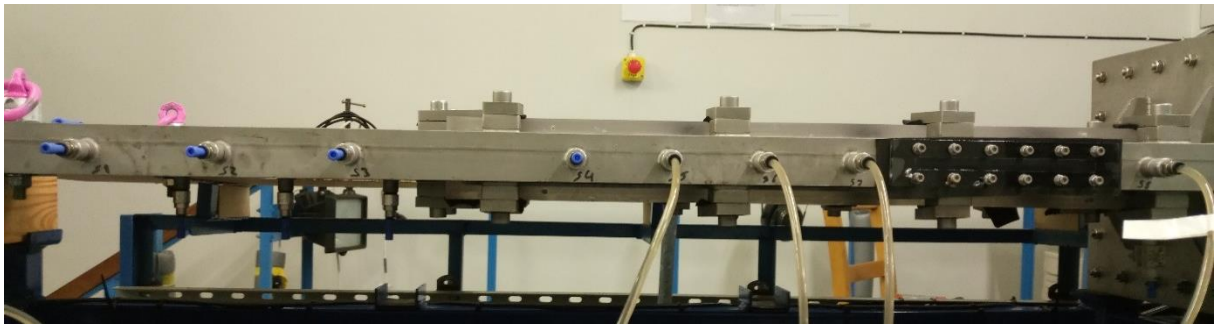

Figure 6.3: Pressure taps along the side wall of the test section

Two XMD Process Plant DP cell differential pressure transmitters (as shown in **Figure 6.4**) are installed near the test section for measuring the pressure differences. Each pressure transmitter can continuously measure the pressure drops between any two of the pressure taps. The measuring ranges of the pressure transmitters are up to 75 and 500 mbar, respectively, with an accuracy of ±0.1% of the full scale. A side glass windows (with a cross-section of 10 ×

150 mm) is installed between pressure taps 7 and 8 to allow laser beam access to the channel for detailed flow measurements by using Laser Doppler Velocimetry (LDV) and Particle Image Velocimetry (PIV) systems.

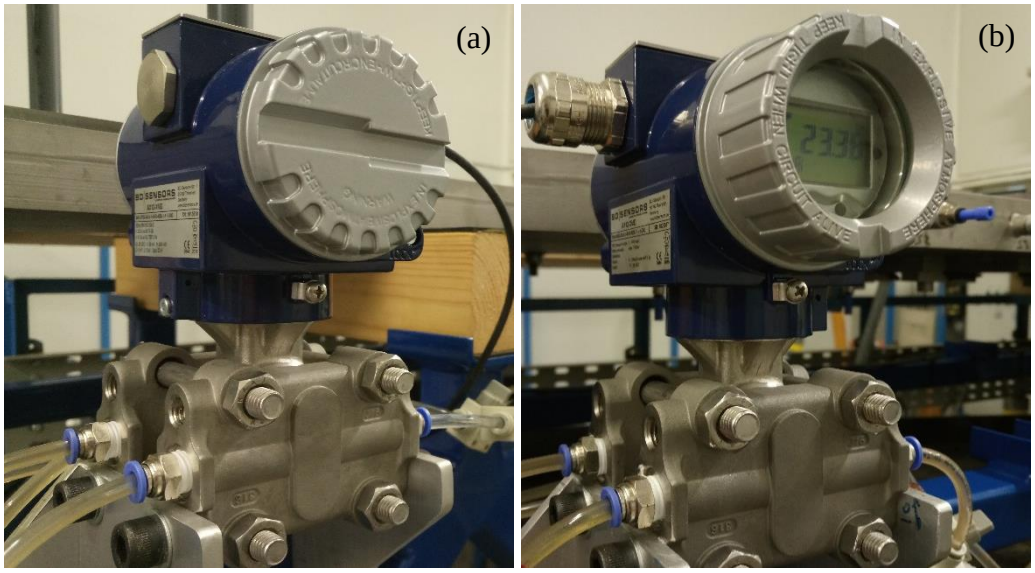

Figure 6.4: XMD Process Plant DP cell differential pressure transmitters with measurement range of 0-75 mbar (left) and 0-500 mbar (right)

6.3 Experimental Set-up

During this investigation, to provide a high Reynolds number, the pump speed was varied from 400 rpm to 1600 rpm using 200rpm increments. Before the pressure drop tests, the maximum velocity and the bulk mean velocity of the test section were calibrated against the requested pump speed by using a two-dimensional LDV system. The relationship of the known pump speeds vs the bulk mean velocity are shown in **Figure 4.11**. Seven bulk mean velocities: 1.62ms^{-1}, 2.87ms^{-1}, 4.10ms^{-1}, 5.17ms^{-1}, 6.29ms^{-1}, 7.45ms^{-1}and 8.30ms^{-1} were applied to the subsequent frictional drag calculation based on the results of pressure drop measurements.

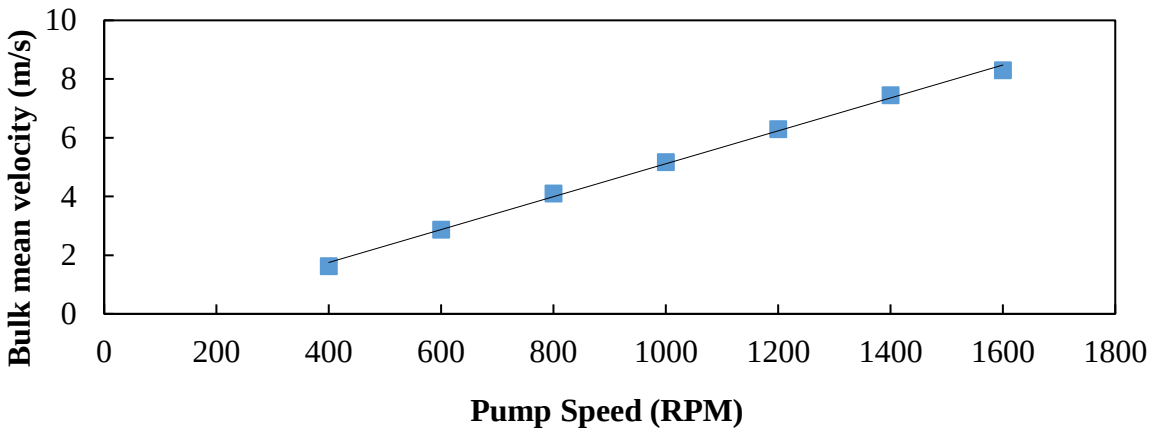

Figure 6.5: The calibration curve of the bulk mean velocity against the pump speed

Four pressure taps from No.5 ($x = 209H$) to No.8 ($x = 249H$) were used for the pressure drop measurements. As the pressure differential transmitter can be connected to two taps at a time, these four pressure taps give six different combinations (as tabulated in **Table 4.1**) with five different pressure drop distances. The pressure drop data was collected by an in-house LabVIEW programme with a sample rate of 10Hz for a sampling period of 100s so that 10,000 data points were captured at each pressure drop distance for each bulk velocity. The collected data was exported in LVM format and then imported into Excel for further analysis.

Table 6.1: Details of the pressure taps combinations

Pressure taps Combines	No.5-6	No.5-7	No.5-8	No.6-7	No.6-8	No.7-8
Pressure Drop Distance (mm)	75	150	400	75	325	250

The kinematic viscosity and density of the water at different temperatures throughout the tests were taken from the ITTC–recommended proceduresfreshwater and seawater properties (ITTC Specialist Committee, 2011). Equation **6.1**, which results from combining Equations **3.76**, **3.77** and **3.79**, illustrates that the channel height directly affects the final frictional coefficient results. Considering machining tolerance while manufacturing the panels, accurately determining the actual channel inner height would be most important

$$C_f = \frac{2hb}{h+b} \times \frac{dp}{dx} \frac{1}{\rho \bar{U}^2} \qquad \textbf{6.1}$$

To precisely determine the channel height, as shown in **Figure 4.6** (**a**), plastic inserts of size 11cm × 2cm × 2cm ($L \times W \times H$) were made from a synthetic rubber compound. By using the plasticity of the synthetic rubber compound, the inserts will be compressed and their average remaining thickness would be the actual channel height.

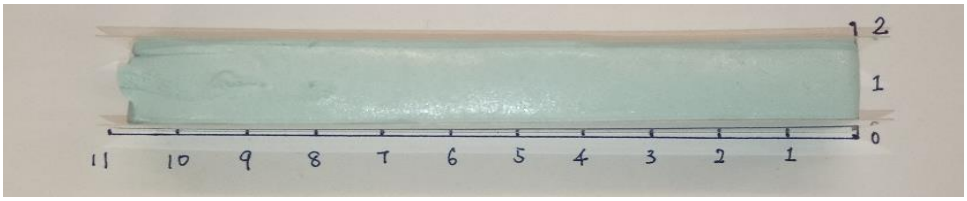

(**a**). Plastic insert for measuring the channel height

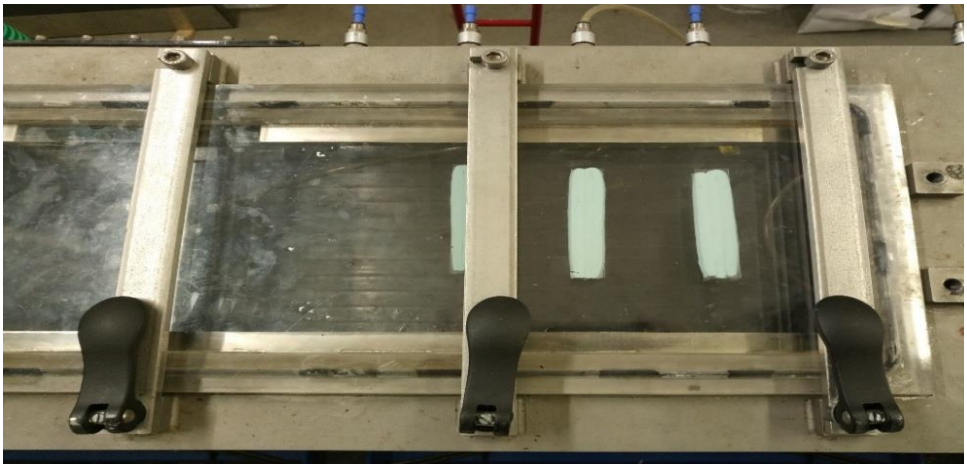

(**b**). Plastic inserts placed in the tests section with reference acrylic panels

Figure 6.6 (**a**)−(**b**)**:** The setup for measuring the channel inner height

As shown in **Figure 4.6** (**b**), before each measurement, the plastic inserts were placed between the testing panels with their positions aligned with each pressure tap (from No.5 to No.8 respectively). The advantage of using these inserts was that they can provide an accurate measurement of the channel inner height, but also without causing any contact damage to the test surfaces.

6.4 Uncertainty Analysis

The uncertainty estimates for the drag coefficients and roughness function calculations were measured through repeatability tests using the procedure defined by Coleman and Steele Jr (1990), including the uncertainty sources such as disturbances caused by the coating finish quality, scratches caused during the tests, issues with the panel installation, temperature fluctuations, etc. The pressure drop tests for each test specimen were repeated five times within the entire experimental test Reynolds number range. The 95% precision confidence limits for a given quantity were obtained by using the standard errors of the statistical variables multiplied by the related two-tailed t value which equals 2.776 for four degrees of freedom according to Coleman and Steele Jr (1990).

Table 6.2 and **Table 6.3** give the detailed uncertainty percentages in frictional coefficients for the Cu_2O applied test surfaces after the 1^{st} and 2^{nd} applications respectively. The uncertainty

percentages from both tables are found to have a decreasing trend as the test flow speed increases. According to **Table 6.2**, for the pressure drop tests of the 1st set of surface applications, the overall uncertainties in skin-friction coefficient, C_f, are found to be typically in the range of ±3.0%−±6.0%, at the lowest Reynolds number ($Re_D \approx 3 \times 10^4$). The lowest uncertainty percentage in the skin-friction coefficient is ±3.2%, whilst ±9.2% is the highest. When at the highest Reynolds number range ($Re_D > 3 \times 10^4$), the uncertainty values of skin-friction coefficient rapidly drop to ±0.8%−±1.5%.

Table 6.2: Uncertainty in C_f for pressure drop tests of panels with 1st applications

Specimens	Bulk mean velocity (m/s)						
	1.62	**2.87**	**4.10**	**5.17**	**6.29**	**7.45**	**8.30**
Smooth	6.2%	2.3%	2.3%	2.2%	1.6%	1.4%	0.8%
C2	9.2%	1.9%	2.4%	1.7%	1.7%	0.9%	1.4%
C7	3.9%	1.9%	2.6%	1.4%	2.2%	1.4%	1.0%
C12	6.5%	2.9%	2.1%	1.4%	0.8%	1.2%	1.0%
C17	5.7%	2.5%	1.5%	1.2%	1.6%	1.4%	1.2%
C25	3.9%	2.5%	1.5%	1.3%	1.0%	1.2%	1.3%
C60	3.2%	2.8%	2.5%	2.0%	0.9%	1.6%	1.5%
C100	7.8%	2.3%	2.4%	1.0%	1.5%	1.2%	1.5%
C250	3.8%	2.9%	2.0%	1.8%	1.4%	1.2%	1.0%

For the pressure drop tests on the 2nd set of surface applications, **Table 6.3** shows that the resulting overall uncertainties in C_f are in the range of ±3.0%−±6.0% at the lowest Reynolds number. The lowest uncertainty in the skin-friction coefficient is ±2.1%, whilst ±6.2% is the highest value. At the highest Reynolds number, the uncertainty percentages of the skin-friction coefficient for all of the tested surfaces were within ±0.8%−±1.2%.

Table 6.3: Uncertainty in C_f for pressure drop tests of panels with 2nd applications

Specimens	Bulk mean velocity (m/s)						
	1.62	**2.87**	**4.10**	**5.17**	**6.29**	**7.45**	**8.30**
Smooth	6.2%	2.3%	2.3%	2.2%	1.6%	1.4%	0.8%
C2	3.9%	2.2%	2.5%	1.4%	2.1%	1.3%	1.0%
C7	4.6%	1.9%	2.0%	1.4%	1.6%	1.2%	1.2%
C12	4.2%	2.3%	2.1%	1.7%	0.8%	1.3%	1.2%
C17	3.5%	1.7%	1.1%	1.6%	1.5%	1.0%	1.0%
C25	4.4%	2.1%	1.9%	1.3%	1.4%	1.3%	0.8%
C60	3.3%	4.3%	2.4%	1.3%	1.6%	1.2%	0.8%
C100	2.1%	1.8%	2.4%	1.8%	0.8%	1.1%	1.1%
C250	5.1%	3.0%	1.3%	2.5%	1.5%	2.1%	1.9%

Table 6.4 and **Table 6.5** give the detailed uncertainty percentages in roughness function for the Cu_2O applied surfaces after the 1st and 2nd applications, respectively. A similar decreasing tendency can be observed in roughness function uncertainty percentage results as the testing flow speed increases.

Table 6.4: Uncertainty in ΔU^+ for pressure drop tests of panels with 1st applications

Specimens	Bulk mean velocity (m/s)						
	1.62	**2.87**	**4.1**	**5.17**	**6.29**	**7.45**	**8.3**
C2	9.8%	3.1%	3.3%	2.9%	2.2%	1.6%	1.5%
C7	7.8%	2.8%	2.9%	2.5%	2.5%	1.8%	1.0%
C12	14.9%	15.0%	9.3%	6.6%	5.8%	3.1%	3.4%
C17	17.0%	6.9%	4.6%	4.5%	4.4%	3.3%	2.1%
C25	8.1%	2.7%	3.3%	2.5%	2.1%	1.2%	1.9%
C60	8.8%	2.7%	3.3%	2.3%	2.3%	1.9%	1.5%
C100	8.4%	2.2%	2.4%	1.8%	1.1%	1.3%	0.8%
C250	3.3%	1.4%	1.2%	1.2%	1.1%	0.7%	0.5%

Table 6.5: Uncertainty in ΔU^+ for pressure drop tests of panels with 2nd applications

Specimens	Bulk mean velocity (m/s)						
	1.62	**2.87**	**4.1**	**5.17**	**6.29**	**7.45**	**8.3**
C2	6.8%	3.5%	3.3%	2.5%	1.7%	1.4%	0.8%
C7	15.4%	6.2%	7.4%	5.3%	5.3%	3.4%	3.2%
C12	13.8%	5.9%	6.7%	5.6%	4.0%	3.9%	2.0%
C17	11.1%	6.5%	4.8%	5.5%	4.4%	3.4%	2.5%
C25	11.9%	5.4%	3.4%	3.6%	2.8%	2.6%	1.4%
C60	6.3%	3.5%	2.7%	2.3%	1.9%	1.1%	0.8%
C100	6.5%	2.7%	2.9%	2.2%	1.4%	1.0%	0.8%
C250	4.0%	1.5%	1.2%	1.5%	0.9%	0.9%	0.6%

Table 6.4 and **Table 6.5** present the uncertainties in roughness function, ΔU^+ for the pressure drop tests of the 1st and 2nd set of surface applications. It can be found that the uncertainties in roughness function are concentrated in the ±8.0% to ±10.0% for the 1st applications and ±6.0%−±12.0% for 2nd applications at the lowest Reynolds number. At the highest Reynolds number, the uncertainty percentages of the majority of the roughness function results for all the 1st application of test surfaces are within the range ±1.0%−±2.0%, and ±0.8%−±2.0% for all the 2nd application of test surfaces.

It has to be noted that, in the present investigations, no relationship can be deduced from surfaces coated with different sizes of Cu_2O particles to the resulting uncertainty percentage changes in skin friction coefficient or roughness function.

6.5 Results and Discussion

The frictional coefficient results of surfaces coated with different size Cu_2O with the 1st and 2nd applications are presented and discussed in **Section 4.4.1**. The roughness functions for all of the tested surfaces are then presented and discussed in **Section 6.5.3**.

6.5.1 Frictional Coefficient

The un-coated cast acrylic panels were used to represent smooth reference surfaces. For the smooth surface results comparison, two empirical power relationships for the smooth wall are employed by the present work according to Dean (1978) and Zanoun *et al*. (2009). Equation **6.2** expresses the empirical power relationship which was proposed by Dean (1978), while equation **6.3** was given by Zanoun *et al*. (2009).

$$C_f = 0.073Re^{-0.25} \qquad \textbf{6.2}$$

for the Reynolds number range: $6 \times 10^3 < Re < 6 \times 10^5$.

$$C_f = 0.0743Re^{-0.25} \qquad \textbf{6.3}$$

Friction coefficient results from surfaces coated with eight different sized Cu_2O specimens by the 1st set of surface applications as well as the smooth surfaces are plotted in **Figure 6.7**, in the meanwhile, the results of the 2nd surface applications are presented in **Figure 6.8**. The results from both figures indicate that the smooth surface measurements show agreement with the mean line of Dean (1978) and Zanoun *et al.* (2009) over the entire Reynolds number range.

Apart from the smooth surfaces, within the 1st applications (**Figure 6.7**), the lowest skin friction coefficients resulted from the surfaces coated with Cu_2O particle size of 12µm (C12), and this is followed by the surfaces coated with C17 which produced slightly higher frictional drag than that of C12. Unlike the results of the 1st application, the lowest skin friction coefficients from the 2nd applications (**Figure 6.8**) were obtained from the surfaces coated with Cu_2O particle size of 7µm (C7) which was close to, but had a lower C_f curve than, C12 and C17. According to **Section 4.3.2**, the differences of the C7 between 1st and 2nd application due to the specimen C7 was better dispersed into the binder during the 2nd application process, without agglomeration. As a result, an improved surface for C7 in the 2nd application was achieved, with the lowest roughness characteristic. Moreover, within the Reynolds number range tested, the C_f curves of C12, C17 (both 1st and 2nd applications) and C7 (2nd application) had a similar

trend to the smooth surface at $Re_D > 1.0 \times 10^5$, which may indicate that these surfaces were between the hydraulically smooth regime and the transitional regime.

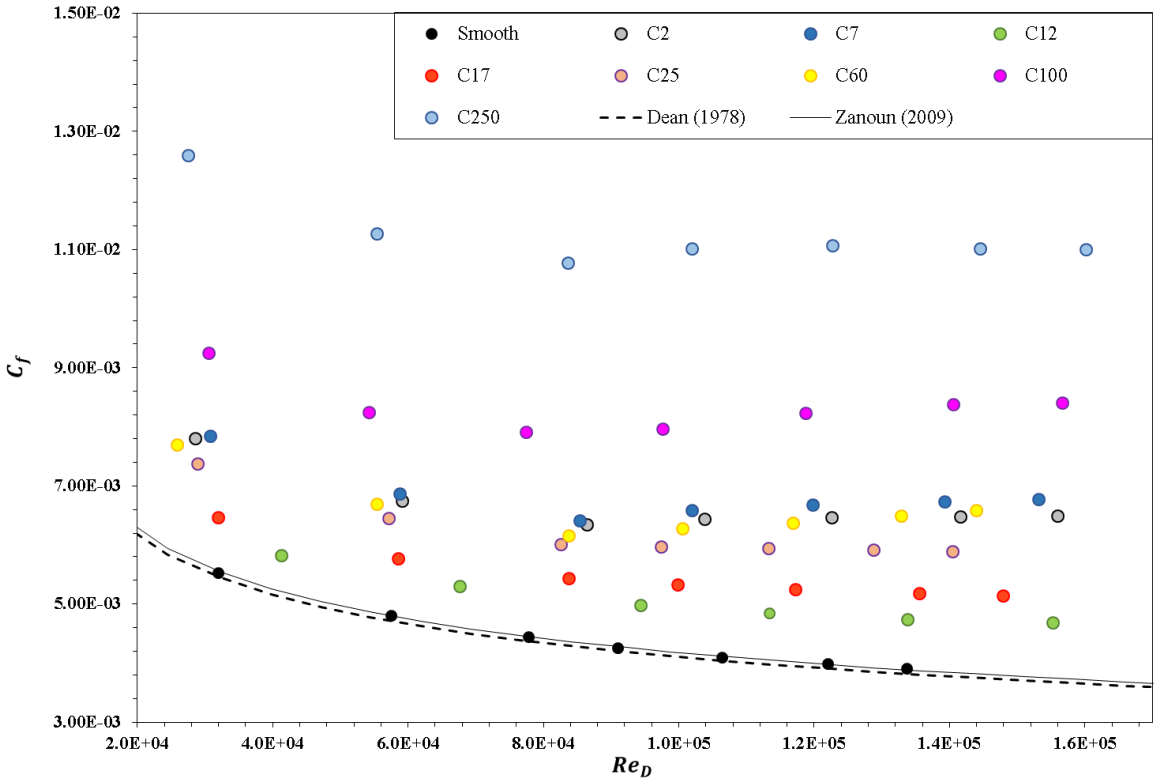

Figure 6.7: Frictional coefficient results for the 1st pressure drop test

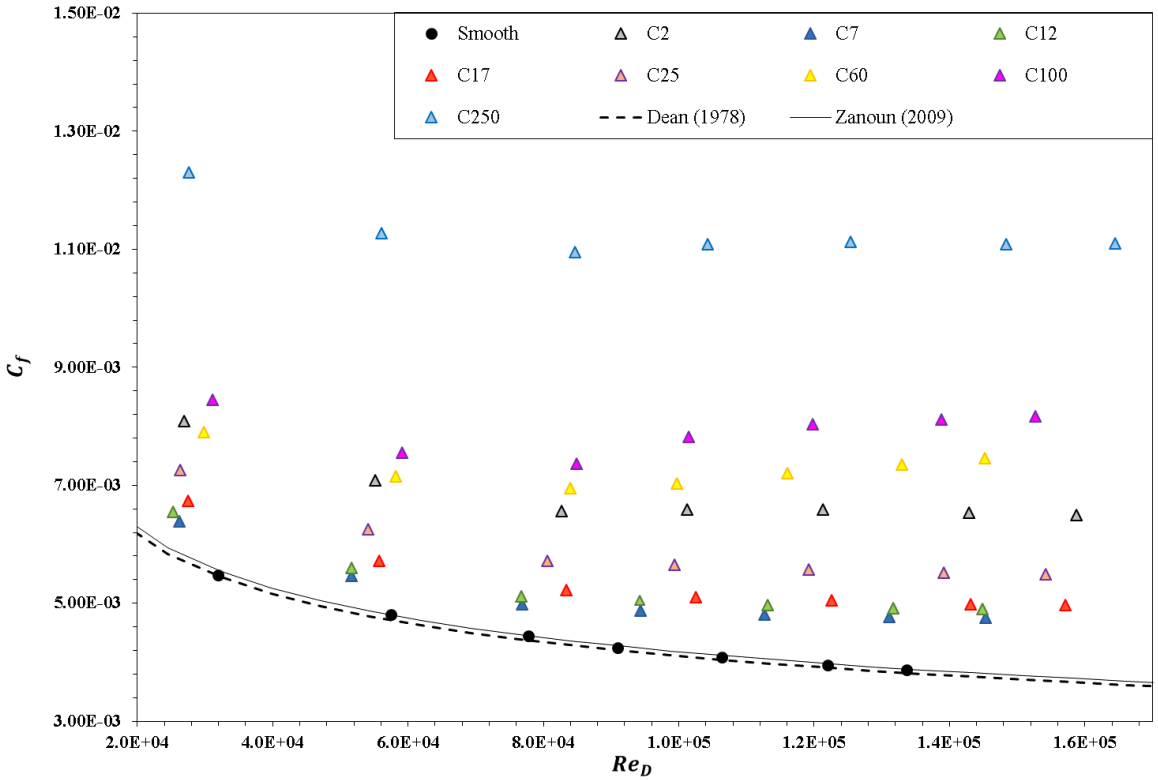

Figure 6.8: Frictional coefficient results for the 2nd pressure drop test

Compared to the smooth surface, rather than C12 and C17, more obvious skin frictional drag resulted from the surfaces coated with Cu_2O specimens of C25 and C60. It can also be noticed that, in **Figure 6.7**, for surfaces coated with the very small sized Cu_2O particles after the 1st application, C2 and C7, presented higher skin frictional drag than C25, but had very similar results to C60 over the entire Reynolds number range. As previously explained in **Section 4.3.2**, due to the coagulation that happened on these minuscule particles and subsequently caused larger coagulated matter to jam the spray gun chamber and block the spray nozzle, the surfaces of C2 and C7 were finished with inconsistently pulsed spraying which resulted in rougher surface textures. For surfaces coated with very large Cu_2O particles, more significant skin frictional drag resulted from the surfaces with C100 and C250, especially the latter which had the highest drag penalties of all the tested surfaces.

Apparent inflectional behaviours in which the friction coefficient curve slightly turns-upward at $Re_D > 8 \times 10^4$ were observed for all specimens except C7 (2nd application), C12 and C17. According to the discussion of Allen *et al*. (2005), inflectional behaviour can be observed in the transitional regime, when $R_q/D < 2.5 \times 10^{-3}$ (where R_q/D is the relative surface roughness). The apparent inflectional behaviours indicated by those tested specimens in the transitional regime is the function of both the Reynolds number and the surface roughness characteristics (Nikuradse, 1933). In this research, due to the closed channel, an average value of relative surface roughness from each pair of panels (top and bottom) was taken into account. The relative surface roughness values of the surfaces coated with tested specimens by the 1st and 2nd applications are tabulated in **Table 6.6**.

Table 6.6: The relative surface roughness for the test specimens

1st surface application								
Specimens	**C2**	**C7**	**C12**	**C17**	**C25**	**C60**	**C100**	**C250**
$Rq/D \times 10^{-4}$	5.3	7.5	1.6	2.6	3.1	4.5	13.1	37.7
2nd surface application								
Specimens	**C2**	**C7**	**C12**	**C17**	**C25**	**C60**	**C100**	**C250**
$Rq/D \times 10^{-4}$	7.5	1.6	1.7	1.9	2.7	10.0	12.7	42.6

Also, up-turned inflectional behaviours of the very large specimen (C250) from both experiments show a mild inflectional behaviour, which diminishes at higher Reynolds numbers, $Re_D > 1.4 \times 10^5$, where the curve becomes parallel to the horizontal axis. This shows that the roughness effects of C100 and C250 are independent of the Reynolds number and lying in the fully rough regime.

The detailed skin friction coefficients of all of the tested surfaces are presented in **Table 6.7**. Except the very small size particles (i.e. C2 and C7) which brought unexpected results, generally, it shows a good agreement for friction coefficient results between two sets of the surface application as more similar surface characteristics can be engineered by using these Cu_2O specimens.

Table 6.7: C_f for the pressure drop measurements of panels

1st surface application									
Bulk mean velocity m/s	**Frictional coefficient $C_f \times 10^3$**								
	Smooth	**C2**	**C7**	**C12**	**C17**	**C25**	**C60**	**C100**	**C250**
1.62	5.5	7.8	7.8	5.8	6.5	7.4	7.7	9.2	12.6
2.87	4.8	6.7	6.9	5.3	5.8	6.5	6.7	8.2	11.3
4.1	4.4	6.3	6.4	5.0	5.4	6.0	6.2	7.9	10.8
5.17	4.3	6.4	6.6	4.8	5.3	6.0	6.3	8.0	11.0
6.29	4.1	6.5	6.7	4.7	5.3	5.9	6.4	8.2	11.1
7.45	4.0	6.5	6.7	4.7	5.2	5.9	6.5	8.4	11.0
8.3	3.9	6.5	6.8	4.7	5.1	5.9	6.6	8.4	11.0
2nd surface application									
Bulk mean velocity m/s	**Frictional coefficient $C_f \times 10^3$**								
	Smooth	**C2**	**C7**	**C12**	**C17**	**C25**	**C60**	**C100**	**C250**
1.62	5.5	8.1	6.4	6.6	6.7	7.3	8.1	8.4	12.3
2.87	4.8	7.1	5.5	5.6	5.7	6.3	7.1	7.6	11.3
4.1	4.4	6.6	5.0	5.1	5.2	5.7	7.0	7.4	10.9
5.17	4.3	6.6	4.9	5.0	5.1	5.7	7.0	7.8	11.1
6.29	4.1	6.6	4.8	5.0	5.0	5.6	7.2	8.0	11.1
7.45	4.0	6.5	4.8	4.9	5.0	5.5	7.4	8.1	11.1
8.3	3.9	6.5	4.8	4.9	5.0	5.5	7.5	8.2	11.1

To provide further insight into the friction drag vs different surface roughness condition with their cuprous oxide specimens, the skin frictional drag increments (%) were calculated for the test surfaces with respect to the acrylic reference surfaces and these are presented in **Table 6.8**.

Overall, the 1st and 2nd experiments indicated that frictional coefficient increased from that of the smooth surface with the increase in particle size, from between approximately 10%–160%. For the 1st experiment, the surfaces coated with 12μm sized Cu2O particles (C12) demonstrated the lowest frictional drag which had an average increase of 13.5% over the smooth surfaces. This was closely followed by the surfaces coated with C17 which presented a slightly higher average frictional drag (24.9%) than that of C12 across the entire Reynolds number range. For those very small size particles, on average, specimen C2 had about 52% increase in C_f, and C7 resulted in 55.6% higher than smooth surface.

Table 6.8: Increase in overall C_f(%) for 1st application compared to the acrylic surface

1st surface application			
Specimen	R_t (μm)**average**	**Average Increase in C_f (%)**	**Range of Increase in C_f (%)**
C2	53.7	51.7	40.5−66.3
C7	69.1	55.6	41.9−73.5
C12	17.2	13.5	5.4−19.8
C17	27.1	24.9	17.0−31.5
C25	32.2	41.0	33.4−50.9
C60	45.6	50.3	38.7−68.7
C100	122.0	90.0	67.2−115.2
C250	337.9	155.9	127.9−181.6
2nd surface application			
Specimen	R_t (μm)**average**	**Average Increase in C_f (%)**	**Range of Increase in C_f (%)**
C2	74.4	56.0	47.3−67.7
C7	17.2	16.9	12.1−22.7
C12	18.0	20.4	15.1−26.7
C17	20.0	22.5	17.4−28.1
C25	28.3	34.6	28.7−41.9
C60	91.9	67.6	47.4−92.4
C100	119.5	82.0	54.1−110.8
C250	324.4	158.0	124.3−186.5

For surfaces coated after the 2nd applications, the specimen C7 resulted in a much lower C_f value, only 16.9% higher than the smooth surface, which is imperceptibly lower than those of C12 (20.4%) and C17 (22.5%). At the same time, specimen C2 in the 2nd experiment still resulted in considerably high values of C_f for its particle size (an average 56% increase). From both 1st and 2nd experiments, the highest average friction was approximately 160% and, this was obtained from C250. Then this is followed by C100 (80%−90%) and C60 (50%−70%).

Based on the experiments presented here, it can be noted that the relative higher C_f values of specimen C2 and the dramatic difference between the two C7 tests are dependent on their surface macro finish quality.

6.5.2 Empirical Correlation between C_f with Particle Size D_{50}

As the frictional drag was seen to increase with the particle size of the surface coating, it would be very useful to determine if a relationship exists between the coated Cu_2O particle sizes and frictional drag. Based on the results of the 1st and 2nd tests, the frictional drags associated

with the coating mean Cu_2O particle size (D_{50}) at the testing bulk velocity 1.62ms^{-1} are plotted in **Figure 6.9**. It should be noted that, considering the poor surface finish quality and unexpectedly higher frictional drag, the C2, C7 of the 1st tests and C2 of the 2nd tests are excluded from the graph deliberately.

The equations of both trend lines indicate that the frictional drag of the tested surfaces may suggest a linear relationship with the Cu_2O particle size. The linear equations $C_f = 0.026 \times D_{50} + 6.2$ for the 1st tests and $C_f = 0.024 \times D_{50} + 6.4$ for the 2nd test, have regression analysis R-squared values of $R^2 = 96.7\%$ and $R^2 = 99.1\%$ respectively indicating good agreement between with the equation and the frictional drag results. Accordingly, the linear relationships of frictional drag $C_f(\times 10^3)$ for each test are tabulated in **Table 6.9** at each testing bulk mean velocity, $\overline{U}$.

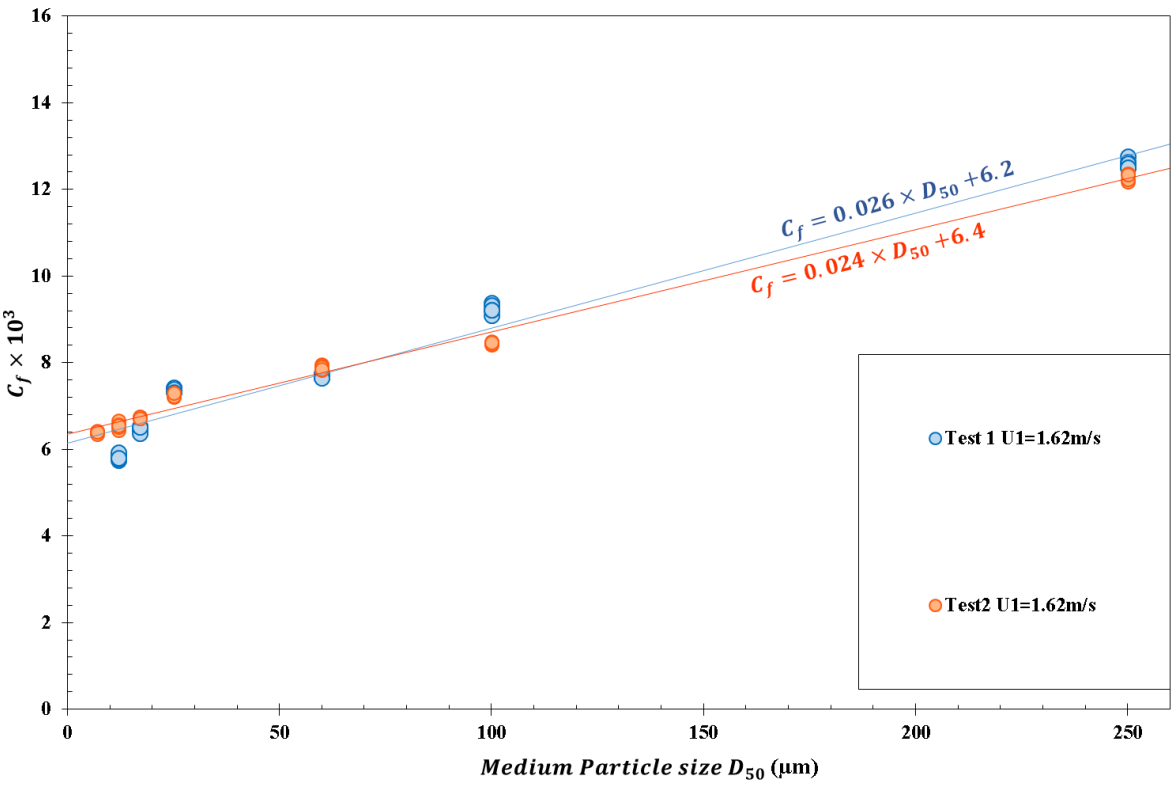

Figure 6.9: Correlation of C_f (%) with Cu_2O particle sizes (D_{50}) for 1st and 2nd applications

Overall, the slopes of these linear equations range between $0.024-0.026$. Meanwhile, the intercepts range between $5.0-6.4$, with most concentrated at 5.0. Moreover, no obvious velocity effects can be observed from these slope and intercept values. Therefore, for the present research, a linear experimental relationship, $C_f(\times 10^3) = A \times D_{50} + B$, can be assumed for

Cu_2O surfaces coated with different size particles with respect to the frictional drag, where the slope value A varies between $0.025-0.026$, and the intercept B is 5.0. To further prove this experimental relationship, more tests of surfaces coated with different sized Cu_2O particles would be required.

Table 6.9: Linear relationship equations of Cu_2O particle size with frictional drag

$\bar{U}$(m/s)	1st applications	2nd applications
1.62	$C_f = 0.026 \times D_{50} + 6.2$	$C_f = 0.024 \times D_{50} + 6.4$
2.87	$C_f = 0.024 \times D_{50} + 5.4$	$C_f = 0.024 \times D_{50} + 5.4$
4.10	$C_f = 0.024 \times D_{50} + 5.1$	$C_f = 0.024 \times D_{50} + 5.0$
5.17	$C_f = 0.026 \times D_{50} + 5.0$	$C_f = 0.025 \times D_{50} + 5.0$
6.29	$C_f = 0.026 \times D_{50} + 5.0$	$C_f = 0.026 \times D_{50} + 5.0$
7.45	$C_f = 0.026 \times D_{50} + 5.0$	$C_f = 0.026 \times D_{50} + 5.0$
8.30	$C_f = 0.026 \times D_{50} + 5.0$	$C_f = 0.026 \times D_{50} + 5.0$

Moreover, a further correlation equation that includes the effects of fluid speed and above mentioned variables has also been obtained. It was found that, 94.6% of the observed variation (i.e. $R^2 = 0.946$) can be explained by this general correlation function at $7\mu m \leq D_{50} \leq 250\mu m$ and $1.62 m/s \leq U \leq 8.3 m/s$.

$$C_f(\times 10^3) = 0.025 \times D_{50} - 0.145U + 5.962$$

6.5.3 Roughness Functions of Surfaces

For pressure drop tests, the roughness function were calculated by using the Granville (1987) method (Equation **3.62**). The results of the roughness function, ΔU^+, for the 1st and 2nd set of tested surfaces are plotted in **Figure 6.10** and **Figure 6.11** against the roughness Reynolds number, k^+. Shown for comparison, the figure also includes the correlation of Townsin and Dey (1990) which is given in Equation **5.6**; the well-known Colebrook-White type roughness function (Colebrook *et al*., 1939) which is given in Equation **5.7** and Nikuradse type roughness function (Nikuradse, 1933) which is given in Equation **5.8**. A multiple of the peak to trough roughness height, $k = AR_t$ was used as the roughness length scale for the present investigation of this Chapter. It has to be noted that the choice of a roughness length scale only affects the abscissa of roughness function profiles along with the roughness Reynolds number, without affecting roughness function values.

The subsequent regression analysis indicated that, for the 1st tests, with $k = 1.1\ R_t$ the resulting values showed a good agreement with the Colebrook type roughness function behaviour,

especially in the transitional rough regime. Some 97.5% (i.e. $R^2 = 0.975$) of the variance in the 1st test results can be explained by the Colebrook type roughness function. For the surfaces with the 2nd application, the equation $k = 1.1\ R_t$ was used as the roughness length scale for scaling the roughness function with the roughness Reynolds number. According to the regression analysis, the results can be observed to present a good agreement with the Colebrook type roughness function behaviour with 97.1% (i.e. $R^2 = 0.971$) variance.

Nevertheless, based on the observations from the SEM images, even though these tested surfaces were like "micro-scale sandpaper", the roughness function results obviously did not exhibit the uniform sand grain results of Nikuradse type roughness function behaviour in the transitionally rough regime. According to **Figure 6.10** and **Figure 6.11**, all the roughness function results are lying in the transitionally and fully rough regimes. For C12, C17 and C25 after the 1st application and for C7, C12, C17 and C25 after the 2nd application, the roughness functions were in the transitionally rough regime within the testing Reynolds number ranges, whereas for those of C2, C7 (1st application) C60, C100 and C250 was passing from the transitional rough regime into the fully rough regime.

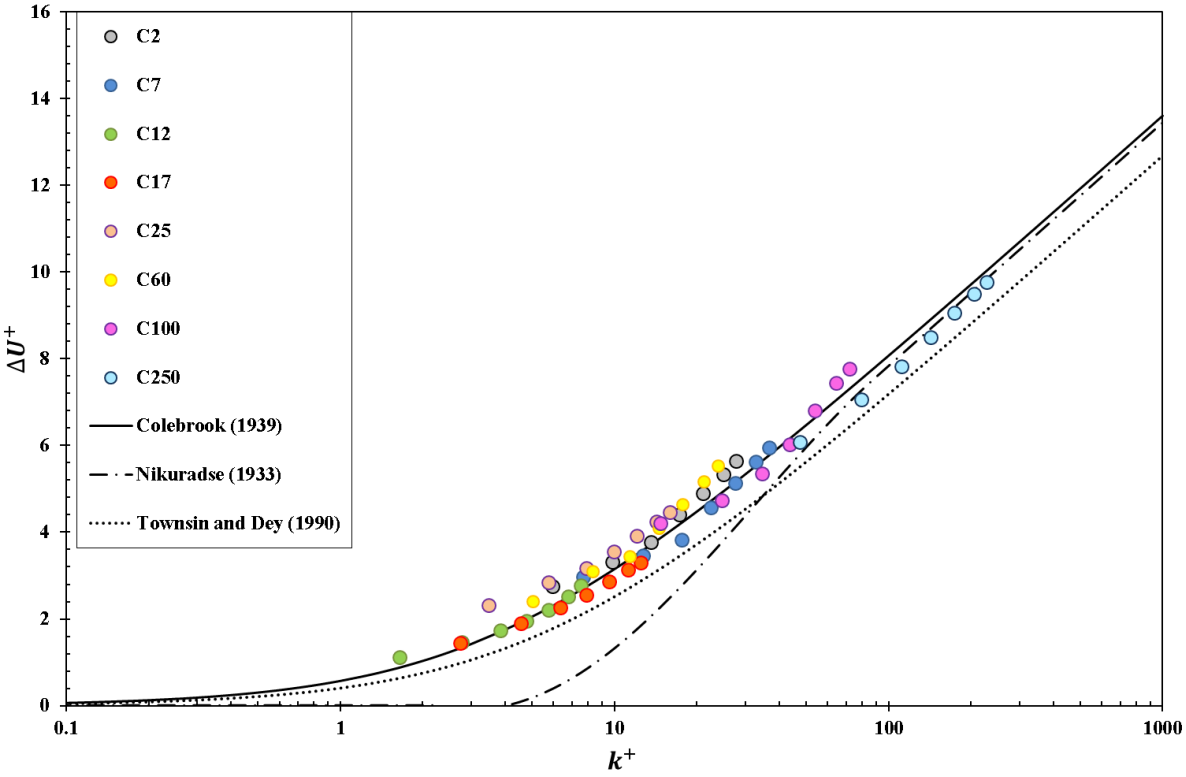

Figure 6.10: Roughness function results for 1st pressure drop test scaled on k=1.1R_t

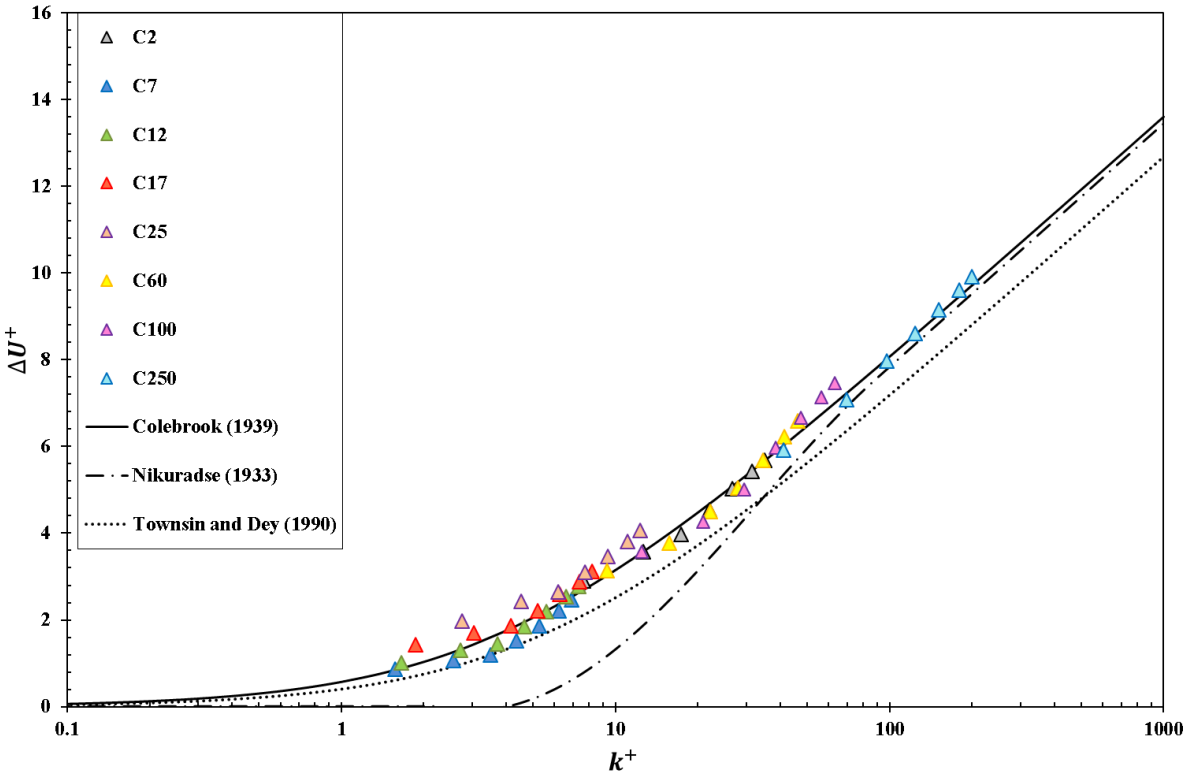

Figure 6.11: Roughness function results for 2nd pressure drop test scaled on k=1.1R_t

The fully rough regime can be found starting at a roughness Reynolds number, $k^+ \approx 20$ to 30 as the scattered ΔU^+ values agree with the full flow asymptotic line of Colebrook's behaviours. These results show good agreement with Schultz and Flack (2007) and Shockling *et al.* (2006) who defined the upper critical range of the transitionally rough regime at $k^+ < 25$ and $k^+ < 30$ respectively. These phenomena show good agreement with the findings of flow properties above these testing surfaces in **Section 6.5.1**. However for the onset of the transitionally rough regime, no k^+ could be identified in the present work.

The further detailed roughness function results along with the associated k^+ of all test surface are all presented in **Table 6.10**. In the transitionally rough regime, $k^+ = 1.6$ was the lowest experimental roughness Reynolds number given by C12 from the 1st surface application and C7 from the 2nd surface application, respectively. The transitional rough regime was within $1.6 < k^+ < 20$ for the present results.

Table 6.10: Results of roughness function ΔU^+ with associated k^+ from coated panels

1st surface application															
C2		**C7**		**C12**		**C17**		**C25**		**C60**		**C100**		**C250**	
$\mathbf{k^+}$	$\mathbf{\Delta U^+}$	$\mathbf{k^+}$	$\mathbf{\Delta U^+}$	$\mathbf{k^+}$	$\mathbf{\Delta U^+}$	$\mathbf{k^+}$	$\mathbf{\Delta U^+}$	$\mathbf{k^+}$	$\mathbf{\Delta U^+}$	$\mathbf{k^+}$	$\mathbf{\Delta U^+}$	$\mathbf{k^+}$	$\mathbf{\Delta U^+}$	$\mathbf{k^+}$	$\mathbf{\Delta U^+}$
6.0	2.8	7.7	3.0	1.6	1.1	2.7	1.4	3.5	2.3	5.0	2.4	14.7	4.2	47.6	6.1
9.8	3.3	12.7	3.5	2.8	1.5	4.6	1.9	5.7	2.8	8.3	3.1	24.6	4.7	79.8	7.1
13.6	3.8	17.6	3.8	3.9	1.7	6.3	2.3	7.9	3.2	11.4	3.4	34.5	5.4	111.4	7.8
17.3	4.4	22.5	4.6	4.8	1.9	7.9	2.6	9.9	3.6	14.5	4.1	43.6	6.0	142.0	8.5
21.0	4.9	27.5	5.1	5.8	2.2	9.6	2.9	12.1	3.9	17.8	4.7	53.9	6.8	173.3	9.1
25.0	5.3	32.7	5.6	6.8	2.5	11.2	3.1	14.3	4.2	21.2	5.2	64.5	7.4	204.7	9.5
27.8	5.6	36.6	6.0	7.6	2.8	12.5	3.3	15.9	4.5	23.8	5.5	71.9	7.8	227.9	9.8
2nd surface application															
C2		**C7**		**C12**		**C17**		**C25**		**C60**		**C100**		**C250**	
$\mathbf{k^+}$	$\mathbf{\Delta U^+}$	$\mathbf{k^+}$	$\mathbf{\Delta U^+}$	$\mathbf{k^+}$	$\mathbf{\Delta U^+}$	$\mathbf{k^+}$	$\mathbf{\Delta U^+}$	$\mathbf{k^+}$	$\mathbf{\Delta U^+}$	$\mathbf{k^+}$	$\mathbf{\Delta U^+}$	$\mathbf{k^+}$	$\mathbf{\Delta U^+}$	$\mathbf{k^+}$	$\mathbf{\Delta U^+}$
7.6	2.9	1.6	0.9	1.7	1.0	1.9	1.4	2.8	2.0	9.4	3.1	12.5	3.6	41.0	5.9
12.7	3.6	2.6	1.1	2.7	1.3	3.1	1.7	4.5	2.4	15.7	3.8	20.9	4.3	69.6	7.1
17.4	4.0	3.5	1.2	3.7	1.4	4.2	1.9	6.2	2.7	22.1	4.5	29.5	5.0	98.0	8.0
22.0	4.5	4.4	1.5	4.6	1.8	5.2	2.2	7.7	3.1	28.0	5.1	38.4	6.0	124.3	8.6
26.7	5.0	5.3	1.9	5.6	2.2	6.3	2.6	9.4	3.5	34.5	5.7	47.3	6.7	151.5	9.2
31.5	5.4	6.2	2.2	6.6	2.5	7.4	2.9	11.0	3.8	41.3	6.2	56.3	7.1	179.1	9.6
35.0	5.7	6.9	2.5	7.4	2.8	8.2	3.1	12.3	4.1	46.4	6.6	63.0	7.5	199.7	9.9

6.6 Chapter Summary

The pressure drop tests of the panels coated with eight different sizes of cuprous oxide particles, along with the acrylic smooth reference panels, were conducted by using the UNEW FTFC. The experimental investigations of Cu_2O surfaces were carried out in two groups: the 1st applications and the 2nd applications. The main objectives of these measurements were to run a systematic study of the effects of the various sizes of cuprous oxide particles on the frictional drag characteristics.

According to the test results, the smaller particle sizes (i.e. specimen C12 and C17) usually produce relatively lower roughness profile surfaces, and this resulted in lower frictional coefficients. For example, in comparison to the reference surface, an average increase of 13.5% and 19.7% resulted from surfaces coated with C12, while an average increase of 29.4% and 21.8% were given by C17 according to the 1st and 2nd tests. Moreover, within the test Reynolds number range, C_f curves of C12 and C17 showed similar performances to the smooth surfaces, and these indicated that the C12 and C17 surfaces were between the hydraulically smooth and transitionally rough regimes.

As for the surfaces coated with the smallest size particles (i.e. C2 and C7), their frictional drags were directly affected by the finish surface condition and surface waviness profile of the macrostructure. The average frictional drag was as high as 51.7% and 55.2% for C2 from the 1st and 2nd tests respectively. However, there was a dramatic difference between the 1st and 2nd surface applications of C7 with 55.6% and 16.9% respectively. For the rest of the larger size particles, the surface roughness was directly affected by the particle size, increasing from C25 to C250, and more apparent frictional drag also resulted, 40% to 160% respectively. Also, inflectional behaviours of the C_f curves of the tested surfaces coated with C2, C25, C60, C100 and C250 at $Re_D > 8 \times 10^4$ can be observed and show that the frictional drag of these transitionally rough surfaces were dependent on both surface roughness effects and the Reynolds number. Moreover, for $Re_D > 1.4 \times 10^5$ and $Re_D > 1.0 \times 10^5$, the C_f curves of C100 and C250 became independent of the Reynolds number indicating that the surface were fully rough at higher Reynolds numbers.

The surface Cu_2O particle sizes correlated with their associated frictional drag and linear relationships. The linear experimental relationship of $C_f(\times 10^3) = A \times D_{50} + B$ was derived for the presented frictional drag of Cu_2O surfaces, where the slope value A was found to vary between $0.025-0.026$, and the intercept B was 5.0. There was no obvious velocity dependence impacts can be observed on affecting the slope and intercept values. Even though this linear relationship needs to be further verified, it can be effectively used for estimating the frictional drag of different Cu_2O surfaces.

The roughness functions of all of the test surfaces were calculated using the Granville (1987) method. The roughness length scale of a multiple of the peak to trough roughness height, R_t (with model $k = AR_t$) made the roughness function results of both tests show a good agreement (with $R^2 = 0.97$) with the Colebrook type roughness function behaviour in the transitionally rough regime. All the roughness function results lay in the transitionally and fully rough regimes, and the fully rough regime was found to start at a roughness Reynolds number, $k^+ \approx$ 20 to 30 which shows good agreement with Schultz and Flack (2007) and Shockling *et al.* (2006). The larger size specimens, such as C100 and C250 as well as the low quality finished surfaces, C2 and C7 could affect the results and passing from the transitionally rough regime into the fully rough regime. In the present work, no k^+ could be identified for the onset of the transitionally rough regime.

Apart from evaluating the initial friction resistance brought by the newly antifouling painted ship underwater surface, people also are showing more concerns on their ship resistance and powering penalties/benefits when antifouling paint vs fouling organisms, especially under in-service condition. In the next chapter, the drag evaluation of Cu_2O surfaces fouled with "in-service" biofilm have been carried out by using the same hydrodynamic assessments (UNEW's FTFC facility). The investigation details and results have been described and discussed in **Chapter 7**.

Chapter 7 Pressure Drop Measurements of Biofilm Fouled Cu_2O Surfaces

7.1 Introduction

This chapter aims to present an investigation of biofilm impacts on the frictional drag characteristics of marine surfaces coated with different sized cuprous oxide (Cu_2O) particles through pressure drop measurements.

In order to meet **Objective 6 (Section 1.3**) of the research study, this chapter included the following tasks:

- To evaluate the biofilm impact on the frictional drag of Cu_2O surfaces which were formed with different size testing particles by using a fully turbulent flow channel;
- To periodically test frictional drag changes from these Cu_2O surfaces and evaluate the drag penalties at the different biofilm development period;
- To calculate and compare the frictional coefficient and roughness functions of each testing surface at the different biofilm development period;

In order to associate this with real-life conditions, the marine surfaces were deployed on a research vessel to allow the biofilm to develop while the vessel was in its service conditions so that the time-dependent biofilm impacts on the surfaces coated with Cu_2O antifouling could be evaluated periodically.

The repeatability and uncertainty of the tests are discussed in **Section 7.2,** and the detailed frictional drag results are presented and discussed in **Section 7.3**, with experiments carried out every 1.5 months for a total of 6 months fouling growth deployment. Based on the experimental frictional drag, the roughness function of all of the tested surfaces is discussed in **Section 7.4**. Finally, the chapter is summarised in **Section 7.5**.

It has to be noted that, the deployment work set-up and biofilm fouled surface condition have been fully described in **Section 4.3.3** and **Section 4.4**. Therefore, no further test surface descriptions would be given in this chapter. Moreover, detailed descriptions of the turbulent flow channel and the experimental set-up are not presented in this chapter as they have already been discussed in **Section 6.2** and **Section 6.3**.

7.2 Uncertainty Analysis

The uncertainty estimates for the present drag coefficients and roughness function calculations were measured through repeatability tests using the procedure defined by Coleman and Steele Jr (1990) which has been explained in the previous chapter (**Section 6.4**). The 95% precision confidence limits for a given quantity were obtained by using the standard errors of the statistical variables multiplied by the related two-tailed t value which equals 2.776 for four degrees of freedom according to Coleman and Steele Jr (1990).

The resulting precision and bias uncertainty span in the skin-friction coefficient, C_f, are tabulated in **Table 7.1**. The overall uncertainty of all tested specimens is C_f: ±1.2% to ±6.8% at the lowest Reynolds number, ±0.6% to ±1.4% at the highest Reynolds number.

Table 7.1: Uncertainty in C_f for all tested surfaces fouled with biofilm

	1.5 Months	**3 Months**	**4.5 Months**	**6 Months**
C12	±1.2% − ±3.6%	±1.2% − ±6.8%	±1.0% − ±1.6%	±1.2% − ±3.1%
C17	±1.0% − ±3.3%	±1.1% − ±3.4%	±1.1% − ±3.4%	±1.1% − ±2.8%
C25	±0.9% − ±4.5%	±0.8% − ±2.7%	±0.6% − ±1.2%	±1.1% − ±3.1%
C60	±1.2% − ±3.6%	±1.1% − ±4.6%	±1.4% − ±3.1%	±1.1% − ±4.8%

The overall precision and bias error for the roughness function, ΔU^+, of all tested specimens, is tabulated in **Table 7.2**. The overall uncertainty in ΔU^+ ranges from ±6.0% to ±10.8% at the lowest Reynolds number, ±0.7% to ±1.5% at the highest Reynolds number.

Table 7.2: Uncertainty in ΔU^+ for all tested surfaces fouled with biofilm

	1.5 Months	**3 Months**	**4.5 Months**	**6 Months**
C12	±1.5% − ±9.2%	±1.2% − ±9.2%	±1.2% − ±6.8%	±1.0% − ±8.9%
C17	±1.1% − ±9.7%	±1.1% − ±7.8%	±1.0% − ±7.7%	±1.1% − ±8.4%
C25	±1.2%−±10.8%	±0.9% − ±7.4%	±0.9% − ±6.3%	±1.2% − ±7.2%
C60	±0.8% − ±6.0%	±0.7% − ±7.5%	±0.9% − ±6.7%	±0.9% − ±7.9%

Generally, it was found that there was no evidence for a specific relationship between the tested surface biofilm accumulations and the experimental uncertainty percentage. In the following sections, all measured results were within the above uncertainty level.

7.3 The Results and Discussion for the Frictional Coefficient

The overall frictional coefficients of the surfaces, from the clean condition through to the surfaces with a total of 6 months fouling, at 1.5-month intervals, are presented in **Figure 7.1**.

The frictional drag of all tested surfaces increased under the effects of biofilm growth. For surfaces coated with 12µm (C12), 17µm (C17) and 25µm (C25) Cu_2O particles, the drag results gradually increased, eventually reaching a relatively constant level by the end of the tests (after 6 months).

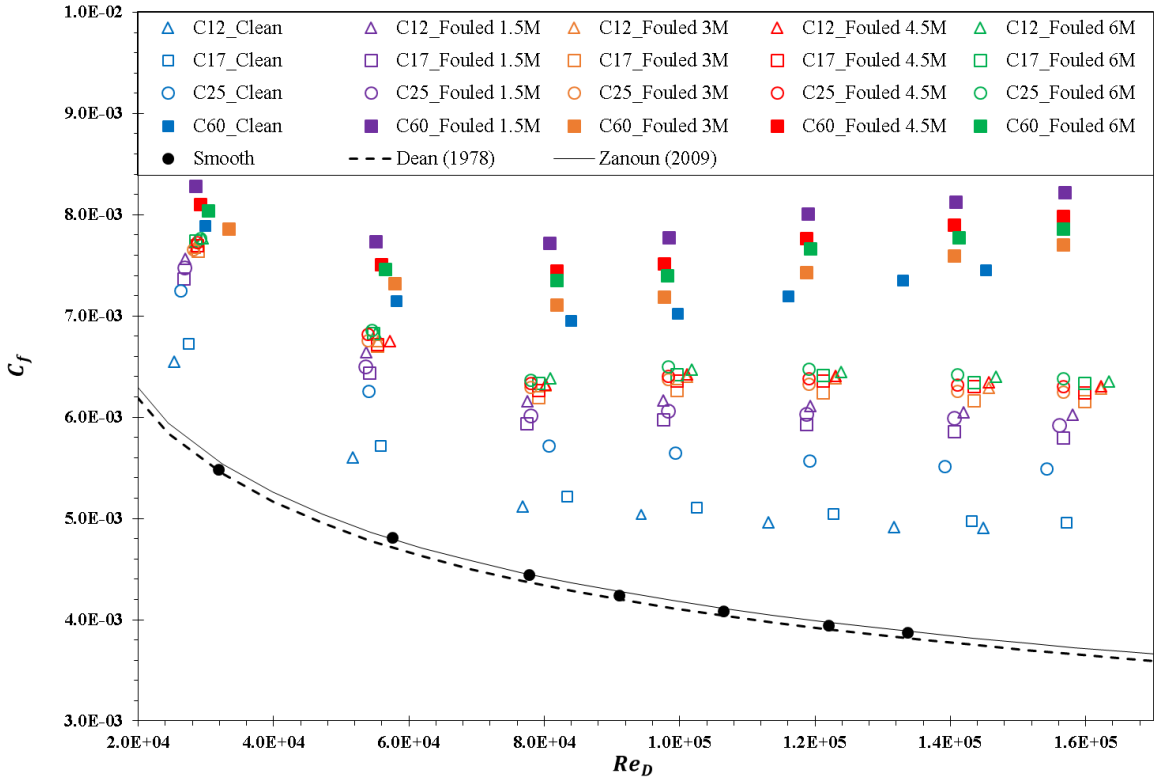

Figure 7.1: Frictional coefficient results for pressure drop test of all fouled panels

The highest frictional drag values were produced by surfaces coated with 60µm (C60) Cu_2O particles in all periods, although there were some drops in the results at 3-months and 6-months. Hereinafter, the following detailed discussion is separated by surface status with every 1.5-month deployment, i.e. 1.5, 3, 4.5 and 6-month. Therefore, the frictional coefficient results of the surfaces fouled at each testing stage of biofilm are presented and discussed in **Section 7.3.1** to **Section 7.3.4** respectively. It also has to be noted that, as illustrated in **Figure 4.14**, the pressure drop tests were conducted using the surfaces after the 2nd applications only.

7.3.1 Frictional Coefficient of Surfaces Fouled with 1.5-Month Biofilm

Figure 7.2 presents the frictional coefficient results of the tested surfaces C12, C17, C25 and C60 fouled with 1.5-month biofilm. For the reference as the clean surface condition, the C_f of the un-coated cast acrylic panels and clean tested Cu_2O surfaces are also plotted. Compared to the results of their original clean surface condition, the frictional drag of surfaces covered with

1.5-month developed biofilm had obviously increased. In particular, there was a dramatic frictional drag increase for the C12 and C17 surfaces fouled with 1.5-month biofilm. The surfaces coated with C17 presented the lowest frictional coefficient after 1.5 months. The clean surfaces coated with C25 had slightly higher frictional drag than those of C12. However, when coated with biofilm after 1.5 months, the surfaces coated with C12 were observed to have slightly higher frictional drag than surfaces coated with C25. Meanwhile, the highest frictional drag was produced by C60 which also had a significant increase over its clean condition.

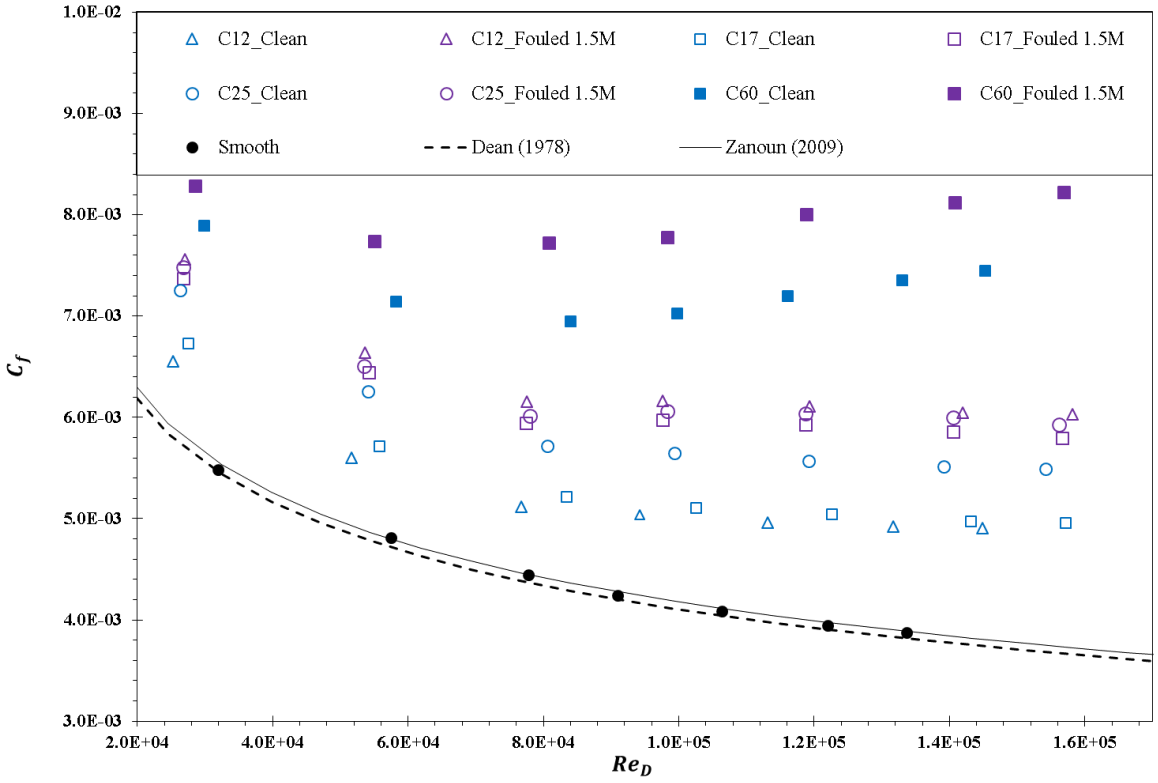

Figure 7.2: C_f for pressure drop measurements of surfaces fouled for 1.5-month

The C_f curves of C12, C17 and C25, are seen to be decreasing within the Reynolds number range, with apparent inflectional behaviours as their frictional coefficient curves slightly turns-upwards at $Re_D > 8 \times 10^4$. The C_f curve of C60 presented a more obvious up-turn at $Re_D > 8 \times 10^4$ and tended to be parallel to the horizontal axis at $Re_D > 1.6 \times 10^5$. This indicated that the C60 surface covered with 1.5-month biofilm showed Reynolds number independent behaviour at higher velocities.

The detailed skin friction coefficients of all 1.5-month biofilm fouled test surfaces are presented in **Table 7.3**. To provide further insight into the frictional drag differences between clean and

fouled surface conditions, the changes in friction coefficients, C_f (%) with respect to the smooth reference panel are given in **Table 7.4**.

Table 7.3: C_f for surfaces fouled with 1.5 months biofilm

Bulk mean velocity m/s	**Frictional coefficient $C_f \times 10^3$**				
	Acrylic	**C12**	**C17**	**C25**	**C60**
1.62	5.5	7.6	7.4	7.5	8.3
2.87	4.8	6.6	6.4	6.5	7.7
4.1	4.4	6.2	5.9	6.0	7.7
5.17	4.3	6.2	6.0	6.1	7.8
6.29	4.1	6.1	5.9	6.0	8.0
7.45	4.0	6.0	5.9	6.0	8.1
8.3	3.9	6.0	5.8	5.9	8.2

Table 7.4: Increase in overall C_f (%) for surfaces fouled for 1.5-month compared to acrylic surface

	Specimen	**R_t (μm)average**	**Average Increase in C_f (%)**	**Range of Increase in C_f (%)**
Clean	**C12**	18.0	20.4	15.1−26.7
	C17	20.0	22.5	17.4−28.1
	C25	28.3	34.6	28.7−41.9
	C60	91.9	67.6	47.4−92.4
1.5 Months	**C12**	50.4	45.4	37.9−55.6
	C17	41.3	40.9	33.7−49.7
	C25	41.7	43.2	35.2−53.0
	C60	99.3	83.3	51.1−112.2

For surfaces coated with C12, the 1.5-month biofilm resulted in the frictional drag having a 45% increase with respect to the reference surface and was about 25% higher than its own clean condition before the submersion. This was followed by the surface coated with C17, for which an increase of 41% in frictional drag was caused by the 1.5-month biofilm, and this was nearly 18% higher than the results of its original surface condition. Slightly higher than the C17 fouled surface, the C25 resulted in a 43% increase in the frictional coefficient. However, compared to the C25 clean surface condition, it had about a 9% increment which was the lowest drag change caused by the 1.5-month biofilm among all of the tested surfaces. The C60 surfaces, as the roughest surfaces in the present test scenario, had an approximately 83% drag increase with respect to the reference surface, and 16% frictional drag difference with respect to the surface before the sea deployment work.

7.3.2 Frictional Coefficient of Surfaces Fouled with 3-Month Biofilm

The friction coefficient curves of the tested surfaces fouled with 3-month biofilm are plotted in **Figure 7.3** along with results of the smooth reference panels. Also, shown for comparison are the C_f curves of 1.5-month fouling.

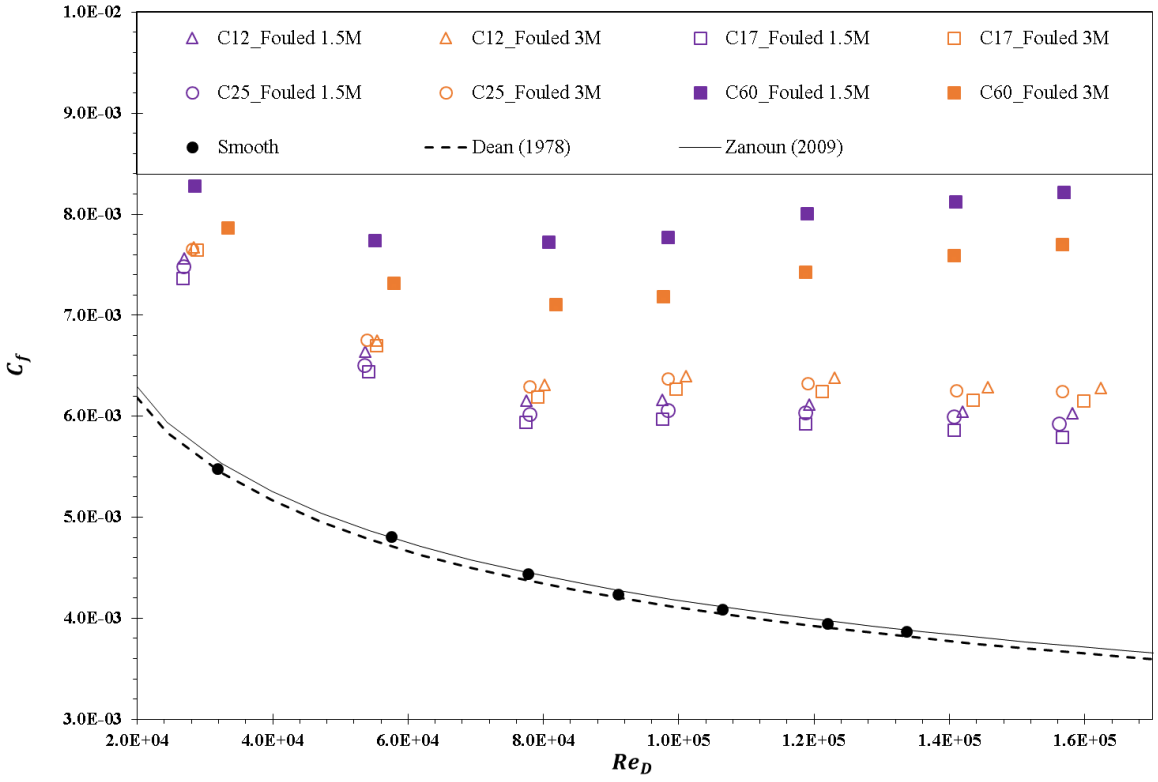

Figure 7.3: C_f for pressure drop measurements of surfaces fouled for 3-month

For the surfaces coated with C12, C17 and C25, the frictional drag was increased by the 3-month biofilm as their surface roughness was further increased. It can be seen that by the end of the 3-month deployment, the lowest frictional coefficients resulted from the surfaces coated with C17, which was closely followed by C25 and C12. However, there were no obvious frictional drag differences at the lowest Reynolds number, $Re_D < 8 \times 10^4$, for these surfaces. In addition, within the Reynolds number range, the C_f curves of C12, C17 and C25 kept a similar trend to their 1.5-month fouled equivalents with the frictional coefficient curve slightly turning-upward at $Re_D > 8 \times 10^4$, which indicated that these fouled surfaces were transitionally rough surfaces. With 3 months of biofilm development, even though surfaces coated with C60 still resulted in the highest frictional drag values, **Figure 7.3** shows that the C_f values of C60 had a significant decrease compared to those of the 1.5-month fouled surfaces. Moreover, the trend of the C_f curve of C60 also presented a similar behaviour to its 1.5-month results and

tended to be parallel to the horizontal axis at $Re_D > 1.6 \times 10^5$. This observation suggests that the C60 with 3-month biofilm presented as a transitionally rough surface, whereas it would behave as a fully rough surface at higher testing velocities.

Table 7.5: C_f for surfaces fouled with 3 months biofilm

Bulk mean velocity m/s	**Frictional coefficient $C_f \times 10^3$**				
	Acrylic	**C12**	**C17**	**C25**	**C60**
1.62	5.5	7.7	7.6	7.7	7.9
2.87	4.8	6.8	6.7	6.8	7.3
4.1	4.4	6.3	6.2	6.3	7.1
5.17	4.3	6.4	6.3	6.4	7.2
6.29	4.1	6.4	6.2	6.3	7.4
7.45	4.0	6.3	6.2	6.3	7.6
8.3	3.9	6.3	6.2	6.3	7.7

The detailed skin friction coefficients of all 3-month biofilm fouled tested surfaces are presented in **Table 7.5**. **Table 7.6** gives the changes in friction coefficients, C_f (%) with respect to the acrylic reference panels, between 1.5-month and 3-month biofilm.

Table 7.6: Increase in overall C_f (%) for surfaces fouled for 3-month compared to acrylic surface

	Specimen	R_t (μm)**average**	**Average Increase in C_f (%)**	**Range of Increase in C_f (%)**
1.5 Months	**C12**	50.4	45.4	37.9−55.6
	C17	41.3	40.9	33.7−49.7
	C25	41.7	43.2	35.2−53.0
	C60	99.3	83.3	51.1−112.2
3 Months	**C12**	58.5	50.1	39.9−62.2
	C17	51.8	47.7	39.3−58.9
	C25	55.3	49.6	39.6−61.4
	C60	95.8	71.2	43.4−98.9

After 3 months of biofilm development, on average, there was about a 50.1% drag increment resulting from surfaces coated with C12. For the C_f differences compared to C12 with 1.5-month of biofilm present, the drag had increased by 5%. A similar C_f increment, 7% was presented by 3-month biofilm on C17, compared to the 1.5-month results, whilst, the overall C_f of C17 had increased by 47.7% with respect to the reference surface. Slightly lower than the results of C12, there was a 49.6% increase in frictional coefficient for the 3-month biofilm on surfaces coated with C25. Also, there was a 6% increase in the friction drag from the results of 1.5-month biofouling, and it can be noted as the highest C_f change during this set of

experiments.

For surfaces coated with C60, the average measured overall frictional drag was about 71.2% compared with the hydraulically smooth surface. However, instead of increasing, the frictional coefficient of C60 fouled with 3-month biofilm was found to have a 12% decrease relative to the 1.5-month case.

7.3.3 Frictional Coefficient of Surfaces Fouled with 4.5-Month Biofilm

The friction coefficient curves of tested surfaces fouled with 4.5-month biofilm are presented in **Figure 7.4** along with results of the smooth reference surface. Also, shown for comparison are the frictional coefficients of surfaces fouled for 3 months.

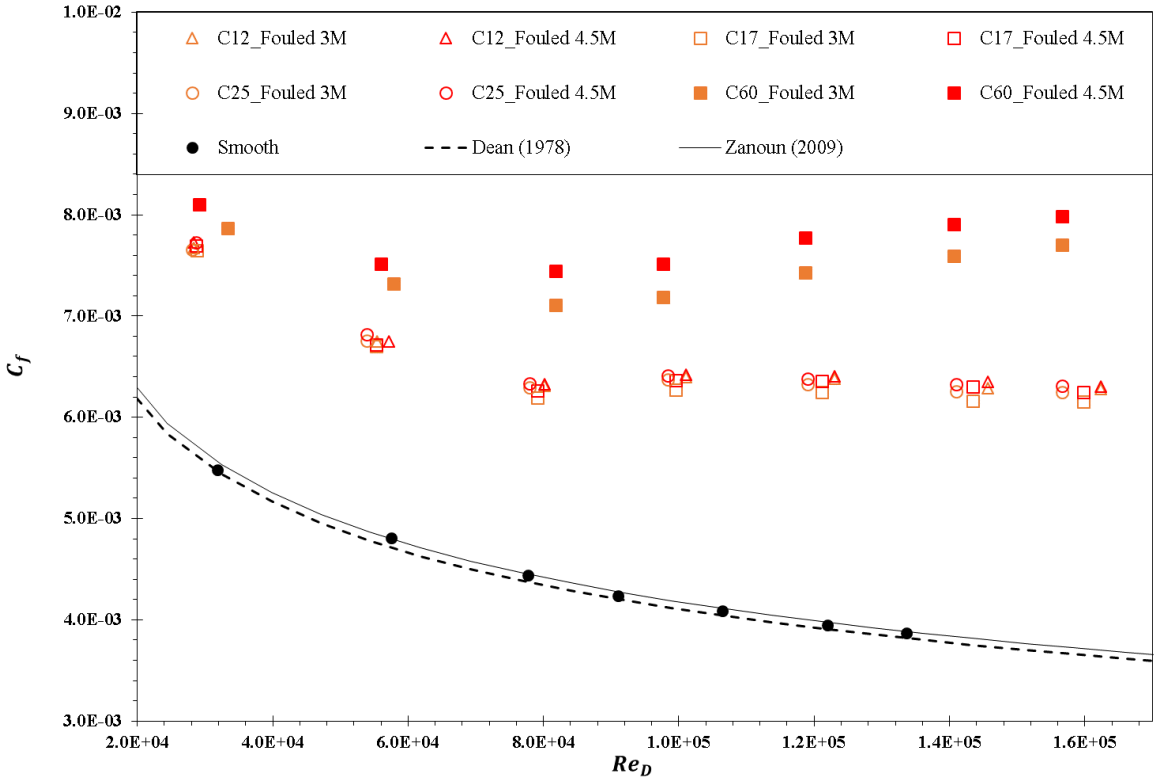

Figure 7.4: C_f for pressure drop measurements of surfaces fouled for 4.5-month

The measured frictional coefficients of C12, C17 and C25 were closer to each other with the covering of 4.5-month biofilm. It can be seen that the lowest frictional coefficients resulted from the C17 surfaces, whereas for those of C12 and C25 were at a very similar level. Moreover, compared to the C_f curves of 3-month biofouling, there were less significant differences between surfaces C12, C17 and C25 fouled with 4.5-month biofilm, especially at the lower Reynolds number, $Re_D < 8 \times 10^4$. Also, within the Reynolds number range, the inflectional

behaviour of the C_f curves at $Re_D > 8.0 \times 10^4$ indicated that the tested surfaces C12, C17 and C25 fouled with 4.5-month biofilm present as transitionally rough surfaces. Meanwhile, there were slightly higher frictional drag values for the 4.5 months biofilm growth on the C60 surfaces. Also, the C_f curve of the C60 surfaces fouled with 4.5-month biofilm show very similar behaviour to its 3-month results which indicated that the biofilm had made the surface fully rough at higher testing velocities.

The detailed skin friction coefficients of all 4.5-month biofilm fouled test surfaces are presented in **Table 7.7**. For the further comparison between surfaces fouled with 3-month and 4.5-month biofilm, with respect to acrylic reference panels, **Table 7.8** gives the changes in friction coefficients, C_f (%).

Table 7.7: C_f for surfaces fouled with 4.5 months biofilm

Bulk mean velocity m/s	**Frictional coefficient $C_f \times 10^3$**				
	Acrylic	**C12**	**C17**	**C25**	**C60**
1.62	5.5	7.7	7.7	7.7	8.1
2.87	4.8	6.8	6.7	6.8	7.5
4.1	4.4	6.3	6.3	6.3	7.4
5.17	4.3	6.4	6.4	6.4	7.5
6.29	4.1	6.4	6.4	6.4	7.8
7.45	4.0	6.3	6.3	6.3	7.9
8.3	3.9	6.3	6.2	6.3	8.0

Table 7.8: Increase in overall C_f (%) for surfaces fouled for 4.5-month compared to acrylic surface

	Specimen	**R_t (μm)average**	**Average Increase in C_f (%)**	**Range of Increase in C_f (%)**
3 Months	**C12**	58.5	50.1	39.9−62.2
	C17	51.8	47.7	39.3−58.9
	C25	55.3	49.6	39.6−61.4
	C60	95.8	71.2	43.4−98.9
4.5 Months	**C12**	61.6	50.8	40.3−62.8
	C17	56.5	49.7	39.6−61.3
	C25	60.0	50.8	40.9−62.9
	C60	112.1	77.9	47.7−106.2

After 4.5-month sea deployment for biofilm growth on the tested surfaces, on average, there was a 50% drag increment for surfaces coated with C12, C17 and C25. Compared to the 3-month fouled results, almost imperceptible drag increments can be noticed from those surfaces which were about 1%−2%. These slight drag differences found between the 3-month and 4.5-

month fouled conditions showed that the biofilm impacts on these surfaces had become almost minimal and no further dramatic drag increase would occur unless the environment was changed. For surfaces coated with C60, the average measured overall frictional drag was about 78% compared with a hydraulically smooth surface and about 7% higher than that of the surface fouled with 3-month biofilm.

7.3.4 Frictional Coefficient of Surfaces Fouled with 6-Month Biofilm

It has to be reminded that, the deployment work from 4.5-month to 6-month was carried out at the yacht harbour (introduced in **Section 4.3.3.2**) instead of on the research vessel. Normally, increasing shear force at the walls can alter the biofilm thickness (Kornegay and Andrews, 1968; Rijnaarts *et al.*, 1993; Zheng *et al.*, 1994). Theoretically, for testing surface fouled with the biofilm at yacht harbour would be expected to be developed thicker and lead to higher frictional resistance. Have to say that, during the current investigation, for the research vessel, the static conditions of the total activities was 85% which equivalent to the static harbour deployment. Plus under the lower water temperature (6.7°C and 15.3°C) and short deployment period (1.5 months). Consequently, the effects of the water current difference between harbour and vessel development set-up would be far difficult to be analysed and therefore neglected.

Figure 7.5 presents the friction coefficient curves of tested surfaces fouled with 6-month biofilm along with results of the smooth reference panels. Shown for comparison, the frictional coefficients of surfaces fouled with 4.5-month are also presented.

The frictional coefficients of C12, C17 and C25 surfaces fouled with 6-month biofilm were all at a very similar level. The lowest C_f values resulted from the biofilm of C17, whilst for those of C12 and C25 were marginally higher. Moreover, comparing the C_f curves of 6-month with 4.5-month fouling shows that there were insignificant differences between those tested surfaces, especially at the lower Reynolds numbers, $Re_D < 8 \times 10^4$. Also, the inflectional behaviour of the C_f curves at $Re_D > 8 \times 10^4$ indicated that the tested surfaces C12, C17 and C25 fouled with 6-month biofilm presented as transitionally rough surfaces. Additionally, the C_f curves were found to have a tendency of becoming parallel to the x-axis at the higher flow speeds, meaning that the C12, C17 and C25 surfaces with 6-month fouling were likely to present as fully rough surfaces as well. Also, a few dips can be noted from the C60 surfaces fouled with 6-month biofilm when compared to the 4.5-month condition. Moreover, the C_f curve of C60 surfaces fouled with 6-month biofilm shows very similar behaviour to that of the 4.5-month results

which indicated that the biofilm had made the surface fully rough at higher testing velocities.

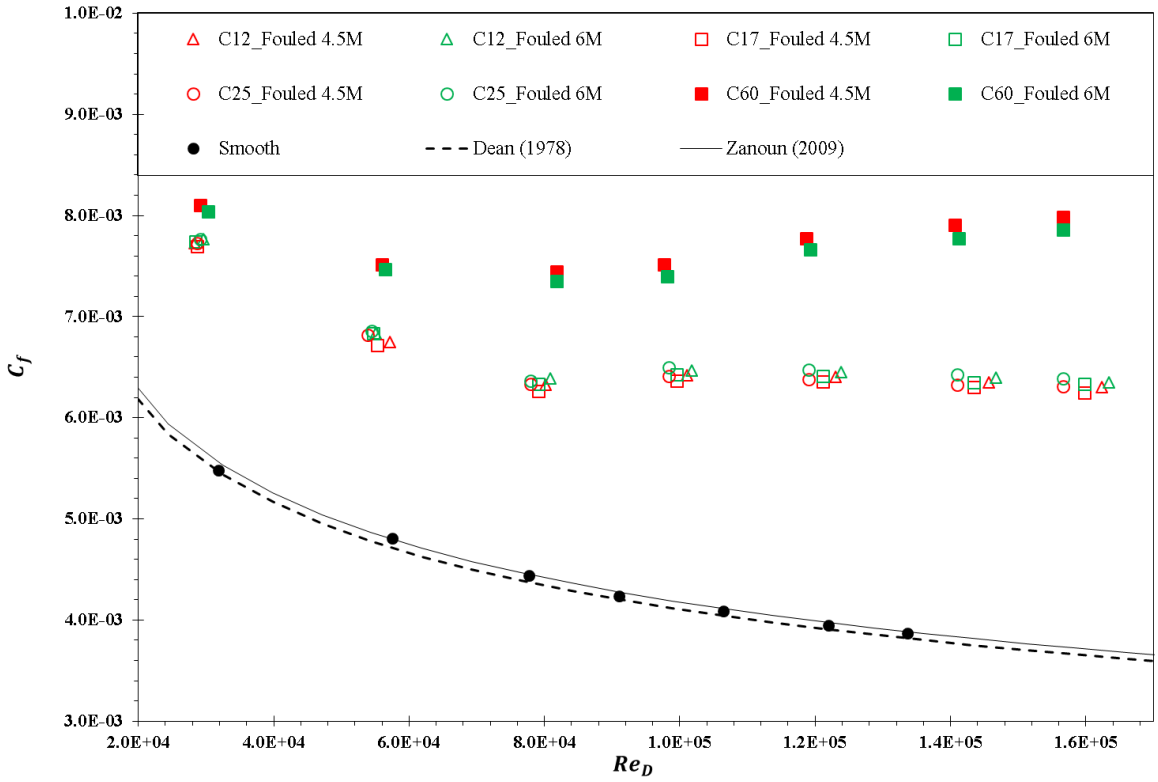

Figure 7.5: C_f for pressure drop measurements of surfaces fouled for 6-month

The detailed skin friction coefficients of all 6-month biofilm fouled test surfaces are presented in **Table 7.9**. For further comparison between surfaces fouled with 4.5-month and 6-month biofilm, with respect to the acrylic reference panels, **Table 7.10** gives the changes in friction coefficients, C_f (%).

Table 7.9: C_f for surfaces fouled with 6 months biofilm

Bulk mean velocity m/s	**Frictional coefficient $C_f \times 10^3$**				
	Acrylic	**C12**	**C17**	**C25**	**C60**
1.62	5.5	7.8	7.7	7.8	8.0
2.87	4.8	6.8	6.8	6.9	7.5
4.1	4.4	6.4	6.3	6.4	7.4
5.17	4.3	6.5	6.4	6.5	7.4
6.29	4.1	6.4	6.4	6.5	7.7
7.45	4.0	6.4	6.3	6.4	7.8
8.3	3.9	6.4	6.3	6.4	7.9

On average, there were 50%-51% drag increments resulting from 6-month biofilm of surfaces coated with C12, C17 and C25. Also, there were very slight drag increases of 1%-2% compared to the results of the 4.5-month fouled surface condition. For the surfaces coated with C60, the

average measured overall frictional drag was about 76% compared with the hydraulically smooth surface and about 2% lower than that of the surface fouled with 4.5-month biofilm.

Table 7.10: Increase in overall C_f (%) for surfaces fouled for 6-month compared to acrylic surface

	Specimen	R_t (μm)average	Average Increase in C_f (%)	Range of Increase in C_f (%)
4.5 Months	C12	61.6	50.8	40.3−62.8
	C17	56.5	49.7	39.6−61.3
	C25	60.0	50.8	40.9−62.9
	C60	112.1	77.9	47.7−106.2
6 Months	C12	63.6	52.0	41.6−64.0
	C17	57.2	51.2	41.2−63.5
	C25	67.1	52.4	41.6−64.9
	C60	112.5	75.6	46.7−103.0

7.3.5 Overall Frictional Coefficient Time-dependent Changes with Biofilm Present

To have a more visual cross comparison, with respect to the reference smooth surfaces, the overall frictional drag changes for all of the experimental tests are shown in **Figure 7.6**.

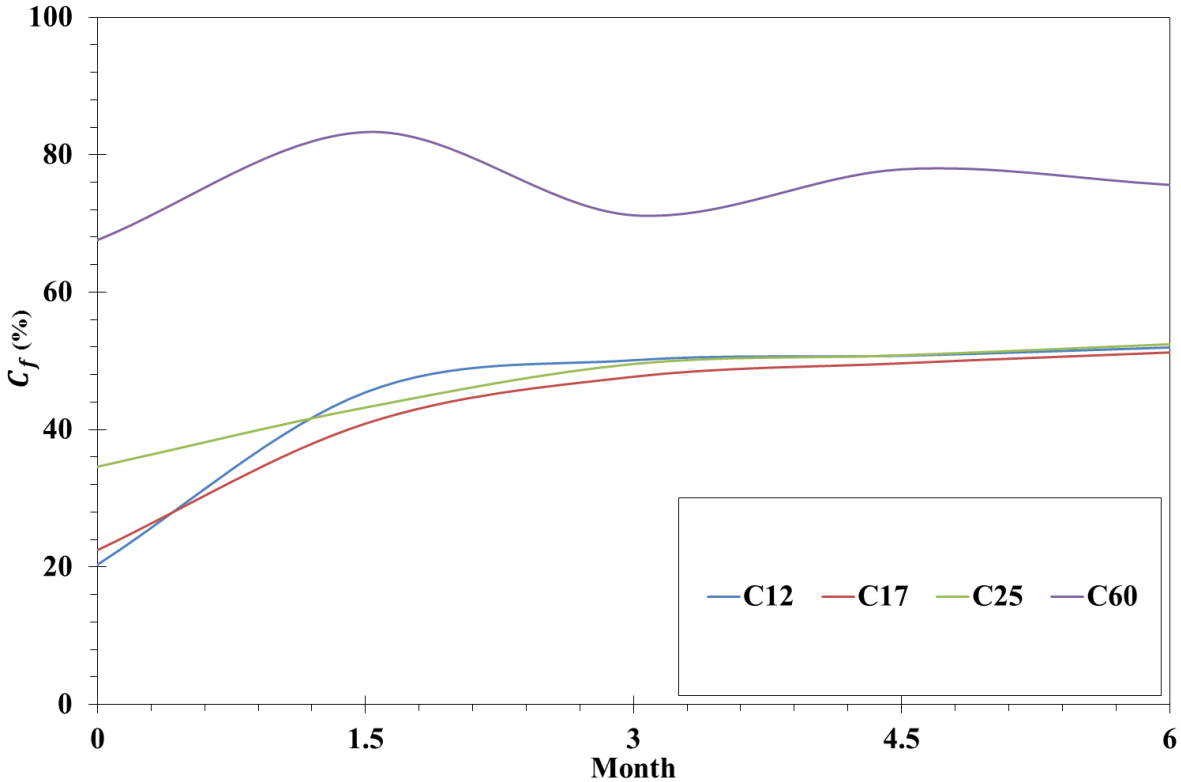

Figure 7.6: Frictional coefficient results for pressure drop test of all fouled panels

According to the figure, before the sea biofilm growth deployment was carried out, the surfaces coated with specimen C60 gave the highest frictional drag among all the tested surfaces. It was

followed by the surface coated with C25 which presented obviously higher drag values than C17 and C12. With surfaces fouled with 1.5-month biofilm covering, the frictional coefficients of all tested surfaces had dramatically increased. Combining this with the surface analysis which was discussed in **Section 4.4.4** the frictional drag is immediately increased once the biofilm starts to attach and develop on a clean surface. The more obvious frictional drag changes can be measured from a surface with a smoother original condition.

However, as the subsequent experiments were processed with time, the frictional drag results of all fouled test surfaces approached an asymptote value by the end of 6-months. Further information is given in **Table 7.11** which shows the changes in C_f (%) between adjacent stages with respect to the acrylic surface.

Table 7.11: Increase in C_f (%) for fouled panels compared for each deployment stage

Specimen	Changes in C_f (%) between adjacent stages with respect to smooth reference			
	Clean-1.5M	**1.5M-3.0M**	**3.0M-4.5M**	**4.5M-6.0M**
C12	25.1	4.7	0.7	1.2
C17	18.4	6.8	2.0	1.6
C25	8.6	6.3	1.3	1.6
C60	15.7	-12.1	6.7	-2.3

As the results of the surface condition demonstrate, the increment rate of frictional drag gradually decreased. This was especially the case for C12, which changed from a 25% increment per 1.5-months to 1.2% per 1.5-months. This is followed by C17 and C25 which both had dramatic drops: from 18% and 9% per 1.5-month to 1.5% and 1.6% per 1.5-month respectively. These phenomena indicate that once the initial biofilm had settled on the smoother or lower profile surfaces, no large drag increases would be expected until other larger fouling attachments formed, or other external factors changed (e.g. water speed, temperature, PH and mechanical damage). These can also be approved by the SEM findings according to **Figure 4.25** and **Figure 4.28** in the (**Chapter 4**) However, for C60, because of the interaction between the biofilm and the rougher microstructure profile and larger interspaces, the changes of roughness and subsequent frictional drag are uncertain. The further support information can be found from SEM scanning images: **Figure 4.26**, **Figure 4.27** and **Figure 4.29**. As a result, some decreases of frictional drag happened and were observed at 3-months and 6-months.

According to **Figure 7.6**, for C12, C17 and C25 surfaces, the asymptote value of the frictional drag changes at the end of 6-months was around a 50% increase with respect to the acrylic

reference. Whereas for the surface coated with C60, this value tended to be 70%−80% with respect to the reference surface.

7.4 Roughness Functions of Surfaces Fouled with Biofilm

According to the Granville (1987) method (Equation **3.62**), the roughness function values for all of the fouled test surfaces were obtained by using the above experimental data. **Figure 7.7** illustrates the roughness function results of the surfaces from every test stage and includes the classical roughness function trend lines according to Townsin and Dey (1990) (Equation **5.6**), Colebrook *et al.* (1939) (Equation **5.7**) and Nikuradse (1933) (Equation **5.8**).

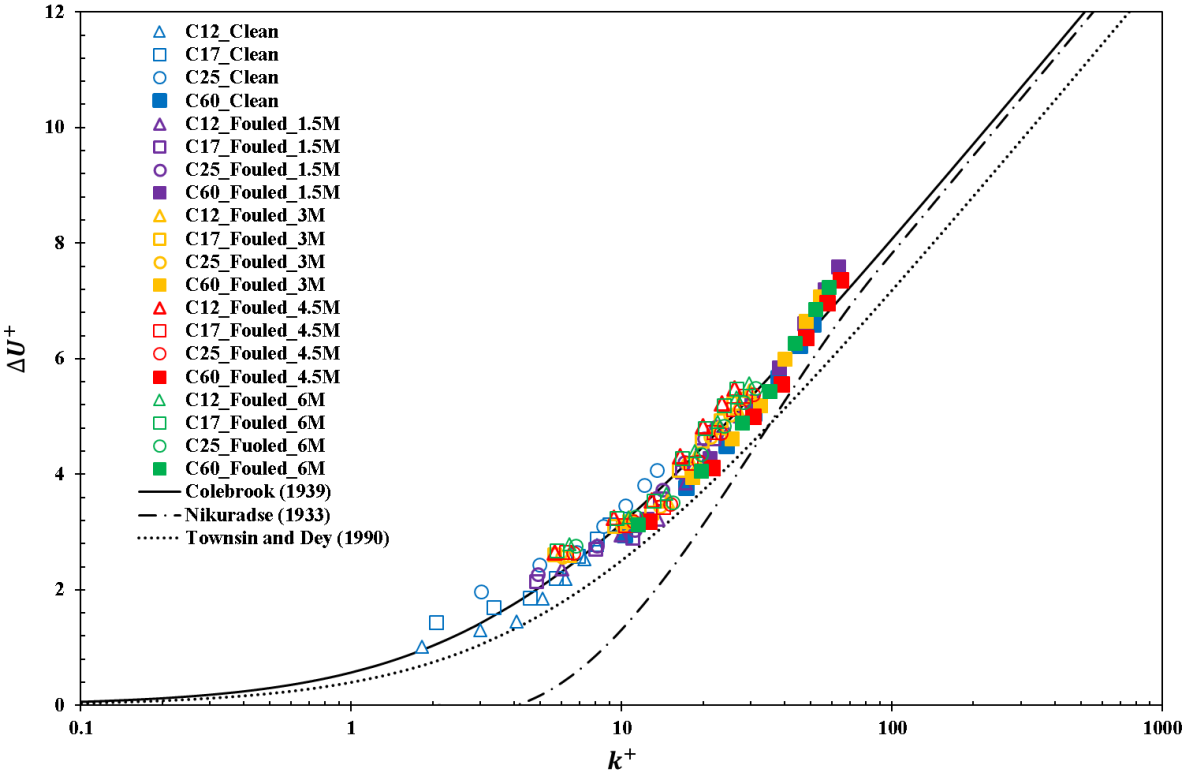

Figure 7.7: Roughness function for pressure drop test of unfouled and fouled surfaces

A multiple of the peak to trough roughness height, $k = AR_t$ was used and it was found to have the best roughness length scale to fit the Colebrook type roughness function. The subsequent regression analysis results indicated that the experimental roughness function result values showed a reasonable agreement with the Colebrook type roughness function behaviour in the transitionally rough regime throughout all testing stages (i.e. 1.5-months, 3-months, 4.5-months and 6-months), with $k = 1.2\,R_t$ ($R^2 = 0.973$), $k = 1.1\,R_t$ ($R^2 = 0.972$), $k = 1.1\,R_t$ ($R^2 = 0.972$) and $k = R_t$ ($R^2 = 0.973$), respectively.

Taken the deployment time into account, a further equation for determining the natural constant has been derived, where M is the deployment time period in month. It was found that, 90% of the observed variation (i.e. $R^2 = 0.90$) can be explained by this equation, at 1.5 months $\leq$ M $\leq$ 6 months.

$$A = -0.04M + 1.25$$

According to **Figure 7.7**, no observation of k^+ values can be addressed for the onset of the transitionally rough regime, whereas the fully rough regime overall started at the roughness Reynolds number of about $k^+ = 20$. Furthermore, the results of the roughness function along with the associated k^+ values are presented in **Table 7.12**. It can be noticed that, when comparing the tested surfaces within the same fouled stage, the transitionally rough regime was within $1.5 < k^+ < 20$ for the present results.

Table 7.12: Roughness function ΔU^+ and associated k^+ from all fouled panels

1.5 Months								**3 Months**							
C12		**C17**		**C25**		**C60**		**C12**		**C17**		**C25**		**C60**	
k^+	ΔU^+	k^+	ΔU^+	k^+	ΔU^+	k^+	ΔU^+	k^+	ΔU^+	k^+	ΔU^+	k^+	ΔU^+	k^+	ΔU^+
6.0	2.4	4.8	2.1	4.9	2.3	12.4	3.2	6.4	2.6	5.7	2.6	6.1	2.6	10.7	3.2
10.0	2.9	8.0	2.7	8.1	2.8	21.2	4.3	10.7	3.2	9.4	3.1	10.1	3.1	18.2	4.0
13.7	3.2	11.0	2.9	11.2	3.0	30.2	5.3	14.7	3.5	12.9	3.3	13.9	3.4	25.6	4.6
17.2	3.8	13.9	3.6	14.2	3.7	38.3	5.8	18.7	4.3	16.4	4.1	17.6	4.2	32.5	5.2
20.9	4.3	16.8	4.0	17.2	4.2	47.2	6.6	22.7	4.8	19.9	4.6	21.4	4.6	40.2	6.0
24.6	4.7	19.8	4.4	20.3	4.6	56.4	7.2	26.7	5.1	23.4	4.9	25.2	5.0	48.1	6.7
27.4	5.0	22.0	4.6	22.5	4.8	63.2	7.6	29.7	5.4	26.0	5.2	28.1	5.3	54.0	7.1
4.5 Months								**6 Months**							
C12		**C17**		**C25**		**C60**		**C12**		**C17**		**C25**		**C60**	
k^+	ΔU^+	k^+	ΔU^+	k^+	ΔU^+	k^+	ΔU^+	k^+	ΔU^+	k^+	ΔU^+	k^+	ΔU^+	k^+	ΔU^+
5.7	2.7	6.2	2.7	6.6	2.6	12.7	3.2	6.4	2.8	5.7	2.7	6.7	2.8	11.5	3.1
9.4	3.2	10.3	3.1	11.0	3.2	21.6	4.1	10.6	3.3	9.6	3.2	11.2	3.3	19.6	4.1
12.9	3.6	14.2	3.4	15.2	3.5	30.7	5.0	14.7	3.7	13.2	3.5	15.4	3.5	27.8	4.9
16.4	4.3	18.0	4.2	19.2	4.2	38.9	5.6	18.6	4.4	16.7	4.3	19.7	4.3	35.2	5.4
20.0	4.8	21.9	4.7	23.3	4.7	48.1	6.4	22.6	4.9	20.3	4.8	23.9	4.8	43.6	6.3
23.5	5.2	25.9	5.1	27.5	5.1	57.5	7.0	26.6	5.3	23.9	5.2	28.2	5.2	52.0	6.9
26.1	5.5	28.7	5.4	30.6	5.4	64.3	7.4	29.6	5.6	26.6	5.5	31.3	5.5	58.2	7.2

In the transitionally rough regime, during each biofilm stage, the lowest ΔU^+ values were obtained for C17 among all of the tested surfaces, and this was followed by C12 and C25, whereas C60 resulted in the highest values. Moreover, the transitionally rough regime of each test specimen was shifted backwards, so that they were concentrated at the side of higher Reynolds number, due to the surface roughness effect of the biofilm from the beginning to the

end of the tests. Moreover, the ΔU^+ values scattered in the fully rough regime show good agreement with the full flow asymptotic lines of Colebrook's behaviours at $k^+ > 20$.

7.5 Chapter Summary

The pressure drop tests of the biofilm fouled surfaces which were coated with different sized cuprous oxide particles along with the acrylic smooth reference panel were conducted by using the turbulent flow channel. Prior to six months of immersion in the sea, different surface roughness profiles were formed using Cu_2O sizes of 12μm (C12), 17μm (C17), 25μm (C25) and 60μm (C60). The investigations consisted of four stages of tests that were carried out after every 1.5 months of the fouling growth deployment.

The main objectives of these measurements were to have a systematic study about the effects of the various sizes of cuprous oxide particles on the frictional drag characteristics.

During the beginning stage of the experiment (i.e. surfaces fouled with 1.5-month biofilm), the frictional drag values of the tested surfaces were found to have dramatically increased due to the biofilm. When compared to the smooth reference surfaces, the drag of surfaces coated with C12 and C17 had increased by 45% and 41%, and these were about 25% and 18% higher compared to the results of their original clean states. For the C25 and C60 surfaces, the 1.5-month biofilm resulted in 43% and 83% drag increments with respect to the acrylic surface results and 9% and 16%, respectively, compared to the clean condition. The frictional drag is obviously increased by the biofilm once it starts to attach and develop on an immersed surface. The more dramatic frictional drag changes can be measured from smoother and lower roughness profile surfaces.

With the biofilm developing on the tested surfaces, the experimental results showed that the frictional drag increments of all tested surfaces gradually slowed down. Even though the overall frictional drag of C12, C17 and C25 had increased from about 40%−45% after 1.5-month, it had only increased to 50%−51% by the end of 6 months. The drag increment rate changed from 5%−7% to 1%−2% every 1.5-month. Combining this with the results of the surface analyses, once the biofilm had fully developed, there were no further changes to the roughness, and the frictional resistance settled to a steady value. However, for surfaces covered with the larger size Cu_2O particles, especially C60, the biofilm effect on the relatively rougher surfaces was found to be delayed due to the initially rougher microstructure. Rough surfaces were found to provide zones of low shear stress that minimised biofilm removal (Alnnasouri *et al*., 2011),

and with more contact areas for microorganisms to attach (Geesey *et al*., 1996). Therefore, it took a long time for the biofilm to fully develop on the rougher surfaces. Meanwhile, the surface microstructure kept changing all the time, and this resulted in roughness and frictional drag values that fluctuated.

Based on the roughness function results, the peak-to-trough roughness height was used as the roughness length scale. The regression value indicated that there was a good agreement between all of the roughness function results with the Colebrook type roughness function. All the roughness function results lay in the transitionally and fully rough regimes, and the fully rough regime can be found to start at the roughness Reynolds number, $k^+ \approx 20$ to 30. Moreover, due to the surface roughness being affected by the biofilm, the transitional rough regime of each fouled surface was found to be shifted into the fully rough regime.

It would always be helpful for the shipowner, or paint developer can easily access to the ship resistance and powering evaluations when a ship coated with an antifouling product or presents a fouling condition. For this case, the next chapter has presented and discussed the additional resistance prediction results for the full-scale ship by using Granville's similarity law scaling procedure based on the laboratory hydrodynamic assessment results. This demonstrates the ultimate effect of different sizes of Cu_2O particles on full-scale ship performance, including with the biofilm effect.

Chapter 8 Frictional Drag Prediction of Full Ship Length Scaled Flat Plates

8.1 Introduction

This chapter aims to predict the frictional drag of full-scale ship hull, which is assumed to be a flat plate with the same wetted length and wetted surface area of the vessel, as assumed in the classical Froude approach to approximate the frictional drag of ship hull. This approach can be combined with Granville's procedure for more accurate prediction of the flat plate frictional drag in the presence of physical surface roughness including biofouling (Granville, 1958; Granville, 1987). The procedure was established based on experimentally derived roughness functions and the boundary layer wall-similarity method.

In this chapter, the frictional drag predictions were conducted for flat plates with six different sizes to represent commercial ship types. They were assumed to be newly coated with Cu_2O coatings, and also included up to six-months in-service conditions. These selected six commercial ship categories are to cover the lengths of almost all ship types, ranging from the yacht to Ultra Large Crude Carrier (ULCC).

Within the above framework, the selection of the data used for the drag predictions and its limitations are discussed in **Section 8.2**. After the experimental data selection, the frictional drag predictions of the newly finished ship surface conditions are presented in **Section 7.3**. In this section, the overall frictional drag coefficient, C_F, of different ship types coated with different sized Cu_2O are compared within a range of commercial service speeds. The additional frictional drag, ΔC_F, has also been compared and discussed. For the ship in-service condition fouled with different stages of biofilm, the frictional drag and its increments for each tested surface are discussed and presented in detail in **Section 8.4** and **Section 8.5** respectively. Finally, the chapter is summarized in **Section 8.6**.

8.2 Data Selection

The experimental work presented previously produced a large number of roughness function results that could be processed to give the frictional drag prediction for the full ship length scaled flat plates. It is not feasible to present every single case in this chapter. Therefore selected cases were chosen to represent the general experimental conditions. The test cases were selected by considering the following aspects:

a. Compared to the boundary layer measurements, which express the skin frictional

coefficients at the local measuring position, the results of pressure drop tests present the frictional drag penalties of the overall coated surface conditions. In considering the frictional drag evaluation of a ship surface, therefore, it would be more appropriate to use the results from pressure drop tests rather than boundary layer measurements.

b. The pressure drop tests and boundary layer measurements were carried out by using the same size UNEW testing panels. However, compared to the boundary layer measurements, a larger range of the velocities have been covered by the pressure drop tests. This indicates that a range of $5-30$knots of predicted ship velocities can be covered by using pressure drop test data, rather than $4-18$ knots based on boundary layer test data. Accordingly, the frictional drag prediction for high-speed vessels can be achieved by using pressure drop results.
c. As discussed in **Chapter 4**, the testing surfaces were prepared with two sets of spray applications: the 1st and 2nd. It should be noted that only the 2nd set of finished surfaces were involved in the biofilm development work and tests.

Given the above, the frictional drag prediction work was conducted and completed based on the pressure drop test results using the 2nd set finished surfaces.

8.3 Frictional Drag of Newly Coated Ship Surfaces

The procedure of the Granville similarity law (Granville, 1958; Granville, 1987) and Froude's flat plate approach for frictional drag prediction of a full-size ship was introduced in **Section 3.6**. For each tested condition, the frictional drag predictions were carried out for 50 different lengths of full-scale flat plates which ranged from 10m to 415m. It is impractical to report all the examples here, therefore, six full-scale flat plate lengths were selected according to their equivalent length to the actual ship wetted length, and used to represent several typical commercial ship types. A yacht of 30m, a Handysize vessel of 100m, a Handymax vessel of 170m, a Panamax vessel of 290m, a VLCC of 350m and a ULCC of 415m, were used for the frictional coefficient calculations. Moreover, for the clean (unfouled) and biofilm fouled surface condition, the additional frictional drag ΔC_F of all full ship length scaled flat plates coated with test Cu_2O specimens can be found in **Appendix F** and **Appendix G**, respectively.

8.3.1 Predicted Frictional Drag of Ship Surfaces Coated with Different Cu_2O Particles

The frictional drag diagrams of all tested specimens have been integrated into **Figure 8.1**, which was generated according to the C_F prediction results.

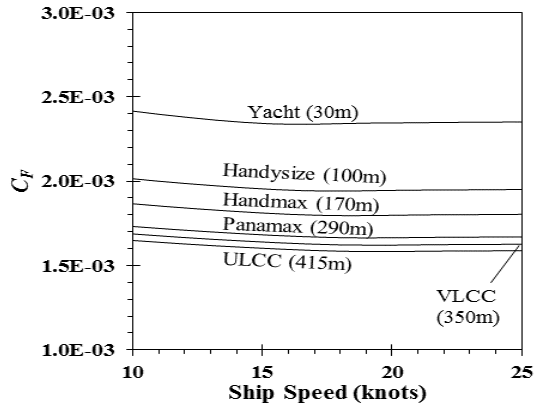

(**a**). For surface coated with C2

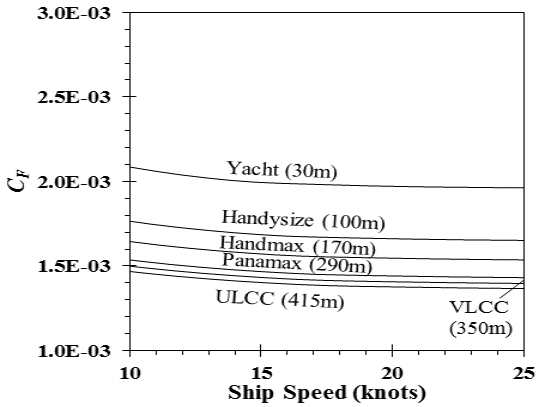

(**b**). For surface coated with C7

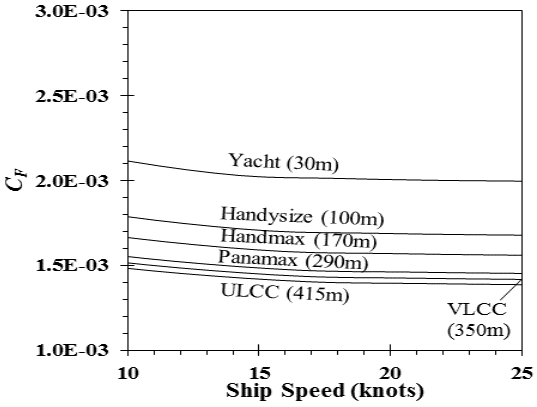

(**c**). For surface coated with C12

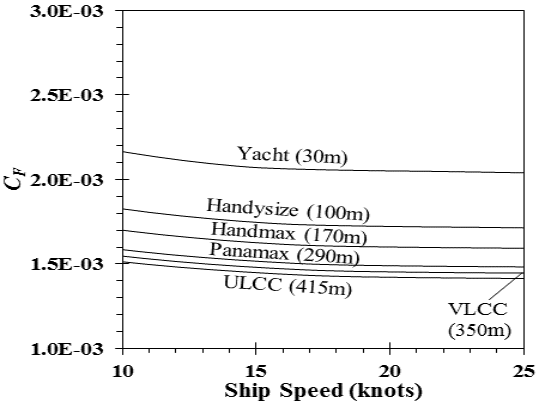

(**d**). For surface coated with C17

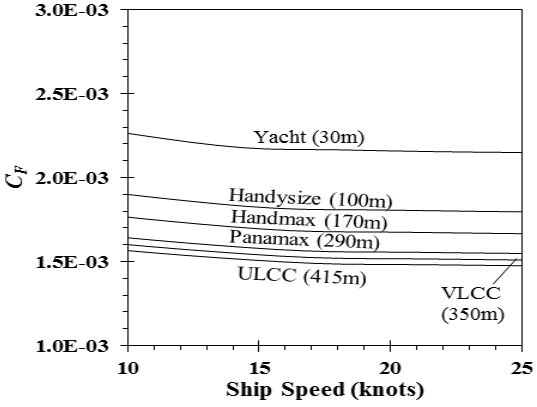

(**e**). For surface coated with C25

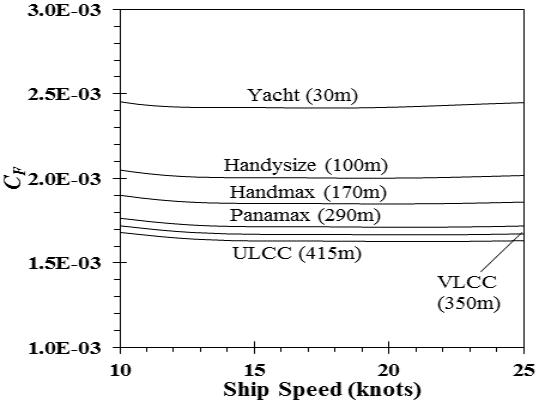

(**f**). For surface coated with C60

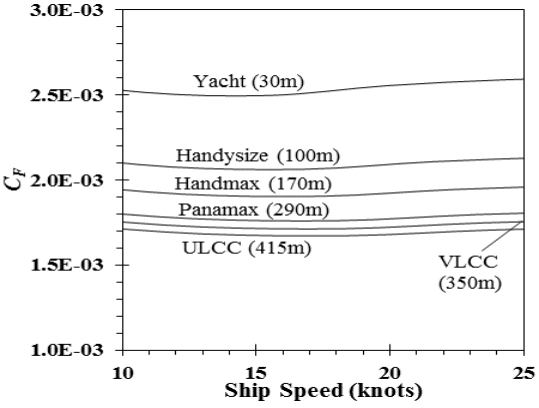

(**g**). For surface coated with C100

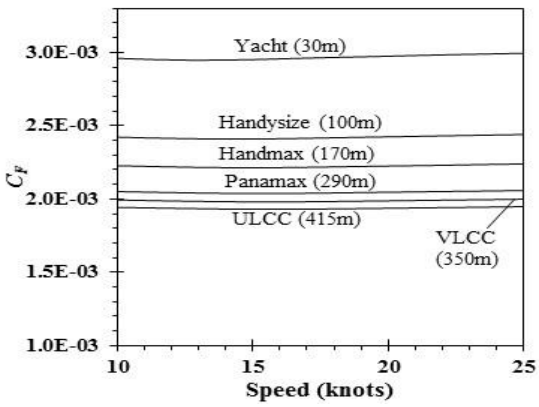

(**h**). For surface coated with C250

Figure 8.1 (a)−(h): Frictional coefficients, C_F, for full ship length scaled flat plates newly coated with tested Cu_2O specimens

Furthermore, in order to present the resistance penalties of each full-scale ship length in the newly coated condition, the additional drag increments, ΔC_F, with respect to the hydraulically smooth hull condition have been calculated based on the C_F diagrams. It also should be noted that the predictions were made over a limited range of ship speeds, given that the concern was with the practical commercial ship service speed limits.

Table 8.1 presents the predicted C_F values of full-scale flat plates according to each type of ship, with surfaces coated with the tested Cu_2O specimens at a service speed of 19knots. Have to say that the realistic average design ship speed varies with the ship type. Globally, as stated by Ross (2005), the new ships being launched in the shipyards certainly not many except for tankers are as slow as 19knots. Therefore, the assumed average design ship speed used for the results presentation in this chapter has been taken at 19 knots. **Figure 8.1 and Table 8.1** both indicate that for surfaces coated with the same Cu_2O specimen, the overall frictional coefficients decrease as the flat plate (ship) length increases. Overall, to achieve lowest frictional drag, the preferred option would be for the surface to be coated with the specimen C7, C12 or C17 rather than being coated with the other specimens.

Table 8.1: C_F for clean ship surfaces coated with tested Cu_2O at 19 knots

Surfaces		**Ship Types and Their Equivalent Full-scale Flat Plate Lengths**					
		Yacht	**Handysize**	**Handymax**	**Panamax**	**VLCC**	**ULCC**
		30m	100m	170m	290m	350m	415m
$C_F \times 10^3$	**C2**	2.34	1.94	1.80	1.67	1.62	1.58
	C7	2.01	1.69	1.57	1.46	1.42	1.39
	C12	2.03	1.70	1.58	1.47	1.44	1.40
	C17	2.08	1.74	1.62	1.50	1.47	1.43
	C25	2.18	1.82	1.68	1.56	1.52	1.49
	C60	2.42	2.00	1.85	1.71	1.67	1.63
	C100	2.50	2.06	1.90	1.76	1.71	1.67
	C250	2.96	2.42	2.23	2.05	1.99	1.94

8.3.2 Added Frictional Drag of Ship Surface Coated with Different Cu_2O

Figure 8.2 presents the diagrams of the additional drag increments, ΔC_F, with respect to the hydraulically smooth hull condition. According to the diagrams the additional drag increments increase with the ship speed, whilst, especially at higher speeds, there are more obvious drag increments for the smaller ships. For example, the yacht (30m) when compared with those for the larger ships, such as the Panamax (290m), VLCC (350m) and ULCC (415m).

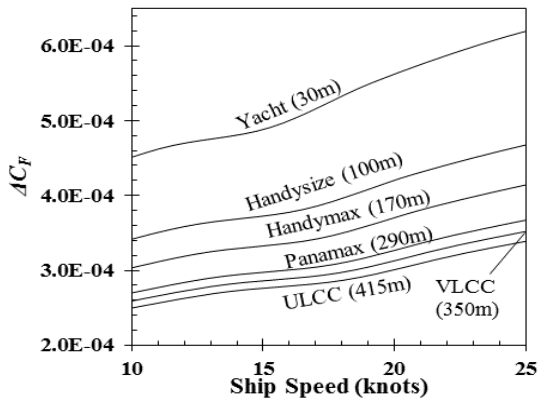

(**a**). For surface coated with C2

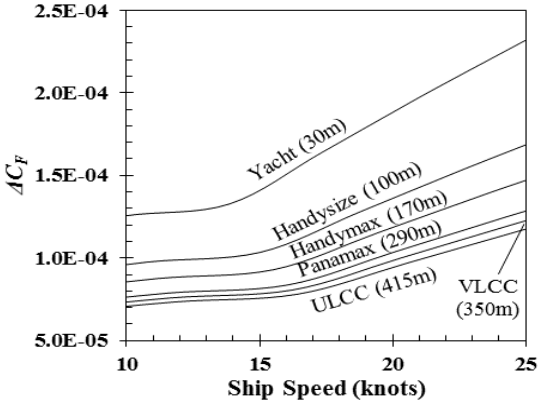

(**b**). For surface coated with C7

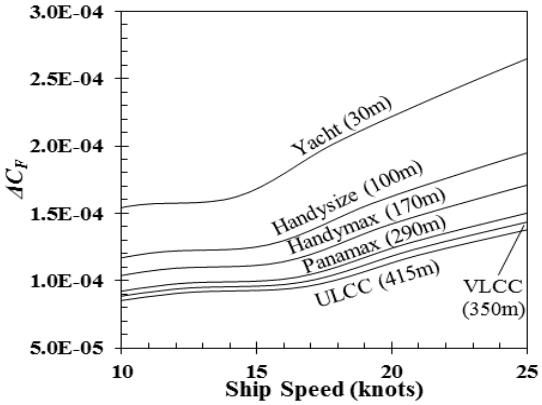

(**c**). For surface coated with C12

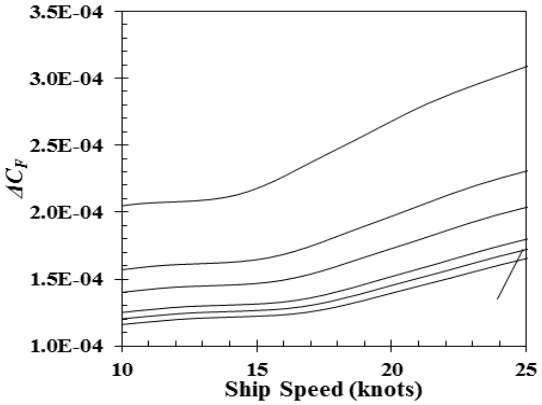

(**d**). For surface coated with C17

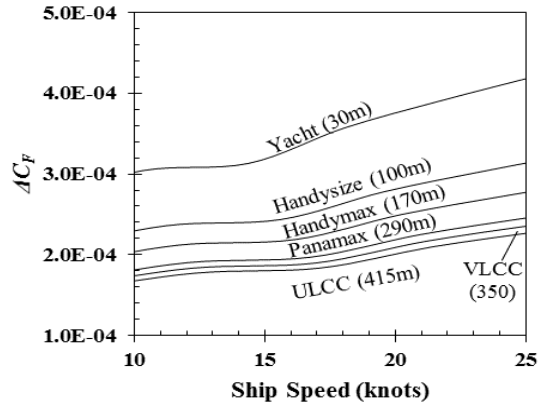

(**e**). For surface coated with C25

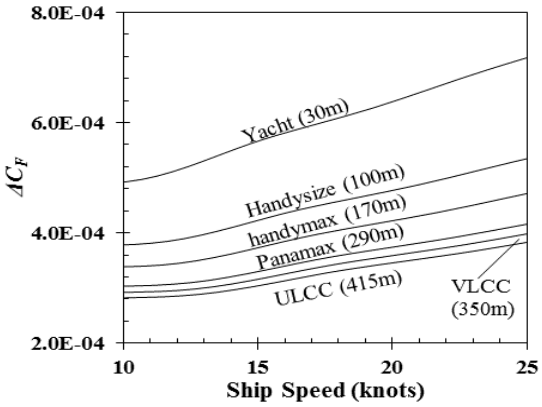

(**f**). For surface coated with C60

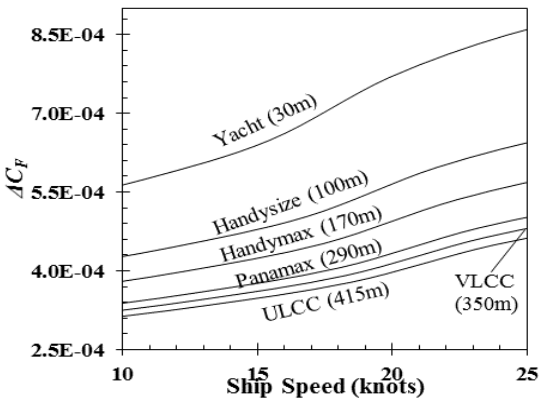

(**g**). For surface coated with C100

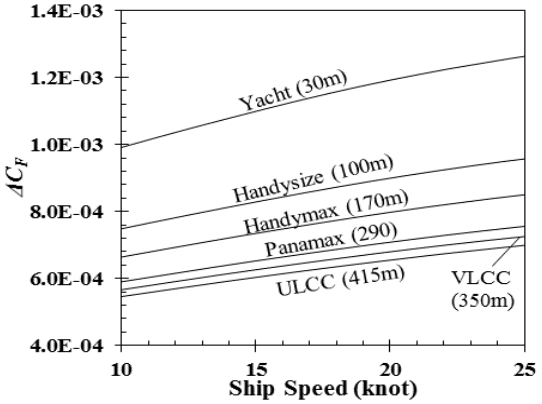

(**h**). For surface coated with C250

Figure 8.2 (**a**)−(**h**)**:** Additional drag increments, ΔC_F, for full ship length scaled flat plates coated with Cu_2O specimens

Based on the C_F results, with respect to the hydraulically smooth hull condition, **Table 8.2** presents the predicted the additional drag increments, ΔC_F(%), of each full-scale ship length with surfaces coated with all of tested Cu_2O specimens at a service speed of 19 nots.

Table 8.2: ΔC_F (%) for clean ship surfaces coated with tested Cu_2O at 19 knots

Surfaces		Ship Types and Their Equivalent Full-scale Flat Plate Lengths					
		Yacht	**Handysize**	**Handymax**	**Panamax**	**VLCC**	**ULCC**
		30m	100m	170m	290m	350m	415m
ΔC_F(%)	**C2**	30.7%	24.4%	23.5%	22.7%	22.4%	22.1%
	C7	9.0%	6.5%	6.3%	6.1%	6.0%	5.9%
	C12	11.1%	8.0%	7.7%	7.5%	7.4%	7.3%
	C17	13.5%	10.5%	10.2%	9.8%	9.7%	9.6%
	C25	19.7%	15.5%	14.9%	14.4%	14.2%	14.0%
	C60	35.0%	28.3%	27.3%	26.3%	26.0%	25.7%
	C100	43.0%	32.3%	31.1%	30.0%	29.6%	29.2%
	C250	69.8%	58.1%	55.9%	53.7%	53.0%	52.3%

According to the ΔC_F(%) results in **Table 8.2**, the specimens C100 and C250 had the highest ΔC_F(%) increments which approximately ranged from 30% to 70%. This was followed by the overall average frictional drag increments for the surfaces coated with C2 and C60 which increased from 22% to 35% for all the predicted ship types.

It is evident from the results that the use of specimens C7, C12 and C17 can effectively lower the frictional drag increments for the full-scale ship. They resulted in 6% to 13.5% frictional drag increments for all ship types. Therefore, in achieving relatively smooth surfaces with lower consequential frictional drag increases, both state-of-the-art commercial products, i.e. C12 and C17, have shown significant advantages.

8.4 C_F Diagrams of Ship Surfaces Fouled with Biofilm

In this section, the same six-ship lengths were used to estimate the frictional drag penalties under in-service conditions: a yacht of 30m, a Handysize vessel of 100m, a Handymax vessel of 170m, a Panamax vessel of 290m, a VLCC of 350m and ULCC of 415m. In order to have a cross-comparison of frictional drag changes at every stage of the fouling condition, the C_F diagrams of the clean (no biofilm) condition have been integrated into the results.

8.4.1 Surfaces Coated with C12 Fouled with Biofilm

Based on the results from each of the surface fouled conditions, the frictional drag diagrams of

specimen C12 are presented in **Figure 8.3** (**a**)−(**e**). Comparison of **Figure 8.3** (**a**) and (**b**) indicates that, for surfaces coated with C12, the initial stage of the biofilm can have a more obvious impact on increased C_F for all types of vessel. As time progressed, according to **Figure 8.3** (**c**)−(**e**), the increments of C_F from C12 surfaces became imperceptible after the biofilm had fully developed at 3 months.

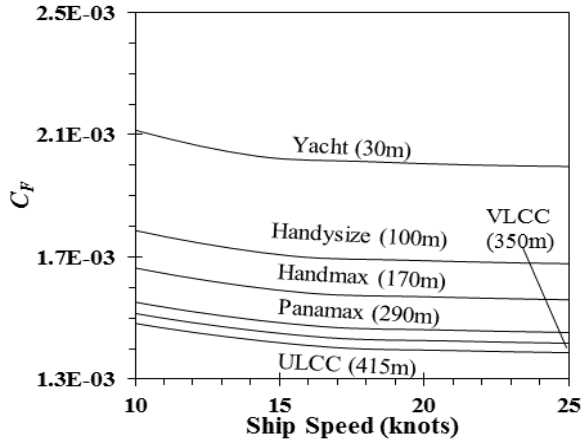

(**a**). Clean (unfouled)

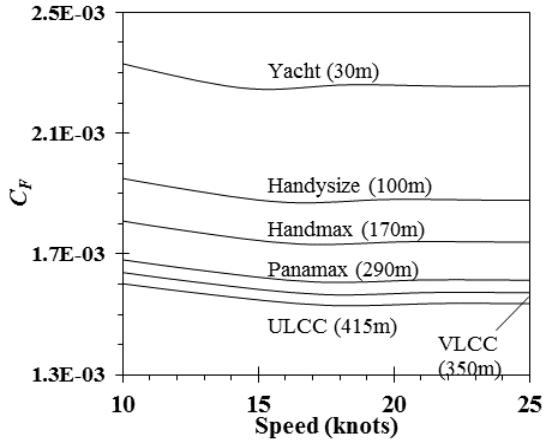

(**b**). Fouled for 1.5-month

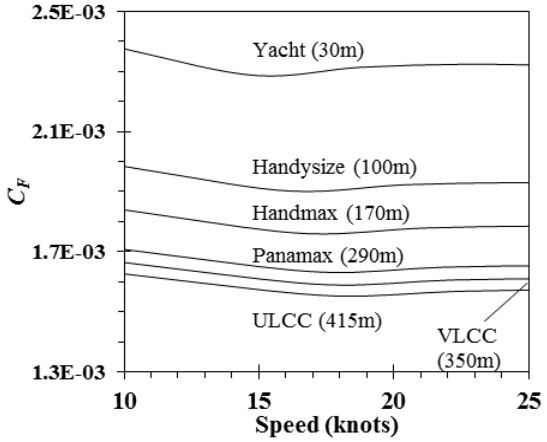

(**c**). Fouled for 3-month

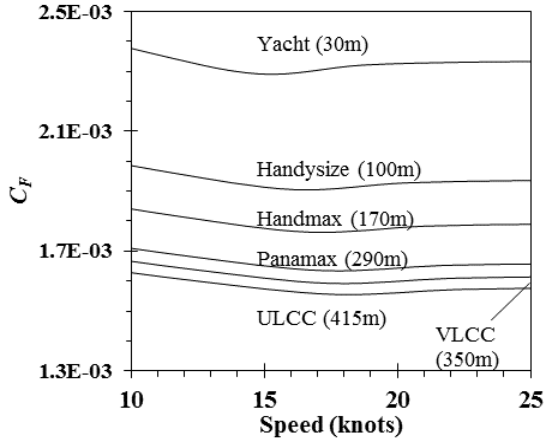

(**d**). Fouled for 4.5-month

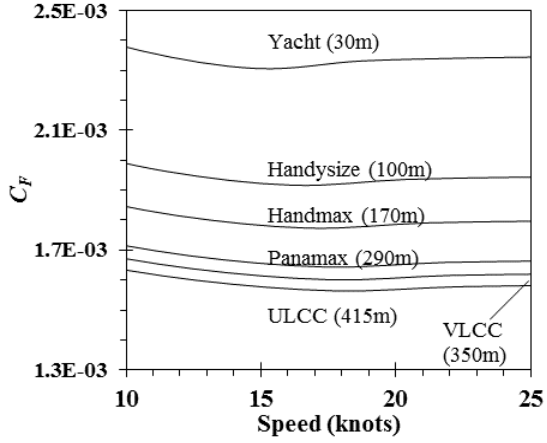

(**e**). Fouled for 6-month

Figure 8.3 (**a**)−(**e**)**:** Biofilm impacts on C_F of full-scale flat plates coated with C12

8.4.2 Surfaces Coated with C17 Fouled with Biofilm

The frictional drag diagrams of specimen C17 fouled over different periods with biofilm are shown in **Figure 8.4** (**a**)−(**e**).

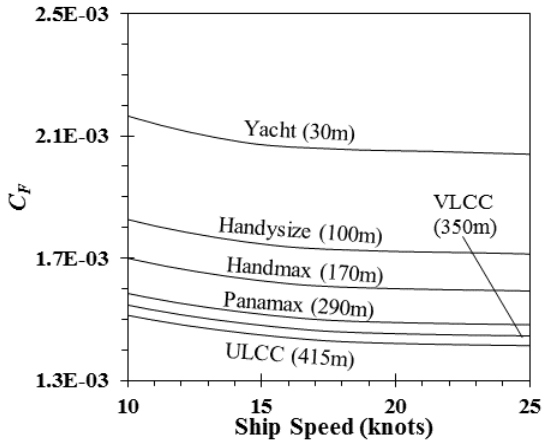

(**a**). Clean (unfouled)

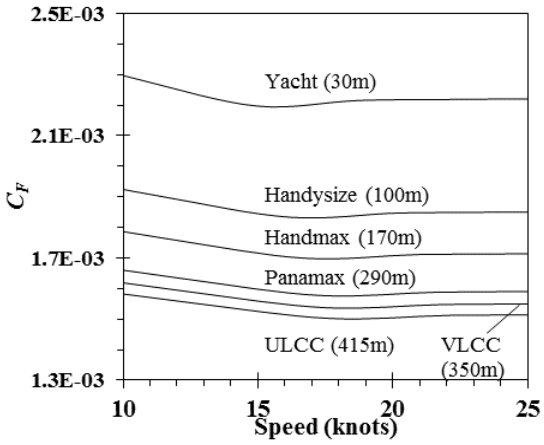

(**b**). Fouled for 1.5-month

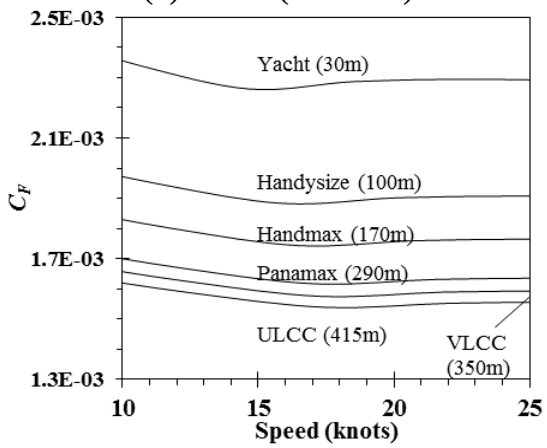

(**c**). Fouled for 3-month

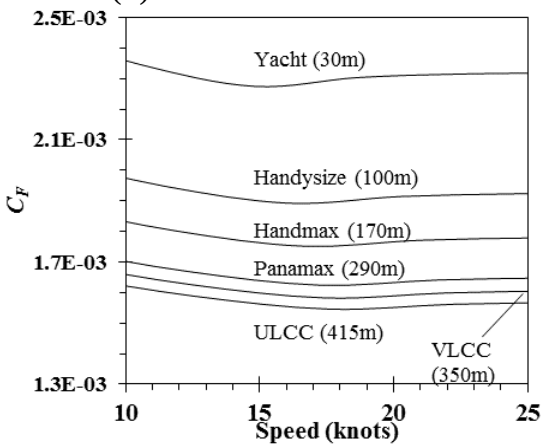

(**d**). Fouled for 4.5-month

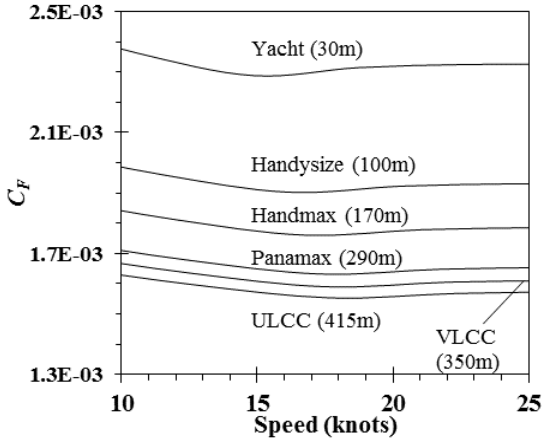

(**e**). Fouled for 6-month

Figure 8.4 (**a**)−(**e**)**:** Biofilm impacts on C_F of full-scale flat plates coated with C17

The difference between **Figure 8.4** (**a**) and (**b**) shows that, for surfaces coated with C17, the initial stage of the biofilm resulted in significant increments of C_F for all types of vessel. For ship hulls coated with C17, after more than 3 months immersion, **Figure 8.4** (c)−(**e**)

indicate the C_F increment rate became significantly lower as the biofilm had fully developed on the top surfaces.

8.4.3 Surfaces Coated with C25 Fouled with Biofilm

Figure 8.5 (**a**)−(**e**) show the frictional drag diagrams of specimen C25 fouled with different periods of biofilm.

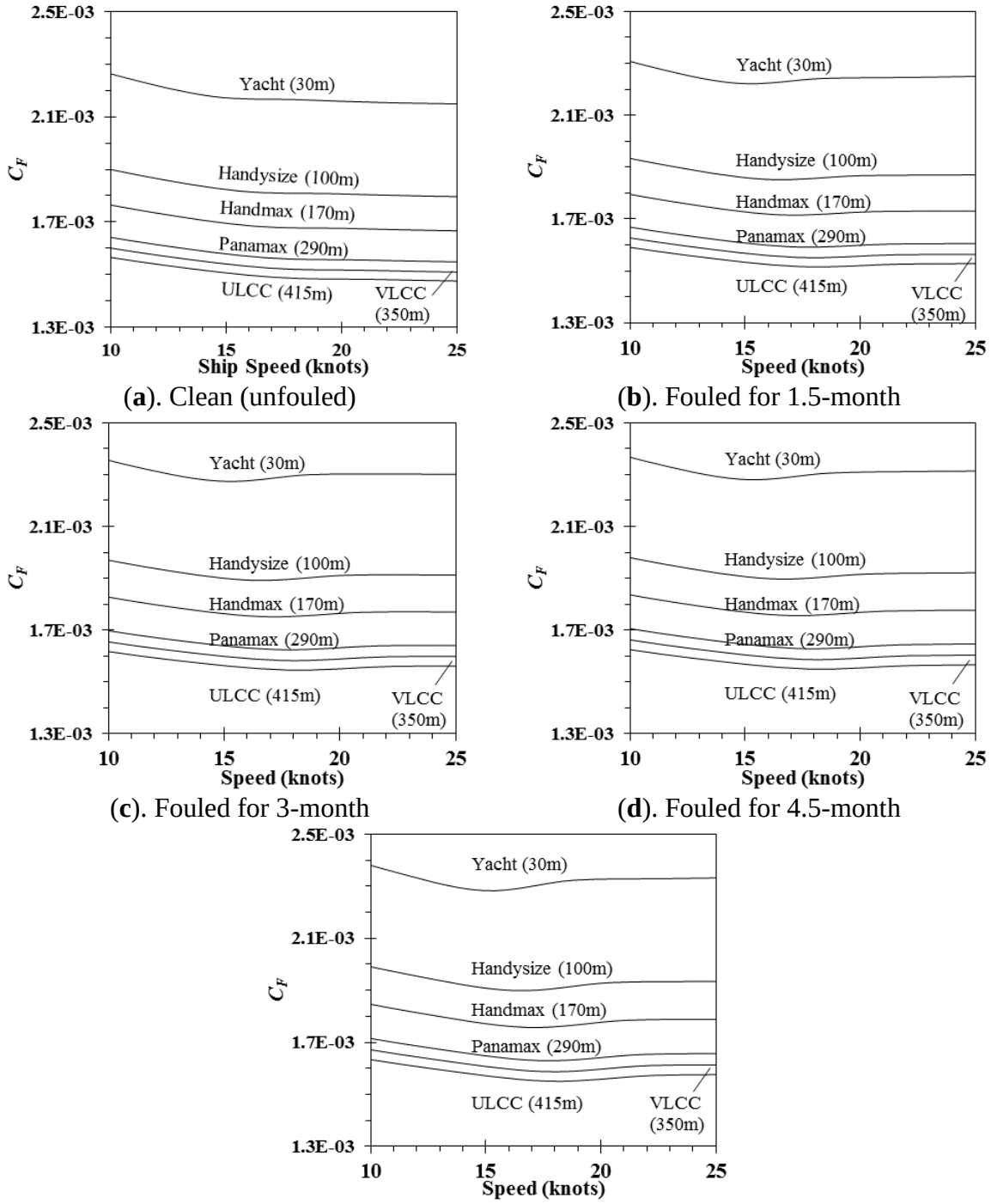

(**a**). Clean (unfouled)

(**b**). Fouled for 1.5-month

(**c**). Fouled for 3-month

(**d**). Fouled for 4.5-month

(**e**). Fouled for 6-month

Figure 8.5 (**a**)−(**e**)**:** Biofilm impacts on C_F of full-scale flat plates coated with C25

Comparing **Figure 8.5** (**a**)−(**c**), unlike the cases of C12 and C17, the initial stage of the biofilm did not show significant impacts on C_F for ships coated with C25. It took about 3 months for the biofilm to be fully developed on top of the C25 surfaces.

8.4.4 Surfaces Coated with C60 Fouled with Biofilm

Figure 8.6 (**a**)−(**e**) present the frictional drag diagrams of specimen C60 fouled with different periods of biofilm.

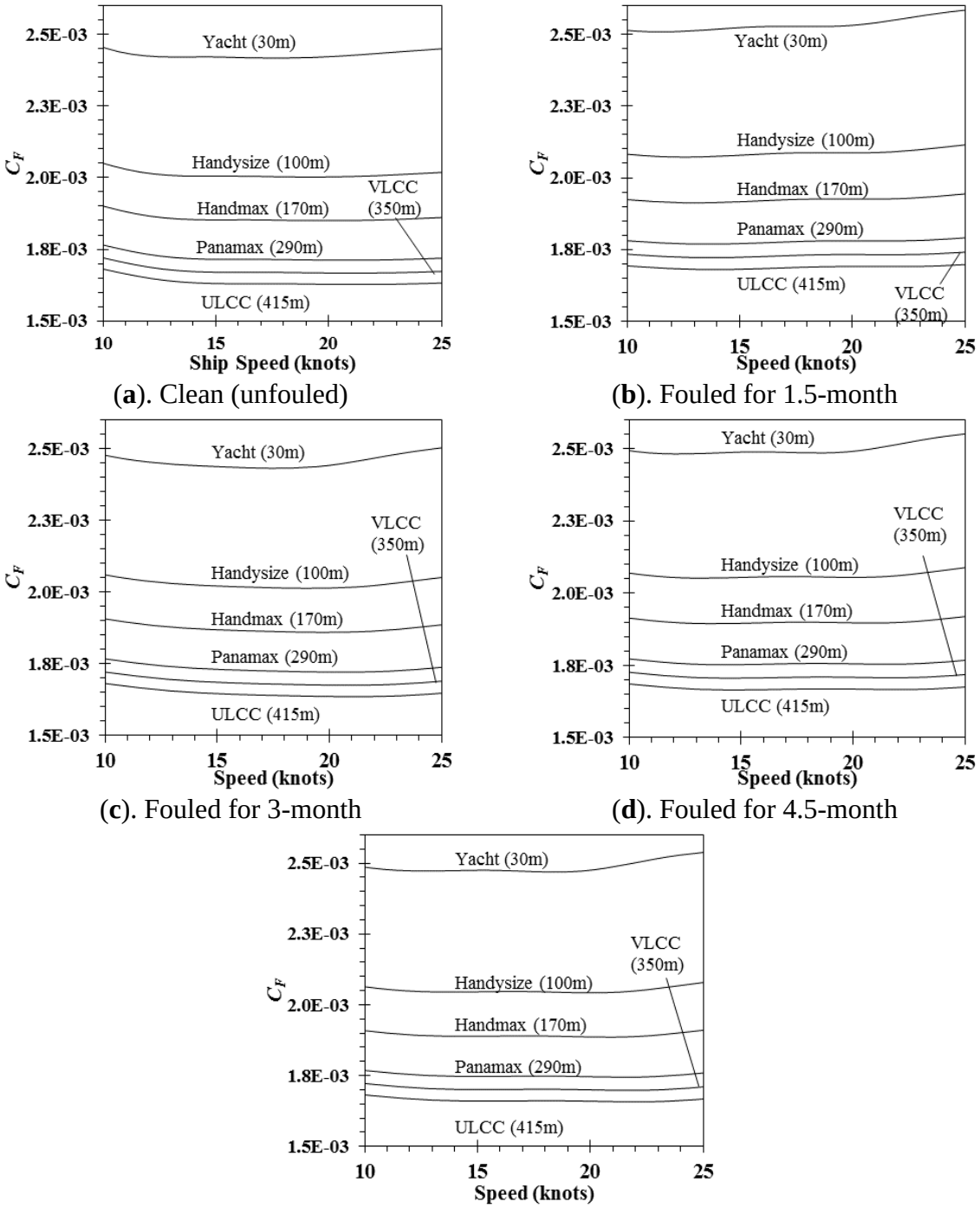

(**a**). Clean (unfouled)

(**b**). Fouled for 1.5-month

(**c**). Fouled for 3-month

(**d**). Fouled for 4.5-month

(**e**). Fouled for 6-month

Figure 8.6 (**a**)−(**e**)**:** Biofilm impacts on C_F of full-scale flat plates coated with C60

The initial stage of the biofilm can be seen to have had a much less significant impact on C_F increases for ships coated with specimen C60. Moreover, because of the interaction between the biofilm and the surface roughness, a fluctuating frictional coefficient increase can be identified. However, compared to the overall full-scale frictional coefficient, especially for large ship lengths, these fluctuating increments may be negligible.

The detailed C_F values at a service speed of 19 knots for all of the predicted ship lengths have been tabulated into **Table 8.3**.

Table 8.3: C_F ($\times 10^3$) for surfaces coated with all tested Cu_2O specimens fouled with different periods of biofilm at service speed of 19knots

Surfaces		Ship Types and Their Equivalent Full-scale Flat Plate Lengths					
		Yacht	**Handysize**	**Handymax**	**Panamax**	**VLCC**	**ULCC**
		30m	100m	170m	290m	350m	415m
C12	**Unfouled**	2.03	1.70	1.58	1.47	1.44	1.40
	1.5M	2.25	1.87	1.73	1.61	1.57	1.53
	3M	2.29	1.90	1.76	1.63	1.59	1.55
	4.5M	2.29	1.91	1.76	1.63	1.59	1.56
	6M	2.31	1.92	1.77	1.64	1.60	1.56
C17	**Unfouled**	2.08	1.74	1.62	1.50	1.47	1.43
	1.5M	2.20	1.83	1.70	1.58	1.54	1.50
	3M	2.26	1.88	1.74	1.62	1.58	1.54
	4.5M	2.27	1.89	1.75	1.62	1.58	1.55
	6M	2.29	1.90	1.76	1.63	1.59	1.55
C25	**Unfouled**	2.18	1.82	1.68	1.56	1.52	1.49
	1.5M	2.22	1.85	1.72	1.59	1.55	1.52
	3M	2.27	1.89	1.75	1.62	1.58	1.55
	4.5M	2.28	1.90	1.76	1.63	1.59	1.55
	6M	2.28	1.90	1.76	1.63	1.59	1.55
C60	**Unfouled**	2.42	2.00	1.85	1.71	1.67	1.63
	1.5M	2.53	2.09	1.93	1.78	1.73	1.69
	3M	2.44	2.02	1.86	1.72	1.68	1.64
	4.5M	2.49	2.06	1.90	1.76	1.71	1.67
	6M	2.47	2.05	1.89	1.75	1.70	1.66

For the conditions in which biofilm was present, the smallest vessel, i.e. yacht (30m), had the highest C_F values. As the ship lengths increased, the overall C_F values gradually decreased, and the values for the ultra-size ships had similar levels, i.e. the VLCC (350m) and ULCC (415m).

8.5 Additional Drag Increments ΔC_F(%) due to Biofilm

The additional drag increments, ΔC_F(%), of the in-service condition with respect to the hydraulically smooth condition of each surface, were calculated based on the six different ship types at a service speed of 19 knots. All results of for the surfaces coated with specimens C12, C17, C25 and C60 are plotted in **Figure 8.7** to **Figure 8.10**. For comparison, with respect to the same hydraulically smooth condition, the added frictional resistances of the clean surfaces were also calculated based on the roughness function and included in these figures.

For the surfaces coated with the tested Cu_2O specimens, the drag prediction indicated that the biofilm would increase frictional drag penalties on the surfaces coated with C12 and C17 (on average of 11.2% and 6.7%, respectively) more than on surfaces coated with C25 and C60 (on average of 2.7% and 5.8% respectively) after the first 1.5-month period. By the end of the tests, these average frictional drag increments of the surfaces coated with C12, C17 and C25 were 14.3%, 11.0% and 6.1%, respectively. However, after six months, only 2.9% of C_F had increased from C60**.** In other words, this value was 2.9% less than the average value of 1.5-month.

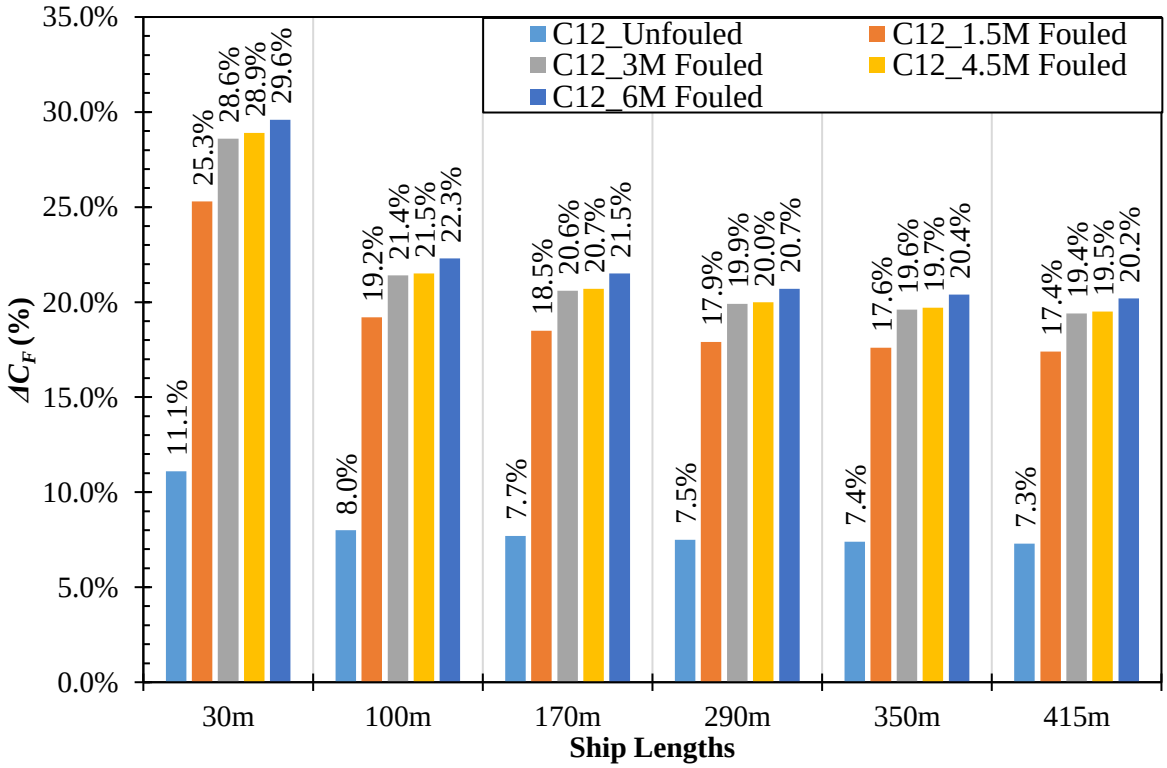

Figure 8.7: Aadditional drag increments, ΔC_F(%), for surfaces coated with C12 resulting from biofilm for various ship lengths at a service speed of 19 knots with respect to the hydraulically smooth hull condition

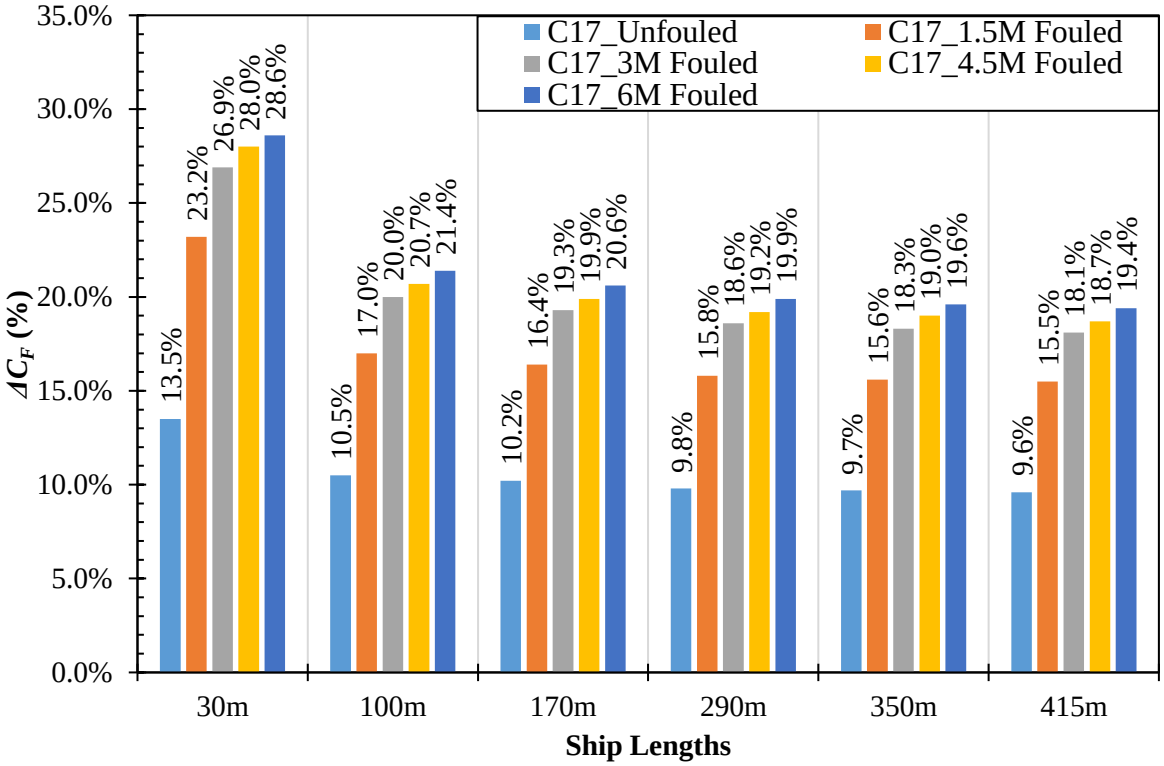

Figure 8.8: Additional drag increments, ΔC_F(%), for surfaces coated with C17 resulting from biofilm for various ship lengths at a service speed of 19 knots with respect to the hydraulically smooth hull condition

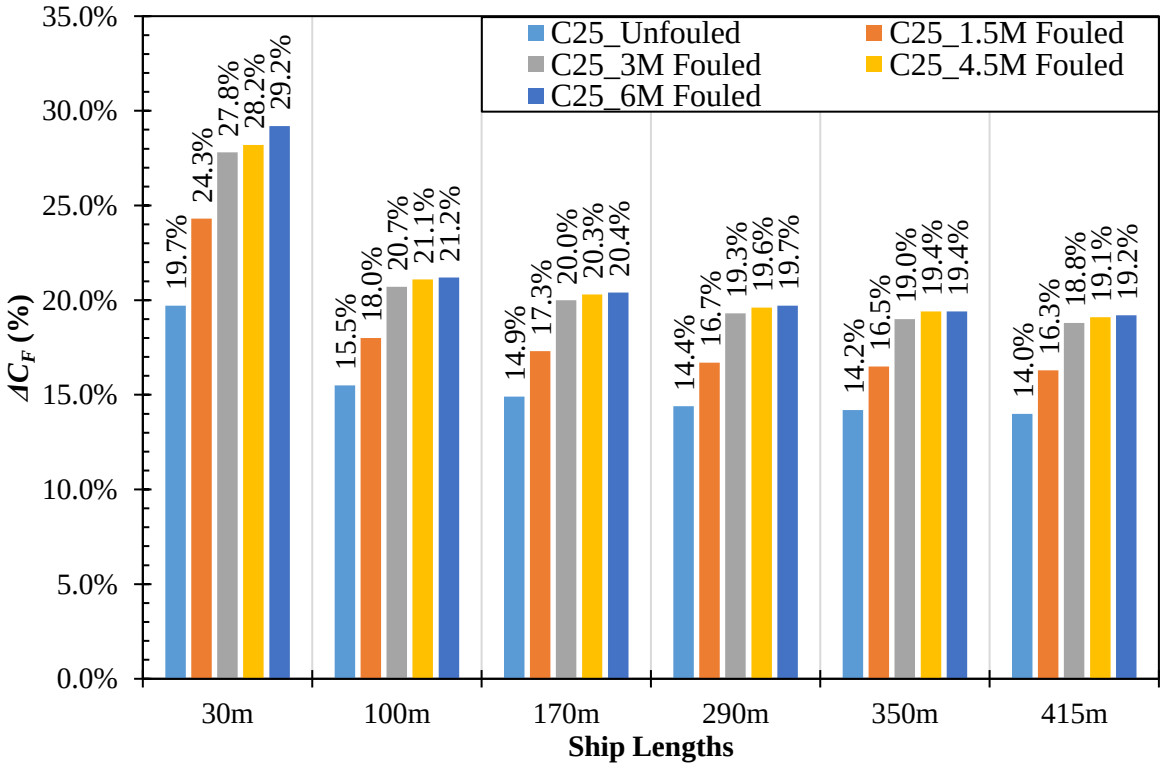

Figure 8.9: Additional drag increments, ΔC_F(%), for surfaces coated with C25 resulting from biofilm for various ship lengths at a service speed of 19 knots with respect to the hydraulic smooth hull condition

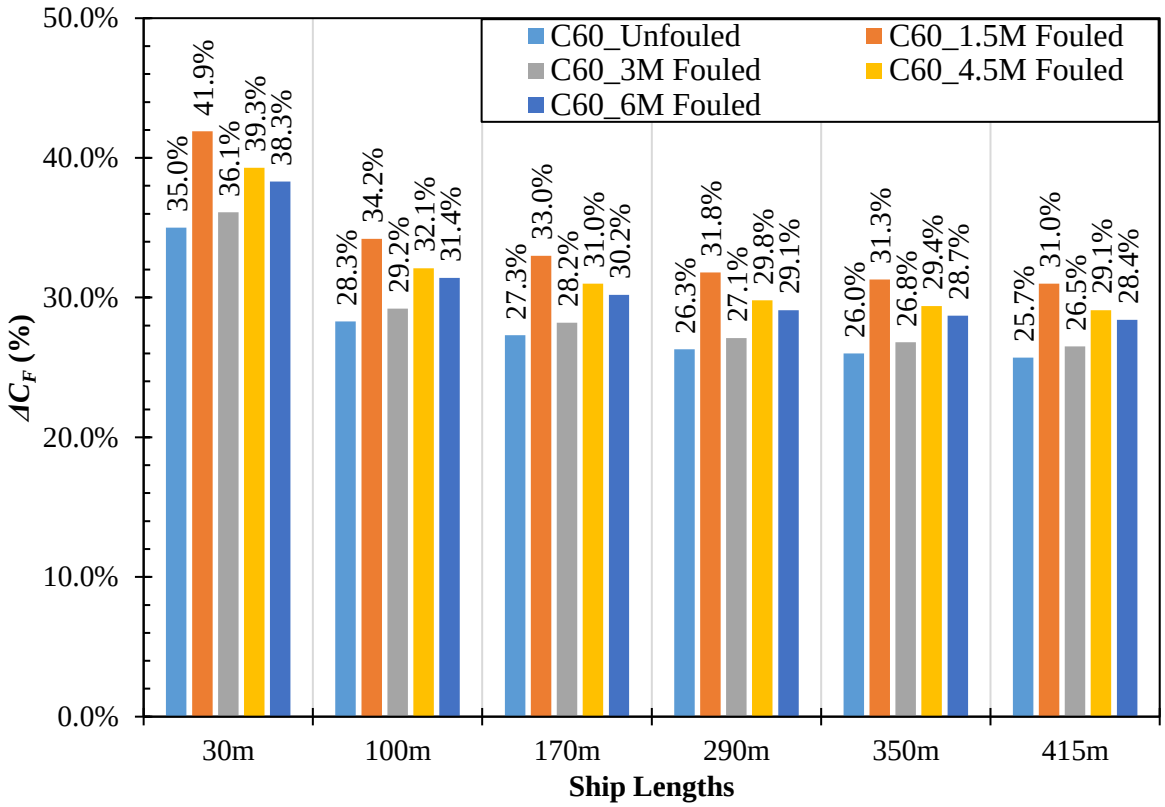

Figure 8.10: Additional drag increments, ΔC_F(%), for surfaces coated with C60 resulting from biofilm for various ship lengths at a service speed of 19 knots with respect to the hydraulically smooth hull condition

Even though the C60 coating shows the lowest frictional drag increments by the end of the tests, the frictional drag of C60 (6-months) was 8.6%−9.5% more than C12, C17 and C25, at the same stage. Meanwhile, C12, C17 and C25 had similar frictional drag after 6-months. Moreover, for each experimental case, the added frictional drag decreased as the prediction length increased.

It should also be noted that for the yacht (30m), the surface roughness can result in a dramatic frictional drag for a small ship length. As the surface length increased, this effect gradually decreased to a steady frictional drag level when surface length ≥ 170m (Handymax).

Therefore, from above, no linear added frictional drag increment can be observed from Cu_2O surface when fouled with biofilm. As the biofilm can immediately alter the surface condition, especially for the smoother surfaces (i.e. C12 and C17), at the beginning of the immersion and resulted in a higher added frictional drag increment. However, from C12, C17 and C25, with the biofilm fully developed, the drag increment rate had slowed down and finally presented similar values. Whereas, due to the interaction between rougher microstructure with biofilm, it presented more fluctuant added frictional drag increment from the C60.

The overall rate of increase of frictional drag related to the surface roughness due to biofilm can be estimated according to the above prediction results. Therefore, as shown in **Table 8.4**, the average increments in drag are expected to be 2.8−4.1% for C12, 2.6%−4.1% for C17, 1.3%−2.5% for C25 and 1.3%−1.6% for C60 per 10μm increment in R_t.

Table 8.4: The additional drag increments of fouled surface per 10μm increment in R_t

Surface	Yacht	Handysize	Handymax	Panamax	VLCC	ULCC
	30m	100m	170m	290m	350m	415m
C12	4.1%	3.1%	3.0%	2.9%	2.9%	2.8%
C17	4.1%	2.9%	2.8%	2.7%	2.7%	2.6%
C25	2.5%	1.5%	1.4%	1.4%	1.3%	1.3%
C60	1.6%	1.5%	1.4%	1.4%	1.3%	1.3%

8.6 Chapter Summary

This chapter has presented a practical method for predicting the frictional drag for full-scale ship hulls, by following the Froude's flat plate approach combined with the similarity law procedure that was proposed by Granville (1958) and Granville (1978). The drag predictions were established based on the roughness function results from pressure drop tests that were carried out with clean Cu_2O coated surfaces (**Chapter 7**), and Cu_2O surfaces fouled with 1.5 to 6 months biofilm (**Chapter 8**). The predictions were conducted for 50 different ship lengths which ranged from 10m to 415m. Six ship lengths of representative ship types: a yacht of 30m, a Handysize vessel of 100m, a Handymax vessel of 170m, a Panamax vessel of 290m, a VLCC of 350m and ULCC of 415m, were used for the presentation in this chapter. Graphs of additional frictional resistance coefficients with respect to the hydraulic smooth hull condition were generated based on the predicted frictional drag results.

The frictional drag increments from surfaces coated with varying sizes of Cu_2O particles (i.e. C2−C250) demonstrated the advantage of the use of specimens C7, C12 and C17 which resulted in 6% to 13.5% frictional drag increments for full-scale prediction cases. However, there were problems with the C7 specimen during the paint preparation process, and this can subsequently cause surface preparation difficulties and rougher surface profiles. The state-of-the-art commercial products, C12 and C17, gave more promising smoother surface conditions with significantly lower drag penalties according to the predictions.

Using the prediction procedure, the effects of a range of periods of biofilm development on the frictional drag of the Cu_2O surfaces (i.e. C12, C17, C25 and C60) have been evaluated. Based

on the roughness function of the biofilm fouled surfaces, the further added frictional drag predictions indicated that even though C60 had the smallest added frictional drag increase, the overall frictional drag level for this was still the highest at each experimental stage, compared to surfaces coated with other smaller Cu_2O particles. For surfaces coated with C12, C17 and C25 size particles, the results indicated similar frictional drag values.

Moreover, according to the additional frictional drag diagrams, the frictional drag of C12 and C17 were more likely to be increased due to the initial biofilm attachment. Therefore, to control the drag penalties, effective anti-biofilm pre-actions should be applied during the biofilm initial development process. This is especially needed for high-speed craft or high-speed container ships as their frictional drags are proportional to the square of the speed.

Regarding the advantages of generating the prediction diagrams, one of the key highlights is the detailed description of the time-dependent influence of biofilms on AF surfaces, especially different roughness profiles, engineered by using varying sizes of Cu_2O. Also, based on these time-dependent diagrams, the frictional drag changes on different size full-scale ships under similar surface conditions are more predictable. For the biofilm fouled surfaces, it was observed that significant fluctuation occurs in the values of roughness and frictional drag for surfaces coated with larger sizes of Cu_2O particles. Therefore, similar behaviours are expected for ship surfaces which have similar or rougher characteristics than C60. For low profile AF surfaces, the roughness and frictional drag after a certain period of biofilm development show much less fluctuation. The overall rate of the increments in drag is expected to be $2.8-4.1\%$ for C12, $2.6\%-4.1\%$ for C17, $1.3\%-2.5\%$ for C25 and $1.3\%-1.6\%$ for C60 per 10μm increment in R_t.

Chapter 9 Conclusions and Recommendations

9.1 Introduction

This chapter presents an overview of the research study presented in this thesis and its major findings within the framework of the aims and objectives of the study (**Section 9.2**). The main contributions made to the-state-of-the-art in the field are presented (**Section 9.3**) and recommendations for future work are given (**Section 9.4**).

9.2 Research Study Overview

Copper and its compounds have historically been widely used as antifouling agents to efficiently maintain marine surfaces in a fouling-free condition and control drag increments. Being one of the more common copper compounds, Cu_2O plays a key role in antifouling as it can provide effective fouling defence mechanisms for marine coatings. A large number of laboratory experiments and sea trials have demonstrated the advantage of using Cu_2O in antifouling functions for extending the dry-docking maintenance cycle and improving ship performance.

However, for any processed surface, understanding the impact of natural irregular particles on coating microstructure and surface roughness is essential. In particular, to minimise the frictional drag penalties on seagoing vessels, the selection of the optimal size of Cu_2O particles for the paint production has been identified in this study, as this is highly significant in terms of their contributions in the roughness and hydrodynamic drag characteristics. However, the selection process may be complicated by the effects of marine biofilm development that may adversely affect the roughness characteristics of these particles.

Accordingly, the principal aim of this research study was to understand the effects of Cu_2O particles on the roughness and hydrodynamic characteristics of marine coatings, as well as to understand the combined effects of biofilm. To systematically support the research aim, the study was completed by achieving several specific objectives (**Section 1.3**). By systematically comparing the roughness, boundary-layer and drag characteristics of these different sized Cu_2O particle coated surfaces, the Cu_2O particle size selection for the paint production could be optimised.

The surface microgeometry and roughness analysis (**Objective 3**) under clean conditions were investigated for surfaces coated with three different kinds of commercial Cu_2O products (C7,

C12 and C17) and five laboratory experimental Cu_2O products (C2, C25, C60, C100 and C250). During the surface preparation process, the particle aggregations were examined for the surfaces coated with the smallest Cu_2O specimens (i.e. C2) and these were found to result in unexpectedly poor finish quality. The microstructure SEM images and roughness results both indicated that the surface microstructures were significantly rougher than expected, for example, the average R_t after both applications was about 64.1μm. The analysis results also demonstrated a similar aggregation phenomenon was likely to have occurred on the surfaces coated with specimen C7. For surfaces coated with aggraded and non-aggraded C7 particles, the difference of the average R_t was found to be 69.1μm and 17.2μm, respectively. For a newly coated hull, the particle aggregation could significantly increase the initial frictional drag and cause an additional fuel consumption demand. Moreover, during the paint preparation, aggregation from the fine particles is usually irreversible. The size of the aggregated matter is also unpredictable and uncontrollable. Therefore, for paint production, these undesirable issues could bring more challenges in terms of surface quality control.

For the surfaces coated with other specimens, the commercial products, C12 ($R_t \approx$17.6μm) and C17 ($R_t \approx$23.5μm) both gave quite low roughness levels. The experimental specimens (C25−C250) gave obviously larger roughness values which were found to increase with particle size. As a consequence, the frictional drag was directly affected and aligned with the associated roughness level from each tested specimen. With respect to the hydraulically smooth surfaces, apart from the aggregated specimens, the pressure drop tests (**Objective 5**) indicated that the lowest frictional drag penalty was about 17% which was measured from C12, and this value was followed by 23.7% from C17. The highest frictional drag increment was about 157.0% from C250 which was followed by 86% from C100. It has to be further noted that, based on the measurements, an empirical linear relationship was noticed when correlating the frictional coefficients C_f ($\times 10^3$) against the particle medium size D_{50} (μm). According to the overall results, the slopes of the linear equations were found to be concentrated at 0.025−0.026, whilst the intercepts were concentrated at 5.0.

It should be noted that these test coatings were formulated in a laboratory environment, mainly consisting of Cu_2O particles (>90% by weight) and that they do not represent commercial products. The commercial antifoulings generally have a Cu_2O content of <50% (dry film weight), and would consequently result in different test results. However, for the initial stage of the paint production or dry-docking application processing, this empirical linear equation

could still provide a good reference estimation for the preliminary frictional coefficients of the antifouling top coats. Furthermore, a range of general surface roughness conditions (17.2μm<R_t<337.1μm) was presented by the coatings with these Cu_2O specimens. For any commercial antifouling coatings with similar surface roughness levels, their resulting friction coefficients could be simply estimated according to the experimental results.

The boundary layer characteristics (**Objective 4**) were analysed based on the measurements from a two-dimensional DANTEC Laser Doppler Velocimetry (LDV) system. Throughout the logarithmic and outer part of the boundary layer (0.01<y/δ), a very good collapse of the velocity defect profiles of hydraulically smooth and Cu_2O coated rough walls was observed and provided support for the universality of the velocity defect law.

To correlate the roughness characteristics and roughness functions within the testing Reynolds number range, for the results of boundary layer tests, a roughness length scale was determined by using a multi-parameter combination, $k = AR_q^2(1 + R_{sk})^B/Sd_4$. The correlation showed a good agreement with Colebrook type roughness function behaviour in the transitionally rough regime, and a reasonable agreement with the Townsin and Dey (1990) roughness function correlation. The roughness length scale for the results of pressure drop tests was decided by an arbitrary constant multiplying with the peak to trough roughness height, $k = AR_t$. A correlation of roughness function variations of the present data with the Colebrook-White law was observed. Moreover, the roughness function results from both boundary layer tests and pressure drop measurements indicated that fully rough surfaces were formed by coating with specimens C100 and C250, whereas others presented as being transitionally rough surfaces. However, no hydraulically smooth antifouling surfaces were achieved by using the current specimens.

The friction of a surface in fluid flow is caused by viscous effects and turbulence production in the boundary layer close to the wall. As the roughness Reynolds number, k^+, increases, the near-wall high peak profiles of the streamwise Reynolds normal stress decreases. For surfaces coated with C100 and C250, the near-wall high peak profile completely disappeared due to the breakdown of the viscous region by the roughness. Once again, this phenomenon indicated that the boundary layer reached the fully rough regime over surfaces coated with C100 and C250. Because the fluid was suddenly transited from a smooth to a rough surface, when comparing the Reynolds stress in the boundary outer layer, the C100 and C250 surfaces had a discrepancy in the values over the range, 0.15< $(y + \varepsilon)/\delta$. When the outer scaling normalization was modified by using the freestream velocity, the Reynolds stress in the outer layer similarity was

observed for all rough and smooth walls. The wall similarity hypothesis can further be approved by the turbulence intensity which found that, at the outer region $0.44 < (y + \varepsilon)/\delta$, a good collapse between the smooth and rough surface profiles was observed. It is worth reiterating that, because of the observation about the outer layer similarity from both smooth and rough walls, the roughness function (or the shift in the log layer) is then a possible way of characterising the roughness impacts on the mean flow and the frictional drag.

The marine biofilm impacts on the surface roughness (**Objective 3**) and frictional drag characteristics (**Objective 6**) were evaluated for surfaces which were coated with both commercial specimens (C12 and C17) and experimental products (C25 and C60). At the same time, a practical and efficient method to grow marine biofilm dynamically in a natural environment was presented in this study.

The SEM observations clearly indicated that the bacteria attached and developed biofilm quickly on the relatively smooth surfaces, with EPS films fully covering the coating top surface. As a consequence, for surfaces covered with smaller Cu_2O particles (i.e. 12μm and 17μm), the roughness and frictional resistance were significantly increased. Once the biofilm had fully developed, there were no further changes to the roughness, and the frictional resistance settled to a steady value. For surfaces covered with the larger size Cu_2O particles, especially C60, the biofilm effect on the relatively rougher surfaces was found to be delayed due to the higher initial rougher microstructure. Rough surfaces were found to provide zones of low shear stress that minimised biofilm removal (Alnnasouri *et al*., 2011), and they had more contact areas for microorganisms to attach (Geesey *et al*., 1996). Therefore, it took a long time for biofilms to become fully developed on the rougher surfaces. Meanwhile, the surface microstructure kept changing all the time, and this resulted in roughness and frictional drag values that fluctuated.

Accordingly, for paint development and marine surface protection, the above results brought further insight into the time-dependent influence of biofilms on AF surfaces, especially different roughness profiles which were engineered by varying the Cu_2O particle size. Similar frictional drag fluctuation increments would be expected for a ship surface which has equivalent or rougher characteristics than the surface C60. For low profile AF surfaces, the roughness and frictional drag after a period of biofilm development show a much slower rate of increase.

For correlating the roughness characteristics of fouled surfaces and their roughness functions within the investigated Reynolds range, the peak-to-trough roughness height was used as the

roughness length scale. The regression value pointed to a good agreement between all of the roughness function results with the Colebrook type roughness function. When testing at the same speed, the effect of the biofilm was to shift the roughness function from the transitionally-rough regime towards the fully-rough regime. It is worth noting that the roughness measurements were carried out using an optical roughness measurement device while keeping the testing plate in seawater.

The Granville similarity procedure (Granville, 1958; Granville, 1987) provides a straightforward extrapolation method that can scale up the frictional drag of a flat plate in experimental tests to that of a full-scale plate under `the same surface conditions (**Objective 7**). The results showed that, for the AF surfaces, the size of the Cu_2O particles in the top coat significantly affect the full-scale ship hull frictional resistance. At a service speed of 19knots, for surfaces with biofilm developed, the overall rate of increase in frictional drag for surfaces coated with particle sizes of 12μm and 17μm was similar, at 3.0% per 10μm increment in R_t, whereas these values were found to be around 1.5% for surfaces coated with particle sizes of 25μm and 60μm.

9.3 Contributions

Within the framework of its overall aim, this research study has systematically explored the effect of different sized Cu_2O on the drag and roughness characteristics of marine coatings for the first time in the open literature and hence demonstrated the significant potential impact of this effect on ship performance in-service. The main contributions from this research work are:

- It was found that the lowest roughness surface was not demonstrated by the smallest sized particles because of aggregations which caused an unexpectedly rougher surface resulting in higher frictional drag.
- Apart from the aggregated particles, the overall frictional drag was found to increase with particle size, and an empirical linear equation was derived and can express this relationship. Moreover, considering the effect of testing fluid speed, another equation was developed and expressed the correlation betwwen frictional drag, particle size and fluid speed.
- In the present research, the roughness length scale for biofilm fouled surfaces was determined by a natural constant (A) multiplied with peak to trough roughness height (R_t). A new equation for finding this natural constant has been proposed by taking the

deployment time for the biofilm development into account.

- Details of the time-dependent influence of biofilms on the Cu_2O surfaces have been tested and presented. The results indicated that, for the Cu_2O surfaces, there was no linear relation between the frictional drag increment and biofilm development time. Moreover, based on this data, the frictional drag changes on different size full-scale ships under similar surface conditions could be predicted.
- For the biofilm fouled surfaces, it was also observed that significant fluctuation occurs on the roughness and frictional drag values for surfaces coated with larger sizes of Cu_2O particles, e.g. D50=60μm, and therefore, similar behaviours are expected for ship surfaces which have similar or rougher characteristics than this particle size.
- The additional resistance estimation process could be simplified by using the frictional drag predictions diagrams. Therefore, based on the roughness functions, which were collected from any specific surface condition, the new full-scale frictional drag diagrams can be quickly and easily generated by again operating the developed MATLAB in-house code.
- Moreover, because the roughness functions of the present work were obtained from fieldwork conditions with in-service biofilms, these diagrams could be used as a set of very practical prediction tools or as a benchmark for ship owners or paint developers to carry out estimations in advance for the in-service condition after a certain period.

9.4 Recommendations for Further Work

In the present study, the test coatings were purely designed for experimental test purposes, with high Cu_2O contents (>90% by weight) in the dry film, and do not correspond to commercial antifoulings (<50% by weight). Therefore, the recommendations for future work have been established from a 3-stage perspective.

Based on the Cu_2O particle size impacts on the marine surfaces, the first stage is to control the Cu_2O contents (by weight) in the dry film at different levels with a decreasing gradient of the Cu_2O content from >90% to <50% in the dry film. The test specimens and binder system should then be applied, and by controlling all variables except the Cu_2O particle content, a systematic range of Cu_2O particle content surfaces could be built up. Therefore, all the experiments or the selected ones reported in this thesis should then be repeated using the new Cu_2O surfaces.

Based on the results from the first set of work, the second stage could be established by

gradually adding other coating pigments, such as Ti_2O and ZnO particles which are commonly used in commercial antifouling products. The use of the Cu_2O and the binder system would be the same as in the previous tests. The content and size of the other added pigments should be systematically controlled and the experiments repeated using the new Cu_2O surfaces. It should be noted that the investigation of coatings that mimic commercial products should be carried out from the point of view of the surface physical characteristics of the antifouling.

Moreover, during the in-service condition, the surface roughness characteristics of the different types of antifouling top surface will vary based on the different binder systems used, such as rosin (CDP) and silyl acrylate (SPC). Based on the results from the second stage, the third phase of the work would be to investigate the interactions between biofilms and the different sized Cu_2O particle and their impacts on the surface roughness and drag characteristics with different matrix materials. The development of the biofilm can be achieved either in an artificial environment or through on-board growth. Then, the roughness functions would be processed for the full-scale frictional drag predictions completing the database before undertaking any commercial or experimental benchmark activities.

The biofilm development in the present study was undertaken around the port of Blyth, on the Northeast coast of England where the annual sea temperature varies between 6.7° and 15.3°C on average. It should be noted that the water temperature can also affect the biofilm growth, and may result in different roughness and drag. Accordingly, to further investigate these effects, experiments should be repeated at a range of temperatures.

Also, the biofilm development activities on the test surfaces were carried out for six months. The frictional coefficients of surfaces coated with C12, C17 and C25 tended to approach similar and constant values while, those of C60 showed a higher but less significant fluctuating increment near the end of tests. Further changes beyond the current testing period could be predicted according to these results, but a valuable contribution in this field could be made by extending the biofilm development to a longer period, for example over a year, in order to have a more comprehensive study about the time-dependent biofilm impacts on the antifouling surface.

In the present study, the velocity profile distributions over the biofilm fouled antifouling surfaces are unknown, especially when considering that the structure of the biofilm is dynamically changing against the flow fluid. Moreover, due to the temperature, ocean location,

species of the microorganism and other factors, the biofilm would be largely different from each circumstance. As a results, the flow structure over the biofilm fouled surfaces still remains as largely unknown. Boundary layer measurements need to be conducted for those biofilm fouled surfaces.

Finally, the present study has provided invaluable systematic roughness, and hydrodynamic data for different size of Cu_2O particles applied surfaces. While the use of this data to estimate the effect of the different size particles on the ship hull resistance has been presented based on the Granville procedure for very practical purposes, more elaborative way of estimating this effect is to use this data in combination with the Computational Fluid Dynamics methods.

References

Adamson, N.E. (1937) Technology of Ship-bottom Paints and Its Importance to Commercial and Naval Activities. Bureau C & R Bull. No. 10, US Government Printing Office.

Afzal, N., Seena, A. and Bushra, A. (2013) 'Turbulent flow in a machine honed rough pipe for large Reynolds numbers: general roughness scaling laws', Journal of hydro-environment research, 7(1), pp. 81-90.

Allen, J.J., Shockling, M.A. and Smits, A.J. (2005) 'Evaluation of a universal transitional resistance diagram for pipes with honed surfaces', Physics of Fluids, 17(12), p. 121702.

Alnnasouri, M., Lemaitre, C., Gentric, C., Dagot, C. and Pons, M.-N. (2011) 'Influence of surface topography on biofilm development: Experiment and modeling', Biochemical engineering journal, 57, pp. 38-45.

Ammar, Y., Swailes, D., Bridgens, B. and Chen, J. (2015) 'Influence of surface roughness on the initial formation of biofilm', Surface and Coatings Technology, 284, pp. 410-416.

Anderson, C. (2012) 'Coatings, Antifoulings', in Kirk-Othmer Encyclopedia of Chemical Technology, (Ed.). pp. 1-28.

Anderson, C., Atlar, M., Callow, M., Candries, M., Milne, A. and Townsin, R.L. (2003) 'The development of foul-release coatings for seagoing vessels', Journal of Marine Design and Operations B, 4, p. 11.

Anderson, C.D. (2008) 'The science of antifoulings', lecture notes, Newcastle University.

Angst, E.C. (1923) 'The fouling of ships bottoms by bacteria', Report, bureau construction and repair.

Antonia, R.A. and Krogstad, P.Å. (2001) 'Turbulence structure in boundary layers over different types of surface roughness', Fluid Dynamics Research, 28(2), p. 139.

Antonia, R.A. and Luxton, R.E. (1971) 'The response of a turbulent boundary layer to a step change in surface roughness Part 1. Smooth to rough', Journal of Fluid Mechanics, 48(4), pp. 721-761.

ASME (2003) American Society of Mechanical Engineers. Standards Committee, B. Classification Designation of Surface, Qualities "Surface texture: Surface roughness, waviness and lay" Amer Society of Mechanical.

Atherton, W.H. (1899) The fouling of ships. Trans. North-East Coast Inst: Engineers and Ship-builders.

Atlar, M. (2011) 'Recent upgrading of marine testing facilities at Newcastle University', AMT'11 – The 2nd International Conference on Advanced Model Measurement Technology for the EU Maritime Industry, Newcastle upon Tyne, UK. , pp. p: 1-32.

Atlar, M., Bashir, M., Turkmen, S., Yeginbayeva, I., Carchen, A. and Politis, G. (2015a) 'Design, manufacture and operation of a strut system deployed on a research catamaran to collect samples of dynamically grown biofilms in-service', The 4th International Conference on Advanced Model Measurement Technology for the Maritime Industry (AMT'15), Istanbul, Istanbul Technical University Press, pp. 67-82.

Atlar, M., Glover, E.J., Candries, M., Mutton, R.J. and Anderson, C.D. (2002) International conference on Marine Science and Technology for Environmental Sustainability (ENSUS 2002). University of Newcastle upon Tyne.

Atlar, M., Turkmen, S. and Bashir, M. (2015b) Design of a strut system for RV -The Princess Royal to collect samples of dynamically grown biofilms in-service (SEAFRONT project Deliverable D5.10).

Atlar, M., Turkmen, S., Yeginbayeva, I. and Carchen, A. (2015c) Commissioning and deployment of a strut arrangement on board The Princess Royal for dynamic biofilm sample collection (SEAFRONT project Deliverable D5.11).

Aupoix, B. (2015) 'Roughness corrections for the k–ω shear stress transport model: status and proposals', Journal of Fluids Engineering, 137(2), p. 021202.

Baier, R.E. (1973) 'Influence of the initial surface condition of materials on bioadhesion', The Third International Congress on Marine Corrosion and Fouling, Gaithersburg, MD, USA, Northwestern University Press, pp. 633-639.

Baier, R.E. (1980) 'Substrata influences on adhesion of microorganisms and their resultant new surface properties', in Adsorption of microorganisms to surfaces. John Wiley, New York, pp. 59-104.

Baier, R.E. and DePalma, V.A. (1971) 'Management of occlusive arterial disease', Yearbook Medical, Chicago, p. 147.

Baier, R.E., Meyer, A.E. and Forsberg, R.L. (1997) 'Certification of properties of nontoxic fouling-release coatings exposed to abrasion and long-term immersion', Naval Research Reviews, 49, pp. 60-65.

Bandyopadhyay, P.R. (1987) 'Rough-wall turbulent boundary layers in the transition regime', Journal of Fluid Mechanics, 180, pp. 231-266.

Barnaby, N. (1860) 'On mechanical invention in its relation to the improvement of naval architecture', Trans, Inst. Nav. Arch, 1, pp. 145-159.

Baysan, A., Sleibi, A., Ozel, B. and Anderson, P. (2018) 'The quantification of surface roughness on root caries using Noncontact Optical Profilometry—An in vitro study', Lasers in Dental Science, 2(4), pp. 229-237.

Benedict, L.H. and Gould, R.D. (1996) 'Towards better uncertainty estimates for turbulence statistics', Experiments in fluids, 22(2), pp. 129-136.

Berman, T. and Passow, U. (2007) 'Transparent Exopolymer Particles (TEP): an overlooked factor in the process of biofilm formation in aquatic environments', Nature, preceedings.

Bertram, V. (2011) Practical ship hydrodynamics. 2nd edn. Elsevier.

Bhushan, B. (2000) Modern tribology handbook, two volume set. CRC press.

Bingeman, J.M., Bethell, J.P., Goodwin, P. and Mack, A.T. (2000) 'Copper and other sheathing in the Royal Navy', International Journal of Nautical Archaeology, 29(2), pp. 218-229.

Bott, T.R. (1990) Fouling notebook. 1st edn. Inst of Chemical Engineers.

Brady Jr, R.F. (1999) 'Properties which influence marine fouling resistance in polymers containing silicon and fluorine', Progress in organic coatings, 35(1-4), pp. 31-35.

Brady Jr, R.F. and Singer, I.L. (2000) 'Mechanical factors favoring release from fouling release coatings', Biofouling, 15(1-3), pp. 73-81.

Bressy, C. and Lejars, M. (2014) 'Marine fouling: an overview', The Journal of Ocean Technology, 9, pp. 19-28.

Brooks, W.K. (1880) Development of the American oyster: (Ostrea Virginiana List). Reprinted from the Report of the Commissioners of Fisheries of Maryland.

Bryers, J.D. (1994) 'Biofilms and the technological implications of microbial cell adhesion', Colloids and Surfaces B: Biointerfaces, 2(1-3), pp. 9-23.

Brzek, B., Cal, R.B., Johansson, G. and Castillo, L. (2007) 'Inner and outer scalings in rough surface zero pressure gradient turbulent boundary layers', Physics of fluids, 19(6), p. 065101.

Brzek, B., Torres-Nieves, S., Lebrón, J., Cal, R., Meneveau, C. and Castillo, L. (2009) 'Effects of free-stream turbulence on rough surface turbulent boundary layers', Journal of Fluid Mechanics, 635, pp. 207-243.

Brzek, B.G., Cal, R.B., Johansson, G. and Castillo, L. (2008) 'Transitionally rough zero pressure gradient turbulent boundary layers', Experiments in Fluids, 44(1), pp. 115-124.

Byrne, D. (1980) The hull roughness of ships in service. Master thesis. University of Newcastle upon Tyne.

Callow, M. (1990) 'Ship fouling: problems and solutions', Chemistry and Industry (London), (5), pp. 123-127.

Callow, M.E. (1993) 'A review of fouling in freshwaters', Biofouling, 7(4), pp. 313-327.

Callow, M.E. and Callow, J.A. (2002) 'Marine biofouling: a sticky problem', Biologist, 49(1), pp. 1-5.

Callow, M.E. and Edyvean, R.G. (1990) 'Algal fouling and corrosion', Introduction to Applied Phycology, pp. 367-387.

Callow, M.E., Pitchers, R.A. and Milne, A. (1986) 'The control of fouling by non-biocidal systems', in Studies in Environmental Science. Elsevier, pp. 145-158.

Candries, M. (2001) Drag, boundary-layer and roughness characteristics of marine surfaces coated with antifoulings. Doctoral thesis. University of Newcastle upon Tyne Newcastle upon Tyne, UK.

Candries, M. and Atlar, M. (2005) 'Experimental investigation of the turbulent boundary layer of surfaces coated with marine antifoulings', Journal of Fluids Engineering, 127(2), pp. 219-232.

Candries, M., Atlar, M. and Anderson, C.D. (2000) 'Considering the use of alternative antifoulings: the advantages of foul release systems', Proceedings ENSUS 2000, pp. 88-95.

Candries, M., Atlar, M. and Anderson, C.D. (2003a) 'Estimating the impact of new-generation antifoulings on ship performance: the presence of slime', Journal of Marine Engineering & Technology, 2(1), pp. 13-22.

Candries, M., Atlar, M., Mesbahi, E. and Pazouki, K. (2003b) 'The measurement of the drag characteristics of tin-free self-polishing co-polymers and fouling release coatings using a rotor apparatus', Biofouling, 19(S1), pp. 27-36.

Carlton, J.N. (1998) 'Composite cuprous oxide powder', U.S. Patent 5,707,438.

Casse, F. and Swain, G.W. (2006) 'The development of microfouling on four commercial antifouling coatings under static and dynamic immersion', International biodeterioration & biodegradation, 57(3), pp. 179-185.

Castro, I.P. (2007) 'Rough-wall boundary layers: mean flow universality', Journal of Fluid Mechanics, 585, pp. 469-485.

Cebeci, T. and Chang, K.C. (1978) 'Calculation of incompressible rough-wall boundary-layer flows', AIAA Journal, 16(7), pp. 730-735.

Chamberlain, A.H.L. (1992) 'The role of adsorbed layers in bacterial adhesion', in Biofilms—Science and Technology. Springer, pp. 59-67.

Characklis, W.G. (1971) 'Effect of hypochlorite on microbial slimes', 26th Industrial Waste Conference, Indiana, USA, Purdue University, pp. 171-181.

Characklis, W.G. and Cooksey, K.E. (1983) 'Biofilms and microbial fouling', in Advances in applied microbiology. Elsevier, pp. 93-138.

Characklis, W.G., McFeters, G.A. and Marshall, K.C. (1990) 'Physiological ecology in biofilm systems', Biofilms, 37, pp. 67-72.

Chen, C.L., Maki, J.S., Rittschof, D. and Teo, S.L.M. (2013) 'Early marine bacterial biofilm on a copper-based antifouling paint', International Biodeterioration & Biodegradation, 83, pp. 71-76.

Chin, M.Y.H., Sandham, A., De Vries, J., van der Mei, H.C. and Busscher, H.J. (2007) 'Biofilm formation on surface characterized micro-implants for skeletal anchorage in orthodontics', Biomaterials, 28(11), pp. 2032-2040.

Christensen, B.E. and Characklis, W.G. (1990) 'Physical and chemical properties of biofilms', Biofilms, 93, p. 130.

Clauser, F.H. (1954a) 'Turbulent boundary layers in adverse pressure gradients', J. aeronaut. Sci, 21(2), pp. 91-108.

Clauser, F.H. (1954b) 'Turbulent boundary layers in adverse pressure gradients', Journal of the Aeronautical Sciences, 21(2), pp. 91-108.

Cock, R. (2001) '‘The finest invention in the world’: the Royal Navy's early trials of copper sheathing, 1708–1770', The Mariner's Mirror, 87(4), pp. 446-459.

Coe, W.R. and Allen, W.E. (1937) Growth of sedentary marine organisms on experimental blocks and plates for nine successive years at the pier of the scripps institution of oceanography. University of California Press.

Colebrook, C.F., Blench, T., Chatley, H., Essex, E.H., Finniecome, J.R., Lacey, G., Williamson, J. and Macdonald, G.G. (1939) 'Correspondence turbulent flow in pipes, with particular reference to the transition region between the smooth and rough pipe laws. (include plates)', Journal of the Institution of Civil engineers, 12(8), pp. 393-422.

Colebrook, C.F. and White, C.M. (1937) 'Experiments with fluid friction in roughened pipes', Proceedings of the royal society of london. Series A-Mathematical and Physical Sciences, 161(906), pp. 367-381.

Coleman, H.W. and Steele Jr, G. (1990) Experimentation and uncertainty analysis for engineers. John Wiley and Sons, New York.

Coles, D. (1956) 'The law of the wake in the turbulent boundary layer', Journal of Fluid Mechanics, 1(02), pp. 191-226.

Conover, J.T. and Sieburth, J.M. (1964) 'Effect of sargassum distribution on its epibiota and antibacterial activity', Botanica Marina, 6(1-2), pp. 147-157.

Curtis, E.J.C. and Curds, C.R. (1971) 'Sewage fungus in rivers in the United Kingdom: the slime community and its constituent organisms', Water Research, 5(12), pp. 1147-1159.

Darcy, H. (1857) Recherches expérimentales relatives au mouvement de l'eau dans les tuyaux. Mallet-Bachelier.

Dean, R.B. (1978) 'Reynolds number dependence of skin friction and other bulk flow variables in two-dimensional rectangular duct flow', Journal of Fluids Engineering, 100(2), pp. 215-223.

Demirel, Y.K. (2015) Modelling the roughness effects of marine coatings and biofouling on ship frictional resistance. Doctoral thesis. University of Strathclyde.

Dempsey, M.J. (1981) 'Colonisation of antifouling paints by marine bacteria', Botanica Marina, 24(4), pp. 185-192.

Den Hartog, C. (1959) 'The epilithic algal communities occurring along the coast of the Netherlands', Plant Biology, 1, pp. 1-241.

DeNicola, D.M. and McIntire, C.D. (1990) 'Effects of substrate relief on the distribution of periphyton in laboratory streams, I. hydrology 1', Journal of Phycology, 26(4), pp. 624-633.

Denny, M.E. (1951) 'BSRA resistance experiments on the Lucy Ashton: Part I—Full-scale measurements', Trans. Institution of Naval Architects, 93, pp. 40-57.

Deutsches Institut für Normung (1982) 4760-1980: Surface irregularities, terms and definitions, classification system.

Dey, S.K. (1989) Parametric representation of hull painted surfaces and the correlation with fluid drag. Doctoral thesis. University of Newcastle upon Tyne.

Donlan, R.M. (2002) 'Biofilms: microbial life on surfaces', Emerging infectious diseases, 8(9), p. 881.

Donlan, R.M., Pipes, W.O. and Yohe, T.L. (1994) 'Biofilm formation on cast iron substrata in water distribution systems', Water Research, 28(6), pp. 1497-1503.

Durst, F., Fischer, M., Jovanović, J. and Kikura, H. (1998) 'Methods to set up and investigate low Reynolds number, fully developed turbulent plane channel flows', Journal of fluids engineering, 120(3), pp. 496-503.

El Din, A.M.S., El-Dahshan, M.E. and El Din, A.M.T. (2003) 'Bio-film formation on stainless steels Part 2. The role of seasonal changes, seawater composition and surface roughness', Desalination, 154(3), pp. 267-276.

Ettl, P., Schmidt, B.E., Schenk, M., Laszlo, I. and Haeusler, G. (1998) International Conference on Applied Optical Metrology. International Society for Optics and Photonics.

Fera, P., Siebel, M.A., Characklis, W.G. and Prieur, D. (1989) 'Seasonal variations in bacterial colonisation of stainless steel, aluminium and polycarbonate surfaces in a sea water flow system', Biofouling, 1(3), pp. 251-261.

Field, B. (1981) 'Marine biofouling and its control: history and state-of-the-art review', OCEANS 81, pp. 542-544.

Fincham, J. (1851) A History of Naval Architecture: To which is Prefixed, an Introductory Disertation on the Application of Mathematical Science to the Art of Naval Construction. . Whittaker.

Fischer-Piette, E. (1932) Répartition des principales espèces fixées sur les rochers battus des côtes et des îles de la Manche, de Lannion à Fécamp. Masson et Cie.

Flack, K.A. and Schultz, M.P. (2010) 'Review of hydraulic roughness scales in the fully rough regime', Journal of Fluids Engineering, 132(4), p. 041203.

Flack, K.A. and Schultz, M.P. (2014) 'Roughness effects on wall-bounded turbulent flows', Physics of Fluids, 26(10), p. 101305.

Flack, K.A., Schultz, M.P. and Connelly, J.S. (2007) 'Examination of a critical roughness height for outer layer similarity', Physics of Fluids, 19(9), p. 095104.

Flack, K.A., Schultz, M.P. and Shapiro, T.A. (2005) 'Experimental support for Townsend's Reynolds number similarity hypothesis on rough walls', Physics of Fluids, 17(3), p. 035102.

Fletcher, R.L. and Chamberlain, A.H.L. (1975) 'Marine fouling algae', Technical series.

Flint, S.H., Brooks, J.D. and Bremer, P.J. (2000) 'Properties of the stainless steel substrate, influencing the adhesion of thermo-resistant streptococci', Journal of Food Engineering, 43(4), pp. 235-242.

Forbes, E. (1999) Paul Revere and the world he lived in. Houghton Mifflin Harcourt.

Foster, M.S. (1975) 'Regulation of algal community development in a Macrocystis pyrifera forest', Marine biology, 32(4), pp. 331-342.

Fratesi, S.E., Lynch, F.L., Kirkland, B.L. and Brown, L.R. (2004) 'Effects of SEM preparation techniques on the appearance of bacteria and biofilms in the carter sandstone', Journal of Sedimentary Research, 74(6), pp. 858-867.

Frei, W. (2013) Which turbulence model should I choose for my CFD application? Available at: https://uk.comsol.com/blogs/which-turbulence-model-should-choose-cfd-application/ (Accessed: Sep 2018).

Froude, W. (1872) 'Experiments on the surface-friction experienced by a plane moving through water', British Association for the Advancement of Science, 42, pp. 118-124.

Froude, W. (1874) Report to the Lords Commissioners of the Admiralty on Experiments for the Determination of the Frictional Resistance of Water on a Surface, Under Various Conditions, Performed at Chelston Cross, Under the Authority of Their Lordships. 44th Report by the British Association for the Advancement of Science.

Gadelmawla, E.S., Koura, M.M., Maksoud, T.M.A., Elewa, I.M. and Soliman, H.H. (2002) 'Roughness parameters', Journal of Materials Processing Technology, 123(1), pp. 133-145.

Gardner, H.A. (1922) 'Modern research on antifouling paints', Scientific Section, Educational Bureau, Circular No. 157, Washington US. pp. 35-72.

Geesey, G.G., Gillis, R.J., Avci, R., Daly, D., Hamilton, M., Shope, P. and Harkin, G. (1996) 'The influence of surface features on bacterial colonization and subsequent substratum chemical changes of 316L stainless steel', Corrosion Science, 38(1), pp. 73-95.

Geesey, G.G., Mutch, R., Costerton, J.W.t. and Green, R.B. (1978) 'Sessile bacteria: an important component of the microbial population in small mountain streams', Limnology and oceanography, 23(6), pp. 1214-1223.

George, W.K. and Castillo, L. (1997) 'Zero-pressure-gradient turbulent boundary layer', Applied Mechanics Reviews, 50(12), pp. 689-729.

Gerhart, D.J., Rittschof, D., Hooper, I.R., Eisenman, K., Meyer, A.E., Baier, R.E. and Young, C. (1992) 'Rapid and inexpensive quantification of the combined polar components of surface wettability: application to biofouling', Biofouling, 5(4), pp. 251-259.

Glover, T.J. (1982) 'Copper–nickel alloy for the construction of ship and boat hulls', British corrosion journal, 17(4), pp. 155-158.

Gonzalez, M.A. and Goff, L.J. (1989) 'The red algal epiphytes Microcladia coulteri and M. californica (Rhodophyceae, Ceramiaceae). II. Basiphyte specificity', Journal of phycology, 25(3), pp. 558-567.

Good, R.J. and van Oss, C.J. (1992) 'The modern theory of contact angles and the hydrogen bond components of surface energies', in Modern approaches to wettability. Springer, pp. 1-27.

Grant, G. and Culver, H.B. (1935) The book of old ships: Their Beginnings, Their Life Histories, Their Ultimate Fate. 1st edn. Doubleday, Doran & Company.

Granville, P.S. (1958) 'The frictional resistance and turbulent boundary layer of rough surfaces', Journal of Ship Research, 2, pp. 52-74.

Granville, P.S. (1978) Similarity-law characterization methods for arbitrary hydrodynamic roughnesses. Final Report Naval Ship Research and Development Center, Bethesda, MD. Ship Performance Dept., 1.

Granville, P.S. (1987) 'Three indirect methods for the drag characterization of arbitrarily rough surfaces on flat plates', Journal of Ship Research, 31, pp. 70-77.

Grass, A.J. (1971) 'Structural features of turbulent flow over smooth and rough boundaries', Journal of Fluid Mechanics, 50(2), pp. 233-255.

Grave, C. (1920) 'Amaroucium pellucidum (Leidy) form constellatum (Verrill). I. The activities and reactions of the tadpole larva', Journal of Experimental Zoology Part A: Ecological Genetics and Physiology, 30(2), pp. 239-257.

Grave, C. and McCosh, G. (1923) 'Perophora viridis (Verrill). The activities and structure of the free-swimming larva', Wash. Univ. Stud. Scient. Ser, 11(89), p. 116.

Grigson, C.W. (1990) 'Towards Reliable Estimates of Full-Scale Viscous Drag', RINA Intl Workshop on Marine Roughness and Drag pp. 8-13.

Gudala, M., Banerjee, S., Kumar, R., Rao, T.R.M., Mandal, A. and Naiya, T.K. (2018) 'Experimental Investigation on Hydrodynamics of Two-Phase Crude Oil Flow in Horizontal Pipe With Novel Surfactant', Journal of Fluids Engineering, 140(6), p. 061302.

Hama, F.R. (1954) 'Boundary-layer characteristics for smooth and rough surfaces', SNAME, 62, pp. 333-358.

Harris, J.R. (1966) 'Copper and shipping in the eighteenth century', The economic history review, 19(3), pp. 550-568.

Haslbeck, E.G. and Bohlander, G.S. (1992) Microbial biofilm effects on drag-lab and field. No. CONF-PAPER-3A-1, Naval Surface Warfare Centre Carderock DIV Annapolis MD.

Hay, W.J. (1863) 'On copper and other sheathing for the Navy', Trans. Inst. Nav. Arch., 4, pp. 79-96.

Heath, C.R., Leadbeater, B.S.C. and Callow, M.E. (1993) 'Formation and calcification of biofilms on antifouling paints in hard waters', Biofouling, 7(1), pp. 29-55.

Heslin, T., Heaney, J. and Harper, M. (1974) The effects of particle size on the optical properties and surface roughness of a glass-balloon-filled black paint. No. NASA-G-7432. National Aeronautics and Space Administration Greenbelt MD Goddard Space Flight Centre.: DTIC Document.

Heukelekian, H. and Crosby, E.S. (1956a) 'Slime Formation in Polluted Waters: II. Factors Affecting Slime Growth', Sewage and Industrial Wastes, pp. 78-92.

Heukelekian, H. and Crosby, E.S. (1956b) 'Slime Formation in Sewage: III. Nature and Composition of Slimes', Sewage and Industrial Wastes, pp. 206-210.

Hilen, E.J. (1923) 'Report on a bacteriological study of ocean slime', Report Bureau Construction and Repair, United States Navy Department, Washington.

Hinze, J.O. (1975) 'Turbulence McGraw-Hill', New York, 218, p. p457.

Hoagland, K.D., Roemer, S.C. and Rosowski, J.R. (1982) 'Colonization and community structure of two periphyton assemblages, with emphasis on the diatoms (Bacillariophyceae)', American Journal of Botany, pp. 188-213.

Hoagland, K.D., Rosowski, J.R., Gretz, M.R. and Roemer, S.C. (1993) 'Diatom extracellular polymeric substances: function, fine structure, chemistry, and physiology', Journal of phycology, 29(5), pp. 537-566.

Hoerner, S.F. (1965) Fluid-dynamic drag: practical information on aerodynamic drag and hydrodynamic resistance. SF Hoerner, Midland Park, New Jersey, USA.

Holm, E., Schultz, M., Haslbeck, E., Talbott, W. and Field, A. (2004) 'Evaluation of hydrodynamic drag on experimental fouling-release surfaces, using rotating disks', Biofouling, 20(4-5), pp. 219-226.

Honda, Y. (1997) 'Quantum Leap Technology After Ban of TBT in Japan', Proceedings of Emerging Nonmetallic Materials for the Marine Environment, Honolulu, HI, 18, p. 20.

Hopf, L. (1923) 'Die Messung der hydraulischen Rauhigkeit', ZAMM-Journal of Applied Mathematics and Mechanics/Zeitschrift für Angewandte Mathematik und Mechanik, 3(5), pp. 329-339.

Horbund, H.M. and Freiberger, A. (1970) 'Slime films and their role in marine fouling: A review', Ocean Engineering, 1(6), pp. 631-634.

Houghton, D.R., Pearman, I. and Tierney, D. (1973) 'The effect of water velocity on the settlement of swarmers of Enteromorpha spp', 3rd Intternational Congress of Marine Corrosion and Fouling. Northwestern University Press, Evanston, pp. 682-689.

Howell, D. and Behrends, B. (2006) 'A review of surface roughness in antifouling coatings illustrating the importance of cutoff length', Biofouling, 22(6), pp. 401-410.

Hutson, R., Leadbeater, B. and Sedgwick, R. (1987) 'Algal interference with water treatment processes', Progress in Phycological research, 5, pp. 266-299.

Ingram, H.A. (1944) 'Research in the Bureau of Ships', Journal of Applied Physics, 15(3), pp. 215-220.

International Maritime Organization (2001) 'International convention on the control of harmful anti-fouling systems on ships'. London.

Irzaman, I., Darmasetiawan, H., Hardhienata, H., Hikam, M., Arifin, P., Jusoh, S.N., Taking, S., Jamal, Z. and Idris, M.A. (2011) 'Surface roughness and grain size characterization of annealing temperature effect for growth gallium and tantalum doped Ba 0.5 Sr 0.5 TiO 3 thin film', Atom Indonesia, 35(1), pp. 57-67.

ISO3274 (1996) 'Geometrical Product Specifications (GPS) - Surface texture: Profile method - Nominal characteristics of contact stylus instruments Replaces ISO 1880:1979 and ISO 3274:1975'.

ISO4287 (1997) 'Geometrical product specifications (GPS)–Surface texture: Profile method–Terms, definitions and surface texture parameters'.

ITTC Specialist Committee (2011) 'ITTC–recommended procedures fresh water and seawater properties'. ITTC.

Jimenez, J. (2004) 'Turbulent flows over rough walls', Annu. Rev. Fluid Mech., 36, pp. 173-196.

Johansson, L. (1985) 'The Local Effect of Hull Roughness on Skin Friction: Calculations Based On Floating Element Data and Three-Dimensional Boundary Layer Theory', Royal Institution of Naval Architects Transactions, 127.

Kempf, G. (1937) 'On the effect of roughness on the resistance of ships', Trans INA, 79, pp. 109-119.

Kendall, K. (1971) 'The adhesion and surface energy of elastic solids', Journal of Physics D: Applied Physics, 4(8), p. 1186.

Kinloch, A.J. (1987) Adhesion and adhesives: science and technology. Springer Science & Business Media.

Kjaer, E.B. (1992) 'Bioactive materials for antifouling coatings', Progress in organic coatings, 20(3-4), pp. 339-352.

Kline, S.J., Coles, D.E. and Hirst, E.A. (1969) Computation of turbulent boundary layers--1968 AFOSR-IFP-Stanford Conference: proceedings held at Stanford University, August 18-25, 1968. Thermosciences Division, Stanford University.

Kong, C.Y., Carroll, P.A., Brown, P. and Scudamore, R.J. (2007) 'The effect of average powder particle size on deposition efficiency, deposit height and surface roughness in the direct metal laser deposition process', 14th International Conference on Joining of Materials, Helsingør, Denmark, 2 May 2007.

Kornegay, B.H. and Andrews, J.F. (1968) 'Kinetics of fixed-film biological reactors', Journal of Water Pollution Control Federation, 40(11), pp. R460-R468.

Kovach, B.S. and Swain, G.W. (1998) 'A boat mounted foil to measure the drag properties of antifouling coatings applied to static immersion panels', Proceedings of the International Symposium on Seawater Drag Reduction, pp. 169-173.

Krazer, A. (1905) Verhandlungen des dritten internationalen Mathematiker-Kongresses in Heidelberg vom 8. bis 13. August 1904. BG Teubner.

Krogstad, P.Å., Andersson, H.I., Bakken, O.M. and Ashrafian, A. (2005) 'An experimental and numerical study of channel flow with rough walls', Journal of Fluid Mechanics, 530, pp. 327-352.

Krogstad, P.Å. and Antonia, R.A. (1994) 'Structure of turbulent boundary layers on smooth and rough walls', Journal of Fluid Mechanics, 277, pp. 1-21.

Krogstad, P.Å., Antonia, R.A. and Browne, L.W.B. (1992) 'Comparison between rough-and smooth-wall turbulent boundary layers', Journal of Fluid Mechanics, 245, pp. 599-617.

Krogstadt, P.Å. and Antonia, R.A. (1999) 'Surface roughness effects in turbulent boundary layers', Experiments in fluids, 27(5), pp. 450-460.

Kutlar, A.I. and Lewkowicz, A.K. (1990) 'Investigation of the Effect of a Paint Coat on the Turbulence near a Rough Flat Plate', RINA Intl Workshop on Marine Roughness and Drag, London 29 March 1990, p. 7.

Langelandsvik, L.I., Kunkel, G.J. and Smits, A.J. (2008) 'Flow in a commercial steel pipe', Journal of Fluid Mechanics, 595, pp. 323-339.

Leadbeater, B.S.C. and Callow, M.E. (1992) 'Formation, composition and physiology of algal biofilms', in Biofilms—Science and Technology. Springer, pp. 149-162.

Leitch, E.G. (1992) 'Evaluation of coating to control zebra mussel colonization: preliminary results 1990-1991', J. Protect. Coat. Linings, pp. 28-41.

Leonardi, S., Orlandi, P., Djenidi, L. and Antonia, R.A. (2004) 'Structure of turbulent channel flow with square bars on one wall', International journal of heat and fluid flow, 25(3), pp. 384-392.

Lewis, J.A. (1998) 'Marine Biofonling and its Prevention', Materials Forum, 22, pp. 41-61.

Lewthwaite, J.C., Molland, A.F. and Thomas, K.W. (1985) 'An investigation into the variation of ship skin frictional resistance with fouling', Royal Institution of Naval Architects Transactions, 127.

Li, B. and Logan, B.E. (2004) 'Bacterial adhesion to glass and metal-oxide surfaces', Colloids and Surfaces B: Biointerfaces, 36(2), pp. 81-90.

Ligrani, P.M. (1989) 'Structure of turbulent boundary layers', Encyclopedia of fluid mechanics. Houston: Gulf Professional Publishing, pp. 121-187.

Ligrani, P.M. and Moffat, R.J. (1986) 'Structure of transitionally rough and fully rough turbulent boundary layers', Journal of Fluid Mechanics, 162, pp. 69-98.

Loeb, G.I. and Neihof, R.A. (1975) 'Marine conditioning films', American Chemical Society, Washington, D.C., 145, pp. 319-335.

Lubbock, J. (1882) Ants, bees, and wasps. K. Paul, Trench, Trubner.

Luther, G. (1976) 'Bewuchsuntersuchungen auf Natursteinsubstraten im Gezeitenbereich des Nordsylter Wattenmeeres: Algen', Helgoländer Wissenschaftliche Meeresuntersuchungen, 28(3), p. 318.

Mackie, G.L. (1991) 'Biology of the exotic zebra mussel, Dreissena polymorpha, in relation to native bivalves and its potential impact in Lake St. Clair', in Environmental assessment and habitat evaluation of the upper Great Lakes connecting channels. Springer, pp. 251-268.

Maier, W.J. (1968) Mass Transfer and Growth Kinetics on a Slime Layer, a Simulation of the Trickling Filter. Doctoral thesis. Cornell University, Ithaca, New York, USA.

Mallet, R. (1872) 'On the Corrosion and Fouling of Iron Ships', Trans. Inst. Nav. Archit., 13, pp. 90-152.

Manzolillo, J.L., Thiele, E.W. and Tuthill, A.H. (1976) 'CA-706 Copper-Nickel Alloy Hulls: The Copper Mariner's Experience and Economics', Society of Naval Architects and Marine Engineers-Transactions, 84.

Marszalek, D.S., Gerchakov, S.M. and Udey, L.R. (1979) 'Influence of substrate composition on marine microfouling', Applied and environmental microbiology, 38(5), pp. 987-995.

Mast, S.O. (1911) Light and the Behavior of Organisms. Wiley.

Matsunaga, T. and Lim, T.K. (2000) 'Electrochemical prevention of biofouling', Electrochemistry, 68(11), pp. 847-852.

Maurer, M. (1945) ' Coppered Bottoms for the United States Navy, 1794-1803', US Naval Institute Proceedings LXXI, (71), pp. 693-699. .

McEntee, W. (1916) 'Variation of Frictional Resistance of Ships with Condition of Wetted Surface', Journal of the American Society of Naval Engineers, 28(1), pp. 311-314.

Medhurst, J.S. (1990) 'Outline of a draft international standard for the measurement and characterisation of roughness topography in fluid flow', RINA Intl Workshop on Marine Roughness and Drag; London 29 March 1990.

Medilanski, E., Kaufmann, K., Wick, L.Y., Wanner, O. and Harms, H. (2002) 'Influence of the surface topography of stainless steel on bacterial adhesion', Biofouling, 18(3), pp. 193-203.

Melo, L.L., Vaz, A.R., Salvadori, M.C. and Cattani, M. (2004) 'Grain sizes and surface roughness in platinum and gold thin films', in Metastable and Nanocrystalline Materials. Trans Tech Publ: Trans Tech Publications, pp. 623-628.

Meyer, A.E., Baier, R.E. and King, R.W. (1988) 'Initial fouling of nontoxic coatings in fresh, brackish, and sea water', The canadian journal of chemical engineering, 66(1), pp. 55-62.

Millett, J. and Anderson, C.D. (1997) 'Fighting fast ferry fouling', Fast'97. pp. 493-495.

Mises, R.V. (1914) Elemente der technischen Hydrodynamik. Teubner, Leipzig.

Mittelman, M. and Geesey, G.G. (1987) Biological fouling of industrial water systems: a problem solving approach. Water Micro Assoc.

Mittelman, M.W. (1996) 'Adhesion to biomaterials', Bacterial adhesion: molecular and ecological diversity. New York: Wiley-Liss, Inc, pp. 89-127.

Monin, A.S., Lumley, J.L. and ÍAglom, A.M. (1971) Statistical fluid mechanics: mechanics of turbulence. Vol. 1. MIT press.

Monteiro, P. (2000) lecture notes.

Monty, J.P. (2005) Developments in smooth wall turbulent duct flows. Doctoral thesis. University of Melbourne, Department of Mechanical and Manufacturing Engineering.

Moody, L.F. (1944) 'Friction factors for pipe flow', Trans. Asme, 66(8), pp. 671-684.

Moore, H.B. (1933) 'Change of orientation of a barnacle after metamorphosis', Nature, 132(3347), p. 969.

Moore, H.B. (1935) 'The biology of Balanus balanoides. IV. Relation to environmental factors', Journal of the Marine Biological Association of the United Kingdom, 20(2), pp. 279-307.

Moore, H.B. and Kitching, J.A. (1939) 'The biology of Chthamalus stellatus (Poli)', Journal of the Marine Biological Association of the United Kingdom, 23(2), pp. 521-541.

Morgan, P. and Roger, W. (2015) Fitz's Atlas of Coating Defects: A Comprehensive Visual Guide to Coatings and Application Defects. M. P. I. Group: Bukupedia.

Mosaad, M.A. (1990) International Workshop on Drag and Roughness RINA London, March 1990.

Moss, B. and Marsland, A. (1976) 'The effects of underwater scrubbing on marine fouling algae', Proceedings, International Marine and Shipping Conference, pp. 39-43.

Musker, A.J. (1990) 'Turbulence Measurements in a Shear-Layer Associated with a Ship-Hull Roughness', RINA Intl Workshop on Marine Roughness and Drag; London 29 March 1990, p. 11.

Nakasono, S., Burgess, J.G., Takahashi, K., Koike, M., Murayama, C., Nakamura, S. and Matsunaga, T. (1993) 'Electrochemical prevention of marine biofouling with a carbon-chloroprene sheet', Applied and environmental microbiology, 59(11), pp. 3757-3762.

Neushul, M. (1972) 'Functional interpretation of benthic marine algal morphology', Contribution to Systematics of Benthic Algae in the North Pacific, pp. p47-74.

Neushul, M., Foster, M.S., Coon, D.A., Woessner, J.W. and Harger, B.W.W. (1976) 'An in situ study of recruitment, growth and survival of subtidal marine algae: techniques and preliminary results', Journal of Phycology, 12(4), pp. 397-408.

Newman, J. (1896) Metallic Structures: Corrosion and Fouling and Their Prevention: A Practical Aidbook to the Safety of Works in Iron and Steel and of Ships, and to the Selection of Paints for Them. Spon.

Nikuradse, J. (1933) 'Laws of flow in rough pipes.', N.A.C.A. Technical Memorandum, 1292, pp. 60-68.

Ninnis, H. (1871) 'On Sheathing Iron Ships', (12), pp. 270-281.

North, W.J. (1970) 'Culturing and dispersing Macrocystis embryos', Kelp Habitat Improvement Project, Annual Report, 1971, pp. 42-54.

Ofek, I. and Doyle, R.J. (2012) Bacterial adhesion to cells and tissues. Springer Science & Business Media.

Ogata, E. (1953) 'Some experiments on the settling of spores of red algae', Bull. Soc. Plant Ecol., Tokyo, 3, pp. 128-134.

Parker, G.H. (1924) 'The growth of marine animals on submerged metals', The Biological Bulletin, 47(3), pp. 127-142-1.

Paul Jr, R.W., Kuhn, D.L., Plafkin, J.L., Cairns Jr, J. and Croxdale, J.G. (1977) 'Evaluation of natural and artificial substrate colonization by scanning electron microscopy', Transactions of the American Microscopical Society, pp. 506-519.

Perron, A., Politano, O. and Vignal, V. (2008) 'Grain size, stress and surface roughness', Surface and Interface Analysis, 40(3-4), pp. 518-521.

Perry, A.E. and Li, J.D. (1990) 'Experimental support for the attached-eddy hypothesis in zero-pressure-gradient turbulent boundary layers', Journal of Fluid Mechanics, 218, pp. 405-438.

Perry, A.E., Schofield, W.H. and Joubert, P.N. (1969) 'Rough wall turbulent boundary layers', Journal of Fluid Mechanics, 37(2), pp. 383-413.

Phelps, A. (1942) 'Observations on reactions of barnacle larvae and growth of metamorphosed forms at Beaufort, NC, June, 1941 to Sept. 1941', Fourth semi-annual Report from

Woods Hole Oceanographic Institution to Bureau of Ships. I., Paper VII.(Unpublished.).

Piatek, A. (1967) 'Preventing filamentous scale in well water', Water and Wastes Engineering, 4(12), pp. 54-55.

Picologlou, B.F., Zelver, N. and Characklis, W.G. (1980) 'Biofilm growth and hydraulic performance', Journal of the Hydraulics Division, 106, pp. 733-746.

Pomerat, C.M. and Weiss, C.M. (1946) 'The influence of texture and composition of surface on the attachment of sedentary marine organisms', The Biological Bulletin, 91(1), pp. 57-65.

Powell, C.A. (1994) 'Copper-nickel sheathing and its use for ship hulls and offshore structures', International biodeterioration & biodegradation, 34(3-4), pp. 321-331.

Powell, C.A. and Michels, H.T. (2000) 'Copper-Nickel for Seawater Corrosion Resistance and Antifouling: A State of the Art Review', NACE International Conference, 90, p. 10.

Raupach, M.R., Antonia, R.A. and Rajagopalan, S. (1991) 'Rough-wall turbulent boundary layers', Applied mechanics reviews, 44(1), pp. 1-25.

Rawle, A. (2002) 'The importance of particle sizing to the coatings industry Part 1: Particle size measurement', Advances in Colour Science and Technology, 5(1), pp. 1-12.

Rees, T.K. (1940) 'Algal colonization at Mumbles Head', Journal of Ecology, 28(2), pp. 403-437.

Rijnaarts, H.H.M., Norde, W., Bouwer, E.J., Lyklema, J. and Zehnder, A.J.B. (1993) 'Bacterial adhesion under static and dynamic conditions', Applied and Environmental Microbiology, 59(10), pp. 3255-3265.

Ross, D. (2005) 'Ship sources of ambient noise', IEEE Journal of Oceanic Engineering, 30(2), pp. 257-261.

Russell, G. and Morris, O.P. (1971) 'A ship model in antifouling research', Sea Breezes, pp. 512-513.

Sabin, A.H. (1900) 'Iron Corrosion: Anti-fouling and Anti-corrosive Paints', Journal of the American Chemical Society, 23(7), pp. 521-521.

Saito, Y. and Atobe, S. (1970) 'Phytosociological Study of Intertidal Marine Algae: I. Usujiri Benten-Jima, Hokkaido', Bulletin of the Faculty of Fisheries Hokkaido University, 21(2), pp. 37-69.

Saroyan, J.R. (1968) 'Antifouling Palnts-The Fouling Problem', Naval Engineers Journal, 80(4), pp. 593-604.

Schetz, J.A. and Bowersox, R.D.W. (1933) Boundary layer analysis. American Institute of Aeronautics and Astronautics.

Schiller, L. (1923) 'Über den strömungswiderstand von rohren verschiedenen querschnitts und rauhigkeitsgrades', ZAMM-Journal of Applied Mathematics and Mechanics/Zeitschrift für Angewandte Mathematik und Mechanik, 3(1), pp. 2-13.

Schlichting, H. (1974) Boundary-layer theory. Springer.

Schlichting, H. (1979) 'Boundary-layer theory'. McGraw-Hill, New York.

Schmidt, D.L., Brady, R.F., Lam, K., Schmidt, D.C. and Chaudhury, M.K. (2004) 'Contact angle hysteresis, adhesion, and marine biofouling', Langmuir, 20(7), pp. 2830-2836.

Schultz, M.P. (1998) The effect of biofilms on turbulent boundary layer structure. Doctoral thesis. Florida Institute of Technology Melbourne, FL.

Schultz, M.P. (2000) 'Turbulent boundary layers on surfaces covered with filamentous algae', Journal of fluids engineering, 122(2), pp. 357-363.

Schultz, M.P. (2002) 'The relationship between frictional resistance and roughness for surfaces smoothed by sanding', Journal of fluids engineering, 124(2), pp. 492-499.

Schultz, M.P. (2004) 'Frictional resistance of antifouling coating systems', Journal of Fluids Engineering, 126(6), pp. 1039-1047.

Schultz, M.P., Bendick, J.A., Holm, E.R. and Hertel, W.M. (2011) 'Economic impact of biofouling on a naval surface ship', Biofouling, 27(1), pp. 87-98.

Schultz, M.P., Finlay, J.A., Callow, M.E. and Callow, J.A. (2000) 'A turbulent channel flow apparatus for the determination of the adhesion strength of microfouling organisms', Biofouling, 15(4), pp. 243-251.

Schultz, M.P., Finlay, J.A., Callow, M.E. and Callow, J.A. (2003) 'Three models to relate detachment of low form fouling at laboratory and ship scale', Biofouling, 19(S1), pp. 17-26.

Schultz, M.P. and Flack, K.A. (2003) 'Turbulent boundary layers over surfaces smoothed by sanding', Journal of fluids engineering, 125(5), pp. 863-870.

Schultz, M.P. and Flack, K.A. (2007) 'The rough-wall turbulent boundary layer from the hydraulically smooth to the fully rough regime', Journal of Fluid Mechanics, 580, pp. 381-405.

Schultz, M.P. and Flack, K.A. (2013) 'Reynolds-number scaling of turbulent channel flow', Physics of Fluids (1994-present), 25(2), p. 025104.

Schultz, M.P. and Swain, G.W. (1999) 'The effect of biofilms on turbulent boundary layers', Journal of Fluids Engineering, 121(1), pp. 44-51.

Schultz, M.P., Walker, J.M., Steppe, C.N. and Flack, K.A. (2015) 'Impact of diatomaceous biofilms on the frictional drag of fouling-release coatings', Biofouling, 31(9-10), pp. 759-773.

Shibata, J., Kimura, M., Ueda, K. and Seika, Y. (1972) Ship hull anti-fouling system utilizing electrolyzed sea water. Report No. MTB-80 Tech Bull.

Shockling, M.A., Allen, J.J. and Smits, A.J. (2006) 'Roughness effects in turbulent pipe flow', Journal of Fluid Mechanics, 564, pp. 267-285.

Smith, F.G.W. (1946) 'Effect of water currents upon the attachment and growth of barnacles', The Biological Bulletin, 90(1), pp. 51-70.

Spalding, D.B. (1961) 'A single formula for the "law of the wall"', Journal of Applied Mechanics, 28(3), pp. 455-458.

Standard ISO 4287 (1997) 'Geometrical product specifications (GPS)–Surface texture: Profile method–Terms, definitions and surface texture parameters'.

Staniforth, M. (1985) 'The introduction and use of copper sheathing-A history', Bulletin of the Australian Institute for Maritime Archaeology, The, 9(1/2), p. 21.

Stanton, T.E. (1911) 'The mechanical viscosity of fluids', Proceedings of the Royal Society of London. Series A, Containing Papers of a Mathematical and Physical Character, 85(579), pp. 366-376.

Stoodley, P., Boyle, J., Cunningham, A.B., Dodds, I., Lappin-Scott, H.M. and Lewandowski, Z. (1999) 'Biofilm structure and influence on biofouling under laminar and turbulent flows', Special Publication-Royal Society of Chemistry, 242, pp. 13-24.

Swain, G. (1999) 'Redefining antifouling coatings', Journal of Protective Coatings and Linings, 16, pp. 26-35.

Swain, G.W., Kovach, B., Touzot, A., Casse, F. and Kavanagh, C.J. (2007) 'Measuring the performance of today's antifouling coatings', Journal of Ship Production, 23(3), pp. 164-170.

Swain, G.W. and Schultz, M.P. (1996) 'The testing and evaluation of non-toxic antifouling coatings', Biofouling, 10(1-3), pp. 187-197.

Taylor, G.T., Zheng, D., Lee, M., Troy, P.J., Gyananath, G. and Sharma, S.K. (1997) 'Influence of surface properties on accumulation of conditioning films and marine bacteria on substrata exposed to oligotrophic waters', Biofouling, 11(1), pp. 31-57.

Tebbs, S.E., Sawyer, A. and Elliott, T.S.J. (1994) 'Influence of surface morphology on in vitro bacterial adherence to central venous catheters', BJA: British Journal of Anaesthesia, 72(5), pp. 587-591.

Thomas, T.R. (1999) Rough surfaces. Imperial College Press London.

Tittley, I. (1985) 'Seaweed communities on the artificial coastline of south-eastern England. 1. Reclaimed saline wetland and estuaries', Transactions of the Suffolk Naturalists' Society, 21, pp. 54-64.

Todd, F.H. and Taylor, D. (1967) 'Resistance and propulsion', Principles of Naval Architecture, pp. 288-462.

Townsend, A.A. (1980) The structure of turbulent shear flow. Cambridge university press.

Townsin, R.L. (2003) 'The ship hull fouling penalty', Biofouling, 19(S1), pp. 9-15.

Townsin, R.L. and Anderson, C.D. (2009) 'Fouling control coatings using low surface energy, foul release technology', in Advances in marine antifouling coatings and technologies. Elsevier, pp. 693-708.

Townsin, R.L. and Dey, S.K. (1990) 'The correlation of roughness drag with surface characteristics', Proceedings of the RINA International Workshop on Marine Roughness and Drag.

Tyler, P.A. and Marshall, K.C. (1967) 'Microbial oxidation of manganese in hydro-electric pipelines', Antonie van Leeuwenhoek, 33(1), pp. 171-183.

Ünal, B. (2012) Effect of surface roughness on the turbulent boundary layer. Doctoral thesis. Istanbul technical university, graduate school of science engineering and technology.

Ünal, U.O. (2015) 'Correlation of frictional drag and roughness length scale for transitionally and fully rough turbulent boundary layers', Ocean Engineering, 107, pp. 283-298.

Ünal, U.O., Ünal, B. and Atlar, M. (2012) 'Turbulent boundary layer measurements over flat surfaces coated by nanostructured marine antifoulings', Experiments in fluids, 52(6), pp. 1431-1448.

Visscher, J.P. (1928) Nature and extent of fouling of ships' bottoms. US Government Printing Office.

Watanuki, A. and Yamamoto, A. (1990) 'Settlement of seaweeds on coastal structures', Hydrobiologia, 204(1), pp. 275-280.

Weinell, C.E., Olsen, K.N., Christoffersen, M.W. and Kiil, S. (2003) 'Experimental study of drag resistance using a laboratory scale rotary set-up', Biofouling, 19(S1), pp. 45-51.

Wells, S. and Sytsma, M. (2013) Estimating costs of using foul-release type coatings to mitigate Dreissena sp. mussel macrofouling at a FCRPS facility. Bonneville Power Administration and Pacific States Marine Fisheries Commission.

White, F.M. and Corfield, I. (2006) Viscous Fluid Flow. McGraw-Hill, New York.

Whitehead, K.A. and Verran, J. (2006) 'The effect of surface topography on the retention of microorganisms', Food and bioproducts processing, 84(4), pp. 253-259.

Whitehouse, D.J. (2010) Handbook of surface and nanometrology. CRC press.

Williams, H. (1923) 'Notes on Fouling Of Ships 'Bottoms and the Effect on Fuel Consumption', Journal of the American Society for Naval Engineers, 35(2), pp. 357-374.

Woods Hole Oceanographic Institution (1952) Marine fouling and its prevention. United States Naval Institute, Annapolis, Maryland, United States.

Xin, Z., Xiao-Hui, S. and Dian-Lin, Z. (2010) 'Thickness dependence of grain size and surface roughness for dc magnetron sputtered Au films', Chinese Physics B, 19(8), p. 086802.

Yaglom, A.M. (1979) 'Similarity laws for constant-pressure and pressure-gradient turbulent wall flows', Annual Review of Fluid Mechanics, 11(1), pp. 505-540.

Young, C.F.T. (1867) The fouling and corrosion of iron ships: Their causes and means of prevention, with the mode of application to the existing iron-clads. London Drawing Association.

Zaidi, B.R., Bard, R.F. and Tosteson, T.R. (1984) 'Microbial specificity of metallic surfaces exposed to ambient seawater', Applied and environmental microbiology, 48(3), pp. 519-524.

Zanoun, E.S., Nagib, H. and Durst, F. (2009) 'Refined cf relation for turbulent channels and consequences for high-Re experiments', Fluid dynamics research, 41(2), p. 021405.

Zhao, W. and Wang, X. (2015) 'Antifouling based on biocides: From toxic to green', in Antifouling Surfaces and Materials. Springer, pp. 105-134.

Zheng, D., Taylor, G.T. and Gyananath, G. (1994) 'Influence of laminar flow velocity and nutrient concentration on attachment of marine bacterioplankton', Biofouling, 8(2), pp. 107-120.

Zobell, C.E. (1938) 'The sequence of events in the fouling of submerged surfaces', Paint and Varnish Production Manager, 11, pp. 379-385.

Zobell, C.E. (1939) 'Primary film formation by bacteria and fouling', Collecting Net, 14(5), pp. 105-106.

Zobell, C.E. (1943) 'The effect of solid surfaces upon bacterial activity', Journal of bacteriology, 46(1), p. 39.

Zobell, C.E. and Allen, E.C. (1935) 'The significance of marine bacteria in the fouling of submerged surfaces', Journal of bacteriology, 29(3), p. 239.

Appendix A Dynamic/Static Deployments of Test Panels

C12 Panels

C17 Panels

C25 Panels

Test panels installed on strut

Unfouled test panels installed on strut

6-month fouled test panels installed on strut

The strut is installing on *The Princess Royal*

The strut installed on *The Princess Royal*

Dynamic deployment area

Static deployment area

Appendix B Roughness Topography for Unfouled Surfaces

Appendix B.1 Roughness Topography for 1st Surface Applications

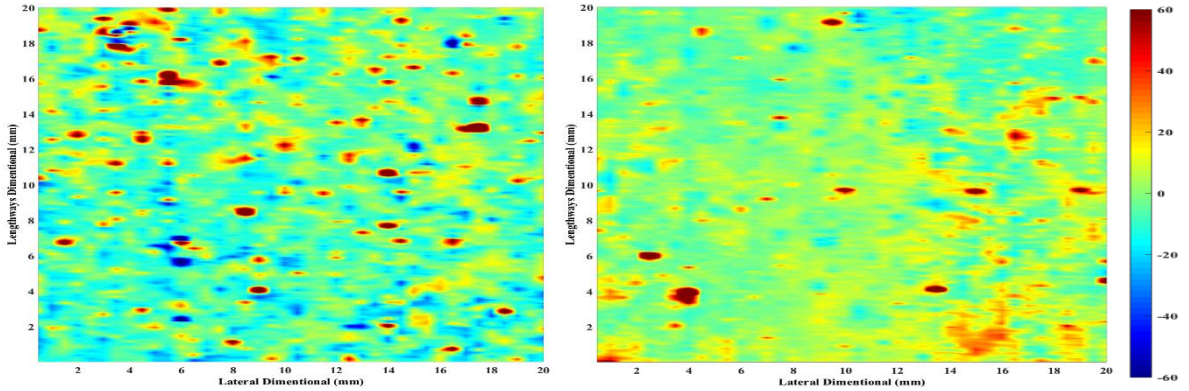

C2 Panel_A C2_Panel_B

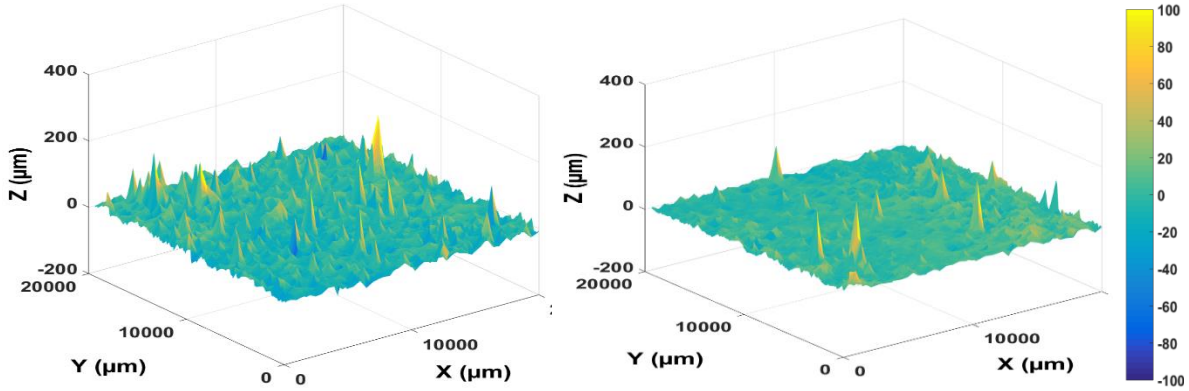

C2 Panel_A C2 Panel_B

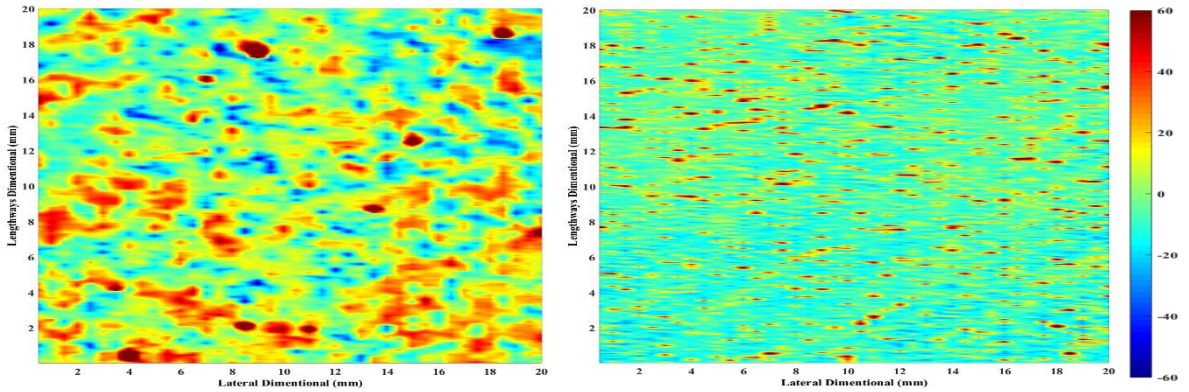

C7 Panel_A C7 Panel_B

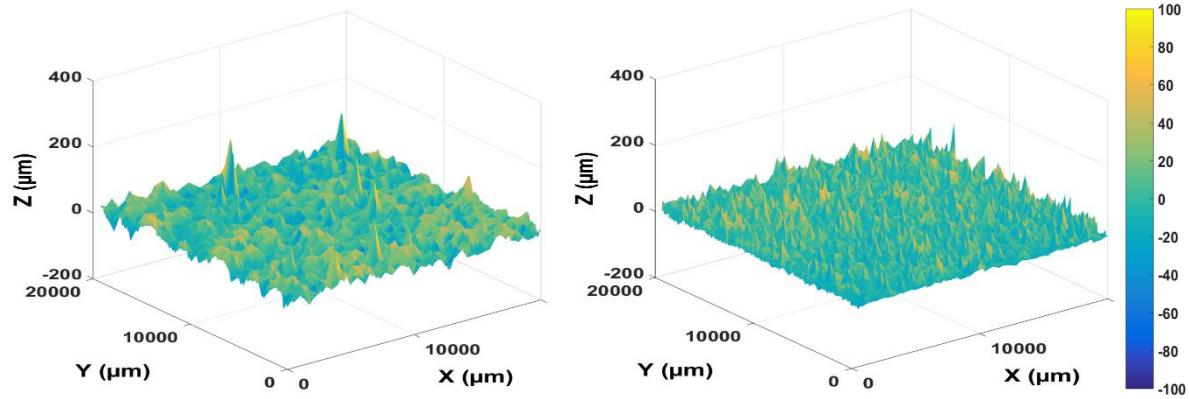

C7 Panel_A C7 Panel_B

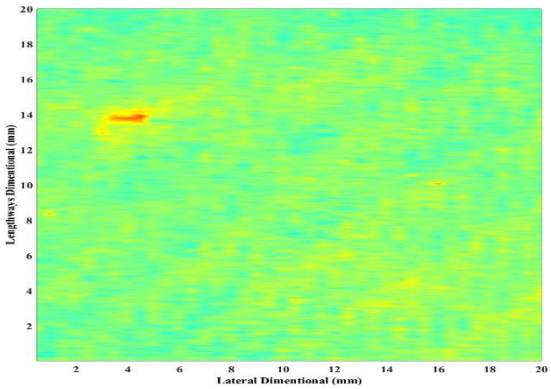

C12 Panel_A

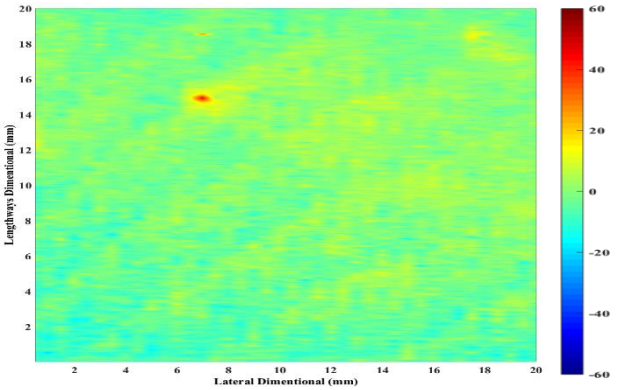

C12 Panel_B

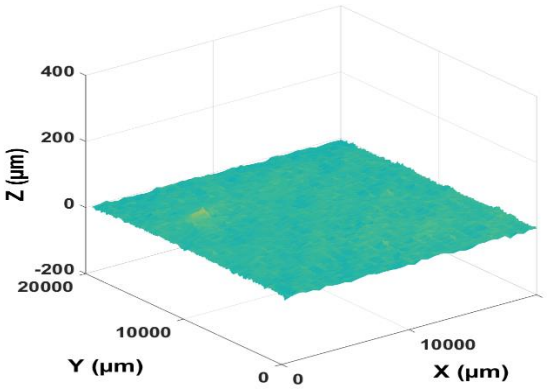

C12 Panel_A

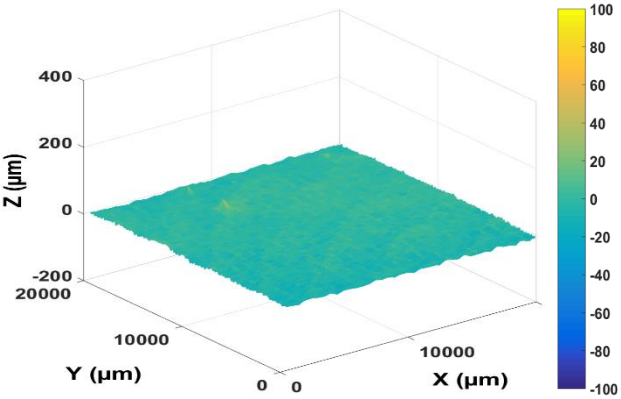

C12 Panel_B

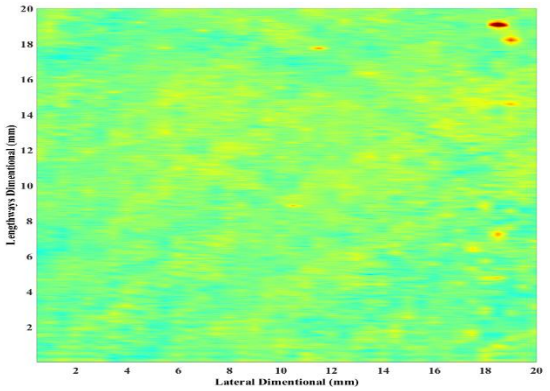

C17 Panel_A

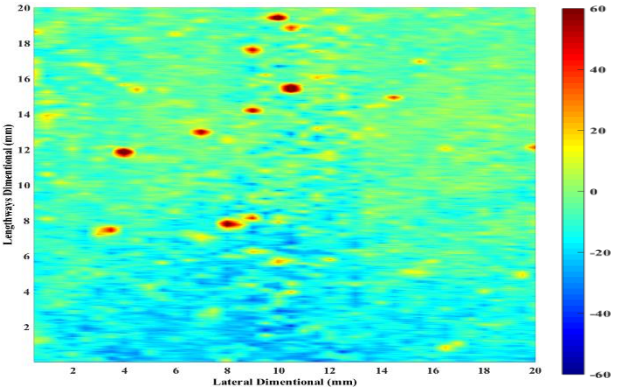

C17 Panel_B

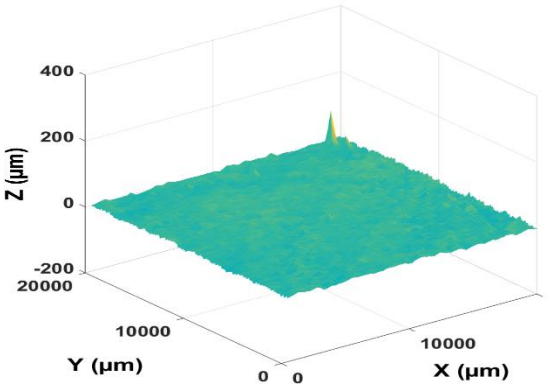

C17 Panel_A

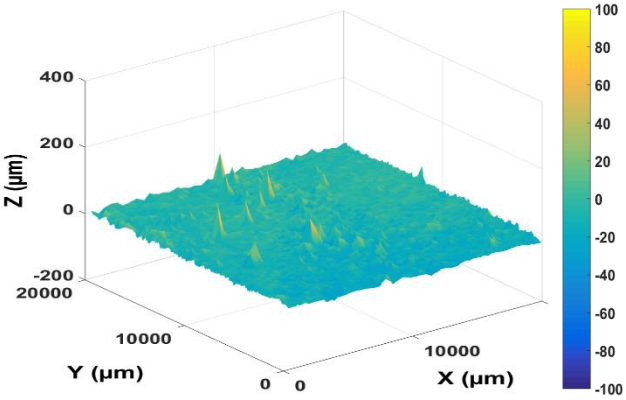

C17 Panel_B

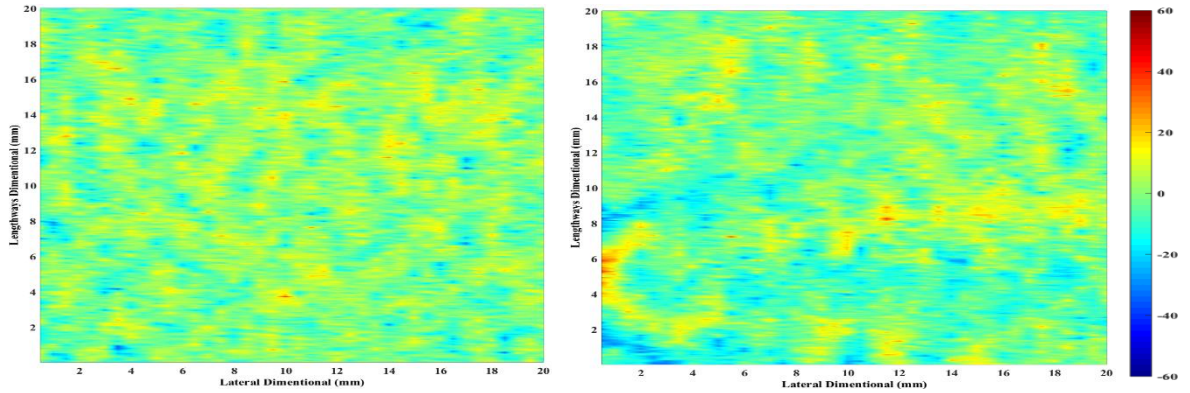

C25 Panel_A C25 Panel_B

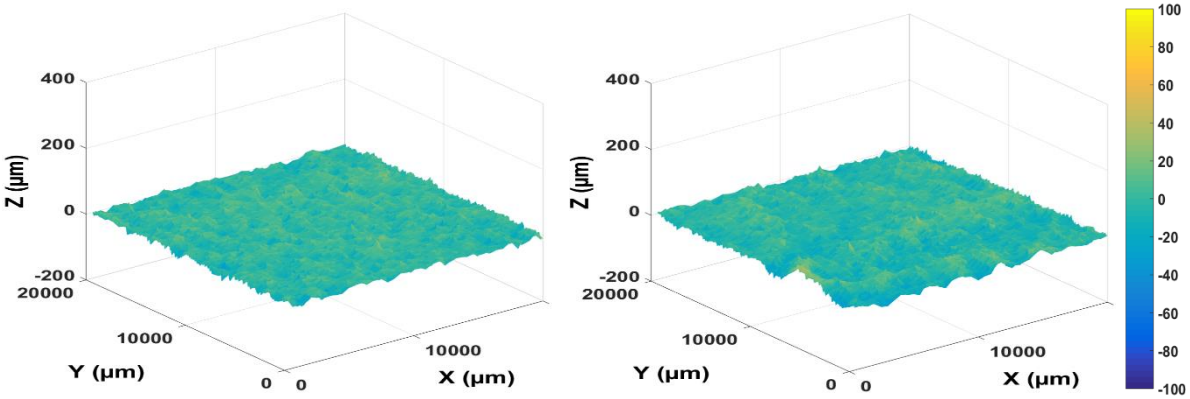

C25 Panel_A C25 Panel_B

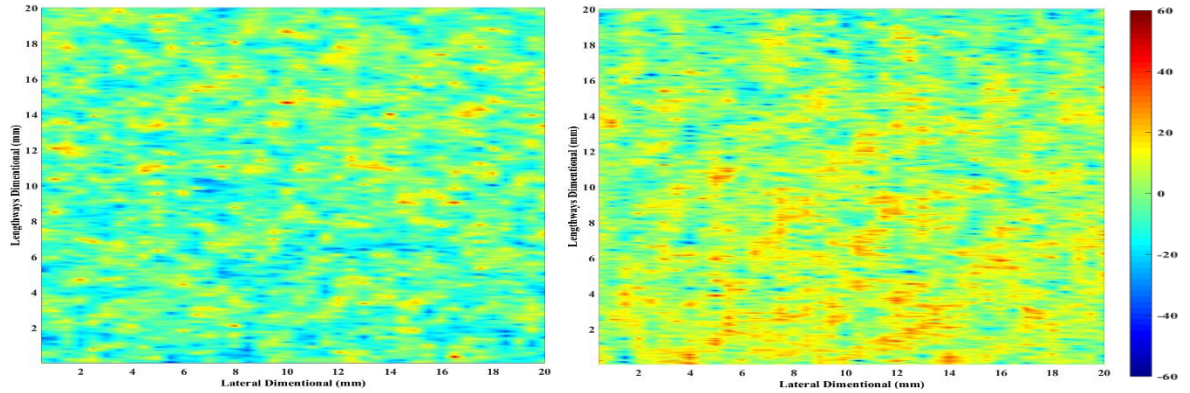

C60 Panel_A C60 Panel_B

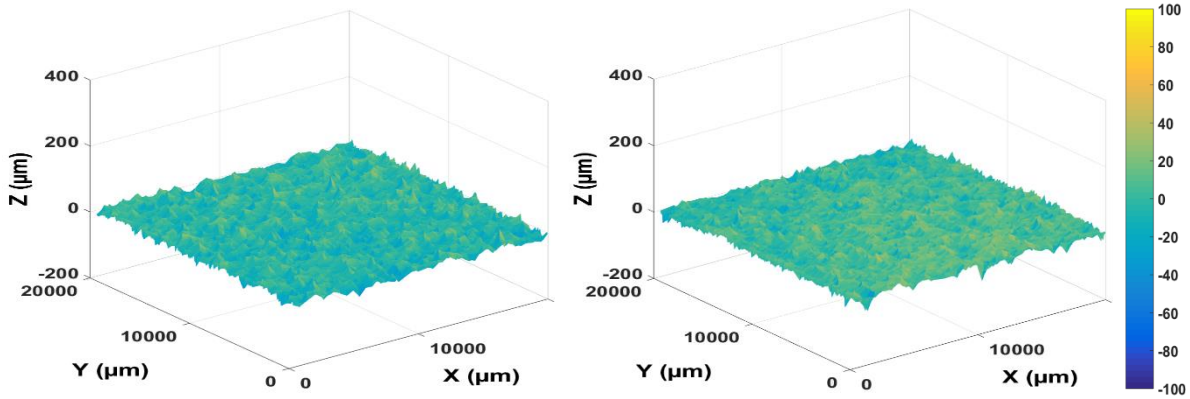

C60 Panel_A C60 Panel_B

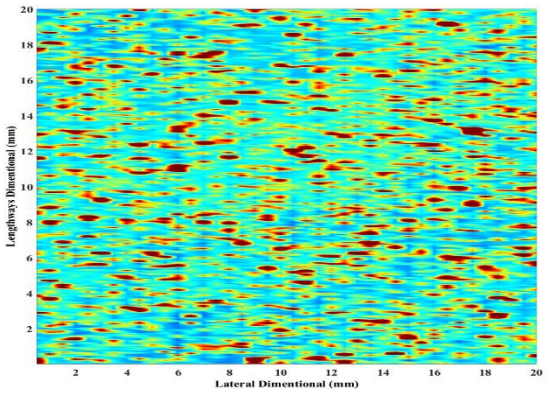

C100 Panel_A

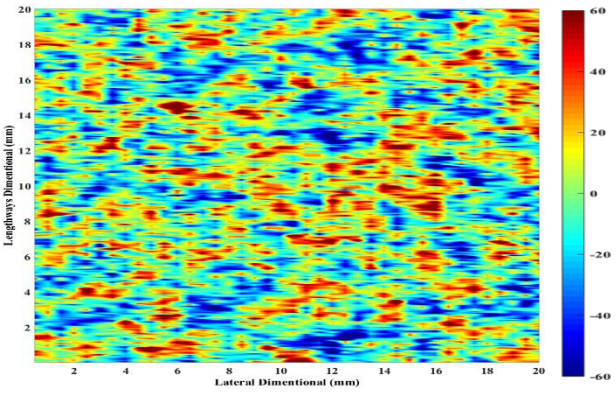

C100 Panel_B

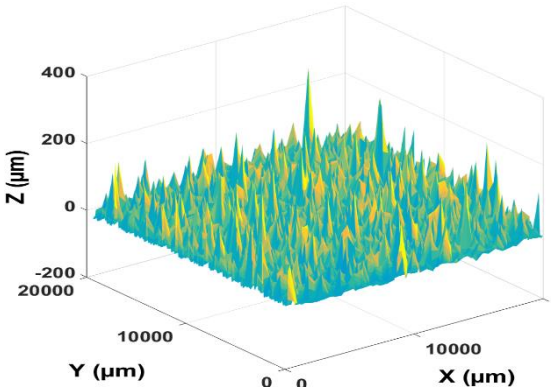

C100 Panel_A

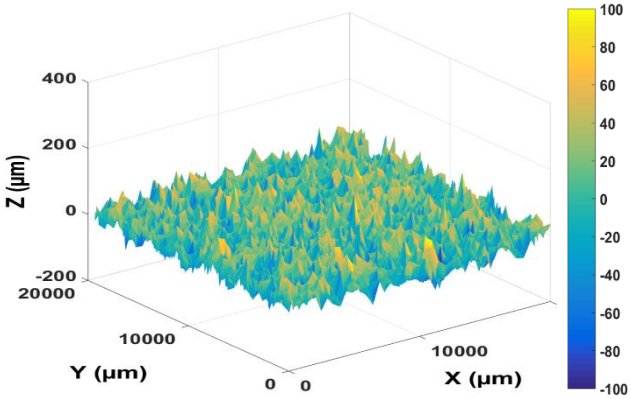

C100 Panel_B

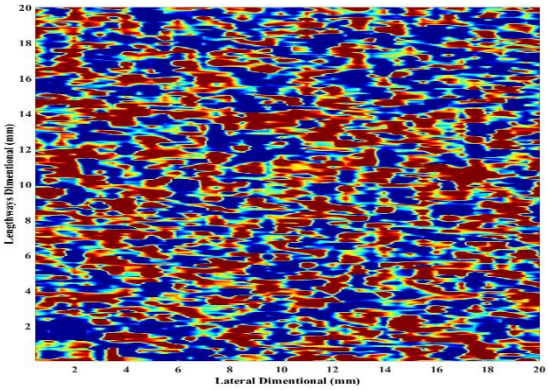

C250 Panel_A

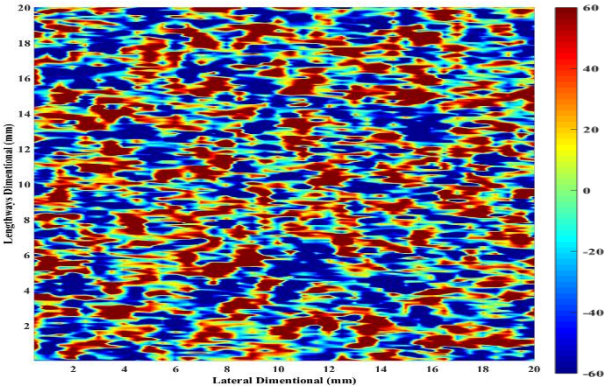

C250 Panel_B

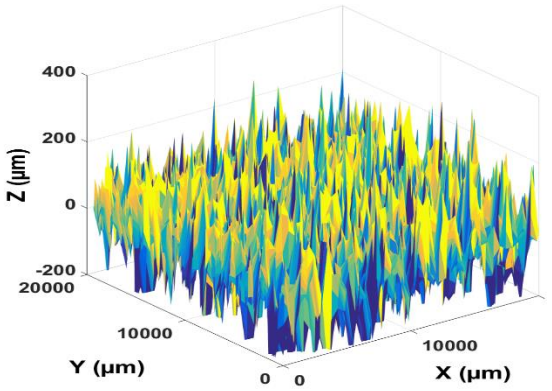

C250 Panel_A

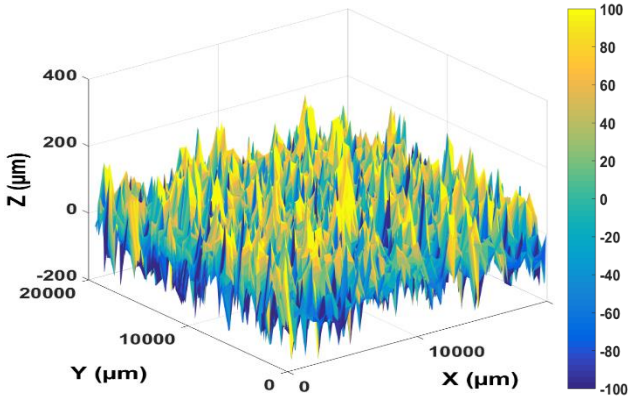

C250 Panel_B

Appendix B.2 Roughness Topography for 2nd Surface Application

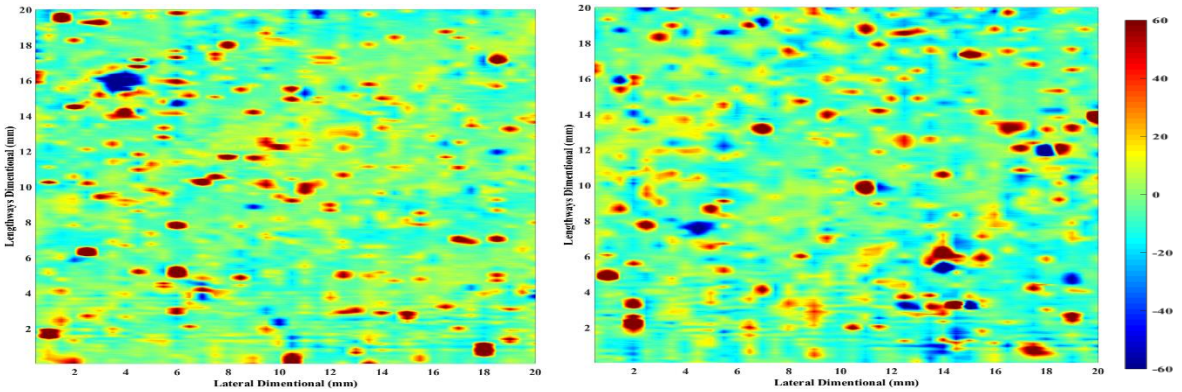

C2 Panel_A C2_Panel_B

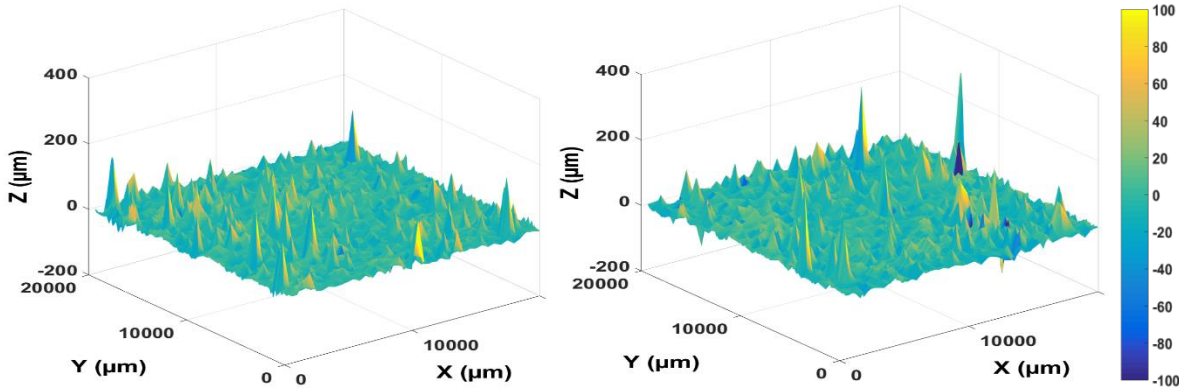

C2 Panel_A C2 Panel_B

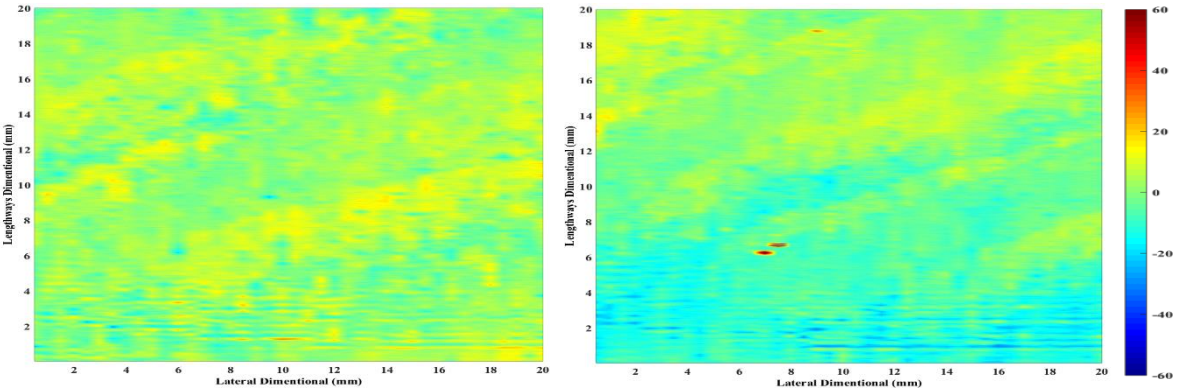

C7 Panel_A C7 Panel_B

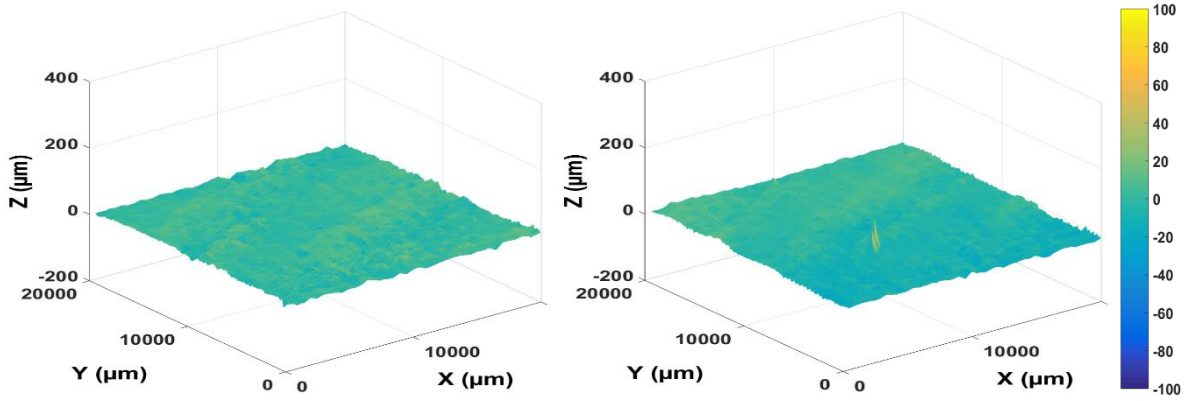

C7 Panel_A C7 Panel_B

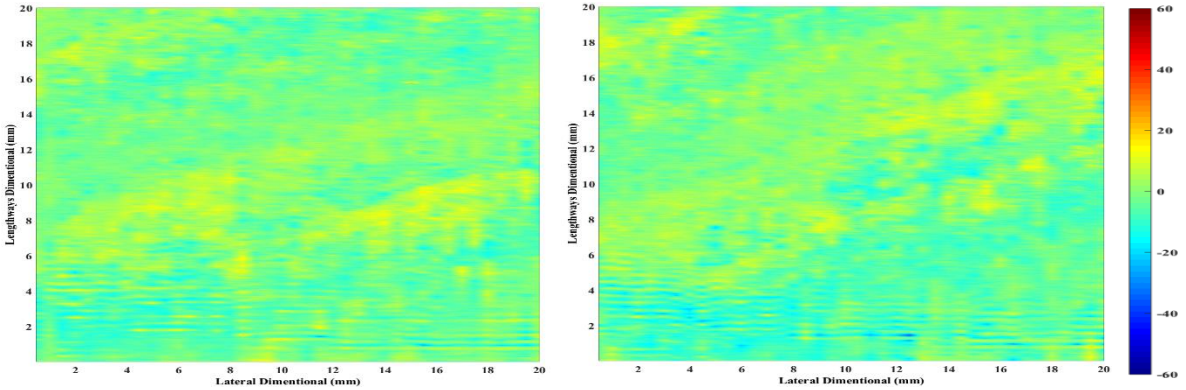

C12 Panel_A C12 Panel_B

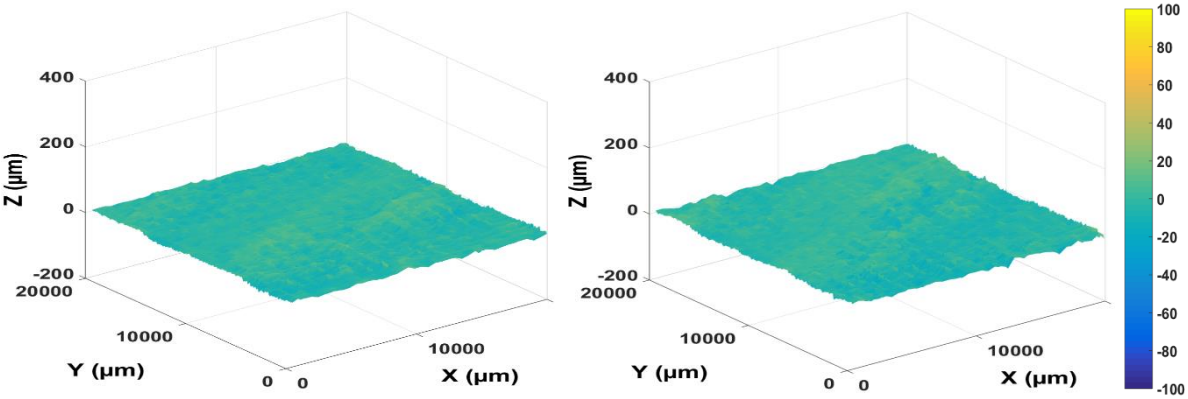

C12 Panel_A C12 Panel_B

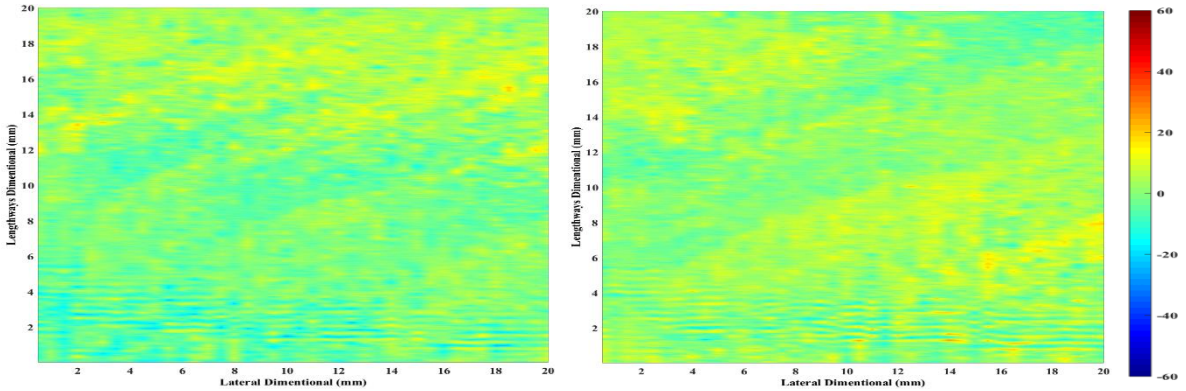

C17 Panel_A C17 Panel_B

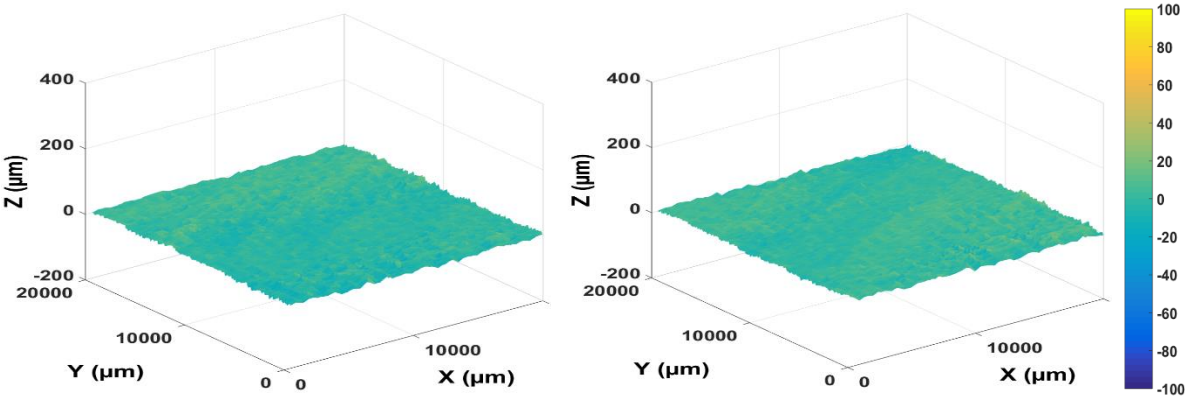

C17 Panel_A C17 Panel_B

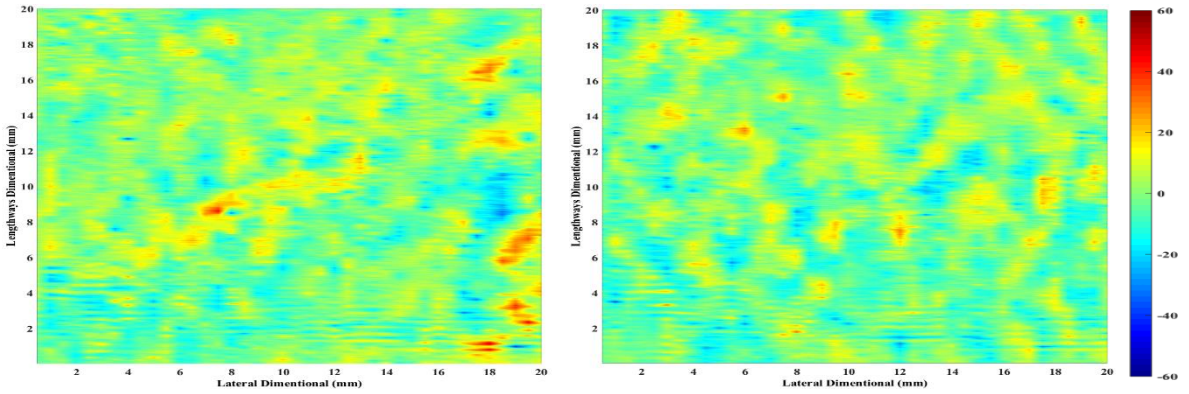

C25 Panel_A C25 Panel_B

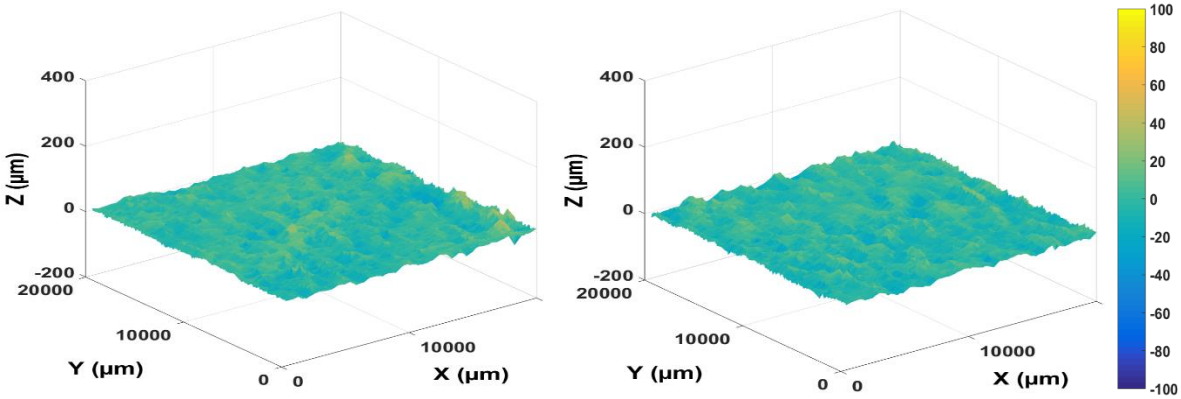

C25 Panel_A C25 Panel_B

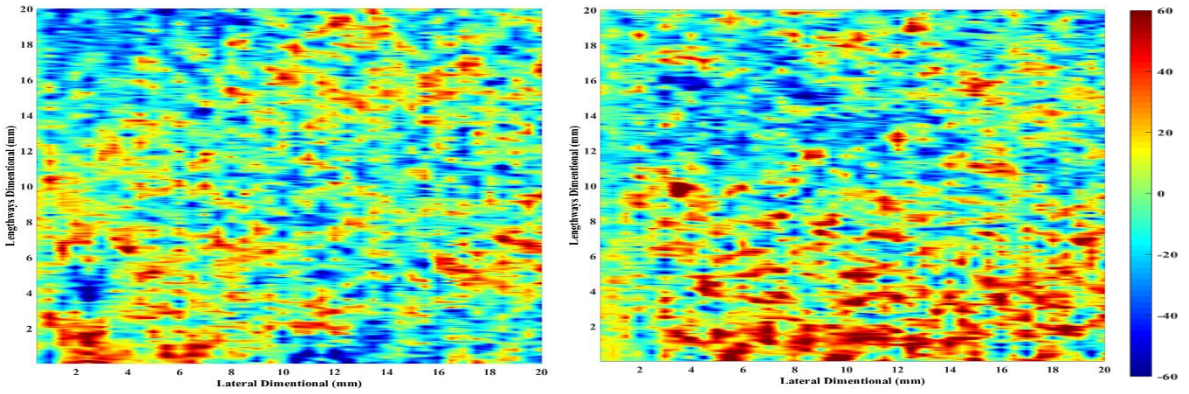

C60 Panel_A C60 Panel_B

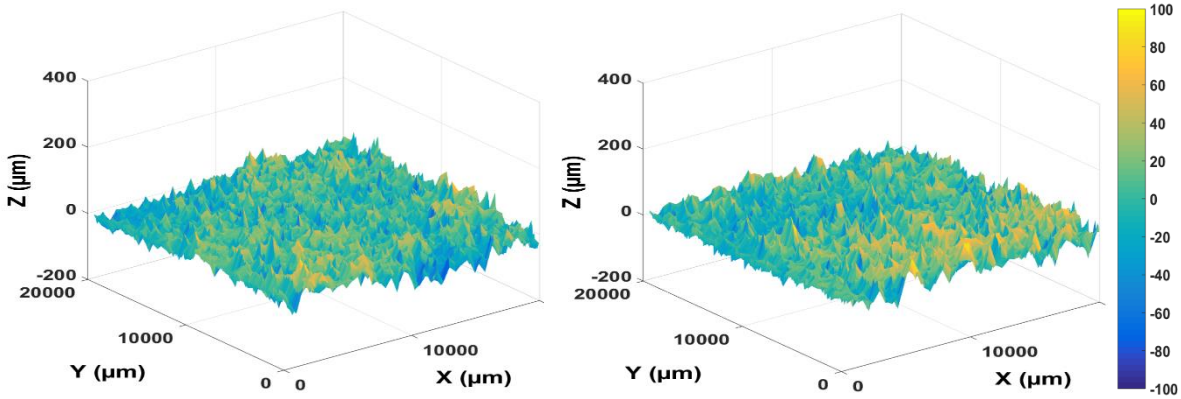

C60 Panel_A C60 Panel_B

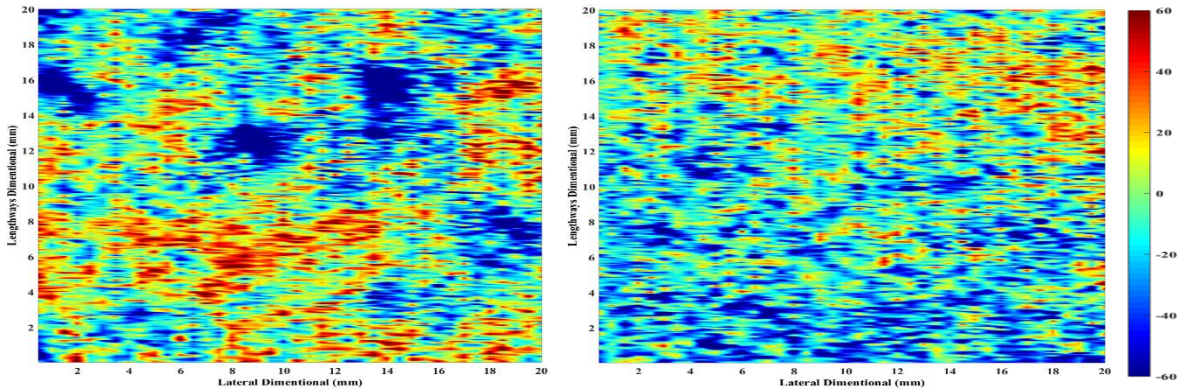

C100 Panel_A C100 Panel_B

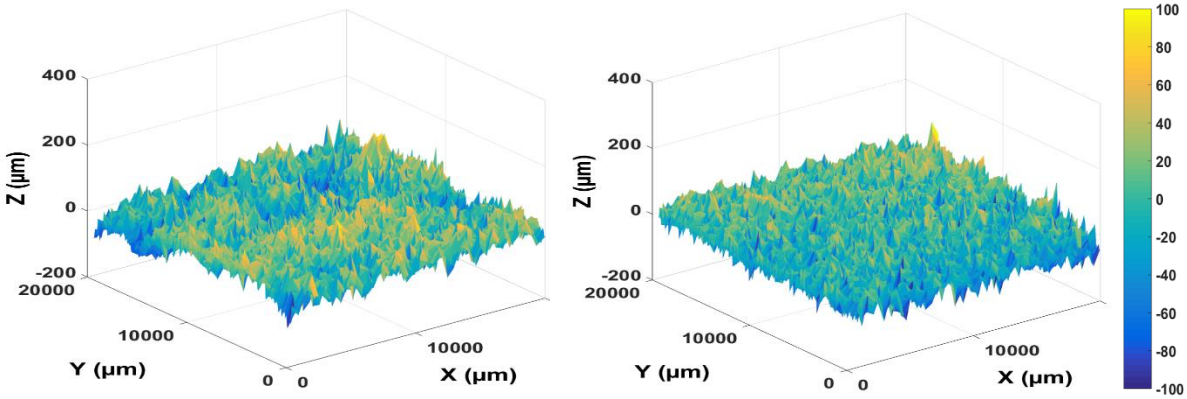

C100 Panel_A C100 Panel_B

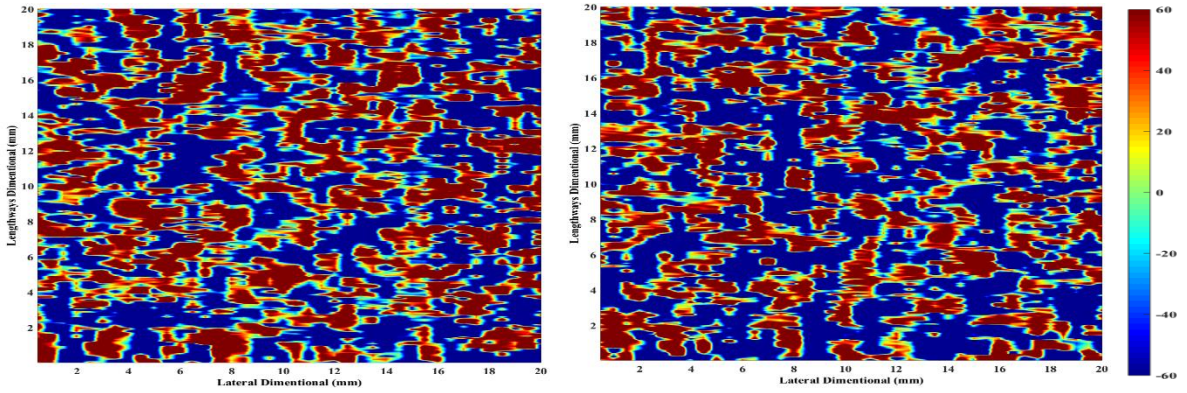

C250 Panel_A C250 Panel_B

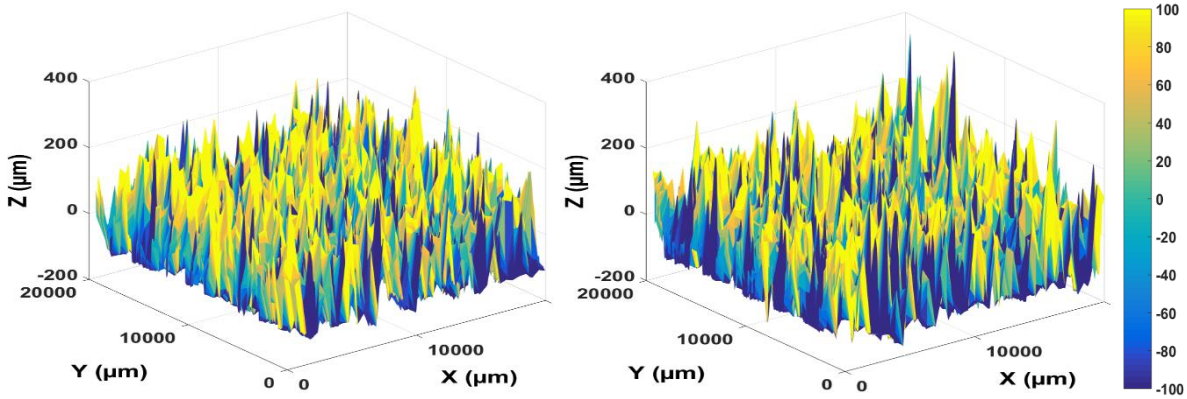

C250 Panel_A C250 Panel_B

Appendix C Roughness Topography for Biofilm Fouled Surfaces

Appendix C.1 Roughness Topography for Surfaces Fouled with 1.5-Month Biofilm

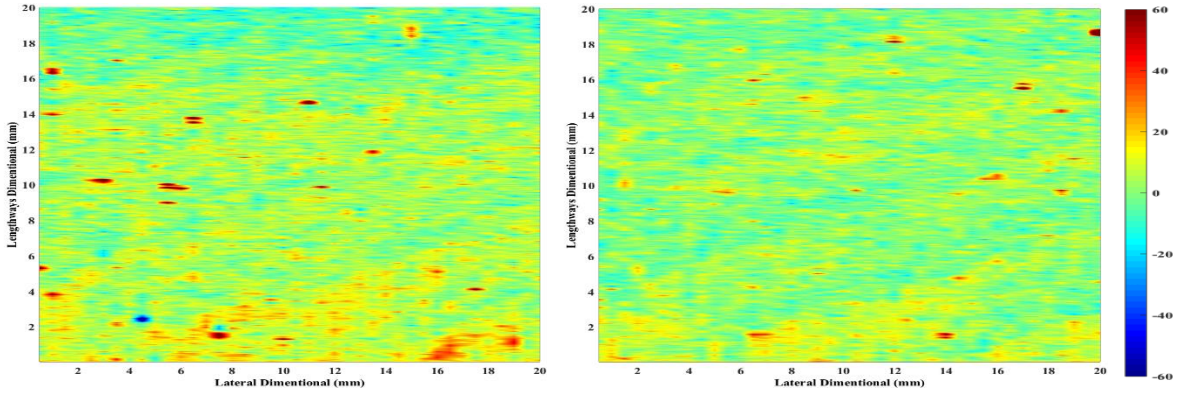

C12 Panel_A C12_Panel_B

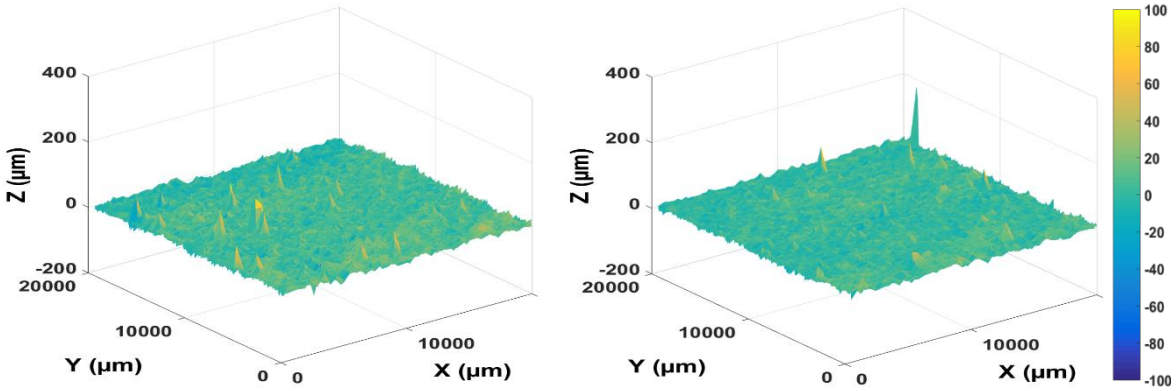

C12 Panel_A C12 Panel_B

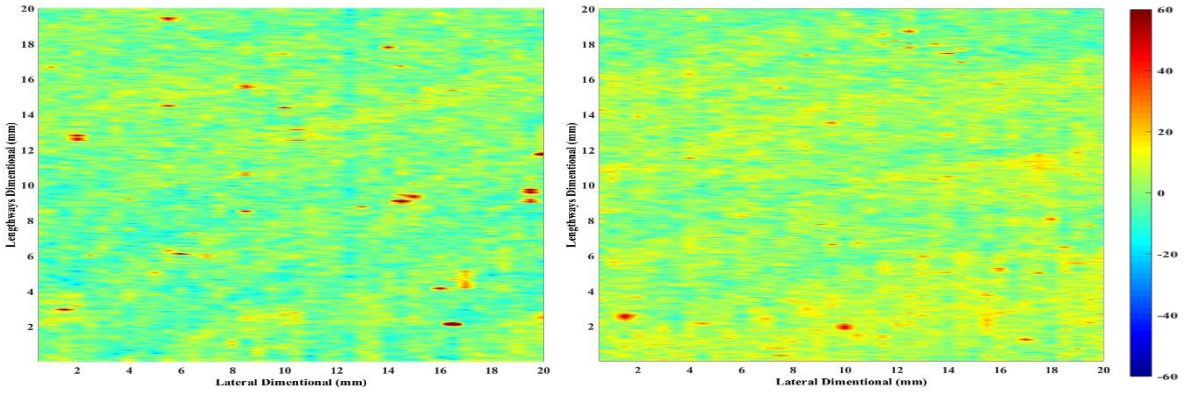

C17 Panel_A C17 Panel_B

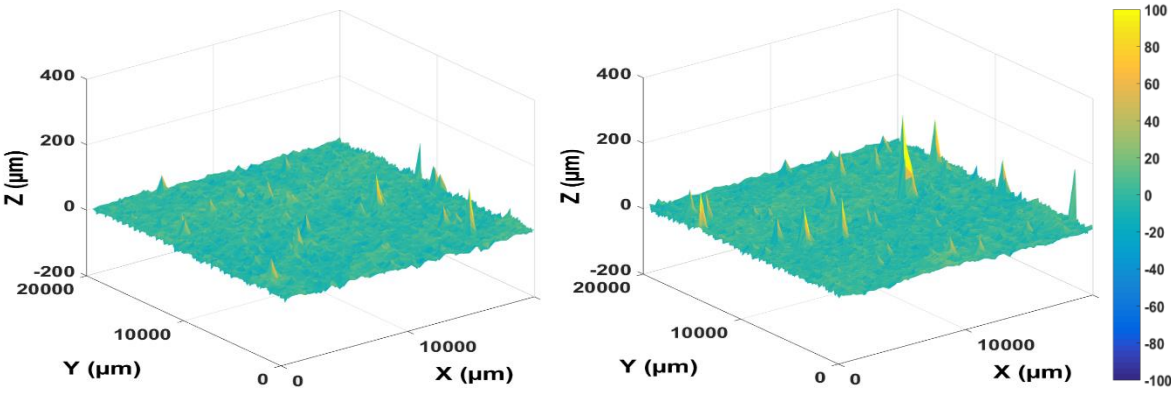

C17 Panel_A C17 Panel_B

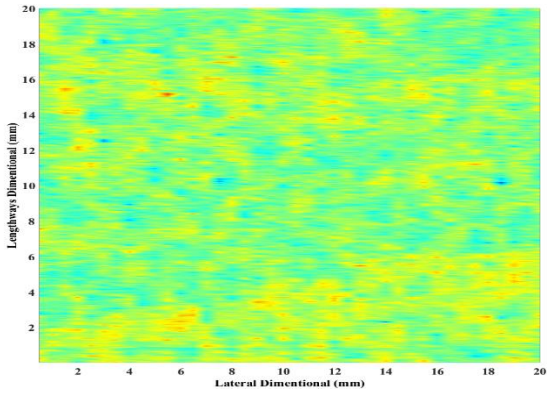

C25 Panel_A

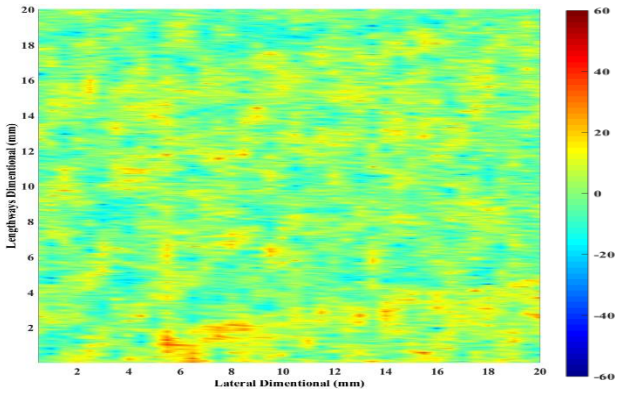

C25 Panel_B

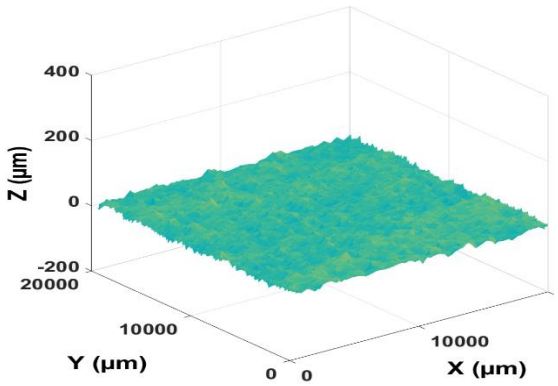

C25 Panel_A

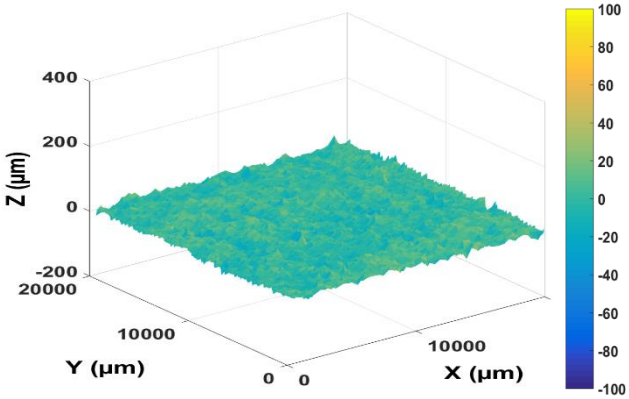

C25 Panel_B

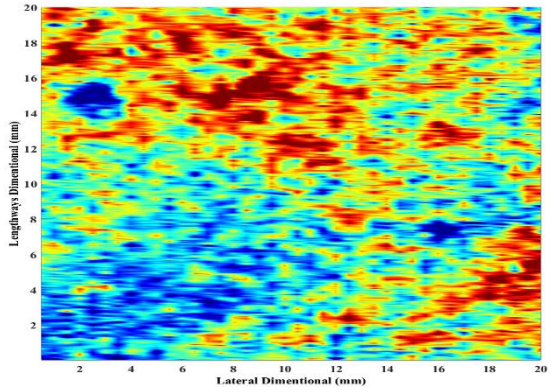

C60 Panel_A

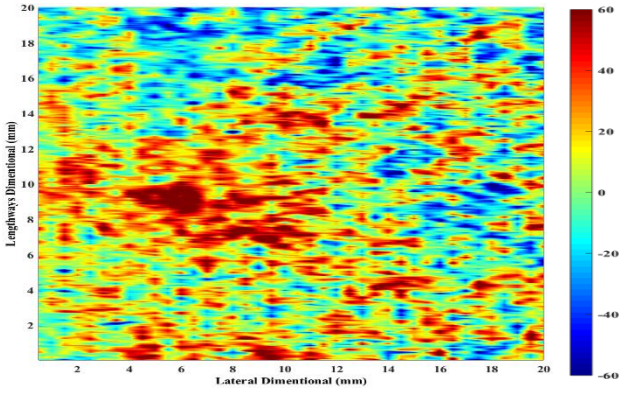

C60 Panel_B

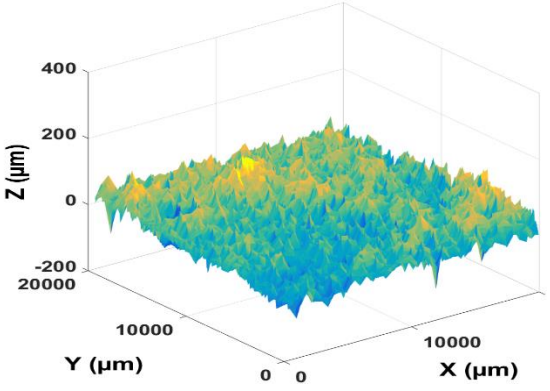

C60 Panel_A

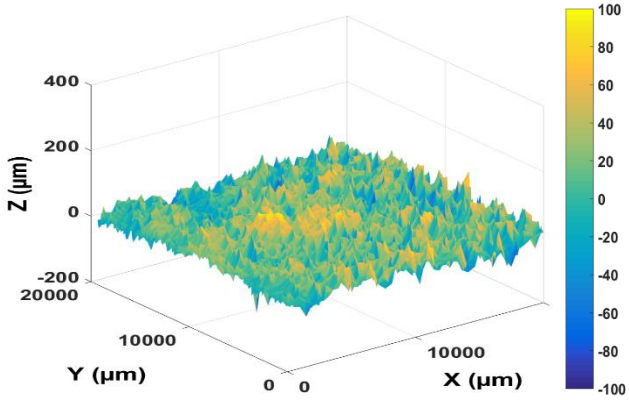

C60 Panel_B

Appendix C.2 Roughness Topography for Surfaces Fouled with 3-Month Biofilm

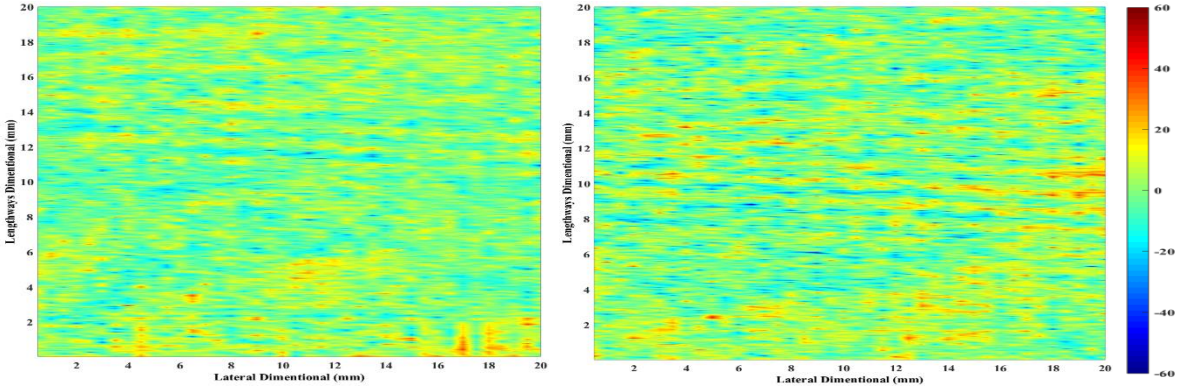

C12 Panel_A C12_Panel_B

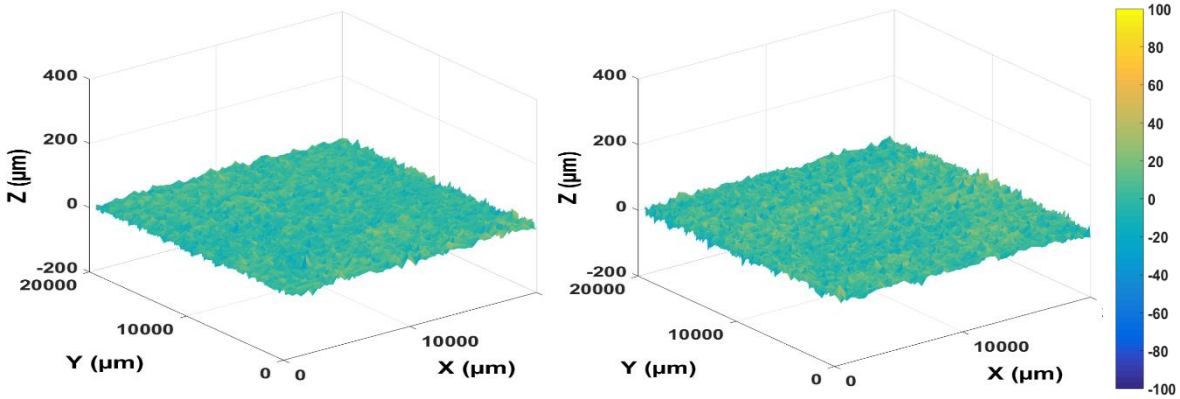

C12 Panel_A C12 Panel_B

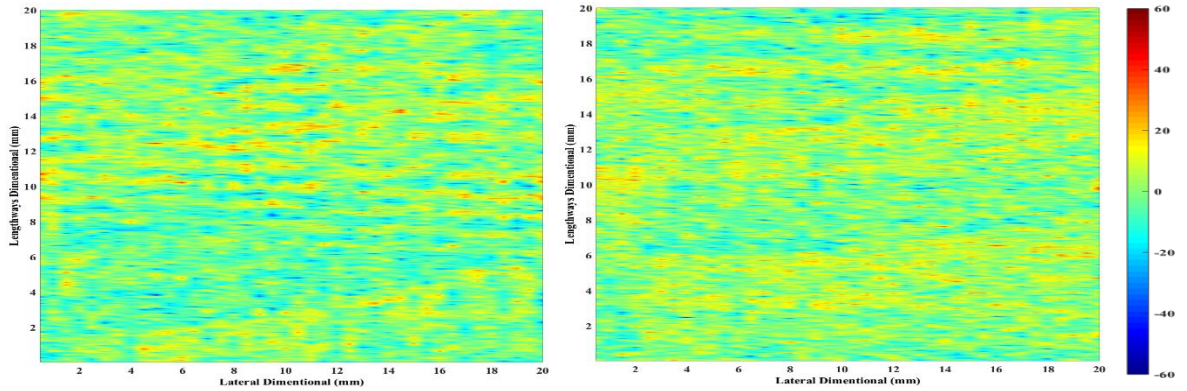

C17 Panel_A C17 Panel_B

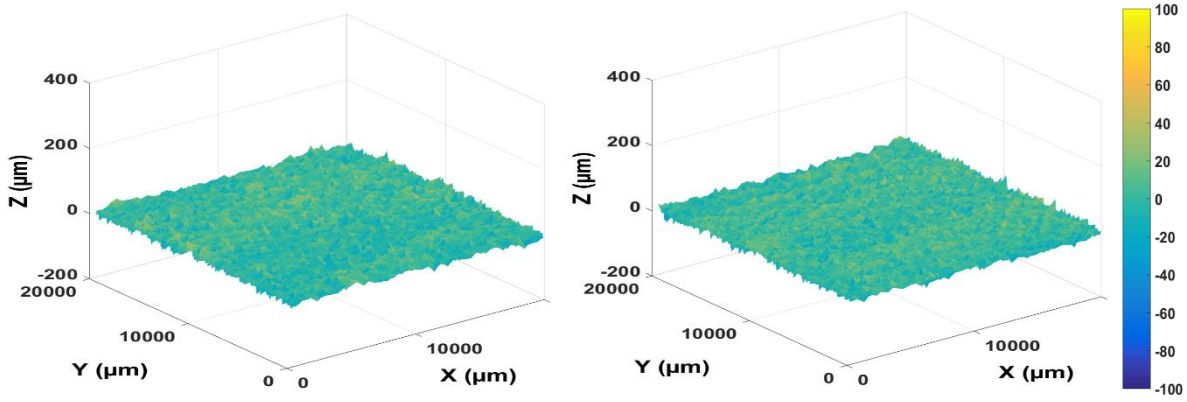

C17 Panel_A C17 Panel_B

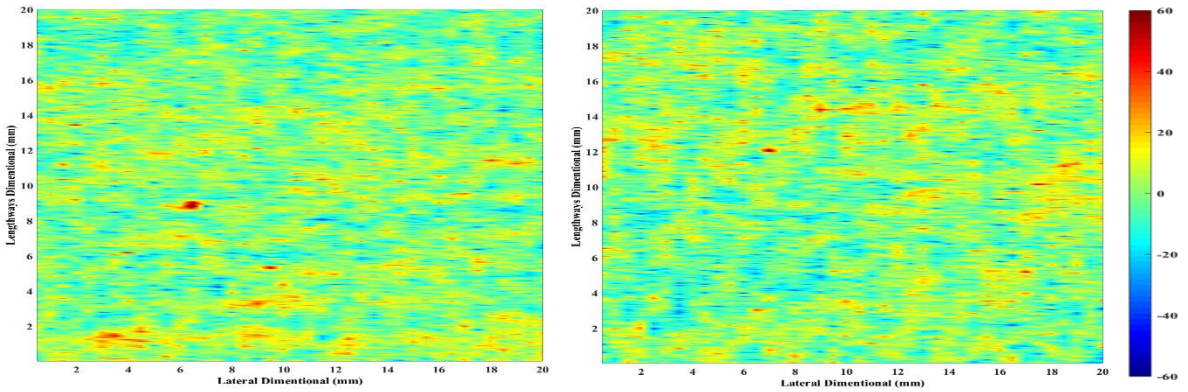

C25 Panel_A C25 Panel_B

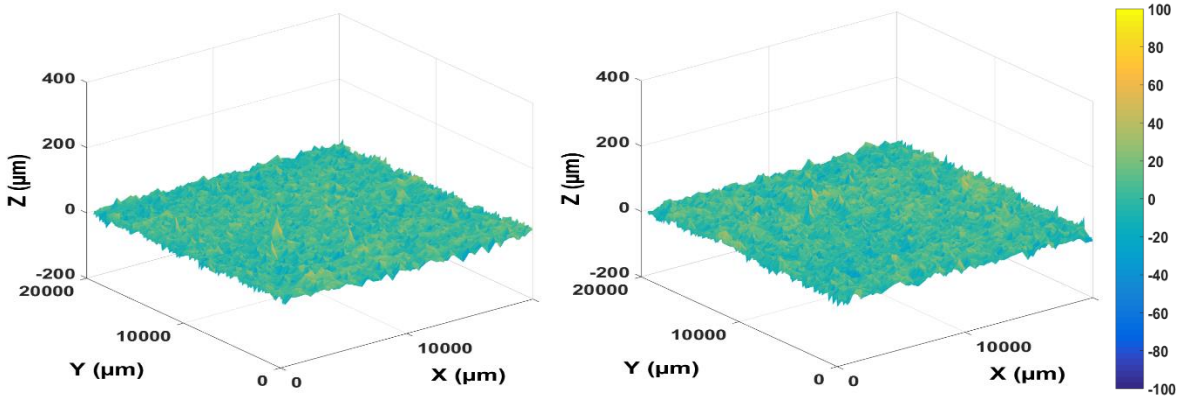

C25 Panel_A C25 Panel_B

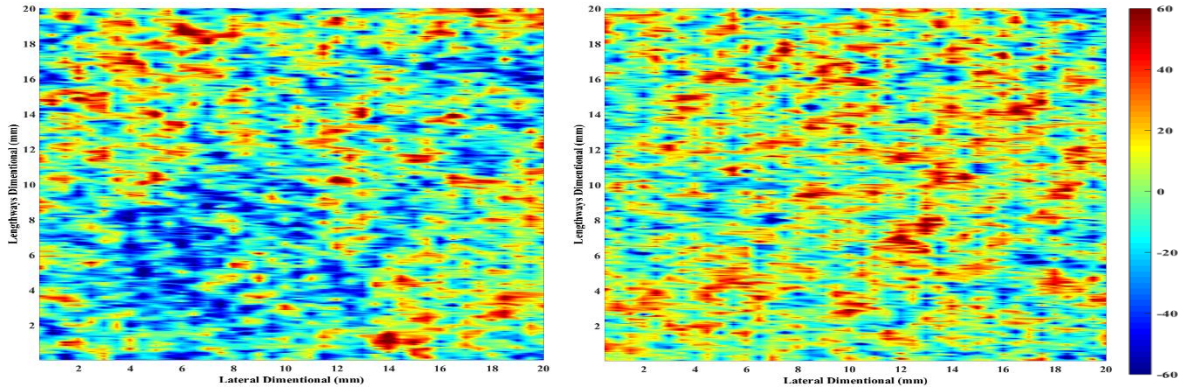

C60 Panel_A C60 Panel_B

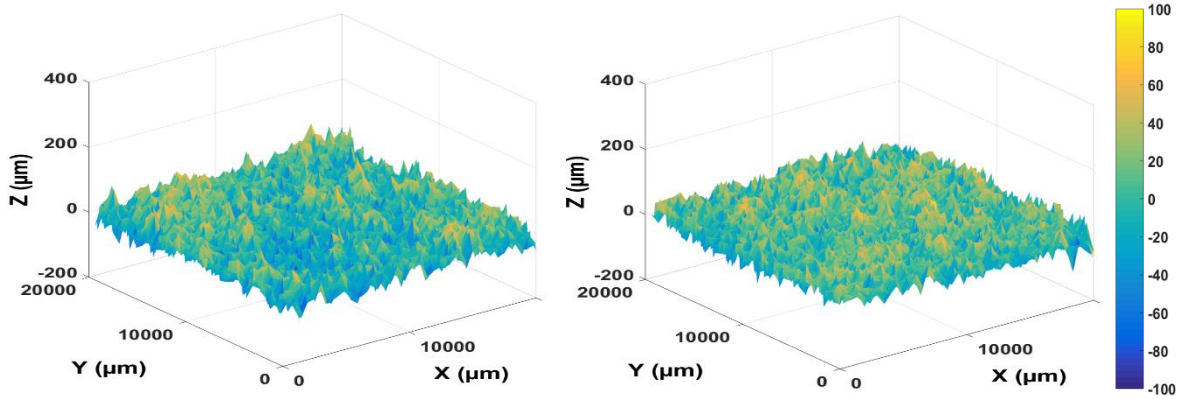

C60 Panel_A C60 Panel_B

Appendix C.3 Roughness Topography for Surfaces Fouled with 4.5-Month Biofilm

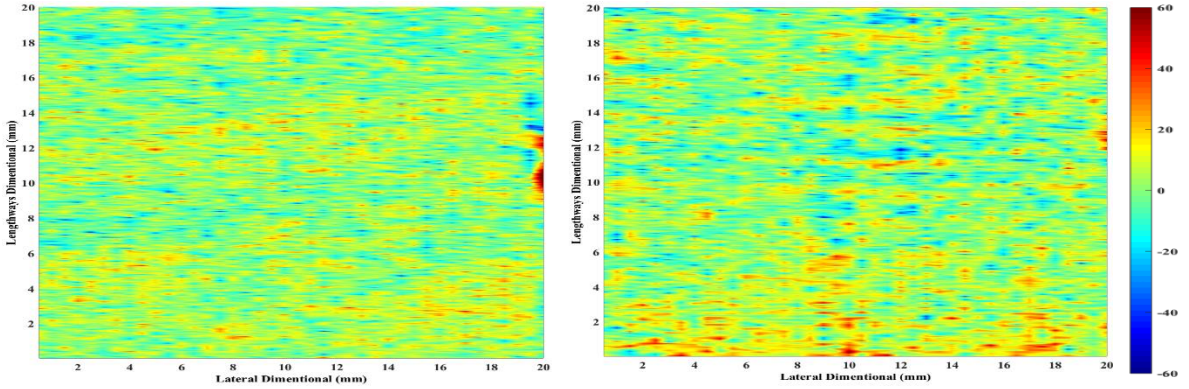

C12 Panel_A C12_Panel_B

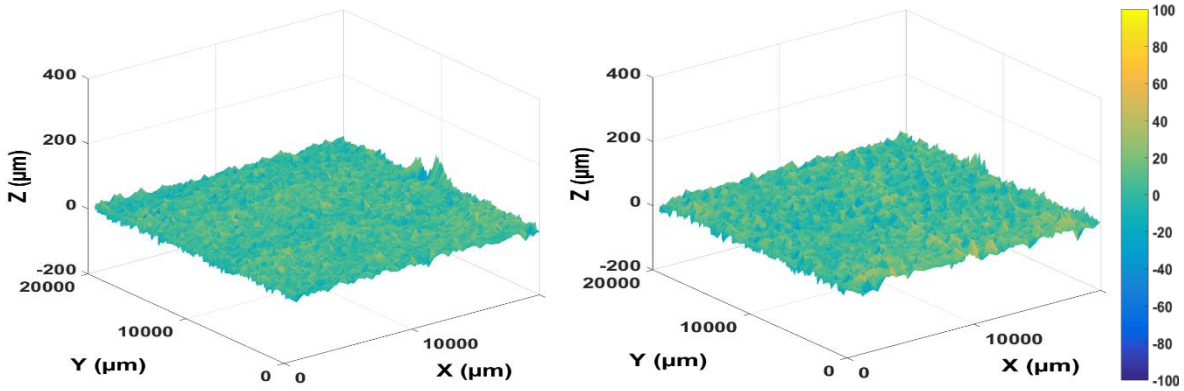

C12 Panel_A C12 Panel_B

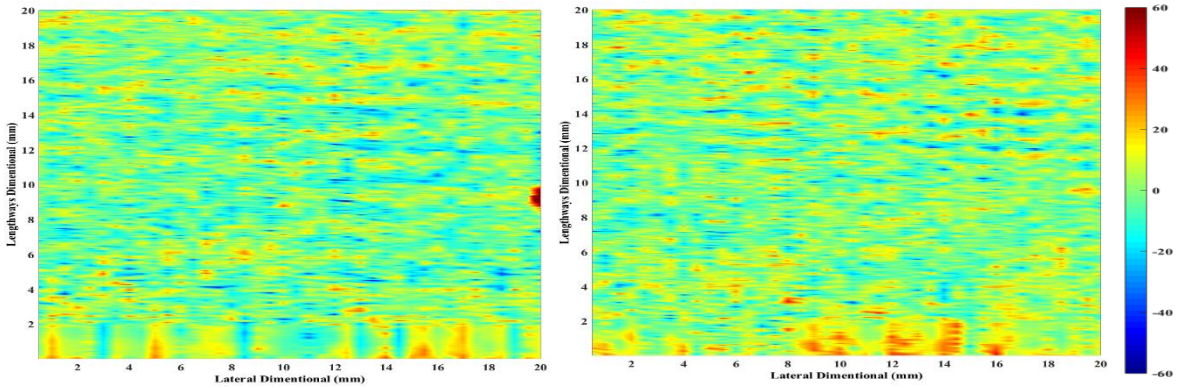

C17 Panel_A C17 Panel_B

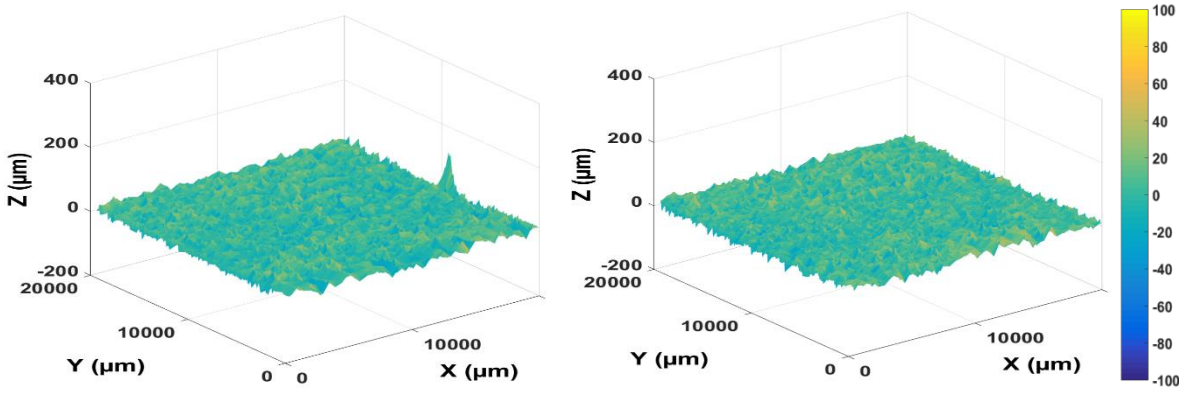

C17 Panel_A C17 Panel_B

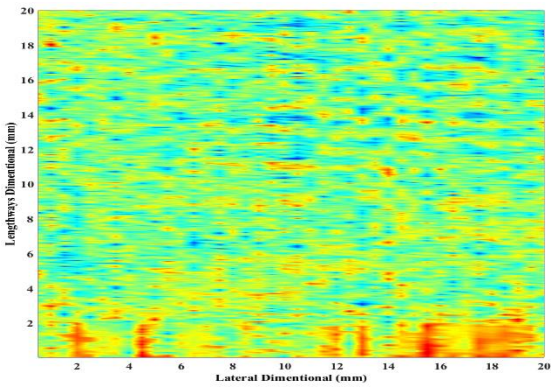

C25 Panel_A

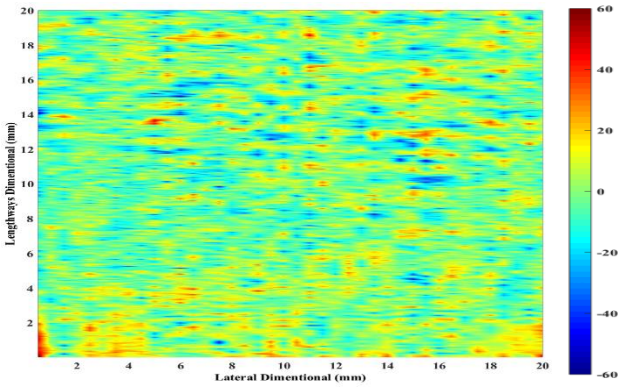

C25 Panel_B

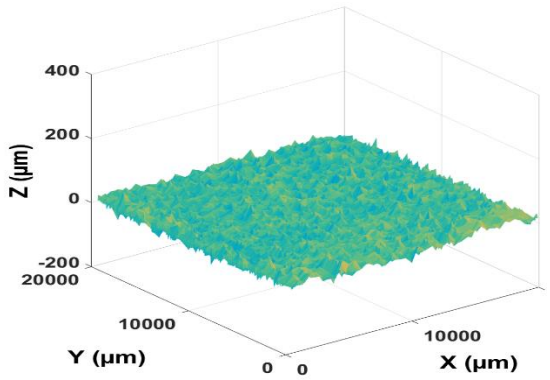

C25 Panel_A

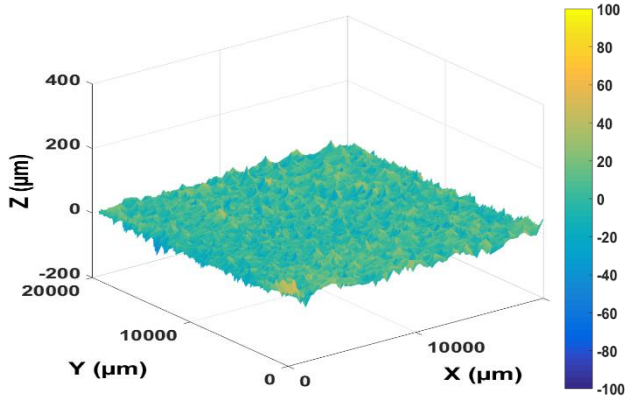

C25 Panel_B

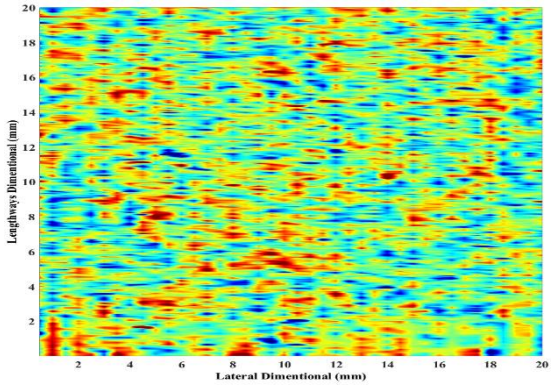

C60 Panel_A

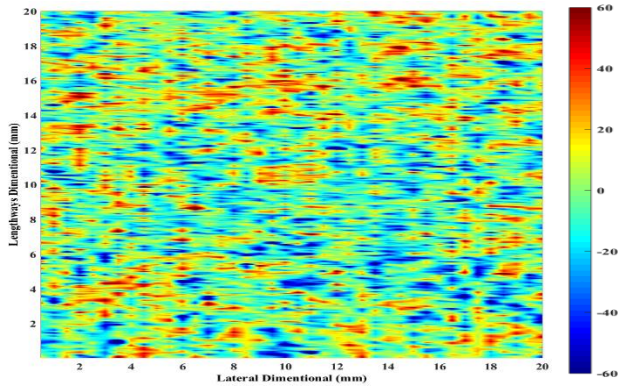

C60 Panel_B

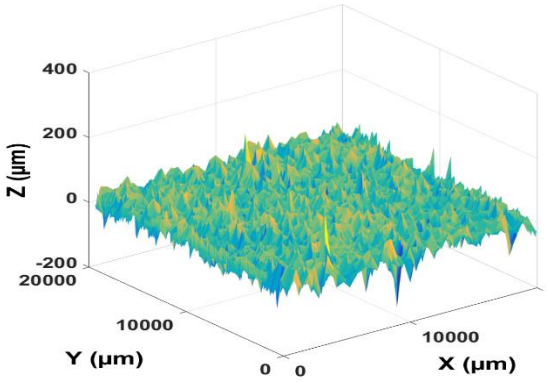

C60 Panel_A

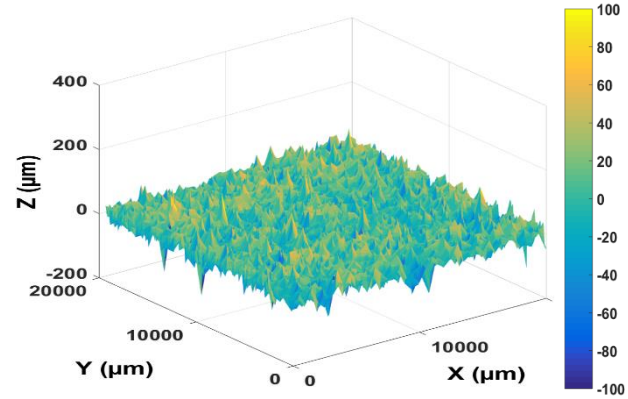

C60 Panel_B

Appendix C.4 Roughness Topography for Surfaces Fouled with 6-Month Biofilm

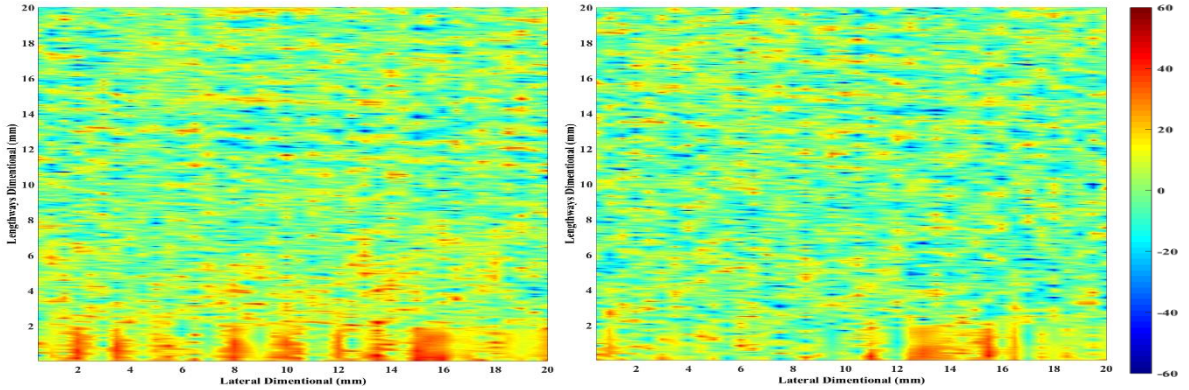

C12 Panel_A C12_Panel_B

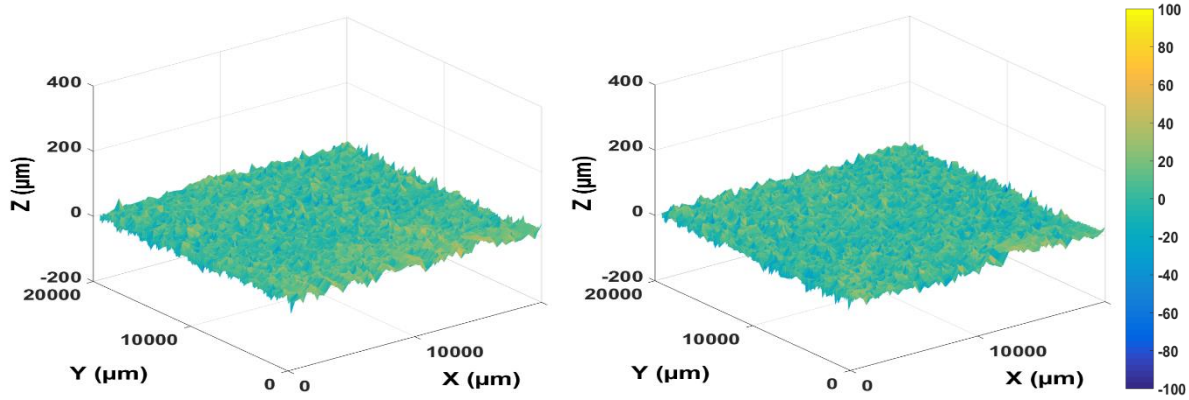

C12 Panel_A C12 Panel_B

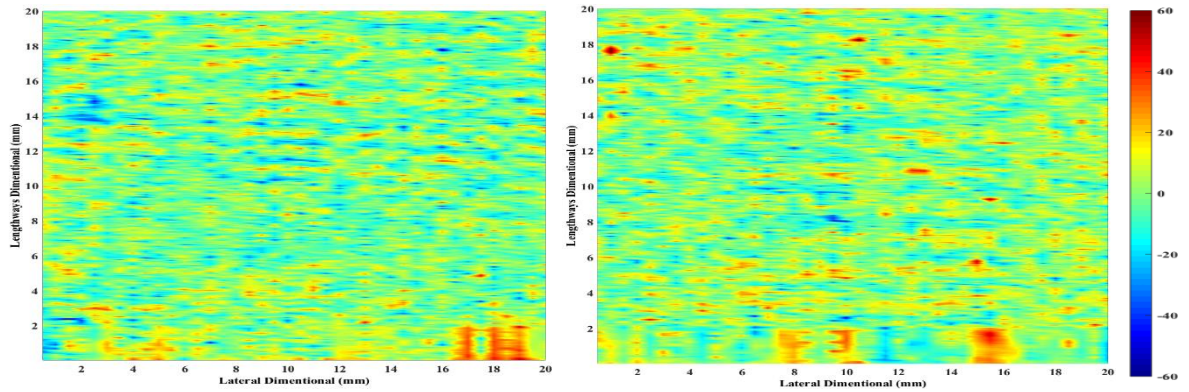

C17 Panel_A C17 Panel_B

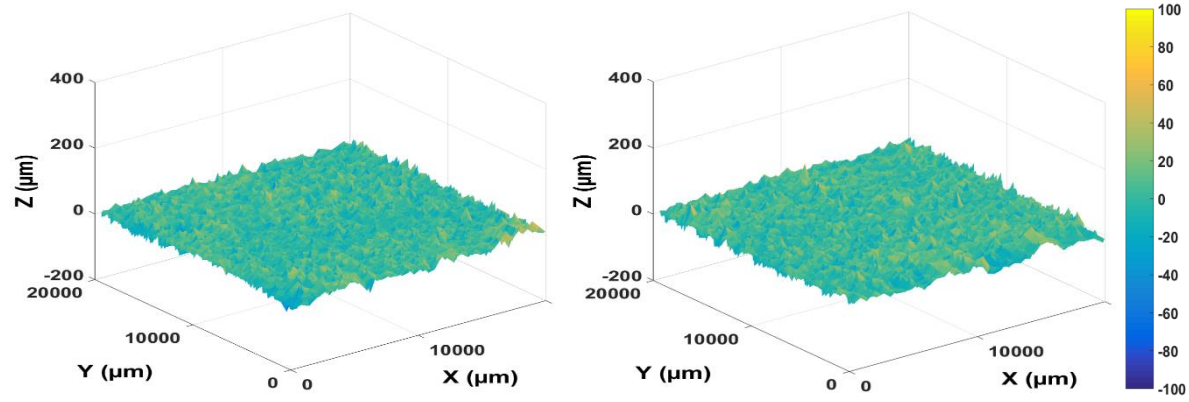

C17 Panel_A C17 Panel_B

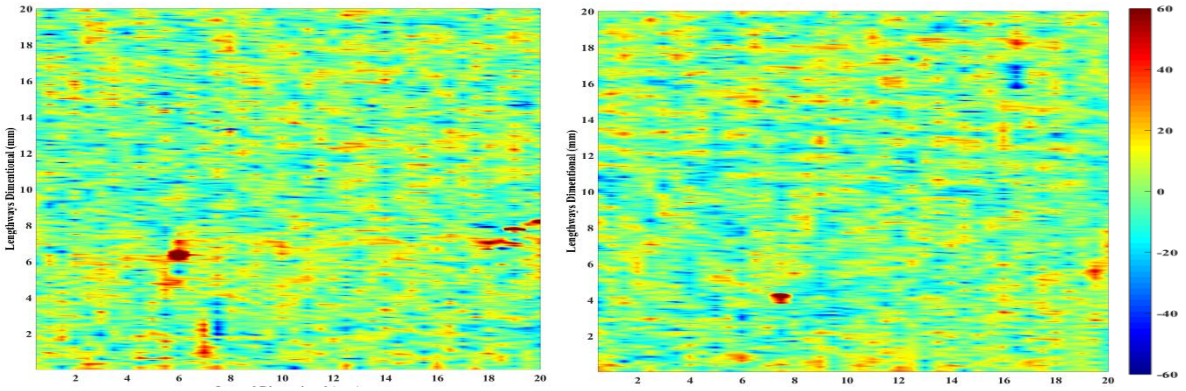

C25 Panel_A C25 Panel_B

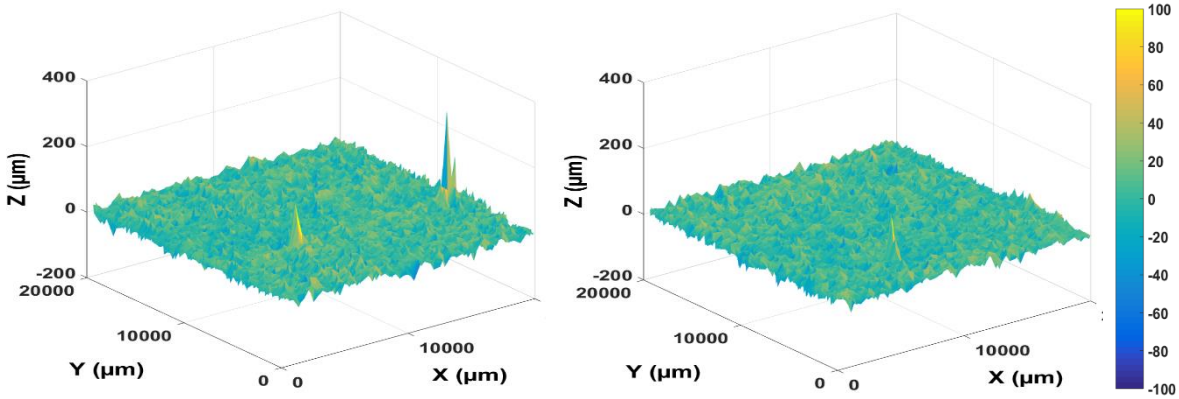

C25 Panel_A C25 Panel_B

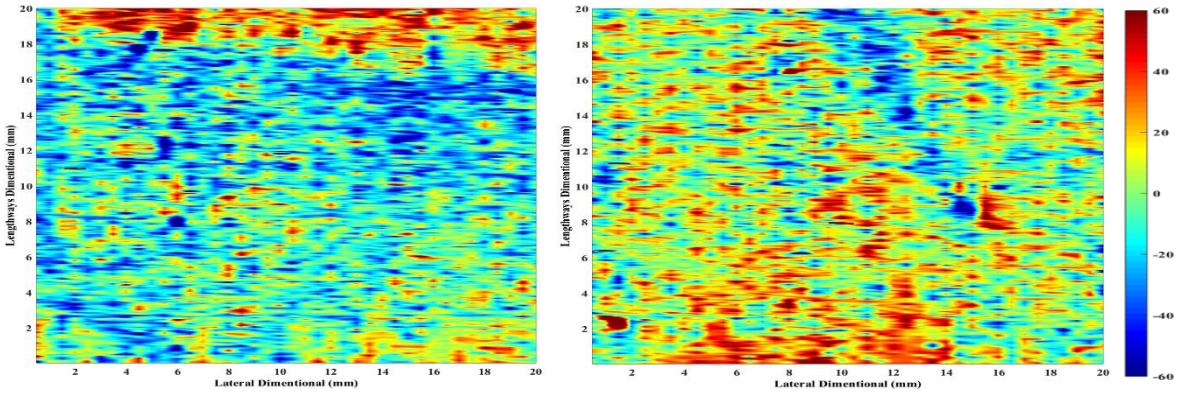

C60 Panel_A C60 Panel_B

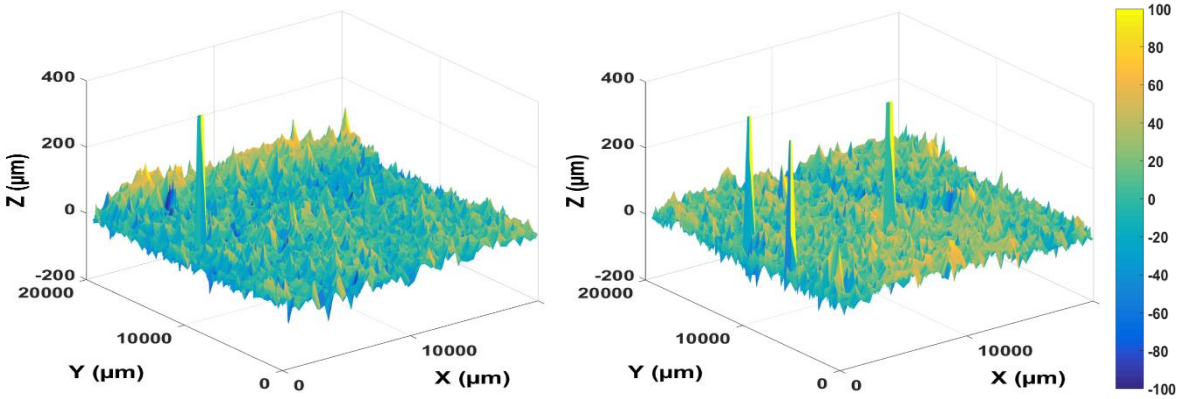

C60 Panel_A C60 Panel_B

Appendix D SEM Images Results

Appendix D.1 SEM Results about Bacterial Colonies and Filiform Fibre

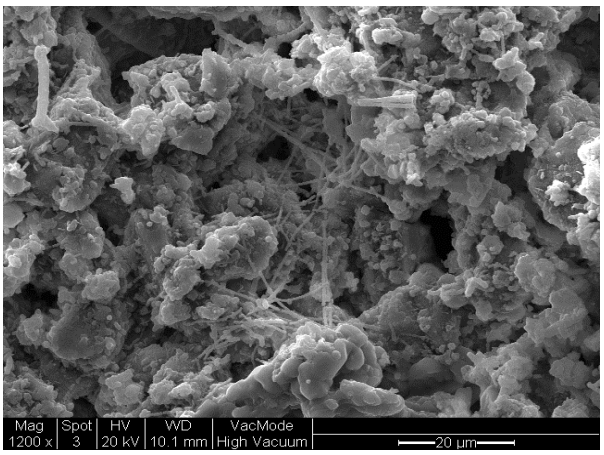

Surface C25 after 1.5-month dynamic deployment (1200× magnification)

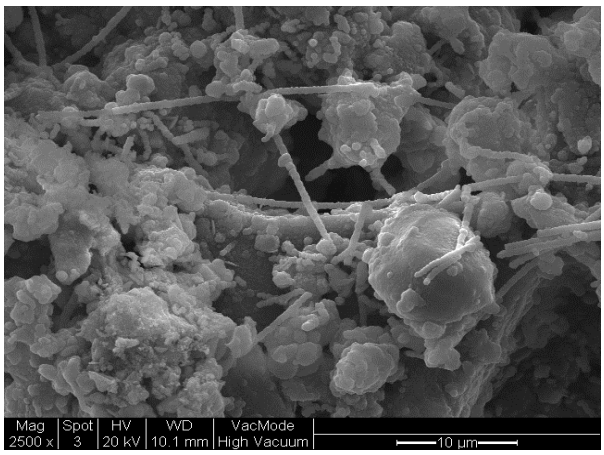

Surface C25 after 1.5-month dynamic deployment (2500× magnification)

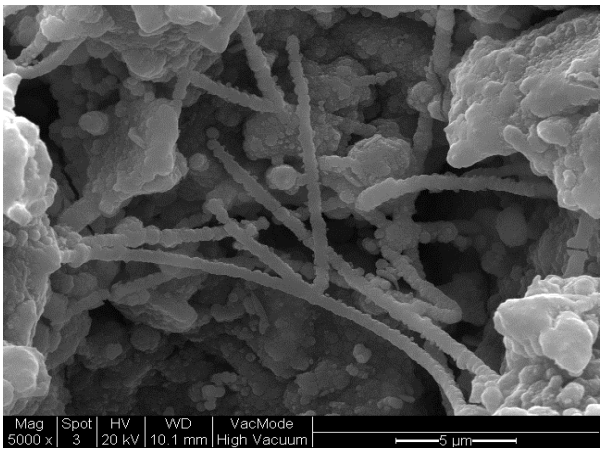

Surface C25 after 1.5-month dynamic deployment (5000× magnification)

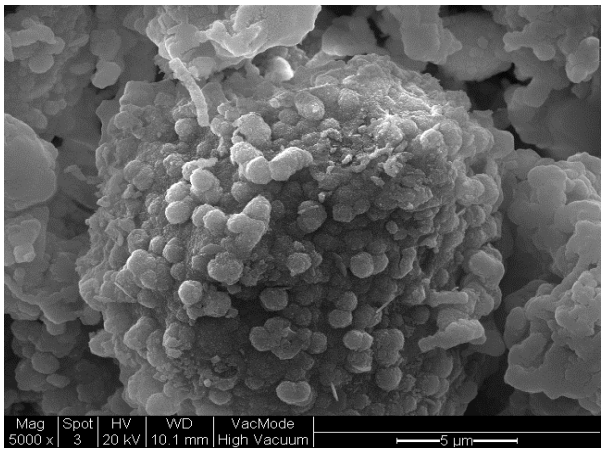

Surface C25 after 1.5-month dynamic deployment (5000× magnification)

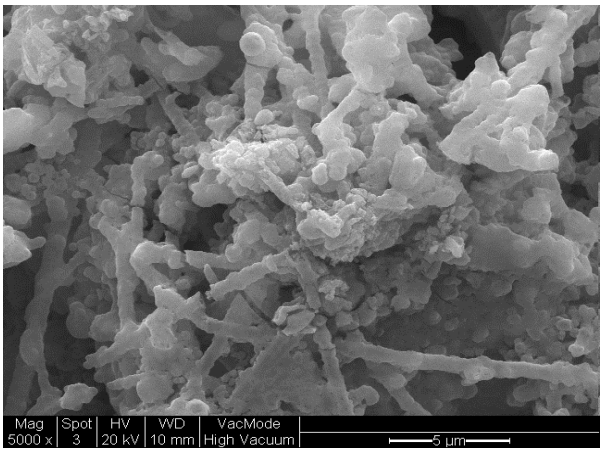

Surface C60 after 1.5-month dynamic deployment (5000× magnification)

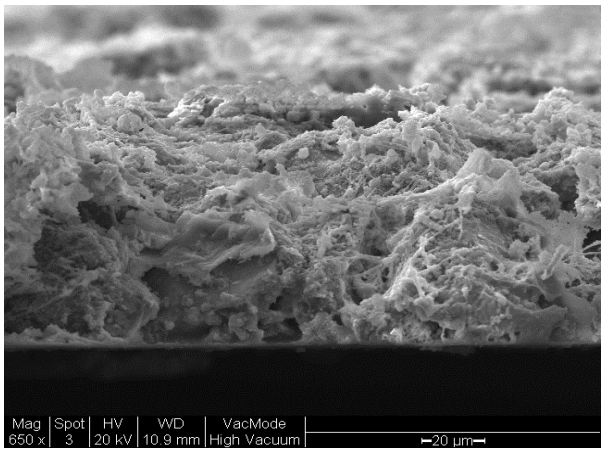

Cross-section of C60 after 1.5-month dynamic deployment (650× magnification)

Appendix D.2 SEM Results about Algae and Other Microorganisms

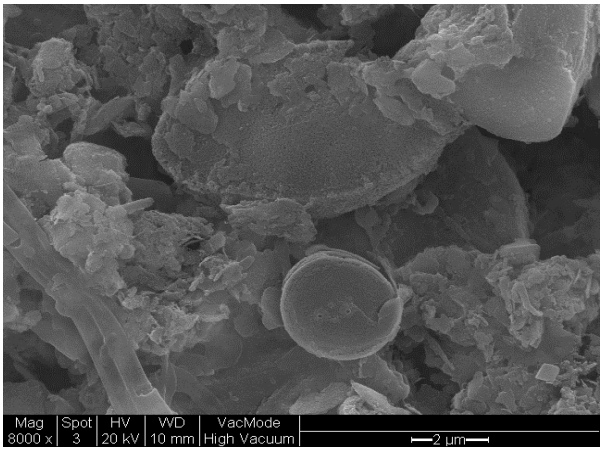

Surface C12 after 4.5-month dynamic deployment (8000× magnification)

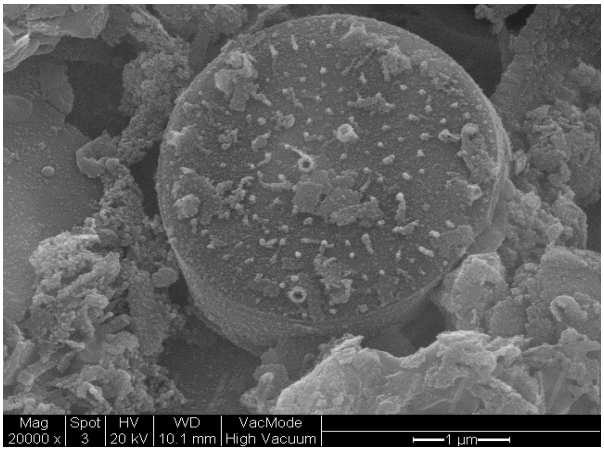

Surface C12 after 4.5-month dynamic deployment (20000× magnification)

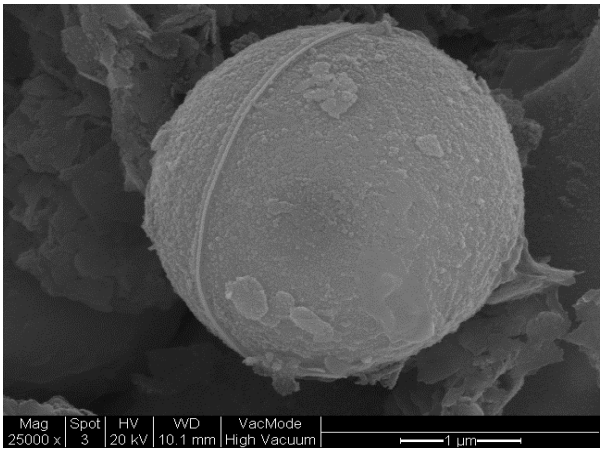

Surface C12 after 4.5-month dynamic deployment (25000× magnification)

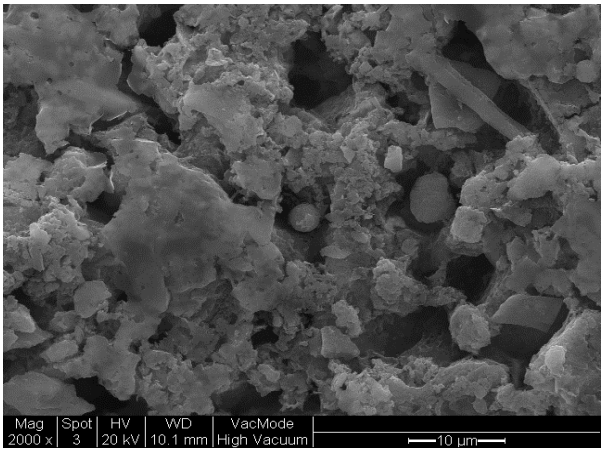

Surface C25 after 4.5-month dynamic deployment (2000× magnification)

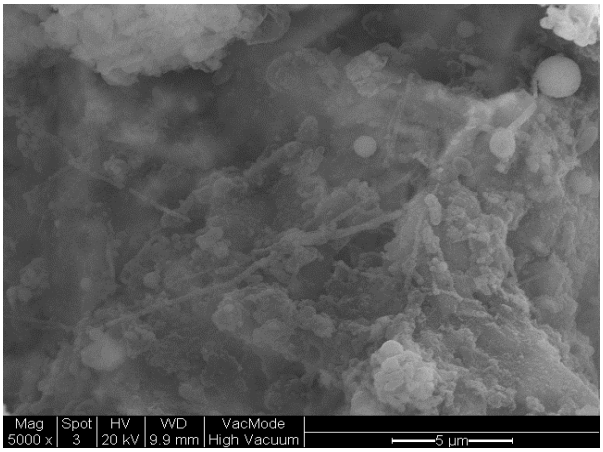

Surface C60 after 4.5-month dynamic deployment (5000× magnification)

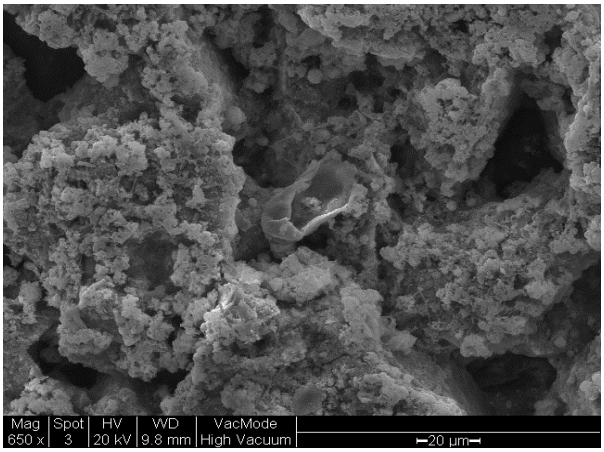

Cross-section of C60 after 4.5-month dynamic deployment (650× magnification)

Appendix E Turbulence Intensity Profiles

Appendix E.1 Turbulence Intensity Profiles in Inner Scaling

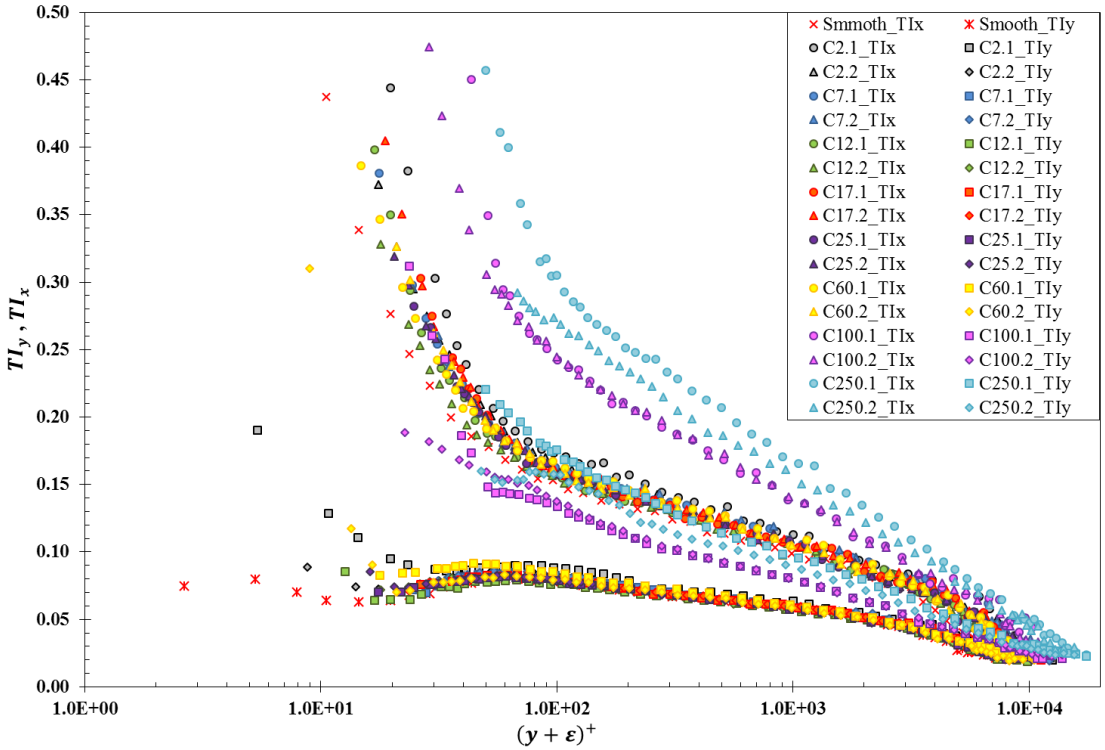

Figure E.1: Turbulence intensity profiles in inner scaling at inflow velocity of 4m/s

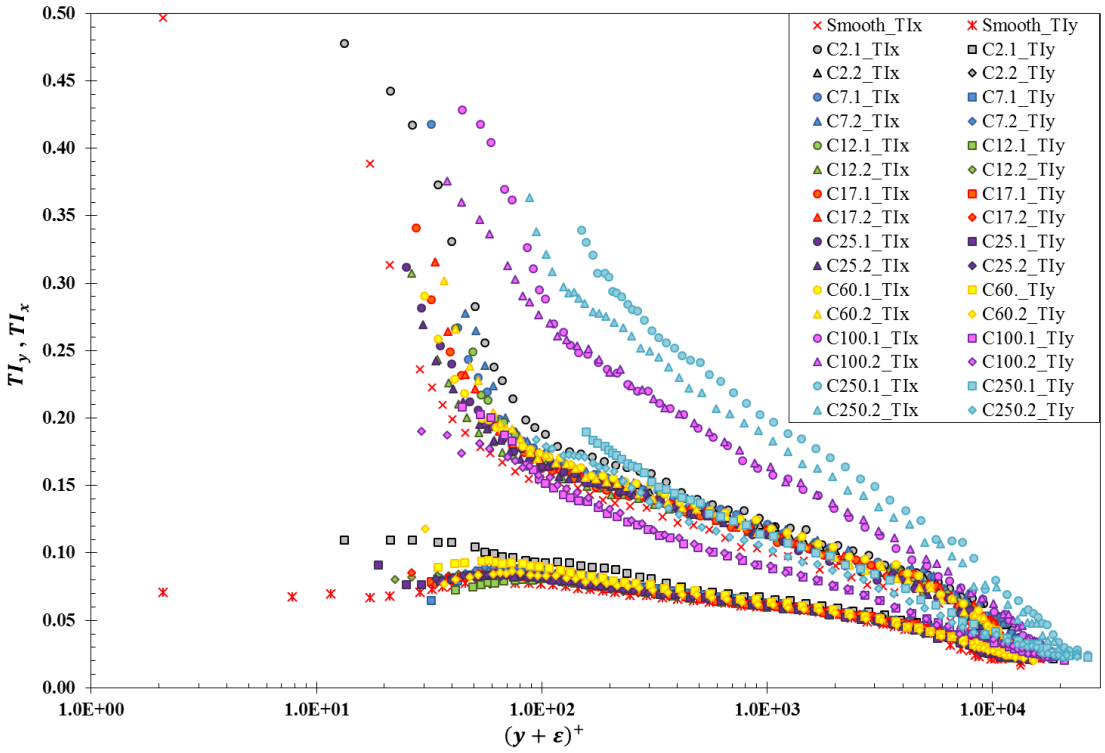

Figure E.2: Turbulence intensity profiles in inner scaling at inflow velocity of 6m/s

Appendix E.2 Turbulence Intensity Profiles in Inner Scaling

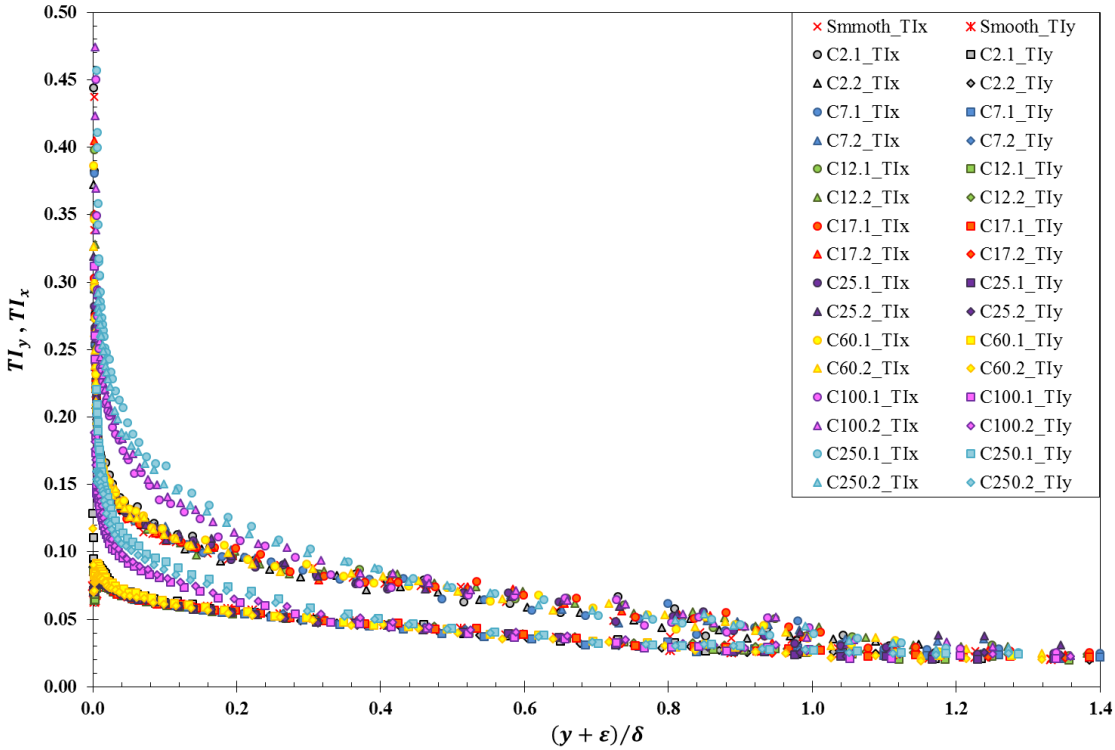

Figure E.3: Turbulence intensity profiles in outer scaling at inflow velocity of 4m/s

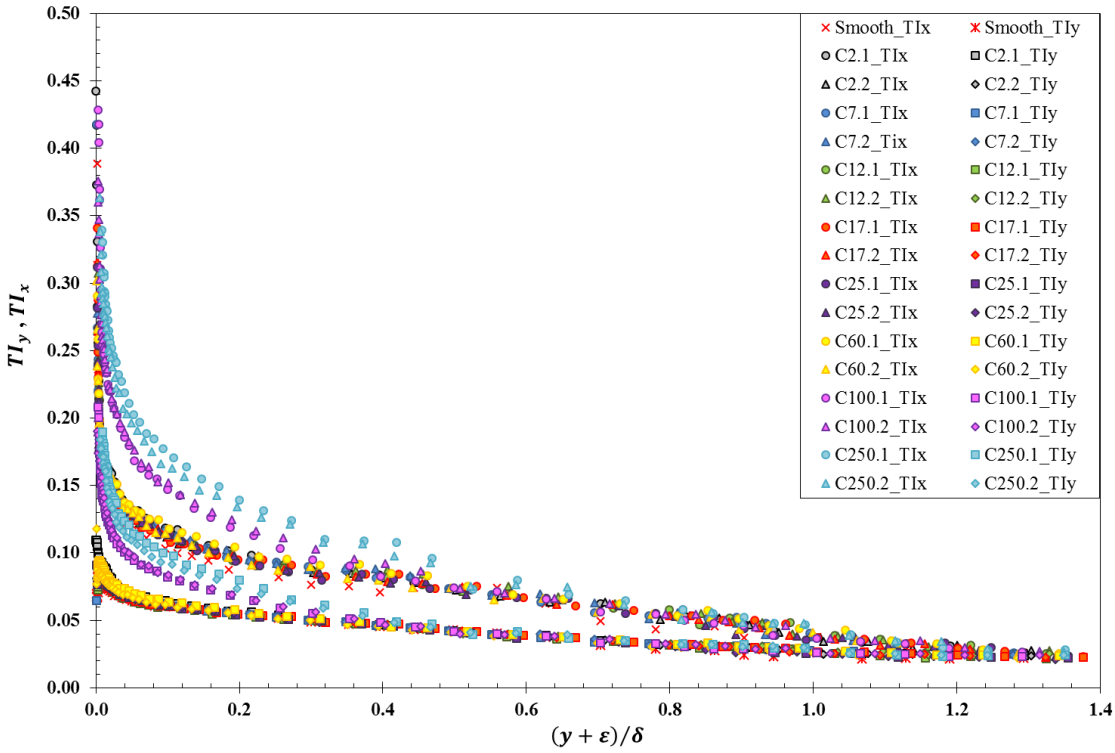

Figure E.4: Turbulence intensity profiles in outer scaling at inflow velocity of 6m/s

Appendix F ΔC_F for Full Ship Length Scaled Flat Plates Coated with Different Cu_2O under Unfouled Condition

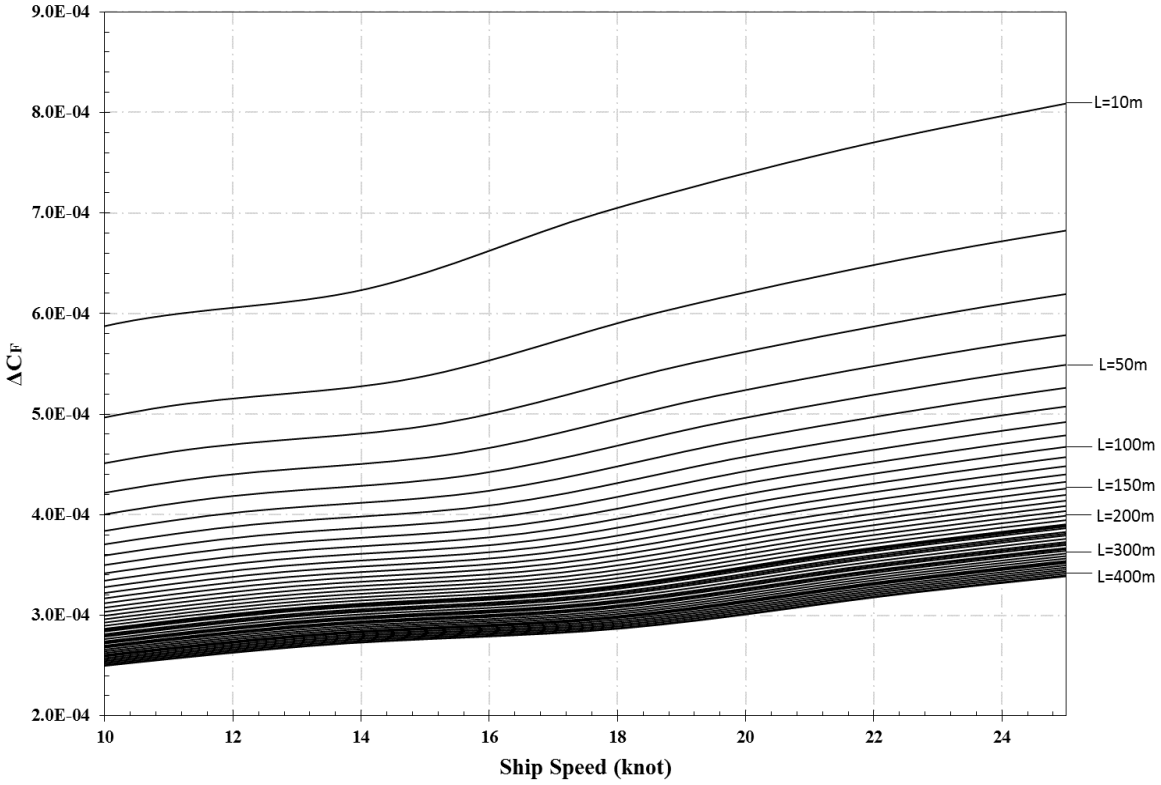

Figure F.1: For surfaces coated with C2

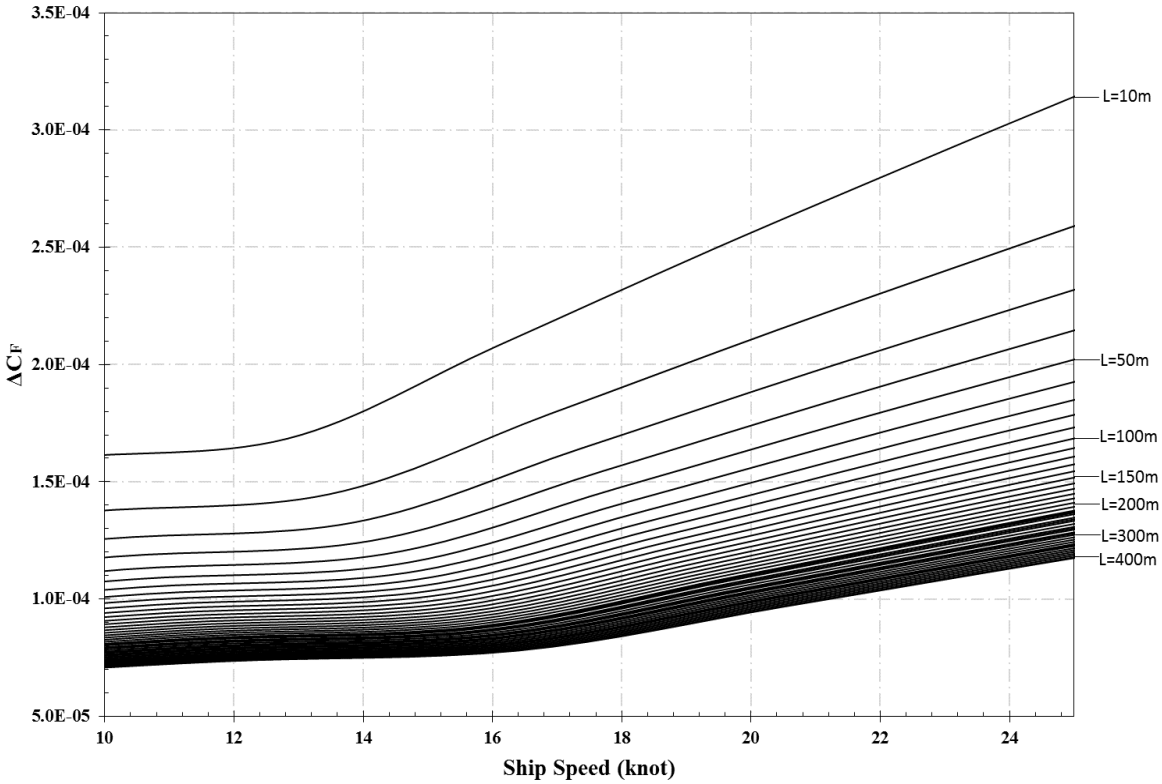

Figure F.2: For surfaces coated with C7

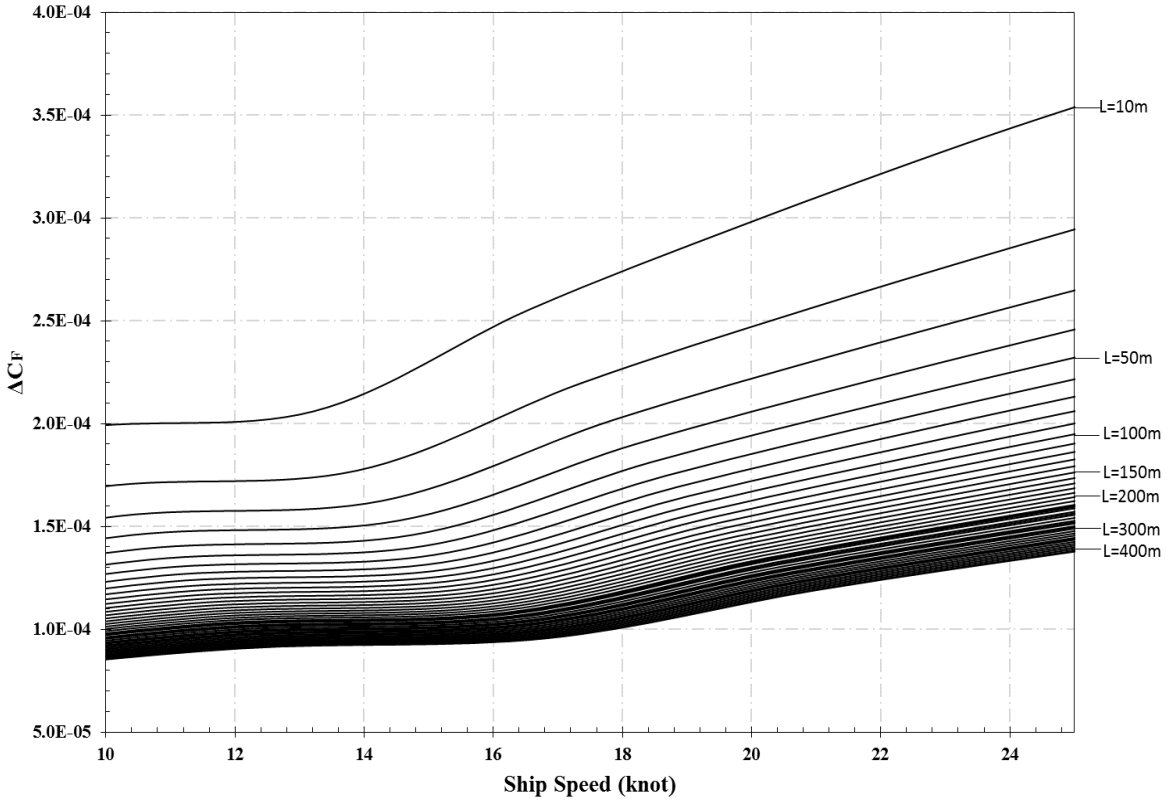

Figure F.3: For surfaces coated with C12

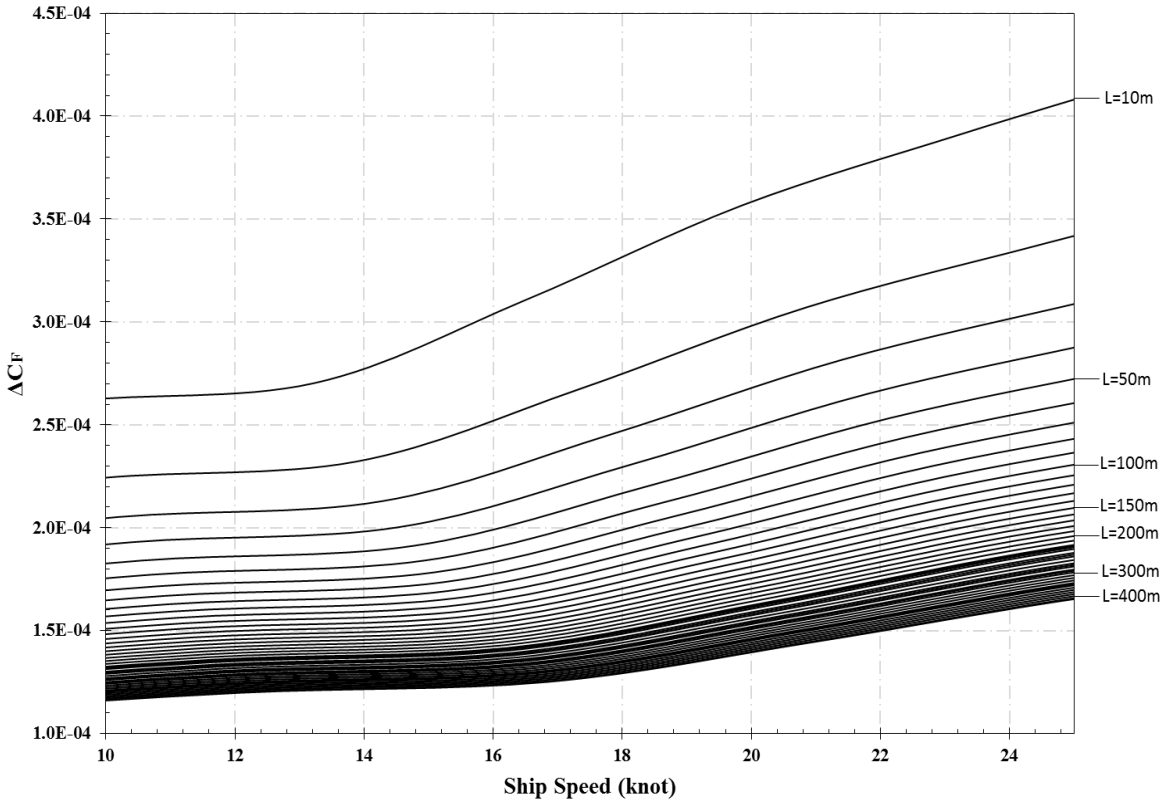

Figure F.4: For surfaces coated with C17

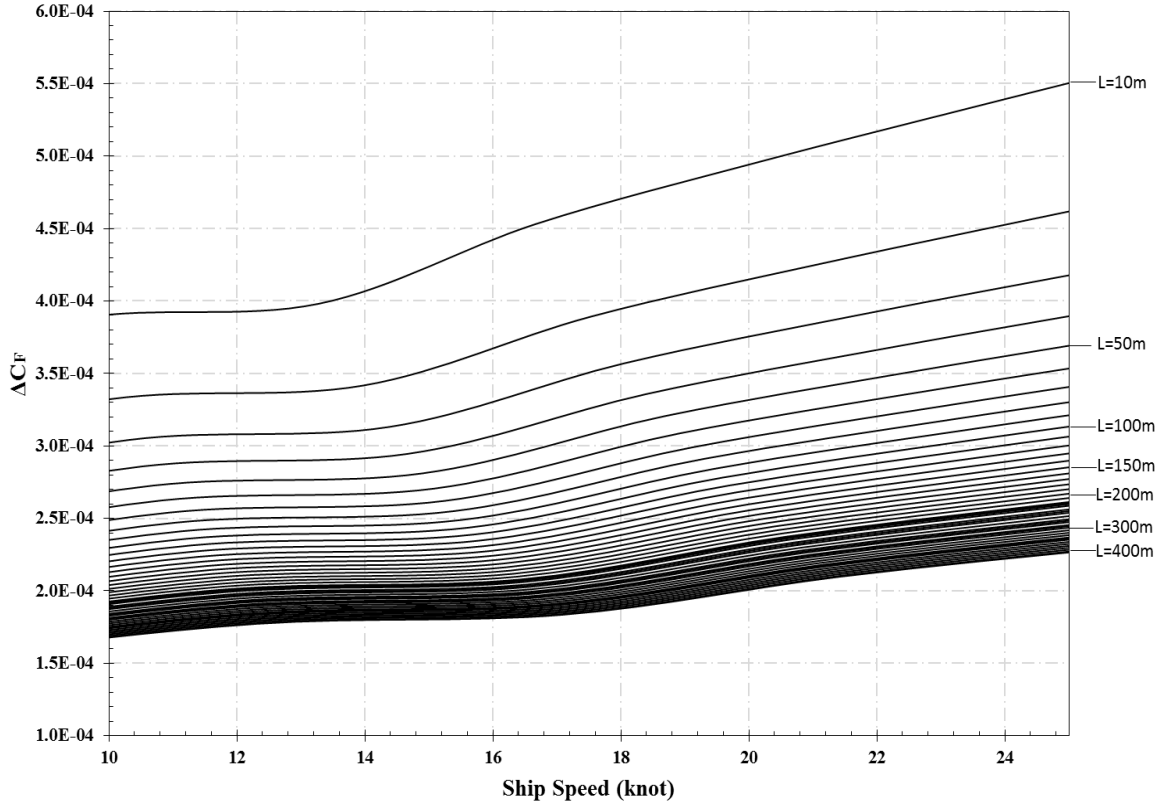

Figure F.5: For surfaces coated with C25

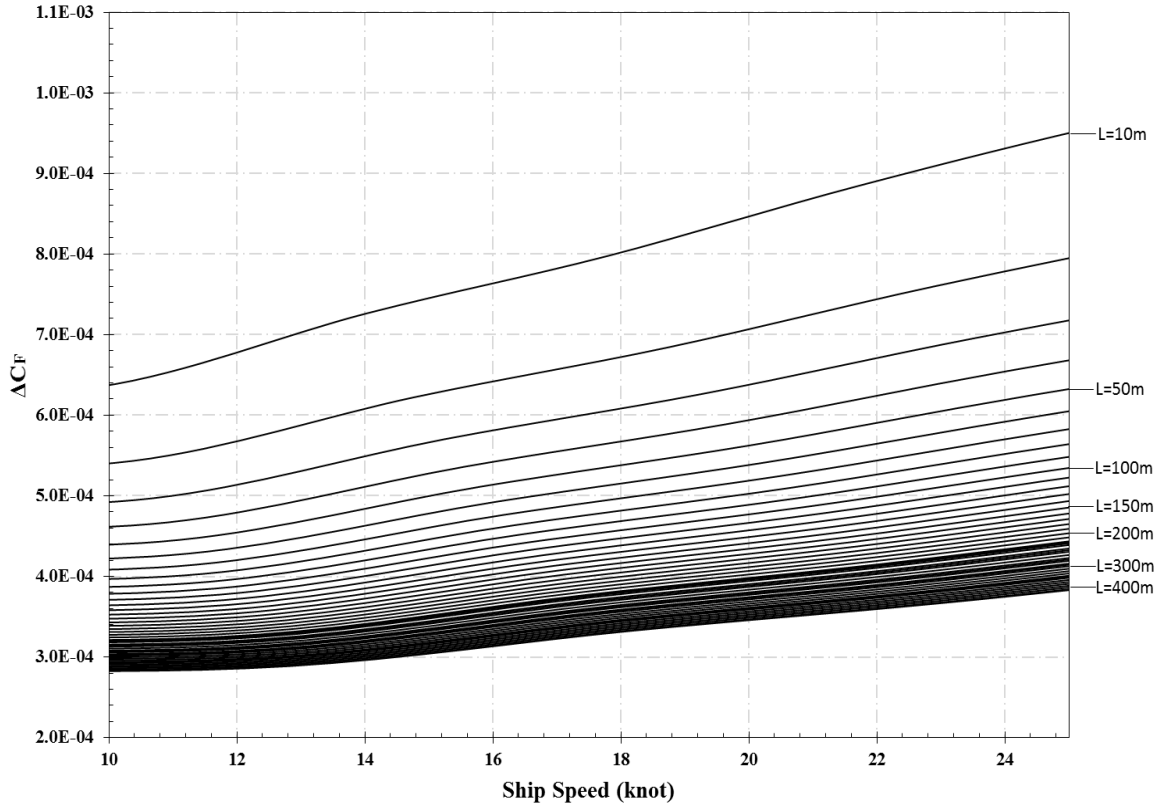

Figure F.6: For surfaces coated with C60

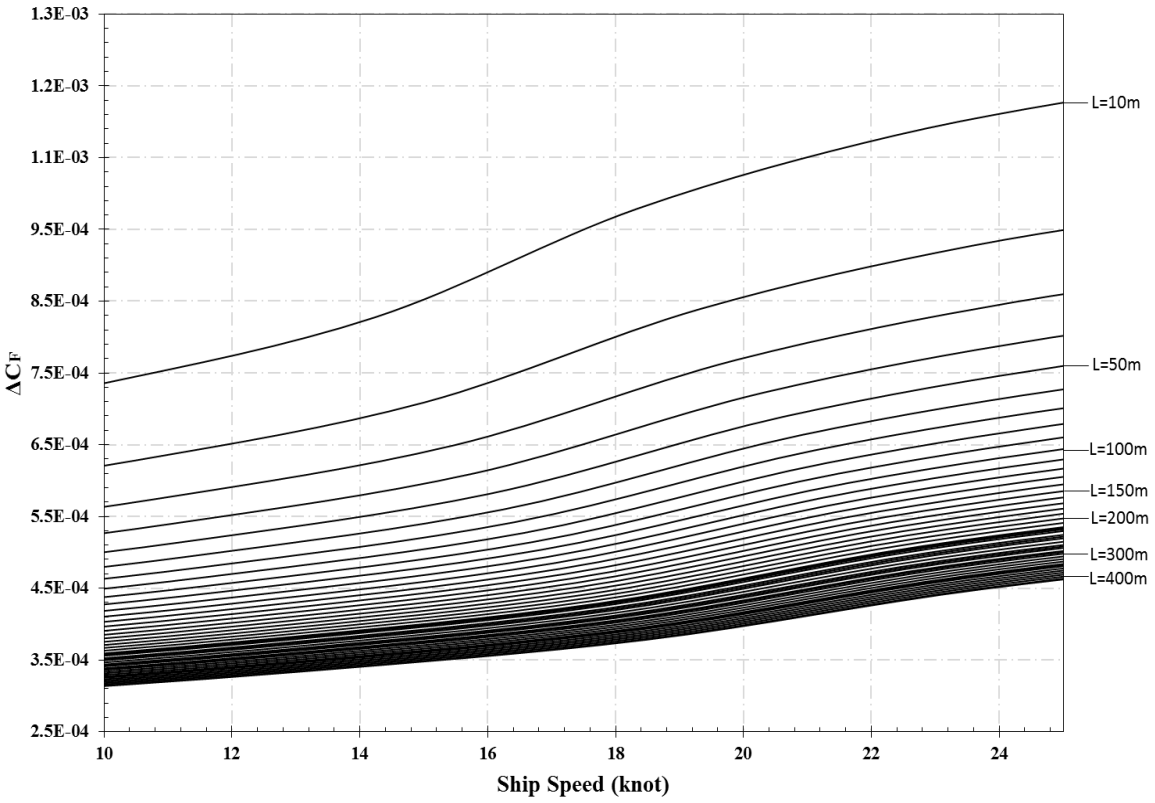

Figure F.7: For surfaces coated with C100

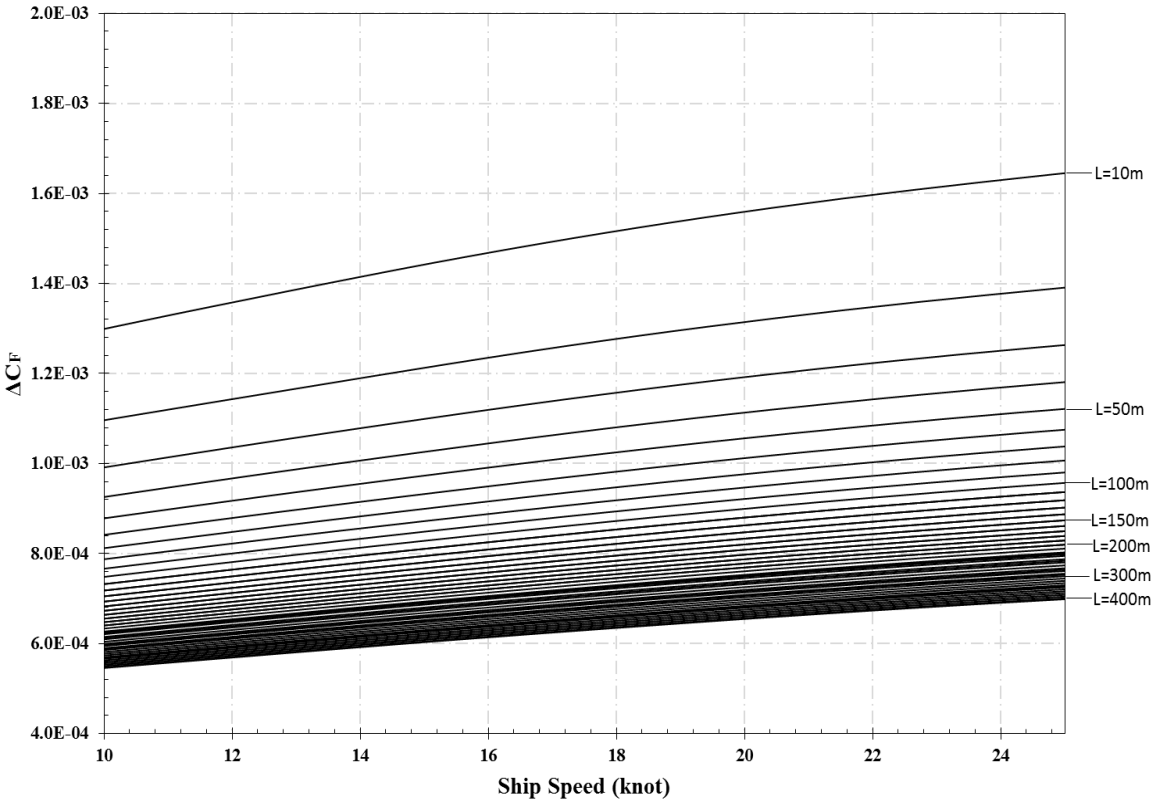

Figure F.8: For surfaces coated with C250

Appendix G ΔC_F for Full Ship Length Scaled Flat Plates Coated with Different Cu_2O under Fouled Condition

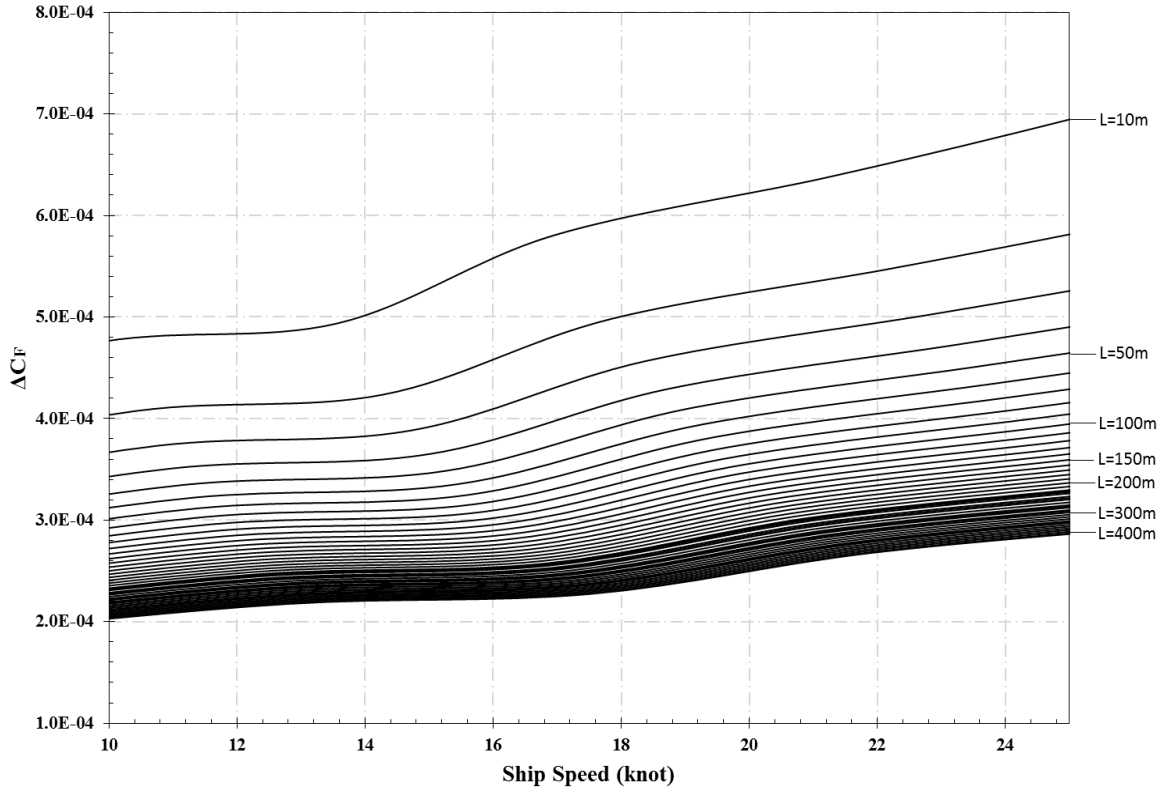

Figure G.1: For surfaces coated with C12 fouled with 1.5-month biofilm

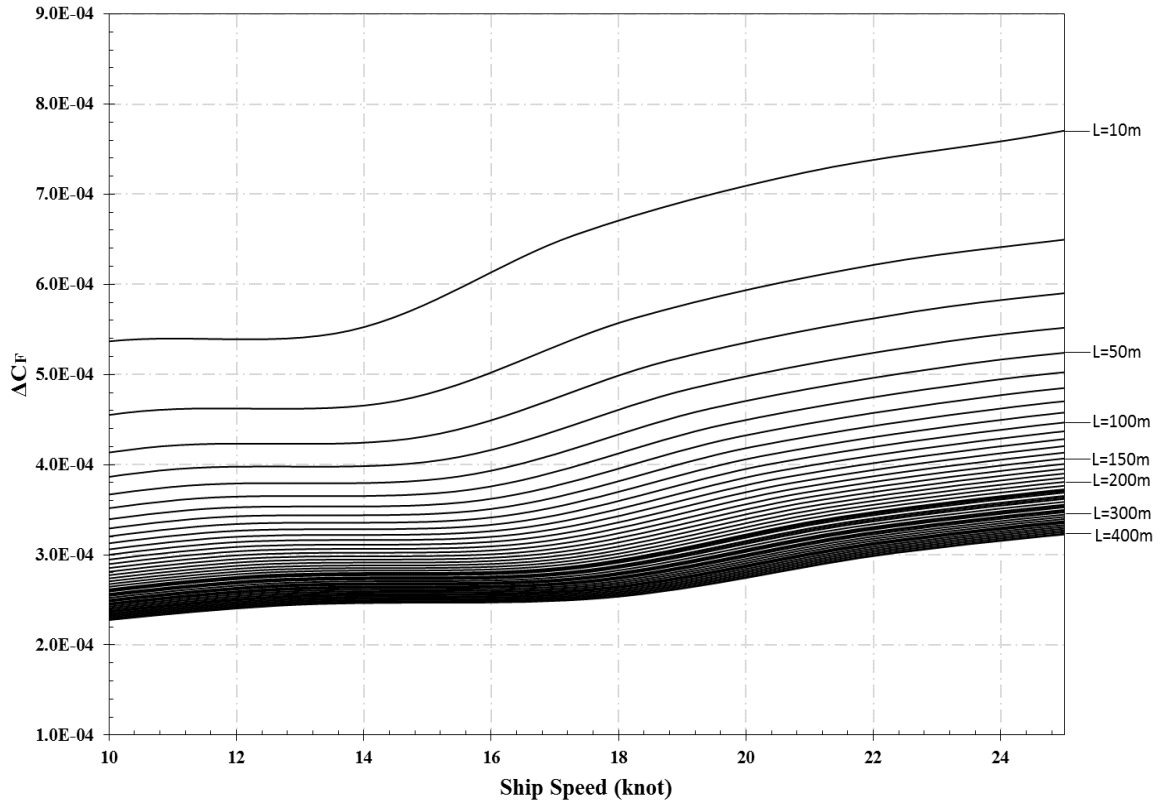

Figure G.2: For surfaces coated with C12 fouled with 3-month biofilm

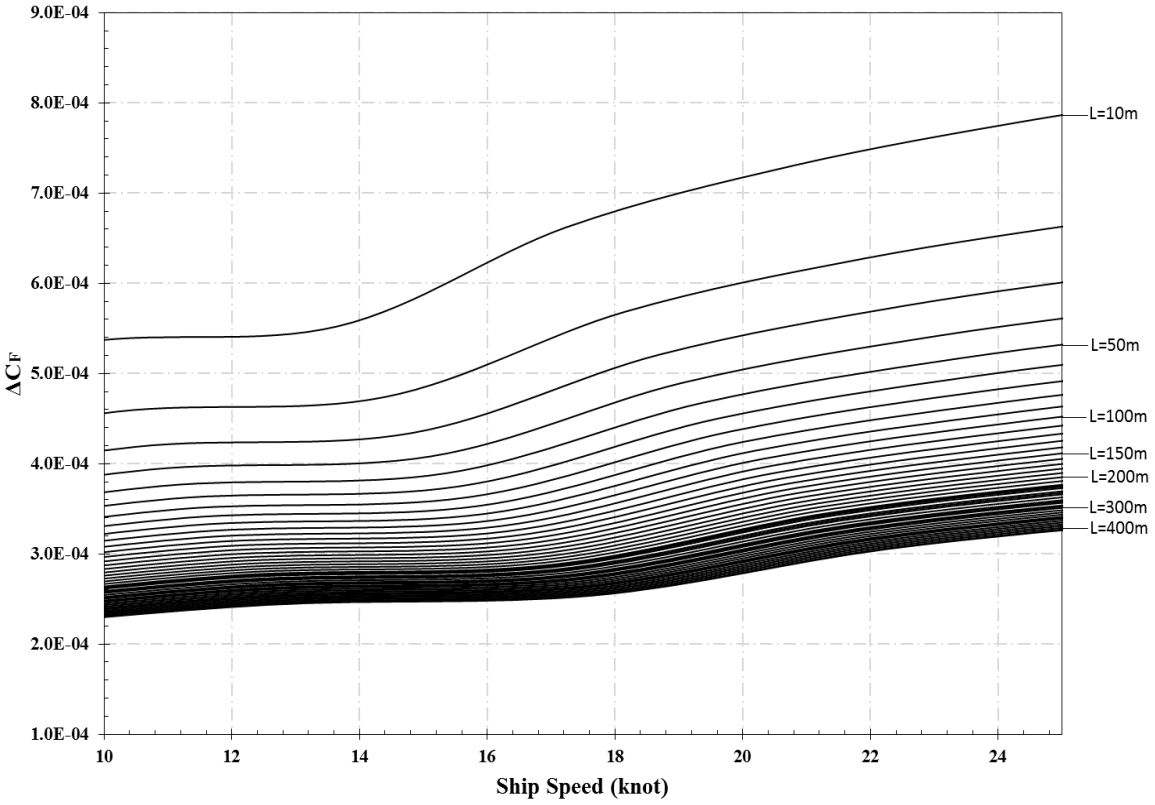

Figure G.3: For surfaces coated with C12 fouled with 4.5-month biofilm

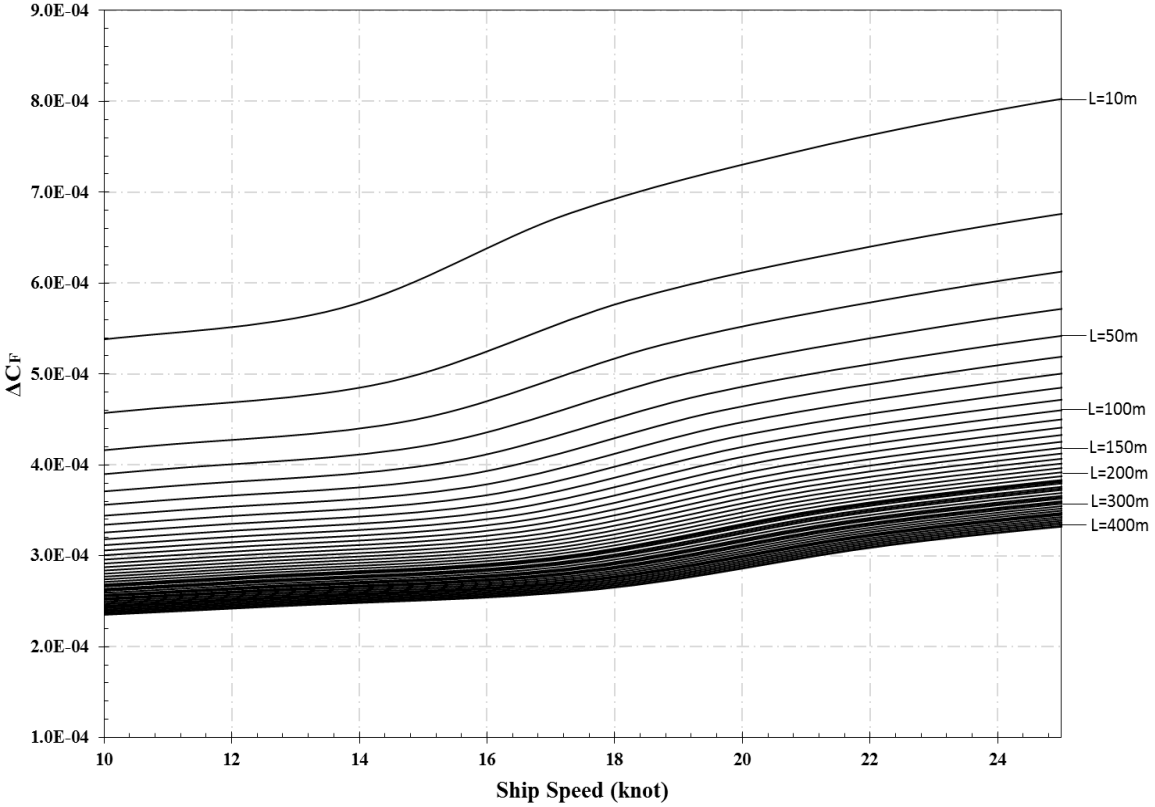

Figure G.4: For surfaces coated with C12 fouled with 6-month biofilm

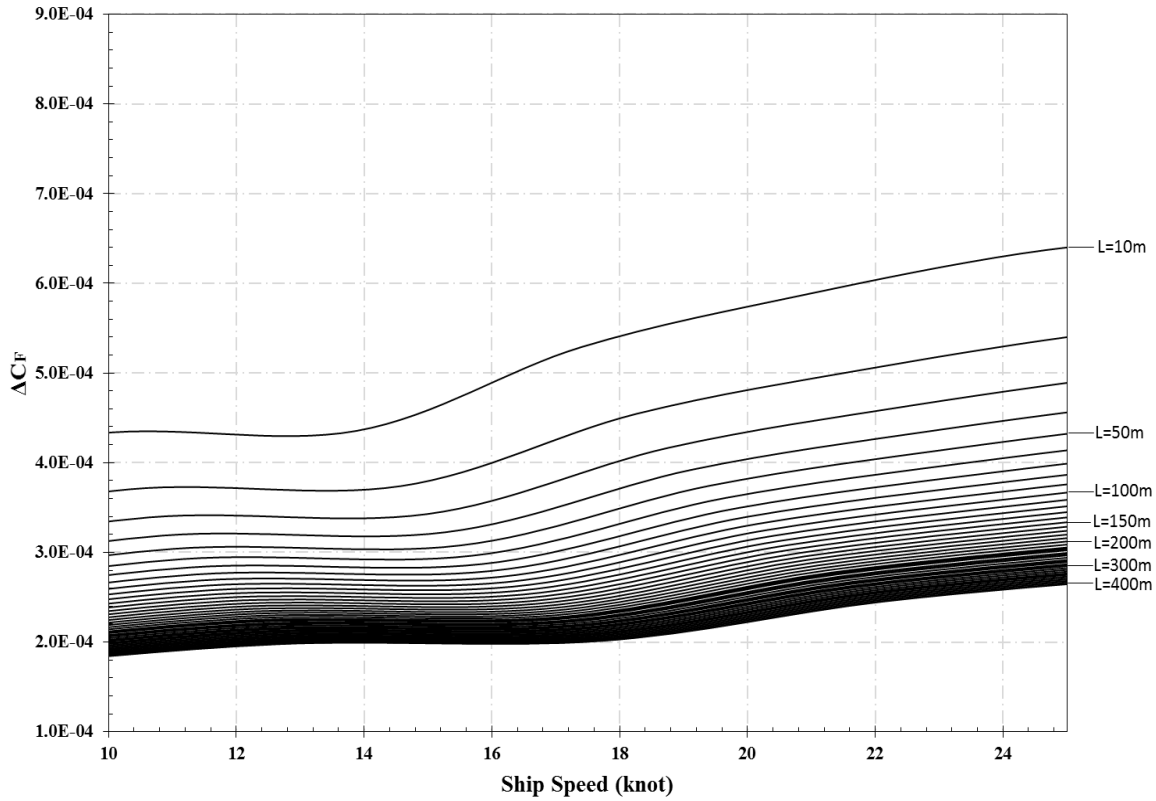

Figure G.5: For surfaces coated with C17 fouled with 1.5-month biofilm

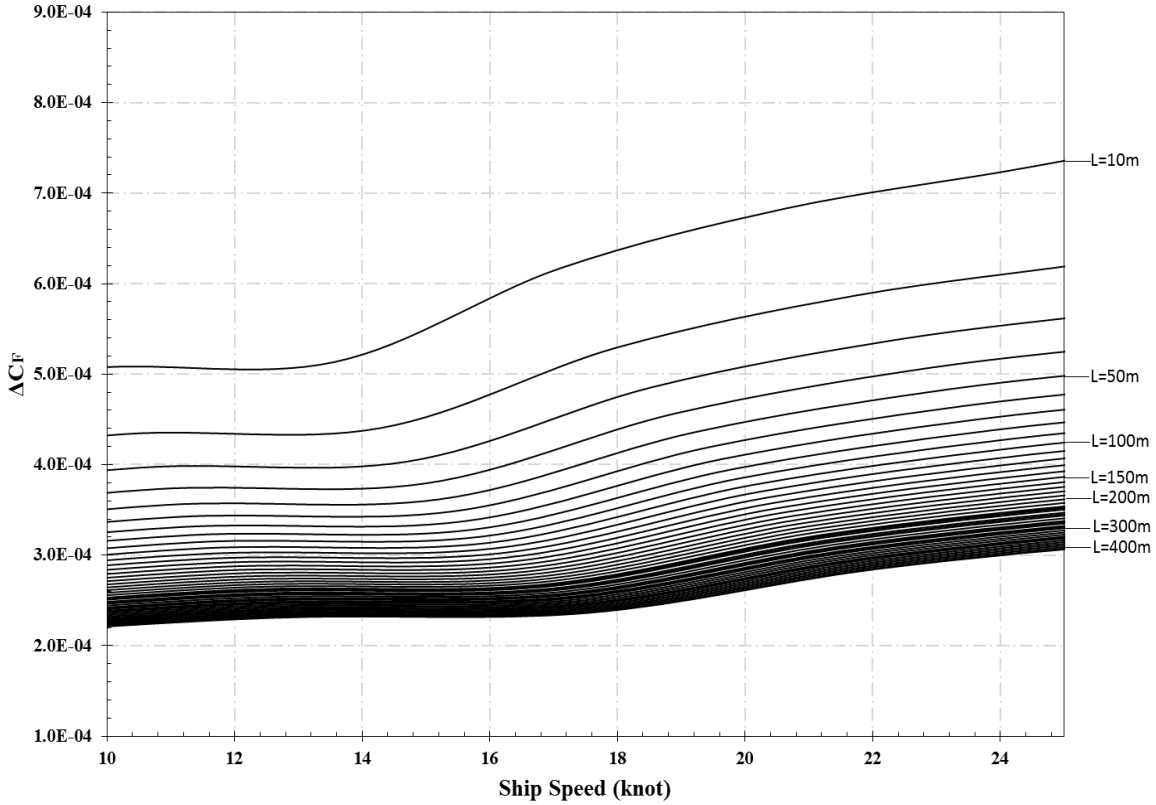

Figure G.6: For surfaces coated with C17 fouled with 3-month biofilm

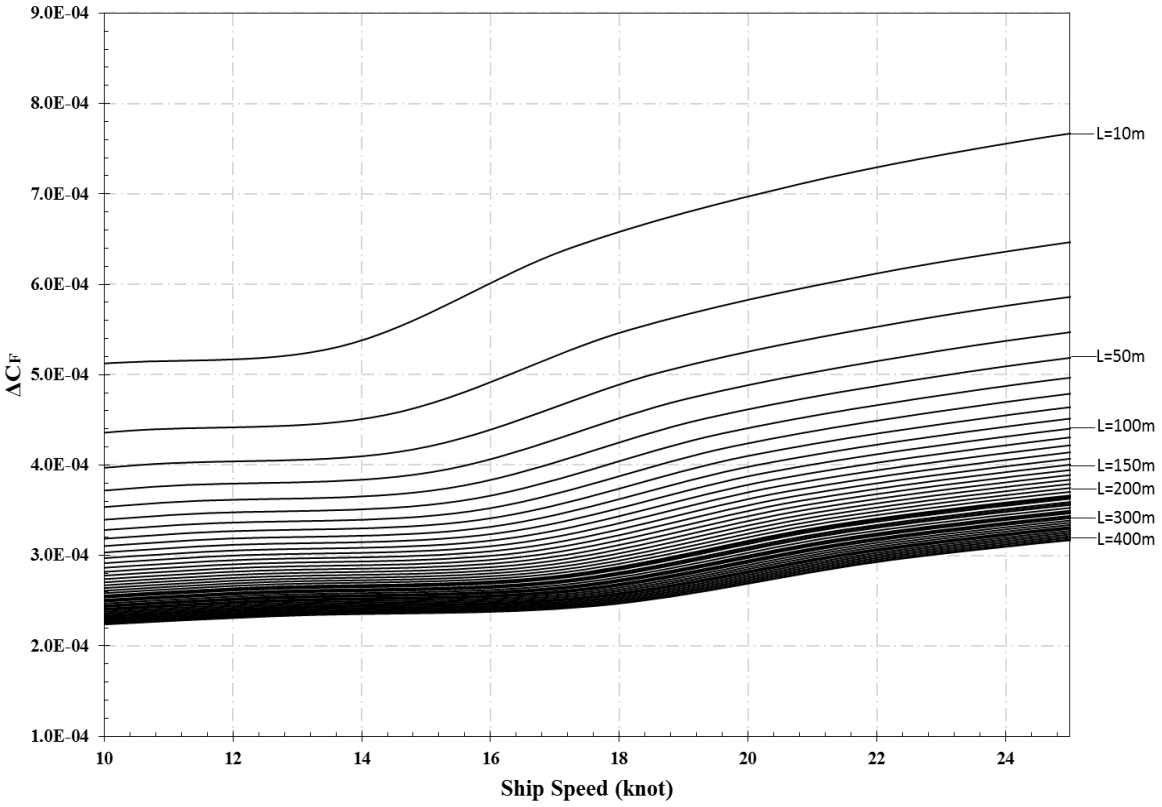

Figure G.7: For surfaces coated with C17 fouled with 4.5-month biofilm

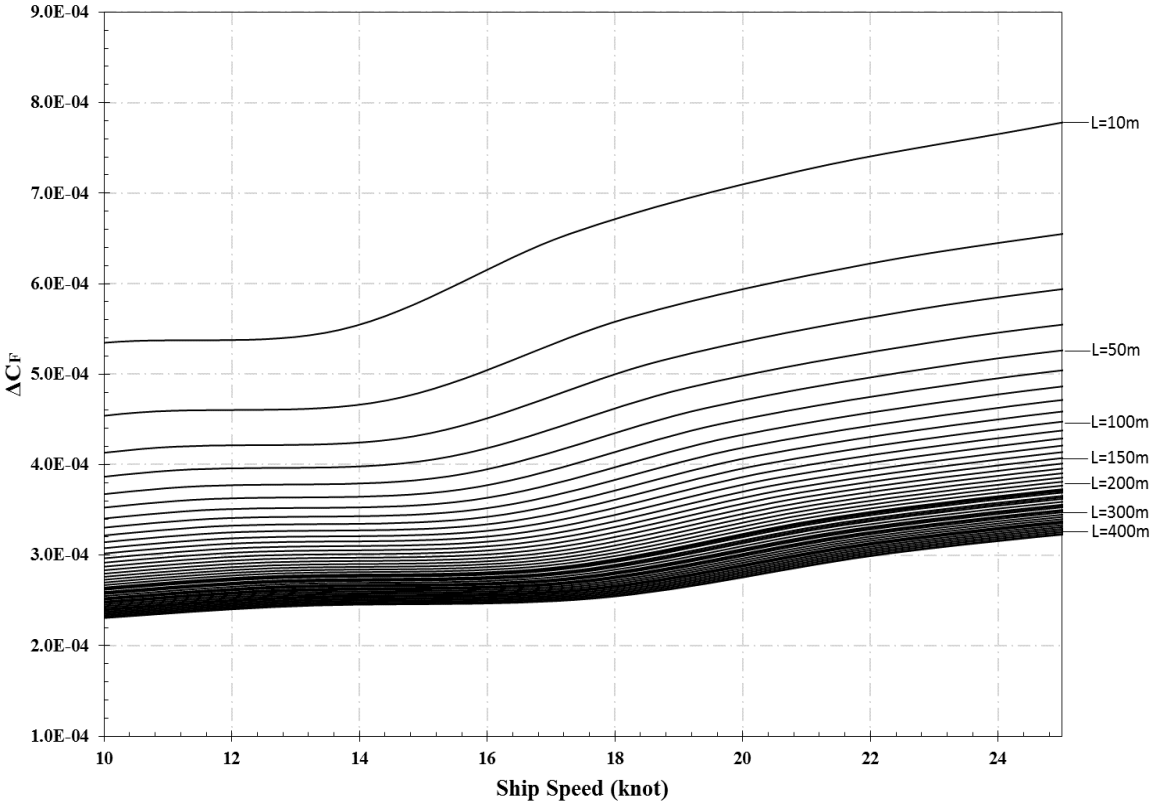

Figure G.8: For surfaces coated with C17 fouled with 6-month biofilm

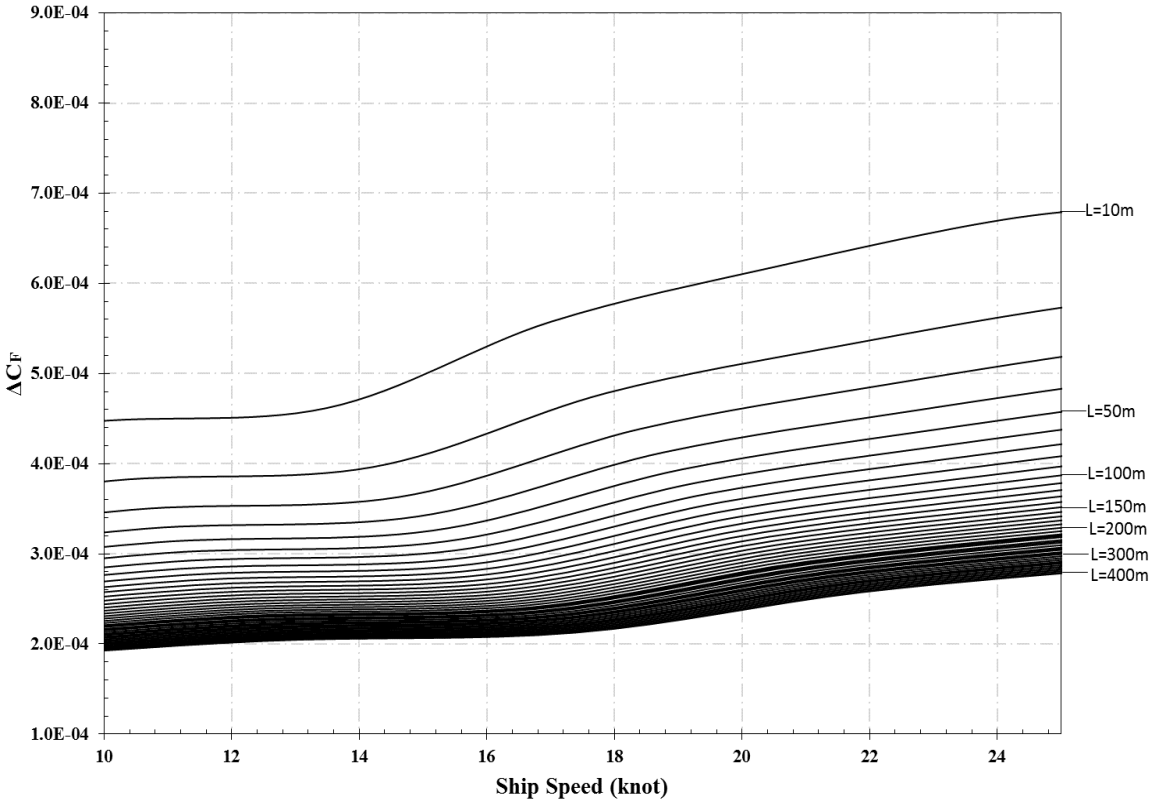

Figure G.9: For surfaces coated with C25 fouled with 1.5-month biofilm

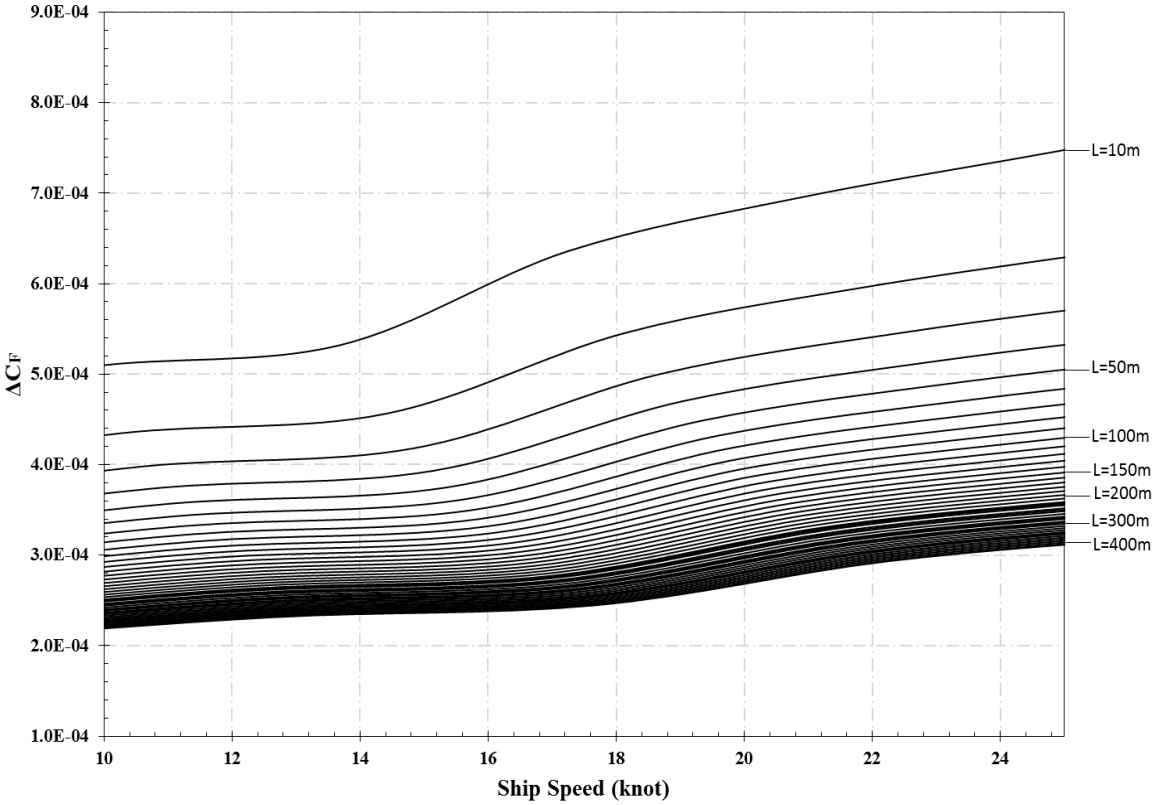

Figure G.10: For surfaces coated with C25 fouled with 3-month biofilm

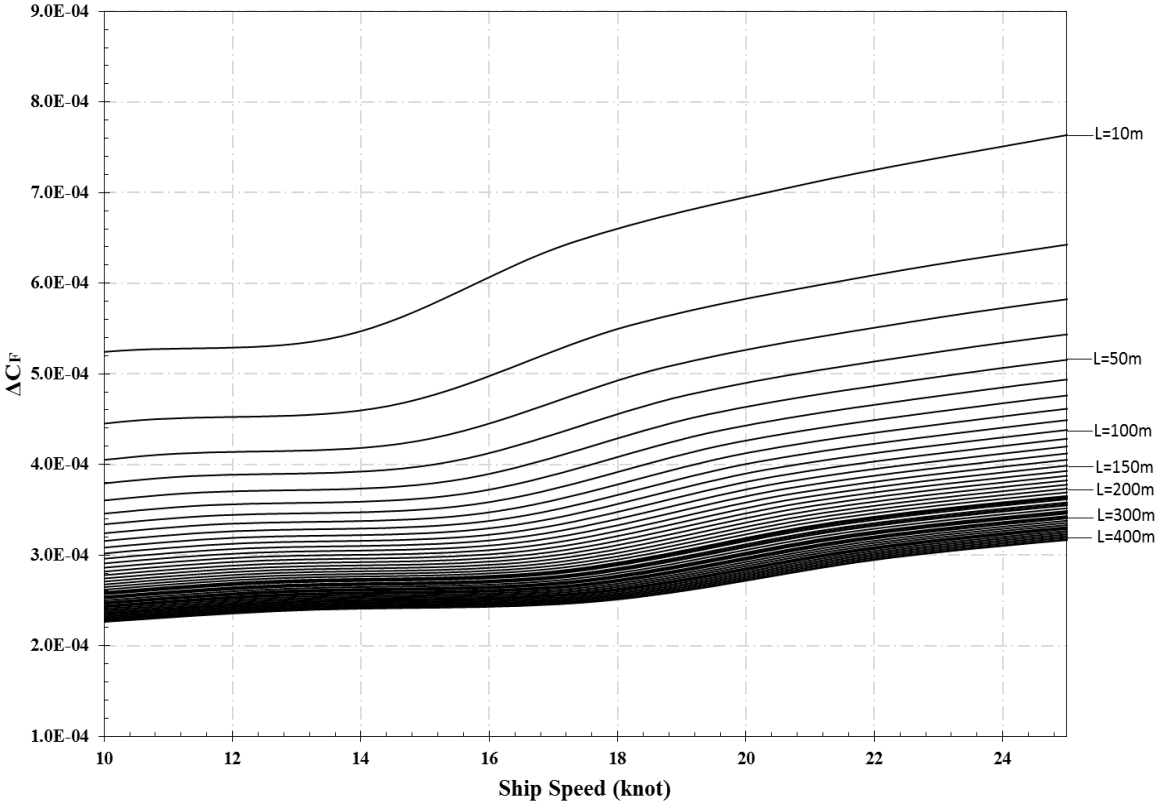

Figure G.11: For surfaces coated with C25 fouled with 4.5-month biofilm

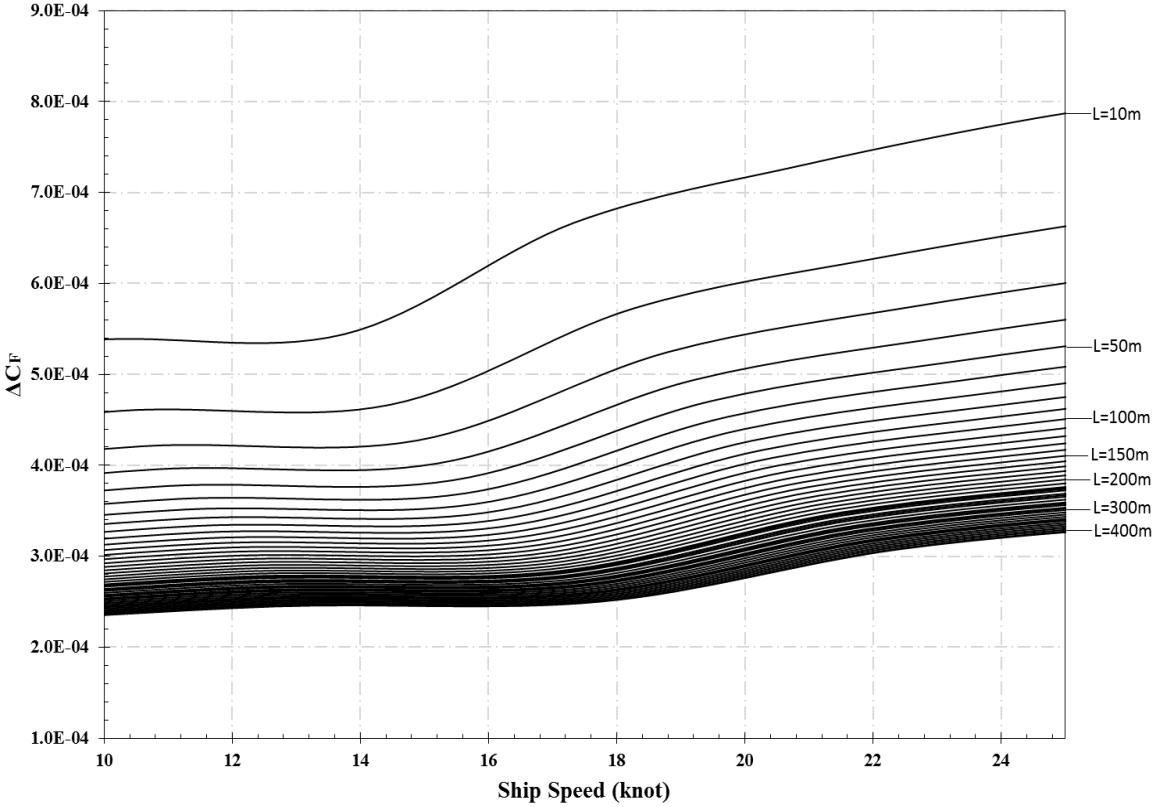

Figure G.12: For surfaces coated with C25 fouled with 6-month biofilm

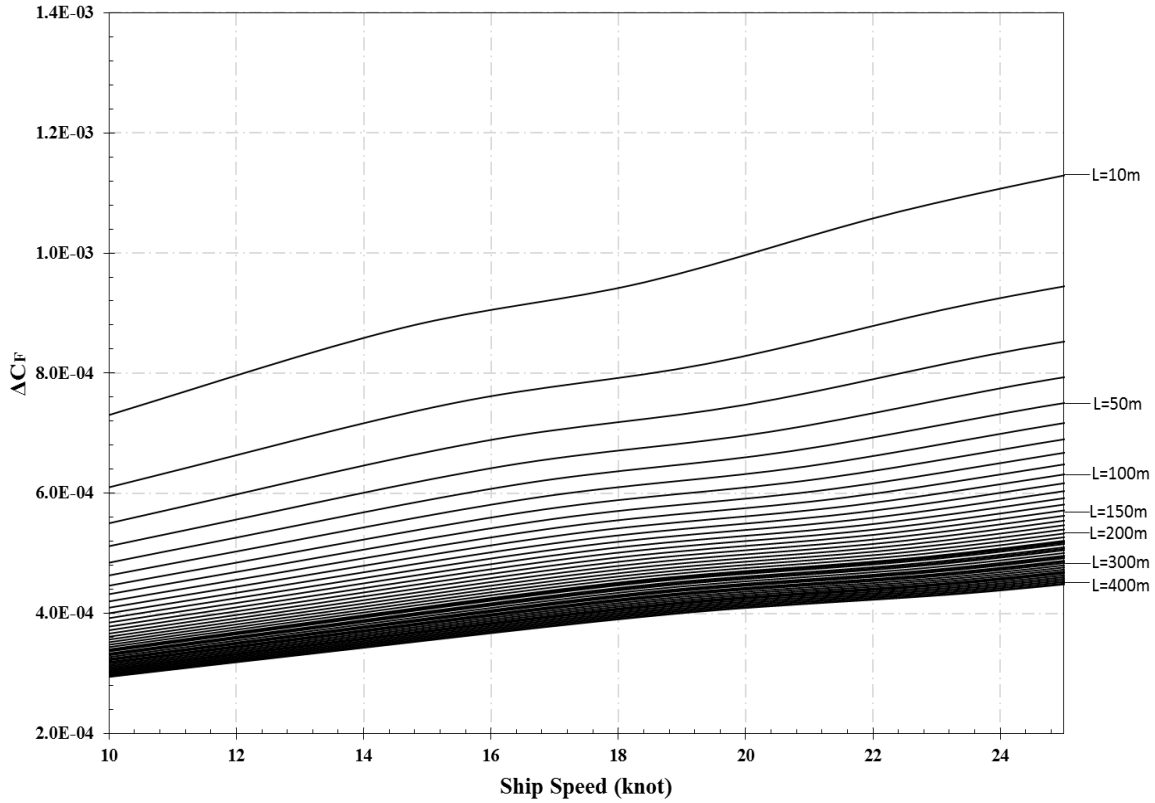

Figure G.13: For surfaces coated with C60 fouled with 1.5-month biofilm

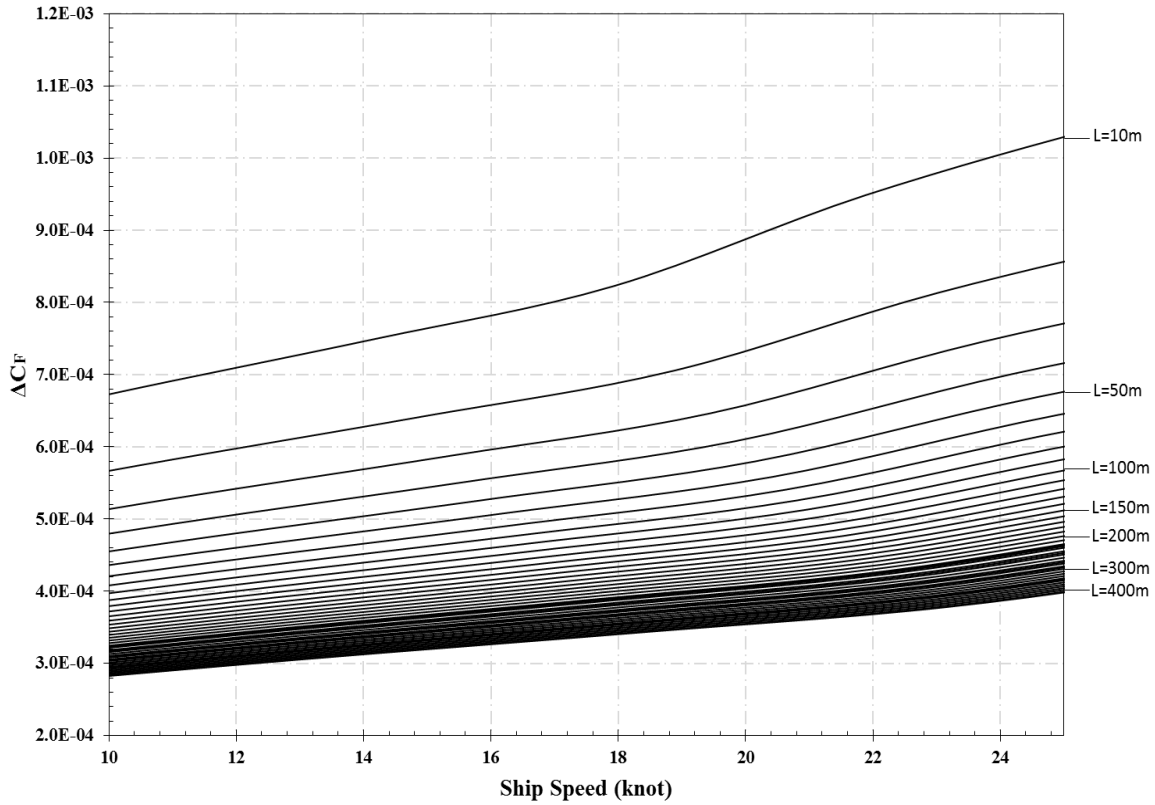

Figure G.14: For surfaces coated with C60 fouled with 3-month biofilm

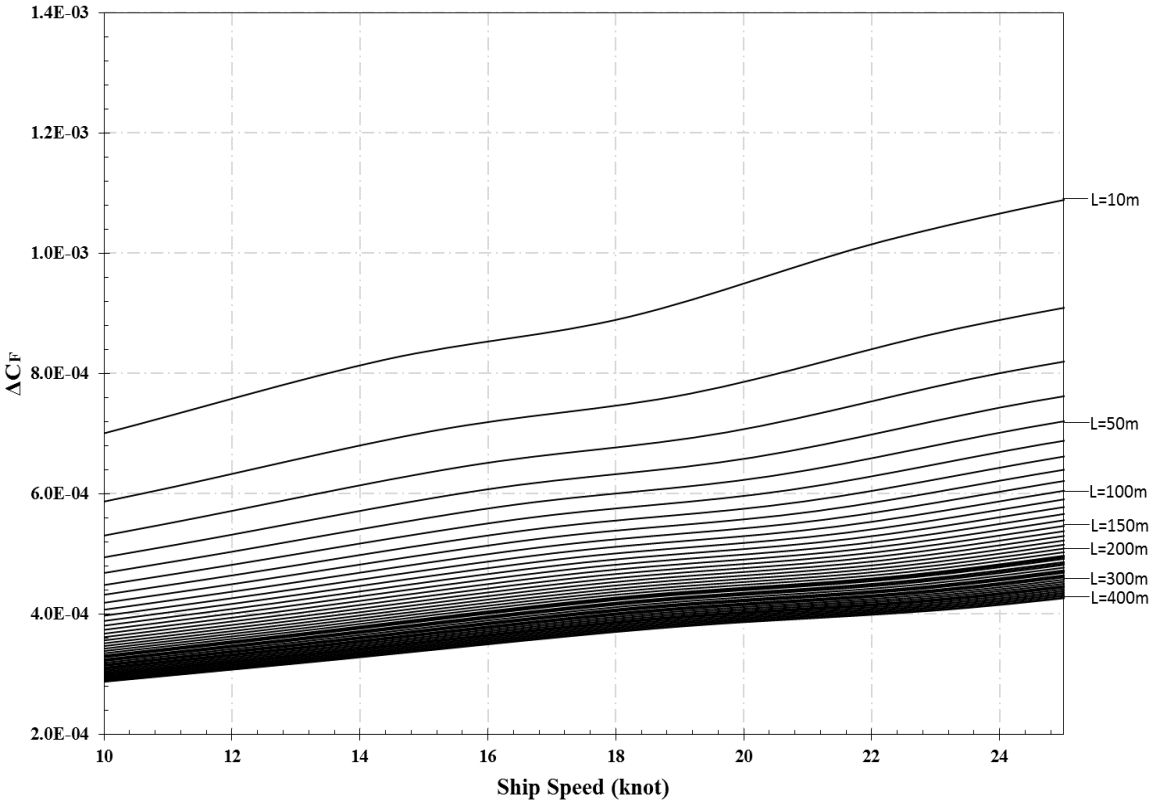

Figure G.15: For surfaces coated with C60 fouled with 4.5-month biofilm

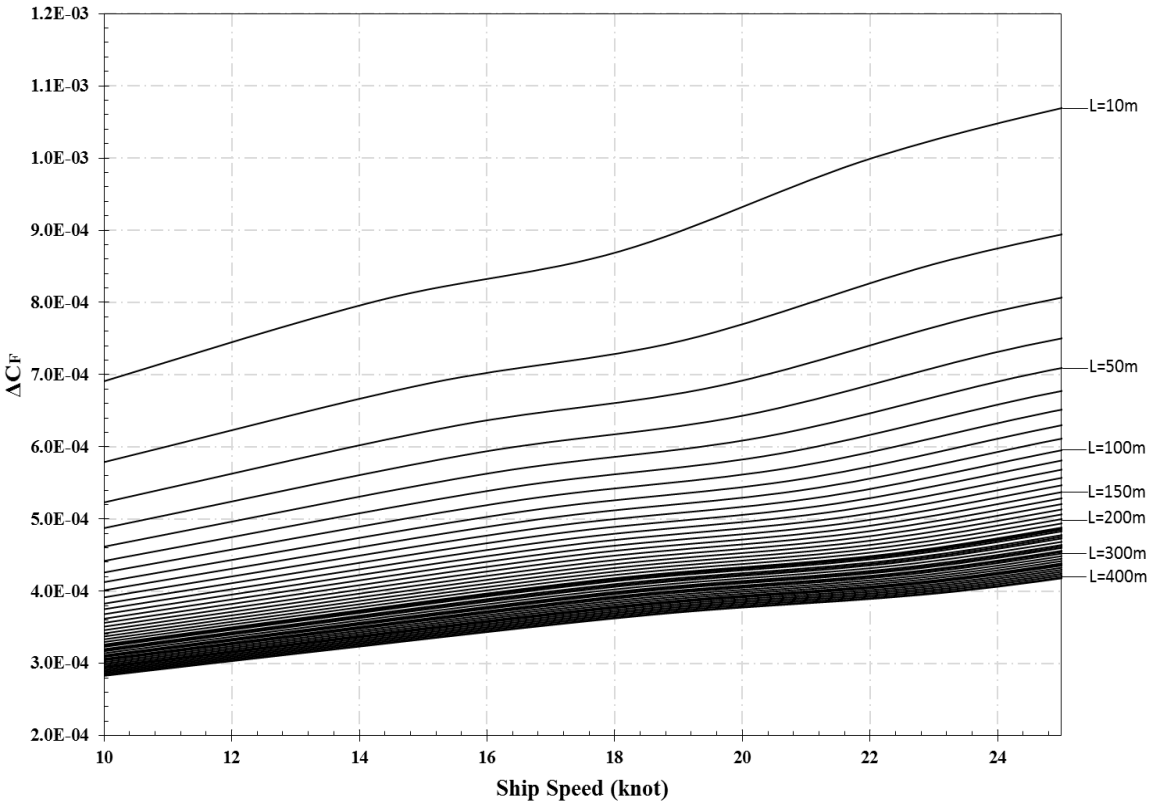

Figure G.16: For surfaces coated with C60 fouled with 6-month biofilm